Journal of Experimental and Theoretical Physics, Vol. 99, No. 6, 2004, pp. 1119–1123.
Translated from Zhurnal Éksperimental’noĭ i Teoreticheskoĭ Fiziki, Vol. 126, No. 6, 2004, pp. 1283–1289.
Original Russian Text Copyright © 2004 by Elizarov, Tupitsyn.

NUCLEI, PARTICLES, AND THEIR INTERACTION

Spin Polarization and Angular Distribution of Auger Electrons Formed as a Result of Decay of the $3d^{-1}5p$ State in the Kr Atom

A. Yu. Elizarov[a],* **and I. I. Tupitsyn**[b],**
[a]*Ioffe Physicotechnical Institute, Russian Academy of Sciences, St. Petersburg, 194021 Russia*
[b]*St. Petersburg State University, St. Petersburg, 198904 Russia*
**e-mail: a.elizarov@mail.ioffe.ru*
***e-mail: tup@tup.usr.pu.ru*

Received March 4, 2004

Abstract—The results of numerical calculations of the energies of Auger transitions, as well as the angular distribution (α_2) and spin polarization (β_2) anisotropy parameters, are presented for transitions in a photoexcited Kr* atom with two open shells. Matrix elements are calculated by the multiconfigurational Fock–Dirac relativistic method using an intermediate type of coupling. The wavefunctions of the initial and final states of the Auger transition are calculated with allowance for relaxation effects. The one-electron wavefunction of the continuous spectrum for an Auger electron is obtained using the single-configuration Fock–Dirac method. The results are compared with experiment and a new experiment is proposed for identifying the Auger state not only from the energy, but also from the total angular momentum of the Auger state. *© 2004 MAIK “Nauka/Interperiodica”.*

1. INTRODUCTION

Analysis of spin polarization and angular distribution of electrons makes it possible to obtain complete information on the dynamics of Auger decay in atoms. A general theory of the anisotropy in the angular distribution of Auger electrons was developed in [1–5] using the density matrix formalism. The first theoretical computations of the angular distribution coefficients were performed by several groups [6–8]. Advances made in experimental studies, including the realization of a complete quantum-mechanical experiment for an Auger process [9, 10], in which the amplitudes of Auger transitions and the phase differences in the partial waves of Auger electrons were measured, have stimulated further theoretical investigations.

Here, we employ the theory of angular distribution of Auger electrons developed in [5–7]. This theory is generalized to the case of atoms with open valence shells.

The wavefunctions of the Kr* atom were calculated using the multiconfigurational Fock–Dirac relativistic method taking into account relaxation for energy levels of both the initial and the final states. Such a relaxation substantially complicates computations since it necessitates the computation of matrix elements of an Auger transition with nonorthogonal one-electron functions. As a rule, relaxation effects were disregarded by other authors. Here, we also calculated the energy levels of the final state disregarding relaxation to clarify the role of these effects. In this case, the energy levels of the final state were calculated by the method of configurational interaction using the frozen one-electron functions obtained for the initial state of the atom.

In multiconfigurational computations, we included all relativistic configurations corresponding to a nonrelativistic configuration. For example, for the excited configuration $3d^95p^1$ of the Kr atom, this means that four different relativistic configurations ($3d^4_{3/2}3d^5_{5/2}5p^1_{1/2}$, $3d^3_{3/2}3d^6_{5/2}5p^1_{1/2}$, $3d^4_{3/2}3d^5_{5/2}5p^1_{3/2}$, and $3d^3_{3/2}3d^6_{5/2}5p^1_{3/2}$) were included in computations. This computational method in fact implements an intermediate coupling (IC) and leads to more reliable results as compared to those obtained earlier in our [11] and other publications in the framework of purely *LS* or *jj* couplings.

The one-electron wavefunction of the continuous spectrum of an Auger electron was calculated using single-configuration Fock–Dirac relativistic method taking into account nonlocal exchange and nondiagonal Lagrangian multipliers ensuring that the wavefunction is orthogonal to the core states of the ion. A detailed description of the method for calculating the wavefunction of the continuum is given in [11]. The influence of relativistic effects in calculations of the wavefunction of the continuum on the value of the angular distribution anisotropy parameter α_2 might be significant since the contribution to the values of parameters α_2 and β_2 (spin polarization anisotropy parameter) is mainly

1063-7761/04/9906-1119$26.00 © 2004 MAIK “Nauka/Interperiodica”

determined by the behavior of the function for the continuum in the atomic core region.

In Section 2, basic relations used for calculating parameters α_2 and β_2 are presented and the method for calculating the matrix elements with nonorthogonal wavefunctions of the initial and final states is described. In Section 3, the results of theoretical calculations of the energies of Auger states $4s^{-1}4p^{-1}5p$, $4s^{-1}4p^{-1}6p$, and $4s^{-1}5p$ of the Kr atom performed in the IC approximation are considered and compared with the results of precision experiment [12]. In the same section, the results of calculations of parameters α_2 and β_2 are presented and the possibility of performing an experiment leading to determination of the total angular momentum of the final state of an atom in an Auger transition is considered.

2. THEORY

2.1. Parameters of Asymmetry in the Angular Distribution of Auger Electrons

The parameter of angular distributions and spin polarization are calculated using a two-stage model of Auger decay proposed in [1]. The general theory of Auger decay is described in many publications (see, for example, [6]). The expression for the angular distribution of Auger electrons has the form

$$\frac{dW_{\mathrm{A}^+ \to \mathrm{A}^{2+}}}{d\Omega} = \frac{dW^{\Sigma}_{\mathrm{A}^+ \to \mathrm{A}^{2+}}}{4\pi}[1 + \alpha_2 A_{20} P_2(\sin\theta)], \quad (1)$$

where $dW^{\Sigma}_{\mathrm{A}^+ \to \mathrm{A}^{2+}}$ is the probability of the Auger process integrated over the direction of trajectories of Auger electrons, A_{20} is the population magnetic sublevels of a singly charged ion, α_2 is the anisotropy parameter of the angular distribution of Auger electrons, P_2 is the quadratic Legendre polynomial, and θ is the angle between the direction of emission of Auger electrons and the polarization of radiation. The expressions for anisotropy parameters of the angular distribution of Auger electrons and spin polarization are borrowed from [5, 6]:

$$\alpha_2 = \frac{A(200)}{A(000)}, \quad \beta_2 = -\frac{1}{\sqrt{3}}\,\mathrm{Im}\,\frac{A(211)}{A(000)}. \quad (2)$$

Here, $A(KkQ)$ are the angular distribution coefficients defined by the expression [6, 11]

$$A(KkQ) = \frac{1}{4\pi p}\sqrt{(2K+1)(2k+1)}$$

$$\times \sum_{l,l'} i^{l'-l} \exp[i(\sigma_l - \sigma_{l'})] \sum_{j,j'} (-1)^{J+J_1+j+Q+l'}$$

$$\times \sqrt{(2l+1)(2l'+1)(2j+1)(2j'+1)} \begin{Bmatrix} J & J_1 & j \\ K & j' & J_1 \end{Bmatrix} \quad (3)$$

$$\times \sum_X C^{X0}_{l0,\,l'0} C^{X0}_{K-Q,\,kQ} \begin{Bmatrix} \frac{1}{2} & \frac{1}{2} & k \\ j' & j & K \\ l' & l & X \end{Bmatrix}$$

$$\times \left\langle (J, \varepsilon lj) J_1 \middle\| \hat{V} \middle\| J_1 \right\rangle \left\langle (J, \varepsilon l'j') J_1 \middle\| \hat{V} \middle\| J_1 \right\rangle,$$

where J_1 is the total angular momentum of the initial state of the A^+ ion, J is the total angular momentum of the final state of the A^{2+} ion, ε is the free electron energy, l is the orbital angular momentum, j is the total angular momentum, and σ_{lj} is the phase of the Auger electron wavefunction.

The above matrix elements $\langle J_1 \| \hat{V} \| (Jj)J_1 \rangle$ of the transition operator $\hat{V}$ are defined for the initial and final multielectron states of an arbitrary atom. These matrix elements can be obtained in the general case by using the Wigner–Eckart theorem if the multielectron wavefunction Ψ_{J_1, M_1} of the initial state of the $\mathrm{A}^+(J_1)$ ion, the wavefunction $\Psi_{J, M}$ of the final state of the $\mathrm{A}^{2+}(J)$ ion, and the one-electron wavefunction ψ_{jm} of the Auger electron are known:

$$\langle (J, \varepsilon l'j') J_1 \| \hat{V} \| J_1 \rangle = \frac{\sqrt{2J_1+1}}{C^{J_1 M_1}_{JM,\,jm}} \langle JM, jm | \hat{V} | J_1 M_1 \rangle. \quad (4)$$

In calculating matrix elements (amplitudes) of the transition with orthogonal orbitals, the transition operator $\hat{V}$ in the Auger process may be the electron interaction operator or operator $\hat{H} - E$, where $\hat{H}$ is the total Hamiltonian of the system. The equivalence of these two versions stems from the fact that the initial and the final states differ in the two-electron excitation; consequently, all one-electron matrix elements vanish (at least in the single-configuration technique). If the one-electron functions of the initial and final states are different, we must choose operator $\hat{H} - E$ as the transition operator. We will now calculate the amplitude $\langle F | \hat{H} - E | I \rangle$ of the Auger transition between the initial state I with quantum numbers $J_1 M_1$ and the final state F with quantum numbers JM, jm.

2.2. Calculation of the Matrix Elements of the Transition Operator with Nonorthogonal Functions

The multiconfigurational Fock–Dirac method was used in all calculations of the multielectron wavefunctions of a singly charged ion in the initial state and a doubly charged ion in the final state. The wavefunctions for the initial and final state in an Auger process are usually calculated in the frozen orbitals approximation according to which the one-electron functions of the initial and final states form a unified set of orthonormal functions. This computational method is usually called calculation disregarding relaxation. Allowance for relaxation necessitates the use of two mutually nonorthogonal sets of orbitals of the final and initial states. Let us consider in greater detail the method for calculating the matrix elements of an Auger transition with nonorthogonal orbitals.

In the multiconfigurational Fock–Dirac method, the wavefunctions Ψ^I and Ψ^F of the initial and final states of an N-electron system can be presented as a linear combination of the Slater determinants $\det_\alpha$ constructed from one-electron wavefunctions $\{\phi_j^I(x)\}$ and $\{\phi_j^F(x)\}$, respectively:

$$\Psi^I = \sum_\alpha C_\alpha^I \det\nolimits_\alpha\{\phi_j^I(x_i)\},$$
$$\Psi^F = \sum_\alpha C_\alpha^F \det\nolimits_\alpha\{\phi_j^F(x_i)\}. \qquad (5)$$

For an Auger process in which the total energy of an atom is conserved during the Auger decay (E = const), the amplitude of transition from the initial state $|I\rangle$ to the final state $|F\rangle$ has the form

$$\langle F|\hat{H} - E|I\rangle = \sum_{\alpha\beta} C_\alpha^{F*} C_\beta^I (H_{\alpha\beta}^{FI} - EB_{\alpha\beta}^{FI}), \qquad (6)$$

where the indices α and β enumerate the Slater determinants for the initial and final states, H^{FI} is the matrix of Hamiltonian $\hat{H}$ in the basis of the Slater determinants, and B^{FI} is the nonorthogonality matrix in the same basis.

Matrix B^{FI} is not equal to the unit matrix since the determinants formed by one-electron wavefunctions of the initial and final states are not orthogonal. This matrix can be presented in the form [13]

$$B_{\alpha\beta}^{FI} = \langle \det\nolimits_\alpha | \det\nolimits_\beta \rangle = (D_{\alpha\alpha}D_{\beta\beta})^{-1/2} D_{\alpha\beta}, \qquad (7)$$

where $D_{\alpha\beta}$ is the determinant of the overlap integral matrix $S^{\alpha\beta}$ in the basis of one-electron orbitals:

$$D_{\alpha\beta} = \det\left|S_{i,j}^{\alpha\beta}\right|, \quad S_{i,j}^{\alpha\beta} = \langle \phi_i^F | \phi_j^I \rangle. \qquad (8)$$

The elements of matrix $S^{\alpha\beta}$ are calculated between two sets of orbitals $\{\phi_i^F\}_\alpha$ and $\{\phi_j^I\}_\beta$ forming the two Slater determinants α and β, respectively.

The matrix elements of the transition for one-electron and two-electron operators can be calculated using expressions for one- and two-particle density matrices of the transition between two states, which are described by Slater determinants α and β. The expression for the one-particle density matrix has the form

$$\rho_1^{\alpha,\beta}(x, x') = (D_{\alpha\alpha}D_{\beta\beta})^{-1/2} D_{\alpha\beta} \sum_{i,j}^N (S^{-1})_{i,j}^{\alpha,\beta} \phi_i^F(x) \phi_j^{I*}(x'). \qquad (9)$$

The two-particle density matrix can be represented in terms of the one-particle matrix and is defined by the expression

$$\rho_2^{\alpha,\beta}(x_1, x_2|x_1', x_2') = (D_{\alpha\alpha}D_{\beta\beta})^{-1/2} \times \sum_{\substack{i\neq k\\ j\neq l}} D_{i,j,k,l}^{\alpha\beta} \phi_i^F(x_1) \phi_j^{F*}(x_1') \phi_k^I(x_2) \phi_l^{I*}(x_2'), \qquad (10)$$

where

$$D_{i,j,k,l}^{\alpha\beta} = D_{\alpha\beta}\varepsilon_{i,k}\varepsilon_{j,l} \times [(S^{-1})_{i,j}^{\alpha,\beta}(S^{-1})_{k,l}^{\alpha,\beta} - (S^{-1})_{i,l}^{\alpha,\beta}(S^{-1})_{k,j}^{\alpha,\beta}], \qquad (11)$$

$$\varepsilon_{i,k} = \begin{cases} 1, & i < k, \\ -1, & i > k. \end{cases}$$

Hamiltonian $\hat{H}$ can be represented as the sum of one- and two-particle operators:

$$\hat{H} = \sum_{i=1,N} \hat{h}_i + \sum_{i\neq j}^N \hat{v}_{i,j}. \qquad (12)$$

The matrix elements have the form

$$H_{\alpha\beta}^{FI} = \langle \alpha|\hat{H}|\beta\rangle = \mathrm{Tr}(\hat{h}\rho_1^{\alpha\beta}) + \mathrm{Tr}(\hat{v}\rho_2^{\alpha\beta}). \qquad (13)$$

Using formulas (9) and (10) for one- and two-particle density matrices, we obtain

$$\langle\alpha|\sum_i \hat{h}_i|\beta\rangle = (D_{\alpha\alpha}D_{\beta\beta})^{-1/2} D_{\alpha\beta} \times \sum_{i\neq j}^N (S^{-1})_{i,j}\alpha, \beta\langle i|\hat{v}|j\rangle, \qquad (14)$$

$$\langle\alpha|\sum_{i\neq j} \hat{v}_{i,j}|\beta\rangle = (D_{\alpha\alpha}D_{\beta\beta})^{-1/2} \times \sum_{i\neq k}^N \sum_{j\neq l}^N D_{i,j,k,l}^{\alpha\beta} \langle i, j|\hat{v}|k, l\rangle. \qquad (15)$$

It was mentioned above that the multiconfigurational Fock–Dirac method was used in this study. All

Table 1. Energies E of the Auger transitions and anisotropy coefficients of angular distribution (α_2) and spin polarization (β_2) calculated taking into account (+) and disregarding (–) relaxation for Auger transitions $4s^{-1}4p^{-1}5p$ in Kr atom

Final state	E^-, eV	α_2^-	β_2^-	E^+, eV	α_2^+	β_2^+
$^4S_{3/2}$	47.7	0.565	0.0	44.3	0.565	0.0
$^4D_{7/2}$	47.4	0.673	0.0	44.0	0.673	0.0
$^4D_{5/2}$	47.4	0.608	0.018	43.9	0.604	0.019
$^4D_{3/2}$	47.2	0.565	0.0	43.8	0.565	0.0
$^2D_{5/2}$	47.2	0.437	0.067	43.7	0.419	0.071
$^4D_{1/2}$	47.0	0.0	0.0	43.6	0.0	0.0
$^2P_{3/2}$	46.8	–0.409	–0.068	43.4	–0.390	–0.075
$^4P_{5/2}$	46.8	0.680	–0.026	43.4	0.679	–0.024
$^4P_{3/2}$	46.8	–0.636	0.050	43.3	–0.636	0.050
$^4D_{1/2}$	46.8	–1.351	0.025	43.3	–1.358	0.025
$^4P_{1/2}$	46.7	0.420	–0.023	43.2	0.463	–0.023
$^2D_{3/2}$	46.5	0.703	–0.005	43.1	0.697	–0.004
$^2S_{1/2}$*	46.3	–1.409	0.023	42.9	–1.392	0.021
$^2S_{1/2}$**	40.5	–0.675	0.0	37.0	–0.727	0.0
$^2D_{3/2}$	40.4	0.149	–0.187	37.0	0.033	–0.173
$^2D_{5/2}$	40.3	0.570	0.032	36.9	0.527	0.045
$^2P_{1/2}$	40.1	–0.700	0.0	36.7	–0.706	0.0
$^2P_{3/2}$	40.1	–0.052	–0.159	36.7	0.003	–0.169

Note: * For the initial state $^1P_1$; ** for the initial state $^3P_2$.

Table 2. Energies E of Auger transitions and anisotropy coefficients of angular distribution (α_2) and spin polarization (β_2) calculated for Auger transitions $4s^{-2}5p$ in Kr atom

Final state	E^-, eV	α_2^-	β_2^-	E^+, eV	α_2^+	β_2^+
$^2P_{1/2}$	24.7	–0.707	0.0	21.5	–0.707	0.0
$^2P_{3/2}$	24.6	–0.530	0.0	21.4	–0.556	0.0

relativistic configurations corresponding to one nonrelativistic configuration were taken into consideration. Such an approach in fact employs the intermediate type of coupling. In the nonrelativistic limit, when the velocity of light tends to infinity, such an intermediate coupling is transformed into a purely *LS* coupling. It should be noted that the single-configuration Fock–Dirac method corresponding to the *jj* coupling does not possess a regular relativistic limit for atoms with open shells. For atoms with closed shells, the approach used by us here is equivalent to the method developed in [5–7].

3. RESULTS AND DISCUSSION

Tables 1–3 show the results of computation of energy and parameters α_2 and β_2 for Auger electrons formed as a result of decay of states $3d^{-1}_{5/2}5p$ and $3d^{-1}_{3/2}5p$ excited by a single-photon process from the ground state to the final state $4s^{-1}4p^{-1}5p$ of the Kr^+ ion. In our calculations, we used the intermediate coupling (IC). Two versions of computations are presented. The first version corresponds to the "frozen core" approximation. In the second version, relaxation of one-electron states for both the initial and the final state is taken into account. It is well known that a comparison of the results of computations performed in the frozen core approximation with those performed for nonorthogonal orbitals of the initial and final states demonstrated that the relaxation effect weakly influences the value of the angular distribution anisotropy parameters for Auger transitions in atoms with filled shells [14] and for atoms with unfilled shells [15]. It can be seen that for atoms in the excited state the relaxation effect noticeably modifies the value of the angular distribution anisotropy parameters and especially the value of the Auger transition energy. This follows from the results presented in Tables 1–3. Table 4 is compiled using the experimental spectrum of the above states given in [12]. States were identified in [12] on the basis of a relativistic multiconfigurational computation, and averaging was carried out over experimentally observed groups of resonances; for this reason, direct comparison with the results of our computations is difficult in our opinion. A comparison can be carried out only on the basis of identification of groups of resonances (see Table 4). Comparison of the experimental data with the results of our computations demonstrates the coincidence of the results of identification of Auger resonances except for one group of resonances to which configuration ($4p^{-3}4d5p$) of double Auger decay is ascribed in [12]. In our computations, this energy range of Auger states corresponds to the results of calculations presented in Table 1.

The identification of Auger states according to the total angular momentum can be carried out using an experimental technique based of the selection rules for three-stage photoexcitation of Auger states by polarized radiation. In this case, Auger states with a certain total angular momentum are excited depending on the total angular momentum projection imparted to the atom by radiation. By varying the combinations of mutual orientation of polarizations of radiation for three stages, we can introduce different total angular projections of the photon momenta for each stage of excitation and, hence, identify Auger states according to the total angular momentum. This method can be used for identifying Auger states of a Ba atom in the

Table 3. Anisotropy coefficients of angular distribution (α_2) and spin polarization (β_2) calculated for Auger transitions $4s^{-1}4p^{-1}6p$ for the Kr atom

Final state	E^-, eV	α_2^-	β_2^-	E^+, eV	α_2^+	β_2^+
$^4S_{3/2}$	45.1	0.706	–0.005	41.8	0.706	–0.005
$^4D_{7/2}$	45.0	0.673	0.0	41.7	0.673	0.0
$^4D_{5/2}$	45.0	0.545	0.040	41.7	0.535	0.043
$^2D_{5/2}$	44.9	0.646	0.0	41.6	–0.768	–0.038
$^2P_{3/2}$	44.9	0.706	–0.006	41.6	0.705	–0.006
$^2S_{1/2}$	44.8	–1.16	0.023	41.5	–1.15	0.023
$^4D_{3/2}$	44.6	0.565	0.0	41.3	–0.666	0.023
$^4D_{5/2}$	44.5	0.672	–0.017	41.2	0.673	–0.018
$^2D_{3/2}$	44.5	0.538	0.0	41.2	–0.667	0.070
$^4D_{1/2}$	44.5	–1.26	0.024	41.2	–1.27	0.024
$^4P_{1/2}$	44.4	–0.845	0.003	41.2	–0.825	0.003
$^2D_{3/2}$	44.2	0.696	–0.004	40.9	0.687	–0.004
$^2P_{1/2}$	40.9	–0.707	0.0	40.9	–0.707	0.0
$^2S_{1/2}$	38.0	0.0	0.0	34.7	–0.707	0.0
$^2D_{3/2}$	38.0	0.563	0.004	34.7	0.564	0.0
$^2D_{5/2}$	38.0	0.546	0.040	34.7	0.515	0.049
$^2P_{1/2}$	37.9	0.0	0.0	34.6	–0.707	0.0
$^2P_{3/2}$	37.9	0.555	0.0	34.6	0.562	0.0

Table 4. Experimental energies and intensities of Auger transitions from state $3d_15p$ for the Kr atom [12]

Final state	E, eV	Intensity, rel. units
$4s^{-1}4p^{-1}(^1P)5p$	42–45	≈4.2
$4s^{-1}4p^{-1}(^1P)6p$	39–41	≈2.0
$4p^{-3}4d5p$ (double Auger decay)	35–39	≈3.7
$4s^{-2}(^1S)5p^2P$	28–32	≈4.3

$6p7p$ configuration [16]. The application of this method will make it possible to compare the results of computations with experiment more fruitfully.

We calculated the energies and anisotropy parameters of the angular distribution and spin polarization of Auger electrons for the decay of the $3d^{-1}5p$ state to the final states $4s^{-1}4p^{-1}5p$, $4s^{-2}5p$, and $4s^{-1}4p^{-1}6p$ of the Kr atom, which are allowed by the selection rules for one-stage photoexcitation from the ground state. The computations were performed using the relativistic multielectron approximation with superposition of the configuration in intermediate coupling taking into account relaxation. The wavefunctions of an Auger electron are orthogonal to the core wavefunctions. The exchange interaction is taken into account. Satisfactory agreement between the calculated energies of Auger decay and experimental results has been reached.

ACKNOWLEDGMENTS

This study was supported by the program "Integration" (project no. L-01-02). Computations were made using the Cluster multiprocessor MISD computer at the Ioffe Physicotechnical Institute, Russian Academy of Sciences.

REFERENCES

1. W. Mehlhorn, Phys. Lett. **26**, 166 (1968).
2. J. Eichler and W. Fritsch, J. Phys. B **9**, 1477 (1976).
3. E. G. Berezhko and N. M. Kabachnik, J. Phys. B **10**, 2467 (1977).
4. H. Klar, J. Phys. B **13**, 4741 (1980).
5. K. Blum, B. Lohmann, and E. Taute, J. Phys. B **19**, 3915 (1986).
6. B. Lohmann, J. Phys. B **23**, 3147 (1990).
7. N. M. Kabachnik, H. Aksela, and S. Ricz, Phys. Rev. A **49**, 4653 (1994).
8. M. H. Chen, Phys. Rev. A **45**, 1684 (1992).
9. U. Hergenhahn, G. Snell, M. Drescher, *et al.*, Phys. Rev. Lett. **82**, 5020 (1999).
10. B. Schmidtke, M. Drescher, N. Müller, *et al.*, J. Phys. B **34**, 4293 (2001).
11. A. Yu. Elizarov and I. I. Tupitsyn, Zh. Éksp. Teor. Fiz. **124**, 733 (2003) [JETP **97**, 658 (2003)].
12. M. Drescher, T. Khalil, N. Müller, *et al.*, J. Phys. B **36**, 3337 (2003).
13. R. McWeeny, in *Methods in Computational Molecular Physics*, Ed. by S. Wilson and G. H. F. Diercksen (Plenum, New York, 1992), Ser. B.
14. J. Tulkki, N. M. Kabachnik, and H. Aksela, Phys. Rev. A **48**, 1277 (1993).
15. A. Yu. Elizarov and I. I. Tupitsyn, Phys. Scr. **70**, 139 (2004).
16. A. Yu. Elizarov and N. A. Cherepkov, Pis'ma Zh. Éksp. Teor. Fiz. **44**, 3 (1986) [JETP Lett. **44**, 1 (1986)].

Translated by N. Wadhwa

Journal of Experimental and Theoretical Physics, Vol. 99, No. 6, 2004, pp. 1124–1128.
Translated from Zhurnal Éksperimental'noĭ i Teoreticheskoĭ Fiziki, Vol. 126, No. 6, 2004, pp. 1290–1295.
Original Russian Text Copyright © 2004 by Il'ichev.

NUCLEI, PARTICLES, AND THEIR INTERACTION

Spin Correlations in a Pair of Atoms Induced by Spontaneous Emission of Photons

L. V. Il'ichev
Institute of Automation and Electrometry, Siberian Division, Russian Academy of Sciences, Novosibirsk, 630090 Russia
e-mail: leonid@iae.nsk.su

Received May 20, 2004

Abstract—An analysis is presented of the state that arises after photons have been spontaneously emitted by a pair of spatially separated excited two-level atoms with spin-1/2 ground and excited states. Selection of possible decay scenarios conditioned on the helicities of the photons (even on the helicity of the one emitted first) makes it possible to reveal ground-state spin-projection correlations between atoms. The correlations are due to quantum interference between alternative scenarios (the atom that has emitted a particular photon cannot be identified). The correlations obtained by the chosen selection method are classical. *© 2004 MAIK "Nauka/Interperiodica".*

1. INTRODUCTION

Growing interest in classification of correlated states of quantum many-body systems and in methods for creating them is motivated by the importance of entanglement, as a special type of correlation, for quantum information processing. The importance of correlations between particles in optics (e.g., their key role in Dicke superradiance [1]) was realized much earlier. Entanglement of subsystems of a closed quantum system must be explained by their interaction. Entanglement in an open system is a more complicated phenomenon: subsystems A and B can be entangled by indirect interaction via some external system (e.g., common environment [2]). In [3], a pair of spontaneously emitting atoms in a resonant light field was used as an example to show how an entangled state of noninteracting subsystems of the same system can be prepared. In this study, we note that the *n*th-order probability amplitudes for interaction with an external field (associated with stimulated transitions involving *n* photons) provide a natural basis for representing the state vector of an atomic system as a superposition of entangled states. In the case of Λ atoms, certain spontaneous decay events can be used as physical "filters" for these states, and it is impossible in principle to attribute a detected spontaneous photon to a particular atom. In the context of an analysis of preparation of entangled states, the phenomenon known as entanglement swapping should also be mentioned [4]. One swapping scenario can be described as follows. Consider a quantum system consisting of subsystems A, A', B, and B'. Suppose that the reduced states represented by density matrices $\hat{\varrho}_{AB}$ and $\hat{\varrho}_{A'B'}$ are entangled, while subsystems A ∪ B and A' ∪ B' are uncorrelated, i.e.,

$$\hat{\varrho}_{ABA'B'} = \hat{\varrho}_{AB} \otimes \hat{\varrho}_{A'B'}.$$

If a post-selective measurement (with a definite outcome) is now performed on A and A' in the entangled basis, then the "posterior" state of the subsystem B ∪ B' corresponding to the given outcome will be entangled, whereas the prior state $\hat{\varrho}_{BB'}$ is strictly uncorrelated both before and after the measurement on A ∪ A'. An example of a natural process in which spin correlations are swapped between particles was considered in [5, 6].

Selection conditioned on the results of interference between product states leads to entanglement in a system of two spatially separated atomic Bose–Einstein condensates [7] or two photonic modes [8]. An analogous selection plays a key role in the present study of the correlations induced by spontaneous decay of the excited states of two spatially separated atoms. The present model, albeit similar to those considered in [2, 3], takes into account polarization of the emitted photons and degeneracy of the atoms with respect to spin direction. The analysis is focused on characterization of the induced ground-state spin-projection correlations.

2. DESCRIPTION OF THE MODEL AND BASIC RELATIONS

Consider a pair of identical atoms A and B with spin-1/2 ground and excited states. Let the atoms be localized at points $\mathbf{r}_A$ and $\mathbf{r}_B$ within a region much smaller than the spontaneous emission wavelength.

Suppose that the atoms are heavy enough that their displacement over the decay time is negligible. When prepared in excited states, the atoms can emit two spontaneous photons. In this system, alternative decay scenarios interfere in a natural manner: an emitted photon cannot be attributed to either atom. To examine this phenomenon in more detail, assume that the emitted photon is absorbed at a point lying on the perpendicular bisector of the line segment that joins two two-level atoms separated by the distance $r = |\mathbf{r}_B - \mathbf{r}_A|$ after it has traveled a distance L (see figure). (Angular momentum is tentatively ignored.) This geometry corresponds to optimal conditions for identifying the photon source. It is clear that the alternative scenarios of emission by A or B will not interfere if the detector can distinguish between the transverse recoil momenta $\mathbf{p}_A$ and $\mathbf{p}_B = -\mathbf{p}_A$ due to absorption. The corresponding quantum uncertainty l in the detector location must satisfy the condition

$$l^{-1} < 2|\mathbf{p}_A| = 2k\sin\theta \equiv \frac{kr}{L}, \qquad (1)$$

where k is the wavevector magnitude characteristic of the emitted photon (Planck's constant is set to unity). However, any difference between $\mathbf{p}_A$ and $\mathbf{p}_B$ can arise only if

$$l \ll r. \qquad (2)$$

It follows from (1) and (2) that the noninterference condition is

$$r \gg \sqrt{\frac{L}{k}}. \qquad (3)$$

Accordingly, if

$$r \lesssim \sqrt{\frac{L}{k}}, \qquad (4)$$

then the alternative scenarios of emission by either atom mutually interfere. This is a necessary condition for the onset of entanglement in the atom pair. Now, consider the optical system in which the detector of spontaneous photons is replaced by a monochromatic light source with wavelength $2\pi/k$. For this system, condition (3) means that the distance between the atoms is many times greater than the Fresnel zone, and condition (4) implies that both atoms are located within the first Fresnel zone. Note also that the present analysis is focused on the ground-state spin correlations induced after two photons have been emitted. Thus, the intermediate energy-spin-projection entanglement that arises after the first photon has been detected is not considered here (see discussion in [3]). It is essential that the correlations in question arise because the atom that has emitted a particular photon cannot be identified.

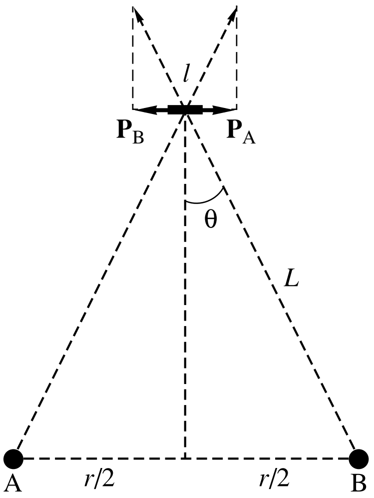

Schematic setup for distinguishing between photon sources.

Now, let us discuss selection of two-atom states conditioned on experimentally distinguishable scenarios of spontaneous decay. The ideal result of this study would be the formulation of a simple method for creating entangled states of the system. The straightforward argumentation presented below shows that the resulting prior state (averaged over all spontaneous decay histories) cannot be entangled if the initial excited state is isotropic and uncorrelated, i.e., described by the density matrix $(1/4)\hat{P}_e \otimes \hat{P}_e$, where $\hat{P}_e$ is the projector on the excited-state subspace of an atom. (The first and second multiplicands in tensor products act on the respective state spaces of A and B.) The atom pair in the ground state can be treated as a two-qubit system. Its geometry is defined by the unit vector $\mathbf{s} = \mathbf{r}/r$ directed from A to B. In standard notation ($\hat{1} \equiv \hat{P}_g$ is the projector onto the ground-state subspace of an atom), the corresponding joint density matrix has the form

$$\hat{\sigma}_x \equiv |g+\rangle\langle g-| + |g-\rangle\langle g+|,$$

$$\hat{\sigma}_y \equiv i|g-\rangle\langle g+| - i|g+\rangle\langle g-|,$$

$$\hat{\sigma}_z \equiv |g+\rangle\langle g+| - |g-\rangle\langle g-|,$$

where "+" and "–" denote the signs of angular-momentum projections on the z axis. It may involve contributions of the following terms:

$$\hat{1} \otimes \hat{1}, \quad \mathbf{s}\cdot\hat{\boldsymbol{\sigma}} \otimes \mathbf{s}\cdot\hat{\boldsymbol{\sigma}},$$

$$\hat{1} \otimes \mathbf{s}\cdot\hat{\boldsymbol{\sigma}}, \quad \mathbf{s}\cdot\hat{\boldsymbol{\sigma}} \otimes \hat{1}, \quad (\mathbf{s}\times\hat{\boldsymbol{\sigma}}) \otimes \hat{\boldsymbol{\sigma}}.$$

The term $\hat{\boldsymbol{\sigma}} \otimes \hat{\boldsymbol{\sigma}}$ is not listed here, because it represents correlations that are isotropic and independent of $\mathbf{s}$, which cannot be the case. The last three terms (linear in the components of $\mathbf{s}$) must therefore be discarded by virtue of mirror symmetry, because they are pseudoscalar operators. Thus, the most general form of the averaged final density matrix is

$$\hat{\varrho} = \frac{1}{4}(\hat{1} \otimes \hat{1} + \rho \mathbf{s} \cdot \hat{\boldsymbol{\sigma}} \otimes \mathbf{s} \cdot \hat{\boldsymbol{\sigma}}). \tag{5}$$

For systems of two spin 1/2 particles, the Peres–Horodecki criterion [9, 10] implies that the initial density matrix involves only classical correlations if and only if the transpose of (5) with respect to the quantum numbers of one of the atoms is positive. It is obvious that this partial transpose is positive (e.g., in a basis where the quantization axis z is aligned with $\mathbf{s}$). Therefore, entanglement cannot be created in this system without performing selection conditioned on the spontaneous decay history. It is shown below that the averaged density matrix does not involve any correlation.

Let us proceed to calculations. Suppose that condition (4) holds. The Lindblad-type master equation for the two-particle density matrix $\hat{\varrho}$ is (e.g., see [11])[1]

$$\begin{aligned}\partial_t \hat{\varrho} = \sum_{q = \pm 1} \int d^2 n \Big[\hat{L}(q, \mathbf{n}) \hat{\varrho} \hat{L}^{\dagger}(q, \mathbf{n}) \\ - \frac{1}{2} \{ \hat{L}^{\dagger}(q, \mathbf{n}) \hat{L}((q, \mathbf{n}), \hat{\varrho}) \}_{+} \Big].\end{aligned} \tag{6}$$

It is written in the Heisenberg representation based on the unperturbed Hamiltonian of the atom pair. Motion of the atoms, their interactions with external fields, and the recoil due to emission of photons are neglected. In this model, the evolution of the density matrix is completely determined by spontaneous decay. Equation (6) contains the Lindblad operator $\hat{L}(q, \mathbf{n})$ corresponding to the emission a photon with helicity $q \in \{\pm 1\}$ in the direction of $\mathbf{n}$. These operators (defined on the state space of the atoms) are the part of the Hamiltonian that represents interaction between intra-atomic currents and a spontaneous photon with definite q and $\mathbf{n}$ (up to a factor). Interference between the alternative scenarios of spontaneous emission by either atom is equivalent to joint action of both atoms as sources of both photons. Therefore,

$$\begin{aligned}\hat{L}(q, \mathbf{n}) = \hat{L}_{\mathrm{A}}(q, \mathbf{n}) \exp(-ik\mathbf{n} \cdot \mathbf{r}_{\mathrm{A}}) \\ + \hat{L}_{\mathrm{B}}(q, \mathbf{n}) \exp(-ik\mathbf{n} \cdot \mathbf{r}_{\mathrm{B}}),\end{aligned} \tag{7}$$

where

$$\begin{aligned}\hat{L}_{\mathrm{A}}(q, \mathbf{n}) = \hat{\mathbf{d}} \cdot \mathbf{e}_q^*(\mathbf{n}) \otimes \hat{I}, \\ \hat{L}_{\mathrm{B}}(q, \mathbf{n}) = \hat{I} \otimes \hat{\mathbf{d}} \cdot \mathbf{e}_q^*(\mathbf{n})\end{aligned} \tag{8}$$

are the operators representing the emission of a photon by A and B, respectively. These definitions involve the identity operator $\hat{I}$ in the state space of an atom and the part of the dipole moment operator responsible for deexcitation,[2]

$$\hat{\mathbf{d}} = \sqrt{\frac{3}{4\pi}}$$

$$\times \sum_{q' = 0, \pm 1} \sum_{m, m' = \pm} |gm\rangle\langle em'| \left\langle \frac{1}{2} m' \frac{1}{2} 1 q' \middle| \frac{1}{2} m \frac{1}{2} \right\rangle \mathbf{e}_{q'}^*,$$

where $\mathbf{e}_{q'}$ denotes the cyclic unit vectors in a laboratory frame ($\mathbf{e}_0 = \mathbf{e}_z$, $\mathbf{e}_{\pm 1} = \mp(\mathbf{e}_x \pm i\mathbf{e}_y)/\sqrt{2}$) and

$$\mathbf{e}_q(\mathbf{n}) = \sum_{q' = 0, \pm 1} D^{(1)}_{q'q}(\mathbf{n}) \mathbf{e}_{q'}$$

denotes the cyclic unit vectors in a reference frame where the z axis is aligned with $\mathbf{n}$. The numerical factor in the expression for $\hat{\mathbf{d}}$ is introduced for convenience. When condition (4) is violated, Eq. (6) should be rearranged so as to reduce the relative contributions of the cross terms containing products of operators associated with different atoms. In the limit of (3), these products vanish, i.e., the photon sources can be distinguished, and right-hand side of Eq. (6) is replaced by the sum of the right-hand sides of the Lindblad equations corresponding to $\hat{L}_{\mathrm{A}}(q, \mathbf{n})$ and $\hat{L}_{\mathrm{B}}(q, \mathbf{n})$.

The procedure for selecting different spontaneous decay histories examined here is conditioned on the helicities of the emitted photons. Accordingly, consider the four ensembles defined by the pair of helicities (q_1, q_2), where q_1 and q_2 denote the helicities of the first and second emitted photons, respectively. The density matrix corresponding to the emission of photons with given helicities at instants t_1 and t_2 is found by solving Eq. (6):

$$\begin{aligned}\hat{\varrho}(t_1, q_1; t_2, q_2) = \int d^2 n_2 \int d^2 n_1 \hat{L}(q_2, \mathbf{n}_2) \\ \times \exp[-\hat{K}(t_2 - t_1)] \hat{L}(q_1, \mathbf{n}_1) \exp[-\hat{K}(t_1 - t_0)] \hat{\varrho}(t_0) \\ \times \exp[-\hat{K}(t_1 - t_0)] \hat{L}^{\dagger}(q_1, \mathbf{n}_1) \\ \times \exp[-\hat{K}(t_2 - t_1)] \hat{L}^{\dagger}(q_2, \mathbf{n}_2),\end{aligned} \tag{9}$$

where

$$\hat{K} = \frac{1}{2} \sum_{q = \pm 1} \int d^2 n \hat{L}^{\dagger}(q, \mathbf{n}) \hat{L}(q, \mathbf{n})$$

---

[1] An alternative approach makes use of quantum stochastic differential equations (e.g., see [3]).

[2] In Eq. (6), time is normalized to the rate constant for spontaneous decay.

is the Hermitian operator of evolution of the two-atom system during the time interval between the acts of emission (equivalent to Hamiltonian-like evolution in imaginary time) and $\hat{\varrho}(t_0)$ is the initial density matrix ($t_0 = 0$ hereinafter). The trace of operator (9) defines the probability distribution of the emission instants and the helicities of the emitted photons. The integral calculated over the admissible set of t_1 and t_2 yields

$$\begin{aligned}&\hat{\varrho}(q_1; q_2)\\ &= \int_0^{\infty} dt_2 \int_0^{t_2} dt_1 \hat{\varrho}(t_1, q_1; t_2, q_2) = \mathcal{E}_{q2}[\mathcal{E}_{q1}\hat{\varrho}(0))].\end{aligned} \tag{10}$$

The superoperator $\mathcal{E}_q$ corresponding to the emission characterized by q is defined as

$$\mathcal{E}_q[\hat{\varrho}] = \sum_{i,j} \int d^2 n \frac{\hat{L}(q, \mathbf{n})\hat{P}_i \hat{\varrho} \hat{P}_j \hat{L}^{\dagger}(q, \mathbf{n})}{\lambda_i + \lambda_j} \tag{11}$$

in terms of elements of the spectral decomposition of $\hat{K}$,

$$\hat{K} = \sum_i \lambda_i \hat{P}_i. \tag{12}$$

Calculation of $\{\lambda_i, \hat{P}_i\}$ yields the following results if the z axis is aligned with the line segment that joins the atoms:

$\lambda_0 = 0$ corresponds to the projector $\hat{P}_0 = \hat{P}_g \otimes \hat{P}_g$;

$\lambda_1 = 1 + \alpha/3$ corresponds to the projector $\hat{P}_1$ onto the subspace

$\mathrm{span}\{|g+\rangle \otimes |e+\rangle + |e+\rangle \otimes |g+\rangle, |g-\rangle \otimes |e-\rangle + |e-\rangle \otimes |g-\rangle\}$;

$\lambda_2 = 1 - \alpha/3$ corresponds to the projector $\hat{P}_2$ onto the subspace

$\mathrm{span}\{|g+\rangle \otimes |e+\rangle - |e+\rangle \otimes |g+\rangle, |g-\rangle \otimes |e-\rangle - |e-\rangle \otimes |g-\rangle\}$;

$\lambda_3 = 1 + (\alpha + \beta + \beta^*)/3$ corresponds to the projector $\hat{P}_3$ onto the subspace

$(|g+\rangle \otimes |e-\rangle - |e+\rangle \otimes |g-\rangle - |g-\rangle \otimes |e+\rangle + |e-\rangle \otimes |g+\rangle)/2$;

$\lambda_4 = 1 - (\alpha + \beta + \beta^*)/3$ corresponds to the projector $\hat{P}_4$ onto the subspace

$(|g+\rangle \otimes |e-\rangle + |e+\rangle \otimes |g-\rangle - |g-\rangle \otimes |e+\rangle - |e-\rangle \otimes |g+\rangle)/2$;

$\lambda_5 = 1 + (\alpha - \beta - \beta^*)/3$ corresponds to the projector $\hat{P}_5$ onto the subspace

$(|g+\rangle \otimes |e-\rangle - |e+\rangle \otimes |g-\rangle + |g-\rangle \otimes |e+\rangle - |e-\rangle \otimes |g+\rangle)/2$;

$\lambda_6 = 1 - (\alpha - \beta - \beta^*)/3$ corresponds to the projector $\hat{P}_6$ onto the subspace

$(|g+\rangle \otimes |e-\rangle + |e+\rangle \otimes |g-\rangle + |g-\rangle \otimes |e+\rangle + |e-\rangle \otimes |g+\rangle)/2$;

$\lambda_7 = 2$ corresponds to the projector $\hat{P}_7 = \hat{P}_e \otimes \hat{P}_e$.

The parameters

$$\alpha = \alpha(r) = 3\frac{\sin(kr) - kr\cos(kr)}{(kr)^3} \tag{13}$$

and

$$\begin{aligned}&\beta = \beta(r)\\ &= \frac{3}{2}\left[\frac{\sin(kr)}{kr} - \frac{\sin(kr) - kr\cos(kr)}{(kr)^3}(1 - ikr)\right]\end{aligned} \tag{14}$$

are defined so that $\alpha(r) \longrightarrow 1$ and $\beta(r) \longrightarrow 1$ as $r = |\mathbf{r}_B - \mathbf{r}_A| \longrightarrow 0$.

3. ANALYSIS OF THE CORRELATED STATE

If the initial state corresponds to uncorrelated isotropic excitation of both atoms,

$$\hat{\varrho}(0) = \frac{1}{4}\hat{P}_e \otimes \hat{P}_e, \tag{15}$$

then expression (10) yields

$$\begin{aligned}\hat{\varrho}(q_1; q_2) &= \frac{1}{16}\left(1 - \frac{1}{2}q_1 q_2 \frac{(\beta - \beta^*)^2}{9 - \alpha^2}\right)\hat{1} \otimes \hat{1}\\ &- \frac{1}{32}q_1 q_2 \frac{(\beta - \beta^*)^2}{9 - \alpha^2}\hat{\sigma}_z \otimes \hat{\sigma}_z\\ &+ \frac{1}{24}q_1 \frac{\alpha(\beta - \beta^*)}{9 - \alpha^2}(\hat{\sigma}_+ \otimes \hat{\sigma}_- - \hat{\sigma}_- \otimes \hat{\sigma}_+),\end{aligned} \tag{16}$$

where

$$\hat{\sigma}_+ \equiv |g+\rangle\langle g-|, \quad \hat{\sigma}_- \equiv |g-\rangle\langle g+|.$$

Note that the last summand contains the operator $(\mathbf{s} \times \hat{\boldsymbol{\sigma}}) \otimes \hat{\boldsymbol{\sigma}}$ written in a different form. Mirror symmetry is not violated here, since the operator is multiplied by the pseudoscalar q_1.

The probability $p(q_1, q_2)$ of emission of a pair of photons with given helicities is proportional to the coefficient of the first summand in (16):

$$\begin{aligned}p(q_1; q_2) &= \mathrm{Tr}_{A,B}\hat{\varrho}(q_1; q_2) = \frac{1}{4}\\ &+ \frac{q_1 q_2}{8}\frac{[kr\cos(kr) - \sin(kr)]^2(kr)^2}{(kr)^6 - [kr\cos(kr) - \sin(kr)]^2}.\end{aligned} \tag{17}$$

The probability of emission of photons having equal helicities is the highest and reaches a maximum value of 0.55 at $kr \approx 2.04$. The ensuing asymptotic expressions are

$$p(q_1; q_2) \longrightarrow \frac{1}{4} + \frac{q_1 q_2}{64}(kr)^2, \quad kr \ll 1, \tag{18}$$

$$p(q_1; q_2) \longrightarrow \frac{1}{4} + \frac{q_1 q_2}{8}\left(\frac{\cos(kr)}{kr}\right)^2, \quad kr \gg 1. \tag{19}$$

The ratio $\hat{\varrho}(q_1; q_2)/p(q_1; q_2)$ is the (posterior) density matrix conditioned on given helicities of the emitted photons. The corresponding density matrices of the respective atoms represent the state characterized by the maximal spin-projection entanglement:

$$\begin{aligned} \hat{\varrho}_{\mathrm{A}} &= \frac{\mathrm{Tr}_{\mathrm{B}}\hat{\varrho}(q_1; q_2)}{\mathrm{Tr}_{\mathrm{A,B}}\hat{\varrho}(q_1; q_2)} = \frac{1}{2}\hat{P}_{\mathrm{gA}}, \\ \hat{\varrho}_{\mathrm{B}} &= \frac{\mathrm{Tr}_{\mathrm{A}}\hat{\varrho}(q_1; q_2)}{\mathrm{Tr}_{\mathrm{A,B}}\hat{\varrho}(q_1; q_2)} = \frac{1}{2}\hat{P}_{\mathrm{gB}}. \end{aligned} \tag{20}$$

The two-particle density matrix averaged over all admissible helicity values exhibits perfect isotropy and complete decoherence:

$$\sum_{q_1, q_2} \hat{\varrho}(q_1; q_2) = \frac{1}{4}\hat{P}_{\mathrm{g}} \otimes \hat{P}_{\mathrm{g}}. \tag{21}$$

However, correlation between atomic states is induced by the last summand in (16) after the helicity of the first photon has been specified. The correlation induced by specifying the value of q_2 can only be stronger. Note also that correlations vanish when either $kr = \tan(kr)$ or the distance between the atoms is much greater than the spontaneous decay wavelength.

According to the Peres–Horodecki criterion, the correlations are classical.

4. CONCLUSIONS

The onset of spin-projection entanglement after spontaneous emission of photons by a pair of atoms is analyzed. The correlation arises from the fundamental impossibility to identify the atom that has emitted a particular photon. The presence of an observer is obviously not required to establish this impossibility, because it should be interpreted as the lack of a parameter of the environment that is entangled with any particular history of spontaneous decay (emission of a photon by a particular atom). This explains the interference between alternative scenarios. The example analyzed here illustrates a general principle: the state of an open quantum system is determined by the information received by the environment [12]. The averaged density matrix does not involve any correlation after the photons have been emitted, and selection conditioned on spontaneous-decay history is required to single out a subensemble in which the ground states of the atoms are correlated. The present analysis uses the simplest (discrete) procedure of selection conditioned on the helicities of the emitted photons. The selection is amenable to a comprehensive analysis, but is not sufficient to identify entangled states, since the resulting correlations are classical. The possibility of entanglement under selection conditioned on the emission directions remains an open question.

ACKNOWLEDGMENTS

I am deeply grateful to P.L. Chapovskii for detailed discussion of the problems considered in this study. This work was supported by the Russian Foundation for Basic Research, project no. 03-02-17553 and by the Siberian Division of the Russian Academy of Sciences under the project "Laser Cooling of Gases in Magneto-optical Traps."

REFERENCES

1. R. H. Dicke, Phys. Rev. **93**, 99 (1954).
2. A. M. Basharov, Zh. Éksp. Teor. Fiz. **121**, 1249 (2002) [JETP **94**, 1070 (2002)].
3. A. M. Basharov and É. A. Manykin, Opt. Spektrosk. **96**, 91 (2004) [Opt. Spectrosc. **96**, 81 (2004)].
4. M. Zukowski, A. Zeilinger, M. A. Horne, and A. K. Ekert, Phys. Rev. Lett. **71**, 4287 (1993).
5. L. V. Il'ichev, Zh. Éksp. Teor. Fiz. **117**, 248 (2000) [JETP **90**, 222 (2000)].
6. L. V. Il'ichev, Teor. Mat. Fiz. **127**, 168 (2001).
7. Y. Castin and J. Dalibard, Phys. Rev. A **55**, 4330 (1997).
8. G. Nienhuis, J. Phys. A **34**, 7867 (2001).
9. A. Peres, Phys. Rev. Lett. **77**, 1413 (1996).
10. M. Horodecki, P. Horodecki, and R. Horodecki, Phys. Lett. A **223**, 1 (1996).
11. C. W. Gardiner, *Handbook of Stochastic Methods for Physics, Chemistry, and the Natural Sciences* (Springer, Berlin, 1985; Mir, Moscow, 1986).
12. M. B. Menskiĭ, *Quantum Measurements and Decoherence* (Kluwer Academic, Dordrecht, 2000; Fizmatlit, Moscow, 2001).

Translated by A. Betev

Journal of Experimental and Theoretical Physics, Vol. 99, No. 6, 2004, pp. 1129–1136.
From Zhurnal Éksperimental'noĭ i Teoreticheskoĭ Fiziki, Vol. 126, No. 6, 2004, pp. 1296–1302.

Resonant Transmittance through Periodically Modulated Films[¶]

Z. D. Genchev and D. G. Dosev

Institute of Electronics, Bulgarian Academy of Sciences, 1784, Sofia, Bulgaria

e-mail: zgenchev@ie.bas.bg; dian_dosev2002@yahoo.com

Received May 31, 2004

Abstract—We analyze the optical transmittance at normal incidence for an electron gas without losses. The electron gas is supposed to have a plane parallel slab geometry and its dielectric permittivity is assumed to be periodically modulated in one direction parallel to the interfaces. Due to surface plasmon polariton mode excitation, there exist resonance frequencies where the transmittance equals to unity. The number and positions of peaks are investigated analytically and a comparison with the analytic theory by Dykhne *et al.* [6] is made. *© 2004 MAIK "Nauka/Interperiodica".*

1. INTRODUCTION

In the past, it had been thought that subwavelength apertures have a very low transmission efficiency of light [1]. Recently, however, high transmission efficiencies from arrays of subwavelength structures in metal films have been reported. Since the publication of [2], many experimental and theoretical studies were carried out in order to determine the physical origin of the extraordinarily enhanced transmission. They focused on the description of complicated electromagnetic modes of the metal, originating from the interaction between photons and surface electrons, considering disordered arrays of holes in a metal film [3], organized nanoparticles [4] or periodic rough surfaces [5].

In this paper, we restrict ourselves to the case where the metal film occupying the space

$$|z| < \frac{d}{2}, \quad -\infty < x < \infty, \quad \frac{\partial}{\partial y} = 0$$

is in a vacuum environment ($|z| > d/2$, $-\infty < x < \infty$) and the dielectric permittivity has the simple form

$$\varepsilon(x) = \tilde{\varepsilon}_0 + \tilde{\varepsilon}_1 \cos(qx),$$

with some prescribed periodicity $a = 2\pi/q$ in the $\hat{x}$ direction. Only transverse magnetic waves (TM mode)

$$(H_y(x, z), E_x(x, z), E_z(x, z))\exp(-i\omega t)$$

are considered in the two-wave approximation

$$F(x, z) = F_0(z) + F_1(z)\cos(qx),$$

where a full analytic treatment of the complicated boundary value problem can be easily done. We follow the notation and the method of solution outlined in [6] in order to obtain a clear physical understanding of the phenomenon of enhanced transmission. We also derive definite results for the dissipationless free-electron gas with

$$\tilde{\varepsilon}_0 = 1 - \frac{\omega_p^2}{\omega^2}$$

(ω_p is the electron plasma frequency). In future studies, these results will be extended to more realistic optical characteristics of metal films, including the experimentally available data for optical constants [7].

2. GENERAL ANALYTIC FORMULATION OF THE PROBLEM

We consider the two-dimensional electromagnetic problem shown schematically in Fig. 1. The magnetic permeability in the whole space is denoted by μ_0 and the dielectric permittivity of the free space is denoted by ε_0. The physical system considered in this work consists of a vacuum (the relative dielectric permittivity is $\varepsilon(\omega) = 1$) in two regions $|z| > d/2$ and a metal slab (in the region $|z| < d/2$) characterized by the relative dielectric function

$$\varepsilon(\omega, x) = -n^2(1 - g\cos(qx))^{-1}. \qquad (1)$$

If the modulation factor $g = 0$, the dielectric function of the slab (Eq. (1)) is assumed to be real and to satisfy the condition $n^2 > 1$ in some frequency range. It is within

---

[¶] This article was submitted by authors in English.

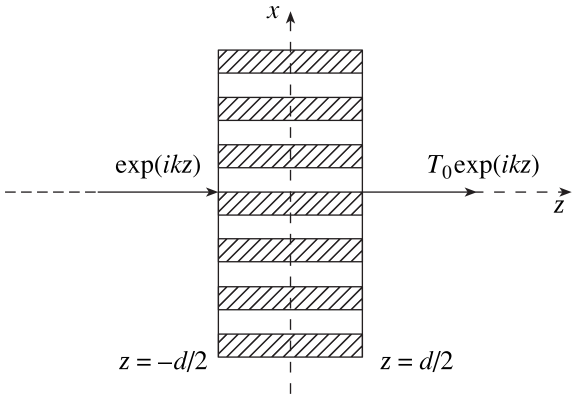

Fig. 1. A plane wave is incident normally on a modulated film $|z| < d/2$. The two arrows show the direction of propagation of the beam incident from $z = -\infty$ and the zero-order transmitted beam ($T_0\exp(ikz)$) at $z = \infty$. The transmittance is defined as $T = |T_0|^2$.

this frequency range that surface-plasmon polaritons exist. The particular periodic x dependence in (1) facilitates the comparison with the analytic results given in [6]. The Maxwell equations in the linear harmonic approximation ($\exp(-i\omega t)$),

$$\mathrm{curl}\mathbf{E}(\omega, \mathbf{r}) = i\omega\mu_0\mathbf{H}(\omega, \mathbf{r}), \tag{2}$$

$$\mathrm{curl}\mathbf{H}(\omega, \mathbf{r}) = -i\omega\varepsilon_0\varepsilon(\omega, x, z)\mathbf{E}(\omega, \mathbf{r}), \tag{3}$$

are treated for transverse magnetic waves (p polarization) $\mathbf{E}(E_x, 0, E_z)$, $\mathbf{H}(0, H_y, 0)$ under the assumption

$$\frac{\partial}{\partial y} = 0.$$

In the region $|z| < d/2$, we have

$$\frac{\partial^2 H_y}{\partial z^2} + \varepsilon(x)\frac{\partial}{\partial x}\left[\frac{1}{\varepsilon(x)}\frac{\partial H_y}{\partial x}\right] + k^2\varepsilon(x)H_y(x, z) = 0, \tag{4}$$

$$E_x = -\frac{i}{\omega\varepsilon_0\varepsilon(x)}\frac{\partial H_y}{\partial z}, \quad E_z = \frac{i}{\omega\varepsilon_0\varepsilon(x)}\frac{\partial H_y}{\partial x}, \tag{5}$$

where

$$k = \omega(\varepsilon_0\mu_0)^{1/2} = \frac{\omega}{c}.$$

Equations (1) and (4) can be written as

$$[1 - g\cos(qx)]\frac{\partial^2 H_y}{\partial z^2} + \frac{\partial}{\partial x}\left[(1 - g\cos(qx))\frac{\partial H_y}{\partial x}\right] - k^2n^2H_y(x, z) = 0. \tag{6}$$

Neglecting the generation of the $\cos(lqx)$ harmonics with l higher than one and recalling the Floquet theorem, we find

$$H_y\left(x, |z| < \frac{d}{2}\right) = [A_1 + 2A_2\cos(qx)][X] + [B_1 + 2B_2\cos(qx)][Y], \tag{7}$$

where

$$[X] = \mathrm{sech}\left(\frac{dkn}{2}\lambda_1\right) \times [X_1\cosh(knz\lambda_1) - X_2\sinh(knz\lambda_1)], \tag{8}$$

$$[Y] = \mathrm{sech}\left(\frac{dkn}{2}\lambda_2\right) \times [Y_1\cosh(knz\lambda_2) - Y_2\sinh(knz\lambda_2)]. \tag{9}$$

In formulas (8) and (9), X_1, X_2, Y_1, and Y_2 are arbitrary constants and $\lambda_{1,2}^2$ are dimensionless eigenvalues given by [6]

$$\lambda_1^2 = \frac{2 - Q + q_1^2}{2 - g^2}, \quad \lambda_2^2 = \frac{2 + Q + q_1^2}{2 - g^2}, \tag{10}$$

where

$$Q^2 = q_1^4 + 2g^2(1 - q_1^2), \quad q_1 = \frac{q}{kn}; \tag{11}$$

A_1, A_2 and B_1, B_2 are eigenvectors that satisfy the four relations

$$A_1(\lambda_1^2 - 1) - gA_2\lambda_1^2 = 0, \tag{12}$$

$$-g\lambda_1^2A_1 + 2(\lambda_1^2 - 1 - q_1^2)A_2 = 0, \tag{13}$$

$$B_1(\lambda_2^2 - 1) - gB_2\lambda_2^2 = 0, \tag{14}$$

$$-g\lambda_2^2B_1 + 2(\lambda_2^2 - 1 - q_1^2)B_2 = 0. \tag{15}$$

If the modulation amplitude is small ($q \ll 1$), it is straightforward to obtain the following expansions up to the order $O(g^4)$:

$$A_1 = 1 + \frac{g^2}{4q_1^2} + \frac{g^4}{4q_1^2}(2F + q_1^{-2}), \tag{16}$$

$$A_2 = -\frac{g}{2q_1^2}\left[1 - \frac{g^2}{2q_1^2} - \frac{g^2}{4}(2F + q_1^{-2})\right], \tag{17}$$

$$\begin{aligned} B_1 = \frac{g}{2q_1^2}\Big[& 1 + q_1^2 - \frac{g^2}{2}(q_1 + q_1^{-1})^2 \\ & + \frac{g^4}{4}(2F + q_1^2 + q_1^{-2})\Big], \end{aligned} \tag{18}$$

$$\begin{aligned} B_2 = \frac{1}{2}\Big\{ & 1 + \frac{g^2}{2q_1^2}(q_1 + q_1^{-1})^2 \\ & + \frac{g^4}{4}(2F + 2 + q_1^2 + q_1^{-2})\Big\}, \end{aligned} \tag{19}$$

$$\lambda_1^2 = 1 - \frac{g^2}{2q_1^2} - \frac{g^4}{4}(2F + q_1^{-2}), \tag{20}$$

$$\begin{aligned} \lambda_2^2 = {} & 1 + q_1^2 + \frac{g^2}{2}(2 + q_1^2 + q_1^{-2}) \\ & + \frac{g^4}{4}(2F + 2 + q_1^2 + q_1^{-2}), \end{aligned} \tag{21}$$

where

$$F = -\frac{(1 + q_1^{-2})^2}{2q_1^2}. \tag{22}$$

Because of a misprint or error (reversed signs in A_2^D, B_1^D), the coefficients in [6] (formula (12)), denoted with the superscript D here, must be corrected according to the relations

$$\begin{aligned} A_1 &= A_1^D = \frac{Q + q_1^2 - g^2(1 + q_1^2)}{q_1^2(2 - g^2)}, \\ A_2^D &= 2A_2 = -\frac{g[2 + q_1^2 - Q]}{q_1^2[2 - g^2]}, \end{aligned} \tag{23}$$

$$\begin{aligned} B_1 &= B_1^D = -\frac{g[2 + q_1^2 + Q]}{2q_1^2[2 - g^2]}, \\ B_2^D &= 2B_2 = \frac{q_1^2 + Q + g^2}{q_1^2(2 - g^2)}. \end{aligned} \tag{24}$$

Obviously, Eqs. (5), (7), (8), and (9) imply that the tangential electric field in the slab is given by

$$\begin{aligned} \frac{\omega\varepsilon_0}{k}E_x &= e_x\left(x, |z| < \frac{d}{2}\right) \\ &= \frac{i}{n}\{[X'](A_1 - gA_2 + \cos(qx)(2A_2 - gA_1)) \\ &\quad + [Y'](B_1 - gB_2 + \cos(qx)(2B_2 - gB_1))\}, \end{aligned} \tag{25}$$

where, analogously to (8) and (9), we have defined the z-dependent functions

$$\begin{aligned} [X'] &= \lambda_1 \operatorname{sech}\left(\frac{dkn\lambda_1}{2}\right) \\ &\times [X_1 \sinh(knz\lambda_1) - X_2 \cosh(knz\lambda_1)], \end{aligned} \tag{26}$$

$$\begin{aligned} [Y'] &= \lambda_2 \operatorname{sech}\left(\frac{dkn\lambda_2}{2}\right) \\ &\times [Y_1 \sinh(knz\lambda_2) - Y_2 \cosh(knz\lambda_2)]. \end{aligned} \tag{27}$$

In the vacuum regions, we have the following fields: in the left half-space in Fig. 1,

$$\begin{aligned} H_y\left(x, z + \frac{d}{2} < 0\right) &= \exp(ik\zeta_+) \\ &+ \sum_{p = 0, \pm 1} R_p \exp[ik(\gamma_p x - \beta_p \zeta_+)], \end{aligned} \tag{28}$$

$$\begin{aligned} &\zeta_+ = z + \frac{d}{2}, \quad \gamma_p = p\frac{q}{k}, \quad R_1 = R_{-1}, \\ &\beta_p = [1 - \gamma_p^2]^{1/2} = iV_p, \quad \operatorname{Im}\beta_p = \operatorname{Re}V_p \geq 0, \end{aligned} \tag{29}$$

and in the right half-space in Fig. 1,

$$\begin{aligned} & H_y\left(x, z - \frac{d}{2} > 0\right) \\ &= \sum_{p = 0, \mp 1} T_p \exp[ik(\gamma_p x + \beta_p \zeta_-)], \end{aligned} \tag{30}$$

where

$$\zeta_- \equiv z - \frac{d}{2} > 0, \quad T_1 = T_{-1}.$$

The continuity condition for the tangential electromagnetic field on the interfaces $z = \mp d/2$ leads to the following four equations containing eight unknown quantities X_1, X_2, Y_1, Y_2, R_0, R_1, T_0, T_1:

$$\begin{aligned} &A_1[X_1 + X_2t_1] + B_1[Y_1 + Y_2t_2] \\ &+ 2\cos(qx)[A_2[X_1 + X_2t_1] + B_2[Y_1 + Y_2t_2]] \\ &= 1 + R_0 + 2\cos(qx)R_1, \end{aligned} \tag{31}$$

$$\begin{aligned} &A_1[X_1 - X_2t_1] + B_1[Y_1 - Y_2t_2] \\ &+ 2\cos(qx)[A_2[X_1 - X_2t_1] + B_2[Y_1 - Y_2t_2]] \\ &= T_0 + 2\cos(qx)T_1, \end{aligned} \tag{32}$$

$$\begin{aligned} &\lambda_1(A_1 - gA_2)[X_1t_1 - X_2] + \lambda_2(B_1 - gB_2)[Y_1t_1 - Y_2] \\ &+ \cos(qx)[\lambda_1(2A_2 - gA_1)[X_1t_1 - X_2] \\ &+ \lambda_2(2B_2 - gB_1)[Y_1t_2 - Y_2]] \\ &= -inT_0 + 2n\nu T_1\cos(qx), \end{aligned} \tag{33}$$

$$\begin{aligned} &\lambda_1(A_1 - gA_2)[X_1t_1 + X_2] + \lambda_2(B_1 - gB_2)[Y_1t_2 + Y_2] \\ &+ \cos(qx)[\lambda_1(2A_2 - gA_1)[X_1t_1 + X_2] \\ &+ \lambda_2(2B_2 - gB_1)[Y_1t_2 + Y_2]] \\ &= in(1 - R_0) + 2n\nu R_1\cos(qx). \end{aligned} \tag{34}$$

Here, we use the notation

$$\begin{aligned} t_{1,2} &\equiv \tanh\left(kn\frac{d}{2}\lambda_{1,2}\right), \\ \nu &= \sqrt{\left(\frac{q}{k}\right)^2 - 1}, \quad \operatorname{Re}\nu \ge 0. \end{aligned} \tag{35}$$

The introduction of the $\operatorname{sech}((dkn/2)\lambda_{1,2})$ coefficients in (8), (9) and in (26), (27) is not obligatory, but simplifies the calculations because only tanh-terms defined in (35) then simultaneously appear in all four equations (31)–(34).

3. CALCULATION OF THE RESONANT TRANSMITTANCE THROUGH A MODULATED SLAB

It is convenient to first equate the terms proportional to $\cos(qx)$ in (31)–(34) and to eliminate the unknowns R_1 and T_1 that are not interesting in this study. Thus we derive the following two relations between the constants (X_1, X_2) corresponding to the fundamental beam and the constants (Y_1, Y_2) describing the $\cos(qx)$ mode:

$$Y_1 = k_1X_1 = \frac{\lambda_1(2A_2 - gA_1)t_1 - 2n\nu A_2}{2nB_2\nu - \lambda_2(2B_2 - gB_1)t_2}X_1, \tag{36}$$

$$Y_2 = k_2X_2 = \frac{\lambda_1(2A_2 - gA_1) - 2n\nu A_2t_1}{2nB_2t_2\nu - \lambda_2(2B_2 - gB_1)}X_2. \tag{37}$$

We note that these expressions are exact in the accepted two-mode ($F_0(z) + 2F_1(z)\cos(qx)$) approximation. We now equate the zero-order terms in boundary conditions (31)–(34) (the fundamental x-independent mode); eliminating R_0 and T_0 from these four equations, we then have

$$\begin{aligned} &X_1 \\ &= \frac{in}{inA_1 + inB_1k_1 + \lambda_1(A_1 - gA_2)t_1 + \lambda_2t_2k_1(B_1 - gB_2)}, \end{aligned} \tag{38}$$

$$\begin{aligned} &X_2 \\ &= \frac{in}{inA_1t_1 + inB_1k_1t_2 + \lambda_1(A_1 - gA_2) + \lambda_2k_2(B_1 - gB_2)}. \end{aligned} \tag{39}$$

The transmission coefficient is given by

$$T_0 = X_1(A_1 + k_1B_1) - X_2(t_1A_1 + k_2t_2B_1), \tag{40}$$

which can also be written as

$$T_0 = \frac{\beta(q_1) - \alpha(q_1)}{(1 + \alpha(q_1))(1 + \beta(q_1))}, \tag{41}$$

where $\alpha(q_1)$ and $\beta(q_1)$ can be written as simple functions of q_1, n, t_1, t_2, k_1, k_2 using formulas (16)–(21) for A_1, B_1, A_2, B_2, λ_1, λ_2 with $O(g^4)$ terms neglected,

$$\begin{aligned} &\alpha(q_1) \\ &= \frac{t_1\left[1 + \frac{g^2}{4}(q_1^{-2} + 2q_1^{-4})\right] + t_2k_1g\frac{\sqrt{1 + q_1^2}}{2}q_1^{-2}}{in\left\{1 + \frac{g^2}{2}q_1^{-4} + \frac{k_1g}{2}(1 + q_1^{-2})\right\}}, \end{aligned} \tag{42}$$

$$\begin{aligned} &\beta(q_1) \\ &= \frac{1 + \frac{g^2}{4}(q_1^{-2} + q_1^{-4}) + k_2g\frac{g_1^{-2}}{2}\sqrt{1 + q_1^2}}{in\left\{t_1\left(1 + \frac{g^2}{2}q_1^{-4}\right) + t_2k_2g\frac{1 + q_1^{-2}}{2}\right\}}. \end{aligned} \tag{43}$$

We first consider two trivial consequences of formulas (42) and (43). If the film thickness vanishes ($t_1 = t_2 = 0$), we have

$$\alpha = 0, \quad \beta = \infty,$$

and therefore

$$T_0 = 1.$$

If there is no modulation, then

$$g = 0, \quad \alpha = \frac{t_1}{in}, \quad \beta = \frac{1}{int_1},$$

and we have the well-known result

$$T_0(g = 0) = \frac{2n}{2n\cosh(knd) + im^2\sinh(knd)}, \qquad m^2 = n^2 - 1. \tag{44}$$

We next consider the most interesting case of a thick metal film with thickness d greater than the skin depth, that is,

$$t_1 = 1 - 2\zeta_1, \quad t_2 = 1 - 2\zeta_2, \tag{45}$$

where

$$\zeta_1 = \exp(-knd), \quad \zeta_2 = \exp\left(-knd\sqrt{1 + q_1^2}\right), \tag{46}$$

and $\zeta_1 \ll 1$, $\zeta_2 \ll 1$. In (46), we approximate $\lambda_{1,2}$ from (20) and (21) as

$$\lambda_1 = 1, \quad \lambda_2 = \sqrt{1 + q_1^2}.$$

Moreover, for an SPP resonance,

$$\frac{k}{q} = \frac{m}{n}, \quad m = \sqrt{n^2 - 1},$$

as we see in what follows, and therefore

$$q_1^{-1} = m$$

and

$$\zeta_2 = \exp\left(-knd\sqrt{1 + \frac{1}{m^2}}\right) = \exp\left(-\frac{kdn^2}{m}\right). \tag{47}$$

In this regime, we derive from the definitions of $k_{1,2}$ in (36) and (37) that

$$k_1 = \frac{2gm(n - m)}{\frac{2m(1 + n^2)}{n^2}(q_1^{-1} - m) - 4\zeta_2 - \frac{n^2 g^2}{2}}, \tag{48}$$

$$k_2 = \frac{2gm(n - m)}{\frac{2m(1 + n^2)}{n^2}(q_1^{-1} - m) + 4\zeta_2 - \frac{n^2 g^2}{2}}. \tag{49}$$

It is important to note that the general formula (41) considered in the complex wavenumber plane ($\mathrm{Re}\, q_1$, $\mathrm{Im}\, q_1$) has two poles at the points where

$$\alpha(Q_1^+) = \beta(Q_1^-) = -1.$$

With the aid of (48) and (49), we can show that these complex wavenumbers are given by

$$(Q_1^+)^{-1} = m + \frac{2n^2\zeta_2}{m(1 + n^2)} + \frac{g^2 n^3}{4m(1 + n^2)^2} \times [n(1 + n^2) - 2m(n - m)(n + m^3)] - ig^2\frac{n^5(n - m)^2}{2(1 + n^2)^2}, \tag{50}$$

$$Q_1^-(\zeta_2) = Q_1^+(-\zeta_2). \tag{51}$$

Two remarks are appropriate to formulas (50) and (51). The first concerns the absence of terms proportional to ζ_1, that is, the limit $t_1 = 1$ is appropriate, but the finite penetration depth for the cos(qx) mode is crucial because there is no resonant enhancement of the transmission at $\zeta_2 = 0$. The second remark is that we neglect terms of the order $O(g^4)$ in (50) and (51). It is now clear that if we set

$$\begin{aligned} \xi &= (q_1^{-1} - m)\frac{2m(1 + n^2)}{n^2} \\ &= \left(\frac{k}{q} - \frac{m}{n}\right)\frac{2m(1 + n^2)}{n}, \end{aligned} \tag{52}$$

then for small values of ξ such that terms of the order $\xi\zeta_2$, ξg^2 can be neglected, we have

$$\begin{aligned} \alpha &= \frac{\xi - 4\zeta_2 + g^2 M_1}{in[\xi - 4\zeta_2 + g^2 M_2]}, \\ \beta &= \frac{\xi + 4\zeta_2 + g^2 M_1}{in[\xi + 4\zeta_2 + g^2 M_2]}, \end{aligned} \tag{53}$$

where

$$\begin{aligned} M_1 &= m^2 n(n - m) - \frac{n^2}{2}, \\ M_2 &= mn^2(n - m) - \frac{n^2}{2}. \end{aligned} \tag{54}$$

From (41), (53), and (54), we derive the transmittance of a dissipationless film in the form

$$T = |T_0|^2 = \frac{4\tilde{g}^4}{[(\tilde{\Delta} - 1)^2 + \tilde{g}^4][(\tilde{\Delta}^2 + 1)^2 + \tilde{g}^4]}, \tag{55}$$

where we have introduced the renormalized modulation

$$\tilde{g}^2 = \frac{g^2 n^2 m(n-m)^2}{4\zeta_2(n^2+1)} \quad (56)$$

and the detuning from the surface plasmon polariton frequency

$$\begin{aligned}\tilde{\Delta} &= -\frac{m(1+n^2)}{2n\zeta_2}\left(\frac{k}{q}-\frac{m}{n}\right) \\ &+ \frac{g^2 n}{8\zeta_2(1+n^2)}[n^3+n-2m(n-m)(n^3+m)].\end{aligned} \quad (57)$$

Due to the equality

$$(n-m)^2(n+n^3+2m) \equiv n^3+n-2m(n-m)(n^3+m),$$

our formulas (56) and (57) are analogous to formulas (33) and (34) in [6], but ζ_2 is given by (47) and not by $\zeta = \zeta_1$ as defined in [6]. Only in the limit $n \longrightarrow \infty$ do both formulations coincide,

$$\lim_{n\to\infty}\left(n - \frac{n^2}{m}\right) = 0.$$

The physical effects associated with the two small parameters ζ_1 and ζ_2 were not discussed in [6]. Although this was not written explicitly, these authors assumed that $n \gg 1$ in order to consider the influence of a single small parameter $\zeta = \zeta_1 \approx \zeta_2$. Our treatment of the strong skin effect in the modulated slab (summarized in formulas (55)–(57)) is free of the restriction $n \gg 1$, that is, the formulas are valid for all $1 < n < \infty$ provided of course that the less restrictive conditions written after formula (46) are fulfilled. Our new and (as we believe) more correct analytic formulation (55)–(57) leads to appreciable differences from the previously proposed analytic formulation [6] for a concrete plasma parameterization given in Section 4.

4. TRANSMISSION OF ELECTROMAGNETIC WAVES THROUGH A SLAB OF COLLISIONLESS PLASMA

As a specific example, we consider the case where

$$\begin{aligned} n^2 &= \frac{\omega_p^2}{\omega^2} - 1 = \frac{2-x^2}{x^2}, \\ \omega &= \frac{\omega_p}{\sqrt{2}}x, \quad 0 < x < 1. \end{aligned} \quad (58)$$

If we introduce the dimensionless parameters

$$D = \frac{\omega_p d}{c}, \quad p = \frac{\omega_p}{cq}, \quad (59)$$

the zero-order resonance frequency that follows from the condition

$$\frac{k}{q} = \frac{m}{n}$$

is equal to the following value of x:

$$x_0 = \sqrt{1 + \frac{2}{p^2} - \sqrt{1 + \frac{4}{p^4}}}, \quad 0 < x_0 < 1. \quad (60)$$

The value $x_0(p)$ is defined for all $0 < p < \infty$. In the special case where $p \gg 1$, $x_0(p)$ is very small, i.e., $x_0 \approx \sqrt{2}/p$. On the other hand, if $p \ll 1$, x_0 is very close to one,

$$x_0 \approx 1 - \frac{p^2}{8}.$$

It is instructive to note that

$$\zeta_2(x) = \exp\left(-D\frac{1-x^2/2}{\sqrt{1-x^2}}\right) \quad (61)$$

tends to the constant value exp(–D) for small x, but if x is close to one, then

$$\zeta_2 \approx \exp\left(-\frac{D}{p}\right), \quad (62)$$

whereas

$$\zeta_1(x=1) = \exp\left(-\frac{D}{\sqrt{2}}\right),$$

and therefore using the result in [6] for $p \ll 1$ gives substantial deviations from the present theory. We consider the number and exact positions of points where the transmittance T is equal to one. We first note that formula (55) can be represented in the form

$$2\sqrt{T^{-1}-1} = \left(\frac{\tilde{\Delta}}{\tilde{g}}\right)^2 - \tilde{g}^{-2} + \tilde{g}^2 = A(n, p, D, g). \quad (63)$$

In writing Eq. (63), we have fixed

$$\omega = \omega_p/\sqrt{1+n^2},$$

also bearing in mind the definitions in Eq. (59). The transcendental equation

$$A(n, p, D, g) = 0 \tag{64}$$

can be solved numerically or approximately by analytic treatment using the fact that $g \ll 1$ and D is of the order of one, and hence

$$\zeta_2(n) = \exp\left[-\frac{Dn^2}{\sqrt{n^4 - 1}}\right] \ll 1 \tag{65}$$

for every $n > 1$. An analysis of Eq. (64) for the model in [6] must be based on

$$\zeta_1(n) = \exp\left[-\frac{Dn}{\sqrt{n^2 + 1}}\right] \ll 1 \tag{66}$$

instead of Eq. (65). Using formulas (56) and (57), we rewrite Eq. (64) as

$$\begin{aligned} a^2(n) = \exp\left[-\frac{2Dn^2}{\sqrt{n^4 - 1}}\right] + 2g^2 a(n) b(n) \\ - g^4[b^2(n) + c^2(n)] = B(n), \end{aligned} \tag{67}$$

where

$$\begin{gathered} a(n) = \frac{1 + n^2}{2n} m\left[\frac{p}{(1 + n^2)^{1/2}} - \frac{m}{n}\right], \\ m^2 \equiv n^2 - 1, \end{gathered} \tag{68}$$

$$b(n) = \frac{n(n - m)^2(n^3 + n + 2m)}{8(1 + n^2)}, \tag{69}$$

$$c(n) = \frac{n^2 m(n - m)^2}{4(1 + n^2)}. \tag{70}$$

If we neglect the right-hand side of Eq. (67), we derive the zero-order solution n_0, given by formula (60), that is,

$$n_0 = \sqrt{\frac{p^2 + \sqrt{p^4 + 4}}{2}}. \tag{71}$$

If $B(n_0) > 0$, we find two formal maxima of the transmittance ($T_{\max} = 1$) at points $n_\pm$, where

$$n_\pm = n_0 \pm \frac{2n_0^3}{1 + n_0^4}\sqrt{B(n_0)}, \tag{72}$$

within first-order perturbation theory. The minus sign in Eq. (72) can lead to a nonphysical solution $n_- < 1$ if the correction term in (72) is sufficiently large. In the limiting case where $B(n) < 0$ for every n, the transmittance never attains a maximum value of one. Nevertheless, the transmittance can have maximum values that are smaller than one (Figs. 2b, 2c). This quantitative analysis was confirmed by numerical calculations shown in Fig. 2. Here, $D = 1$, $g = 0.2$, and $p = 0.1$, 1, and 10 in the respective Figs. 2a–2c. The numerical results based on formula (66), that is, the Dykhne model [6], are shown by dashed lines. We see not more than two maxima in all cases. The Dykhne model predicts only one peak in the cases $p = 0.1$ and $p = 1$, whereas our model leads to two maxima in these two cases.

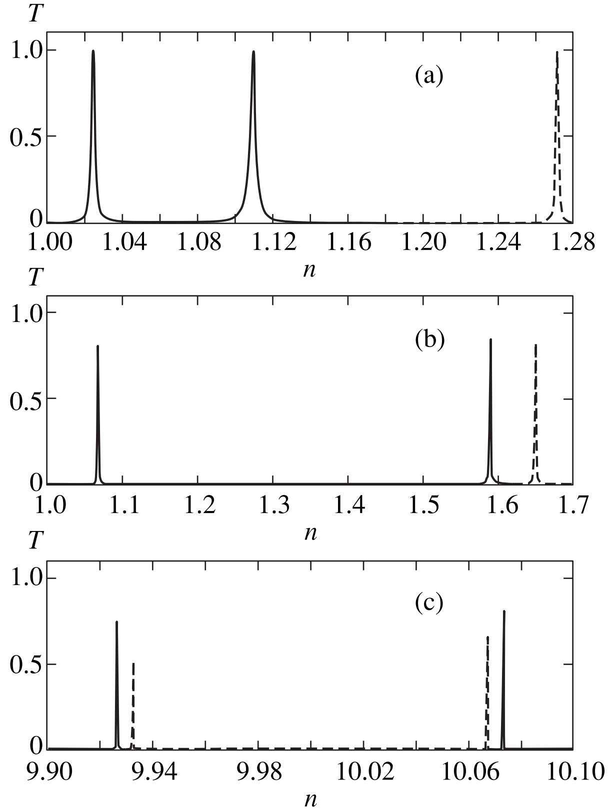

Fig. 2. Transmittance as a function of n at $D = 1$, $g = 0.2$, and $p = 0.1$ (a), 1 (b), 10 (c). Our results—continuous lines; model [6]—dashed lines.

5. CONCLUSIONS

We have presented a method to analytically describe the resonant transmittance of electromagnetic waves through periodically modulated films. The phenomenological description of the medium $|z| < d/2$ through Eq. (1) allows complex values of the parameters

$$n = n_1 - in_2, \quad g = g_1 + ig_2,$$

but in this paper, we analyze in detail only the dissipationless case (real values of n and g). In the framework of the same physical model, it is not difficult to analyze the more general parameterization

$$\varepsilon(x) = \tilde{\varepsilon}_0 + \tilde{\varepsilon}_1 \cos(qx)$$

(where both numbers $\tilde{\varepsilon}_0$, $\tilde{\varepsilon}_1$ are complex) and to consider oblique incidence of the primary field. The investigation of the interaction of incident light with surface plasmon modes complements the study in [6] as well as the analytical results in [8].

ACKNOWLEDGMENTS

We thank Drs. J.R. Ockendon and G. Kozyreff for bringing the transmission problem to our attention and for interesting discussions. Dr. Genchev was supported by the Royal Society (UK) through a scientific project with OCTAM (Oxford, UK) and the Institute of Electronics (Sofia, Bulgaria).

REFERENCES

1. H. A. Bethe, Phys. Rev. **66**, 163 (1944).
2. T. W. Ebbesen, H. J. Lezec, H. F. Ghaemi, *et al.*, Nature **391**, 667 (1998).
3. A. K. Sarychev, V. A. Podolsky, A. M. Dykhne, and V. M. Shalaev, IEEE J. Quantum Electron. **38**, 956 (2002).
4. F. J. Garcia-Vidal and J. B. Pendry, Phys. Rev. Lett. **77**, 1163 (1996).
5. A. Barbara, P. Quemerais, E. Busfaret, *et al.*, Eur. Phys. J. D **23**, 143 (2003).
6. A. M. Dykhne, A. K. Sarychev, and V. M. Shalaev, Phys. Rev. B **67**, 195402 (2003).
7. P. B. Johnson and R. W. Cristy, Phys. Rev. B **6**, 4370 (1972).
8. S. A. Darmanyan and A. V. Zayats, Phys. Rev. B **67**, 035424 (2003).

Journal of Experimental and Theoretical Physics, Vol. 99, No. 6, 2004, pp. 1137–1149.
Translated from Zhurnal Éksperimental'noĭ i Teoreticheskoĭ Fiziki, Vol. 126, No. 6, 2004, pp. 1303–1316.
Original Russian Text Copyright © 2004 by Prudnikov, Taĭchenachev, Tumaĭkin, Yudin, Nienhuis.

NUCLEI, PARTICLES, AND THEIR INTERACTION

Basis of Polarization-Dressed States of an Atom in an Elliptically Polarized Resonant Field

O. N. Prudnikov[a,b], A. V. Taĭchenachev[a,b], A. M. Tumaĭkin[a,b],
V. I. Yudin[a,b], and G. Nienhuis[c]
[a]*Novosibirsk State University, Novosibirsk, 630090 Russia*
[b]*Institute of Laser Physics, Siberian Division, Russian Academy of Sciences, Novosibirsk, 630090 Russia*
[c]*Huygens Laboratorium, University of Leiden, 2300 RA Leiden, The Netherlands*
e-mail: llf@admin.nsu.ru, llf@laser.nsc.ru

Received June 21, 2004

Abstract—A basis of polarization-dressed states is proposed for atomic energy levels degenerate in the total angular momentum projections in the case of interaction with elliptically polarized light. It is shown that instead of selection rules for the magnetic quantum number, the interaction in this basis can be presented as the sum of direct transitions between corresponding pairs of polarization-dressed states of the upper and lower levels. The explicit form of the basis is derived for ten possible combinations of dipole transitions between energy levels with angular momenta $J = 0$, 1/2, 1, 3/2, and 2. The problem of Rabi oscillations in such a system is considered as an application. *© 2004 MAIK “Nauka/Interperiodica”.*

1. INTRODUCTION

The problem of interaction of resonant polarized monochromatic light with an atom whose energy levels are degenerate in the total angular momentum projections is one of the central problems in quantum optics; this problem was solved by many authors in various approximations [1–5]. Using light polarization (generally elliptical), it is possible to control both intrinsic degrees of freedom of atoms (e.g., the anisotropy state of atoms) and their translatory motion. It is well known that allowance for degeneracy of atomic levels reduces the pattern of the nonlinear interaction of polarized light to a complex multilevel diagram. It is difficult to obtain an analytic solution to this problem in view of the large number of equations for magnetic sublevels associated with the nonlinear interaction with various components of the light field polarization. The interaction pattern is simplified to a certain extent in particular cases of purely linear and circular polarization, when a multilevel system can be reduced to a set of independent nondegenerate two-level systems governed by the magnetic quantum number selection rules. Such a simplification is associated with the appropriate choice of the quantization axis (which is chosen along the field in the case of linear polarization and at right angles to the polarization plane in the case of circular polarization of light). The appropriate choice of the quantization axis along the axis of the cylinder whose cross section coincides with the polarization ellipse also simplifies the analysis of resonant interaction of degenerate atoms with elliptically polarized light [6].

It should be noted that transitions $1 \longleftrightarrow 0$, $1 \longrightarrow 1$, and $1/2 \longrightarrow 1/2$ are preferred in polarization problems since these transitions are characterized by only one effective interaction parameter [7]. In particular, it is possible in these cases to prove exact integrability of the Maxwell–Bloch equations and to obtain one- and two-soliton solutions in problems of propagation of light pulses in a nonlinear medium [7].

A general formulation of the problem of interaction of resonant elliptically polarized light with a two-level system degenerate in the total angular momentum projections was proposed in [8]. However, only particular solutions, which are associated with the existence of stationary coherent states (also referred to as elliptically dark states) describing the effect of coherent population trapping (CPT), were determined in [8]. As a continuation of [8] and a series of our subsequent publications [9–14], here we attempt to obtain all the remaining analytic solutions to the Schrödinger equation from the complete orthonormal set of states of a degenerate atom in elliptically polarized light.

The basic idea of our approach to the problem lies in determining a basis set of the wavefunctions of the unperturbed Hamiltonian, in which light-induced dipole transitions between degenerate energy levels can be presented as a set of independent nondegenerate two-level systems (as in the case of purely linear or circular polarization) and which would take into account all peculiarities of the interaction with elliptic polarization of the light field. The determination of such a polarization-dressed basis is equivalent to representing the tensor part of the interaction operator in block-diagonal form.

It should be noted that the problem of reduction of a degenerate two-level system to a set of independent non degenerate two-level systems was formulated for the first time in general form in [15], where transition $J_a = 2 \longrightarrow J_b = 1$ was considered as an example. A basis of polarization-dressed states was used in [9] in implicit form in the problem of determining the stationary state of the density matrix of atoms in an elliptically polarized field. Here, we propose a new basis instead of the generally accepted Zeeman basis of angular momentum for problems of interaction of resonant elliptically polarized light with atomic and molecular energy levels degenerate in angular momentum projections. This basis, which will be referred to as a polarization-dressed basis, is defined as the proper basis of optical shift operators. It is presented as an expansion in the basis of magnetic sublevels with coefficients depending only on the light field polarization; i.e., the basis is initially "tuned" to the field polarization. After the application of the light field, the selection rules in the dipole interaction change: only direct dipole transitions between states with identical eigenvalues $\lambda_i^b - \lambda_i^\alpha = 0$ are realized in the new basis instead of dipole transitions between magnetic sublevels $m_a - m_b = 0, \pm 1$ of the lower and upper levels. In Section 3, general properties of the new basis are considered. The explicit analytic form of new states and their eigenvalues is determined in Section 5 for ten possible combinations of dipole transitions between energy levels with angular momenta $J = 0$, 1/2, 1, 3/2, and 2; it is shown that the problem can be presented as the sum of independent two-level systems. By way of example, the solution of the problem of Rabi oscillations in a system with degenerate energy levels is considered in Section 4.

2. FORMULATION OF THE PROBLEM

In the dipole approximation, the Hamiltonian describing the interaction of an atom degenerate in the angular momentum projections with a monochromatic elliptically polarized resonant field can be written in the form

$$\hat{H}_{\text{int}} = -\mathbf{E}\hat{\mathbf{d}} = \Omega\hat{V}\exp(-i\omega t) + \text{h.c.}, \tag{1}$$

where the polarization-angular part

$$\hat{V} = q_+\hat{d}_{1,-1} + q_-\hat{d}_{1,+1} \tag{2}$$

and field amplitude E_0 appearing in the Rabi frequency

$$\Omega = -E_0\langle J_a\|d\|J_b\rangle/\hbar$$

are singled out as cofactors. In the coordinate system in which the principal semiaxes of the polarization ellipse coincide with the x and y axes and the angular momentum quantization axis z is orthogonal to the ellipse plane, the circular field components $q_\pm$ can be written in the form

$$q_+ = \sin(\varepsilon + \pi/4), \quad q_- = \cos(\varepsilon + \pi/4), \tag{3}$$

where ε is the light ellipticity parameter defined in the interval $-\pi/4 \le \varepsilon \le +\pi/4$ and $|\tan\varepsilon|$ is the ratio of the semiminor axis of the ellipse to the semimajor axis. The matrix elements of the angular part of the dipole momentum operator $\hat{d}_{1,\pm1}$ in the standard basis of the magnetic sublevels $|J_a, m_a\rangle$ and $|J_b, m_b\rangle$ of the lower and upper levels can be expressed in terms of the Clebsch–Gordan coefficients

$$\langle J_b, m_b|\hat{d}_{1,\pm1}|J_a, m_a\rangle = C^{J_b, m_b}_{J_a, m_b;\, 1, \pm1}. \tag{4}$$

We seek the solution to the time-dependent Schrödinger equation

$$i\frac{\partial\Psi}{\partial t} = (\hat{H}_0 + \hat{H}_{\text{int}})\Psi \tag{5}$$

in the form of an expansion in a certain orthonormal basis of vectors of state of degenerate lower $|(a)j\rangle$ and upper $|(b)k\rangle$ levels:

$$\begin{aligned}\Psi &= \exp\left(-i\frac{E_a}{\hbar}t\right)\sum_{j=1}^{2J_a+1} a_j(t)|(a)j\rangle \\ &+ \exp\left(-i\frac{E_b}{\hbar}t\right)\sum_{k=1}^{2J_b+1} b_k(t)|(b)k\rangle.\end{aligned} \tag{6}$$

Indices $k = 1, 2, \ldots, 2J_b + 1$, and $j = 1, 2, \ldots, 2J_a + 1$ label the states of this basis for the upper and lower energy levels, respectively. The orthonormality condition indicates that

$$\begin{gathered}\langle(a)i|(a)j\rangle = \delta_{i,j}, \quad \langle(b)i|(b)j\rangle = \delta_{i,j}, \\ \langle(a)i|(b)j\rangle = 0.\end{gathered} \tag{7}$$

Obviously, the generally accepted Zeeman basis of angular momentum eigenstates $|J_b, m_b\rangle$, $|J_a, m_a\rangle$ is a particular case of this basis.

The equations for probability amplitudes $a_j(t)$ and $b_k(t)$ follow from expressions (5) and (6):

$$\dot{a}_k = -i\Omega\exp(-i\delta t)\sum_{i=1}^{2J_b+1}\langle(a)k|\hat{V}^+|(b)i\rangle b_i, \tag{8}$$

$$\dot{b}_j = -i\Omega^*\exp(i\delta t)\sum_{k=1}^{2J_a+1}\langle(b)j|\hat{V}|(a)k\rangle a_k. \tag{9}$$

In the general case of an arbitrary basis, system of equations (8), (9) is as complex as in the case of the standard basis of magnetic sublevels since states with different values of $i \ne j$ are entangled. However, this system can be substantially simplified in a basis in which interaction operators $\hat{V}$ and $\hat{V}^+$ connect only pairs of states $|(a)j\rangle$ and $|(b)k\rangle$ of the upper and lower levels. It will be shown below that such a diagonalization of the tensor part of the interaction is always possible and the resultant eigenstates define the basis which will be referred to as the basis of polarization-dressed states (PDS) $|(a)i\rangle$ and $|(b)j\rangle$ of the lower and upper levels, respectively. This is because it takes into account peculiarities of interaction with the light field only as regards its polarization and it can be expanded in the magnetic sublevel basis with coefficients depending on the field polarization:

$$\begin{aligned} |(a)i\rangle &= \sum_{m_a=-J_a}^{m_a=+J_a} A_{i,m_\alpha}(\varepsilon)|J_a, m_a\rangle, \\ |(b)i\rangle &= \sum_{m_b=-J_b}^{m_b=+J_b} B_{i,m_b}(\varepsilon)|J_b, m_b\rangle. \end{aligned} \tag{10}$$

Here, matrices $\hat{A}$ and $\hat{B}$ realize a transition from the magnetic sublevel basis to a new PDS basis. In solving Eqs. (5), (8), and (9), one encounters operators $\hat{V}^+\hat{V}$ and $\hat{V}\hat{V}^+$ which, being bilinear combinations of the interaction Hamiltonian, describe quadratic Stark shifts of levels depending on ellipticity. It can be seen that these operators are Hermitian matrices and, hence, can always be transformed to diagonal form using appropriate unitary transformations. It will be shown in the next section that PDSs are eigenstates of operators $\hat{V}^+\hat{V}$ and $\hat{V}\hat{V}^+$, which are diagonalized by matrices $\hat{A}$ and $\hat{B}$:

$$\begin{aligned} \hat{A}\hat{V}^+\hat{V}\hat{A}^+ &= \mathrm{diag}\{\lambda_i^a\}, \\ \hat{B}\hat{V}\hat{V}^+\hat{B}^+ &= \mathrm{diag}\{\lambda_i^b\}. \end{aligned} \tag{11}$$

It should be noted that, in the general state of elliptic polarization, matrices $\hat{A}$ and $\hat{B}$ are not rotation operators, which complicates analysis. The problem of determination of the proper basis of optical shift operators was considered earlier in [9, 15, 16]. Proceeding from these studies, we will consider the properties of the PDS basis in the general form without determining the explicit form of matrices $\hat{A}$ and $\hat{B}$.

3. PROPERTIES OF THE PDS BASIS

Operator $\hat{V}^+\hat{V}$ acts on the lower level and has eigenvalues λ_i^a in the new orthonormal basis of PDSs, which can be determined from the equation

$$\hat{V}^+\hat{V}|(a)i\rangle = \lambda_i^a|(a)i\rangle, \quad \langle(a)i|(a)j\rangle = \delta_{i,j}. \tag{12}$$

Analogously, operator $\hat{V}\hat{V}^+$ acts on states $|(b)j\rangle$ of the upper level:

$$\hat{V}\hat{V}^+|(b)j\rangle = \lambda_j^b|(b)j\rangle, \quad \langle(b)j|(b)k\rangle = \delta_{k,j}. \tag{13}$$

Eigenvalues of operators $\hat{V}^+\hat{V}$ and $\hat{V}\hat{V}^+$ are real nonnegative numbers $\lambda_i^a \ge 0$ and $\lambda_j^b \ge 0$. Zero eigenvalues $\lambda_i^a = 0$ and $\lambda_j^b = 0$ correspond to CPT states at the upper and lower levels. In our earlier publications [8, 10, 11], we derived analytic expressions for CPT states for various types of dipole transitions. It should be noted once again that CPT states are a part of the complete orthonormal set of the PDS basis with corresponding zero eigenvalues.

It can be proved that if we eliminate zero subspaces from matrices $\hat{V}^+\hat{V}$ and $\hat{V}\hat{V}^+$ and label eigenvalues at each sublevel, the sets of eigenvalues of matrices $\hat{V}^+\hat{V}$ and $\hat{V}\hat{V}^+$ in the truncated space will coincide. Indeed, we have

$$(\hat{V}\hat{V}^+)\hat{V}|(a)i\rangle = \lambda_i^a\hat{V}|(a)i\rangle, \tag{14}$$

$$(\hat{V}^+\hat{V})\hat{V}^+|(b)j\rangle = \lambda_j^b\hat{V}^+|(b)j\rangle. \tag{15}$$

Consequently, $\hat{V}|(a)i\rangle$ is an eigenvector of

$$\hat{V}^+\hat{V} \longrightarrow \hat{V}|(a)i\rangle \sim |(b)i\rangle,$$

while $\hat{V}^+|(b)j\rangle$ is an eigenvector of

$$\hat{V}\hat{V}^+ \longrightarrow \hat{V}^+|(b)j\rangle \sim |(a)j\rangle.$$

Thus, nonzero eigenvalues of $\hat{V}^+\hat{V}$ give a set of eigenvectors $|(a)i\rangle$, such that

$$|(b)i\rangle = \frac{\hat{V}|(a)i\rangle}{\sqrt{\langle(a)i|\hat{V}^+\hat{V}|(a)i\rangle}} = \frac{\hat{V}|(a)i\rangle}{\sqrt{\lambda_i^a}}, \tag{16}$$

$$|(a)i\rangle = \frac{\hat{V}^+|(b)i\rangle}{\sqrt{\langle(b)i|\hat{V}\hat{V}^+|(b)i\rangle}} = \frac{\hat{V}^+|(b)i\rangle}{\sqrt{\lambda_i^b}}. \tag{17}$$

It follows hence that the set of eigenvalues of operators $\hat{V}^+\hat{V}$ and $\hat{V}\hat{V}^+$ is the same:

$$\lambda_i^b = \lambda_i^a = \lambda_i. \tag{18}$$

Light-induced transitions combine only *i* pairs of basis vectors of different levels corresponding to the same (nonzero!) eigenvalues. In this case, index $i = 1, 2, \ldots$, r labels states in the truncated space (without zero subspace). The number r of such transitions in the new basis is equal to $r = 2J_a$ for transitions $J_a = J \longrightarrow J_b = J$ (J is an integer), $r = 2J_a - 1$ for transitions $J_a = J \longrightarrow J_b = J - 1$, and $r = 2J_a + 1$ for transitions $J_a = J \longrightarrow J_b = J + 1$ and $J_a = J \longrightarrow J_b = J$ (J is a half-integer). Substituting now expressions (16) and (17) into (8) and (9), we find that the interaction matrices on the right-hand sides of Eqs. (8) and (9) become diagonal with eigenvalues equal to $\sqrt{\lambda_j}$, and the interaction Hamiltonian can be reduced to the diagonal form:

$$\hat{V} = \sum_i \sqrt{\lambda_i}|(a)i\rangle\langle(b)i|. \tag{19}$$

The interaction Hamiltonian $\hat{V}$ presented in such a form essentially defines the new selection rules

$$\lambda_i^b - \lambda_i^a = 0$$

between the states of the upper and lower levels, while values $\sqrt{\lambda_j}$ themselves can be regarded as new quantum numbers replacing angular momentum and its projections.

Thus, for preset ellipticity of light and angular momenta of energy levels, we can first construct a polarization-dressed basis determined by the polarization alone and independent of the intensity of light and then solve the problem of interaction analogous in many respects to the problem of interaction with a nondegenerate two-level atom. By way of example of application of PDSs, we consider the modification of the solutions to the well-known problem of Rabi oscillations when degeneracy of energy levels is taken into account.

4. PROBLEM OF RABI OSCILLATIONS FOR DEGENERATE LEVELS

Substituting expression (19) into Eqs. (8), (9), we find that the equation for probability amplitudes of an individual pair of states with identical eigenvalues, which are coupled by the field in light-induced transition $|(a)j\rangle \longrightarrow |(b)j\rangle$, can be transformed to the equation known from the theory of a two-level atom [17, 18]:

$$\dot{b}_j = i\Omega_j^* \exp(-i\delta t)a_j, \tag{20}$$

$$\dot{a}_j = i\Omega_j \exp(i\delta t)b_j, \tag{21}$$

with renormalized Rabi frequency Ω_j

$$\Omega_j = \Omega\sqrt{\lambda_j}. \tag{22}$$

It can be seen that the dependence on the external field intensity is contained in Ω and the entire possible dependence on ellipticity for a specific transition is contained in factor $\sqrt{\lambda_j}$. The solution to dynamic equations (20), (21) is well known and its explicit form is determined by the initial conditions and by the interaction initiation mode. For example, when interaction appears suddenly, we assume that the atom at instant $t = 0$ is at the lower level with an isotropic distribution over magnetic sublevels, which is also isotropic in the new basis states

$$a_j(t=0) = \frac{1}{\sqrt{2J_a+1}}, \quad b_j(t=0) = 0.$$

Using the normalization condition for the wavefunction of the atom in the whole,

$$\sum_{i=1}^{2J_a+1} |a_i(t)|^2 + \sum_{i=1}^{2J_b+1} |b_i(t)|^2 = 1,$$

under the chosen initial conditions, we can single out the normalization for each transition between the upper and lower PDSs separately,

$$|a_i(t)|^2 + |b_i(t)|^2 = \frac{1}{2J_a+1}, \tag{23}$$

and treat this transition as an independent two-level system. In this case, the solution to system (20), (21) for each *j*th pair of states of the upper and lower levels formally coincides with the solution to the problem of Rabi oscillations for a two-level atom [17]:

$$a_j = \frac{\exp(-i\delta t/2)}{\sqrt{2J_a+1}}\left[\cos(\Delta_j t) + i\frac{\delta}{2\Delta_j}\sin(\Delta_j t)\right], \tag{24}$$

$$b_j = -i\frac{1}{\sqrt{2J_a+1}}\frac{\Omega_j}{\Delta_j}\exp\left(\frac{i\delta t}{2}\right)\sin(\Delta_j t). \tag{25}$$

Here, $\Delta_j = \sqrt{\delta^2/4 + \lambda_j\Omega^2}$ is the effective Rabi frequency for the *j*th transition and $\delta = \omega_{ba} - \omega$ is the detuning of the laser field from the atomic resonance. The wavefunction of an atom in the field is the sum of such two-level systems and CPT states that do not interact with light. Consequently, analogously to a conventional two-level system, new states of the upper and lower levels (except CPT states) are split by the field and shifted relative to the unperturbed states with energies E_a and E_b [17]. Substituting solutions (24), (25) into Eq. (6), we find that the wavefunction $\Psi(t)$ of the atom is a superposition of $4r$ stationary states (four states in each two-level transition) whose quasi-energies, taking into account of eigenvalues λ_j determined above, have the form

$$\begin{aligned} E_a^+(j) &= E_a + \delta/2 + \Delta_j, \\ E_a^-(j) &= E_a + \delta/2 - \Delta_j, \end{aligned} \tag{26}$$

$$\begin{aligned} E_b^+(j) &= E_b - \delta/2 + \Delta_j, \\ E_b^-(j) &= E_b - \delta/2 - \Delta_j. \end{aligned} \tag{27}$$

Thus, a transition to the PDS basis is equivalent to the reduction of a complex multilevel system to a set of *r* independent two-level systems. Energy level splitting in a two-level system is due to nonzero field amplitude (Rabi frequency). In addition, the solution should be supplemented with the corresponding stationary CPT

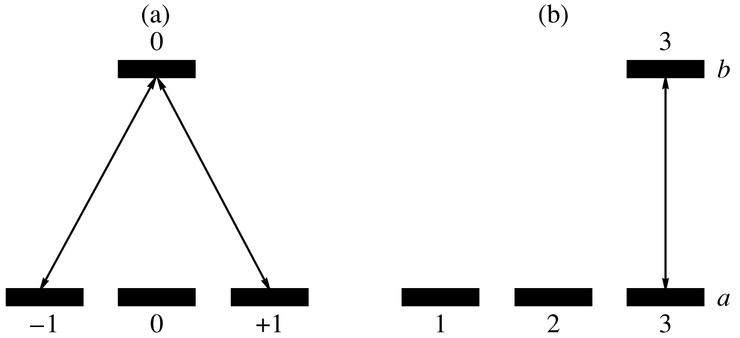

Fig. 1. Diagram of interaction of elliptically polarized light in the (a) magnetic sublevel and (b) PDS basis for optical transition $J_a = 1 \longrightarrow J_b = 0$.

states with unperturbed energies E_a and E_b, which completely defines the solution to the dynamic problem for a two-level degenerate atom in an arbitrarily polarized resonant field. It should also be noted that such a proper PDS basis can be used both for stationary problems with relaxation [9] and for nonstationary problems in the limit $\gamma t \ll 1$ since the PDS basis is constructed from the basis of nonsplit magnetic sublevels taking into account only the tensor part of the interaction. The main property of the new basis is the absence of coherence between PDSs at each level in density matrix $\hat{\rho}$,

$$\begin{aligned}\langle (a)i|\hat{\rho}_{aa}|(a)j\rangle &= |a_j|^2\delta_{i,j},\\ \langle (b)i|\hat{\rho}_{bb}|(b)j\rangle &= |b_j|^2\delta_{i,j},\end{aligned} \tag{28}$$

while Zeeman coherence of the levels in the magnetic sublevel basis differs from zero.

5. EXAMPLES OF POLARIZATION-DRESSED STATES

In the general case, a new basis with an explicit dependence on the ellipticity of eigenstates and eigenvalues can be found using the procedures of diagonalization of matrices, which are well known in linear algebra [15]. Unfortunately, it is extremely difficult to derive analytic expressions for eigenvectors and eigenvalues of PDSs for large values of angular momenta. However, for transitions with small values of the angular momentum of levels (J = 0, 1/2, 1, 3/2, and 2), we can easily construct a PDS basis as a linear superposition of the wavefunctions of magnetic sublevels proceeding from the explicit form of elliptically dark states, which must be orthogonal to PDSs since they are a part of the PDS basis [12]. These states $|\Psi_i^{(NC)}(a)\rangle$ for the lower level and $|\Psi_i^{(NC)}(b)\rangle$ for the upper level can be determined from the equations

$$\hat{V}|\Psi_i^{(NC)}(a)\rangle = 0, \quad \hat{V}^{+}|\Psi_i^{(NC)}(b)\rangle = 0. \tag{29}$$

The corresponding eigenvalues are

$$\lambda_i^a = \lambda_i^b = 0.$$

In addition, we observe the following symmetry in the basis states for reversed pairs of optical transitions (i.e., for optical transitions that transform into each other upon the replacement of the upper level by the lower level, $a \longleftrightarrow b$. The PDS basis vectors of reversed optical transitions can be obtained by changing the indices $a \longleftrightarrow b$ and reversing the sign of projection m_i of the Zeeman wavefunctions. Thus, the procedure of transformation of coefficients in matrices A and B (10) of basis vectors for reversed optical transitions has the form

$$\begin{aligned}A_{i,m}(J_b \longrightarrow J_a) &= B_{i,-m}(J_a \longrightarrow J_b),\\ B_{i,m}(J_b \longrightarrow J_a) &= A_{i,-m}(J_a \longrightarrow J_b).\end{aligned} \tag{30}$$

Bearing this symmetry in mind, we will henceforth for brevity write the expressions for PDS basis vectors and their eigenvalues only for one of reversed transitions.

5.1. Transition $J_a = 1 \longrightarrow J_b = 0$ ($J_a = 0 \longrightarrow J_b = 1$)

In the optical transition $J_a = 1 \longrightarrow J_b = 0$, the excited level contains only one degenerate state (Fig. 1a) that also remains unchanged in the new basis,

$$|(b)3\rangle \equiv |0, 0\rangle. \tag{31}$$

The lower level contains two elliptical dark states which, in accordance with relations (29), are a linear combination of the wavefunctions of magnetic sublevels with coefficients depending only on the polarization of light and independent of the light intensity:

$$|(a)1\rangle \equiv |\Psi_1^{(NC)}(a)\rangle = |1, 0\rangle, \tag{32}$$

$$|(a)2\rangle \equiv |\Psi_2^{(NC)}(a)\rangle = q_{+}|1, -1\rangle - q_{-}|1, +1\rangle. \tag{33}$$

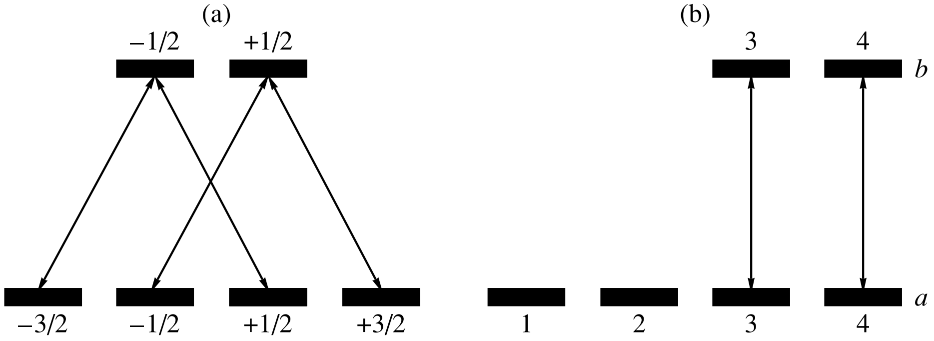

Fig. 2. The same for optical transition $J_a = 3/2 \longrightarrow J_b = 1/2$.

In this case, the third state associated with light and orthogonal to these states has the form

$$|(a)3\rangle = q_-|1,-1\rangle + q_+|1,+1\rangle. \qquad (34)$$

The light field couples only two states in the transition

$$|(a)3\rangle \longrightarrow |(b)3\rangle.$$

The corresponding eigenvalues are given by

$$\lambda_3 = 1/3, \quad \lambda_1 = \lambda_2 = 0.$$

Figure 1b shows the new diagram of the transition. Figure 1a all subsequent figures (a) show the diagrams of the corresponding transitions in the basis of magnetic sublevels, while figures (b) show the transitions in the PDS basis. The PDS basis and the eigenvalues for the optical transition $J = 0 \longrightarrow J = 1$ can be easily found using the expressions for the PDS basis vectors and their eigenvalues for the optical transition $J = 1 \longrightarrow J = 0$ and procedure (30).

5.2. Transition $J_a = 3/2 \longrightarrow J_b = 1/2$
($J_a = 1/2 \longrightarrow J_b = 3/2$)

Fig. 2a shows that the lower state of the optical transition

$$J_a = 3/2 \longrightarrow J_b = 1/2$$

contains two independent simple Λ links corresponding to two elliptic dark states [8, 14]:

$$|(a)1\rangle \equiv |\Psi_1^{(NC)}(a)\rangle$$
$$= \frac{\sqrt{3}q_-|3/2,+1/2\rangle - q_+|3/2,-3/2\rangle}{\sqrt{(q_+^2 + 3q_-^2)}}, \qquad (35)$$

$$|(a)2\rangle \equiv |\Psi_2^{(NC)}(a)\rangle$$
$$= \frac{\sqrt{3}q_+|3/2,-1/2\rangle - q_-|3/2,+3/2\rangle}{\sqrt{(q_-^2 + 3q_+^2)}}. \qquad (36)$$

In this case, the remaining part of the PDS basis, which is orthogonal to these dark states, can be constructed in the following obvious way:

$$|(a)3\rangle = \frac{q_+|3/2,+1/2\rangle + \sqrt{3}q_-|3/2,-3/2\rangle}{\sqrt{(q_+^2 + 3q_-^2)}}, \qquad (37)$$

$$|(a)4\rangle = \frac{q_-|3/2,-1/2\rangle + \sqrt{3}q_+|3/2,+3/2\rangle}{\sqrt{(q_-^2 + 3q_+^2)}}. \qquad (38)$$

Supplementing these states with two renumbered upper states of the Zeeman basis,

$$|(b)3\rangle \equiv |1/2,-1/2\rangle, \qquad (39)$$

$$|(b)4\rangle \equiv |1/2,+1/2\rangle, \qquad (40)$$

we obtain the complete set of states forming the orthonormal PDS basis; light-induced transitions occur only between the states

$$|(a)3\rangle \longrightarrow |(b)3\rangle$$

and

$$|(a)4\rangle \longrightarrow |(b)4\rangle.$$

The corresponding eigenvalues are given by

$$\lambda_3 = \frac{1}{4}q_-^2 + \frac{1}{12}q_+^2, \quad \lambda_4 = \frac{1}{4}q_+^2 + \frac{1}{12}q_-^2, \qquad (41)$$
$$\lambda_1^a = \lambda_2^a = 0.$$

The modified diagram of transitions in the PDS basis is shown in Fig. 2b. An analogous diagram for the reversed transition

$$J_a = 1/2 \longrightarrow J_b = 3/2$$

is presented in Fig. 3.

5.3. Transition $J_a = 1 \longrightarrow J_b = 2$
($J_a = 2 \longrightarrow J_b = 1$)

The upper level of the optical transition

$$J_a = 1 \longrightarrow J_b = 2$$

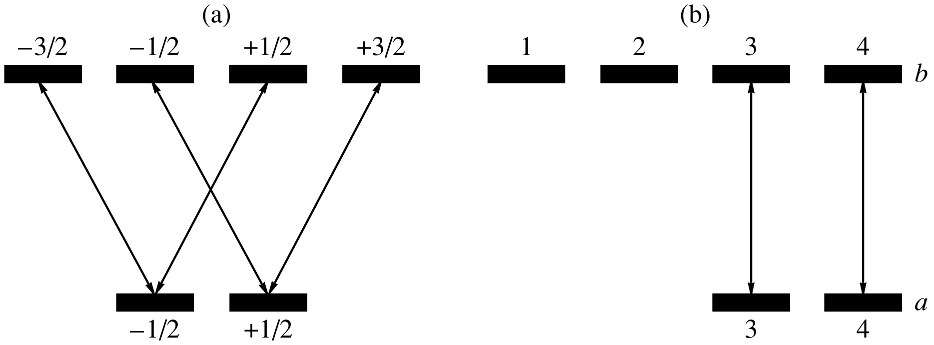

Fig. 3. The same for optical transition $J_a = 1/2 \longrightarrow J_b = 3/2$.

contains two CPT states:

$$|(b)1\rangle \equiv |\Psi_1^{(NC)}(b)\rangle = q_-|2,-1\rangle - q_+|2,+1\rangle, \tag{42}$$

$$|(b)2\rangle \equiv |\Psi_2^{(NC)}(b)\rangle = \frac{q_-^2|2,-2\rangle - \sqrt{6}q_-q_+|2,0\rangle + q_+^2|2,+2\rangle}{\sqrt{q_+^4 + 6q_-^2q_+^2 + q_-^4}}. \tag{43}$$

The corresponding eigenvalues for the CPT states are given by

$$\lambda_1 = \lambda_2 = 0.$$

The field-coupled orthogonal PDSs can be written in the form

$$|(a)3\rangle = |1,0\rangle, \tag{44}$$

$$|(b)3\rangle = q_+|2,-1\rangle + q_-|2,+1\rangle \tag{45}$$

with the eigenvalue

$$\lambda_3 = \frac{1}{10}.$$

Further, we have the pair of states

$$|(a)4\rangle = -\frac{\sqrt{2}}{2}\frac{(5\sin 2\varepsilon + \sqrt{25 - 24\cos^2 2\varepsilon})}{\sqrt{N_4^a}}|1,-1\rangle + \frac{\sqrt{2}}{2}\frac{\cos 2\varepsilon}{\sqrt{N_4^a}}|1,+1\rangle, \tag{46}$$

$$|(b)4\rangle = \frac{(1 + \sin 2\varepsilon)(1 - 6\sin 2\varepsilon - \sqrt{25 - 24\cos^2 2\varepsilon})}{\sqrt{N_4^b}}|2,-2\rangle + \sqrt{6}\frac{\sin 4\varepsilon}{\sqrt{N_4^b}}|2,0\rangle + \frac{(1 - \sin 2\varepsilon)(1 + 6\sin 2\varepsilon - \sqrt{25 - 24\cos^2 2\varepsilon})}{\sqrt{N_4^b}}|2,+2\rangle \tag{47}$$

with the eigenvalue

$$\lambda_4 = \frac{7 + \sqrt{25 - 24\cos^2 2\varepsilon}}{60}.$$

Finally, the last pair of states have the form

$$|(a)5\rangle = -\frac{\sqrt{2}}{2}\frac{(5\sin 2\varepsilon - \sqrt{25 - 24\cos^2 2\varepsilon})}{\sqrt{N_5^a}}|1,-1\rangle + \frac{\sqrt{2}}{2}\frac{\cos 2\varepsilon}{\sqrt{N_5^a}}|1,+1\rangle, \tag{48}$$

$$|(b)5\rangle = \frac{(1 + \sin 2\varepsilon)(1 - 6\sin 2\varepsilon + \sqrt{25 - 24\cos^2 2\varepsilon})}{\sqrt{N_5^b}} \times |2,-2\rangle + \sqrt{6}\frac{\sin 4\varepsilon}{\sqrt{N_5^b}}|2,0\rangle + \frac{(1 - \sin 2\varepsilon)(1 + 6\sin 2\varepsilon + \sqrt{25 - 24\cos^2 2\varepsilon})}{\sqrt{N_5^b}}|2,+2\rangle, \tag{49}$$

$$\lambda_5 = \frac{7 - \sqrt{25 - 24\cos^2 2\varepsilon}}{60}.$$

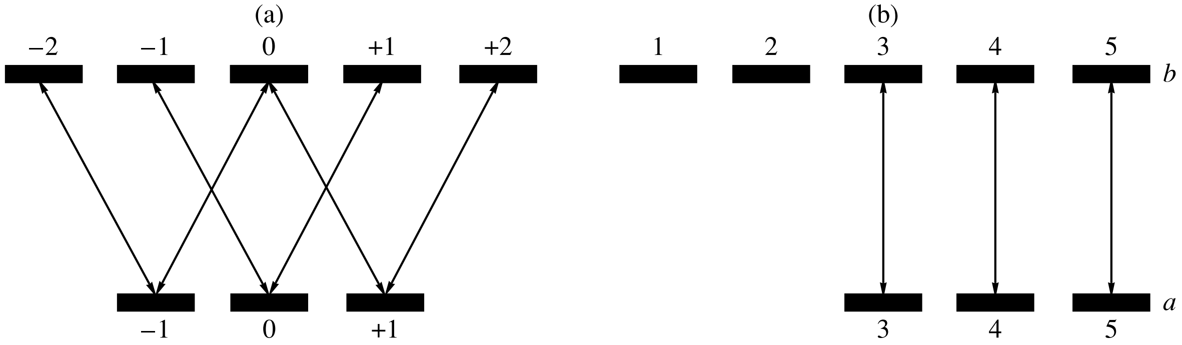

Fig. 4. The same for optical transition $J_a = 1 \longrightarrow J_b = 2$.

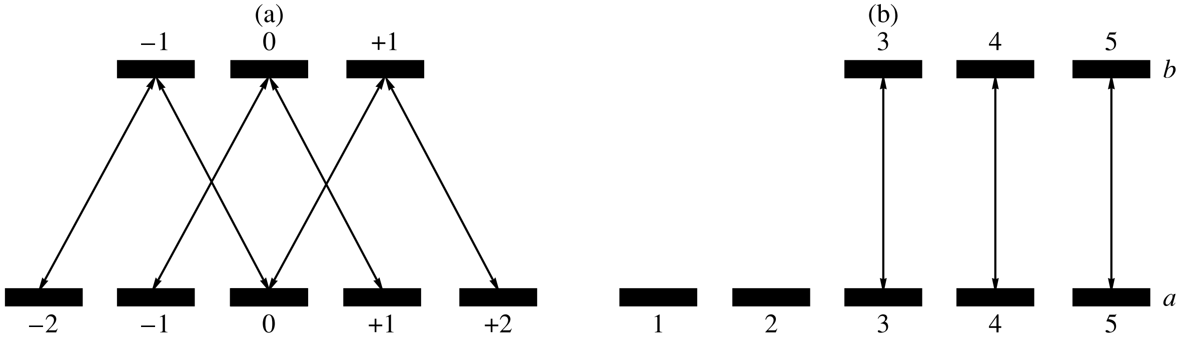

Fig. 5. The same for optical transition $J_a = 2 \longrightarrow J_b = 1$.

The normalization factors have the form

$$\begin{gathered} N_4^a = 25 - 24\cos^2 2\varepsilon \\ + 5\sin 2\varepsilon\sqrt{25 - 24\cos^2 2\varepsilon}, \\ N_4^b = \frac{8}{3}[50 - 73\cos^2 2\varepsilon + 24\cos^4 2\varepsilon \\ + (10 - 11\cos^2 2\varepsilon)\sqrt{25 - 24\cos^2 2\varepsilon}], \qquad (50) \\ N_5^a = 25 - 24\cos^2 2\varepsilon \\ - 5\sin 2\varepsilon\sqrt{25 - 24\cos^2 2\varepsilon}, \\ N_5^b = \frac{8}{3}[50 - 73\cos^2 2\varepsilon + 24\cos^4 2\varepsilon \\ - (10 - 11\cos^2 2\varepsilon)\sqrt{25 - 24\cos^2 2\varepsilon}]. \end{gathered}$$

Figure 4 shows the optical transition

$$J_a = 1 \longrightarrow J_b = 2$$

in the old and new bases; Fig. 5 shows the corresponding reversed transition

$$J_a = 2 \longrightarrow J_b = 1.$$

5.4. Transition $J_a = 1 \longrightarrow J_b = 1$

For this transition, each energy level contains a single CPT state [12] (Fig. 6)

$$|(a)1\rangle \equiv |\Psi_1^{(NC)}(a)\rangle = q_+|1, -1\rangle + q_-|1, +1\rangle, \qquad (51)$$

$$|(b)1\rangle \equiv |\Psi_1^{(NC)}(b)\rangle = -q_-|1, -1\rangle - q_+|1, +1\rangle. \qquad (52)$$

The orthogonal states interacting with light at the lower level can be expressed in terms of the magnetic sublevel states,

$$|(a)2\rangle \equiv |1, 0\rangle, \qquad (53)$$

$$|(a)3\rangle = q_-|1, -1\rangle - q_+|1, +1\rangle; \qquad (54)$$

the corresponding expressions for the states at the upper level are

$$|(b)2\rangle = -q_+|1, -1\rangle + q_-|1, +1\rangle, \qquad (55)$$

$$|(b)3\rangle \equiv |1, 0\rangle. \qquad (56)$$

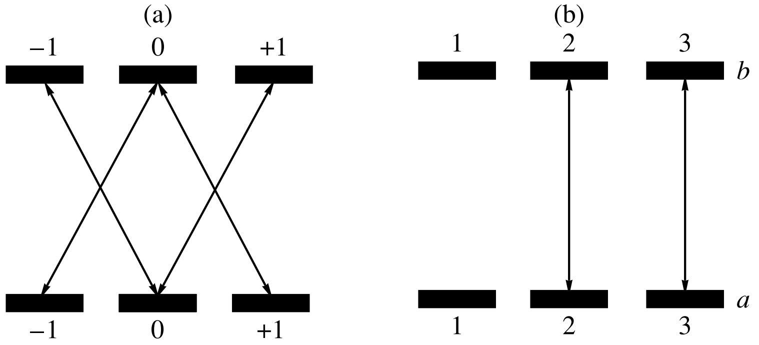

Fig. 6. The same for optical transition $J_a = 1 \longrightarrow J_b = 1$.

The system splits into two independent transitions between PDSs (see Fig. 6b),

$$|(a)2\rangle \longrightarrow |(b)2\rangle, \quad |(a)3\rangle \longrightarrow |(b)3\rangle,$$

in addition, each level contains a CPT state, which is not coupled by the field. The corresponding eigenvalues are given by

$$\lambda_1^a = \lambda_1^b = 0, \quad \lambda_2 = \lambda_3 = \frac{1}{6}.$$

It should be noted that, for the given transition in the new basis, double degeneracy in energy (identical Rabi frequencies) is preserved for the two PDSs interacting with the field and exhibiting field splitting which is independent of ellipticity.

5.5. Transition $J_a = 2 \longrightarrow J_b = 2$

The lower and upper levels contain one elliptical dark state each:

$$\begin{aligned}|(a)1\rangle = {} & \sqrt{3}\frac{(1+\sin 2\varepsilon)}{\sqrt{N_1}}|2,-2\rangle + \sqrt{2}\frac{\cos 2\varepsilon)}{\sqrt{N_1}}|2,0\rangle \\ & + \sqrt{3}\frac{(1-\sin 2\varepsilon)}{\sqrt{N_1}}|2,+2\rangle,\end{aligned} \tag{57}$$

$$\begin{aligned}|(b)1\rangle = {} & \sqrt{3}\frac{(1-\sin 2\varepsilon)}{\sqrt{N_1}}|2,-2\rangle + \sqrt{2}\frac{\cos 2\varepsilon)}{\sqrt{N_1}}|2,0\rangle \\ & + \sqrt{3}\frac{(1+\sin 2\varepsilon)}{\sqrt{N_1}}|2,+2\rangle.\end{aligned} \tag{58}$$

These states have zero eigenvalues. The states of the lower and upper levels, which interact with light, are defined as

$$\begin{aligned}|(a)2\rangle = {} & \frac{\sin 2\varepsilon - \sqrt{1+8\cos^2 2\varepsilon}}{\sqrt{N_2}}|2,-1\rangle \\ & + \frac{3\cos 2\varepsilon}{\sqrt{N_2}}|2,+1\rangle,\end{aligned} \tag{59}$$

$$\begin{aligned}|(b)2\rangle = {} & \frac{3\cos 2\varepsilon}{\sqrt{N_2}}|2,-1\rangle \\ & + \frac{\sin 2\varepsilon - \sqrt{1+8\cos^2 2\varepsilon}}{\sqrt{N_2}}|2,+1\rangle.\end{aligned} \tag{60}$$

The next pair of vectors has the form

$$\begin{aligned}& |(a)3\rangle \\ & = -\frac{(1-\sin 2\varepsilon)(3+2\sin 2\varepsilon - \sqrt{1+8\cos^2 2\varepsilon})}{\sqrt{N_3}}|2,-2\rangle \\ & + 2\frac{\sin 4\varepsilon}{\sqrt{N_3}}|2,0\rangle \\ & + \frac{(1+\sin 2\varepsilon)(3-2\sin 2\varepsilon - \sqrt{1+8\cos^2 2\varepsilon})}{\sqrt{N_3}}|2,+2\rangle,\end{aligned} \tag{61}$$

$$\begin{aligned}|(b)3\rangle = {} & \frac{(1+\sin 2\varepsilon)(3-2\sin 2\varepsilon - \sqrt{1+8\cos^2 2\varepsilon})}{\sqrt{N_3}} \\ & \times |2,-2\rangle + 2\frac{\sin 4\varepsilon}{\sqrt{N_3}}|2,0\rangle \\ & - \frac{(1-\sin 2\varepsilon)(3+2\sin 2\varepsilon - \sqrt{1+8\cos^2 2\varepsilon})}{\sqrt{N_3}}|2,+2\rangle.\end{aligned} \tag{62}$$

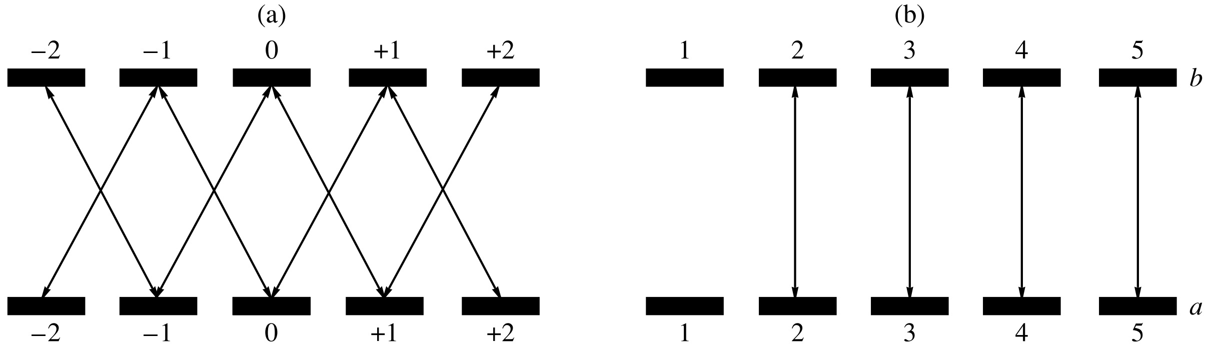

Fig. 7. The same for optical transition $J_a = 2 \longrightarrow J_b = 2$.

This is followed by the pair of states

$$|(a)4\rangle = \frac{\sin 2\varepsilon + \sqrt{1 + 8\cos^2 2\varepsilon}}{\sqrt{N_4}}|2, -1\rangle + \frac{3\cos 2\varepsilon}{\sqrt{N_4}}|2, +1\rangle, \tag{63}$$

$$|(b)4\rangle = \frac{3\cos 2\varepsilon}{\sqrt{N_4}}|2, -1\rangle + \frac{\sin 2\varepsilon + \sqrt{1 + 8\cos^2 2\varepsilon}}{\sqrt{N_4}}|2, +1\rangle. \tag{64}$$

The last pair of states has the form

$$|(a)5\rangle = -\frac{(1 - \sin 2\varepsilon)(3 + 2\sin 2\varepsilon + \sqrt{1 + 8\cos^2 2\varepsilon})}{\sqrt{N_5}} \times |2, -2\rangle + 2\frac{\sin 4\varepsilon}{\sqrt{N_5}}|2, 0\rangle + \frac{(1 + \sin 2\varepsilon)(3 - 2\sin 2\varepsilon + \sqrt{1 + 8\cos^2 2\varepsilon})}{\sqrt{N_5}}|2, +2\rangle, \tag{65}$$

$$|(b)5\rangle = \frac{(1 + \sin 2\varepsilon)(3 - 2\sin 2\varepsilon + \sqrt{1 + 8\cos^2 2\varepsilon})}{\sqrt{N_5}} \times |2, -2\rangle + 2\frac{\sin 4\varepsilon}{\sqrt{N_5}}|2, 0\rangle - \frac{(1 - \sin 2\varepsilon)(3 + 2\sin 2\varepsilon + \sqrt{1 + 8\cos^2 2\varepsilon})}{\sqrt{N_5}}|2, +2\rangle. \tag{66}$$

The normalization coefficients appearing in these formulas are given by

$$\begin{aligned} N_1 &= 12 - 4\cos^2 2\varepsilon, \\ N_2 &= 2 + 16\cos^2 2\varepsilon - 2\sin 2\varepsilon\sqrt{1 + 8\cos^2 2\varepsilon}, \\ N_3 &= \frac{8}{3}[2 + 15\cos^2 2\varepsilon - 8\cos^4 2\varepsilon \\ &\quad - (2 + \cos^2 2\varepsilon)\sqrt{1 + 8\cos^2 2\varepsilon}], \\ N_4 &= 2 + 16\cos^2 2\varepsilon + 2\sin 2\varepsilon\sqrt{1 + 8\cos^2 2\varepsilon}, \\ N_5 &= \frac{8}{3}[2 + 15\cos^2 2\varepsilon - 8\cos^4 2\varepsilon \\ &\quad + (2 + \cos^2 2\varepsilon)\sqrt{1 + 8\cos^2 2\varepsilon}]. \end{aligned} \tag{67}$$

The corresponding eigenvalues are

$$\begin{aligned} \lambda_1^a &= \lambda_1^b = 0, \\ \lambda_2 &= \lambda_3 = \frac{1}{12} + \frac{1}{60}\sqrt{1 + 8\cos^2 2\varepsilon}, \\ \lambda_4 &= \lambda_5 = \frac{1}{12} - \frac{1}{60}\sqrt{1 + 8\cos^2 2\varepsilon}. \end{aligned}$$

It can be seen that nonzero eigenvalues λ_i for this transition as well as for transition $J_a = 1 \longrightarrow J_b = 1$ are doubly degenerate, which is a common property of all transitions $J \longrightarrow J$ (where J is an integer). Figure 7 shows the diagrams of these transitions in the old and new bases.

Transitions

$$J_a = J \longrightarrow J_b = J$$

(J is a half-integer) should be considered separately, since these transitions do not involve CPT states and the method used for constructing the new basis becomes inapplicable. However, the PDS basis for transitions

$$J_a = 1/2 \longrightarrow J_b = 1/2$$

and

$$J_a = 3/2 \longrightarrow J_b = 3/2$$

can easily be constructed with the help of standard algebraic methods in view of the low rank of the system of linear equations.

5.6. *Transition $J_a = 1/2 \longrightarrow J_b = 1/2$*

It follows from the selection rules and the level diagram (Fig. 8) that the interaction for this simplest degenerate transition has already been diagonalized (to within a notation); i.e., the eigenstates are given by

$$|(b)1\rangle = |1/2, -1/2\rangle, \quad |(b)2\rangle = |1/2, +1/2\rangle, \qquad (68)$$

$$|(a)1\rangle = |1/2, +1/2\rangle, \quad |(a)2\rangle = |1/2, -1/2\rangle, \qquad (69)$$

and the corresponding eigenvalues are

$$\lambda_1 = \frac{q_-^2}{3}, \quad \lambda_2 = \frac{q_+^2}{3}.$$

Figure 8 shows the diagrams of these transitions in the old and new bases.

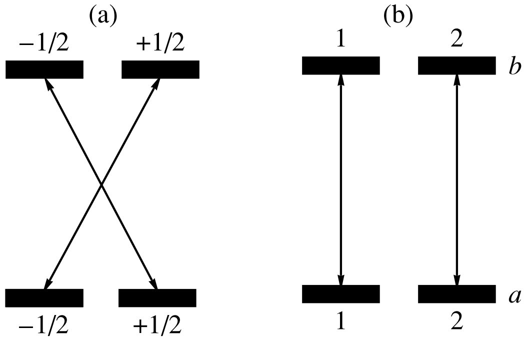

Fig. 8. The same for optical transition $J_a = 1/2 \longrightarrow J_b = 1/2$.

5.7. *Transition $J_a = 3/2 \longrightarrow J_b = 3/2$*

In this transition, the energy levels contain no dark states and the PDS basis can be determined directly by solving a system of fourth-degree linear equations. All states of the lower and upper levels, which explicitly depend on ellipticity, have the form

$$\begin{aligned}|(a)1\rangle &= -\frac{\sqrt{2}}{4} \\ &\times \frac{(1-\sin 2\varepsilon + \sqrt{2 + 2\cos^2 2\varepsilon - 2\sin 2\varepsilon})}{\sqrt{N_1}q_-}|3/2, -1/2\rangle \\ &+ \sqrt{\frac{6}{2}}\frac{q_+}{\sqrt{N_1}}|3/2, +3/2\rangle,\end{aligned} \qquad (70)$$

$$\begin{aligned}|(a)2\rangle &= -\frac{\sqrt{2}}{4} \\ &\times \frac{(1-\sin 2\varepsilon - \sqrt{2 + 2\cos^2 2\varepsilon - 2\sin 2\varepsilon})}{\sqrt{N_1}q_-}|3/2, -1/2\rangle \\ &+ \sqrt{\frac{6}{2}}\frac{q_+}{\sqrt{N_2}}|3/2, +3/2\rangle,\end{aligned} \qquad (71)$$

$$\begin{aligned}|(a)3\rangle &= \sqrt{\frac{3}{2}}\frac{q_-}{\sqrt{N_3}}|3/2, -3/2\rangle - \frac{\sqrt{2}}{4} \\ &\times \frac{(1+\sin 2\varepsilon + \sqrt{2 + 2\sin 2\varepsilon + 2\cos^2 2\varepsilon})}{\sqrt{N_3}q_+}|3/2, +1/2\rangle,\end{aligned} \qquad (72)$$

$$\begin{aligned}|(a)4\rangle &= \sqrt{\frac{3}{2}}\frac{q_-}{\sqrt{N_4}}|3/2, -3/2\rangle - \frac{\sqrt{2}}{4} \\ &\times \frac{(1+\sin 2\varepsilon - \sqrt{2 + 2\sin 2\varepsilon + 2\cos^2 2\varepsilon})}{\sqrt{N_4}q_+}|3/2, +1/2\rangle.\end{aligned} \qquad (73)$$

The PDSs for the upper level are given by

$$\begin{aligned}|(b)1\rangle &= -\frac{\sqrt{2}}{4}\frac{(1-\sin 2\varepsilon + \sqrt{2 + 2\cos^2 2\varepsilon - 2\sin 2\varepsilon})}{\sqrt{N_1}q_-} \\ &\times |3/2, +1/2\rangle + \sqrt{\frac{6}{2}}\frac{q_+}{\sqrt{N_1}}|3/2, -3/2\rangle,\end{aligned} \qquad (74)$$

$$\begin{aligned}|(b)2\rangle &= -\frac{\sqrt{2}}{4}\frac{(1-\sin 2\varepsilon - \sqrt{2 + 2\cos^2 2\varepsilon - 2\sin 2\varepsilon})}{\sqrt{N_2}q_-} \\ &\times |3/2, +1/2\rangle + \sqrt{\frac{6}{2}}\frac{q_+}{\sqrt{N_2}}|3/2, -3/2\rangle,\end{aligned} \qquad (75)$$

$$\begin{aligned}|(b)3\rangle &= \sqrt{\frac{3}{2}}\frac{q_-}{\sqrt{N_3}}|3/2, +3/2\rangle \\ &- \frac{\sqrt{2}}{4}\frac{(1+\sin 2\varepsilon + \sqrt{2 + 2\sin 2\varepsilon + 2\cos^2 2\varepsilon})}{\sqrt{N_3}q_+} \\ &\times |3/2, -1/2\rangle,\end{aligned} \qquad (76)$$

$$\begin{aligned}|(b)4\rangle &= \sqrt{\frac{3}{2}}\frac{q_-}{\sqrt{N_4}}|3/2, 3/2\rangle \\ &- \frac{\sqrt{2}}{4}\frac{(1+\sin 2\varepsilon - \sqrt{2 + 2\sin 2\varepsilon + 2\cos^2 2\varepsilon})}{\sqrt{N_4}q_+} \\ &\times |3/2, -1/2\rangle.\end{aligned} \qquad (77)$$

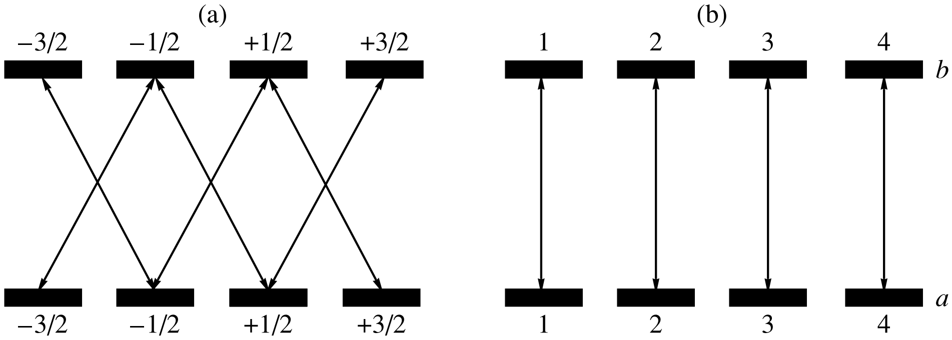

Fig. 9. The same for optical transition $J_a = 3/2 \longrightarrow J_b = 3/2$.

All eigenvalues are different and have the form

$$\lambda_1 = \frac{1}{12} + \frac{1}{60}\sin 2\varepsilon + \frac{1}{30}\sqrt{2 + 2\cos^2 2\varepsilon - 2\sin 2\varepsilon},$$

$$\lambda_2 = \frac{1}{12} + \frac{1}{60}\sin 2\varepsilon - \frac{1}{30}\sqrt{2 + 2\cos^2 2\varepsilon - 2\sin 2\varepsilon},$$

$$\lambda_3 = \frac{1}{12} - \frac{1}{60}\sin 2\varepsilon + \frac{1}{30}\sqrt{2 + 2\cos^2 2\varepsilon + 2\sin 2\varepsilon},$$

$$\lambda_4 = \frac{1}{12} - \frac{1}{60}\sin 2\varepsilon - \frac{1}{30}\sqrt{2 + 2\cos^2 2\varepsilon + 2\sin 2\varepsilon}.$$

The normalization coefficients are given by

$$\begin{aligned} N_1 &= 2 + \sin 2\varepsilon + 1/2\sqrt{2 + 2\cos^2 2\varepsilon - 2\sin 2\varepsilon}, \\ N_2 &= 2 + \sin 2\varepsilon - 1/2\sqrt{2 + 2\cos^2 2\varepsilon - 2\sin 2\varepsilon}, \\ N_3 &= 2 - \sin 2\varepsilon + 1/2\sqrt{2 + 2\sin 2\varepsilon + 2\cos^2 2\varepsilon}, \\ N_4 &= 2 - \sin 2\varepsilon - 1/2\sqrt{2 + 2\sin 2\varepsilon + 2\cos^2 2\varepsilon}. \end{aligned} \tag{78}$$

Figure 9 shows the diagrams of this transition in the old and new bases. Substituting the eigenvalues λ_j obtained in this section into Eqs. (24) and (25), we find that the probability density for an atom being at certain energy levels oscillates in time at r independent Rabi frequencies (except for the cases when eigenvalues are degenerate). The explicit dependence of these frequencies on ellipticity is defined by the formulas corresponding to each specific transition.

6. CONCLUSIONS

Thus, the examples considered above visually demonstrate that the selection rules for light-induced dipole transitions between the states of the upper and lower levels change in the new PDS basis. In contrast to the magnetic sublevel basis, the light-induced coherence between PDSs of each level is eliminated in this case, which simplifies analysis of the interaction between elliptically polarized light and atomic levels degenerate in the angular momentum projections and makes it possible to use the results obtained for a simple nondegenerate two-level model of the atom. In this case, the new basis is "tuned" only to the polarization of light, it does not depend on the light intensity, and it can be used instead of the basis of magnetic sublevels for finding exact solutions (e.g., for studying the propagation of ultrashort polarized pulses [19], effects of electromagnetically induced transparency in degenerate systems [20] and in processes of scattering of resonant polarized radiation [21], and other problems taking into account the interaction with additional magnetic and electromagnetic fields as a perturbation).

Derivation of the explicit form of the PDS basis for arbitrary values of angular momenta remains an urgent problem.

ACKNOWLEDGMENTS

This study was supported financially by the Russian Foundation for Basic Research (project no. 04-02-16488).

REFERENCES

1. A. Kastler, J. Phys. Radium **11**, 255 (1950).
2. D. Lenstra, Phys. Rep. **59**, 3 (1980).
3. G. Grynberg, B. Lounis, P. Verkerk, *et al.*, Phys. Rev. Lett. **70**, 2249 (1993).
4. S. G. Schirmer, A. I. Solom, and J. V. Leahy, J. Phys. A: Math. Gen. **35**, 4125 (2002).
5. V. Milner, B. Chernobrod, and Y. Prior, Phys. Rev. A **60**, 1293 (1999).
6. A. M. Tumaĭkin and V. I. Yudin, Zh. Éksp. Teor. Fiz. **98**, 81 (1990) [Sov. Phys. JETP **71**, 43 (1990)].
7. A. M. Basharov and A. I. Maĭmistov, Zh. Éksp. Teor. Fiz. **87**, 1594 (1984) [Sov. Phys. JETP **60**, 913 (1984)]; A. M. Basharov, A. I. Maĭmistov, and Yu. M. Sklyarov, Opt. Spektrosk. **63**, 707 (1987) [Opt. Spectrosc. **63**, 418 (1987)]; A. M. Basharov and A. I. Maĭmistov, Zh. Éksp. Teor. Fiz. **94** (12), 61 (1988) [Sov. Phys. JETP **67**, 2426

(1988)]; A. M. Basharov and A. I. Maĭmistov, Opt. Spektrosk. **68**, 1112 (1990) [Opt. Spectrosc. **68**, 649 (1990)].

8. V. S. Smirnov, A. M. Tumaĭkin, and V. I. Yudin, Zh. Éksp. Teor. Fiz. **96**, 1613 (1989) [Sov. Phys. JETP **69**, 913 (1989)].
9. A. V. Taichenachev, A. M. Tumaikin, V. I. Yudin, and G. Nienhuis, Phys. Rev. A **69**, 033410 (2004).
10. A. V. Taĭchenachev, A. M. Tumaĭkin, and V. I. Yudin, Zh. Éksp. Teor. Fiz. **110**, 1727 (1996) [JETP **83**, 949 (1996)].
11. A. V. Taĭchenachev, A. M. Tumaĭkin, and V. I. Yudin, Zh. Éksp. Teor. Fiz. **118**, 77 (2000) [JETP **91**, 67 (2000)].
12. A. V. Taĭchenachev, A. M. Tumaĭkin, V. I. Yudin, and M. A. Ol'shanyĭ, Pis'ma Zh. Éksp. Teor. Fiz. **53**, 336 (1991) [JETP Lett. **53**, 351 (1991)]; Zh. Éksp. Teor. Fiz. **101**, 1787 (1992) [Sov. Phys. JETP **74**, 952 (1992)].
13. A. V. Taĭchenachev, A. M. Tumaĭkin, V. I. Yudin, and G. Nienhuis, Zh. Éksp. Teor. Fiz. **114**, 125 (1998) [JETP **87**, 70 (1998)].
14. A. V. Taĭchenachev, A. M. Tumaĭkin, V. I. Yudin, and G. Nienhuis, Zh. Éksp. Teor. Fiz. **108**, 415 (1995) [JETP **81**, 224 (1995)].
15. J. R. Morris and B. W. Shore, Phys. Rev. A **27**, 906 (1983).
16. G. Nienhuis, Opt. Commun. **59**, 353 (1986).
17. N. B. Delone and V. P. Kraĭnov, *Atom in a Strong Light Field* (Atomizdat, Moscow, 1978) [in Russian].
18. A. Allen and J. Eberly, *Optical Resonance and Two-Level Atoms* (Wiley, New York, 1975; Atomizdat, Moscow, 1978).
19. A. A. Zabolotskiĭ, Zh. Éksp. Teor. Fiz. **121**, 1012 (2002) [JETP **94**, 869 (2002)].
20. I. V. Zelenskiĭ and E. A. Mironov, Zh. Éksp. Teor. Fiz. **121**, 1068 (2002) [JETP **94**, 916 (2002)].
21. L. P. Rapoport, B. A. Zon, and N. L. Manakov, *Theory of Multiphoton Processes in Atoms* (Atomizdat, Moscow, 1978) [in Russian].

Translated by N. Wadhwa

Journal of Experimental and Theoretical Physics, Vol. 99, No. 6, 2004, pp. 1150–1172.
Translated from Zhurnal Éksperimental'noĭ i Teoreticheskoĭ Fiziki, Vol. 126, No. 6, 2004, pp. 1317–1343.

Characteristics of High-Power Radiating Imploding Discharge with Cold Start

V. V. Alexandrov[a], E. V. Grabovsky[a], M. V. Zurin[a], I. V. Krasovsky[a], K. N. Mitrofanov[a], S. L. Nedoseev[a],*, G. M. Oleinik[a], I. Yu. Porofeev[a], A. A. Samokhin[a], P. V. Sasorov[b], V. P. Smirnov[a], M. V. Fedulov[a], and I. N. Frolov[a]

[a]*Troitsk Institute for Innovation and Fusion Research, Russian State Research Center,*
Troitsk, Moscow oblast, 142092 Russia
[b]*Institute of Theoretical and Experimental Physics, Russian State Research Center,*
Moscow, 117218 Russia
**e-mail: nedos@triniti.ru*

Received February 12, 2004

Abstract—A qualitative model of the dynamics of a multiterawatt radiating Z-pinch with cold start and high rate of current rise is proposed. The model is used to analyze discharges with currents $I \sim 2$–5 MA (with $dI/dt > 10^{13}$ A/s) through uniform or structured plasma-producing loads, including wire arrays. The most important consequence of cold start is that spatially nonuniform plasma production is prolonged to almost the entire current rise time. Under these conditions, the Ampére force begins to play a dominant role in the plasma dynamics before the plasma-producing load is completely transformed into an accelerated plasma. The results of computations of wire-array vaporization are presented. A formula is proposed for estimating the highest attainable velocity of plasma flow into a heterogeneous liner driven by the Ampére force. It is shown that local imbalance between radial motion of the produced plasma and supply of the plasma-producing substance to be ionized leads to axially nonuniform breakthrough of magnetic flux into the liner, which precedes plasma collapse. The magnetic-flux breakthrough gives rise to a chaotic azimuthal–axial plasma structure consisting of radial plasma jets of relatively small diameter, which is called a *radial plasma rainstorm*. The breaking-through azimuthal magnetic flux obstructs further current flow in the breakthrough region. Analyses of Z-pinch implosion based on the theory of Rayleigh–Taylor instability or the snowplow model are incorrect under the plasma-rainstorm conditions. The processes taking place in a stagnant Z-pinch include conversion of the energy carried by the current-generated magnetic field into turbulent MHD flow of the ion component of the plasma, its convective mixing with magnetic field, heating, energy transfer from ions to electrons, and emission from the plasma. Under typical experimental conditions, emission plays a key role in the energy balance in an imploding pinch. Z-pinch is modeled by an electric-circuit component that has a time-dependent nonlinear impedance and consumes the magnetic energy supplied by a generator through a magnetically insulated transmission line (MITL). The peak power reached in the circuit is comparable to the peak soft X-ray power output emitted by the pinch in terms of magnitude and timing. Optimum matching conditions are formulated for the generator–MITL–pinch circuit. © *2004 MAIK "Nauka/Interperiodica".*

INTRODUCTION

The Angara-5-1 facility has been used to study imploding discharges (fast Z-pinches) for many years. A considerable amount of experimental data has been amassed [1–5], and it must be summarized in order to develop a physical model of these discharges. In the discharges created in our experiments [1–5], currents having a strength of $I \sim 2$–5 MA, with $dI/dt > 10^{13}$ A/s, were used to heat axially symmetric homogeneous or structured plasma-producing loads or their combinations with outer diameters varying between 1 and 3 cm. Most plasma-producing substances consisted of elements with high atomic numbers or contained them as additives. The plasma-producing loads were either heterogeneous (thin-wire array, solid-state foam in vacuum) or homogeneous (gas puff). The experiments were conducted under "cold-start" discharge conditions; i.e., the phase transformations of the plasma-producing substances (melting, vaporization, dissociation, ionization) were induced by the main current pulse. The mass, shape, and dimensions of the plasma sources were chosen so that the discharge electric power, as well as the soft X-ray power, varied within several terawatts.

Previous models of the processes involved in fast Z-pinches were based on the assumption that the current-carrying plasma shell formed at the earliest stage of the discharge implodes as a whole. In particular, the most comprehensive review of recent studies of fast Z-pinches presented in [6] begins with an analysis of the implosion of a perfectly conducting cylindrical shell. Finite conductivity, emission, instabilities, and multidimensional compression are introduced as complicating factors in the course of the analysis.

However, the results obtained in our studies [1–5] show that this model of the dynamics of a multiterawatt radiating Z-pinch is not valid under the cold-start discharge conditions. Actually, this regime has been implemented in all terawatt-scale Z-pinch experiments (not only ours).

Our experiments on discharges with cold start and high rate of current rise show that the Ampére force driving the implosion comes into effect after only a small portion of the plasma-producing load has been transformed into an accelerated plasma, i.e., at the earliest stage of plasma production. In what follows, plasma production is interpreted as the entire process of transformation of the plasma-producing load into an accelerated plasma. The Ampére force drives the produced current-carrying plasma out of the region occupied by the plasma-producing material, and the zone of heat release due to joule heating moves with the current-carrying plasma. Thus, the plasma production is prolonged to almost the entire current rise time.

Furthermore, our observations show that the plasma production is spatially nonuniform. The current-carrying plasma does not make up a one-piece plasma shell, being disrupted even at the starting radius. This condition strongly affects the subsequent development of an imploding discharge. For this reason, we believe that the classical models of Z-pinch cannot be used in theoretical analysis of such discharges.

To date, prolonged plasma production and turbulent motion in the stagnant state of a fast Z-pinch were taken into account in several theoretical models. Relationship between prolonged plasma production and dynamics of the produced plasma was analyzed in [3]. The analysis presented below relies on the conclusions made in that study. In [7, 8], a model of instability, ablation, and formation of plasma jets was proposed describe wire-array Z-pinches. In what follows, it is referred to as the model of [7, 8]. In [9, 10], energy balance in the stagnant state of a fast Z-pinch was described by the model of MHD turbulent heating of a Z-pinch with toroidal magnetic bubbles penetrating to the pinch axis. However, those studies do not provide sufficient basis for a comprehensive characterization of a multiterawatt radiating Z-pinch with cold start as a multifactorial phenomenon. Moreover, some assumptions of the model of [7, 8] disagree with our experimental results.

In this paper, we summarize the broad variety of factors contributing to the dynamics of a multiterawatt radiating Z-pinch with cold start and high rate of current rise. The phenomenological description proposed here relies on the experimental results reported in [1–5]. We believe that it can serve as a basis for quantitative mathematical modeling of a radiating fast Z-pinch. However, we understand that this root model must be further refined to agree with forthcoming experimental data. Moreover, we realized that our results must be extrapolated to larger scale experiments, including those currently underway at the Z facility [11] and those planned to be conducted at the ZR [12] and Baikal [13] facilities.

To have a clear perspective, we enumerate the key factors that determine the dynamics of a radiating fast Z-pinch in our model in the opening section of the paper, which briefly summarizes the principal conclusions based on an analysis of experimental data. In subsequent sections, these conclusions are elaborated to the extent that is currently possible. Some of the conclusions should be interpreted as working assumptions to be verified by additional experiments.

KEY FACTORS CONTRIBUTING TO THE DYNAMICS OF MULTITERAWATT RADIATING Z-PINCH WITH COLD START AND HIGH RATE OF CURRENT RISE

1. COLD START OF AN IMPLODING DISCHARGE

1.1. The starting characteristics of the plasma-producing materials used in imploding discharges are predetermined by the physics of multiterawatt electrical pulse generation.

1.2. Cold start is inherent in imploding discharges with high rates of current rise that have been studied to this day. The main consequence of cold start is that the plasma production is prolonged to almost the entire current rise time.

1.3. Heterogeneous structure of plasma-producing loads is an essential factor, but effects due to cold start manifest themselves in initially homogeneous plasma-producing loads as well. Plasma production is spatially nonuniform in any event.

1.4. Massive electrodes may play the role of an uncontrollable additional plasma-producing load at cold start.

1.5. Strong preionization not induced by current is an unimplemented alternative to cold start.

2. PROLONGED PLASMA PRODUCTION AS THE PRINCIPAL CONSEQUENCE OF COLD START

2.1. The most important manifestation of prolonged plasma production is that the Ampére force begins to play a dominant role in the dynamics of the produced plasma before the plasma-producing material is used up. The evolution of the produced plasma is controlled by the total azimuthal magnetic field due to the total discharge current.

2.2. Each wire in an electrically heated wire array turns into a high-density heterogeneous core (consisting of droplets and vapor) surrounded by a plasma of relatively low density. Our model of the state of the core describes the evaporation from the droplet surface and the loss of mass due to vapor flow from the core boundary. The source of energy release in the core is the joule heating by current flowing through the ionized vapor.

The current is driven by the voltage drop along the wire array.

2.3. The rate of plasma production required to sustain a steady radial flow of the tungsten plasma from the plasma-producing load with a stationary outer boundary is expressed as

$$\frac{dm}{dt}\left[\frac{\mu\text{g}}{\text{cm}^2\ \text{ns}}\right] \approx 0.2\left(\frac{I_{[\text{MA}]}}{R_{[\text{st}]}}\right)^{1.8}.$$

2.4. At the plasma-production stage, the current-carrying plasma flows into the liner volume.

2.5. A timely termination of plasma production is a crucial factor that determines a high degree of compression in a Z-pinch with cold start.

2.6. In contrast to the model of [7, 8], our time-dependent model of plasma production describes the penetration of the azimuthal magnetic field into the liner volume.

3. BREAKTHROUGH OF MAGNETIC FLUX ACROSS THE DISRUPTED PLASMA-PRODUCING REGION AND PARTIAL PLASMA TRAPPING

3.1. Experimental Observation of Breakthrough of Azimuthal Magnetic Flux across the Wire Array

Spatially nonuniform breakthrough of magnetic flux manifests itself by the radial plasma rainstorm discovered and studied in [5].

3.1a. The rapid contraction of the outer pinch boundary begins with a spatially nonuniform breakthrough of magnetic flux toward the pinch axis. The magnetic-flux breakthrough precedes the subsequent implosion of the plasma.

3.1b. The magnetic-flux breakthrough gives rise to a chaotic azimuthal–axial plasma structure consisting of radial plasma jets of relatively small diameter, which is called the *radial plasma rainstorm.*

3.1c. In the course of the implosion toward the wire-array axis, the plasma jets contract and merge into distinct plasma-current filaments mostly parallel to the pinch axis.

3.1d. Due to an early magnetic-flux breakthrough, an X-ray pulse can be generated before the plasma completely implodes as a whole. The plasma remains spatially nonuniform at the instant when a high-power X-ray pulse is generated by the Z-pinch.

3.1e. The spatial structure of the imploding plasma is so nonuniform that the wholeness of an imploding plasma shell is out of question. Under these conditions, any analysis of Z-pinch implosion based on the theory of Rayleigh–Taylor instability or the snowplow model is incorrect under the plasma-rainstorm conditions.

3.2. Criteria for Breakthrough of Magnetic Flux into the Liner Volume at the Final Plasma-Production Stage

3.2a. The magnetic-flux breakthrough is a consequence of local imbalance between supply and ionization of the plasma-producing substance and radial motion of the produced plasma from the plasma-production region driven by the Ampére force.

3.2b. The minimal discharge current I_{cr} at which magnetic flux can break into the liner volume across an annular gap of length d is estimated as

$$I_{\text{cr}}[\text{A}] \approx 3\times 10^{21}\frac{\sqrt{\rho}}{\sigma}\frac{R\Delta}{d^2},$$

where ρ is the plasma density, σ is electrical conductivity of the plasma, Δ is the plasma-layer thickness, and R is the liner radius. If $\rho \sim 10^{-4}$ g/cm^3, $\sigma \sim 10^{14}$ CGSE units, $\Delta \approx d \approx 0.1$ cm, and $R \approx 1$ cm, then $I_{\text{cr}} \approx 3$ MA.

3.2c. The mass of the plasma moving with the breaking-through frozen-in magnetic flux can be only a fraction of the mass of the plasma-producing material occupying the breakthrough region.

3.2d. The breaking-through azimuthal magnetic field obstructs further current flow in the breakthrough region.

4. MHD TURBULENT HEATING AND RADIATIVE COOLING OF STAGNANT PLASMA

4.1. MHD Turbulent Heating

Stagnation is a natural consequence of the magnetic-flux breakthrough. In the stagnant pinch, the energy of the current-generated magnetic field is converted into the turbulent MHD flow of the ion component of the stagnant plasma. This process involves convective mixing of the plasma with magnetic field, heating, energy transfer from ions to electrons, and emission from the stagnant plasma. The rate of MHD turbulent heating is estimated as

$$W_{\text{th}}\left[\frac{\text{TW}}{\text{cm}}\right] \approx \frac{0.5I^3}{rM^{1/2}},$$

where I, M, and r are measured in megamperes, micrograms per centimeter, and millimeters, respectively [10].

4.2. Energy Balance in a Radiating Turbulent Pinch

4.2a. The electron plasma component is heated by the energy transferred from the ion component. In the high-density pinch plasmas, the corresponding time scale is small as compared to the joule heating time for electrons.

4.2b. Under the conditions of our experiments, radiation plays a key role in the energy balance of an imploding pinch. The tendency of the turbulent current-carrying plasma toward filamentation and transformation of the radial plasma rainstorm into radial “protuberances” observed in our experiments [5] can be explained by radiative cooling of the imploding spatially nonuniform plasma.

5. EFFECTIVE CONVERSION OF STORED MAGNETIC ENERGY INTO Z-PINCH HEATING AND MULTITERAWATT X-RAY EMISSION

5.1. Z-pinch is modeled by an electric-circuit component that has a time-dependent nonlinear impedance and consumes the magnetic energy supplied by a generator through a magnetically insulated transmission line (MITL). The MITL couples the load surface to the water–vacuum interface. In the course of plasma production, the magnetic energy is accumulated in the MITL while the outer current boundary remains at rest. After the magnetic-flux breakthrough, the energy is consumed to implode and heat the radiatively cooled current-carrying plasma. The peak active power W_{act} is comparable to the peak soft X-ray power output in terms of timing.

5.2. The active power produced in the discharge is sustained by consuming the stored magnetic energy (W_{ind}) and the power supplied by the generator (W_{suppl}). In experiments, the relative values of W_{suppl} and W_{ind} depend on the initial liner radius and its mass per unit length.

5.3. At all stages of the implosion (including the stagnant state), the heat accumulated by the radiating pinch plasma is low as compared to the magnetic energy generated by the discharge current. The radiation power emitted by the pinch is determined by the active power W_{act}.

5.4. Optimal Matching Conditions for the Generator– MITL–Pinch Circuit

5.4.1. The circuit parameters must ensure that the magnetic energy accumulated in the MITL reaches its maximum by the starting moment of the pinch implosion.

5.4.2. The impedance of an stagnant MHD-turbulent pinch must be much larger than the generator impedance.

5.4.3. The plasma contained between the electrodes provides a bypass for current leakage in the stagnant pinch. The rate of the magnetic-field influx that sustains the pinch may be limited by the plasma passed by the field on its way toward the pinch. These effects can be the key factors that determine the peak values of both discharge power and X-ray emission intensity.

BASIC CHARACTERISTICS OF HIGH-POWER RADIATING IMPLODING DISCHARGE WITH COLD START

1. COLD START OF IMPLODING DISCHARGE

1.1. Effect of the Physical Characteristics of Multiterawatt Pulse Generation on the Starting Parameters of Plasma-Producing Loads in Imploding Discharges

The implementation of the multiterawatt pulse generation technology in Z-pinches has opened new prospects in the physics and engineering of plasma implosion. In particular, the power supplied by the Marx generator to the fast imploding discharge is higher than the output from the capacitor banks used to power conventional plasma foci (with microsecond-scale current pulses) by two orders of magnitude. We should note here that the conventional and fast power-supply systems are comparable in terms of stored energy and peak current. For example, the power of about 40 TW produced by the generator used in the Z facility at Sandia National Labs generates a current of 20 MA through a wire-array having an inductance of 12 nH in about 100 ns [11]. These are the best characteristics obtained to this day. For comparison, the output characteristics of the Angara-5-1 facility vary from 2 to 5 MA and from 2 to 5 TW.

The power boost was achieved by raising the discharging voltage of the Marx generator and using pulse-forming lines designed to produce shorter pulses. Figures 1a and 1b show, respectively, a schematized circuit diagram and typical oscilloscopic traces of the output voltage pulse $V(t)$, discharge current I, and dI/dt obtained in the experiments reported in [1–5]. The rapidly varying dI/dt trace demonstrates that Z-pinch can be modeled by a time-dependent nonlinear impedance.

The reduction of the current-rise time from 10 μs to 100 ns implies that the starting radius must be about 1 cm rather than tens of centimeters. This requirement necessitates the use of the magnetically insulated transmission line for coupling the output from a meter-sized pulse generator to a centimeter-scale load. The MITL inductance that couples the load (Z-pinch) surface to the water–vacuum interface is denoted by L_0 in Fig. 1a. Thus, power supply to a multiterawatt/megavolt discharge is degraded only by a relatively low spurious inductance (10 to 20 nH). The difference in slope between the portions of the $V(t)$ and dI/dt traces corresponding to rising current through the inductive load (see Fig. 1b) is explained by the electron leakage from the MITL that takes place while the magnetic insulation of the gaps develops [2]. The corresponding leakage currents are not shown in Fig. 1a. However, they can amount to substantial levels.

The MITL accumulates magnetic energy and thereby ensures high rates of energy conversion at the implosion and stagnation phases of a Z-pinch. Figure 2

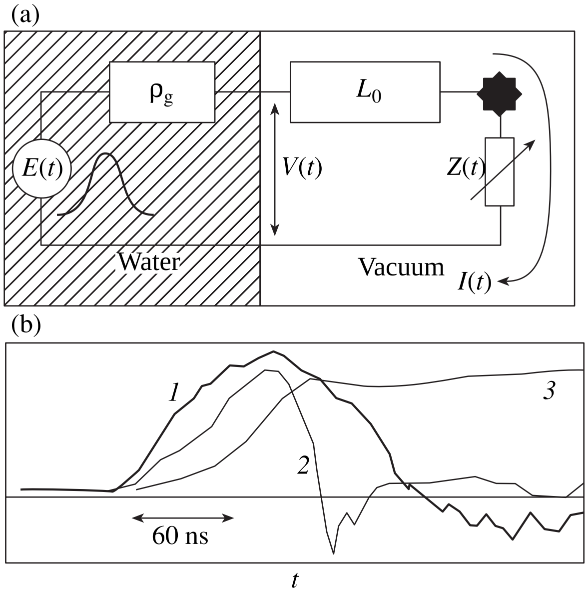

Fig. 1. (a) Schematized circuit diagram: $E(t)$ = emf pulse; $V(t)$ = voltage output from a water-insulated pulse-forming line; $I(t)$ = discharge current; L_0 = MITL inductance; ρ_g = total wave impedance of a water-insulated pulse-forming line; $Z(t)$ = nonlinear total impedance of the load. (b) typical characteristics of high-power imploding discharge: (*1*) $V(t)$ ($V_{max} \approx 1.1$ MV); (*2*) dI/dt ($dI/dt_{max} \approx 4 \times 10^{13}$ A/s); (*3*) $I(t)$ ($I_{max} \approx 3$ MA).

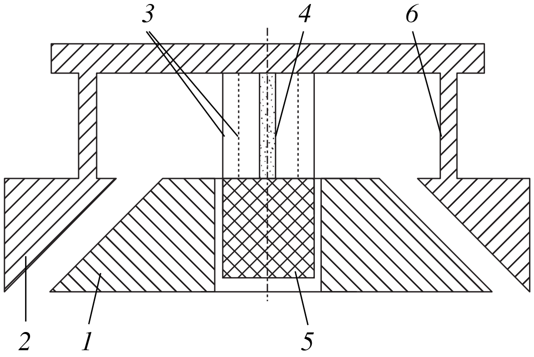

Fig. 2. Schematic of a MITL: (*1*) cathode; (*2*) anode; (*3*) outer and inner wire arrays; (*4*) central load (low-density foam); (*5*) weight for wire-array stressing; (*6*) return current anodes.

schematizes the MITL assembly used in our experiments as one of the numerous variants of the load [1–5].

Current basic and applied studies of multiterawatt fast Z-pinches are focused on the efficiency of conversion of the energy accumulated in the MITL into a soft X-ray pulse. To accomplish this task, plasma-producing materials containing elements with high atomic numbers must be utilized. The drastic reduction of the starting diameter of the plasma-producing load, the stringent constraints imposed on the load geometry, and the changes made in the elemental composition of the load to achieve the desired spectral characteristics of the X-ray pulse stimulated the use of nongaseous plasma-producing media. The typical plasma-producing substance used in up-to-date experiments is a low-density heterogeneous material consisting of micrometer-sized solid grains or fibers. Wire arrays have been frequently used in recent studies. The mass per unit length of the imploding plasma produced from a high-atomic-number material varies between 0.2 and 10 mg/cm in radiating Z-pinches with currents ranging from 3 to 20 MA. It is important to ensure that the plasma-producing load have the strictly required starting geometric parameters and the plasma production be well controlled.

The loads utilized in most present-day experiments are fairly consistent with these requirements in terms of geometry and mass, but the controllability of plasma production from an initially cold matter is yet to be improved.

1.2. Cold Start as an Inherent Stage of All Imploding Discharges with High Rates of Current Rise that Have Been Studied to Date

As mentioned above, the plasma-production process implemented in every terawatt-scale Z-pinch experiment conducted to this day is initiated by electrical breakdown of unionized material with a pulse produced by the generator. This experimental solution, termed *cold start*, is dictated by the need to simplify the design of the power-generating part of the facility. It strongly affects all processes involved in the subsequent implosion. The plasma production initiated by electrical breakdown of the plasma-producing material, but is not completed during the breakdown. Due to the rapid current rise (with $dI/dt \sim (0.5–2.0) \times 10^{14}$ A/s) required to accelerate a mass of 0.1–1.0 mg/cm to a velocity $\sim 3–5 \times 10^7$ cm/s over a length of 1 to 2 cm, the produced plasma is highly nonuniform. As the discharge current grows, the plasma is accelerated by magnetic field before the entire load transforms into an accelerated plasma. As the produced low-density plasma and the current are driven out of the plasma-production region, the energy required to vaporize and ionize the plasma-producing substance is released at a decreasing rate. This trend affects not only the initial stage of the discharge, but also the implosion and stagnation phases.

1.3. Heterogeneity of the Plasma-Producing Load

Heterogeneous structure of plasma-producing loads is an essential factor, but effects due to cold start manifest themselves in initially homogeneous plasma-producing loads as well [2, 3].

Spatially nonuniform plasma production is characteristic of both heterogeneous media (low-density solid-state foam, wire array) and homogeneous (gas-

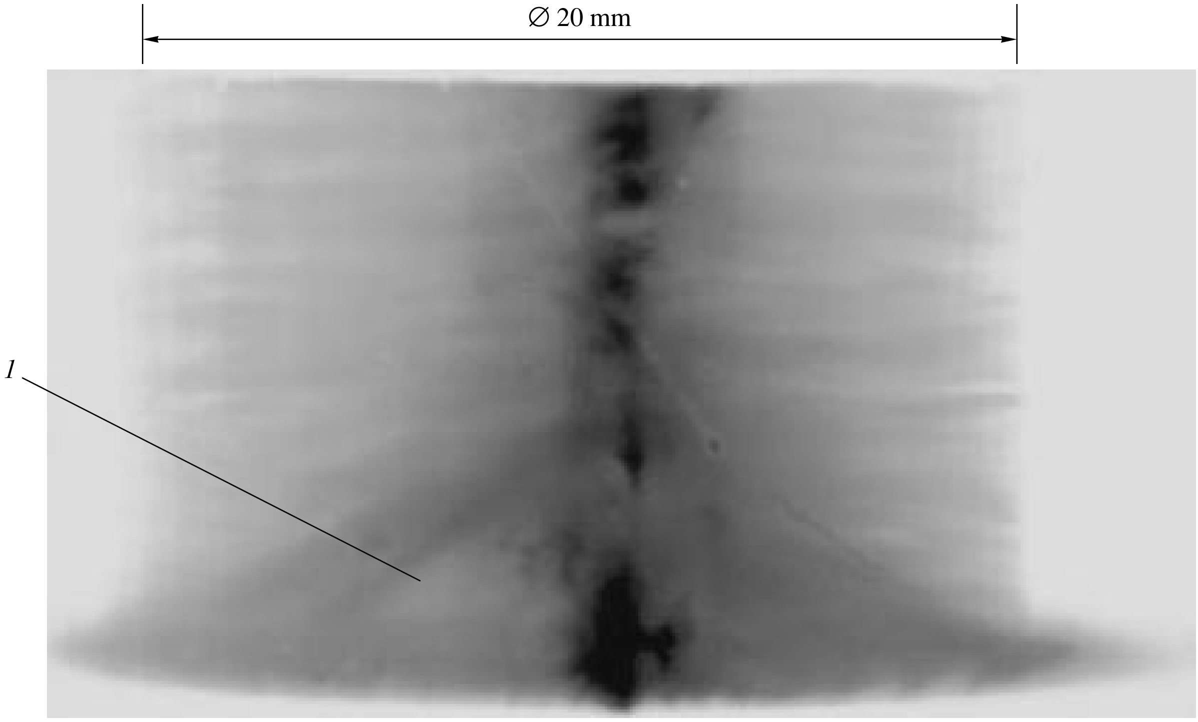

Fig. 3. Time-integrated X-ray photograph of a Z-pinch for wire array with a diameter of 20 mm: (*1*) cone-shaped cathode plasma sheath.

eous) substances, even though the respective mechanisms of breakdown and plasma production are different. A wire array is azimuthally nonuniform by construction, because the wire spacing (200–1000 μm) is much greater than the wire diameter (5–15 μm). The spatial nonuniformity of the plasma produced from a gas puff manifests itself via plasma instability as azimuthal current filamentation followed by axial stratification of the produced plasma. The thermal instability responsible for the filamentation of current-carrying plasma columns develops in any azimuthally uniform medium provided that the rate of current rise is sufficiently high.

1.4. Massive Electrodes as an Additional Plasma-Producing Load in Z-Pinches with Cold Start

Since the Z-pinch length is limited by massive electrodes, one has to deal with another problem associated with cold start: formation of a plasma sheath at the electrodes. In the MITL, which must deliver the current I to the load located on its axis, the linear current density $j_{\mathrm{lin}} = I/2\pi r$ increases with decreasing radius r of the current-carrying plasma. In a high-power Z-pinch, the electric power density created in a load with $r \sim 1$ cm exceeds 1 TW/cm^2. The current density $j \sim 10^8$ A/cm^2 is insufficient to vaporize a conductor in 10–20 ns. When the linear current density exceeds 1 MA/cm, this value of current density is attained when the skin-layer thickness is $\delta \sim 0.01$ cm. For a conductor with conductivity $\sigma \sim 10^{16}$ CGSE units, the skin-layer relaxation time is $t \sim 4\pi\delta^2\sigma/c^2 \sim 10$–15 ns, which corresponds to the durations of the processes involved in our experiments. Electric vaporization from the current-carrying surface leads to plasma formation in the electrode gap. The ensuing uncontrolled nonuniform plasma flow into the imploding-discharge volume strongly affects the dynamics of Z-pinch implosion.

These considerations apply equally to both cathode and anode conductors. However, the effects due to the cathode plasma are stronger. Figure 3 shows an X-ray photograph of a Z-pinch clearly demonstrating the skirt-shaped plasma sheath at the cathode.

The difference in plasma behavior between the anode and cathode sheaths is poorly understood. The formation of the near-cathode plasma sheath may be affected by the effect of electrons involved in the near-cathode magnetic self-insulation region. The ion current incident on the cathode may heat its surface to a higher temperature as compared to the anode surface. However, the results of the experiments reported in [1–5] may be explained in technical rather than fundamental terms. The wire-array cathode is connected to the current-carrying conductor by a sliding contact, which is degraded by azimuthal nonuniformity. The required pinch mass balance in the pinch may be violated by the erosive plasma generated in the contact zone at a linear current density higher than 1 MA/cm and ejected into the volume surrounded by the wire array. Under certain conditions, the uncontrolled plasma flow into the electrode gap can be prevented by using low-density porous solid electrodes adjoining the load. They can be rapidly vaporized, and the resulting plasma can be carried away from the gap by magnetic field to compensate for the plasma ejection into the gap.

1.5. Strong Preionization not Induced by Current as an Unimplemented Alternative to Cold Start

Actually, cold start precludes the implementation of the liner scheme of multiterawatt imploding discharge. Here, the liner is interpreted as a conducting thin massive cylindrical shell accelerated to a high velocity so that its kinetic energy transforms into heat as it hits an obstacle (the inner shell). In a multiterawatt imploding discharge, the liner is obviously a plasma shell. The creation of a compact massive plasma shell with a kinetic energy of at least 100 kJ is a key problem in liner design. In fast imploding discharges with cold start, the desired shell has not been created to this day.

The problem could be resolved by means of strong preionization of the plasma-producing medium. It is essential that preionization must not lead to generation of a spatially nonuniform plasma, as in discharges with cold start. Implementation of liner preionization not induced was attempted for less powerful discharges [14]. The much higher power required to implement preionization in multiterawatt discharges entails much higher costs. Strong preionization by an ion beam (with power up to ~0.1 TW) may be more efficient. The parameters of the plasma generated by this method must be chosen to prevent further ionization processes leading to its filamentation after the main current pulse is fired. An initial electron temperature of about 10 eV seems sufficient to ensure that the thermal instability leading to filamentation is suppressed by radiative loss. However, this method has not been implemented because of its technological complexity and relatively high cost.

Ionization of a foam liner by an auxiliary external shell would be practicable if it were sufficiently slow for the filaments to expand and merge together. Some encouraging results have been obtained in the first experiments on interaction between a megampere-current shell of a microsecond-scale plasma focus with a foam liner [15]. However, the subsequent coupling of the generator producing the main current pulse to the plasma shell obtained by this method has yet to be investigated.

Strong preionization is indispensable, because it provides a unique means to implement liner implosion schemes based on the original ideas put forward in the early 1980s.

2. PROLONGED PLASMA PRODUCTION AS A MAIN CONSEQUENCE OF COLD START [2, 3]

Prolonged plasma production is an experimentally established unquestionable consequence of the cold start of a fast Z-pinch. Many facets of this phenomenon characteristic of various plasma-producing materials have been described in [1–5]. The recently published results of experiments on wire-array implosion in the MAGPIE facility [16] suggest a similar phenomenological pattern of wire-array discharge, but the theoretical interpretations of the results presented in [1–5] and [16] are essentially different. The interpretation of the MAGPIE experiments proposed by their authors relies on the model of [7, 8]. Our interpretation is based on the model of a heterogeneous liner with prolonged plasma production presented below.

2.1. Phenomenology of Prolonged Plasma Production Based on the Experimental Results of [1–5] and Physical Model of Plasma Production in a Heterogeneous Medium

Prolonged plasma production in imploding discharges with cold start manifests itself most clearly in the dominant role played by the Ampére force in the plasma dynamics until the plasma-producing load completely transforms into an accelerated plasma. First of all, the combined effect of the magnetic fields generated by multiple current-carrying filaments on an individual filament drives the filaments and the low-density plasmoids evolving from wires in the radial direction before the plasma begins to implode as a whole. The plasma driven inwards by the total magnetic field generated by the current that flows through it concentrates on the axis into a precursor pinch much earlier than does the wire-array plasma. Moreover, the local magnetic field generated by the current flowing through a current-carrying column (an individual filament or a vaporized wire) affects the column itself. This can lead to magnetically driven filamentation of the column resulting in its axial MHD nonuniformity. It was shown in [2] that the magnetically driven filamentation easily occurs in high-atomic-number plasma-producing gases.

The relative importance of the effects of the total and local magnetic fields on the dynamics of the plasma being produced depends on various conditions. However, experiments demonstrate that the entire pinch evolution at the plasma-production stage is affected by the continuing inward flow of new portions of the accelerated plasma from the plasma-producing region. The generated plasma carries part of the current, but the outer boundary of the plasma remains at the initial outer radius of the plasma-producing load for a long time. Under the conditions of our experiments, the outer plasma boundary remains at rest during the entire interval of current rise. The observed stationarity of the

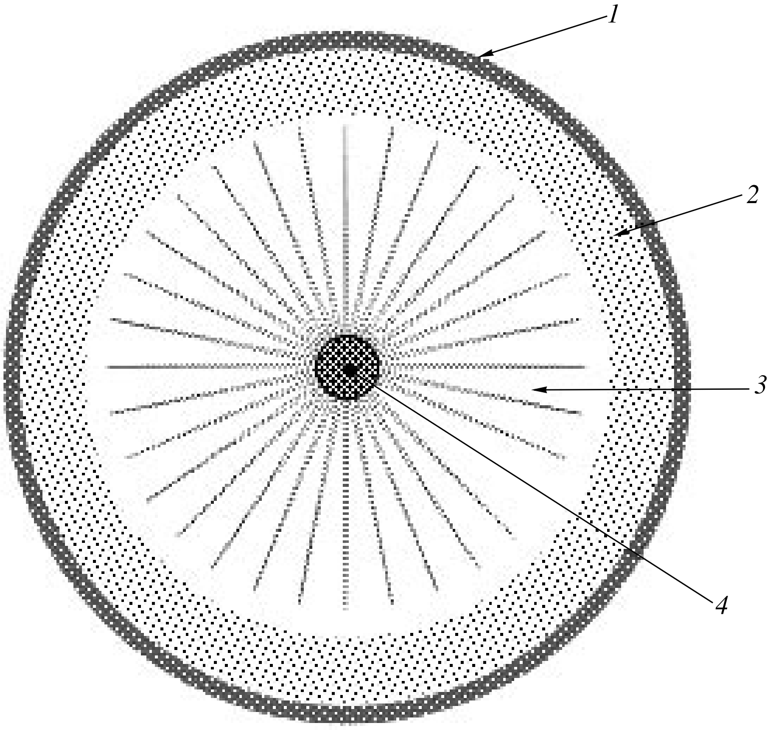

Fig. 4. Plasma-production configuration (not to scale): (*1*) heterogeneous plasma-producing load; (*2*) region of azimuthal magnetic field pumping into plasma; (*3*) radial plasma moving with frozen-in magnetic field; (*4*) precursor pinch. Actual boundaries between regions are not distinct.

outer plasma boundary implies that the rates of plasma production and plasma flow driven by the Ampére force are balanced.

The experimental results reported in [1–5] provide a basis for a physical model of prolonged plasma production. Our approach differs from those developed in the model of [7, 8] and earlier studies, which were focused on the azimuthal structure of the wire-array plasma at the initial stage of the discharge. We also take into account the azimuthal structure of the plasma-producing load in estimating the wire-array vaporization (see Section 2.2). However, we do not consider the azimuthal structure of the plasma-producing load as the factor that plays the dominant role in prolonged plasma production.

In our model of plasma production, it is assumed that the total azimuthal magnetic field B generated by the current I carried by the heterogeneous plasma-producing medium containing a condensed phase plays the dominant role almost from the very start of the discharge. To simplify our analysis of the basic physical characteristics of prolonged plasma production, we assume that the local plasma sources are uniformly distributed over the plasma-producing region and the spacing between them is small as compared to the size of the region. As a suitable model of the medium, we consider an annular cloud of microscopic dust grains in vacuum. The spacing between them is assumed to be much greater than the grain diameter and much smaller than the thickness of the annulus, which is much smaller than its radius. Figure 4 illustrates the radial structure of this liner at the stage of prolonged plasma production.

During the first nanoseconds of the discharge, the current flowing through region *1* in Fig. 4 (occupied by dust grains of the plasma-producing material) switches over to the low-density plasma occupying the space between the grains. The plasma occupying regions *1* and *2* is heated, its conductivity increases, and the azimuthal magnetic field generated by the discharge current is frozen into the plasma. Flow *3* of the plasma carrying the frozen-in magnetic field is driven by the Ampére force toward the axis, giving rise to a precursor pinch. The dust grains are vaporized by heat and radiation fluxes from plasma regions. The corresponding flux intensities are relatively low, and the vaporization lasts for tens of nanoseconds; i.e., its duration is comparable to the current rise time. In the meantime, the outer boundary of the region occupied by current and plasma remains at rest at the location of region *1* until complete vaporization is achieved. Thus, the plasma production involves the following processes: vaporization and ionization in region *1*, diffusive mixing of the plasma and magnetic field in region *2*, and inward radial motion of the produced plasma driven by the Ampére force. These processes are discussed below in more detail. In Section 2.2, we present the results obtained by computing the wire-array vaporization. In

Sections 2.3–2.6, we analyze the dynamics of the plasma flow into the liner volume.

2.2. Model of Vaporization of an Azimuthally Nonuniform Plasma-Producing Load

In this section, we consider an azimuthally structured load consisting of many vaporized tungsten wires. The results obtained by X-ray probing of a vaporized wire array using an X-pinch [4] demonstrate that each vaporized wire consists of a dense core surrounded by a plasma of relatively low density. Since the core spacing is much greater than the core radius, we can consider a single core. Experimental data can be used to describe the core structure after a relatively long time $t_X \approx 60$ ns has passed since the starting instant of current rise and the total current through the wire array has reached about 1 MA. For a wire of radius 6 μm, the core diameter reaches the value $2r_c = 18$ μm in about 60 ns. Assuming that the mass per unit length of the wire has reduced to $m_c \approx 2.6$ μg/cm, we find that the mean core density is $\rho_c \sim 1$ g/cm^3, while the critical density of tungsten is 4.5 g/cm^3. The point in the phase diagram for tungsten where $\rho_c \sim 1$ g/cm^3 corresponds to a temperature above 12×10^3 K [17], i.e., a thermal velocity above 8×10^4 cm/s, whereas the measured velocity of core expansion is about 1.5×10^4 cm/s. Therefore, the core should be considered as a volume occupied by a heterogeneous mixture of ionized vapor and liquid droplets rather than a homogeneous vapor. In this model, we take into account both evaporation from the droplet surface and the loss of mass due to vapor flow from the core boundary. The source of energy release in the core is the joule heating by the current J flowing through the ionized vapor. The current is driven by the electric field E generated by the voltage drop along the wire array (region *1* in Fig. 4). The core can also be heated by the energy fluxes from the outer higher temperature plasma due to radiative transfer and electron heat conduction. The present model ignores these additional energy fluxes, even though they can substantially increase the rate of the liquid-phase evaporation, particularly at its final stage.

We treat the core as a cylinder of radius r_c consisting of a mixture of vapor with liquid droplets of radius r_L and density ρ_L characterized by a droplet concentration N_L per unit length and a concentration $n_L = N_L/\pi r_c^2$ per unit volume. It is obvious that the liquid mass per unit length is smaller than the core mass per unit length. The opacity of the heterogeneous core structure for probing X-rays from an x-pinch suggests the following estimate for the droplet concentration. If the probing photons (with $h\nu \sim 3$ keV) are completely absorbed by the droplets, then the core's opacity implies that $N_L r_L^2 > r_c$. Neglecting the vapor mass contained in the core, we have $r_L\rho_L < r_c\rho_c$, $r_L < 0.35$ μm and $N_L > 10^6$ cm^{-1}; hence, $n_L \sim 3 \times 10^{12}$ cm^{-3}, which is comparable to the concentration of defects in a cold metal (on the order of 10^{12} cm^{-3} [18]).

The mass and energy balance equations for the core at a uniform temperature T are written as follows:

$$\frac{m_L}{\rho_L} + \frac{m_G}{\rho_G} = \pi r_c^2, \quad r_L = \sqrt[3]{\frac{3}{4\pi}\frac{m_L}{N_L\rho_L}},$$

$$u_T = \sqrt{\frac{k_B T}{2\pi M}}, \quad P_L(T, \rho_L) = P_G(T, \rho_G), \tag{1}$$

$$\frac{dm_L}{dt} = -4\pi r_L^2 N_L u_T(\rho_t(T) - \rho_G),$$

$$\frac{d(m_L + m_G)}{dt} = -2\pi r_c u_T \rho_G,$$

$$m_L\frac{d\varepsilon_L}{dt} + m_G\frac{d\varepsilon_G}{dt} - \frac{dm_L}{dt}(\varepsilon_G - \varepsilon_L) + P_G\dot{V} = JE, \tag{2}$$

$$\dot{V} = 2\pi r_c u_T, \quad J = \pi r_c^2 \sigma E,$$

where m is mass, ε is energy per unit mass, P is pressure, $\rho_t(T)$ is the saturated vapor density for tungsten, and V is the core volume; the subscripts L and G refer to liquid and gas, respectively.

To set the value of E in (2), we use the experimental fact that the discharge current flowing through a wire array switches over to the low-density plasma outside the core at an early stage: i.e., the core carries only a small fraction of the current: $J \ll I/N$, where I is the total discharge current and N is the number of wires in the array. Since J has never been measured directly, we have to calculate J from (2) for a given E. The electric field strength at the outer boundary of the plasma-producing region is determined by the global characteristics of the discharge, which can be reliably measured. To find the electric field in region *1*, we consider the motion of a perfectly conducting plasma moving toward the axis with a drift velocity V at the boundary between regions *1* and *2* (see Fig. 4). If B is the azimuthal magnetic field generated by the discharge current I at the outer boundary of region *1*, then the magnetic field B' at the boundary between regions *1* and *2* is weaker, because only a fraction of I penetrates into region *2* with the plasma. In the next section, we show that $B' \sim B/\sqrt{3}$. The plasma motion across the field with velocity V generates the electric field $E' = 10^{-8}VB'$, where E' is measured in volts per centimeter and the remaining quantities are measured in CGSE units. The difference between the electric field E in region *1* and E' is due to induction. If the radial magnetic-field profile is linear across region *1* of small thickness $\delta R \sim 0.1R_a$ (R_a is the array radius) and $I < 3$ MA, then

$$E - E' \approx 2 \times 10^{-9}\frac{\delta R}{R_a}\frac{dI}{dt} < 5\ \frac{\text{kV}}{\text{cm}}.$$

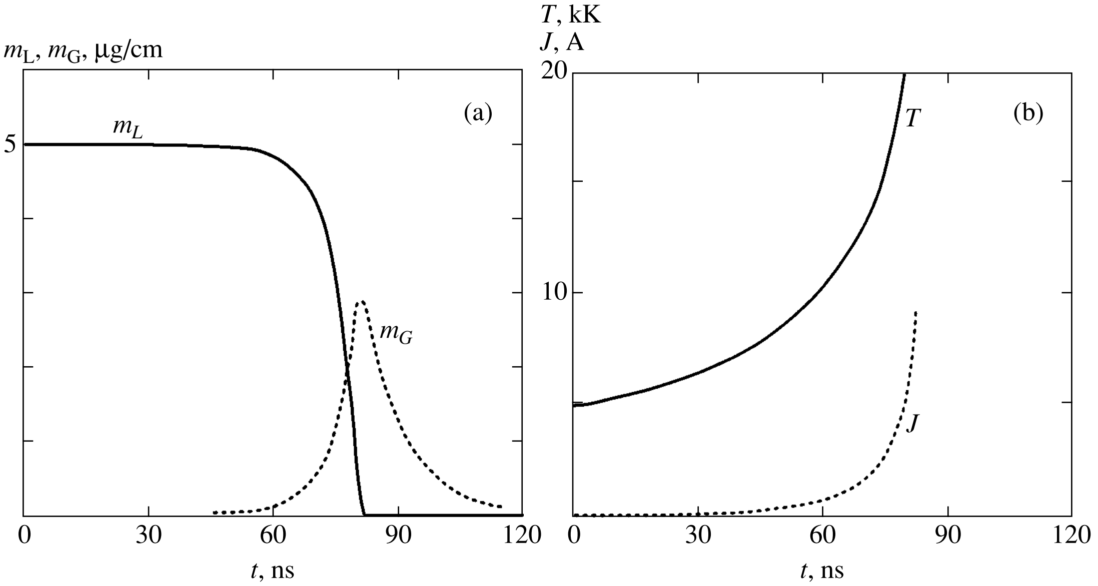

Fig. 5. Computed evolution of heterogeneous core of constant radius r_c = 10 μm for electric field strength E = 30 kV/cm: m_L and m_G are the liquid- and vapor-phase masses per unit core length, T is temperature, and J is current through the core.

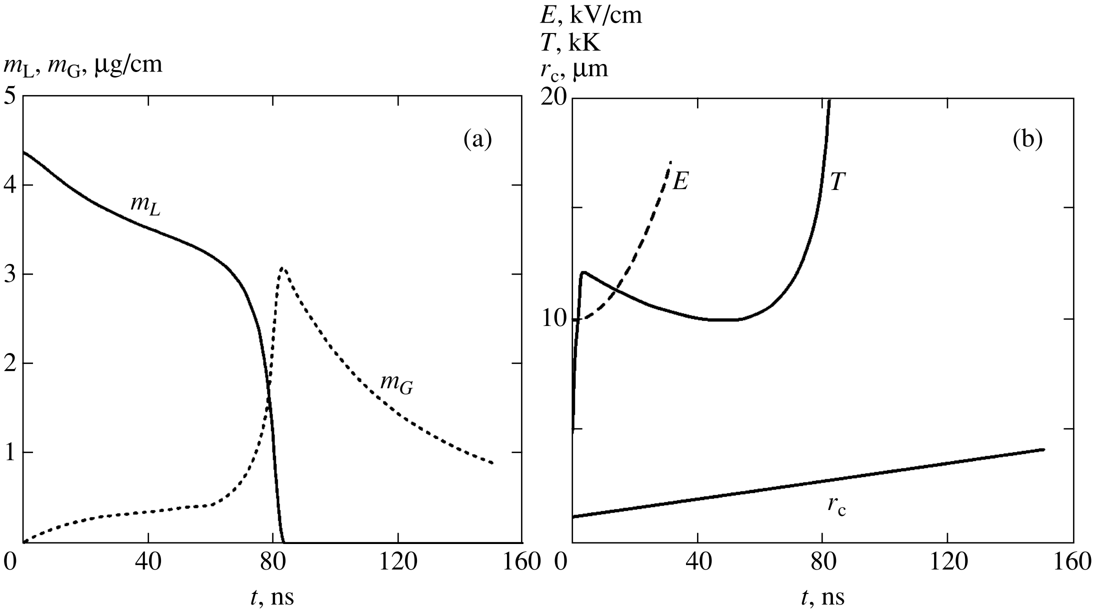

Fig. 6. Computed evolution of heterogeneous core with time-dependent radius r_c and E increasing with time (see Fig. 5 for notation).

According to our experimental results, the radial plasma velocity at the boundary between regions *1* and *2* is $V = (1–2) \times 10^7$ cm/s. Therefore, if I = 2 to 3 MA and R_a = 1 cm, then $E \sim E'$ = 20–60 kV/cm.

In our calculations, Eqs. (1) and (2) were supplemented with equations of state for liquid and gaseous tungsten [19]. The current through the core was calculated as $J = \pi r_c^2 \sigma E$, where the conductivity σ of tungsten was determined by using a Coulomb logarithm model [20]. The effect of the liquid-droplet phase on the current was ignored in view of the condition $m_L/\rho_L < m_G/\rho_G$. Figure 5 shows the evolution of a heterogeneous core computed for r_c = 10 μm and E = 30 kV/cm. Figure 6 shows the evolution of a core with a linearly growing radius for E increasing with time.

The computed results show that rapid droplet evaporation begins only after 60 to 70 ns have passed since the starting instant of current rise. This agrees with the results of our experiments, where a dense phase was detected at 70 ns after the starting instant of current rise. However, quantitative agreement between numerical and experimental results is not required at this stage of our study, because our goal was to elucidate the nature of the process.

The drastic decrease in the mass of the liquid phase at $t \sim 80$ ns and the corresponding increase in the vapor mass inside the core are due to the jump in the core temperature that occurs when the energy consumption required to vaporize the liquid tungsten ceases. Indeed, if $J \sim 10$ A (as in our computations) and $E \sim 3 \times 10^4$ V/cm, then $JE \sim 3 \times 10^5$ W/cm. Assuming that the power thus produced is consumed entirely to vaporize the liquid tungsten in the core, we find that the rate of vaporization is about 0.1 μg/ns per unit length of the core. This agrees with the numerical results shown in Fig. 6: $dm_L/dt \sim 0.1$ μg/cm at $t \sim 70$–80 ns. After the liquid phase has evaporated completely, the vapor mass contained in the core decreases as the vapor flows out of the core into the space between the wires. The rate of vapor-mass loss calculated over the interval from 90 to 100 ns does not exceed 0.05 μg/(ns cm). When $N = 50$, the flow rate of the mass to be ionized and accelerated by the Ampére force is $dm_G/dt \sim 2.5$ μg/(ns cm).

2.3. Plasma Production Rate Required to Sustain a Steady Flow of Tungsten Plasma from the Plasma-Producing Region with a Stationary Boundary

In this section, we analyze the dynamics of the material vaporized in region *1* (see Fig. 4). To simplify analysis, we assume that the local plasma sources are uniformly distributed over the region. The produced plasma having a low density ρ and a conductivity σ occupies region *1* and flows into region *2*. Suppose that the current flowing through the plasma generates an azimuthal magnetic field B at its boundary. In the course of plasma production in regions *1* and *2*, the azimuthal magnetic field is frozen into the produced plasma. The Ampére force drives the current-carrying plasma out of region *2* toward the axis with a velocity on the order of the Alfvén velocity $V_A \sim B/(4\pi\rho)^{1/2}$, giving rise to a transition layer of thickness $\Delta \sim c^2/4\pi\sigma V_A$. Suppose that the energy required to maintain the balance between the rates of plasma outflow and production is provided by the heat flux determined by the electron heat conductivity of the inward-moving plasma. These simplifying assumptions were used in [3] to derive an expression for the radial velocity of the inward-moving plasma under the condition that the mass rate of production of ionizable material by vaporization of condensed phase in the core is sufficient (see Section 2.2):

$$\frac{dm}{dt}\left[\frac{\mu\text{g}}{\text{cm}^2\ \text{ns}}\right] \approx 0.2\left(\frac{I_{[\text{MA}]}}{R_{[\text{st}]}}\right)^{1.8}. \qquad (3)$$

It should be recalled here that the process is analyzed by ignoring both axial and azimuthal nonuniformity of plasma production, which are clearly observed in experiments. Nonetheless, this simplified analysis leads to important results discussed below.

2.4. Mathematical Model of Plasma Inflow into the Liner Volume at the Plasma-Production Stage

Following [3], we use a one-dimensional cylindrical MHD model and assume that thermal-pressure gradients are weak as compared to the Ampére force. Then, we have

$$\frac{\partial}{\partial t}v + v\frac{\partial}{\partial r}v = -\frac{1}{8\pi r^2\rho}\frac{\partial (Br)^2}{\partial r}, \qquad (4)$$

$$\frac{\partial}{\partial t}B + \frac{\partial}{\partial r}(vB) = 0, \qquad (5)$$

$$\frac{\partial}{\partial t}\rho + \frac{1}{r}\frac{\partial}{\partial r}(\rho v r) = 0, \qquad (6)$$

where B is the azimuthal magnetic field, v is the radial plasma velocity, and r is radius. Boundary conditions are set for prolonged plasma production at $r = R_l$ (liner radius):

$$(\rho v)\big|_{r = R_l} = -\dot{m}(t), \qquad (7)$$

$$\left(\rho v^2 + \frac{B^2}{8\pi}\right)\Bigg|_{r = R_l} = \frac{[B_0(t)]^2}{8\pi}, \qquad (8)$$

$$-v\big|_{r = R_l} \le \frac{|B|}{\sqrt{4\pi\rho}}\Bigg|_{r = R_l}. \qquad (9)$$

According to boundary condition (8), the newly generated plasma has zero radial velocity. The magnetic field at the outer liner boundary is determined by the total discharge current $I(t)$:

$$B_0(t) = \frac{2I(t)}{cR_l}, \qquad (10)$$

which is treated as a prescribed function of time. Conditions (7)–(9) imply that a considerable fraction of the total current flows through the region of plasma production inside the liner. In particular, if the inward-moving plasma has the Alfvén velocity, then the magnetic field at the inner boundary of the liner is $B_0/\sqrt{3}$, i.e., about 40% of the current flows inside the liner.

2.5. One-Dimensional Model of Z-Pinch Evolution Allowing for a Finite Interval of Decreasing Plasma Production Rate

Prolonged plasma production must come to an end before the outer boundary of the current-carrying plasma begins to contract into a Z-pinch. It is obvious that the rate of plasma production does not instantly

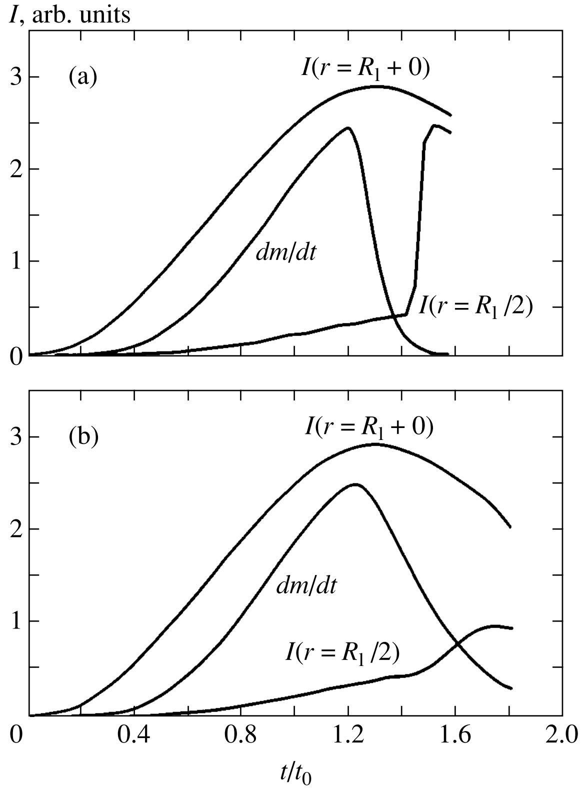

Fig. 7. Time-varying current within the liner half-radius for (a) fast and (b) slow decrease in $\dot{m}(t)$.

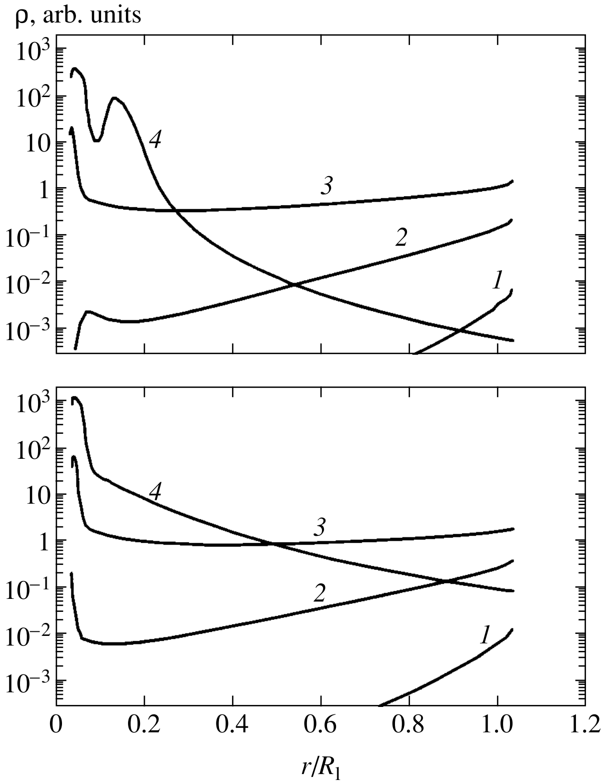

Fig. 8. Computed radial profiles of plasma density at (*1*) $t = 0.25t_0$, (*2*) $t = 0.58t_0$, (*3*) $t = 1.04t_0$, and (*4*) $t = 1.80t_0$ for (a) fast and (b) slow decrease in $\dot{m}(t)$.

drop to zero. Suppose that the plasma production rate initially increases as $\dot{m}(t) = CI^{\mu}$ at $t \le t_q$ and then decreases as $\exp(-(t - t_q)/t_f)$. The total mass of the liner is M_l. To solve Eqs. (4)–(9), we use dimensionless variables defined in terms of the reference current I_0, reference length $R_0 \equiv R_l$, and reference time t_0. The corresponding reference values of velocity, plasma density, and liner mass per unit length are $V_0 = R_l/t_0$, $\rho_0 = I_0^2 t_0^2/\pi c^2 R_l^4$, and $M_0 = (I_0 t_0/cR_l)^2$, respectively. To compare computed results with experimental data, we set $I_0 = 1$ MA, $R_0 = R_l = 1$ cm, and $t_0 = 100$ ns.

Figures 7–10 show the computed results. Figure 7 shows the time-varying current within the liner half-radius; Figs. 8–10, radial profiles of density, discharge current, and velocity at several points in time. Panels (a) and (b) correspond to relatively fast and slow decrease in $\dot{m}(t)$, respectively.

The computed results demonstrate that discharge current penetrates into the liner even at an early stage of plasma production, owing to diffusion of the magnetic field generated by the current into the produced plasma. Another important finding is the strong dependence of basic Z-pinch parameters on $\dot{m}(t)$. When $\dot{m}(t)$ is relatively low, the region inside the liner half-radius carries less than half the total current, whereas almost the entire current flows within the half-radius. The rates of plasma and current concentration near the axis are several times higher in the case of high $\dot{m}(t)$ as compared to low $\dot{m}(t)$. Therefore, timely termination of plasma production is a crucial factor that determines a high degree of compression in a Z-pinch with cold start.

2.6. Penetration of Azimuthal Magnetic Flux into the Liner Volume: Distinction of the Present Model from the Model of [7, 8]

In the model of [7, 8], the axially nonuniform structure of the plasma and magnetic field was analyzed for each wire, and the plasma flows originating in the gaps between the wires were not magnetized. For this reason, it was concluded that current concentrates in around the wires rather than penetrates into the liner volume at the plasma production stage, and the precursor plasma does not carry any current. We have measured the azimuthal magnetic field inside the wire array by means of miniature magnetic probes [5], and there is no reason to question the reliability of the results obtained, at least, before the Z-pinch began to contract as a whole. Figure 11 shows the results of magnetic probing obtained for a 20-mm diameter array of 80 5-μm diameter wires. It demonstrates that current begins to flow through the region within a radius of $0.5R_l$ at the plasma-production stage, amounting to

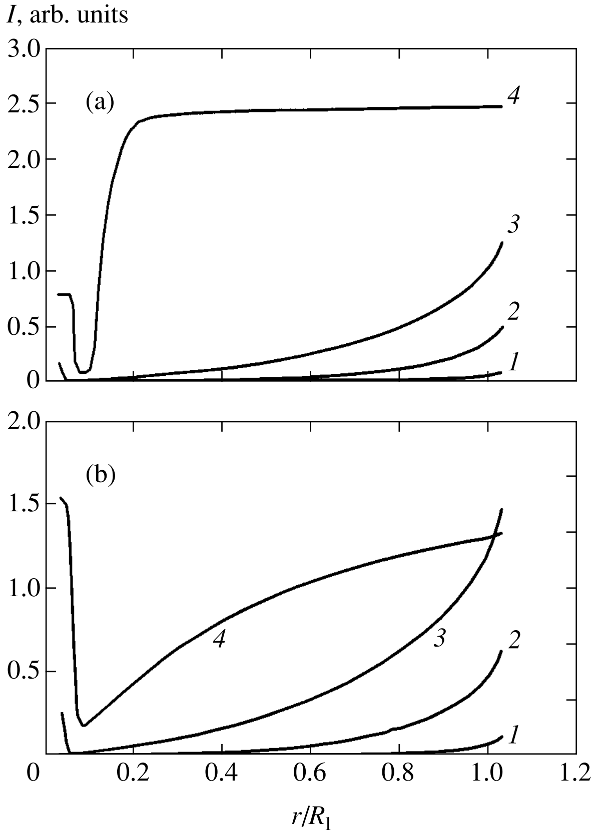

Fig. 9. Computed radial profiles of discharge current at (*1*) $t = 0.25t_0$, (*2*) $t = 0.58t_0$, (*3*) $t = 1.04t_0$, and (*4*) $t = 1.80t_0$ for (a) fast and (b) slow decrease in $\dot{m}(t)$.

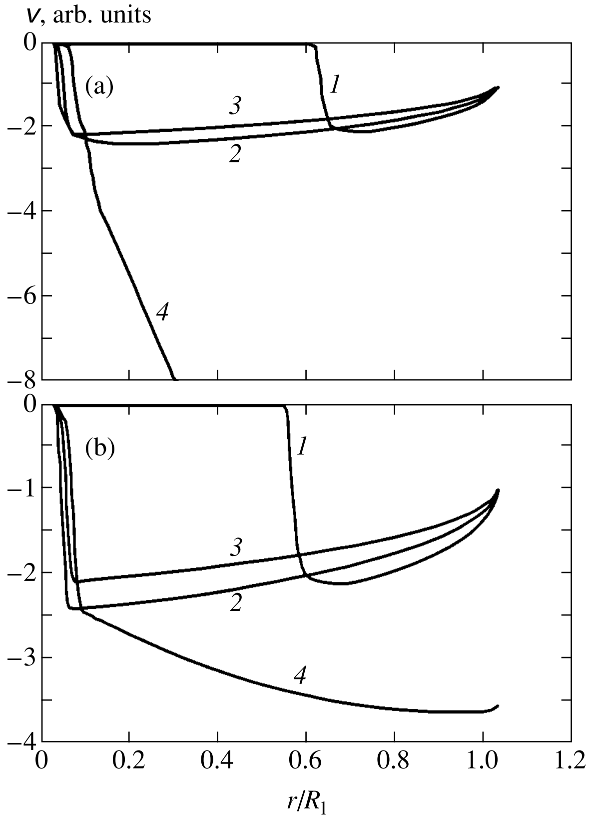

Fig. 10. Computed radial velocity profiles: (a) fast decrease in $\dot{m}(t)$, (*1*) $t = 0.22t_0$, (*2*) $t = 0.50t_0$, (*3*) $t = 0.91t_0$, and (*4*) $t = 1.58t_0$; (b) slow decrease in $\dot{m}(t)$, (*1*) $t = 0.25t_0$, (*2*) $t = 0.58t_0$, (*3*) $t = 1.04t_0$, and (*4*) $t = 1.80t_0$.

about 15% of the total current. In this particular case, less than half the total current was found to flow through the region within the liner half-radius by the moment of peak emission from the Z-pinch. Apparently, the parameters of the plasma-producing load deviated from their optimal values required to achieve the highest rate of implosion, and the decrease in the plasma production rate was relatively slow, as illustrated by Figs. 7b–10b. However, these results support one of the basic points of our model: a current-carrying plasma penetrates into the liner volume at the stage of prolonged plasma production.

In the model of [7, 8], the assumption of zero current through the volume inside the wire array at the plasma-production stage is inferred from the experimental fact that the precursor seems to be macroscopically stable. We claim that this assumption is not well grounded. Indeed, as long as a relatively high rate of plasma production is sustained, the outer boundary of the plasma is tied to the wire-array radius. This observation was made both in our experiments [4] and in those conducted at the MAGPIE facility [16]. The steadiness of the outer boundary is conditioned on a sufficiently high rate of plasma flow into zones where its density drops for any reason. Fast plasma production "cures" transient nonuniformities of plasma density arising at the boundary. We believe that the stability of the outer

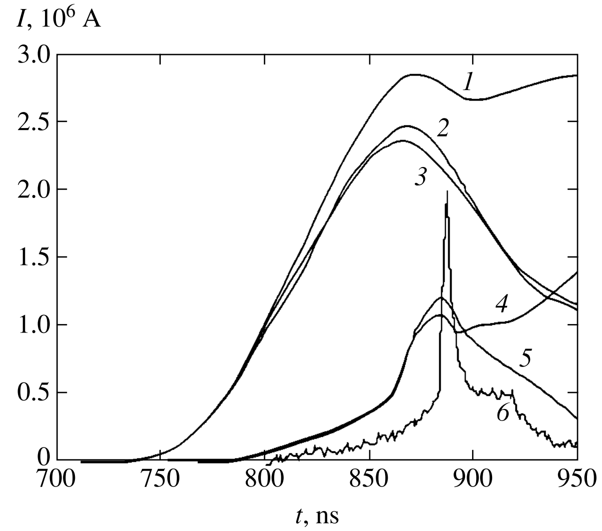

Fig. 11. Currents within the radii (*1*) 55 mm, (*2*) 30 mm, (*3*) 30 mm (two probes), (*4*) 5 mm, and (*5*) 5 mm (two probes) and (*6*) soft X-ray intensity (arbitrary units) for a wire array of radius 10 mm.

plasma boundary can ensure the MHD stability of a current-carrying precursor plasma.

Plasma instabilities develop when balance cannot be maintained between the radial plasma motion driven by the Ampére force and plasma supply to zones where plasma sources are depleted. Magnetic flux breaks through these zones into the volume encompassed by the depleted plasma-producing load.

3. BREAKTHROUGH OF MAGNETIC FLUX ACROSS THE DISRUPTED PLASMA-PRODUCING REGION AND PARTIAL PLASMA TRAPPING

The results of detailed experimental investigation of the magnetic flux breakthrough inside gas and foam liners, which are azimuthally homogeneous in the initial state, have been described in [1, 2]. Below, we will consider analogous phenomena in azimuthally nonuniform systems (wire arrays).

3.1. Experimental Observation of Breakthrough of Azimuthal Magnetic Flux across a Wire Array

Evidence of a spatially inhomogeneous magnetic flux breakthrough is provided by the phenomenon of a radial plasma rainstorm, which has been discovered and investigated in our previous work [5]. It was demonstrated that the current-induced implosion in tungsten wire arrays gives rise to considerable azimuthal and axial inhomogeneity of the plasma. The Ampére forces drive the generated plasma toward the axis in the form of a plasma rainstorm (multiple plasma jets of relatively small diameter, elongated in the radial direction). As these jetlike plasmoids move toward the array axis, they decrease in radial size and merge together to form isolated plasma current filaments elongated predominantly along the discharge axis. The plasma in the thus formed Z-pinch also remains spatially inhomogeneous at the time of intense X-ray emission.

Figure 12 shows an example of the time-integrated pinhole image of the Z-pinch in a double-shell wire array comprising the outer aluminum wire array with a diameter of 12 mm and the inner tungsten wire array with a diameter of 6 mm. The X-ray photograph clearly reveals the rainstorm of aluminum plasma from the outer array, whereas virtually no such rainstorm is observed for the inner array. The qualitative difference between collapse in the outer and inner arrays is explained, in particular, by the different conditions of plasma formation. Indeed, the plasma production in the inner array is influenced by the plasma flow from the outer array. These peculiarities of the plasma production process in the system under consideration require further investigation.

As noted above, the spatial inhomogeneity of the plasma rainstorm is retained upon the onset of intense X-ray emission from the Z-pinch. The breaking-through magnetic flux entrains the plasma in which it is frozen. The mass of the entrained plasma may account for only a fraction of the residual mass of the plasma-producing material. The magnetic flux breakthrough overtakes the subsequent implosion of the plasma. For this reason, the X-ray emission pulse may precede the final collapse of the plasma as a whole. This behavior is clearly illustrated in Fig. 13, which shows a series of pinhole images synchronized with the oscilloscopic trace of the intensity of X-ray emission from tungsten plasma. The first frame corresponds to the end of the first stage of plasma production and the onset of the magnetic flux breakthrough. Here, one can still distinguish a pinch precursor (prepinch), whose emission is masked in the second shot by a superimposed pulse of emission from the plasma rainstorm filling almost the entire space inside the wire array. The second and third frames correspond to the maximum intensity of soft X-ray emission from the pinch. The time interval between second and third frames is about 10 ns. During this period of time, the streams of plasma rainstorm almost completely reach the paraxial region, and the intensity of X-ray emission passes through a maximum and begins to decrease. Note that the image of expanding plasma in the fourth frame has clearer and more smoothened contour as compared to those of turbulent jets of the plasma rainstorm observed in the second and third frames.

The main conclusion following from these experimental results is that the Z-pinch collapse under the conditions studied begins with a spatially inhomogeneous breakthrough of the magnetic flux, followed by plasma contraction toward the axis. The large-scale axial inhomogeneity of this flux even at the start is so pronounced that it is impossible to speak of a continuous plasma current shell. For this reason, it would be incorrect to treat this phenomenon using the formalism of the Rayleigh–Taylor instability or in terms of the classical snowplow model.

Thus, the nonuniform contraction of the outer boundary of discharge is caused primarily by the inhomogeneity of plasma formed at the final stage. On the whole, the plasma production zone may still contain a considerable amount of the plasma-producing material. However, should the plasma production in some parts of the liner be insufficiently intense, the energy of the azimuthal magnetic field accumulated outside a thin cylindrical liner penetrates inside by forming a spatially inhomogeneous flux of magnetic energy and entrained plasma—a radial plasma rainstorm—that is in fact the Z-pinch.

3.2. Criteria for Breakthrough of Magnetic Flux into the Liner Volume at the Final Plasma-Production Stage

As long as the balance between plasma production and its outflow under the action of the Ampére forces is

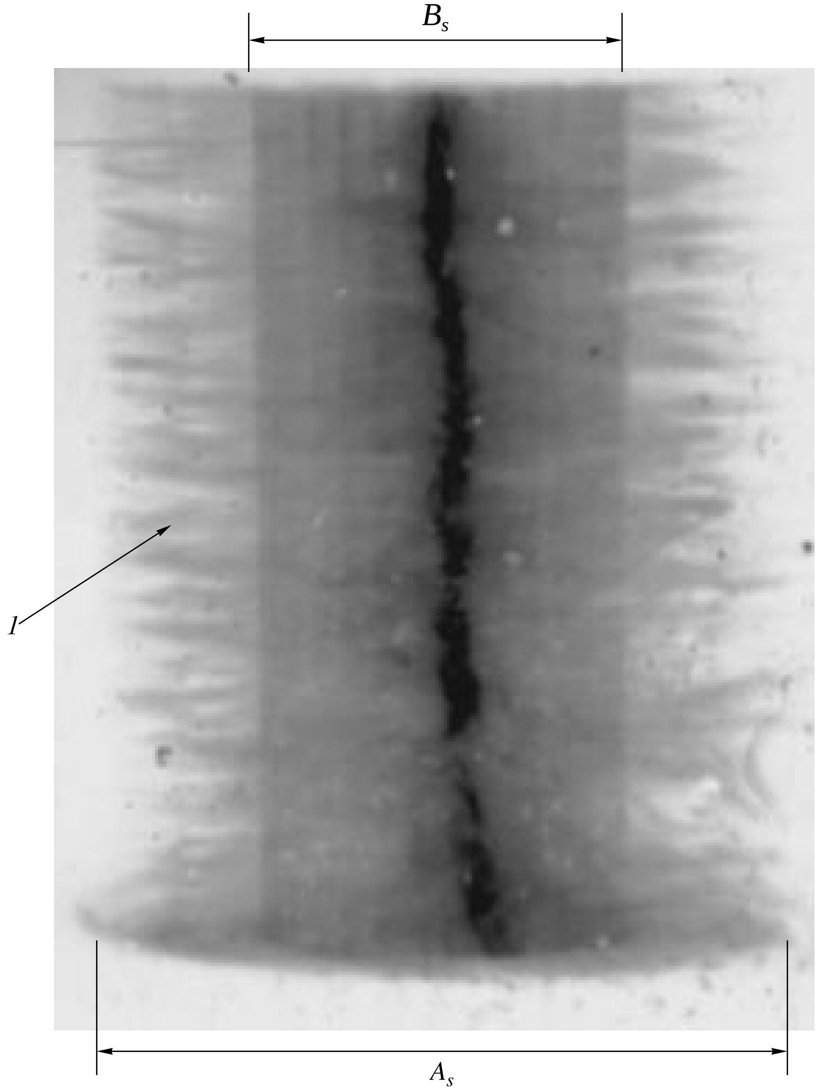

Fig. 12. Time-integrated X-ray photograph of double-shell implosion for an outer array of starting diameter A_s = 12 mm (30 aluminum wires of diameter 20 μm) and inner array of starting diameter B_s = 6 mm (20 tungsten wires of diameter 6 μm): (*1*) plasma rainstorm from the outer array.

ensured, the outer boundary of the current-carrying plasma is determined by the initial geometry of the plasma-producing medium. Evidently, the current-carrying plasma cannot be azimuthally structured: the current channels may feature only the axial local small-scale inhomogeneities, while the outer plasma boundary remains at rest in the scale of the whole liner. The plasma-producing medium (in particular, the dense component of the material of exploding wires), being converted into the plasma state under the action of a heat flux and the emission from discharge, is consumed at a rate of $\dot{m}(t)$ equal to the amount of material removed from the plasma-production region by the Ampére force (with the outer boundary of the current–carrying plasma occurring at rest). An estimate of this rate was obtained in Section 2.4, where it was in fact implied that the necessary amount of the plasma-producing material is available at each point of the zone of plasma production. Yet the stock of this material is exhausted in some time. In addition, the material supply rate may also decrease, for example, because of the reduction in area of the particles of plasma-producing material in the course of their evaporation. The process of the material stock exhaustion and the material supply rate decrease is locally inhomogeneous. As a result, zones will eventually appear in the plasma-producing medium where the balance of the material supply and the plasma outflow under the action of the Ampére forces is shifted toward the latter process. These zones are featuring uncompensated decrease in the plasma density and, as a result, admit the breakthrough of the azimuthal magnetic flux inside the axially inhomogeneous cylindrical liner. Now we will provide a simple

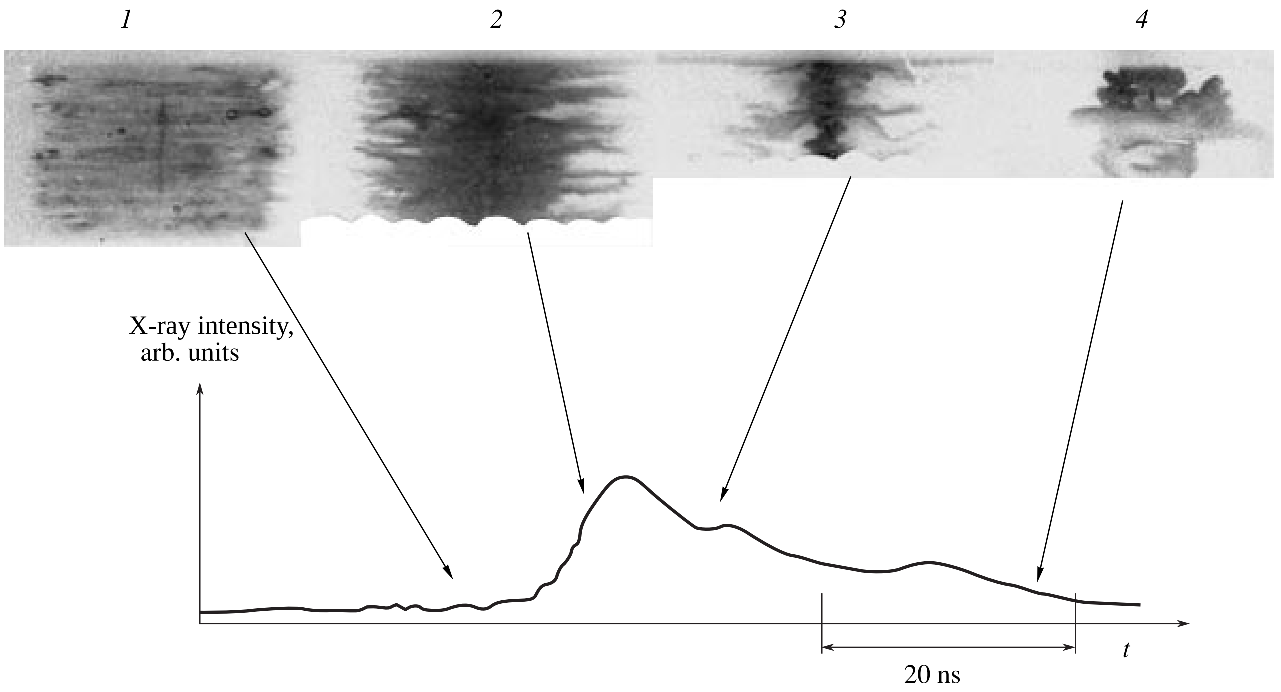

Fig. 13. Pinhole images (exposure time ~2 ns) synchronized with oscilloscopic trace of X-ray intensity for an array of diameter 12 mm (60 tungsten wires of diameter 8 μm) (shot no. 3880): the near-cathode pinch region is not recorded in frames *3* and *4*.

evaluation of this process using the scheme depicted in Fig. 14.

Let an axial gap d deprived of the source of plasma-producing material to appear in a circular zone of plasma production with radius R and thickness Δ. The region of decreased plasma density is supplied with the material at the expense of plasma diffusion across the azimuthal magnetic field B from two sides, so that the total incoming plasma flux is

$$G_{\mathrm{d}} \approx 2\frac{c^2}{4\pi\sigma}(2\pi R\Delta)\frac{\partial\rho}{\partial z}. \qquad (11)$$

At the same time, the plasma outflow at a velocity of V_{A} (on the order of the Alfvén wave velocity) under the action of the Ampére forces accounts for the outgoing radial plasma flux

$$G_s \approx \rho V_{\mathrm{A}}(2\pi R d). \qquad (12)$$

Replacing, for the sake of simplicity, $\partial\rho/\partial z$ by ρ/z and assuming that $V_{\mathrm{A}} = I/5R(4\pi\rho)^{1/2}$, we obtain an estimate for the critical discharge current I_{cr} above which the magnetic flux penetrates inside the liner via the circular gap with the axial length (width) d:

$$I_{\mathrm{cr}}\ [\mathrm{A}] \approx 3\times 10^{21}\frac{\sqrt{\rho}}{\sigma}\frac{R\Delta}{d^2}. \qquad (13)$$

Assuming $\rho \sim 10^{-4}$ g/cm^3, $\sigma \sim 10^{14}$ esu, $\Delta \approx d \approx 0.1$ cm, and $R \approx 1$ cm, we obtain $I_{\mathrm{cr}} \approx 3$ MA.

Since criterion (13) is obtained under very general assumptions, the above relations can be used only for obtaining rough estimates. Nevertheless, weak dependence of the critical current I_{cr} on the density ρ and its

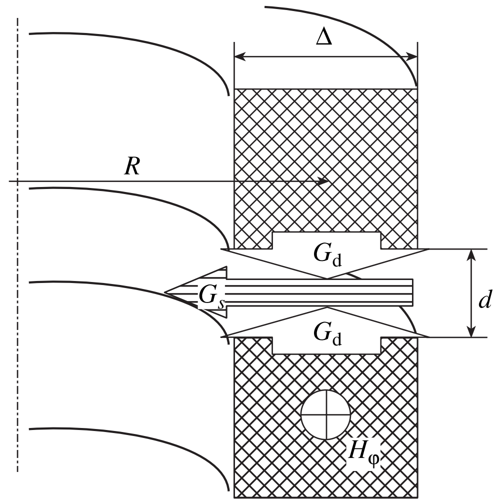

Fig. 14. Breakthrough of azimuthal magnetic flux into an axially nonuniform cylindrical liner: R and Δ are the radius and width of annular plasma-production region, d is the axial gap not occupied by plasma-producing material, G_{d} is diffusive plasma flux, G_s is radial plasma flow, and H_φ is azimuthal magnetic field generated by discharge current.

strong dependence on the gap width d allow us to make some general conclusions based on criterion (13).

First, azimuthal variations of the density ρ (which depend, in particular, on the distance between wires in the wire array) are not as substantial. Therefore, it is not as important whether the plasma-producing medium is azimuthally homogeneous or not (as in a wire array): the produced plasma will unavoidably break into separate coaxial fragments before the complete consumption of the plasma-producing medium.

Second, the most probable are the relatively rough coaxial gaps with the d values comparable with the macroscopic size of the liner plasma in the final stage of plasma production.

The appearance of a circular coaxial gap leads to the radial outflow of current with the residual plasma from gap d, which may result in magnetic insulation of the gap. If the magnetic insulation condition is satisfied, the current ceases to flow through the gap. The simplest condition for such a magnetic insulation is smallness of the Larmor electron radius as compared to the gap width ($r_{\rm L} \ll d$). For electrons with an energy of 0.5 MeV under the conditions studied, the Larmor radius is $r_{\rm L} \sim 5 \times 10^{-3}$ cm and, hence, the magnetic insulation of the gap is quite possible.

Now let us obtain another estimate for the conditions under which the current does not flow through the gap. If the azimuthal magnetic field with a plasma breaking through the axial circular gap moves at a velocity close to the Alfvén velocity, an emf is induced in the gap in the direction opposite to the electric field exciting the current. The magnitude of this emf can be estimated as

$$E_{\rm d}\left[\frac{\rm V}{\rm cm}\right] \sim 10^{-8}V_{\rm A}B \sim 4\times10^{-10}\frac{I^2}{r^2\sqrt{4\pi\rho}}. \qquad (14)$$

For $I = 2 \times 10^6$ A, $r = 0.5$ cm, $\rho = 3 \times 10^{-5}$ g/cm^3, and $V_A \approx 4 \times 10^7$ cm/s, this formula yields $E_{\rm d} \approx 3.3 \times 10^5$ V/cm. This emf can be sufficient to block the current flow through the gap, provided that the gap width d is not very small. Under such conditions, an electric power of $W_{\rm d} = E_{\rm d}Id$ is transferred via the gap inside the liner. Then, using expression (14), we obtain an estimate

$$W_{\rm d}\ [{\rm W}] \sim 4\times10^{-10}I^3\frac{d}{r^2\sqrt{4\pi\rho}}. \qquad (15)$$

4. MHD TURBULENT HEATING AND RADIATIVE COOLING OF STAGNANT PLASMA

4.1. MHD Turbulent Heating

The state of implosion is a natural consequence of magnetic flux breakthrough into the paraxial region. Contraction of the magnetic flux and entrained plasma is followed by the period of stagnant pinch. Spatial inhomogeneity of the Z-pinch plasma is also retained upon the onset of stagnation. The characteristic transverse size of jetlike plasmoids in the paraxial zone, which emit quanta with an energy of 1–2 keV, amounts to 100–200 μm and the maximum length is several times as great.

Previously [5], we demonstrated that, by thoroughly selecting the initial parameters of composite wire arrays, it is possible to obtain a radiative state of the pinch in the form of a straight filament with a diameter of ~400 μm and insignificant spatial inhomogeneity at a total length of 15 mm. The duration (full width at half maximum, FWHM) of the emission pulse from such objects was 6–10 ns at a pulse front width of 1–2 ns. The magnetic energy dissipated in the discharge at the stage of intense emission amounts approximately to 4 TW (see Section 5.2).

Thus, our experiment has demonstrated transformation of a plasma rainstorm with an initial radial size on the order of 1 cm into a plasma column with a diameter below 0.5 mm, possessing a fine internal structure and radiating in a multiterawatt power range. Apparently, this result has to be explained without recourse to the concept of liner as a massive, compact cylindrical plasma shell accelerated by the magnetic field pressure in the radial direction to a kinetic energy on the order of 100 kJ, since such a shell was never observed in our experiments. For this reason, we believe that a stagnant, spatially inhomogeneous pinch features conversion of the energy of the current-generated magnetic field into the turbulent MHD flow of the ion component of the imploded plasma. This process involves convective mixing of the plasma with magnetic field, heating, energy transfer from ions to electrons, and X-ray emission from the stagnant plasma. We have suggested this scheme [2] for a radiating Z-pinch based on the results reported by Lovberg *et al.* [9]. This scheme had been thoroughly studied [10] and, at present, the MHD turbulent heating model can be considered as most adequately describing the experimental data.

The MHD turbulent heating power introduced in the form of the current-generated magnetic field energy into the paraxial region of the pinch can be described by a formula of type (15), modified so as to include the parameters controlled in experiment. For a pinch of radius r [cm] and the current I [A] flowing in the imploded plasma with a mass per unit length M [g/cm] = $\pi r^2\rho$, expression (15) yields the following approximate formula for the MHD turbulent heating power per unit length of imploded pinch:

$$W_{\rm th}\left[\frac{\rm W}{\rm cm}\right] = 10^{-10}\frac{\chi I^3}{rM^{1/2}}, \qquad (16)$$

where χ is a dimensionless factor describing the parameters (including the degree of inhomogeneity) of plasma in the pinch. This parameter was estimated [9, 10] assuming that a certain part of the imploded plasma in the pinch is filled with toroidal magnetic bubbles penetrating from the periphery to paraxial region of the pinch. According to this model, the final approximate expression for the MHD turbulent heating power can be written as [10]

$$W_{\mathrm{th}}\left[\frac{\mathrm{TW}}{\mathrm{cm}}\right] = 0.5\frac{I^3}{rM^{1/2}}, \qquad (17)$$

where I, M, and r are measured in megamperes, micrograms per centimeter, and millimeters, respectively.

In application to real experiment, the accuracy of formulas (16) and (17) should not be overstated. Indeed, inhomogeneities in a plasma rainstorm are represented by radial plasma jets (exhibiting transformation in the course of implosion), rather than by toroidal magnetic bubbles on a homogeneous plasma background. For this reason, the structure of relatively coarse, large-scale inhomogeneities developed in the MHD turbulent plasma rainstorm should be described using factor χ calculated based on some other assumptions. Most reliably, this quantity can be evaluated only in experiment. It should be noted that strong dependence of the transferred power W_{th} on the current and radius of imploded plasma in formulas (16) and (17) implies the need for detailed information on the radial distribution of current in the pinch, but such experimental data are so far not available.

4.2. Energy Balance in a Radiating Turbulent Pinch

Let us assume that the MHD turbulent heating power estimated by formula (17) is transferred to the ion component of plasma, while electrons are heated by the energy transferred from the ion component. Evaluation of the energy transfer from ions to electrons showed that, under the conditions studied, this factor does not limit the radiation power.

An upper estimate for the radiation power W_{rad} can be obtained using the theory developed in [21]. Assuming the mean path of radiation quanta to be l_{v} and the radiation output to be free, we have

$$W_{\mathrm{rad}} = \frac{4V\sigma_{\mathrm{SB}}T^4}{l_{\mathrm{v}}}, \qquad (18)$$

where σ_{SB} is the Stefan–Boltzmann constant. For a plasma of multicharged ions, the l_{v} value is given by the formula [21]

$$l_{\mathrm{v}} = \frac{4.92\times10^{-11}A^2T^{4.5}}{Z_m(Z_m+1)^2I_m\rho^2}\ \mathrm{cm}, \qquad (19)$$

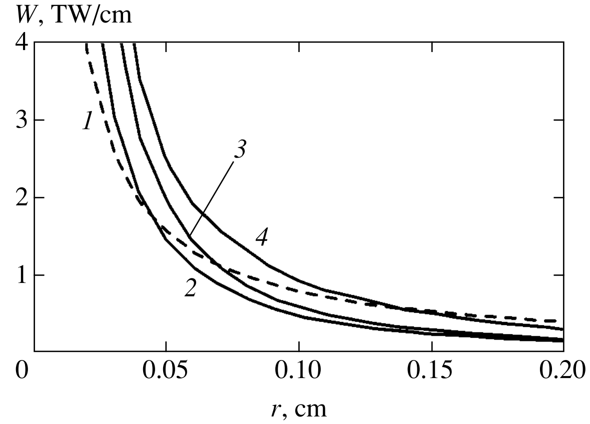

Fig. 15. Radial profiles of turbulent heating rate and X-ray power output for M = 100 μg/cm and I = 2.6 MA: (*1*) W_{th} given by (17); (*2*) W^*_{rad} for T_e = 250 eV; (*3*) W^*_{rad} for T_e = 300 eV; (*4*) W_{rad} for T_e = 200 eV.

where $\rho = M/\pi r^2$, Z_m is the average ion charge, A is the atomic weight, I_m is the average ionization potential (corresponding to the plasma density ρ [g/cm^3] and temperature T [eV]), M [g/cm] is the plasma mass per unit length of the pinch, and r [cm] is the pinch radius. It should be noted that expressions (18) and (19) derived using the method proposed in [21] significantly overstate the contribution of a hard radiation component with quantum energies above I_m. With neglect of the hard radiation component in expressions (18) and (19), the radiation power decreases by factor of three, which provides for a lower estimate (this estimate of the radiation power is denoted W^*_{rad}).

A comparison of the radiation powers for the MHD turbulent heating of the pinch (Eq. (17)) and the radiation power (Eqs. (18) and (19)) shows that these values differently depend on the pinch radius r. Therefore, a pinch radius may exist for which the two powers are equal. For a smaller radius of the pinch, the radiation power estimated using these formulas exceeds the heating power. Once the pinch has contracted to such an extent, the subsequent implosion proceeds in the regime of radiative cooling, and the real radiation power is determined by the MHD turbulent heating rate. As an illustration, Fig. 15 demonstrates that the condition W_{rad}, $W^*_{\mathrm{rad}} \sim W_{\mathrm{th}}$ corresponds to a pinch contracted to a radius of ~1–2 mm when the current is 2.5 MA and the mass per unit length of the tungsten plasma is 100 μg/cm.

Although the above formulas for the turbulent heating power (W_{th}) and the radiation power (W_{rad}, W^*_{rad}) giver only rough estimates, they nevertheless correctly reflect the relationships between Z-pinch parameters typical of our experiments. This allows us to draw certain conclusions that may provide a basis for subsequent experiments. In particular, it can be hypothesized that the condition of approximate equality of the radiation power and heating rate for the Z-pinch in tungsten plasma holds in a wide range of the degrees of pinch implosion. In other words, radiation plays a key role in the energy balance of the imploding pinch under the conditions of our experiments. Thus, radiative cooling of the imploding spatially inhomogeneous plasma explains the formation of radiating filamentous structures in the turbulent current-carrying plasma and the transformation of a radial plasma rainstorm into radial “protuberances” observed in our experiments [5].

5. EFFECTIVE CONVERSION OF ACCUMULATED MAGNETIC ENERGY INTO Z-PINCH HEATING AND MULTITERAWATT X-RAY EMISSION

5.1. Z-pinch as a Time-Dependent Nonlinear Component of the Discharge Circuit

Energetic processes in the Z-pinch are closely related to the magnetic energy supplied from a generator via a magnetically insulated transfer line. For this reason, an analysis of the electric processes in the generator–MITL–Z-pinch circuit is a necessary prerequisite for correct understanding of the physics of Z-pinch and for effective optimization of the pinch parameters. Z-pinch, as an electric circuit component, is time-dependent nonlinear impedance that consumes the energy supplied from the generator creating a magnetic field in the MITL. The character of the Z-pinch impedance varies depending on the stage of discharge.

In the course of plasma production, which lasts for almost the entire period of discharge current rise, the outer current boundary remains at rest. This implies that the MITL inductance (L_0 in Fig. 1) coupling the load (Z-pinch surface) to the water–vacuum interface of the generator remains virtually constant. Even though a fraction of the discharge current is carried by the load during plasma production, the magnetic energy transferred to the load is small as compared to that accumulated in the external inductance ($L_0 \sim 10$–20 nH). The ohmic resistance of the plasma column with a diameter of 1–2 cm is small as compared to the inductive impedance L_0/τ, where $\tau \sim 100$ ns is the current rise time. Therefore, the discharge in the course of plasma production exhibits an inductive character, and the magnetic energy accumulated in the inductance L_0 outside the liner can be estimated as $E_H = 0.5L_0I^2 \sim$ 100–150 kJ.

At the stage of termination of the plasma production, the magnetic flux breakthrough inside the liner sharply changes the character of the load impedance. Moving in the radial direction at a velocity of V_A (on the order of the Alfvén velocity), the magnetic flux generates an emf described by formula (14). From the standpoint of the electric circuit, this emf is equivalent to the active impedance

$$\frac{dL}{dt} \approx 2 \times 10^{-9}\frac{V_A}{r}\left[\frac{\Omega}{\text{cm}}\right],$$

where r is the radius of the current channel. The accumulated magnetic energy E_H is expended to compress and heat the trapped plasma and drive the magnetic field into the space within the starting radius of the array. Upon breakthrough of the magnetic flux with entrained plasma inside the paraxial region, the magnetic flux exhibits implosion and the pinch enters the stage of stagnation. In this stage, the major part of the magnetic energy and the energy supplied from the generator are converted into the MHD turbulent motion of the ion component of the imploded plasma.

5.2. Experimental Determination of Electric Power in the Discharge Circuit

With neglect of the electron losses in the magnetically insulated transfer line, an equation for the current-carrying (generator–MITL–load) circuit depicted in Fig. 1a can be written as follows:

$$2E - \rho_g I - \frac{d(LI)}{dt} - \Omega I = 0. \tag{20}$$

Here, $L = L(t)$ is the total inductance of the circuit and Ω is the ohmic component of the load impedance $Z(t)$.

Experimentally measured quantities are (i) the voltage $V(t) = 2E(t) - \rho_g I(t)$ applied to the MITL and (ii) the derivative $dI(t)/dt$ of the total current. Using these values, it is possible to determine the active power and some other characteristics in the discharge circuit. To this end, Eq. (20) can be represented as the differential equation with respect to the inductance $L(t)$ (with $L(0) = L_0$), involving the known values of $V(t)$, $dI(t)/dt$, and $I(t) = \int(dI/dt)\,dt$:

$$I\frac{dL}{dt} + \frac{dI}{dt}L + (\Omega I - V) = 0. \tag{21}$$

This differential equation can be numerically solved for an arbitrarily set form of the $\Omega(t)$ function. The L_0 value is chosen such that $L_0 dI/dt \sim V(t)$ in the current rise stage (while $L(t) \sim L_0$). In this way, we determine the value of $L(t)$, dL/dt, and $W_{\text{suppl}} = V(t)I(t)$ (the power pumped by the generator into the MITL). In addition, it is possible to calculate the functions $W_{\text{ind}}(t) = L(t)I(t)dI/dt$ (called inductive power in the discharge circuit) and the difference $W_{\text{act}} = W_{\text{suppl}} - W_{\text{ind}}$ (called active power in the discharge circuit). Figure 16 gives an example of the results of such calculations for $\Omega(t) = 0$. As can be seen, the active power in the discharge circuit reaches $W_{\text{act}} \sim 4$ TW, which is about twice the maximum power supplied from the generator

(W_{suppl} ~ 2 TW) in this particular experiment. On the time scale, the maximum of W_{act} is close to the maximum power of the soft X-ray emission pulse.

Note that it is the current derivative, a quantity dramatically changing in the stage of active implosion and emission from the pinch, that determines the time variation of the inductive and active power components in the circuit according to the expression for $W_{\text{ind}}(t) = L(t)I(t)dI/dt$. At the moments of a sharp change in the current derivative (see Figs. 1b and 16), the circuit features dissipative processes involving multiterawatt power related to fast implosion of the current-carrying plasma, heating of the plasma, and X-ray emission from the pinch. During the entire period of time related to the current rise, plasma production, and the prepinch formation, the active power in the discharge circuit is small as compared to that developed at the moment of emission from the pinch.

Figure 16 demonstrates that about half the active power at the moment of maximum W_{act} is provided by consuming the previously accumulated magnetic energy. Indeed, W_{ind} at this moment is negative, and the other part, W_{suppl}, is determined by the operation of the generator, which continues to pump energy into the MITL. In experiment, the relation between W_{suppl} and W_{ind} depends on the choice of the load parameters: the initial radius and mass per unit length of the liner. An increase in these values leads to a delay in pinch implosion and reduces the power W_{suppl} supplied by the generator. On the contrary, when both radius and mass of the liner are small (i.e., for an early pinch implosion), the active power in the circuit is primarily determined by the generator power output.

In all experiments, the soft X-ray emission pulse is strictly related on the time scale to the W_{act} pulse. The leading and trailing fronts of the emission intensity pulse are somewhat steeper as compared to those of the W_{act} pulse. In experiments, the energy that dissipated in the circuit, which is defined as

$$E_{\text{act}} = \int W_{\text{act}} dt,$$

reached a level of ~100 kJ, and the soft X-ray emission output energy was 50–60 kJ.

5.3. Z-Pinch as an Effective Converter of Magnetic Energy into Soft X-Ray Radiation

In order to obtain pulses of soft X-ray emission from the Z-pinch, it is necessary to provide for a number of conditions, otherwise this task will not be solved.

Our experience shows that a real multiterawatt Z-pinch with a cold start is a three-dimensional radiating object characterized by a high degree of spatial inhomogeneity. Nevertheless, high-intensity soft X-ray emission from the Z-pinch was observed in a rather broad range of the initial parameters of the plasma-producing material. From this it follows that the high power and yield of the X-ray emission from the Z-pinch can be obtained provided that the plasma, albeit spatially inhomogeneous, is capable of accepting and radiating the supplied electromagnetic energy and that the system of energy transfer and concentration is capable of delivering this energy from the generator to the plasma. From the standpoint of plasma physics, the problem of inhomogeneity of the radiating plasma was considered in the previous sections. Below, we will consider in more detail the requirements on the electrical characteristics. Assuming that the properties of the first component in the generator–MITL–Z-pinch circuit can be determined independently, we will discuss the necessary features of matching between the remaining two components and between each of these and the generator.

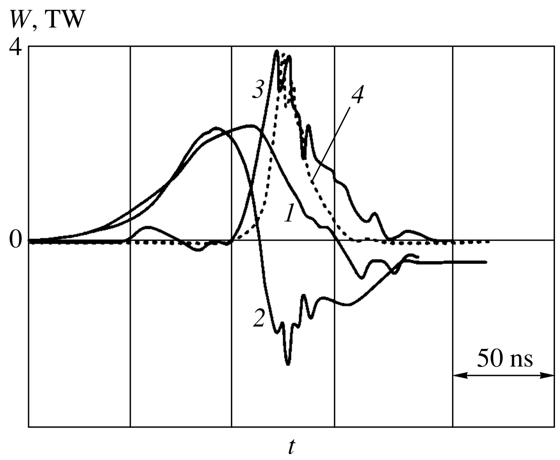

Fig. 16. Computed power characteristics of the discharge circuit: (*1*) $W_{\text{suppl}}(t) = V(t)I(t)$ is the power supplied by the generator to the MITL, (*2*) $W_{\text{ind}}(t) = L(t)I(t)dI/dt$ is inductive power, (*3*) $W_{\text{act}}(t) = W_{\text{suppl}} - W_{\text{ind}}$ is active power, and (*4*) soft X-ray power output (arbitrary units).

5.4. Optimum Matching between the MITL Inductance and the Z-Pinch Impedance

If the Z-pinch were coupled directly to the generator, rather than via an inductance (representing the MITL), the optimum matching condition (ensuring the maximum transmitted power) between the nonstationary pinch impedance $Z(t)$ and the wave resistance ρ_g of the generator would look as follows: $Z(t) \sim \rho_g$ (for the Angara-5-1 facility, $\rho_g = 0.25\ \Omega$).

The presence of an MITL with inductance L_0 and the time-dependent behavior of the pinch impedance $Z(t)$ change the optimum matching conditions for maximum energy transfer to the load. In this case, the parameters of the generator–MITL–Z-pinch circuit have to obey a complex set of requirements. First, it is necessary to ensure that the maximum energy would be accumulated in the MITL by the onset of the effective

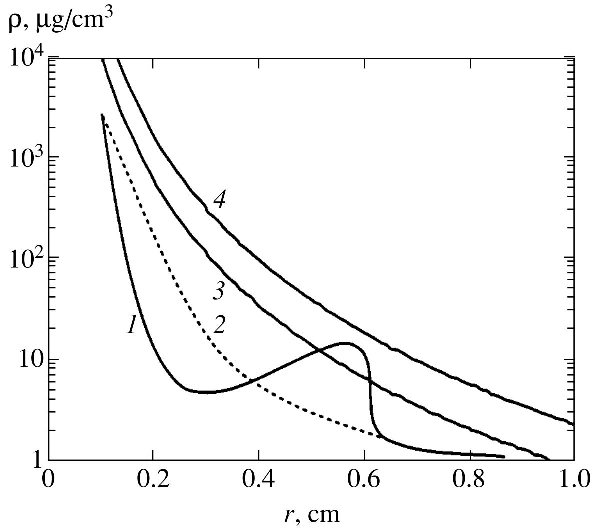

Fig. 17. Estimated radial plasma-density profile in the gap that cannot be exceeded for a given rate of power transfer W_{tr} for the starting radius of plasma-producing load r_0 = 0.6 cm and I = 3 MA: (*1*) and (*2*) are model profiles, (*3*) and (*4*) are computed profiles for W_{tr} = 5 and 3 TW, respectively.

implosion of the current-carrying plasma. Second, the pinch impedance after the onset of effective implosion would increase so as to ensure that the accumulated magnetic energy be dissipated in the imploded plasma within the shortest period of time. Finally, the MITL must ensure the delivery of this energy from the electrode gap to the pinch. Let us consider these requirements in more detail.

5.4.1. Optimum value of L_0. Using Eq. (20), it is possible to determine the optimum inductance L_0 for maximum magnetic energy accumulation corresponding to a preset emf $E(t)$ and $L(t) = L_0$. For the Angara-5-1 facility, $E(t) \sim E_m \sin(\pi t/T)$, where $T \sim 150$ ns. By solving Eq. (20), one can readily determine the optimum value $L_0 \sim 20$ nH. The existence of this optimum reflects the fact that $\rho_g \neq 0$. For L_0 values below this optimum, the characteristic current decay time L_0/ρ_g turns out to be much shorter than T. In this case, the energy cannot be completely pumped into the MITL (L_0) and is partly reflected back to the generator. The L_0 values exceeding the optimum pose limitations on the current I developed by the generator. In the general case, for a semisinusoidal shape of the emf pulse $E(t)$, the optimum L_0 value is related to the generator internal resistance ρ_g as $L_0 \approx \theta \rho_g T$, where $\theta \approx 0.5$–0.6, T is the period [ns], and L is the inductance [nH].

5.4.2. Optimum value of pinch impedance Z_{eff}. In accordance with the results presented in Section 4, the impedance of a stagnant MHD turbulent Z-pinch is proportional to the current: $Z_{eff} \sim I/(rm^{1/2})$. In order to effectively dissipate the accumulated magnetic energy, this impedance must be much higher than that of the generator that pumps magnetic energy into the MITL: $Z_{eff} \gg \rho_g$. Apparently, a value of $Z_{eff} \sim 1\ \Omega$ might provide for a sufficiently high dissipated power ($W_{act} \sim 10$ TW) in the Angara-5-1 facility. It is also important that this impedance would be switched quite rapidly (within ~10 ns). Our experimental results showed that, under real conditions, this level has not yet been achieved. One possible limiting factor, insufficiently high quality of implosion reducing the active pinch impedance, was considered in the preceding sections. Another possible factor responsible for a decrease in W_{act} can be insufficiently effective magnetic insulation of the MITL.

5.4.3. Performance of the MITL magnetic insulation. Magnetic insulation of the gap between current-carrying electrodes has to be effective not only in the stage of current rise and magnetic energy pumping into the gap, but at the stage of magnetic energy transfer to the imploded radiating pinch as well (i.e., ~100 ns after onset of the current rise). This period is of critical importance for reaching a high power of energy dissipation and, hence, high-intensity X-ray emission from the pinch. Indeed, a voltage across the pinch corresponding to $W_{act} \sim 10$ TW must exceed 3 MV at a current of ~3 MA. Therefore, the electric field strength in the electrode gap near the pinch ($d \sim 1.5$ cm) to be hold by the magnetic insulation exceeds 2 MV/cm. The experience shows that a high energy density in the liner system, both at the stage of magnetic energy pumping and in the stage of its maximum consumption in the radiating pinch, leads to the appearance of a dense plasma of the electrode surface material, which moves inside the gap at a velocity on the order of 10^7 cm/s. By the moment of maximum emission from the pinch, the electrode plasma fills up to one- to two-thirds of the electrode gap. The presence of a plasma in the gap gives rise to the leak currents shunting the pinch current in the imploded state. In addition, the rate of the magnetic energy supply to the radiating pinch can be controlled by the plasma through (or with) which the magnetic flux is delivered to the pinch.

The energy dissipated in the pinch is supplied to the paraxial region via the plasma with a density profile $\rho(r)$ in the electrode gap. In the case of delayed plasma production, the plasma density profile may have a rather complicated shape (Fig. 17, curve *1*). The pinch plasma density is maximum in the paraxial region carrying the current I. Another local density maximum can be achieved on the radius r_0 of the plasma-producing material. The plasma may also occur in the region of $r > r_0$ in the magnetically insulated electrode gap, where it appears as a result of the current-induced surface explosion of the electrodes.

In the region of $r < r_0$ in the electrode gap, the plasma is frozen in the magnetic field generated by the current I. For this reason, the velocity of propagation of the magnetic field frozen in the plasma can be considered in the MHD approximation as close to the Alfvén velocity: $V(r) \sim V_A$. Then, by analogy with formulas (14) and (15), the total power that can be transferred via the electrode gap of width d filled with a plasma having the density profile $\rho(r)$ for $r < r_0$ is

$$W(r)\ [\mathrm{W}] \approx \left(\frac{H^2}{8\pi} + \frac{\rho V_A^2}{2}\right)(2\pi r d)V_A \approx 4\times10^{-10} I^3 \frac{d}{r^2\sqrt{4\pi\rho}}. \quad (22)$$

This relation can be also presented in the following form:

$$W = I^2 Z_{\mathrm{act}},$$

where

$$Z_{\mathrm{act}}(I, r, \rho, d)\ [\Omega] \approx 4\times10^{-10} I \frac{d}{r^2\sqrt{4\pi\rho}}$$

is the active nonlinear impedance of the discharge imploding at the Alfvén velocity. This impedance is independent of the electric conductivity of imploded plasma. The nonlinear impedance of the imploded discharge, in contrast to that determined by the Joule losses in the plasma, depends on the discharge current. This nonlinear impedance determines the energy spent to transfer the mass of imploding plasma with the frozen-in magnetic field. At the stage of stagnation of the MHD turbulent pinch, this impedance characterizes the energy consumed for turbulent stirring of the magnetic field and entrained plasma under the conditions of effective radiative cooling of the plasma.

A criterion of applicability of the MHD approximation is $c/\omega_{pi}d \ll 1$, where c is the velocity of light and ω_{pi} is the ion plasma frequency. In the opposite case, when $c/\omega_{pi}d \gg 1$, the motion of the azimuthal magnetic field determined by the current I has to be described in the EMHD approximation [22], according to which the velocity of the magnetic field front propagation in the plasma is evaluated as $V_A(c/\omega_{pi}d)$ and the motion of ions is ignored. The EMHD approximation is typically valid in a gap with the radius $r > r_0$, where the electromagnetic power transmitted through the gap is

$$W(r)\ [\mathrm{W}] \approx 2\times10^{-10} I^3 \frac{d(1 + c/\omega_{pi}d)}{r^2\sqrt{4\pi\rho}} \quad \text{at} \quad r > r_0. \quad (23)$$

For an analysis of energy fluxes in the plasma rainstorm, that is, in the region of $r < r_0$, let us fix the power $W(r) = W_{\mathrm{tr}}$ = const in Eq. (22). This value in fact characterizes the energy transmission capacity of the gap for $r < r_0$. We used Eq. (22) with the experimental set of parameters, I = 3 MA and W_{tr} = 3 or 5 TW, and obtained estimates for the radial profile of plasma density in the gap, $\rho(r) \sim 1/r^4$, which should not be exceeded. These profiles are presented in Fig. 17 (curves *3* and *4*). For example, let a model plasma-producing material array with a starting radius of $r_0 \sim$ 0.6 cm exhibit a local density maximum $\rho(r_0) \sim$ 15 μg/cm^3 (Fig. 17, curve *1*). This density exceeds the value permitted for a power of W_{tr} = 5 TW (which therefore will not be admitted into the pinch). If the $\rho(r)$ profile has no local maxima (Fig. 17, curve *2*), the power W_{tr} = 5 TW will be transmitted to the paraxial plasma region. The power W_{tr} = 3 TW will be transmitted in both cases. Thus, a residual plasma (even with a relatively small density) present at the pinch start radius r_0 poses a limitation on the level of power that can be transmitted to the paraxial region of the pinch.

An analogous analysis can also be performed for $r > r_0$ by using (23) instead of (22). Equations (22) and (23) predict a very sharp radial variation of the admissible density not to be exceeded for a given energy transmission capacity of a magnetically insulated electrode gap: $\rho(r) \sim 1/r^4$. Therefore, a plasma created in the gap at $r > r_0$ during the stage of prolonged plasma production and after the onset of emission from the pinch may control the peak values of both discharge and emission power. The model analyses presented above are by no means quantitatively accurate. Quantitative description requires further study.

ACKNOWLEDGMENTS

The authors are grateful to the staff of the Angara-5-1 facility for their engineering and technical support of experiments.

This study was supported by the Russian Foundation for Basic Research, project no. 02-02-17200.

REFERENCES

1. A. V. Branitskiĭ, S. A. Dan'ko, A. V. Gerusov, *et al.*, Fiz. Plazmy **22**, 307 (1996) [Plasma Phys. Rep. **22**, 277 (1996)].
2. A. V. Branitskiĭ, V. V. Aleksandrov, E. V. Grabovskiĭ, *et al.*, Fiz. Plazmy **25**, 1060 (1999) [Plasma Phys. Rep. **25**, 976 (1999)].
3. V. V. Aleksandrov, A. V. Branitskiĭ, G. S. Volkov, *et al.*, Fiz. Plazmy **27**, 99 (2001) [Plasma Phys. Rep. **27**, 89 (2001)].
4. V. V. Alexandrov, I. N. Frolov, M. V. Fedulov, *et al.*, IEEE Trans. Plasma Sci. **30**, 559 (2002).
5. V. V. Aleksandrov, E. V. Grabovskiĭ, G. G. Zukakishvili, *et al.*, Zh. Éksp. Teor. Fiz. **124**, 829 (2003) [JETP **97**, 745 (2003)].
6. D. D. Ryutov, M. S. Derzon, and M. K. Matzen, Rev. Mod. Phys. **72**, 167 (2000).
7. M. G. Haines, IEEE Trans. Plasma Sci. **30**, 588 (2002).
8. M. G. Haines, S. V. Lebedev, J. P. Chittenden, *et al.*, in *Proceedings of 5th International Conference on Dense Z-pinches* (Albuquerque, New Mexico, 2002); AIP Conf. Proc. **651**, 345 (2002).

9. R. H. Lovberg, R. A. Raily, and J. S. Shlachter, in *Proceedings of 3rd International Conference on Dense Z-pinches* (London, UK, 1993); AIP Conf. Proc. **299**, 59 (1993).
10. L. I. Rudakov, A. L. Velikovich, J. Davis, *et al.*, Phys. Rev. Lett. **84**, 3326 (2000).
11. T. W. L. Sanford, N. R. Roderick, R. C. Mock, *et al.*, IEEE Trans. Plasma Sci. **30**, 538 (2002).
12. D. H. McDaniel, M. G. Mazarakis, D. E. Bliss, *et al.*, in *Proceedings of 5th International Conference on Dense Z-pinches* (Albuquerque, New Mexico, 2002); AIP Conf. Proc. **651**, 23 (2002).
13. E. A. Azizov, V. V. Alexandrov, S. G. Alikhanov, *et al.*, in *Proceedings of 5th International Conference on Dense Z-pinches* (Albuquerque, New Mexico, 2002); AIP Conf. Proc. **651**, 29 (2002).
14. R. B. Baksht, A. G. Russkikh, and A. A. Chagin, Fiz. Plazmy **23**, 195 (1997) [Plasma Phys. Rep. **23**, 175 (1997)].
15. L. Karpinski, M. Scholz, W. Stepnevski, *et al.*, in *Proceedings of 4th International Conference on Dense Z-pinches* (Vancouver, Canada, 1997); AIP Conf. Proc. **409**, 169 (1997).
16. J. P. Chittenden, S. N. Bland, *et al.*, in *Proceedings of 5th International Conference on Dense Z-pinches* (Albuquerque, New Mexico, 2002); AIP Conf. Proc. **651**, 65 (2002).
17. P. R. Levashov, Preprint No. 1-446, OIVT RAN (Joint Inst. for High Temperatures, Russian Academy of Sciences, Moscow, 2000).
18. *Studies of Metals in Liquid and Solid States (to 80-Year Anniversary of I. P. Bardin)* (Nauka, Moscow, 1964) [in Russian].
19. V. E. Fortov and I. T. Yakubov, *Physics of Nonideal Plasma* (Akad. Nauk SSSR, Chernogolovka, 1984) [in Russian].
20. I. T. Yakubov, Usp. Fiz. Nauk **163** (5), 35 (1993) [Phys. Usp. **36**, 365 (1993)].
21. Ya. B. Zel'dovich and Yu. P. Raĭzer, *Physics of Shock Waves and High-Temperature Hydrodynamic Phenomena*, 2nd ed. (Nauka, Moscow, 1966; Academic, New York, 1966 and 1967), Vols. 1 and 2.
22. A. S. Kingsep, *Introduction to the Nonlinear Plasma Physics* (Mosk. Fiz.–Tekh. Inst., Moscow, 1996), p. 207 [in Russian].

Translated by A. Betev and P. Pozdeev

Journal of Experimental and Theoretical Physics, Vol. 99, No. 6, 2004, pp. 1173–1182.
Translated from Zhurnal Éksperimental'noĭ i Teoreticheskoĭ Fiziki, Vol. 126, No. 6, 2004, pp. 1344–1354.
Original Russian Text Copyright © 2004 by B. B. Zelener, B. V. Zelener, Manykin.

**PLASMA,
GASES**

Kinetic Processes in a Nonideal Rydberg Matter

B. B. Zelener[a],*, B. V. Zelener[a], and E. A. Manykin[b]
[a]*Associated Institute for High Temperatures, Russian Academy of Sciences, Moscow, 125412 Russia*
[b]*Russian State Research Center Kurchatov Institute, Moscow, 123182 Russia*
**e-mail: bobozel@mail.ru*

Received June 18, 2004

Abstract—A kinetic model is developed to describe ultracold nonideal Rydberg plasmas, which allows all stages of the generation and decay of such a plasma to be sequentially traced. The plasma kinetics is considered on the basis of available experimental data corresponding to a nonideality parameter of $\gamma \sim 1$. The results of theoretical analysis are in good agreement with experiment. Calculations show evidence of a significantly decreased recombination rate and, hence, of the possible formation of a metastable structure in the plasma under consideration. The distribution of the number of excited atoms is determined for the plasma with $N_e = N_i = 7 \times 10^5$ and $E_e = 9$ K. The observed behavior of the number and density of particles as functions of the time and principal quantum number is explained. It is suggested that the distribution of excited atoms for the given parameters has a maximum for the state with $k = 25$. *© 2004 MAIK “Nauka/Interperiodica”.*

1. INTRODUCTION

Recently, two research groups [1–4] have succeeded in obtaining ultracold Rydberg plasmas with an electron temperature of $T_e = 1$–1000 K and a charged particle density of $n = 2n_e = 10^8$–10^{10} cm^{-3}. The nonideality parameter, defined as

$$\gamma = \frac{e^2 n^{1/3}}{kT}$$

(e is the electron charge and k is the Boltzmann constant), reached 50, while the degeneracy parameter was

$$n_e \lambda_e^3 \ll 1,$$

where

$$\lambda_e = \frac{\hbar}{(m_e kT)^{1/2}}$$

($\hbar$ is the Planck constant and m_e is the electron mass). Killian *et al.* [1–3] obtained an ultracold plasma via complete ionization of cold Xe atoms ($T_a \sim 10^{-4}$ K) by laser radiation. Robinson *et al.* [4] generated a plasma of alkali metals (Rb, Cs) by adding 1% of excited atoms ($T \sim 300$ K) to a cold atomic gas ($T_a \sim 10^{-4}$ K) excited to a Rydberg energy level ($n = 36$–40).

The results of experiments [1–3] showed that the rate of recombination in the obtained plasma at $\gamma \geq 1$ is significantly decreased as compared to that in a plasma with $\gamma \ll 1$, and the characteristic recombination time is $\tau_{rec} \sim 10^{-4}$ s. Analysis of the experimental data reported in [1–3] poses a number of questions requiring additional investigations with respect to the following issues:

(i) low population of excited levels;

(ii) nonmonotonic decrease of the populations with time;

(iii) inconsistent behavior of populations n_k depending on the principal quantum number from the standpoint of a usual recombination mechanism;

(iv) anomalous time variation of small populations n_k;

(v) decrease followed by increase in the total number of excited atoms with time;

(vi) sharp decrease in the plasma density with time.

All these issues have been discussed [5–11] and various kinetic models were proposed to describe the obtained experimental data. The models can be divided into two groups. The first group [5–7] proceeds from the idea that recombination begins in the plasma immediately upon its formation and leads to an increase in the kinetic energy of electrons. This results in a growth of the electron temperature T_e and the kinetic energy of ions. The second group [10, 11] assumes that the Coulomb repulsion between ions in the plasma at the moment of its formation leads to a high positive potential energy of electrons. As the plasma expands, the potential energy is converted into kinetic energy.

Below, we will consider the assumptions made in [5–11] in more detail. Better understanding of the kinetic processes in ultracold plasmas obtained in [1–4] can be reached by considering sequential stages from creation to decay of a Rydberg plasma.

2. PLASMA FORMATION AND ELECTRON TEMPERATURE ESTABLISHMENT

According to Killian *et al.* [1–3], a Rydberg plasma is created within a time of $t \sim 10^{-9}$ s. Electrons generated as a result of the multiphoton ionization of atoms by laser radiation acquire an additional kinetic energy of $E_e = 1$–1000 K, while ions remain at a temperature of $T_i = T_a = 10^{-4}$ K. The accuracy of determining E_e is related to a lower limit for the laser line halfwidth ($0.07\ \mathrm{cm}^{-1}$). The obtained plasma was substantially nonequilibrium, since the equilibrium electron temperature T_e is not established and all electrons occur in the continuum.

The most rapid process in the course of equilibrium plasma evolution is establishment of the electron temperature. In a slightly nonideal plasma ($\gamma \ll 1$), the time of T_e establishment is given by the formula [12]

$$\tau_{ee} \approx \frac{(T_e)^{3/2} m^{1/2}}{8 n_e e^4 L_e}, \qquad (1)$$

where L_e is the Coulomb logarithm. Under specified conditions, this quantity is expressed as

$$\begin{gathered} L_e = \ln \frac{1}{2\sqrt{\pi}\gamma_e^{3/2}}, \\ \gamma_e = e^2 n_e^{1/3}/kT_e. \end{gathered} \qquad (2)$$

Note that Eqs. (1) and (2) have no physical meaning for $\gamma_e^3 \ge 1/4\pi$. Indeed, $\gamma_e^3 = 1/4\pi$ makes $L_e = 0$, while greater γ_e values correspond to negative L_e.

The Coulomb logarithm L_e [12] is involved in calculations of the transport cross section for the interaction between two charges. For the electron–electron interaction, we have

$$L_e = \int_{\rho_{\min}}^{\rho_{\max}} \frac{d\rho}{\rho}, \qquad (3)$$

where ρ is the impact parameter expressed in units of $\beta e^2 = e^2/kT$. Logarithmic divergence of the integral in Eq. (3) determines selection of the finite integration limits. For a slightly nonideal plasma [12],

$$\rho_{\min} = 1, \quad \rho_{\max} = \frac{r_D}{\beta e^2},$$

where

$$r_D = (4\pi n_e \beta e^2)^{-1/2}$$

is the Debye radius. With these integration limits, we obtain expression (2) for L_e.

However, this choice of the integration limits in Eq. (3) becomes senseless even for $\gamma_e = 1/4\pi = 0.08$. In this case, the Debye radius is equal to the average distance between particles,

$$r_D = r_{av} = n_e^{-1/3}. \qquad (4)$$

Although the plasma is still slightly nonideal, the expression $\rho_{\max} = r_D/\beta e^2$ can no longer be used for the upper integration limit.

Calculations of the thermodynamic properties and correlation functions of plasma [13] showed that the correlation of particles in a plasma with $\gamma \ge 0.1$ becomes insignificant even at an average distance. Therefore, the upper integration limit in Eq. (3) in this case is correctly set at $r_{av}/\beta e^2 = \gamma^{-1}$.

The lower integration limit can be chosen at

$$r_D/\beta e^2 = \frac{1}{2\pi^{1/2}\gamma^{3/2}}.$$

This value depends on n and T and is equal to unity only at $\gamma = (1/4\pi)^{-1/3} = 0.43$. Thus, integration in the region $\gamma = 0.08$–0.43 is performed for the angles on the order of (but always smaller than) unity.

With this choice of the integration limits, the Coulomb integral L_e is expressed as

$$L_e = \ln(2\sqrt{\pi}\gamma_e^{1/2}). \qquad (5)$$

Expression (5) (in contrast to (2)) is positive for $\gamma_e > 0.08$ and describes a logarithmic growth of L_e with γ_e. The region of validity of Eq. (5) corresponds to $\gamma_e \le 1$. However, even extrapolation of this expression to the region of $\gamma_e > 1$ does not lead to the loss of meaning and retains the correct trend (whereby the relaxation rate increases with γ_e).

Figure 1 shows the $L_e(\gamma_e)$ curves calculated using expressions (2) and (5). The estimation of τ_{ee} in the region of $\gamma_e \le 1$ using formulas (1) and (5) for the parameters of ultracold plasmas obtained in [1–4] showed that $\tau_{ee} \sim 10^{-11}$–10^{-10} s.

Thus, we may ascertain that, after creation of the plasma within $t \sim 10^{-9}$ s [1–3], the electron temperature $T_e = (2/3)E_e$ is established for $t \sim 10^{-11}$–10^{-10} s. As was noted above, the ion temperature is equal to the temperature of atoms because the fraction of kinetic energy transferred to heavy particles during the ionization and excitation of atoms is insignificant. Thus, the plasma becomes two-temperature, although it still remains nonequilibrium with respect to ionization [14] since the Saha and Boltzmann distributions are not valid.

3. NONEQUILIBRIUM TWO-TEMPERATURE RYDBERG PLASMA AND ESTABLISHMENT OF THERMAL EQUILIBRIUM

When the electron temperature T_e is established, electrons begins to populate levels of the discrete spectrum. This implies the onset of recombination processes. Since all electrons initially occur in the continuum [1–3], recombination begins at the boundary between the discrete and continuous spectra. The main mechanism of recombination is via electron collisions [14], while the intensity of radiative transitions in this region of energies is small. As the binding energy grows, the role of radiative processes increases. Biberman *et al.* [14] defined a boundary energy,

$$E_R = \left(\frac{n_e}{4.5 \times 10^{13}}\right)^{1/4} T_e^{-1/8} \tag{6}$$

(where T_e is expressed in eV and n_e in cm^{-3}), that divides the energy spectrum into two regions:

(i) $E < E_R$ (where the impact processes dominate);

(ii) $E > E_R$ (where the impact excitation is followed by radiative deexcitation).

In the case of an ultracold Rydberg plasma [1–3], the initial states of plasma before the onset of expansion correspond to $E_R \sim 0.1$–1.1 eV, that is, to excitation levels with the principal quantum numbers $k = 4$–11. In the course of plasma expansion, E_R shifts toward the boundary of the continuous spectrum because it depends on n_e stronger than on T_e.

Thus, electron collisions give the main contribution to recombination in major part of the discrete spectrum under the conditions studied. Methods for the calculation of a nonequilibrium distribution of populations are described in [14]. The distribution of atoms over levels under nonequilibrium recombination conditions is illustrated in Fig. 2. Let us analyze this scheme following an approach developed in [14]. In equilibrium, the curve

$$\ln(n_k/g_k) = f(E_k)$$

drawn through the points corresponding to real atomic levels is a straight line whose slope is uniquely related to the temperature. It should be noted that, for temperatures in the interval $T = 1$–10 K, this line is close to the energy axis. Curve *2* schematically shows the behavior of populations under nonequilibrium recombination conditions.

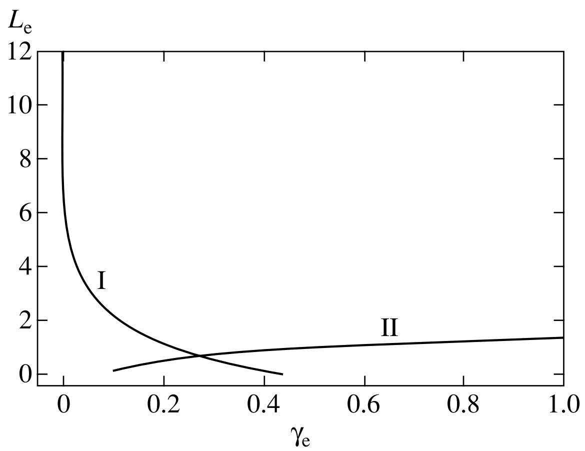

Fig. 1. Plots of $L_e(\gamma_e)$ calculated using (I) Eq. (2) and (II) Eq. (5).

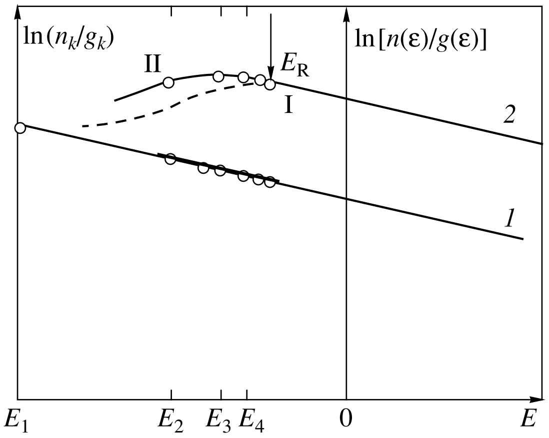

Fig. 2. Schematic diagram illustrating the characteristic distributions of atoms over excited states: (*1*) equilibrium case (using a straight line $\ln(n_k/g_k)$ drawn via points E_1, E_2, … corresponding to real atomic levels, it is possible to determine the electron temperature); (*2*) nonequilibrium recombination regime (dashed curve shows the distribution of populations in the case when radiative processes are substantial; branch I corresponds to the group of states in equilibrium with the continuum; branch II corresponds to the group of nonequilibrium states; E_R is the boundary of the influence of radiative transitions [14]).

The populations can be conditionally separated into two groups. The first group includes the upper excited states occurring in equilibrium with the continuum. The second group represents all the other excited states occurring under substantially nonequilibrium conditions. The transition from one group to another is called a “bottleneck.” The bottleneck position for $E_R > (3/2)T_e$ is determined by collision processes and, in the case under consideration, corresponds to the energy

$$E_m = \frac{3}{2}T_e. \tag{7}$$

For example, at $T_e = 6$ K $= 5.2 \times 10^{-4}$ eV, the number of the Rydberg state determining the bottleneck is

$$k_m = \sqrt{\frac{\text{Ry}}{E_m}} = 132,$$

where Ry = 13.6 eV.

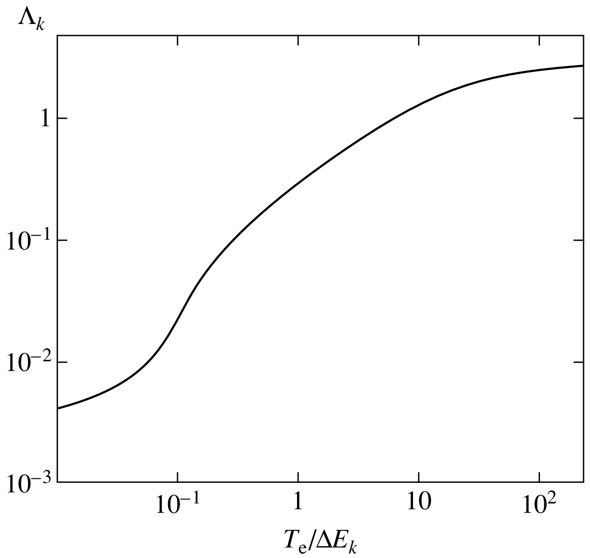

Fig. 3. Plot of the Coulomb logarithm Λ_k versus $T_e/\Delta E_k$ [14].

Methods for the calculation of the nonequilibrium distribution of populations developed in [14] make use of the condition of quasi-stationary excitation. In order to evaluate the relaxation time τ_k of the kth excited state, we use the formula [14]

$$\tau_k^{-1} = 2n_e \frac{4\sqrt{2\pi}e^4 E_{k-1}\Lambda_k}{(E_k - E_{k+1})(E_{k-1} - E_{k+1})\sqrt{mT_e}} \times \exp\left(\frac{E_k - E_{k+1}}{T_e}\right), \tag{8}$$

where Λ_k is the Coulomb logarithm for the interaction between a free electron and a weakly bound one, and $\Delta E_k = |E_k - E_{k-1}|$. It is also assumed that the probabilities of the radiative transitions do not contribute to τ_k^{-1}. Strictly speaking, expression (8) is valid only for a slightly nonideal plasma; yet it can be used to evaluate τ_k and follow the qualitative laws of variation of the relaxation rate. For the Rydberg states, formula (8) can be rewritten as

$$\tau_k^{-1} = \frac{\sqrt{2\pi}n_e e^4 \Lambda_k}{\mathrm{Ry}\sqrt{mT_e}} k^4 \exp\left(\frac{\mathrm{Ry}}{T_e}\frac{2}{k^3}\right). \tag{9}$$

Figure 3 shows the universal dependence of the Coulomb logarithm as a function of the electron temperature: $\Lambda_k = f(T_e/\Delta E_k)$ [14]. As can be seen, Λ_k varies within several orders in magnitude depending on $T_e/\Delta E_k$, which may significantly influence the establishment of quasi-stationary low-energy levels at low T_e. For $10^{-2} < T_e/\Delta E_k < 1$, the Coulomb logarithm is given with quite sufficient accuracy by the expression

$$\Lambda_k \approx 0.1\frac{T_e}{\Delta E_k}. \tag{10}$$

It should be noted that the accuracy of Λ_k determination in the region $T_e/\Delta E_k \ll 1$ is low.

Simultaneously with recombination processes, the plasma features the process of establishment of the equilibrium between electrons and ions. In order to estimate the time τ_{ei} required for the system to attain thermodynamic equilibrium, let us use the formula for a slightly nonideal plasma [12]:

$$\tau_{ei} = \frac{(T_e)^{3/2}M_i}{8n_i z^2 e^4 L_e (2\pi m_e)^{1/2}}, \tag{11}$$

where n_i, M_i, and z are the ion density, mass, and charge, respectively. Similarly to the evaluation of τ_{ee} described above, the Coulomb logarithm L_e for the Debye plasma is calculated using formulas (2), while that for a non-Debye plasma is given by formula (5). For $\gamma \sim 1$, the characteristic time τ_{ei} is on the order of a few microseconds. Thus, the ion temperature in the ultracold Rydberg plasma obtained in [1–3] becomes equal to the electron temperature within a time period of $t \approx 10^{-6}$ s. According to our estimates, this time decreases with increasing nonideality γ.

Now let us use Eqs. (9) and (11) to determine the levels that are quasi-stationary over the time τ_{ei}, that is, the levels for which

$$\tau_{ei} = \tau_k. \tag{12}$$

Taking into account the condition of quasi-neutrality ($n_e = n_i$), using formula (10), and accomplishing simple transformations, we obtain the following approximate relation for a quasi-stationary level with the minimum number k:

$$\exp\left(\frac{2\mathrm{Ry}}{T_e}\frac{1}{k^3}\right) \approx \frac{8m_e}{M_i}\frac{\mathrm{Ry}}{T_e}\frac{L_e}{\Lambda_k k^7}. \tag{13}$$

Calculations using formula (13) for $\gamma \sim 1$ show that the lowest quasi-stationary level has the number $k_{qs} = 24$ at $T_e = 1$ K.

Thus, only levels for which the probabilities of transitions due to electron collisions predominate, while the radiative transitions are insignificant and are quasi-stationary at the electron temperatures T_e of interest in the case under consideration. Moreover, the recombination flow is absent at $k < k_{qs}$, and the populations n_k for such k tend to zero. The radiative lifetime τ_{rad} of these levels is much greater than 10^{-6} s. This lifetime is given by the expression [14]

$$\tau_{rad} = A_k^{-1} = \frac{k^5}{1.6 \times 10^{10}}\ \mathrm{s}, \tag{14}$$

where A_k is the probability of the radiative transition from kth level to the ground state. For example, a radiative lifetime of the level with $k = 16$ is $\tau_{rad} = 6.55 \times 10^{-5}$.

In order to determine the populations n_k of levels with the numbers above $k_{\rm qs}$, let us consider a simple approximation provided by the diffusion approach [14], which is valid primarily in the case of $\Delta E_k/T \le 1$. This approximation yields the following expression for the relative populations y_k:

$$y(E) = \frac{y_1\chi(E/T_{\rm e}) + y_{\rm e}^2[\chi(E_1/T_{\rm e}) - \chi(E/T_{\rm e})]}{\chi(E_1/T_{\rm e})}, \quad (15)$$

where

$$\chi(x) = \frac{4}{3\sqrt{\pi}}\int_0^x t^{3/2}e^{-t}dt. \quad (16)$$

The relative population $y(E)$ is defined as the ratio of the population of a given energy level and the equilibrium population. Let y_1 be the relative population of a level below $k_{\rm qs}$. Taking this value to be zero, we have

$$y(E) = y_{\rm e}^2\left[1 - \frac{\chi(E/T_{\rm e})}{\chi(E_1/T_{\rm e})}\right]. \quad (17)$$

Taking into account that $E_1/T_{\rm e} \gg 1$ for $E_1 \ge E_{\rm qs}$ and that $\chi(x) = 1$ for $x \gg 1$, and passing to the absolute populations, we obtain

$$n_k = n_{\rm e}^2\frac{g_k\lambda^3}{2\Sigma_i}\exp(E_k/T_{\rm e})(1 - \chi(E_k/T_{\rm e})), \quad (18)$$

where

$$\lambda = \frac{h}{\sqrt{2\pi m_{\rm e}T_{\rm e}}},$$

$g_k = 2k^2$ is the statistical weight of the kth level, and $\Sigma_{\rm i} \approx 1$ is the statistical weight for the ion.

Using formula (18), it is possible to evaluate the total populations of all discrete levels by integrating this expression with respect to k from $k_{\rm qs}$ to k_n (possible at a given density and temperature). The main contribution to the total population is due to levels with $E_k/T_{\rm e} \ge 1$, for which

$$\chi(E_k/T_{\rm e}) \approx 1 - (4/3\sqrt{\pi})(E_k/T_{\rm e})^{3/2} \times \exp(-E_k/T), \quad (19)$$

and

$$\sum n_k \approx \frac{4}{3\sqrt{\pi}}n_{\rm e}^2\left(\frac{\rm Ry}{T}\right)^{3/2}\lambda^3\int_{k_{\rm qs}}^{k_n}\frac{dk}{k}. \quad (20)$$

Relation (20) can be approximately rewritten as

$$\sum n_k \approx \frac{4}{3\sqrt{\pi}}n_{\rm e}^2\left(\frac{\rm Ry}{T}\right)^{3/2}\lambda^3\ln k_{\rm qs}. \quad (21)$$

Note that the value of the original in the integral of Eq. (20) at the upper limit k_n is negligibly small and can be ignored. In order to determine the energy released upon recombination for $t \sim 10^{-6}$ s, let us integrate the product $E_kn_k/T_{\rm e}$ with respect to k for the levels with $E_k/T_{\rm e} \ge 1$:

$$u = \frac{4}{3\sqrt{\pi}}\int_{k_{\rm qs}}^{k_n} n_{\rm e}^2\left(\frac{\rm Ry}{T}\right)^{5/2}\lambda^3\frac{dk}{k}. \quad (22)$$

This expression can be approximately rewritten as

$$u = \frac{4}{3\sqrt{\pi}}n_{\rm e}^2\left(\frac{\rm Ry}{T}\right)^{5/2}\lambda^3\frac{2}{2k_{\rm qs}^2}. \quad (23)$$

Our estimates for the experimental point with $n_{\rm e} = 2 \times 10^9$ cm^{-3} and $E_{\rm e} = 9$ K [2, 3] corresponding to the initial electron temperature $T_{\rm e} = 6$ K give $\sum n_k = 7 \times 10^8$ cm^{-3} and $u/2n_{\rm e0} = 2.1$. This result indicates that the number of generated excited states accounts for about 15% of the number of charged particles, and the energy (per particle) converted from potential to kinetic as a result of recombination is about $2kT$. This value is much lower than that suggested in [5–9]. For this reason, we believe that the conclusion made in [5–9] concerning heating of the plasma is rather questionable.

It should be noted that the estimates obtained for the aforementioned experimental point [3] using expressions (21)–(23) is overstated for both $\sum n_k$ and $u/2n_{\rm e}$. This is related primarily to the fact that formulas (21)–(23) are valid for $\Delta E_k/T_{\rm e} \le 1$, whereas the case under consideration corresponds to $k_{\rm qs} = 25$ and, hence, $\Delta E_{25}/T_{\rm e} \approx 3$. The tendency to overstatement is strongly manifested on the passage to still lower temperatures $T_{\rm e} \approx 1$–3 K, where $\Delta E_k/T_{\rm e} > 5$ and the calculated total population $\sum n_k$ is several dozen of times greater than the initial density of charged particles.

We have also attempted to use a more accurate modified diffusion approach (MDA) [14] within the framework of a slightly nonideal plasma model. The MDA is based on a solution of the Fokker–Planck equation in finite differences and retains a discrete character of the energy space. This attempt was unsuccessful, thus suggesting that it is necessary to take into account the effects related to nonideality of the plasma (since the case under consideration corresponds to $\gamma \ge 1$). However, in the case of $\gamma \sim 1$, these effects can be partly taken into account using MDA [14], for which expression (18) acquires the following form:

$$n_k = \frac{n_e^2 g_k \lambda^3}{2}\exp\left(\frac{\mathrm{Ry}}{T_e k^2}\right) \times \frac{\displaystyle\sum_{k_1 = k_{qs}-2}^{k} \frac{2}{g_{k_1}\Lambda_{k_1}k_1^4}\exp\left(-\frac{\mathrm{Ry}}{T_e(k_1+1)^2}\right)}{\displaystyle\sum_{k_1 = k_{qs}-2}^{\infty} \frac{2}{g_{k_1}\Lambda_{k_1}k_1^4}\exp\left(-\frac{\mathrm{Ry}}{T_e(k_1+1)^2}\right)}. \tag{24}$$

An analysis of the sum in the denominator of this expression shows that the main contribution is due to the levels with

$$k \ge k_m = \sqrt{\frac{\mathrm{Ry}}{E_m}}.$$

According to [14], this implies that the energy spectrum in the course of recombination has a bottleneck at $E_m \approx 3kT_e/2$ (see formula (7)). For these k values, we have $\Lambda_k \sim 1$, $\exp(-\mathrm{Ry}/T_e(k+1)^2) \sim 1$, and the sum in the denominator is

$$\sum_{k_1 = k_m = \sqrt{\mathrm{Ry}/E_m}}^{\infty} \frac{1}{k_1^6}.$$

The effects of nonideality are related primarily to the nonrealization of levels whose energies are comparable with or lower than T_e. An increase in the density at T_e = const and $\gamma > 1$ leads to nonrealization of the levels with dimensions exceeding $r_{av} = n^{-1/3}$, primarily those with large orbital moments. We may suggest that, in this case, $g_k/2 = 1$. Taking into account these effects, the above sum in the denominator can be written as

$$\sum_{k_1 = k_m}^{\infty} \frac{1}{k_1^4},$$

and the expression for the populations acquires the following form:

$$n_k = \frac{n_e^2 g_k \lambda^3 k_m^3}{6}\exp\left(\frac{\mathrm{Ry}}{T_e k^2}\right) \times \sum_{k_1 = k_{qs}-2}^{k} \frac{2}{g_{k_1}\Lambda_{k_1}k_1^4}\exp\left(-\frac{\mathrm{Ry}}{T_e(k_1+1)^2}\right). \tag{25}$$

According to this formula, the values of $\sum n_k$ at T_e = 1–3 K are within one percent of the number of free charges and, accordingly, $u/2n_{e0} \approx kT$. The proposed approach leads to the results coinciding with those previously obtained by Hahn [11].

4. EXPANSION OF PLASMA

Recently [15], we calculated the properties of a plasma with an extremely small number of electrons in the bound states. The calculations were performed by the Monte Carlo method within the framework of a pseudopotential model. The values of the internal energy per particle obtained for $\gamma \ge 1$ can be approximated by a simple expression,

$$\frac{E}{NkT} = A\gamma, \tag{26}$$

where $A = 10$ and $\gamma = \beta e^2(n_e + n_i)^{1/3}$. The fact that the internal energy per particle for $\gamma \ge 1$ is positive has to be taken into account in an analysis of the plasma expansion stage.

As the ion temperature increases in the course of their interaction with electrons, the plasma exhibits enhanced expansion. During this, the stored positive potential energy is converted into kinetic energy and the velocity of expansion exhibits a manifold growth. This fact is confirmed by experimental data.

The velocity of plasma expansion [2, 3] was determined using the relation

$$E_{kin} = \frac{3}{2}M_i V_0^2. \tag{27}$$

Here, V_0 is a velocity entering into the expression for the density of the expanding gas [2, 3]:

$$\bar{n} = \frac{N}{[4\pi(\sigma_0^2 + V_0^2 t^2)]^{3/2}}, \tag{28}$$

where N is the number of ions and $\sigma_0 = 180$ μm is the rms radius of the plasma cloud at the moment of plasma formation. It was suggested [2] that the plasma expansion velocity at $E_e > 70$ K obeys the relation

$$V_0 = \sqrt{\frac{E_e}{\alpha M_i}}, \tag{29}$$

where E_e is the kinetic energy of electrons and $\alpha = 1.7$ is a fitting parameter determined from experimental data.

Expression (29) with the fitting parameter α can be also derived theoretically, proceeding from the following considerations. According to a description of the expansion of a spherical gas cloud [16], the average radial velocity of the gaseous mass asymptotically tends to a constant limit

$$V_\infty = \sqrt{\frac{2E_{kin}}{M}} = \frac{V_{max}}{B},$$

where V_{max} is the boundary velocity and B is a constant. An analysis of this problem shows that the velocity given by expression (29) is related to the boundary velocity V_{max} ($V_{max} = \sqrt{3}\,V_0$) rather than to the asymptotic value V_∞ (as was suggested in [3]). In the case of a gas sphere exhibiting automodel expansion [16] with an adiabatic exponent of $\gamma_p = 5/3$ and a constant gas density over the volume (following from (28), we have $B = \sqrt{5/3}$ and

$$V_0 = \sqrt{\frac{10E_{\rm kin}}{9M_{\rm i}}}. \tag{30}$$

In the state of thermal equilibrium, $T_{\rm e} = T_{\rm i}$ and the kinetic energy of ions is $E_{\rm kin} = E_{\rm e}/2$, which yields

$$V_0 = \sqrt{\frac{E_{\rm e}}{1.8M_{\rm i}}}. \tag{31}$$

As can be seen, expressions (29) and (31) coincide with good accuracy. In the case of $\gamma \geq 1$ or $E_{\rm e} > 70$ K, we will determine V_0 from relation (26). After the establishment of thermal equilibrium and complete energy conversion from potential to kinetic, the kinetic energy of ions is

$$E_{\rm kin} = E_{\rm i} + E_{\rm e}/2,$$

where

$$E_{\rm i} = E/N = Ae^2(n_{\rm e} + n_{\rm i})^{1/3}, \quad T_{\rm e} = T_{\rm i},$$
$$n_{\rm e} = n_{\rm i}, \quad A = 10.$$

In this case, we eventually obtain

$$V_0 = B_1\sqrt{\frac{2(E_{\rm i} + E_{\rm e}/2)}{3M_{\rm i}}}, \tag{32}$$

where the coefficient B_1 is determined via the Poisson adiabatic exponent γ_p. Using the results obtained in [15], it can be shown [16] that $\gamma_p = 4/3$ for a nonideality parameter on the order of unity. Then, $B_1 = \sqrt{4/3}$ and formula (32) acquires the following final form:

$$V_0 = \sqrt{\frac{8(Ae^2(2n_{\rm e})^{1/3} + E_{\rm e}/2)}{9M_{\rm i}}}. \tag{33}$$

Figure 4 (reproduced from [2]), shows the plots of V_0 versus $E_{\rm e}$ for $n_{\rm e} = 2 \times 10^9$ and 2×10^8 cm^{-3} in the case of $\gamma \geq 1$. The dependence of V_0 on $E_{\rm e}$ for $\gamma \sim 1$ significantly differs from that for $\gamma \ll 1$. First, the value of V_0 in the former case is several times that according to the formulas obtained for the slightly nonideal plasma ($\gamma \ll 1$), in agreement with experiment [3]. Second, the obtained expression for the velocity (in agreement with [11]) weakly depends on the electron density (on the order of $n_{\rm e}^{1/6}$).

In our calculations, it is possible to pass smoothly from the case of $E_{\rm e} < 70$ K to $E_{\rm e} > 70$ K because the internal energy $E_{\rm i}$ per ion was calculated [15] in the entire range of γ. This dependence can be effectively introduced via the coefficient A in formula (26), by representing it as $A = A(\gamma)$. For small values of the nonideality parameter γ, we have

$$A = -\sqrt{\pi}\gamma^{1/2},$$

and the expansion velocity is given by expression (31); for $\gamma > 0.5$, we have $A > 0$ and describe the plasma expansion using formula (33).

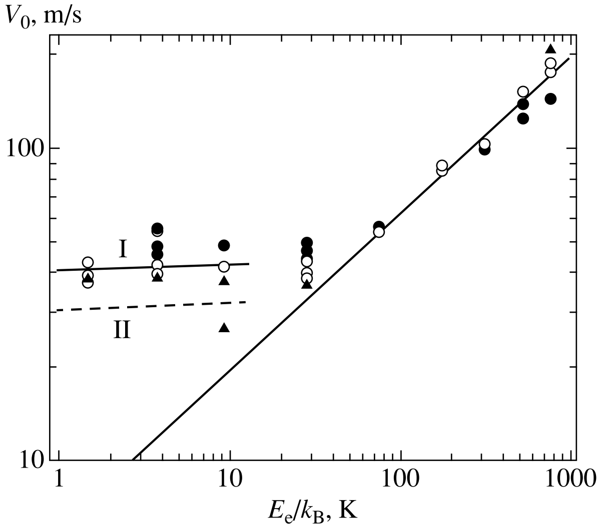

Fig. 4. Plot of the plasma expansion velocity V_0 versus initial kinetic energy $E_{\rm e}$ of electrons for the initial average density $\bar{n}_0$ varied from 6×10^6 to 2.5×10^9 cm^{-3}: (●) $10^9 \leq \bar{n}_0$; (○) $2 \times 10^8 \leq \bar{n}_0 < 10^9$; (▲) $\bar{n}_0 \leq 2 \times 10^8$; straight line corresponds to $V_0 = \sqrt{E_{\rm e}/1.7M_{\rm i}}$ [2]; lines I and II are calculated using formula (33) for $n_{\rm e} = 2 \times 10^9$ and 2×10^8 cm^{-3}, respectively.

It should be noted that, generally speaking, use of the velocity V_0 as a criterion for the comparison of theory and experiment is not quite correct because, as was demonstrated above, this parameter is rather uncertain. A more convenient criterion for this purpose is $\Delta E_{\rm e}/(E_{\rm e}/\alpha)$ [3]. An expression for $\Delta E/(E_{\rm e}/\alpha)$ at $\gamma \geq 1$ can be written as

$$\begin{aligned} \frac{\Delta E}{E_{\rm e}/\alpha} &= \frac{E - E_{\rm e}/\alpha}{E_{\rm e}/\alpha} = \frac{2E_{\rm i}}{E_{\rm e}} = \frac{2A\gamma}{3/2} \\ &= \frac{4}{3 \times 1.28}A\Gamma_{\rm e} = 1.08A\Gamma_{\rm e}, \end{aligned} \tag{34}$$

where

$$\Gamma_{\rm e} = \frac{\beta e^2}{(4\pi n_{\rm e}/3)^{-1/3}}$$

is the nonideality parameter used in [2, 3]. Figure 5 shows a plot constructed using Eq. (34). For $\Gamma_{\rm e} > 1$, the

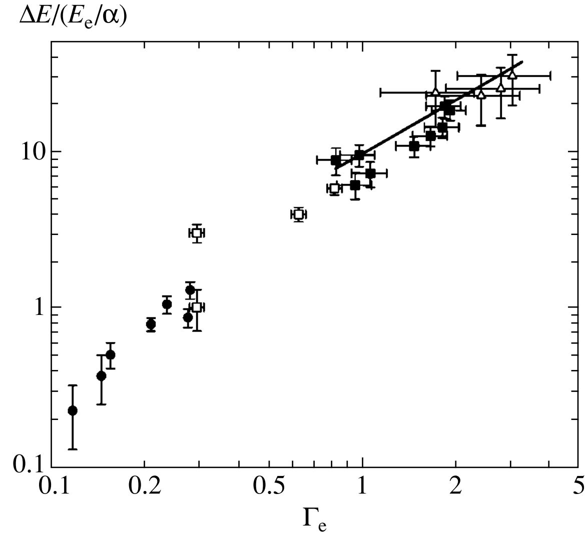

Fig. 5. Plot of the excess energy in expanding plasma versus nonideality parameter Γ_e for E_e/k_B = 28 (●), 9.2 (□), 3.9 (■), and 1.5 K (△) (experimental data from [2]); solid line shows the results of calculations using formula (34).

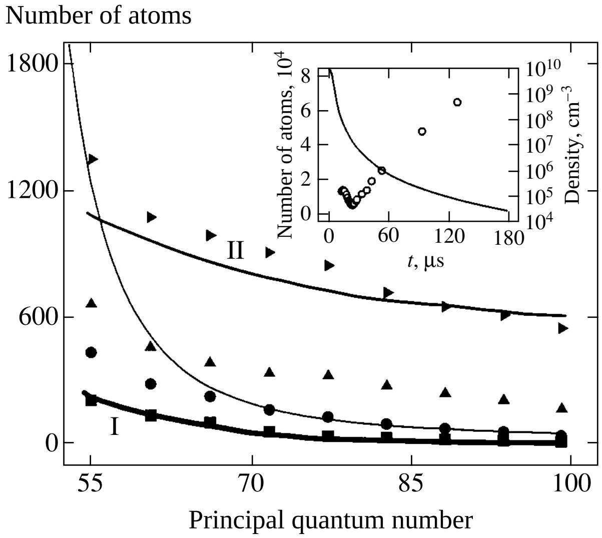

Fig. 6. Rydberg atom distributions for E_e = 9 K and $N_i = 7 \times 10^5$ at various times after photoionization: t = 12 (●), 22 (■), 50 (▲), and 125 μs (▼); thin solid curve is the equilibrium Saha distribution for t = 12 μs, T_e = 8.5 K [3]; curves I and II show the distributions of excited atoms calculated using formula (18) for t = 25 μs, T_{e25} = 2 K (I) and t = 125 μs, T_{e125} = 0.22 K (II). The inset shows the time variation of the total number of Rydberg atoms (circles) and the density of heavy particles (solid curve) [3].

results show good coincidence; in the region $0.1 < \Gamma_e < 0.5$, the E_i values no longer correspond to relation (26) and the coefficient effectively decreases; and in the region $0.5 < \Gamma_e < 1$, the ratio $\Delta E/(E_e/\alpha)$ approaches to the experimental values.

Let us evaluate the time of complete energy conversion from potential to kinetic. Assuming that particles in the plasma are uniformly accelerated, the transition time is

$$\tau_{tr} = \frac{2L}{V_{st} + V_f}, \tag{35}$$

where $V_{st} = \sqrt{4E_e/9M_i}$ is the initial velocity, $V_f = V_0$ is the final velocity according to formula (33), and L is the distance over which this transition takes place. The latter value is determined from the relation

$$\frac{L}{\beta e^2} = \frac{1}{\gamma_1} - \frac{1}{\gamma_0}, \tag{36}$$

where $\gamma_0 \sim n_0^{1/3}$ is the initial interaction parameter and $\gamma_1 \sim n_1^{1/3}$ is the parameter of interaction for $E_i = 0$. Substituting relation (36) into expression (35), we obtain

$$\tau_{tr} = \frac{2(\gamma_0 - \gamma_1)\beta e^2}{\gamma_1\gamma_0(\sqrt{4E_e/9M_i} + V_0)}. \tag{37}$$

For $n = 2 \times 10^9$ cm^{-3} and E_e = 9 K, this formula yields $\tau_{tr} \approx 2 \times 10^{-7}$ s. The results indicate that the energy conversion from potential to kinetic after the establishment of thermal equilibrium ($T_e = T_i$) proceeds much faster than the process of temperature leveling.

5. RECOMBINATION IN EXPANDING PLASMA

An increase in the kinetic energy of particles at the expense of their positive potential energy leads to the following effects.

(i) Highly excited states formed by that moment exhibit partial ionization at the expense of increasing electron temperature T_e and decreasing total number of these states. This is illustrated by experimental data (points) in Fig. 6, which show that the population of excited atoms and their total number (see inset) decreases until t = 25 μs. Starting at t = 25 μs, both the population and the total number of excited atoms increase, the electron temperature ceases to grow and exhibits a decrease, and the recombination process begins.

(ii) The recombination at t > 25 μs proceeds at a slow rate, which is related to a large velocity of expansion leading to the "quenching" effect. This effect (see, e.g., [14, 16]) is caused by the fact that expansion of the plasma proceeds at a higher rate than its cooling.

It was demonstrated [14, 16] that, if the recombination coefficient obeys the relation

$$\alpha = aT_e^{-9/2}, \tag{38}$$

the degree of ionization $x = n_e/n$ can be described by the expression

$$x = x_1\left[1 + 2a_1x_1^2\int_{t_1}^{t}\frac{n^2(t)dt}{T_e^{-9/2}(t)}\right]^{-1/2}. \qquad (39)$$

According to this formula, $x = \text{const}$ provided that $T_e \sim t^{l_1}$, where $l_1 \geq 10/9$ [16]. The parameter l_1 is related to the adiabatic exponent so that the condition $l_1 \geq 10/9$ corresponds to the inequality $\gamma_p < 4/3$. As was indicated above, the nonideality parameter on the order of unity corresponds to $\gamma_p = 4/3 < 1.37$. This result implies that the rate of plasma recombination exhibits a decrease.

As can be seen from Fig. 6, the distribution of populations for the excited atoms with $k = 55$–100 changes rather weakly with time. Therefore, the distribution at every moment of time can be considered as quasi-stationary and, using formula (18), we can estimate the temperature from the distribution of populations.

The results of calculations according to formula (18) for $t = 25$ and 125 μs showed (see Fig. 6) that these moments of time correspond to $T_{e25} = 2$ K and $T_{e125} = 0.22$ K. The temperature weakly depends on the concentration N_a of excited atoms (even for a twofold variation of N_a) to within the accuracy comparable with that in [3]. The data in Fig. 6 show that the electron temperature at $t = 25$ μs is close to T_e at the beginning of expansion and then decreases with time. It is also seen that the results of theoretical calculations of the population distribution well agree with the experimental points.

An analysis of the distribution of Rydberg atoms in Fig. 6 suggests that there is a maximum at $k = 25$. However, this assumption requires experimental verification.

6. CONCLUSIONS

We have followed the entire sequence of stages in the formation and degradation of an ultracold Rydberg plasma. Using the results of our calculations of the thermodynamic properties of such plasmas [15], we constructed a kinetic model and arrived at the following conclusions.

In the region of plasma parameters obtained in [1–3], the electron temperature is established within $\tau_{ee} < 10^{-10}$ s and the ion temperature T_i becomes equal to the electron temperature T_e within $\tau_{ei} \leq 10^{-6}$ s. This circumstance allows the plasma to be considered as occurring in an incomplete thermodynamic equilibrium, whereby $T_i = T_e$, but the equilibrium populations of the energy levels of excited atoms are not yet reached. The results of our calculations [15] for the conditions studied in [1–3] showed that such a system of charged particles featuring no bound states is characterized by strong repulsion, which increases with the nonideality parameter γ (see Eq. (26)). In the stage of plasma expansion, this repulsion favors an increase in the velocity, leads to ionization of a certain fraction of excited atoms (existing at the moment of establishment of the thermal equilibrium), and sets the regime of recombination "quenching."

The idea about strong repulsion in such plasmas was originally formulated (although for ions only) by Hahn [10, 11]. However, this was made on a level of estimates and left unexplained the role of electrons present in the system in equal amount with ions.

An analysis of the radiative professes and collisions in the temperature interval $T = 1$–5 K for the electron densities $n_e = 10^8$–10^{13} cm^{-3} showed that, during plasma evolution up to the establishment of thermal equilibrium within $\tau_{ei} \leq 10^{-6}$, the recombination flow is quasi-stationary only for the levels with $k > 25$, while radiative transitions are substantial only for the levels with $k \leq 10$. The major recombination mechanism in this stage is via collisions. The radiative lifetime of a level with $k \sim 10$ is on the order of 10^{-5} s, which is much greater than the characteristic time of the establishment of thermal equilibrium. This relation indicates that, within $t \sim 10^{-6}$ s, the plasma does not lose energy; the kinetic energy released as a result of recombination is spent for the ionization of excited atoms (the process reverse to recombination) and the heating of ions and electrons.

As was demonstrated above, the former process predominates at $T_e = 6$ K. This implies that heating of plasma due to the radiative energy transfer (suggested in [5–9]) does not take place. The low electron temperature shifts the bottleneck (featuring maximum resistance to the recombination flow) close to the boundary between the discrete spectrum and continuum. For $\gamma < 1$, there are no levels with $E_k \leq kT$ above the bottleneck; as the nonideality parameter γ increases, nonrealized levels with $r_{av} = n^{-1/3}$ appear, primarily those with high orbital moments. All these factors favor a decrease in the recombination flow, leaving only a very small number of excited atoms with $k > k_{qs}$ (much smaller than the number of free electrons and ions). This fact confirms the assumptions underlying a model used for the calculation of thermodynamic properties [15].

In this study, the analysis of plasma kinetics was based on the available experimental data (see Figs. 4–6) corresponding to a nonideality parameter of $\gamma \sim 1$. The theoretical and experimental data on the plasma expansion velocity V_0 and the ratio $\Delta E_e/(E_e/\alpha)$ are in good agreement, although it was pointed out that V_0 (being rather uncertain quantity) is not very convenient for such a comparison. We determined the number of excited atoms for $N_e = N_i = 7 \times 10^5$ and $E_e = 9$ K and explained the observed behavior, as well as the particle number density variation depending on the time and the principal quantum number. We suggest that there might a maximum in the distribution of excited atoms (for the specified parameters) at $k = 25$.

As the nonideality parameter γ increases, it is necessary to take into account the following additional circumstances.

(i) A decrease in the recombination rate in a nonideal plasma (see, e.g., [17, 18]) related to the effects of strong Coulomb interaction on the density of states and the electron diffusion coefficient.

(ii) The absence of excited levels, with dimensions greater than the average distance, below the k_mth level, which leads to an increase in resistance to the recombination flow.

(iii)The appearance of a long-range order and a large positive energy of particles, as established in [15].

All these factors (especially the third, if the plasma state could be stabilized at large γ, for example, by applying external electromagnetic fields) lead to an increase in the characteristic recombination time; in the absence of stabilization, these factors lead to the complete absence of recombination.

The calculations in [15] referred to a plasma with neglect of the bound states between electrons and ions for $k < 100$. Recently [19], we performed calculations for experimental conditions corresponding to various k (e.g., for $k > 36$, see [4]) and determined the energy per particle, E/NkT, in cases where the dependence on γ may substantially differ from that described by formula (26). An analysis of the Rydberg plasma kinetics in such cases is the subject of our subsequent investigations.

ACKNOWLEDGMENTS

The authors are grateful top A.A. Belevtsev and A.G. Leskis for fruitful discussions.

This work was supported in part by the Russian Foundation for Basic Research (project no. 04-02-17474a).

REFERENCES

1. T. C. Killian, S. Kulin, S. D. Bergeson, *et al.*, Phys. Rev. Lett. **83**, 4776 (1999).
2. S. Kulin, T. C. Killian, S. D. Bergeson, and S. L. Rolston, Phys. Rev. Lett. **85**, 318 (2000).
3. T. C. Killian, M. J. Lim, S. Kulin, *et al.*, Phys. Rev. Lett. **86**, 3759 (2001).
4. M. P. Robinson, B. L. Tolra, M. W. Noel, *et al.*, Phys. Rev. Lett. **85**, 4466 (2000).
5. F. Robicheaux and J. D. Hanson, Phys. Rev. Lett. **88**, 055002 (2002).
6. T. Pohl, T. Pattard, and J. M. Rost, Phys. Rev. A **68**, 010703(R) (2003).
7. S. G. Kuzmin and T. M. O'Nail, Phys. Rev. Lett. **88**, 065003 (2002).
8. M. S. Murillo, Phys. Rev. Lett. **87**, 115002 (2001).
9. A. N. Tkachev and S. I. Yakovlenko, Kvantovaya Élektron. (Moscow) **30**, 1077 (2000).
10. Y. Hahn, Phys. Lett. A **293**, 266 (2002).
11. Y. Hahn, Phys. Lett. E **64**, 046409 (2001).
12. E. M. Lifshitz and L. P. Pitaevskiĭ, *Physical Kinetics* (Nauka, Moscow, 1979; Pergamon Press, Oxford, 1981).
13. B. V. Zelener, G. E. Norman, and V. S. Filinov, *Perturbation Theory and Pseudopotential in Statistical Thermodynamics* (Nauka, Moscow, 1981) [in Russian].
14. L. M. Biberman, V. S. Vorob'ev, and I. T. Yakubov, *Kinetics of Nonequilibrium Low-Temperature Plasmas* (Nauka, Moscow, 1982; Consultants Bureau, New York, 1987).
15. M. Bonitz, B. B. Zelener, B. V. Zelener, *et al.*, Zh. Éksp. Teor. Fiz. **125**, 821 (2004) [JETP **98**, 719 (2004)].
16. Ya. B. Zel'dovich and Yu. P. Raĭzer, *Physics of Shock Waves and High-Temperature Hydrodynamic Phenomena*, 2nd ed. (Nauka, Moscow, 1966; Academic, New York, 1966).
17. L. M. Biberman, V. S. Vorob'ev, and I. T. Yakubov, Dokl. Akad. Nauk SSSR **296**, 576 (1987) [Sov. Phys. Dokl. **32**, 752 (1987)].
18. I. T. Yakubov, Teplofiz. Vys. Temp. **30**, 862 (1992).
19. V. S. Filinov, V. E. Fortov, E. A. Manykin, *et al.*, submitted to Phys. Lett. A.

Translated by P. Pozdeev

Journal of Experimental and Theoretical Physics, Vol. 99, No. 6, 2004, pp. 1183–1188.
Translated from Zhurnal Éksperimental'noĭ i Teoreticheskoĭ Fiziki, Vol. 126, No. 6, 2004, pp. 1355–1361.
Original Russian Text Copyright © 2004 by Sushko.

Molecular Light Scattering of Multiplicity 1.5

M. Ya. Sushko
Odessa National University, Odessa, 65026 Ukraine
e-mail: mrs@dtp.odessa.ua

Received June 7, 2004

Abstract—The "interference" contributions from compact groups of scattering centers to the total intensity of molecular scattering in a liquid are analyzed. The result of the algebra of fluctuating quantities has been restored for the case of long-range correlations between the groups. The role of short-range correlations is most significant for moderate deviations (10^{-3}–10^{-2}) of the dimensionless temperature from its critical value. Estimates of the relative value and temperature peculiarities of the contributions of multiplicity 1.5 proportional to the third-order moment of the density fluctuations and an analysis of experimental data indicate that they can be partially observed under conditions deviating from the critical isochore. *© 2004 MAIK "Nauka/Interperiodica".*

1. INTRODUCTION

In this paper, we explore the question of whether the effects of molecular scattering of light in liquids attributable to the third (non-Gaussian) moments of the thermodynamic fluctuations can be observed. At present, the answer to this question is believed to be negative (see reviews [1, 2]). It should be noted, however, that this conclusion is based on an analysis of the effects of the true multiple scattering when the successive reemission events occur between distant scattering centers spaced $|\mathbf{r}_i - \mathbf{r}_j| \gg \lambda \gtrsim r_c$ apart, where r_c is the correlation length and λ is the wavelength in the medium. In the corresponding calculations, the electromagnetic field propagators,

$$T_{\alpha\beta}(r) = -(k^2\delta_{\alpha\beta} + \nabla_\alpha\nabla_\beta)\frac{e^{ikr}}{4\pi k^2 r}, \quad k = \frac{2\pi}{\lambda}$$

are replaced with their asymptotic expressions for the wave zone, and standard asymptotic uncouplings are used in place of multipoint correlation functions. As a result, a quasi-Gaussian fluctuation model is obtained, in which the odd-order fluctuation moments are negligible.

We proceed from the assumption [3] that the intensity $I_{1.5}$ of the molecular light scattering of multiplicity 1.5 has the largest relative value at a certain distance from the critical point where all three scattering centers are spaced $|\mathbf{r}_i - \mathbf{r}_j| \lesssim r_c \ll \lambda$ ($i, j = 1, 2, 3$) apart. In this case, the three-point correlation functions cannot be uncoupled, but the intensity $I_{1.5}$ can be expressed in terms of the third-order fluctuation moments. Preliminary estimates [3] show that the contribution from the third-order moment of density fluctuations to the permittivity fluctuations in a single-component liquid in the appropriate temperature and density ranges is comparable in magnitude to the corresponding contribution from the Gaussian part of the fourth-order moment. If the true double scattering for this region is still relatively weak, then $I_{1.5}$ should be experimentally measurable.

To single out these contributions from the overall scattering pattern and to quantitatively estimate them, we perform a macroscopic analysis of the effects of molecular light scattering by compact groups of scattering centers. A compact group is interpreted here as any group of scattering centers in which $|\mathbf{r}_i - \mathbf{r}_j| \ll \lambda$. From the physical point of view, scattering by such groups is single, but the corresponding scattering intensities I_{nm} are determined by the correlators $\langle[\mathbf{E}^{(n)}, \mathbf{H}^{(m)*})]\rangle$ of individual terms in the iterative series $\mathbf{E}^{(1)} + \mathbf{E}^{(2)} + \mathbf{E}^{(3)} + \ldots$ and $\mathbf{H}^{(1)} + \mathbf{H}^{(2)} + \mathbf{H}^{(3)} + \ldots$ for the electric and magnetic field strengths in the scattered wave. The scattering multiplicity defined as $(n + m)/2$ no longer corresponds to the iteration step number in solving the integral equation that describes the propagation and scattering of a wave in a statistically inhomogeneous medium.

The fact that the domains of integration variables where the internal propagators corresponding to reemissions between the members of a compact group exhibit singular behavior is crucial in calculating the contributions I_{nm}. This allows us to use methods of the theory of generalized functions [4] in our analysis and to single out the leading-order contributions to the total intensity I of single polarized scattering in each iteration step. In the immediate vicinity of the critical point, the expression derived here reduces to the result of the algebra of fluctuating quantities for systems with a conserved order parameter [5]; in addition, an explicit form of the coefficients of the expansion of I in terms of the algebra elements is established.

In the other limit, when there is no nonlocal correlation between fluctuations, individual terms of the series expansion of I are determined by the second or higher order moments of thermodynamic fluctuations. For a single-component system, the moments of density fluctuations, which play a major role, can be expressed in terms of isothermal compressibility β and its derivatives by using the grand canonical ensemble. Thus, we can go beyond the scope of the Gaussian approximation and simultaneously use the van der Waals equation in our estimates. These estimates and the appropriate analysis of experimental data [6] on the depolarization ratio Δ for scattered light in xenon indicate that detection of the contributions due to the third-order moments of density fluctuations to molecular scattering appears to be partially possible and is most probable in the temperature range $10^{-3} \lesssim \tau \lesssim 10^{-2}$, $\tau \equiv |T - T_c|/T_c$ by deviating from the critical isochore to lower densities.

2. ANALYSIS OF THE PECULIARITIES OF THE PROPAGATOR

The most singular contribution to the propagator $T_{\alpha\beta}(r)$ at small values of the argument comes from the derivative $\nabla_\alpha\nabla_\beta r^{-1}$. To analyze it, let us treat r^{-1} as a generalized function and introduce the corresponding linear continuous functional

$$F(\varphi) = \int_V d\mathbf{r}\frac{1}{r}\varphi(\mathbf{r}) \tag{1}$$

defined on the set of smooth functions $\varphi(\mathbf{r})$ that are constant at zero and are such that

$$\varphi(\mathbf{r}),\ \partial\varphi(\mathbf{r})/\partial r,\ r\partial\varphi(\mathbf{r})/\partial r \xrightarrow[r \to \infty]{} 0$$

(e.g., according to the Ornstein–Zernicke law $|\varphi(\mathbf{r})| \underset{r \to \infty}{\propto} e^{-\alpha r}/r$, $\alpha > 0$).

Following standard rules [4], let us define the derivative $\nabla_\alpha\nabla_\beta r^{-1}$ as the generalized function associated with the following functional:

$$\int_V d\mathbf{r}\left(\nabla_\alpha\nabla_\beta\frac{1}{r}\right)\varphi(\mathbf{r}) = \lim_{\varepsilon \to 0}\int_{V_\varepsilon} d\mathbf{r}\frac{1}{r}(\nabla_\alpha\nabla_\beta\varphi(\mathbf{r})). \tag{2}$$

Here, the integral on the right-hand side is taken over the three-dimensional space V_ε from which the sphere of a radius $\varepsilon > 0$ centered at the origin was removed.

Double integration by parts yields the following expression as $\varepsilon \longrightarrow 0$:

$$\begin{aligned}&\int_V d\mathbf{r}\left(\nabla_\alpha\nabla_\beta\frac{1}{r}\right)\varphi(\mathbf{r})\\ &= \int_V d\mathbf{r}\left\{-\frac{4\pi}{3}\delta(\mathbf{r})\delta_{\alpha\beta} + \frac{1}{r^3}(3e_\alpha e_\beta - \delta_{\alpha\beta})\right\}\varphi(\mathbf{r}),\end{aligned} \tag{3}$$

where $\delta(\mathbf{r})$ is the Dirac delta function, $\delta_{\alpha\beta}$ is the Kronecker delta, and e_α is the α component of the unit vector $\mathbf{e} = \mathbf{r}/r$. Thus, we represent the derivative $\nabla_\alpha\nabla_\beta r^{-1}$ as the expression in the braces in (3). It satisfies the symmetry requirements and leads to the well-known result $\Delta r^{-1} = -4\pi\delta(\mathbf{r})$. By analogy, we find the generalized derivative $\nabla_\alpha r^{-1} = -e_\alpha/r^2$.

The propagator $T_{\alpha\beta}(r)$ can be represented as

$$\begin{aligned}\tilde{T}_{\alpha\beta}(r) &= \frac{1}{3k^2}\delta(\mathbf{r})\delta_{\alpha\beta}e^{ikr} - \frac{1}{4\pi r}(\delta_{\alpha\beta} - e_\alpha e_\beta)e^{ikr}\\ &+ \frac{1}{4\pi k^2}\left(\frac{1}{r^3} - \frac{ik}{r^2}\right)(\delta_{\alpha\beta} - 3e_\alpha e_\beta)e^{ikr}.\end{aligned} \tag{4}$$

This representation should be understood in the sense that the following equality holds for any function $\varphi(\mathbf{r})$ from the chosen set:

$$\int_V d\mathbf{r}\tilde{T}_{\alpha\beta}(r)\varphi(\mathbf{r}) = \int_V d\mathbf{r}T_{\alpha\beta}(r)\varphi(\mathbf{r}). \tag{5}$$

Thus, we represent propagator (4) as the sum of three contributions the second of which corresponds to distant reemissions between the scattering centers. The second and third terms are nonzero at $\alpha \neq \beta$; their role in light depolarization due to both true double scattering and the scattering by a compact pair of scattering centers, as well as the relationship of the latter depolarization channel to the general depolarization mechanism due to fluctuations of the thermal fluctuation distribution function [7], were discussed in [8, 9]. The isotropic first term in (4) is the most singular at $\alpha = \beta$; its contributions to polarized scattering are analyzed below.

3. SCATTERING INTENSITY

Given representation (4), the electrodynamic part of the problem can easily be solved. We assume that permittivity fluctuations $\delta\varepsilon = \varepsilon - \varepsilon_0$ lead to relatively small frequency shifts relative to the incident wave (Rayleigh scattering). The equation that describes the wave propagation in such a medium takes the form

$$\Delta\mathbf{E} + k^2\mathbf{E} - \mathrm{grad}\,\mathrm{div}\mathbf{E} = -k_0^2\delta\varepsilon\mathbf{E}, \tag{6}$$

where $k_0 = k/\sqrt{\varepsilon_0}$. To calculate I, we restrict ourselves to a static model and write the equivalent integral equation

$$\mathbf{E}(\mathbf{R}) = \mathbf{E}_0(\mathbf{R}) - k_0^2\int_V d\mathbf{r}\hat{T}(\mathbf{R}, \mathbf{r})\delta\varepsilon(\mathbf{r})\mathbf{E}(\mathbf{r}), \tag{7}$$

where $\mathbf{E}_0(\mathbf{r}) = \mathbf{e}_0E_0\exp(i\mathbf{k}\cdot\mathbf{r})$ is the electric field of the incident wave, and $\mathbf{e}_0$ is the unit polarization vector. Applying an iterative procedure to (7) and replacing all internal propagators with their most singular parts (the first terms in (4)), we use a standard method [10] to obtain the following result for if $|\mathbf{R}| \gg L$ (L is the size of the system):

$$\mathbf{E}^{(n)}(\mathbf{R}) = -\frac{e^{ikR}k_0^2E_0}{4\pi R}[\hat{\mathbf{R}}\times[\hat{\mathbf{R}}\times\mathbf{e}_0]] \times\left(-\frac{1}{3\varepsilon_0}\right)^{n-1}\int_V d\mathbf{r}(\delta\varepsilon(\mathbf{r}))^n e^{-i\mathbf{q}\cdot\mathbf{r}}, \tag{8}$$

where $\hat{\mathbf{R}} = \mathbf{R}/R$ is the unit vector toward the point $\mathbf{R}$ and $\mathbf{q}$ is the change in the wavevector due to the scattering. The magnetic field of the scattered wave is calculated by using the relation

$$\mathbf{H}^{(n)}(\mathbf{R}) = -\frac{i}{k_0}\mathrm{curl}\mathbf{E}^{(n)}(\mathbf{R});$$

its intensity, by using the Poynting vector. We have

$$I = \sum_{n, m \geq 1} I_{nm}, \tag{9}$$

$$I_{nm} = \frac{c}{8\pi}\mathrm{Re}\langle[\mathbf{E}^{(n)}(\mathbf{R})\times\mathbf{H}^{(m)*}(\mathbf{R})]\cdot\hat{\mathbf{R}}\rangle, \tag{10}$$

where the angle brackets denote averaging over the statistic of fluctuations $\delta\varepsilon$. Taking into account (10) and the spatial homogeneity of the medium, we obtain

$$I_{nm} \propto \left(-\frac{1}{3\varepsilon_0}\right)^{n+m-2} \times\int_V d\mathbf{r}\langle(\delta\varepsilon(\mathbf{r}))^n(\delta\varepsilon(\mathbf{0}))^m\rangle e^{-i\mathbf{q}\cdot\mathbf{r}}. \tag{11}$$

In what follows, we omit the factor

$$I_0\frac{k_0^4V}{16\pi^2R^2}[1-(\hat{\mathbf{R}}\cdot\mathbf{e}_0)^2], \quad I_0 = \frac{c}{8\pi}\frac{k}{k_0}|\mathbf{E}_0|^2,$$

where I_0 is the intensity of the incident wave and V is the scattering volume.

Thus, the intensity I is determined by the spatial Fourier transforms of the (irreducible) fluctuation correlators $G_{nm}(r) = \langle\langle\varepsilon^n(\mathbf{r})\varepsilon^m(\mathbf{0})\rangle\rangle$.

Strong permittivity fluctuations are mainly due to fluctuations of the order parameter $\delta\varphi$,

$$\delta\varepsilon \approx \left(\frac{\partial\varepsilon}{\partial\varphi}\right)\delta\varphi.$$

Therefore, the correlators in (11) reduce to the irreducible correlators $\langle\langle\varphi^n(\mathbf{r})\varphi^m(\mathbf{0})\rangle\rangle$. Formulas (9) and (11) directly confirm the hypothesis [5] about the existence of a complete set (algebra) of fluctuating scalar quantities in the problem of molecular scattering of light in liquids; moreover, all coefficients in the expansion of the intensity in terms of the algebra elements can be calculated.

The critical exponents for the contributions I_{nm} can be estimated by using the scaling parameters Δ_n of the algebra elements. Assuming the permittivity and its derivatives with respect to the order parameter to be weakly sensitive to the critical point, we may write in the long-wavelength limit $q \longrightarrow 0$

$$I_{nm} \propto \int_V d\mathbf{r}\langle(\delta\varphi(\mathbf{r}))^n(\delta\varphi(\mathbf{0}))^m\rangle \propto |\tau|^{-\mu_{nm}}. \tag{12}$$

The equality of the scaling dimensions for the left- and right-hand sides of Eq. (12) implies that

$$\mu_{nm} = \frac{d-\Delta_n-\Delta_m}{\Delta_\tau}, \tag{13}$$

where Δ_τ is the scaling parameter for τ.

The first-order ε-expansion (see [5, 11]) yields

$$\Delta_n = n\frac{2-\varepsilon}{2}+\frac{n(n-1)}{6}\varepsilon, \quad \Delta_\tau = 2-\frac{\varepsilon}{3},$$

where $\varepsilon = 4 - d$ characterizes the deviation of spatial dimension from 4. Hence, in particular, we find that $\mu_{12} = 1/2 + \varepsilon/6$, which yields $\mu_{12} \approx 0.67$ at $\varepsilon = 1$.

Thus, the derived temperature dependence of the intensity of multiplicity 1.5 scattering in the fluctuation region is $I_{1.5} \propto \tau^{-0.67}$, which agrees with that obtained in [5]. However, as further estimates show, this temperature regime is reached in a fairly close neighborhood of the critical point, where the effects of true multiple (in particular, double) scattering are more significant. Multiplicity 1.5 scattering can be detected sufficiently far from the critical point, where nonlocal correlation between fluctuations is relatively weak (in the so-called Rayleigh region).

4. SCATTERING IN THE RAYLEIGH REGION

Since the integrand in (11) does not vanish at $\tau \gtrsim 10^{-3}$ only when $|\mathbf{r}| \lesssim r_c \ll \lambda$, we may replace the exponential factor with unity and express the remaining integral in terms of thermodynamic fluctuation moments [10]. Recalling that the integral in (11) is performed with respect to the difference $\mathbf{r} = \mathbf{r}_1 - \mathbf{r}_2$ between the coordinates of fluctuations at distinct points $\mathbf{r}_1$ and $\mathbf{r}_2$, we change to an integral over these coordinates. We obtain

$$I_{nm} \propto \left(-\frac{1}{3\varepsilon_0}\right)^{n+m-2} \tilde{V}\langle(\delta\varepsilon)^n(\delta\varepsilon)^m\rangle_{\tilde{V}}, \qquad (14)$$

where the symbol $\langle\ldots\rangle_{\tilde{V}}$ denotes a correlator averaged over a macroscopic region $\tilde{V}$:

$$\langle(\delta\varepsilon)^n(\delta\varepsilon)^m\rangle_{\tilde{V}} = \frac{1}{\tilde{V}^2}\int\limits_{\tilde{V}} d\mathbf{r}_1 \int\limits_{\tilde{V}} d\mathbf{r}_2 \langle(\delta\varepsilon(\mathbf{r}_1))^n(\delta\varepsilon(\mathbf{r}_2))^m\rangle. \qquad (15)$$

We define the thermodynamic contributions to the fluctuations of ε^n ($n = 1, 2, 3, \ldots$) as

$$\Delta(\varepsilon^n) = \varepsilon^n - \overline{\varepsilon^n} = \frac{1}{\tilde{V}}\int\limits_{\tilde{V}} d\mathbf{r}\,\delta(\varepsilon^n(\mathbf{r})). \qquad (16)$$

For the terms up to the fourth order in $\delta\varepsilon$, we can prove that $\langle(\delta\varepsilon)^n(\delta\varepsilon)^m\rangle_{\tilde{V}} = \langle(\Delta\varepsilon)^{n+m}\rangle$.

Indeed, at $n = m = 1$, this relation follows directly from (15) and (16) and is well known [10]. For $n = 2$ and $m = 1$, we may write

$$\langle(\delta\varepsilon(\mathbf{r}_1))^2(\delta\varepsilon(\mathbf{r}_2))\rangle = \langle\delta(\varepsilon^2(\mathbf{r}_1))\delta\varepsilon(\mathbf{r}_2)\rangle - 2\bar{\varepsilon}\langle\delta\varepsilon(\mathbf{r}_1)\delta\varepsilon(\mathbf{r}_2)\rangle;$$

hence, using (15) and (16) we obtain

$$\langle(\delta\varepsilon)^2(\delta\varepsilon)\rangle_{\tilde{V}} = \overline{\varepsilon^3} - 3\bar{\varepsilon}\overline{\varepsilon^2} + 2\bar{\varepsilon}^3 = \langle(\Delta\varepsilon)^3\rangle.$$

The remaining relations can be proved in a similar way.

Thus, the intensity I_{nm} of molecular scattering in the Rayleigh region is determined by the moments of order $n + m$ of thermodynamic permittivity fluctuations:

$$I_{nm} \propto \left(-\frac{1}{3\varepsilon_0}\right)^{n+m-2} \tilde{V}\langle(\Delta\varepsilon)^{n+m}\rangle. \qquad (17)$$

If light is scattered in a single-component system, where $\Delta\varepsilon$ is mainly due to fluctuations of the particle number density n, $\Delta\varepsilon \approx (\partial\varepsilon/\partial n)\Delta n$, then the moments $\langle(\Delta\varepsilon)^n\rangle$ can be expressed in terms of moments of fluctuations of the number of particles ΔN in a fixed volume by using the relation $\langle(\Delta n)^n\rangle = \tilde{V}^{-n}\langle(\Delta N)^n\rangle$. Denoting $I_1 \equiv I_{11}$ (single scattering), $I_{1.5} \equiv I_{12} + I_{21}$ (scattering of multiplicity 1.5), and $I_2 \equiv I_{13} + I_{22} + I_{31}$ (the contribution of groups of four closely spaced scattering centers), we use formulas from [3, 12] to obtain the following for the first six terms of series (9):

$$I_1 \propto \left(n\frac{\partial\varepsilon}{\partial n}\right)^2 k_B T\beta, \qquad (18)$$

$$I_{1.5} \propto -\frac{2}{3\varepsilon_0}\left(n\frac{\partial\varepsilon}{\partial n}\right)^3 \frac{k_B^2T^2}{\tilde{V}}\left\{2\beta^2 + \left(\frac{\partial\beta}{\partial P}\right)_{T,V}\right\}, \qquad (19)$$

$$I_2 \propto \frac{1}{3\varepsilon_0^2}\left(n\frac{\partial\varepsilon}{\partial n}\right)^4 \left\{\frac{3k_B^2T^2}{\tilde{V}}\beta^2 + \frac{k_B^2T^3}{\tilde{V}^2} \times \left[6\beta^3 + 7\beta\left(\frac{\partial\beta}{\partial P}\right)_{T,V} + \left(\frac{\partial^2\beta}{\partial P^2}\right)_{T,V}\right]\right\}, \qquad (20)$$

where k_B is the Boltzmann constant. Contribution (19) and the second term in (20) are due to the deviation of the statistic of fluctuations ΔN from a Gaussian one.

At present, the explicit form of the derivatives of the compressibility β near the critical point is unknown. However, in the temperature range under consideration, the functional structure of the derivative $(\partial\beta/\partial P)_{T,V}$ can be estimated by using the van der Waals equation. Having performed appropriate calculations, we find that the expression in the braces in (19) is

$$3\omega(3\omega + 2)^{-1}[\beta^2 + 6P_c(1 + \omega)^{-2}\beta^3],$$

where $\omega = \rho_c/\rho - 1$, ρ is the density of the liquid, ρ_c is its critical value, and P_c is the critical pressure.

We see that $I_{1.5} = 0$ on the critical isochore, which satisfies the conformal invariance condition [13]. Deviating from it by ω, we have the lower limit ($\beta \gtrsim 1/6P_c\tau$)

$$|I_{1.5}| \gtrsim \frac{1}{\varepsilon_0}\left(n\frac{\partial\varepsilon}{\partial n}\right)^3 \frac{k_B^2T^2}{\tilde{V}}\frac{|\omega|}{\tau}\beta^2. \qquad (21)$$

Assuming that the Gaussian contribution in (20) is the dominant one, we obtain the following estimate using formula (21):

$$\left|\frac{I_{1.5}}{I_2}\right| \gtrsim \frac{\varepsilon_0|\omega|}{(n\partial\varepsilon/\partial n)\tau}.$$

For liquids characterized by low values of $n\partial\varepsilon/\partial n$, the contribution $I_{1.5}$ can be decisive. In particular, $\varepsilon_0 \approx 1.3$ and $n\partial\varepsilon/\partial n \approx 0.33$ for xenon [6]; therefore, $|I_{1.5}/I_2| \gtrsim 4|\omega|/\tau$.

We also provide other data from [6] used below; $\lambda \approx 4.28 \times 10^{-5}$ cm, $r_c = 2.2 \times 10^{-8}\tau^{-0.63}$ cm, $P_c = 5.84 \times 10^7$ dyn cm^{-2}, $\rho_c = 188.2$ Amagat, and $T_c = 289.765$ K.

To estimate $|I_{1.5}/I_1|$, we note that the linear size of the region $\tilde{V}$ far from the critical point must be much larger than the range of action of intermolecular forces; at the same time, it can remain small compared to λ [10]. Setting $\tilde{V} \approx 2.5 \times 10^{-19}$ cm^3 for $\tau \gtrsim 1 \times 10^{-2}$ (i.e., for correlation lengths $r_c \lesssim 4 \times 10^{-7}$ cm) and $k_BT \approx 4 \times 10^{-14}$ erg, we obtain

$$\left|\frac{I_{1.5}}{I_1}\right| \approx n\frac{\partial\varepsilon}{\partial n}\frac{k_BT\beta|\omega|}{\varepsilon_0\tilde{V}\tau} \gtrsim 1.2\times 10^{-4}|\omega|\tau^{-2},$$

which is ~1% at $|\omega| \approx \tau \approx 1 \times 10^{-2}$. Passing from the compressibility critical exponent $\gamma = 1$ used above to $\gamma \approx 1.2$, slightly reducing $\tilde{V}$, and varying ω and τ, we can increase this estimate by an order of magnitude. Note also that the intensity of the double polarized scattering [2, 9] in this region

$$I_d \propto (n\partial\varepsilon/\partial n)^4 L k_0^4 k_B^2 T^2 \beta^2/15\pi$$

(L is in cm) and the contribution $I_{1.5}$ (if $|\omega| \approx \tau$) exhibit similar temperature dependences, but $|I_{1.5}|$ exceeds I_d for small L:

$$\left|\frac{I_{1.5}}{I_d}\right| \approx 0.1\frac{|\omega|\lambda^4}{\tau L\tilde{V}} \approx 1.3\frac{|\omega|}{\tau L}.$$

In a single-component liquid, the contribution due to fluctuations of the distribution function for thermal fluctuations (see [7]) can be ignored.

For $r_c \gg 4 \times 10^{-7}$ cm, $\tilde{V}$ becomes more certain [5]: $\tilde{V} \sim 4\pi r_c^3/3$. In this case, the pattern of the temperature dependence of contributions (19) and (20) changes significantly. The first term in (20) yields a well-known result predicted by the Gaussian model for order-parameter fluctuations: $I_2 \propto r_c$. Approaching the critical point in such a way that $|\omega|\beta$ = const, we find that $I_{1.5} \propto r_c$, which is close the result [5] of the scaling theory restored in the preceding section. Since $I_1 \propto r_c^2$, the relative role of contributions (19) and (20) in this region decreases sharply. They are additionally suppressed by the contribution $I_d \propto \beta^2$; the growth of the latter as we pass to a range of $\tau \lesssim 10^{-4}$ slows down.

5. OBSERVATION OF 1.5 SCATTERING

As the above estimates show, the most favorable situation for experimentally detecting the effects of the molecular scattering of light of multiplicity 1.5 is realized for liquids with low values of the parameter $n\partial\varepsilon/\partial n$, with the contribution $I_{1.5}$ having the largest relative value in the temperature range $10^{-3} \lesssim \tau \lesssim 10^{-2}$ and at comparable values of ω. The fact that $I_{1.5} < 0$, while the contributions I_1, I_2, I_d, the contribution of the double depolarized scattering I_{dd} (on the order of $I_d/8$ [9]), and the contribution of the depolarized scattering by the fluctuations in anisotropy I_a (relatively small in simple liquids and virtually insensitive to the critical point) are positive, favors its separation from the total scattering intensity.

Consider the depolarization ratio Δ of the scattered light. Taking into account the contributions for a simple liquid listed above, we can write

$$\Delta = \frac{I_a + I_{dd}}{I_1 + I_{1.5} + I_2 + I_d}. \qquad (22)$$

Let us pass from (22) to the relation

$$\frac{I_{dd}}{I_1\Delta} = \frac{1 + I_{1.5}I_1^{-1} + (I_2 + I_d)I_1^{-1}}{1 + I_aI_{dd}^{-1}}. \qquad (23)$$

Given the above temperature dependences for the individual contributions, its structure is

$$\frac{x}{\Delta} \propto \frac{1 - a\tilde{V}^{-1}\omega\tau^{-1}x + bf(x)}{1 + cx^{-2}}, \qquad (24)$$

where a, b, and c are positive constants; $x \equiv k_BT\beta$; and the function f is such that $f(x) \approx x$ for $\tau \gtrsim 10^{-3}$ and a constant value is approached at $\tau < 10^{-4}$. If the contribution of $I_{1.5}$ is zero ($a = 0$), then the right-hand side of (24) is a monotonically increasing function of x that rapidly approaches a linear function as the denominator decreases and then levels off. The contribution of $I_{1.5} < 0$, must violate the monotonic behavior of (24): the initial increase gives way to a decrease, passage through a minimum, and then a possible increase and saturation. No attempts to experimentally test these predictions have been made so far.

The depolarization mechanisms of the molecular scattering of light in xenon were experimentally studied by Trappeniers *et al.* [6], who analyzed in detail the dependence of Δ on

$$D = k_0^{-4}\left[\frac{(\varepsilon_0 - 1)(\varepsilon_0 + 2)}{12\pi}\right]^{-2}(k_BT\beta)^{-1} \propto x^{-1}.$$

Using these data, we plotted (see figure) the values of $(D\Delta)^{-1}$ and D^{-1} for thirty points in the temperature range from 39.1880°C ($\tau = 7.8 \times 10^{-2}$) to 16.6252°C ($\tau = 3.5 \times 10^{-5}$) lying on the isochore ρ = 186.93 Amagat ($\omega = 6.8 \times 10^{-3}$); L = 0.547 cm. A maximum and a minimum are observed at $\tau = 4.1 \times 10^{-3}$ and 1.8×10^{-4}, respectively. The qualitative behavior of the plot and the parameters of its characteristic points are in satisfactory agreement with our estimates.

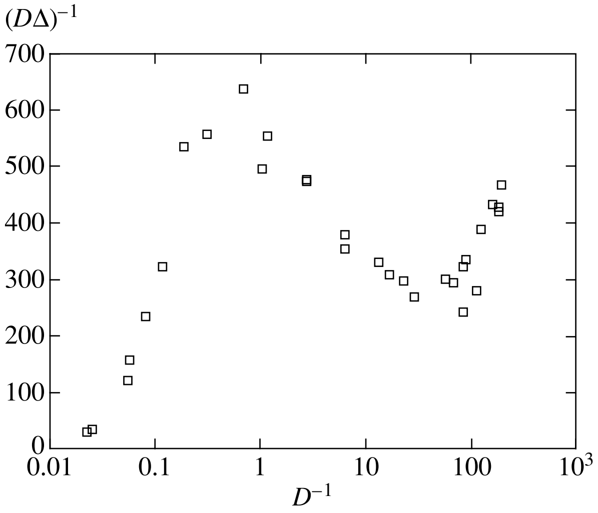

$(D\Delta)^{-1}$ versus D^{-1} along the $\omega = 6.8 \times 10^{-3}$ isochore for xenon, based on data from [6].

Further thorough testing of our conclusions is of considerable interest. Their confirmation in a specially planned experiment would imply that information about the third-order fluctuation moments and related parameters of the liquid could in principle be obtained by the methods of molecular spectroscopy.

REFERENCES

1. B. Crosignani, P. Di Porto, and M. Bertolotti, *Statistical Properties of Scattered Light* (Academic, New York, 1975; Nauka, Moscow, 1980).
2. E. L. Lakoza and A. V. Chalyĭ, Usp. Fiz. Nauk **140**, 393 (1983) [Sov. Phys. Usp. **26**, 573 (1983)].
3. M. Ya. Sushko, Ukr. Fiz. Zh. **49**, 710 (2004).
4. V. S. Vladimirov, *Equations of Mathematical Physics*, 3rd ed. (Nauka, Moscow, 1981; Marcel Dekker, New York, 1971).
5. A. Z. Patashinskiĭ and V. L. Pokrovskiĭ, *Fluctuation Theory of Phase Transitions*, 2nd ed. (Nauka, Moscow, 1982; Pergamon Press, Oxford, 1979).
6. N. J. Trappeniers, A. C. Michels, H. M. J. Boots, and R. H. Huijser, Physica A (Amsterdam) **101**, 431 (1980).
7. A. F. Andreev, Pis'ma Zh. Éksp. Teor. Fiz. **19**, 713 (1974) [JETP Lett. **19**, 368 (1974)].
8. L. V. Adzhemyan, L. Ts. Adzhemyan, L. A. Zubkov, and V. P. Romanov, Pis'ma Zh. Éksp. Teor. Fiz. **22**, 11 (1975) [JETP Lett. **22**, 5 (1975)].
9. N. P. Malomuzh and M. Ya. Sushko, Zh. Éksp. Teor. Fiz. **89**, 435 (1985) [Sov. Phys. JETP **62**, 246 (1985)].
10. L. D. Landau and E. M. Lifshitz, *Course of Theoretical Physics*, Vol. 8: *Electrodynamics of Continuous Media*, 2nd ed. (Nauka, Moscow, 1982; Pergamon Press, Oxford, 1984).
11. K. G. Wilson and M. E. Fisher, Phys. Rev. Lett. **28**, 240 (1972).
12. R. F. Greene and H. B. Callen, Phys. Rev. **83**, 1231 (1951).
13. A. M. Polyakov, Pis'ma Zh. Éksp. Teor. Fiz. **12**, 538 (1970) [JETP Lett. **12**, 381 (1970)].

Translated by V. Astakhov

Journal of Experimental and Theoretical Physics, Vol. 99, No. 6, 2004, pp. 1189–1192.
Translated from Zhurnal Éksperimental’noĭ i Teoreticheskoĭ Fiziki, Vol. 126, No. 6, 2004, pp. 1362–1366.
Original Russian Text Copyright © 2004 by A. Kravets, Dzhezherya, V. Kravets, Klimuk.

SOLIDS
Structure

Specific Features of the Reflection of Infrared Radiation by Crystalline Dielectrics in a Magnetic Field

A. F. Kravets[a], Yu. I. Dzhezherya[a], V. G. Kravets[b], and E. S. Klimuk[a]
[a]*Institute of Magnetism, National Academy of Sciences of Ukraine, Kiev, 03680 Ukraine*
[b]*Institute of Information Recording Problems, National Academy of Sciences of Ukraine, Uzhgorod, 294000 Ukraine*
e-mail: kravets@imag.kiev.ua

Received February 2, 2004

Abstract—Magnetic-field-induced variations in the reflection spectra $R(\lambda)$ of the crystalline dielectrics Al_2O_3, LiF, and MgO in the infrared band ($\lambda = 2.5$–25 μm) are investigated. It is found that the reflection spectra exhibit specific features in the neighborhood of wavelengths corresponding to the excitation of optical phonon modes in the above-mentioned crystals and that a magnetic field causes an appreciable variation in the reflectivity at these wavelengths. To qualitatively describe the effect of a magnetic field on the reflection of light, the magnetoreflection spectra $\Delta R/R$ are investigated. The spectra $\Delta R/R$ exhibit sharp peaks in the neighborhood of wavelengths at which the materials under investigation are characterized by minimal reflectivity. The values of $\Delta R/R$ for *p*-polarized infrared radiation in a magnetic field of about 12 kOe amount to about 0.5% for Al_2O_3 at $\lambda \approx 9.6$ μm, 7% for LiF at $\lambda \approx 11.1$ μm, and 0.07% for MgO at $\lambda \approx 11.7$ μm. *© 2004 MAIK “Nauka/Interperiodica”.*

Nanocomposite materials containing ferromagnetic nanosized grains dispersed in dielectric matrices (Al_2O_3, HfO_2, and MgO) play an important role in the study of tunnel magnetoresistance (TMR). The magnitude of TMR is determined by the type of the magnetic and oxide materials, the stoichiometry of their composition, and the shape and concentration of ferromagnetic inclusions. The recently discovered magnetorefractive effect (MRE) [1] has been widely used for scrutinizing the details of the physical nature of the TMR. This effect consists in the dependence of the reflection, transmission, and absorption coefficients of a material on the applied magnetic field. It is believed [1] that the MRE is associated with the spin dependence of the optical conductivity of materials. The MRE was predicted theoretically in multilayer [1] and granular [2] metallic magnetic structures. It was experimentally verified in [3, 4] in magnetorefractive investigations of multilayer magnetic structures and in experiments with granular metallic [5, 6] and metal-dielectric [7–12] structures.

Investigations of metal-dielectric nanocomposites [7–12] revealed peaks in the spectra of MRE in the range of frequencies close to that where the materials of dielectric matrices exhibit optical phonon modes. However, the nature of these peaks has not been determined. It was also established that the MRE spectra of metal-dielectric films depend on the polarization of the incident light [10–12]. It should be noted that the MRE in reflection experiments attains its maximal value for *p*-polarized light when the angle of incidence approaches the Brewster angle. This is especially clearly manifested in metal-dielectric structures with the content of ferromagnetic grains close to the percolation threshold [11, 12]. The authors of these papers developed a theoretical model to describe the MRE spectra in similar structures that accounts for the relation between the MRE, the TMR, and the optical parameters of the system.

In the present study, we tried to determine the role of the dispersion properties of the materials of dielectric matrices on the reflection of infrared radiation from metal-dielectric nanocomposites in a magnetic field. We measured the infrared reflection spectra of materials frequently used as dielectric matrices in nanocomposites. We also investigated the effect of magnetic field on the reflectivity. The experiments were carried out under the same conditions as those used when investigating the magnetorefractive properties of metal-dielectric films [10].

For magnetooptical measurements, we used the following crystalline samples, were optically polished from one side: Al_2O_3 crystals with orientations [1012] (R-plane) and [1120] (A-plane), a LiF crystal with orientation [001], and a MgO crystal with orientation [100]. The purity of the crystals produced by Goodfellow amounted to 99.99%. The light reflection spectra $R(\lambda)$ in the infrared range of wavelengths from 2.5 to 25 μm were recorded on a Nicolet 670 FTIR spectrometer with an MCT-B photodetector, which was cooled by liquid nitrogen. Spectral measurements in polarized light were carried out with the use of a KRS-5 mesh polarizer. When measuring the light reflection spectra as a function of a magnetic field, the mirrors of the spectrometer were taken outside the device so that

1063-7761/04/9906-1189$26.00 © 2004 MAIK “Nauka/Interperiodica”

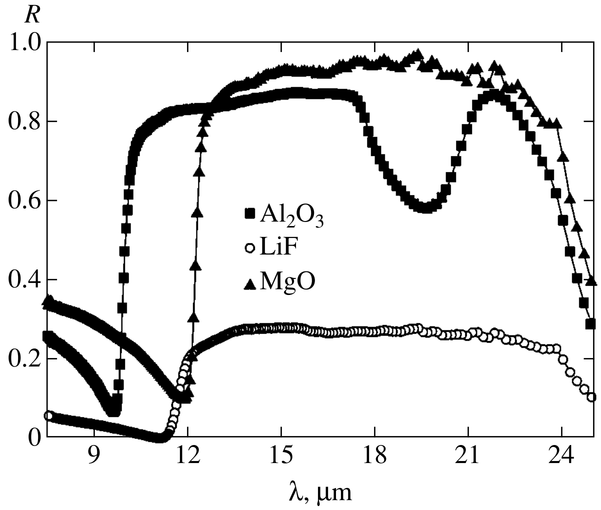

Fig. 1. The reflection spectra of a *p*-polarized infrared radiation for crystalline dielectrics.

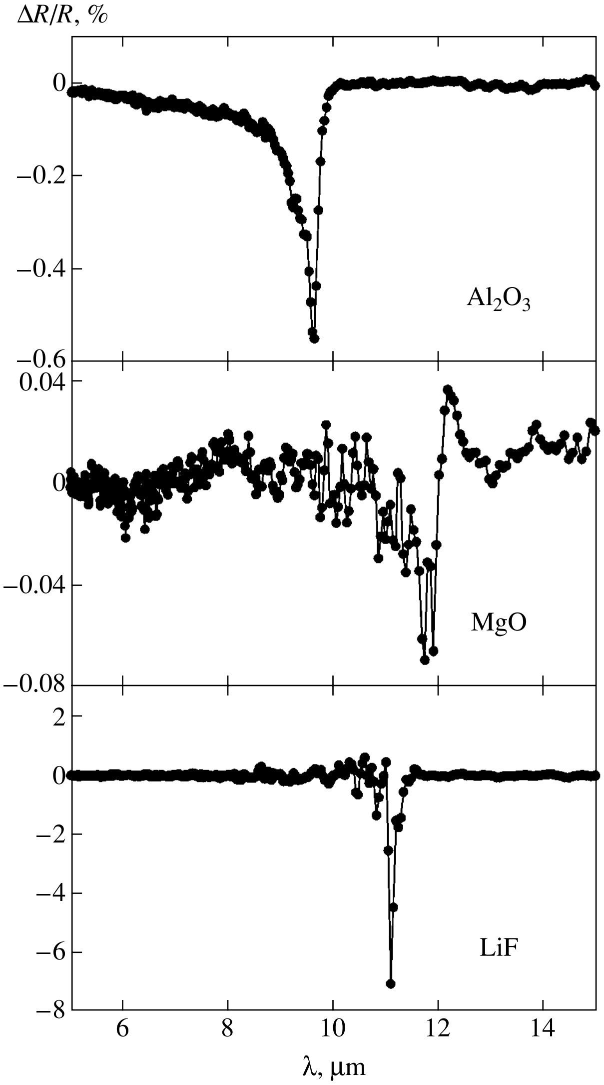

Fig. 2. The $\Delta R/R$ spectra of dielectrics measured in a magnetic field of 12.2 kOe.

infrared radiation could be focused on a sample placed in the gap of an external electromagnet. The samples were fixed on a small copper table that prevented them from being displaced due to the switching on of a magnetic field. The incidence angle of light on the samples was about 65°. This angle was close to the Brewster angle, which guaranteed the maximal effect [8, 11, 12]. The optical reflection spectra were normalized by the relevant spectra of thick silver films, whose reflectivity was about 0.9. Note also that the measurements for Al_2O_3 were performed repeatedly for crystals with different crystallographic orientations as well as for polycrystalline samples. For the Al_2O_3 crystal, the effect was maximal for the reflection from the [1120] plane. The relevant spectra are discussed below.

By analogy with the MRE in nanocomposites, we introduce the magnetoreflection (MR) coefficient for dielectrics, which is defined by the relation

$$\Delta R/R = (R_0 - R_H)/R_0,$$

where R_H and R_0 are the reflection coefficients of a material in the presence and absence of a magnetic field, respectively.

The magnetic field was directed perpendicular to the propagation direction of infrared radiation and parallel to the surface of the samples.

We have found that the MR spectra strongly depend both on the polarization of the incident light and on the magnitude of the magnetic field.

The spectral functions $R(\lambda)$ and $\Delta R/R$ presented in this paper are obtained by averaging over about 400 scans performed with the FTIR spectrometer. As test measurements, we determined the reflection spectra from thick films of pure silver and aluminum in a magnetic field. These measurements showed that the reflection coefficient $R(\lambda)$ does not depend on the magnetic field.

In our previous work [10], we showed that the spectra $\Delta R/R$ of pure Al_2O_3 experience variations in a magnetic field, which are most clearly manifested near the wavelengths corresponding to the excitation of phonon modes in Al_2O_3 at about $\lambda \approx 9.6$ μm.

To give a clear idea of the physical nature of $\Delta R/R$ in dielectrics, in addition to Al_2O_3, which is characterized by covalent dipolar bonds, we measured the reflection spectra $R(\lambda)$ and the $\Delta R/R$ spectra in the covalent polar crystal MgO and in the ionic crystal LiF.

Figure 1 shows the spectra of *p*-polarized infrared radiation reflected from the surface of bulky crystals of Al_2O_3, MgO, and LiF. All the spectra exhibit minima in the neighborhood of wavelengths of $\lambda \approx 9$–12 μm, which correspond to the excitation of optical phonon modes in these materials [13, 14].

Figure 2 shows the $\Delta R/R$ spectra in these dielectrics, measured in a magnetic field of 12.2 kOe. In all these spectra, the MRE manifests itself only in the neighborhood of the wavelength λ_0 where the reflection is minimal: $\lambda_0 \approx 9.6$ μm for Al_2O_3, $\lambda_0 \approx 11.7$ μm for MgO, and $\lambda \approx 11.1$ μm for LiF. One can see that, among all the samples investigated, the greatest value of $\Delta R/R$ is attained in LiF, and the minimal value, in MgO.

Since Al_2O_3 has found wide application in nanocomposite technology owing to its unique physical properties, in the present study, we placed special emphasis on the investigation of magnetoreflection precisely for this material, the investigations of LiF and MgO being carried out to demonstrate the universal character of this phenomenon.

Figure 3 shows the $\Delta R/R$ spectra for Al_2O_3 measured for different values of the magnetic field. As the magnetic field increases from 1 to 12.2 kOe, the absolute value of $\Delta R/R$ increases from 0.15 to 0.57% by a nonlinear law. The minimum of $\Delta R/R$ in Al_2O_3 is attained at a wavelength of $\lambda_0 \approx 9.6$ μm (Fig. 3). We did not observe any variation in the position of this minimum as a function of the magnetic field within the measurement accuracy.

Significant dependence of the reflection coefficient on a magnetic field in Al_2O_3, MgO, and LiF was observed only in those spectral regions where $R(\lambda)$ is small (Fig. 4). The reflection coefficients of both components of a light wave, those polarized in the plane of incidence and perpendicular to it, are small only in the frequency domain where the dielectric permittivity of a substance is characterized by a sharp time dispersion, more precisely, at wavelengths where the permittivity is close to unity. In this case, the refractive indices of a crystal and the surrounding medium become almost equal and the interface between them has negligible reflection. Then, the small corrections due to the magnetic field against the background of weak reflection become noticeable and reach a relatively large value. Naturally, this results in an increase in the MR coefficient because ΔR in $\Delta R/R$ is divided by a small quantity. However, such sharp spectral dependence of MR (Fig. 2) is associated exclusively with the character of variation in the absolute value of $\Delta R = R_0 - R_H$. To support this thesis, we present in Fig. 5 the spectral dependence of ΔR for a *p*-polarized light. When carrying out these measurements, a magnetic field of 13.5 kOe, which was the maximum possible value in our experiments, was applied to the samples. Figures 2 and 5 show that the curves of $\Delta R/R$ and ΔR exhibit similar spectral behavior; this confirms the effect of the magnetic field on the reflection spectra of the dielectrics under investigation. It should also be noted that the effect observed is even with respect to the field because we did not observe a change in the sign of ΔR under the reversal of the magnetic field direction. The function ΔR shows a significant variation only in the neighborhoods of $\lambda \sim 9$–12 μm; everywhere outside these regions, it is constant and close to zero. The ΔR spectrum of the ionic crystal LiF exhibits the narrowest and deepest minimum in the range of wavelengths 11.1–

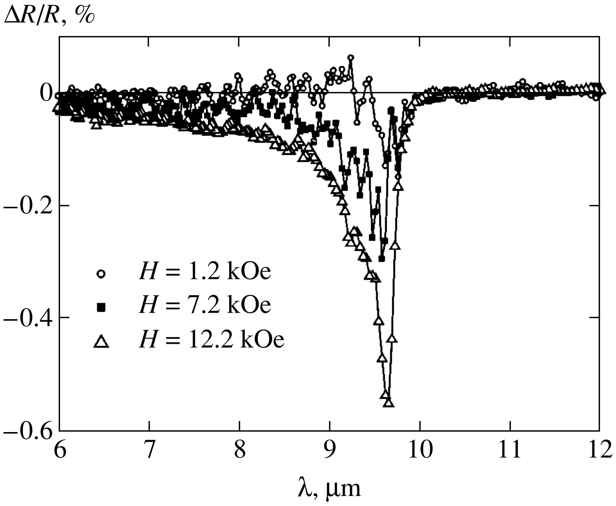

Fig. 3. The $\Delta R/R$ spectra of Al_2O_3 for *p*-polarized radiation for various values of the magnetic field *H*.

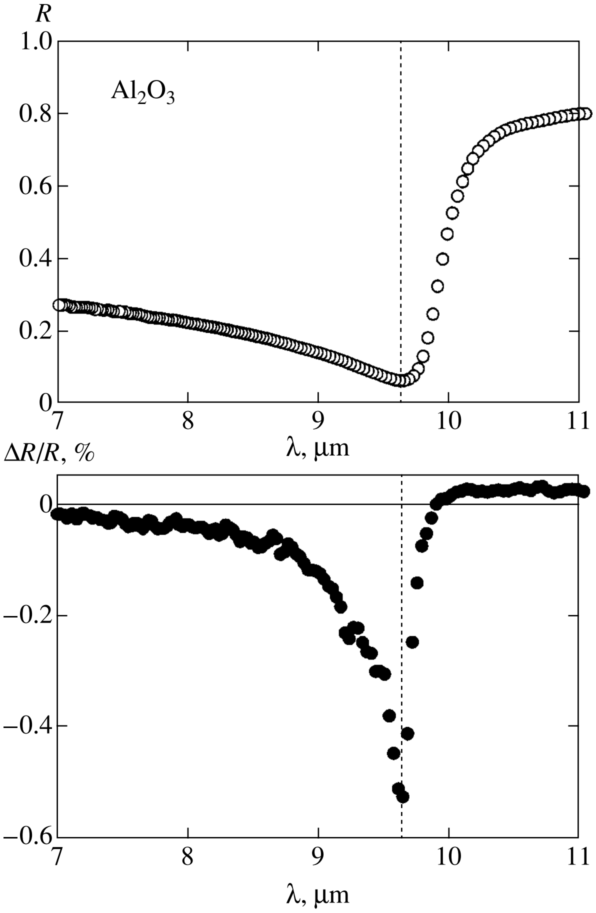

Fig. 4. Comparison of the reflection spectra *R* and magnetoreflection spectra $\Delta R/R$ in Al_2O_3.

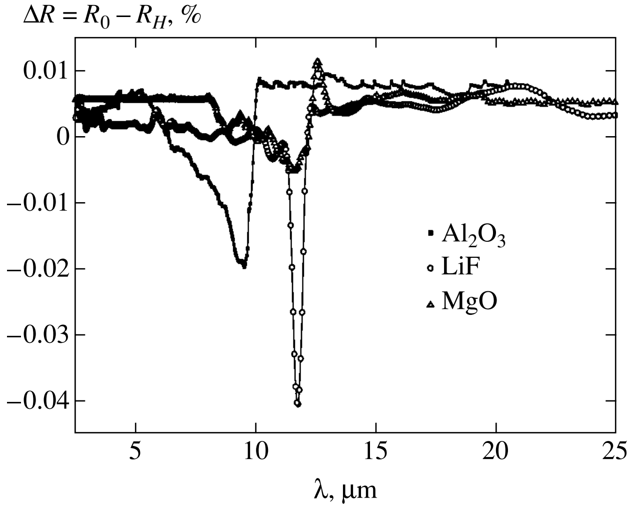

Fig. 5. The $\Delta R = R_0 - R_H$ spectra of dielectrics for *p*-polarized radiation measured in a magnetic field of 13.5 kOe.

12.2 μm, whereas for Al_2O_3, this range is 5.1–10.1 μm, and for MgO, 8–12.4 μm.

Thus, we have shown that the anomalies in the MRE spectra of magnetic nanocomposites in a certain frequency region in the infrared band can be attributed to the dispersion properties of the dielectric matrix.

REFERENCES

1. J. C. Jacquet and T. Valet, Mater. Res. Soc. Symp. Proc. **384**, 477 (1995).
2. A. B. Granovskiĭ, M. V. Kuzmichev, and J. P. Clerc, Zh. Éksp. Teor. Fiz. **116**, 1762 (1999) [JETP **89**, 955 (1999)].
3. S. Uran, M. Grimsditch, E. E. Fullerton, and S. D. Bader, Phys. Rev. B **57**, 2705 (1998).
4. J. van Driel, F. R. de Boer, R. Coehoorn, *et al.*, Phys. Rev. B **61**, 15321 (2000).
5. J. P. Camplin, S. M. Thompson, D. R. Loraine, *et al.*, J. Appl. Phys. **87**, 4846 (2000).
6. V. G. Kravets, D. Bozec, J. A. D. Matthew, *et al.*, Phys. Rev. B **65**, 054415 (2002).
7. I. V. Bykov, E. A. Gan'shina, A. B. Granovskiĭ, and V. S. Gushchin, Fiz. Tverd. Tela (St. Petersburg) **42**, 487 (2000) [Phys. Solid State **42**, 498 (2000)].
8. D. Bozec, V. G. Kravets, J. A. D. Matthew, and S. M. Thompson, J. Appl. Phys. **91**, 8795 (2002).
9. A. Granovskiĭ, V. Gushchin, I. Bykov, *et al.*, Fiz. Tverd. Tela (St. Petersburg) **45**, 868 (2003) [Phys. Solid State **45**, 911 (2003)].
10. V. G. Kravets, A. N. Pogorelyĭ, A. F. Kravets, *et al.*, Fiz. Tverd. Tela (St. Petersburg) **45**, 1456 (2003) [Phys. Solid State **45**, 1530 (2003)].
11. A. B. Granovskiĭ, M. Inoue, J. P. Clerc, and A. N. Yurasov, Fiz. Tverd. Tela (St. Petersburg) **46**, 484 (2004) [Phys. Solid State **46**, 498 (2004)].
12. A. B. Granovskiĭ, I. V. Bykov, E. A. Gan'shina, *et al.*, Zh. Éksp. Teor. Fiz. **123**, 1256 (2003) [JETP **96**, 1104 (2003)].
13. W. Zhu, C. J. Hirschmugl, A. D. Laine, *et al.*, Appl. Phys. Lett. **78**, 3103 (2001).
14. P. Brüesh, R. Kötz, H. Neff, and L. Pietronero, Phys. Rev. B **29**, 4691 (1984).

Translated by I. Nikitin

Journal of Experimental and Theoretical Physics, Vol. 99, No. 6, 2004, pp. 1193–1200.
Translated from Zhurnal Éksperimental'noĭ i Teoreticheskoĭ Fiziki, Vol. 126, No. 6, 2004, pp. 1367–1376.
Original Russian Text Copyright © 2004 by Melkov, Dzyapko, Chumak, Slavin.

SOLIDS
Structure

Two-Magnon Relaxation Reversal in Ferrite Spheres

G. A. Melkov*, A. D. Dzyapko, A. V. Chumak, and A. N. Slavin
Taras Shevchenko National University, Kiev, 01680 Ukraine
**e-mail: melkov@univ.kiev.ua*

Received April 6, 2004

Abstract—The reversal of two-magnon relaxation associated with linear scattering of oscillations of uniform magnetization precession from sample nonuniformities is studied theoretically and experimentally in ferrite spheres of yttrium iron garnet (YIG). Relaxation reversal is performed by parametric phase conjugation of dipole–exchange spin waves formed as a result of scattering of uniform precession from inhomogeneities. As a result of two-magnon backward scattering of dipole–exchange spin waves with a certain time delay, magnetization oscillations are renewed with an amplitude that could exceed the initial amplitude of uniform precession. The relaxation reversal is due to crystallographic anisotropy of the sample and is manifested most strongly when a YIG sphere is magnetized along the intermediate axis [110]. Experiments were carried out on YIG spheres of diameter 0.65–1.05 mm for a parallel pumping frequency $\omega_p/2\pi \approx 9.4$ GHz, which is about twice the uniform precession frequency. The maximal delay time for the restored signal of uniform precession was about 2 μs, while the maximal amplitude exceeded the initial uniform precession amplitude by a factor of about 5. The "latent" relaxation parameters of ferrites, e.g., the natural ferromagnetic resonance linewidth associated with many-particle processes and the linewidth associated with two-magnon scattering at bulk nonuniformities, are determined experimentally. © *2004 MAIK "Nauka/Interperiodica".*

1. INTRODUCTION

The main contribution to the ferromagnetic resonance linewidth ΔH even in perfect samples of yttrium iron garnet (YIG) comes from two-magnon relaxation processes connected with two-magnon elastic scattering of magnetization oscillations from bulk and surface nonuniformities in the sample [1]. As a result of two-magnon scattering, uniform precession of magnetization, or a magnon with wavenumber $k = 0$, excites a spin wave, or a magnon with wavenumber $k' \neq k = 0$ determined by the size a of the nonuniformity. Waves with $k' \sim 2\pi/a$, are excited most intensely. For YIG single crystal with a typical size $a \sim 1$ μm of nonuniformities, this corresponds to excitation of dipole–exchange spin waves with $k' \sim 10^4$ cm^{-1} by uniform precession. In addition to the magnetic dipole interaction, the exchange interaction of magnetic moments proportional to k'^2 becomes significant for such waves.

It should be noted that the momentum conservation law rules out two-magnon scattering and two-magnon relaxation associated with it in a perfect infinitely large crystal. This law can be violated only in a crystal containing nonuniformities and boundaries.

Prior to the irreversible transformation into thermal lattice vibrations, the uniform precession energy is transformed by two-magnon relaxation first to a system of dipole–exchange spin waves, where it can exist even after the termination of uniform precession oscillations, since the lifetimes $T_k = 2/\gamma\Delta H_k$ of dipole–exchange spin waves are several times longer than the lifetimes $T = 2/\gamma\Delta H$ of uniform precession. Here, γ is the gyromagnetic ratio for electron spin and ΔH_k is the resonance linewidth of dipole–exchange spin wave with wavenumber k. Before the attainment of the thermal level by the amplitude of dipole–exchange waves, the energy of these waves can be transferred back to uniform precession, which causes reversal of two-magnon relaxation and partial restoration of the uniform precession of magnetization.

Several methods for reversal of scattering processes are known. We will use the method of phase conjugation by parametric pumping [2]. As applied to the case considered here, this method consists of the following stages. First, a signal electromagnetic pulse of duration τ_s and frequency ω_s close to the ferromagnetic resonance frequency ω_0 excited uniform precession. As a result of interaction with random nonuniformities in the sample, this precession excites a set of $n \gg 1$ dipole–exchange spin waves propagating from these nonuniformities with different wavevectors $\mathbf{k}_n$, frequencies $\omega_n \sim \omega_s$, and group velocities v_n. After the termination of the signal pulse, uniform precession rapidly dies away and spin waves continue to move away from the nonuniformities, attenuating with time at a much lower rate than uniform precession. Then a uniform parametric pump pulse of duration τ_p and frequency $\omega_p \approx 2\omega_s$ is supplied at instant $t = t_p$. Pumping, first, leads to parametric amplification of primary waves (propagating away from nonuniformities) having frequencies ω_n and wavevectors $\mathbf{k}_n$ and, second, excites new idler waves of frequency ω_i, whose wavevectors $\mathbf{k}_i$ satisfy the energy and momentum conservation laws:

$$\omega_i = \omega_p - \omega_n, \quad \mathbf{k}_i = \mathbf{k}_p - \mathbf{k}_n,$$

where vector $\mathbf{k}_p$ is the pump wavevector. In the case of a uniform pumping ($\mathbf{k}_p = 0$), we have $\mathbf{k}_i = -\mathbf{k}_n$; i.e., the idler wave is an reverse wave relative to the primary dipole–exchange spin wave, which propagates along the same path as the primary wave, but in the opposite direction. Such a behavior of the idler wave can be interpreted as phase conjugation (or time reversal) of the primary wave under the action of parametric pulsed pumping [2]. Thus, for all n idler reverse waves, the reverse path to nonuniformities will be the same as for the primary waves and, after the termination of pumping, will take the same time t_p as the time of propagation of primary waves from inhomogeneities to the instant of pump pulse action irrespective of the wave velocity v_n. Consequently, over a time $t = 2t_p$ (for $\tau_p \ll t_p$), all idler waves reach the corresponding nonuniformities at which they form a restored signal of uniform magnetization precession as a result of backward two-magnon scattering.

Parametrically enhanced dipole–exchange waves propagating from inhomogeneities can also make a contribution to restoration of uniform magnetization precession [3]. Prior to parametric pumping, the phases of all spin waves, $\varphi_n = \omega_n t$ ($\omega_s - 1/\tau_s < \omega_n < \omega_s + 1/\tau_s$), are uniformly distributed with time over an interval from 0 to 2π; consequently, their total contribution to uniform magnetization precession is equal to zero in view of backward two-magnon scattering. After the pumping is switched on, the process of amplification of primary spin waves begins. If the pump pulse is long enough ($\tau_p \le T_k$) and, hence, has a narrow frequency range, parametric amplification of spin waves caused by this pulse is characterized by a narrow band: from the entire set of dipole–exchange spin waves, only waves with frequencies close to half the pumping frequency $\omega_p/2$ will be selectively amplified. Thus, the coherence of the system of dephased spin waves will be partially restored and their contribution to uniform precession will differ from zero [3]. This contribution will increase during the operation of a phasing pump pulse and attains its maximal value at the instant of its termination, i.e., for $t = t_p + \tau_p$ and not for $t = 2t_p$ as in the case of phase conjugation for dipole–exchange spin waves. After the termination of the pump pulse, misphasing of dipole–exchange spin waves again comes into play and the contribution of these waves to uniform precession will decrease until it vanishes completely after the attainment of a uniform phase distribution of spin waves (in a time on the order of $1/\tau_s$).

We will confine our analysis to reversal of two-magnon relaxation associated only with the effect of parametric phase conjugation of dipole exchange spin waves. In accordance with the above arguments, we will use short (τ_s, $\tau_p \ll \Gamma_k^{-1}$, t_p) signal and pump pulses. First, we will derive theoretical relations describing the process of two-magnon relaxation reversal, which will be verified experimentally using parametric pumping of 3-cm waves at small ferrite spheres with a diameter from 0.65 to 1.05 mm.

2. THEORY

Oscillations of uniform precession and dipole–exchange spin waves coupled by crystal nonuniformities in the presence of parallel parametric pumping can be written in the form [3, 4]

$$\begin{aligned} &\frac{\partial c_0}{\partial t} + i\omega_0 c_0 + \Gamma_0 c_0 \\ &- i\sum_{\mathbf{k} \ne 0} R_{0\mathbf{k}} c_{\mathbf{k}} = -i\gamma h_s \exp(-i\omega_s t), \end{aligned} \tag{1}$$

$$\begin{aligned} &\frac{\partial c_{\mathbf{k}}}{\partial t} + i\omega_k c_{\mathbf{k}} + \Gamma_{k0} c_{\mathbf{k}} \\ &- i\sum_{\substack{\mathbf{k}' \ne \mathbf{k} \\ \mathbf{k} \ne 0}} R_{\mathbf{k}\mathbf{k}'} c_{\mathbf{k}'} = -iV_{\mathbf{k}} h_p \exp(-i\omega_p t) c^*_{-\mathbf{k}}, \end{aligned} \tag{2}$$

where c_0 and $c_{\mathbf{k}}$ are the amplitudes of uniform precession and dipole–exchange spin waves with natural frequencies ω_0 and ω_k, respectively. Here, h_p, h_s and ω_p, ω_s are the amplitudes and frequencies of varying magnetic field of parallel pumping and the signal exciting uniform precession, respectively, and $V_{\mathbf{k}}$ is the coupling coefficient of dipole–exchange spin waves with parallel pumping [1]; for uniform precession, such a coupling is absent [1] in Eq. (1); $R_{\mathbf{k}\mathbf{k}'}$ is the probability of scattering of a spin wave (or oscillation) with wavevector $\mathbf{k}'$ from a nonuniformity followed by its transformation into a new spin wave (or oscillation) with wavevector $\mathbf{k} \ne \mathbf{k}'$. It was mentioned earlier that the scattering probability depends on linear size a of a nonuniformity; probability $R_{\mathbf{k}\mathbf{k}'}$ has the maximal value for $|\mathbf{k}' - \mathbf{k}| \sim 2\pi/a$. Finally, $\Gamma_0 = \gamma\Delta H_0/2$ and $\Gamma_{k0} = \gamma\Delta H_{k0}/2$ are the parameters of natural relaxation of uniform precession and spin waves, respectively, taking into account only intrinsic multimagnon and magnon–phonon relaxation processes, including those with participation of optical branches. The contributions from two-magnon processes to relaxation, which will be denoted by $\delta\Gamma_0 = \gamma\delta H_0/2$ and $\delta\Gamma_k = \gamma\delta H_k/2$ for uniform precession and spin waves, respectively, should be determined from system of equations (1) and (2). As a result, we obtain the total frequencies of relaxation and total linewidths in the form

$$\Gamma = \Gamma_0 + \delta\Gamma_0, \quad \Delta H = \Delta H_0 + \delta H_0$$

for uniform precession and

$$\Gamma_k = \Gamma_{k0} + \delta\Gamma_k, \quad \Delta H_k = \Delta H_{k0} + \delta H_k$$

for dipole–exchange spin waves.

Analysis of the natural oscillations of infinite system of equations (1), (2) for a low probability of two-magnon scattering, $|R_{\mathbf{kk'}}| \ll \Gamma_0, \Gamma_{k0}$ gives for $k \geq 0$ [5]

$$\delta\Gamma_k = \sum_{\mathbf{k'}} |R_{\mathbf{kk'}}|^2 \frac{\Gamma_{k'}}{\Gamma_{k'}^2 + (\omega_{k'} - \omega_k)^2}. \tag{3}$$

After supplying an electromagnetic signal of frequency $\omega_s \approx \omega_0$ to ferrite, the spin wave with $k = 0$ (i.e., uniform precession) will possess the largest amplitude. Taking this circumstance into account and using expression (3), we can substantially simplify system of equations (1), (2):

$$\frac{\partial c_0}{\partial t} + i\omega_0 c_0 + \Gamma c_0 = -i\gamma h_s \exp(-i\omega_s t), \tag{4}$$

$$\begin{gathered} \frac{\partial c_{\mathbf{k}}}{\partial t} + i\omega_k c_{\mathbf{k}} + \Gamma_k c_{\mathbf{k}} \\ = -iR_{\mathbf{k}0} c_0 - iV_{\mathbf{k}} h_p \exp(-i\omega_p t) c_{-\mathbf{k}}^*. \end{gathered} \tag{5}$$

We will write the expression for the coupling parameter of dipole–exchange spin waves with parallel pumping $V_{\mathbf{k}}$ taking into account the magnetic crystallographic anisotropy field H_a. It is well known that, in spite of its smallness ($H_a \ll 4\pi M_0$, where M_0 is the magnetization of ferrite) crystallographic anisotropy may strongly affect the course of nonlinear processes [4]. It will be shown below that precisely this situation is also observed in the case considered here. For orientation of magnetization $\mathbf{M}_0$ in the $(1\bar{1}0)$ plane, we have

$$\begin{aligned} V_{\mathbf{k}} &= \frac{1}{4}\gamma\frac{\omega_M}{\omega_k}\sin^2\theta_k \exp(2i\varphi_k) \\ &\quad - \frac{3}{4}\gamma^2\frac{H_a}{\omega_k}\left(\sin^2\theta_H - \frac{3}{4}\sin^2 2\theta_H\right), \end{aligned} \tag{6}$$

where θ_k and φ_k are the polar and azimuth angles of spin waves in the reference frame associated with the direction of the external constant magnetic field $\mathbf{H}_0$, θ_H is the angle between vector $\mathbf{H}_0$ and the [001] axis of the crystal, and $\omega_M = 4\pi\gamma M_0$.

We will solve system (4), (5), presuming the following sequence of short signal and pump pulses acting on ferrite (it was mentioned above that $\tau_s, \tau_p \ll \Gamma_0, \Gamma_k, t_p$). At instant $t = 0$, a signal pulse at frequency $\omega_s = \omega_0$ is switched on, which, in accordance with Eq. (4), enhances uniform precession to the amplitude

$$c_0 = A\exp(-i\omega_s t), \quad A = i\gamma h_s \tau_s. \tag{7}$$

After the removal of the signal pulse, the amplitude of uniform precession decays exponentially by transferring partly energy to spin waves. Then, at instant $t = t_p$, a short pump pulse at frequency $\omega_p = 2\omega_s = 2\omega_0$ is switched on. By this time, in accordance with formulas (5) and (7), the amplitudes of spin waves for $\Gamma \gg \Gamma_k$ attain the values

$$\begin{aligned} c_{\mathbf{k}}(t = t_p) &= -A\frac{R_{\mathbf{k}0}}{(\omega_k - \omega_0) - i\Gamma_k} \\ &\quad \times \exp(-i\omega_k t_p)\exp(-\Gamma_k t_p). \end{aligned} \tag{8}$$

After switching on of pumping at $t \geq t_p$, spin waves are first built up with initial condition (8); second, reverse waves propagating in the opposite directions towards nonuniformities appear. In accordance with formula (5) their amplitudes c_k^{rev} for $t \geq t_p$ have the form

$$\begin{aligned} c_{\mathbf{k}}^{\text{rev}} &= \frac{R_{\mathbf{k}0}}{2\nu_k}\frac{V_{\mathbf{k}}h_p}{\Gamma_k - i(\omega_k - \omega_0)} \\ &\quad \times A^*\exp[i\omega_k(t - 2t_p)]\exp(-\Gamma_k t)\exp(\nu_k t), \end{aligned} \tag{9}$$

where $\nu_k^2 = |V_{\mathbf{k}}h_p|^2 - (\omega_k - \omega_0)^2$.

After scattering from nonuniformities, all waves (9) exhibit backward two-magnon scattering, which restores uniform oscillation of magnetization (7) (naturally, with a different amplitude $A^{\text{rev}} \neq A$). To determine A^{rev}, we must use Eq. (1) for $h_s = 0$, substituting Eq. (9) into it. This gives

$$\begin{aligned} A^{\text{rev}} &= iA^*\sum_{\substack{k > 0 \\ \theta_k, \varphi_k}} \frac{V_{\mathbf{k}}h_p}{2\nu_k}\exp[-i\omega_k(t - 2t_p)] \\ &\quad \times \exp(\nu_k\tau_p)\exp(-2\Gamma_k t_p) \\ &\quad \times \frac{|R_{\mathbf{k}0}|^2}{[\Gamma_k - i(\omega_k - \omega_0)][\Gamma_k - \Gamma_0 + i(\omega_k - \omega_0)]}. \end{aligned} \tag{10}$$

It can be seen from this relation that each spin wave makes a contribution to uniform precession with its own phase proportional to $\exp[-i\omega_k(t - 2t_p)]$; as a result, the total contribution from all spin waves averages to zero in the general case. The sum in (10) differs from zero only at instant $t = 2t_p$ since it is only at this instant that the phase of all dipole–exchange spin waves is the same.

The sum in expression (10) for $t = 2t_p$ determines the maximal amplitude $A^{\text{rev}}(2t_p)$ of uniform precession restored as a result of the reversal process. We will obtain an approximate estimate for this sum based on the fact that parametric pumping excites a narrow wave packet in the vicinity of frequency $\omega_p/2$, which possess the minimal parametric excitation threshold. Assuming that the spread in the natural frequencies of excited dipole–exchange spin waves satisfies the inequality

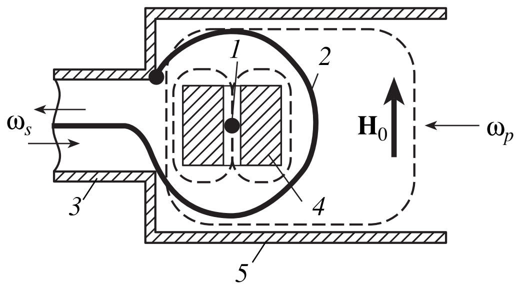

Fig. 1. Experimental model: *1*—ferrite sphere; *2*—loop coupler; *3*—coaxial cable of the signal channel; *4*—open dielectric pumping resonator; *5*—rectangular waveguide of pumping channel. The magnetic microwave field lines of the dielectric resonator and the waveguide are shown by dashed lines; $\mathbf{H}_0$ is the external constant magnetic field.

$|\omega_k - \omega_p/2| \ll \Gamma$, Γ_k and the spread in their wavenumbers is $\Delta k \ll k$, we can take out all constant coefficients and coefficients depending on k from the sum in expression (10). Summation of φ_k in relation (10) nullifies the contribution from the first term in expression (6) for $V_{\mathbf{k}}$ (coupling coefficient of dipole–exchange spin waves with parametric pumping) in view of symmetry in the azimuth angle distribution of dipole–exchange spin waves in the ferrite sphere [4]. Thus, it turns out that the effect of relaxation reversal in a ferrite sphere (or, in the general case, in a sample with identical transverse demagnetizing factors) is due to the influence of the magnetic crystallographic anisotropy described by the second term in expression (6) for $V_{\mathbf{k}}$.

In view of what has been said above and under the assumption that there is a large amplitude of parametric pumping, $h_p V_{\mathbf{k}} \gg \Gamma_k$, we eventually obtain the following expression for the reversal coefficient K of two-magnon relaxation, which is equal to the ratio of the maximal amplitude $A^{\text{rev}}(2t_p)$ of uniform precession restored as a result of reversal of dipole–exchange spin waves to the initial amplitude A excited by input electromagnetic signal (7):

$$K = \frac{|A^{\text{rev}}(2t_p)|}{|A|}, \tag{11}$$

$$K = \frac{\delta\Gamma_0}{\Gamma}\exp(h_p V_{\mathbf{k}}\tau_p)\exp(-2\Gamma_k t_p) \times\left[\frac{3H_a}{8\pi M_0}\left(\sin^2\theta_H - \frac{3}{4}\sin^2 2\theta_H\right)\right]. \tag{12}$$

Analysis of expression (12) shows that the reversal coefficient K attains is maximal value for $\theta_H = 90°$, i.e., for the orientation of the external magnetic field along the intermediate axis [110] of the crystal. For $\theta_H = 0$ (hard axis [001]) and $\theta_H = 55°$ (easy axis [111]), we have $K = 0$. Reversal is also equal to zero in the absence of two-magnon scattering ($\delta\Gamma_0 = \delta\Gamma_k = 0$); for $\delta\Gamma_0$, $\delta\Gamma_k \ll \Gamma_k$, it increases linearly with the scattering probability $|R_{\mathbf{kk'}}|^2$; however, for $\delta\Gamma_k \sim \Gamma_k$, it decreases exponentially due to increasing attenuation of dipole–exchange spin waves, $\Gamma_k = \Gamma_{k0} + \delta\Gamma_k$. Finally, it should be noted that the value of K exponentially increases with amplitude h_p and duration τ_p of the pump pulse and might exceed unity; in other words, restoration of the uniform precession signal with an amplitude larger than its initial amplitude is possible.

3. EXPERIMENT AND DISCUSSION OF RESULTS

The structure of the experimental model for studying two-magnon relaxation reversal under the action of parallel pumping is shown in Fig. 1. A signal of frequency $\omega_s/2\pi \approx 4.7$ GHz was supplied to ferrite sphere *1* and was picked up with the help of loop coupler *2*, which served as a terminal load of 50-Ω coaxial cable *3*. The ferrite sphere was placed in rectangular dielectric resonator *4* tuned to the pumping frequency $\omega_p/2\pi \approx 9.4$ GHz. The type of resonator oscillations was $H_{11\delta}$, and the ac magnetic field in the sphere was parallel to the external constant magnetic field $\mathbf{H}_0$; i.e., the case of parallel pumping of spin-wave instability is realized [1]. The resonator was prepared from a thermostable ceramic material with a dielectric constant of $\varepsilon \approx 80$. A circular hole 1.1 mm in diameter was drilled to accommodate the ferrite sphere. The hole was located at an maximum of magnetic field lines of the resonator and at the minimum of electric field lines; consequently, the shift in the natural frequency of the resonator due to the hole did not exceed 3%. Pumping power P_p with a frequency of $\omega_p \approx 2\omega_s$ was supplied to the dielectric resonator with the help of standard 3-cm waveguide *5* with a rectangular cross section. The pumping source was a magnetron oscillator ensuring a power P_p of 6 W for a pulse duration τ_p of 80 ns. The signal source of power P_s was a klystron generator; to avoid saturation, power P_s did not exceed 10 μW; the duration of signal pulses was $\tau_s = 50$ ns. The signal reflected from the ferrite sphere and the signal emitted by it were supplied from the coaxial cable via a ferrite circulator to the measuring channel of the signal, which contained a low-frequency filter (for suppressing the pump pulse), a low-noise semiconductor amplifier, a power amplifier, and semiconductor detector *1*. The signal from detector *1* was fed to the first channel of a double-beam oscilloscope. The second channel of this oscilloscope was used for detecting the pump pulse incident on the dielectric resonator; this pulse was recorded from semiconductor detector *2* coupled with the waveguide pumping channel via a directional coupler.

Oscillograms of the pulses observed on the screen of the oscilloscope are shown in Fig. 2. Here, the upper and the lower beams describe the voltage across detectors *1* (signal channel) and *2* (pumping channel). Fig-

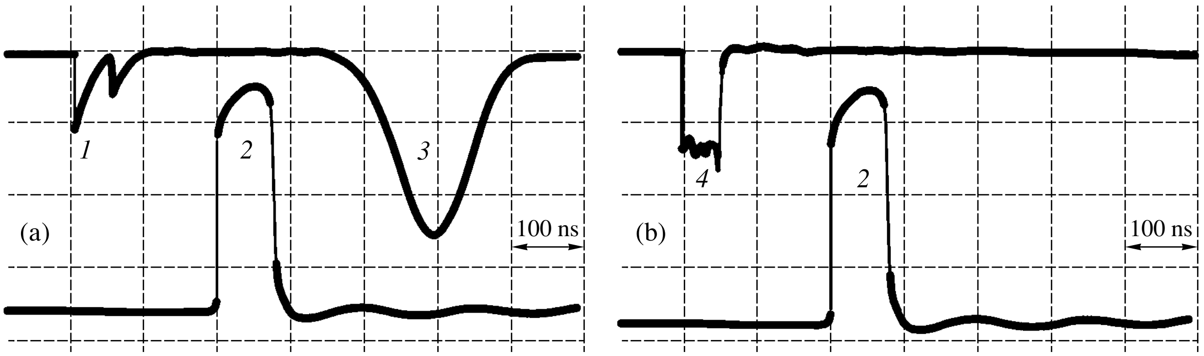

Fig. 2. Oscillograms of pulses in the signal channel (upper beam) and pumping channel (lower beam); one division on the horizontal axis corresponds to 100 ns. (a) Ferromagnetic resonance at the signal frequency: $\omega_0 = \omega_s$; $H_0 = 1650$ Oe. (b) Strong detuning of the signal frequency from the ferromagnetic resonance frequency: $|\omega_0 - \omega_s| \gg \gamma\Delta H$, $H_0 = 2000$ Oe; *1* and *4* are pulses reflected from the loop coupler with ferrite in ferromagnetic resonance and away from it, respectively; *2*—incident pumping pulse; *3*—output pulse emitted by the ferrite sphere as a result of two-magnon relaxation reversal. The sample is a YIG sphere (of diameter 1.05 mm; ΔH = 0.5 Oe) magnetized along the intermediate axis; t_p = 200 ns.

ure 2a corresponds to resonance tuning of uniform precession frequency ω_0 to the signal frequency, $\omega_0 = \omega_s$. In this case, the power of the signal is partly absorbed in the ferrite sphere due to excitation of uniform precession followed by the excitation of dipole–exchange spin waves. As a result (and also due to the effect of transient processes), the shape of the signal pulse reflected from the loop coupler (see pulse *1* in Fig. 2a) differs from the rectangular shape of the signal incident on this loop. After the termination of the signal pulse, the power absorbed by the sample was accumulated in the system of dipole–exchange spin waves, on which pump pulse *2* began to act at instant $t = t_p$. Pumping led to phase conjugation of spin waves and to restoration of oscillations of uniform precession, which induced output signal *3* in the loop coupler at instant $t \approx 2t_p$.

In the other, nonresonant case ($\omega_0 \neq \omega_s$), power absorption in ferrite decreases, causing a decrease in the output signal amplitude, while the power reflected from the loop coupler increases. The oscillogram in Fig. 2b corresponds to strong detuning from resonance: $|\omega - \omega_0| \gg \gamma\Delta H$. In this case, the output pulse vanishes, while pulse *4* reflected from the loop coupler restores its rectangular shape and becomes equal to the input signal pulse incident on the ferrite sample. Thus, under the action of parallel pumping, reversal coefficient *K* for two-magnon relaxation (see formula (11)) could be determined experimentally as the ratio of the output signal amplitude (see pulse *3* in Fig. 2a) to the reflected pulse amplitude (pulse *4* in Fig. 2b) for strong detuning of the constant magnetic field from the ferromagnetic resonance.

The experimental dependence of reversal coefficient *K* of two-magnon relaxation on the crystallographic orientation of the YIG sphere is shown in Fig. 3. In general, this dependence matches the above theory (see formula (12)): the peak is observed for magnetization of the sphere along the intermediate axis [110], and the minima coincide with the magnetic field direction along the easy [111] and hard [001] axes. For convenience of comparison of experimental (squares) and theoretical (solid curve) dependences of the reversal coefficient on the crystallographic orientation, the theoretical curve in Fig. 3 is normalized to the experimental values obtained for $\theta_H = 90°$; the absolute value of reversal coefficient *K* determined by theoretical dependence (12) will be considered later. The discrepancy between the theory and experiment observed in Fig. 3

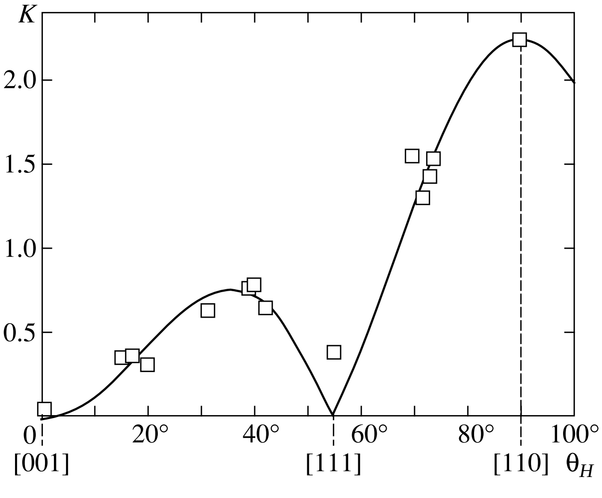

Fig. 3. Dependence of two-magnon relaxation reversal coefficient *K* on angle θ_H between the direction of the constant external magnetic field $\mathbf{H}_0$ and the crystallographic [001] axis in the $(1\bar{1}0)$ plane. The sample is a YIG sphere of diameter 1.05 mm; ΔH = 0.5 Oe. Squares correspond to experiment for t_p = 180 ns, P_p = 6 W; the solid curve describes theoretical dependence (12) normalized to experimental values for $\theta_H = 90°$. The positions of the hard [001], easy [111], and intermediate [110] crystallographic axes are indicated on the abscissa axis.

(especially for $\mathbf{H}_0 \parallel [001]$ and $\mathbf{H}_0 \parallel [111]$; in this case, $K = 0$ according to the theory, the entire experiment gives a finite value of K) can be explained by the approximate nature of the theory (in particular, disregard of the second crystallographic anisotropy constant, magnetoelastic energy, etc.). The error in determining the crystallographic orientation of the sample also plays a certain role. We used a simple method of magnetic orientation [6] whose accuracy was ±3°. Finally, contribution to the output pulse amplitude may also come from processes associated with excitation by the input electromagnetic pulse of not only uniform precession, but also of the entire set of long-wave magnetostatic oscillations whose amplitude may differ from zero in view of nonuniformity of the magnetic fields. These processes can be responsible for experimentally observed ferromagnetic echo [7]. In spite of the fact that a ferromagnetic echo was detected for transverse pumping at a frequency equal to the signal frequency, its presence for parallel pumping at double the frequency also cannot be ruled out in principle, although this problem requires detailed studies. However, in spite of the fact that the contribution of ferrite echo in our experiments with small ferrite spheres must undoubtedly be small in view of uniformity of the constant external magnetic field. It should be recalled that enhanced echo was obtained in [7] only for large samples of an irregular geometrical shape with a specially produced nonuniformity of the internal constant magnetic field.

The results presented in Fig. 3 were obtained for a high-quality YIG sphere with the total width of the ferromagnetic resonance line

$$\Delta H = \Delta H_0 + \delta H_0 = 2(\Gamma_0 + \delta\Gamma_0)/\gamma$$

equal to 0.5 Oe (at a signal frequency of 4.7 GHz). To reduce the contribution from surface nonuniformities and the linewidth ΔH, the sphere was thoroughly polished with an abrasive paste with a grain size of less than 1 μm. In this case, the two-magnon relaxation frequency $\delta\Gamma_0$ and contribution δH_0 to the linewidth associated with it were mainly determined by bulk nonuniformities such as nonmagnetic inclusions, dislocations, and vacancies. In contrast to natural relaxation frequency Γ_0 (and natural linewidth $\Delta H_0 = 2\Gamma_0/\gamma$), which is a parameter of the material, two-magnon relaxation frequency $\delta\Gamma_0$ and the corresponding two-magnon linewidth $\delta H_0 = 2\delta\Gamma_0/\gamma$ are parameters of the sample, which can easily be changed, for example, by introducing additional nonuniformities on the surface of the sphere by polishing with a coarse abrasive paste. The total linewidth $\Delta H = \Delta H_0 + \delta H_0$ of the sample, which can easily be measured in experiments, will change in this case due to an increase in the value of $\delta\Gamma_0 = \gamma\delta H_0/2$. To analyze the effect of the sample surface on reversal coefficient K of two-magnon relaxation, the ferrite sphere was polished twice for a short time using an abrasive paste with a grain size of 10 μm. As a result of polishing, ferromagnetic resonance linewidth ΔH was gradually increased from 0.5 to 0.6 Oe and then to 0.7 Oe. The dependence of two-magnon relaxation reversal coefficient K on the orientation of constant magnetic field $\mathbf{H}_0$ remained unchanged in this case and was analogous to the dependence shown in Fig. 3. However, the absolute value of K increased thereby, which is completely in accordance with the above theory. The value of K increased on the average by a factor of 1.6 as compared to that for a polished sample with $\Delta H = 0.5$ Oe for $\Delta H = 0.6$ Oe and by a factor of 1.9 for $\Delta H = 0.7$ Oe. In accordance with formula (12), the observed increase in coefficient K is associated with an increase in the first term in expression (12),

$$\frac{\delta\Gamma_0}{\Gamma} = \frac{\Delta H - \Delta H_0}{\Delta H} = \frac{\delta H_0}{\Delta H}, \tag{13}$$

where, as noted earlier, ΔH is the total and ΔH_0 is the natural ferromagnetic resonance linewidth, associated with natural relaxation processes and δH_0 is the ferromagnetic resonance linewidth associated with two-magnon scattering processes. The value ΔH appearing in formula (13) is measured experimentally. It also follows from the above results that linewidth $\delta H_0 = \Delta H - \Delta H_0$ responsible for two-magnon scattering increases by 0.1 Oe after each polishing. Comparing the above experimental results on variation of K as a result of polishing with formula (13), we can also approximately estimate the values of other relaxation parameters of the sample and find the corresponding linewidths. To match the theory with experiment, we must assume that the natural linewidth of the ferromagnetic resonance for the ferromagnetic sphere studied here is $\Delta H_0 = 0.35$ Oe, while the two-magnon linewidth associated with the contribution from bulk nonuniformities only is 0.15 Oe. The additional contribution from surface nonuniformities due to polishing gradually increased the two-magnon linewidth to 0.25 and 0.35 Oe. The experimentally obtained results do not contradict the ferromagnetic relaxation theory. For example, for the natural ferromagnetic resonance linewidth of YIG single crystals associated with natural relaxation processes, the theoretical value of ΔH_0 lies in the interval 0.1–0.5 Oe [8, 9].

Figure 4 shows the experimental dependence of the two-magnon relaxation reversal coefficient on time t_p of switching on of the pump pulse. The time of emergence of the restored output pulse in this case is $2t_p$ within the experimental error. In accordance with theoretical dependence (12), curve $K(t_p)$ in Fig. 4 is close to exponential. From the slope of this curve (61 dB/μs), we can determine parameter ΔH_k of relaxation of waves excited as a result of scattering of uniform precession oscillations from nonuniformities: $\Delta H_k = 0.4$ Oe. The results presented in Fig. 4 correspond to a twice-polished YIG sphere.

It was found that polishing of the surface affects the value of ΔH_k noticeably less strongly that the value of ΔH_0; the value of ΔH_k for an unpolished sphere was 0.37 Oe; i.e., the change in ΔH_k as a result of polishing was only 8% against 40% for ΔH. This result is not unexpected since polishing affects only a small number of dipole–exchange spin waves excited near the surface in view of a small mean free path [10]. The values of ΔH_k obtained here are more than twice as high as the minimal value of the linewidth for spin waves excited by the parallel pumping method [1]. As a matter of fact, the value of constant magnetic field H_0 in our experiments corresponded to the condition for the emergence of ferromagnetic resonance at the signal frequency and was approximately 80 Oe higher than the field H_c corresponding to the minimum of the parallel pumping threshold [1]. The maximal polar angle θ_k of the spin waves degenerate with uniform precession did not exceed $\theta_k \approx 65°$. According to [11], the relaxation parameter for such waves is approximately twice as large as that for spin waves with $\theta_k = 90°$, which are excited for $H_0 = H_c$.

Finally, let us estimate the absolute values of two-magnon relaxation reversal coefficients K, which follow from theoretical dependence (12) and compare these values with experimental results. The most complicated problem here is to determine the amplitude h_p of the pumping field in the resonator, which acts on the ferrite sphere. In view of the exponential dependence $K(h_p)$, even a small error in determining the value of the pumping field leads to a substantial spread in values of K. It should be noted that the second exponential factor in formula (12) can easily be determined from experiment (see Fig. 4).

It is impossible at present to calculate field h_p in the resonator from the value of power P_p incident on it in view of the absence of an electrodynamic theory of an open dielectric resonator of rectangular shape with a central cylindrical hole for accommodation of the ferrite sphere. To determine the pumping field amplitude h_p experimentally, we used the calibrated sample method with a preset value of parametric instability threshold field h_c for parallel pumping [12]. The value of h_c was determined with the help of a rectangular cavity, for which the values of ac magnetic fields can easily be determined from the incident power, Q factor, and size of the resonator [13]. The calibrated sample was placed into a dielectric resonator for which the relation between h_p and the incident power was determined experimentally from the observation of the parallel pumping threshold. The maximal amplitude h_p of the ac magnetic field acting on the sample in our measurements was 20 ± 3 Oe.

Substituting the results into formula (12), we can obtain the theoretically expected value of two-magnon relaxation reversal coefficient K. For example, for the situation depicted in Fig. 3, the theory gives values of K varying from 0.5 to 3.0, which does not contradict the experimental value of $K = 2.2$. Thus, in spite of their approximate nature, the theoretical relations derived here provide a correct qualitative and quantitative description of reversal of two-magnon relaxation in ferrite spheres.

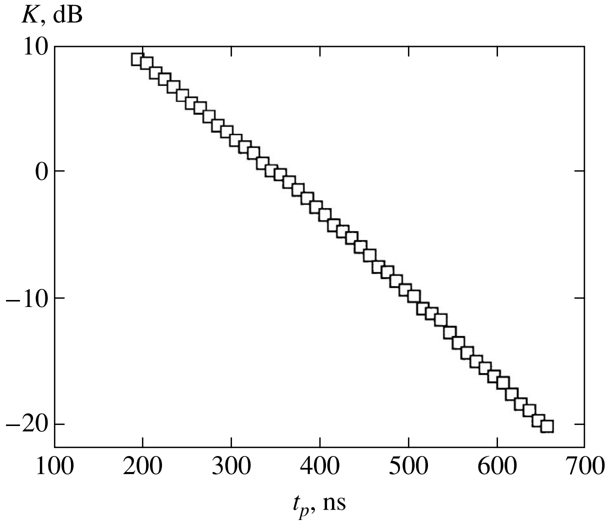

Fig. 4. Dependence of two-magnon relaxation reversal coefficient K on time t_p of switching on of the pump pulse. The sample is a polished YIG sphere of diameter 1.05 mm; $\Delta H = 0.7$ Oe; $P_p = 6$ W.

4. CONCLUSIONS

We have studied the reversal of two-magnon relaxation of uniform precession of magnetization in a YIG ferrite sphere using the method of longitudinal parametric pumping with a frequency twice as high as the uniform precession frequency. As a result of pumping, uniform precession oscillations are restored; the maximal amplitude of restored oscillations could exceed the initial amplitude of uniform precession excited by an external electromagnetic field by a factor of $K > 1$. The theoretical expression for reversal coefficient K of two-magnon relaxation was determined from the system of two coupled equations of uniform precession and short-wave dipole–exchange spin waves excited as a result of scattering of uniform precession oscillations from nonuniformities. In the case of a YIG sphere with cubic crystallographic anisotropy, reversal coefficient K has the maximal value when the magnetization of the crystal coincides with the intermediate axis [110], while $K = 0$ for magnetization along the hard [001] and easy [111] axes. The maximal value of K is attained by choosing an optimal value for the probability of two-magnon scattering of uniform precession with the formation of dipole–exchange spin waves; two-magnon broadening of the natural ferromagnetic resonance line for this value is nearly equal to the width of this line. For stronger scattering, the value of K decreases exponentially due to an increase in the damping parameter of dipole–exchange spin waves, while $K = 0$ in the absence of scattering. The reversal coefficient increases exponentially with the pumping amplitude and duration and decreases exponentially with increasing the delay time of the pumping pulse switching on.

Experimental studies of two-magnon relaxation reversal was carried out on small monocrystalline YIG spheres of diameters 0.65–1.05 mm for a pumping frequency $\omega_p/2\pi \approx 9.4$ GHz. The main conclusions of the theory were confirmed by experiment. In particular, the maximal value of two-magnon relaxation reversal coefficient was observed for spheres magnetized along the intermediate axis. For magnetization along the hard and easy axis, the value of K was minimal, though not equal to zero.

In accordance with the theory, reversal coefficient K increased upon a variation of the efficiency of two-magnon scattering by polishing the spherical surface with a coarse abrasive paste. A comparison of theory with experiment led to the values of the natural ferromagnetic resonance linewidth and the linewidth associated with two-magnon scattering at bulk nonuniformities. These values were found to be 0.35 and 0.15 Oe, respectively. The relaxation parameters ΔH_k of dipole–exchange spin waves were measured from the slope of the curve depicting the dependence of the reversal coefficient K on the delay time.

The experimentally measured value of reversal coefficient K was found to match the theory to within the experimental error. For small delay times, the two-magnon relaxation reversal is accompanied by amplification; i.e., $K > 1$. For a YIG sphere with a diameter of 1.05 mm, a value of $K \approx 5$ was attained for $t_p = 180$ ns. The maximal delay time for the restored signal was about 2 μs.

Two-magnon relaxation of uniform precession of magnetization in YIG ferrite spheres caused by longitudinal parametric pumping studied here can be used for processing microwave information and for measuring "latent" relaxation times, e.g., the natural linewidth of ferromagnetic resonance and the linewidth associated with two-magnon scattering from bulk nonuniformities. In addition, the relaxation reversal effect can be used for directly measuring the dipole–exchange spin-wave relaxation times. The knowledge of these relaxation times is especially important now for developing nanosize magnetic memory elements whose natural excitations are dipole–exchange spin waves.

REFERENCES

1. A. G. Gurevich and G. A. Melkov, *Magnetic Oscillations and Waves* (Nauka, Moscow, 1994) [in Russian].
2. B. Ya. Zel'dovich, N. F. Pilipetskiĭ, and V. V. Shkunov, *Wave Front Reversal* (Nauka, Moscow, 1985) [in Russian].
3. G. A. Melkov, Yu. V. Kobljanskyj, A. A. Serga, *et al.*, Phys. Rev. Lett. **86**, 4918 (2001).
4. V. S. L'vov, *Nonlinear Spin Waves* (Nauka, Moscow, 1987) [in Russian].
5. E. Schlomann, J. J. Green, and U. Milano, J. Appl. Phys. **31**, 3865 (1966).
6. Y. Sato and P. S. Carter, IRE Trans. Microwave Theory Tech. **10**, 611 (1962).
7. D. E. Kaplan, R. M. Hill, and G. F. Herrmann, J. Appl. Phys. **40**, 1164 (1969).
8. M. Sparks, *Ferromagnetic Relaxation Theory* (McGraw-Hill, New York, 1964).
9. V. Cherepanov, I. Kolokolov, and V. L'vov, Phys. Rep. **229**, 81 (1993).
10. G. A. Melkov, Zh. Éksp. Teor. Fiz. **70**, 1324 (1976) [Sov. Phys. JETP **43**, 690 (1976)].
11. Yu. M. Yakovlev and S. Sh. Gendelev, *Ferrite Monocrystals in Radioelectronics* (Sovetskoe Radio, Moscow, 1975) [in Russian].
12. G. A. Melkov, Radiotekh. Élektron. (Moscow) **17**, 2027 (1972).
13. Ya. A. Monosov, *Nonlinear Ferromagnetic Resonance* (Nauka, Moscow, 1971) [in Russian].

Translated by N. Wadhwa

Journal of Experimental and Theoretical Physics, Vol. 99, No. 6, 2004, pp. 1201–1206.
Translated from Zhurnal Éksperimental'noĭ i Teoreticheskoĭ Fiziki, Vol. 126, No. 6, 2004, pp. 1377–1383.
Original Russian Text Copyright © 2004 by Murtazaev, Kamilov, Babaev.

Critical Behavior of a Cubic-Lattice 3D Ising Model for Systems with Quenched Disorder

A. K. Murtazaev*, I. K. Kamilov, and A. B. Babaev
Institute of Physics, Dagestan Scientific Center, Russian Academy of Sciences, Makhachkala, 367003 Russia
**e-mail: m_akai@iwt.ru*

Received May 31, 2004

Abstract—A Monte Carlo method is applied to simulate the static critical behavior of a cubic-lattice 3D Ising model for systems with quenched disorder. Numerical results are presented for the spin concentrations of p = 1.0, 0.95, 0.9, 0.8, 0.6 on $L \times L \times L$ lattices with L = 20–60 under periodic boundary conditions. The critical temperature is determined by the Binder cumulant method. A finite-size scaling technique is used to calculate the static critical exponents α, β, γ, and ν (for specific heat, susceptibility, magnetization, and correlation length, respectively) in the range of p under study. Universality classes of critical behavior are discussed for three-dimensional diluted systems. *© 2004 MAIK "Nauka/Interperiodica".*

1. INTRODUCTION

Analysis of the critical behavior of diluted spin systems with quenched disorder is a topical problem in condensed matter physics. Systems of this kind have been the subject of intensive experimental [1–3], theoretical [4–13], and computational [14–21] studies. The Harris criterion formulated in the framework of renormalized perturbation theory can be used to obtain qualitative predictions of the effects of particular impurities on critical behavior [4]. According to this criterion, weak disorder modifies critical behavior only if the specific-heat critical exponent is positive ($\alpha > 0$), i.e., if specific heat is divergent at the critical point. Conversely, if $\alpha < 0$ (specific heat is finite at the transition point), then weak disorder does not change the critical behavior. This criterion holds only for systems described by effective Hamiltonians that are isomorphic to the Ising model near the corresponding critical points.

Modified critical exponents have been reliably determined for disordered 3D Ising models both in experiments [1–3] and in theoretical studies [4–13]. Even though they agree with the entire body of available evidence, it remains unclear if the modified critical exponents are universal, i.e., whether they are independent of the impurity concentration below the percolation threshold or vary continuously with the concentration along a line of fixed points. Moreover, there are good reasons to expect that the critical exponents depend on the realization of disorder in a particular model. It was found in [19] that the results obtained when disorder was realized in a canonical ensemble (by fixing the fraction of magnetic sites) would be different from those of grand canonical Monte Carlo simulations (when the fraction of magnetic sites in each particular impurity configuration is a fluctuating variable). In the nearest future, accurate analysis of these trends can only be performed by numerical methods.

The renormalization-group analysis using an ε-expansion [8] showed that the critical behavior of the 3D Ising model for systems with quenched disorder is characterized by critical exponents that are different from those corresponding to the pure Ising model. However, the asymptotic convergence of the ε-expansion series is even slower than for pure systems, and predictions obtained by the ε-expansion method are not reliable [6, 14].

Current experimental studies are impeded by the difficulties encountered in calculating the critical exponents and determining the universality class of static behavior for such systems [2, 3]. The results available from current experiments cannot be used to develop a complete and self-consistent model of critical behavior of impure systems. This is explained by strong dependence of experimental results not only on the sample and the method employed, but also on the procedure used to prepare the sample (see references in [13]). Furthermore, no experimental studies have been conducted in which the same method is applied to samples of the same type containing well-controlled amounts of impurities. For this reason, phase transitions and critical phenomena in diluted systems are the subject of intensive current studies performed by different versions of the Monte Carlo (MC) method, including powerful cluster algorithms [14, 15, 17–21]. To date, cluster MC algorithms were mainly applied to dilute systems modeled by grand canonical ensembles. Systems represented as canonical ensembles have been studied to a much lesser extent.

In this paper, we report the results of MC simulations of the static critical behavior of the cubic-lattice Ising model performed for systems with quenched dis-

1063-7761/04/9906-1201$26.00 © 2004 MAIK "Nauka/Interperiodica"

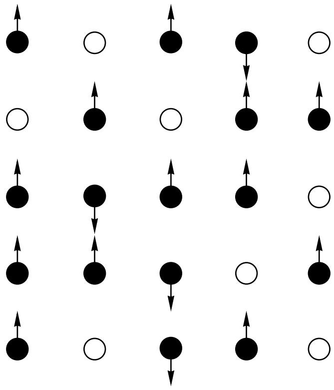

Fig. 1. Weakly diluted 3D Ising model with quenched disorder.

order. The enormous interest in this model is motivated by the following principal reasons.

First, the weakly diluted 3D Ising model for systems with quenched disorder is of great practical importance, because it provides a basis for analyzing disorder-induced macroscopic effects, which are commonly found in real materials.

Second, studies of effects of quenched disorder on universal characteristics of critical behavior are of fundamental, as well as of practical, importance [5].

Third, the first attempts to analyze this model numerically were made at the time when the available computing resources and MC algorithms were insufficient to calculate critical exponents to the required accuracy.

2. ISING MODEL FOR SYSTEMS WITH QUENCHED DISORDER

The weakly diluted 3D Ising model for systems with quenched disorder is schematized in Fig. 1. In the model examined here, the impurity distribution is simulated by means of a canonical ensemble. The model relies on the following assumptions.

1. The sites of a cubic lattice are occupied either by spins $S_i = \pm 1$ or by nonmagnetic impurities. The nonmagnetic impurities are randomly distributed and bound to the corresponding lattice sites.

2. The nearest-neighbor coupling energy is $|J|$ if both sites are occupied by magnetic atoms and zero otherwise.

The corresponding microscopic Hamiltonian is

$$H = -\frac{J}{2}\sum_{i,j}\rho_i S_i \rho_j S_j, \tag{1}$$

where

$$\rho_i = \begin{cases} 1, & \text{if the site is occupied by a spin,} \\ 0, & \text{otherwise.} \end{cases}$$

The spin concentration is the sum of the absolute values of spin at all sites:

$$p = \frac{1}{L^3}\sum_{i=1}^{L^3}\rho_i|S_i|. \tag{2}$$

The cases of $p = 1$ and $p = 0$ correspond to the pure Ising model and the lattice of impurities, respectively.

3. SIMULATION METHOD

Cluster MC algorithms [22, 23] are very effective tools for analyzing critical phenomena in various systems and models [19–21, 24, 25]. The critical exponents based on the results obtained by means of cluster algorithms are highly accurate and reliable [21, 24, 25]. The most effective cluster MC algorithm was proposed by Wolff [22]. Its version employed in the present study consists of the following procedures:

I. The coordinates of a lattice site are taken by generating three random numbers. If the site is occupied by a nonmagnetic impurity, then new random numbers are generated until the coordinates of a spin S_i are obtained.

II. The nearest neighbor sites of S_i are inspected. If a neighbor S_j is occupied by a spin S_j and the values of S_i and S_j are equal for $J > 0$, then the coupling between S_i and S_j is assigned the probability $P = 1 - \exp(-2K)$ with $K = J/k_BT$, where k_B is Boltzmann's constant. Then, the nearest neighbors of S_j are inspected in a similar manner. The process is continued until the boundaries of the system are reached.

III. A cluster is defined as the set of coupled spins.

IV. The cluster is flipped with a probability of one.

Computations were performed under periodic boundary conditions on $L \times L \times L$ lattices with L varied from 20 to 60 for the spin concentrations $p = 1.0$, 0.95, 0.9, 0.8, and 0.6.

In the starting distributions, all spins were parallel to the z axis. In the case of $p = 1.0$, the equilibrium state of the system was obtained by discarding the results of the first 2×10^6 Monte Carlo steps (here, each MC step corresponds to one cluster flip) and averaging the remaining results over five starting distributions. For systems with $p = 0.95$, 0.9, 0.8, and 0.6, the number of discarded Monte Carlo steps was 3×10^6, 4×10^6, 5×10^6, and 6×10^6, respectively, and the results were averaged over 20 to 80 different distributions. We should note here that the number of disorder realizations used to calculate thermodynamic characteristics must increase with decreasing spin concentration to compensate for increasing fluctuations in the impurity distribution.

Note also that the complexity of the computations performed for each impurity distribution rapidly increases with lattice size.

4. RESULTS

The temperature-dependent specific heat and susceptibility of fluctuating systems were calculated as follows [26]:

$$C = (NK^2)(\langle U^2\rangle - \langle U\rangle^2), \tag{3}$$

$$\chi = (NK)(\langle m^2\rangle - \langle m\rangle^2), \tag{4}$$

where $K = |J|/k_B T$, $N = pL^3$ is the number of magnetic sites, U is internal energy, m is magnetization, and angle brackets denote a thermal average.

Figures 2 and 3 show the temperature-dependent specific heat C and susceptibility χ obtained for $p = 1.0$, 0.95, 0.9, 0.8, and 0.6. The errors of the results presented from here on do not exceed the size of symbols in the corresponding figures. Figure 2 demonstrates that the peak in the specific heat is smeared, and the peak value is reduced, by increasing the nonmagnetic-impurity fraction $c = 1 - p$. This behavior is characteristic of diluted 3D Ising spin systems [16, 17]. Note also that the critical behavior of susceptibility is characterized by sharp peaks at each p (see Fig. 3).

The critical temperature $T_c(p)$ was determined by the Binder cumulant method [27], with the fourth-order cumulant U_L defined as

$$U_L(T, p) = 1 - \frac{\langle m^4(T, p; L)\rangle}{3\langle m^2(T, p; L)\rangle_L^2}, \tag{5}$$

where m is the magnetization for a system on the lattice of size L. To calculate T_c, we found the temperature dependence of the cumulant $U_L(T, p)$ obtained by averaging over disorder realizations for $L_1, L_2, \ldots, L_n$. The critical point T_c was defined as the temperature at which $U_{L_1}(T_c, p) = U_{L_2}(T_c, p) = \ldots = U_{L_n}(T_c, p)$. The calculated critical temperatures are listed in the table. Figure 4 illustrates the temperature dependence of the Binder cumulant $U_L(T, p)$ for systems of different size with $p = 0.8$. The point of intersection of the curves corresponds to $T_c = 3.4956(6)$.

According to Fig. 3, the susceptibility peaks for systems with different values of p correspond to the values of $T_c(p)$ determined by the Binder cumulant method up to a numerical error. This demonstrates the high reliability of our calculations of the critical temperature.

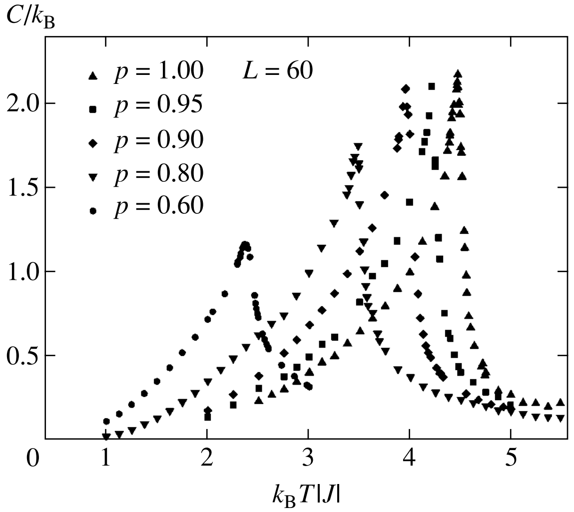

Fig. 2. Specific heat versus temperature for diluted 3D Ising model.

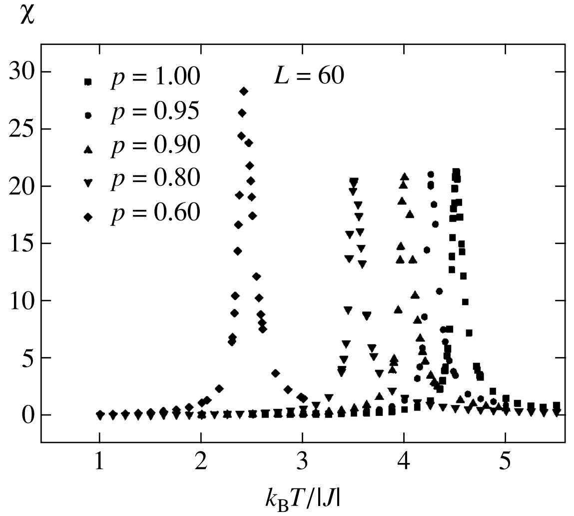

Fig. 3. Susceptibility versus temperature for diluted 3D Ising model.

The static critical exponents α (specific heat), γ (susceptibility), and β (magnetization) were determined by applying the following finite-size scaling ansatz

Critical exponents in weakly diluted 3D Ising model for systems with quenched disorder calculated by using a finite-size scaling technique

p	$k_B T_c/\lvert J\rvert$	ν	α	γ	β
1.00	4.5106(6)	0.624(2)	0.108(2)	1.236(2)	0.322(2)
0.95	4.2591(4)	0.646(2)	–0.010(2)	1.262(2)	0.306(3)
0.90	4.0079(8)	0.664(3)	–0.014(3)	1.285(3)	0.308(3)
0.80	3.4956(6)	0.683(4)	–0.016(3)	1.299(3)	0.310(3)
0.60	2.4173(9)	0.725(6)	–0.093(7)	1.446(4)	0.349(4)

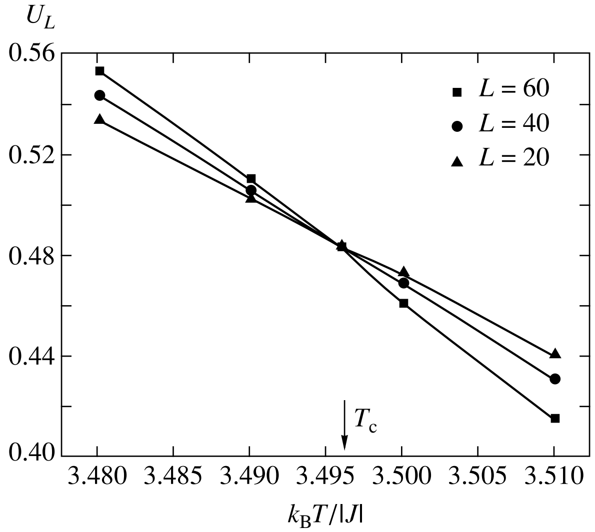

Fig. 4. Cumulant U_L averaged over impurity distributions with different disorder realizations versus temperature for $p = 0.8$.

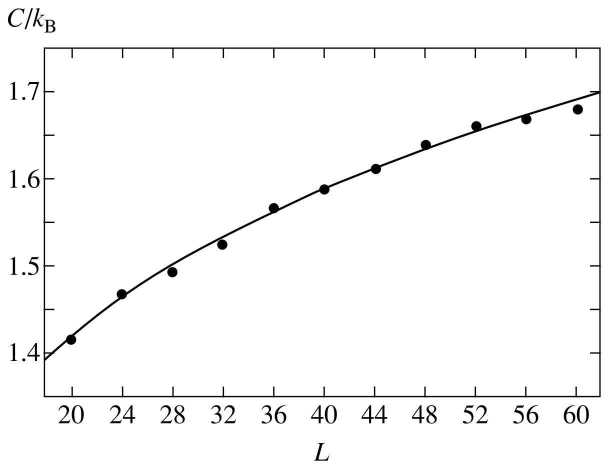

Fig. 5. Specific heat versus lattice size for $p = 0.8$.

proposed for systems with periodic boundary conditions [28]:

$$F(T, L) \propto L^{-d}F_0(tL^{1/\nu}), \tag{6}$$

where $t = |T - T_c|/T_c$, $T_c = T_c(L = \infty)$, and ν is the static correlation-length critical exponent for $L = \infty$. Equation (6) entails analogous equations for specific heat, susceptibility, and spontaneous magnetization per spin:

$$C(T, L) \propto L^{\alpha/\nu}C_0(tL^{1/\nu}), \tag{7}$$

$$\chi(T, L) \propto L^{\gamma/\nu}\chi_0(tL^{1/\nu}), \tag{8}$$

$$m(T, L) \propto L^{-\beta/\nu}m_0(tL^{1/\nu}), \tag{9}$$

where the critical exponents α, γ, and β corresponding to $L = \infty$ satisfy the hyperscaling relation $2 - \alpha = d\nu = 2\beta + \gamma$ [29].

In modern theories, an alternative finite-scaling ansatz is proposed for evaluating ν [30, 31]:

$$V_n = L^{1/\nu}g_{V_n}, \tag{10}$$

where g_{V_n} is a constant parameter, and V_n is defined as

$$V_i = \frac{\langle m^iE\rangle}{\langle m^i\rangle} - \langle E\rangle \quad (i = 1, 2), \tag{11}$$

$$V_3 = \frac{dU_L}{d\beta} = \frac{1}{3\langle m^2\rangle^2} \times\left[\langle m^4\rangle\langle E\rangle - 2\frac{\langle m^4\rangle\langle m^2E\rangle}{\langle m^2\rangle^2} + \langle m^4E\rangle\right], \tag{12}$$

with $\beta = 1/T$.

According to (8) and (9), the susceptibility and magnetization for a sufficiently large $L \times L \times L$ lattice at $T = T_c$ are

$$\chi \propto L^{\gamma/\nu}, \tag{13}$$

$$m \propto L^{-\beta/\nu}. \tag{14}$$

We used these expressions to evaluate γ and β. The corresponding expression for specific heat disagrees with experimental results, as demonstrated in [24]. The temperature-dependent specific heat as a function of L is commonly approximated by different expressions, for example (see [19, 26]),

$$C_{\max}(L) = C_{\max}(L = \infty) - AL^{\alpha/\nu}, \tag{15}$$

where A is a constant factor.

To evaluate α, β, γ, and ν, we calculated C, m, χ, and V_n as functions of L. A nonlinear least-squares regression analysis was performed to determine α/ν, β/ν, γ/ν, and 1/ν. Then, the values of ν obtained in this study were used to find α, β, and γ. It should be noted that the present approach is different from that used in numerous studies where these critical exponents were determined by invoking various scaling relations. Figures 5 and 6 show log–log plots of C and χ versus L for $p = 0.8$. According to Fig. 6, the calculated susceptibility values do not deviate from a line even at small L. Similar results were obtained in [19]. The attainment of asymptotic critical behavior is frequently questioned when systems of the kind considered here are simulated. Apparently, both the number of impurity distributions used here to calculate average quantities and the

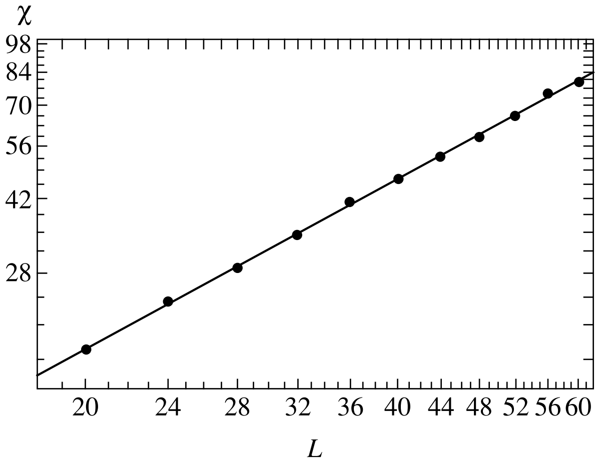

Fig. 6. Susceptibility versus lattice size for $p = 0.8$.

lattice size ($L \geq 20$) were sufficiently large to ensure that the asymptotic critical behavior of susceptibility was attained for $p = 0.8$, as well as in other cases examined in this study.

As noted above, expression (15) is used instead of (7) in actual data processing. Figure 5 demonstrates that the log–log plot of $C(L)$ for $p = 0.8$ is not a line.

The critical exponents listed in the table were obtained for several values of p by using the corresponding $\nu(p)$ and Wolff's single-cluster MC algorithm. Their values differ from those corresponding to the pure Ising model. The weak dependence of the critical exponents on the impurity concentration revealed for weakly diluted systems (with $p \geq 0.8$) can be attributed to a crossover from pure to dilute critical behavior. Note that the sign of α changes in the neighborhood of $p = 0.95$, and its value is equal to the theoretical result obtained in [7] up to a numerical error.

The absolute values of the critical exponents obtained for the highly diluted system ($p = 0.6$) are substantially larger. This can be explained by the existence of an additional random fixed point (which is difficult to find in numerical simulations), because the critical behavior near such a point must be characterized by different values of the scaling exponents. Experimental evidence supporting this conjecture can be found in [2], where critical exponents similar to those obtained here for $p = 0.6$ were reported for the diluted Ising antiferromagnet $\mathrm{Fe}_p\mathrm{Zn}_{1-p}\mathrm{F}_2$ with $p = 0.6$ and 0.5.

The critical behavior observed for $p = 0.6$ in this study is consistent with the influence of an additional ("percolation") fixed point hypothesized in [14, 18]. Note also that the values of α, γ, and β obtained here for $p = 1.0$ are in excellent agreement with $\alpha = 0.109(4)$, $\gamma = 1.2396(13)$, and $\beta = 0.3258(14)$ obtained in [12] by resumming the perturbation series in the scalar φ^4 theory with $d = 3$ in the absence of disordered structure.

5. CONCLUSIONS

The systematic analysis of a weakly diluted 3D Ising model with canonical disorder performed in this study by using the same technique demonstrates that

(i) the critical exponents obtained for low impurity concentrations ($p \geq 0.8$) differ from those in the pure Ising model ($p = 1.0$) and characterize a distinct universality class;

(ii) highly diluted systems ($p \leq 0.6$) are characterized by specific values of the critical exponents corresponding to yet another universality class.

Therefore, the model must exhibit two crossovers: one between the pure ($p = 1.0$) and weakly diluted ($p \geq 0.8$) systems and the other between the weakly ($p \approx 0.8$) and highly ($p \leq 0.6$) diluted systems. The controversial and mutually inconsistent of most results obtained for the model in question may be explained by the existence and substantial width of such crossover regions.

ACKNOWLEDGMENTS

This work was supported by the Russian Foundation for Basic Research, project no. 04-02-16487; under the State Program for Support of Leading Science Schools, grant 2253.2003.2; under the Federal Program "Integratsiya," grant I0228; and by the Foundation for Support of Domestic Science (A.K. Murtazaev).

REFERENCES

1. P. W. Mitchell, R. A. Cowley, H. Yoshizawa, *et al.*, Phys. Rev. B **34**, 4719 (1986).
2. R. J. Birgeneau, R. A. Cowley, G. Shirane, *et al.*, Phys. Rev. B **27**, 6747 (1983).
3. J. Yoon and M. H. Chan, Phys. Rev. Lett. **78**, 4801 (1997).
4. A. B. Harris, J. Phys. C **7**, 1671 (1974).
5. V. S. Dotsenko, Usp. Fiz. Nauk **165**, 481 (1995) [Phys. Usp. **38**, 457 (1995)].
6. V. V. Prudnikov, P. V. Prudnikov, and A. A. Fedorenko, Fiz. Tverd. Tela (St. Petersburg) **43**, 1688 (2001) [Phys. Solid State **43**, 1759 (2001)].
7. I. O. Maĭer and A. I. Sokolov, Fiz. Tverd. Tela (Leningrad) **26**, 3454 (1984) [Sov. Phys. Solid State **26**, 2076 (1984)].
8. D. E. Khmel'nitskiĭ, Zh. Éksp. Teor. Fiz. **68**, 1960 (1975) [Sov. Phys. JETP **41**, 981 (1975)].
9. Yu. Holovatch and T. Yavors'kii, J. Stat. Phys. **92**, 785 (1998).
10. A. I. Sokolov and B. N. Shalaev, Fiz. Tverd. Tela (Leningrad) **23**, 2058 (1981) [Sov. Phys. Solid State **23**, 1200 (1981)].
11. B. N. Shalaev, Phys. Rep. **237**, 129 (1994).
12. R. Guida and J. Zinn-Justin, J. Phys. A **31**, 8103 (1998).
13. R. Folk, Yu. Holovatch, and T. Yavorskiĭ, Usp. Fiz. Nauk **173**, 175 (2003) [Phys. Usp. **46**, 169 (2003)].

14. V. V. Prudnikov and A. N. Vakilov, Zh. Éksp. Teor. Fiz. **103**, 962 (1993) [JETP **76**, 469 (1993)].
15. K. Hukushima, J. Phys. Soc. Jpn. **69**, 631 (2000).
16. S. S. Aplesnin, Fiz. Tverd. Tela (Leningrad) **26**, 3355 (1984) [Sov. Phys. Solid State **26**, 2016 (1984)].
17. H.-O. Heuer, Phys. Rev. B **42**, 6476 (1990).
18. H.-O. Heuer, J. Phys. A **22**, L333 (1993).
19. S. Wiseman and E. Domany, Phys. Rev. E **58**, 2938 (1998).
20. H. G. Ballesteros, L. A. Fernandez, V. Martin-Mayor, *et al.*, Phys. Rev. B **58**, 2740 (1998).
21. O. V. Vasil'ev and L. N. Shchur, Zh. Éksp. Teor. Fiz. **117**, 1110 (2000) [JETP **90**, 964 (2000)].
22. U. Wolff, Phys. Lett. **62**, 361 (1989).
23. J.-S. Wang and R. H. Swendsen, Physica A (Amsterdam) **167**, 565 (1990).
24. A. K. Murtazaev, I. K. Kamilov, and M. A. Magomedov, Zh. Éksp. Teor. Fiz. **120**, 1535 (2001) [JETP **93**, 1330 (2001)].
25. I. K. Kamilov, A. K. Murtazaev, and Kh. A. Aliev, Usp. Fiz. Nauk **169**, 773 (1999) [Phys. Usp. **42**, 689 (1999)].
26. P. Peczak, A. M. Ferrenberg, and D. P. Landau, Phys. Rev. B **43**, 6087 (1991).
27. K. Binder, Phys. Rev. Lett. **47**, 693 (1981).
28. M. E. Fisher and M. N. Barber, Phys. Rev. Lett. **28**, 1516 (1972).
29. A. Z. Patashinskiĭ and V. L. Pokrovskiĭ, *Fluctuation Theory of Phase Transitions*, 2nd ed. (Nauka, Moscow, 1982; Pergamon Press, Oxford, 1979).
30. A. Mailhot, M. L. Plumer, and A. Caille, Phys. Rev. B **50**, 6854 (1994).
31. D. Loison, Phys. Lett. A **257**, 83 (1999).

Translated by A. Betev

Journal of Experimental and Theoretical Physics, Vol. 99, No. 6, 2004, pp. 1207–1213.
Translated from Zhurnal Éksperimental'noĭ i Teoreticheskoĭ Fiziki, Vol. 126, No. 6, 2004, pp. 1384–1390.
Original Russian Text Copyright © 2004 by Gusakova, Vedyaev, Kotel'nikova, Buzdin.

SOLIDS
Structure

Magnetization Distribution in a Helicoidal Structure Containing a Point Defect

D. Yu. Gusakova[a],*, A. V. Vedyaev[a], O. A. Kotel'nikova[a], and A. I. Buzdin[b]

[a]*Moscow State University, Moscow, 119992 Russia*
[b]*Université Bordeaux I, 33405 Talence Cedex, France*
**e-mail: dasha@magn.ru*

Received July 8, 2004

Abstract—The helicoid that forms in an external magnetic field in the presence of a point defect is modeled in the framework of the Landau theory of second-order phase transitions. A general solution to the nonlinear problem retaining all terms in the Helmholtz free-energy functional is obtained by means of Green functions. The magnetization distribution in the plane perpendicular to the helicoid axis and to the external field is calculated. *© 2004 MAIK "Nauka/Interperiodica".*

1. INTRODUCTION

The presence of defects and inhomogeneities in ferromagnetic materials can strongly affect critical properties of magnets. For example, if the local exchange constant in the vicinity of a defect is greater than that in the bulk of the material, then a localized magnetic moment can exist at a temperature above the bulk T_{C0}. However, this is possible only if the defect parameters (effective radius and exchange interaction strength) satisfy certain conditions (e.g., see [1, 2]).

The Helmholtz free-energy functional for a magnet having a noncentrosymmetric crystalline structure contains a term that is linear in spatial derivatives. Owing to this term, the ground state of the system is stabilized, and a helicoidal structure forms at a temperature above the Curie temperature T_{C0} of the paramagnetic–ferromagnetic transition [3]. Helicoidal structures of this kind were found, for example, in MnSi [4] and FeGe [5].

A theoretical analysis of stationary localized states at crystalline-structure defects in noncentrosymmetric cubic magnets was presented in [6]. Solutions describing two- and three-dimensional localized states were obtained for temperatures above the paramagnetic–helicoidal transition point. It was shown that, if the Helmholtz free-energy functional contains the term $-\gamma\mathbf{M}^2\delta(\mathbf{r})$ associated with a defect (where $\mathbf{M}$ is the local magnetic moment) and the parameter γ has a certain small value, then the transition to the helicoidal phase occurs at a temperature T_{CL} above the critical temperature T_{C0} for the paramagnetic–helicoidal transition in a bulk sample without defects.

The stability of solutions describing nonlinear vector fields in models characterized by Lifshitz invariants was examined in [7]. It was shown that the two- and three-dimensional localized states associated with relaxation of the field magnitude are radially unstable. However, the existence of states with lower energies (i.e., radial instability) was established for a Helmholtz free-energy functional that did not contain the δ-function contribution to the energy of the system in the vicinity of the defect. The predicted behavior drastically changes when this contribution is taken into account: stable multidimensional states can be localized at the crystalline-structure defects in a noncentrosymmetric cubic paramagnet.

Helicoidal structures are the subject of intensive ongoing experimental studies. In addition to the long-known materials MnSi [4] and FeGe [5], helimagnetism was revealed, for example, in $Ba_2CuGe_2O_7$ [8, 9] and $K_2V_3O_8$ [10]. These materials are of particular interest for analyzing the Dzyaloshinskii–Moriya exchange interaction. The formation of incommensurate structures of new types, including magnetic vortices (skyrmions), was discussed in [11]. An experimental study of the influence of the Co^{2+} impurity concentration x on the helicoidal structure observed in $Ba_2(Co_xCu_{1-x})Ge_2O_7$ was reported in [12]. However, this phenomenon is poorly understood to this day and should be studied in more detail.

In this paper, we focus on a model analogous to that considered in [6]. In the present model, the expression for the Helmholtz free energy contains an additional term proportional to $\mathbf{M}^4$ and a term representing the Zeeman energy of a magnetic moment in an external field. Our goal here is to calculate the stable helicoidal magnetic state of a system containing a single magnetic impurity. We show that, in addition to uniform magnetization, there exists a localized helicoidal magnetic state in an external magnetic field at a temperature above T_{CL}. It can be observed in neutron scattering experiments.

1063-7761/04/9906-1207$26.00 © 2004 MAIK "Nauka/Interperiodica"

The problem in question can also be of interest in view of the fact that structural analogs of helicoids can be found in various nonlinear models of condensed matter. Apart from magnets [13, 14], interactions associated with invariants that are linear in the first spatial derivatives (Lifshitz invariants) take place in certain classes of ferroelectrics and liquid crystals [15]. Another example of a multidimensional stationary localized state is the Abrikosov vortex in a superconductor [16]. By analogy, a term that is linear in spatial derivatives stabilizes two-dimensional localized states in noncentrosymmetric magnets, and magnetic vortices develop [17].

2. CALCULATION OF THE GROUND STATE OF A MAGNET

Consider the Dzyaloshinskii–Moriya-type weak interaction for a ferromagnet with defect localized at $x = y = z = 0$ in an external field. The Helmholtz free-energy functional of this system is

$$F = \frac{n\theta}{M_S^2}\int\Big(\tau\mathbf{M}^2 + \frac{b}{2}\mathbf{M}^4 + a^2(\nabla M_x)^2 + a^2(\nabla M_y)^2 + a^2(\nabla M_z)^2 + \lambda\mathbf{M}\cdot\mathrm{curl}\mathbf{M} - \gamma\mathbf{M}^2\delta(\mathbf{r}) - HM_z\Big)d^3\mathbf{r}, \qquad (1)$$

where θ is on the order of the Curie temperature T_{C0}, n is the concentration of magnetic moments, M_S is the maximum possible magnetization at zero temperature, $\tau = (T - T_{C0})/T_{C0}$, and H_z is an external magnetic field parallel to the z axis. The first two terms in (1) represent the expansion in powers of $\mathbf{M}$ about the Curie point (magnetization $\mathbf{M}$ is treated as the order parameter in the general theory of second-order phase transitions). Note that T_{C0} is the Curie temperature for the paramagnetic–ferromagnetic transition in the absence of the term proportional to $\mathbf{M}\cdot\mathrm{curl}\mathbf{M}$. When this term is taken into account, transition to a helicoidal magnetic structure occurs at a temperature T_C above the Curie point, i.e., $(T_C - T_{C0})/T_{C0} = \tau_0 = (\lambda/2a)^2$. In a noncentrosymmetric cubic crystal, the small term proportional to $\lambda\mathbf{M}\cdot\mathrm{curl}\mathbf{M}$ (i.e., linear in derivatives) gives rise to a helicoidal magnetic superstructure modulating the ferromagnetic structure. The sign of λ determines the energy-minimizing rotation of $\mathbf{M}$ in a particular material. The term proportional to $-\gamma\mathbf{M}^2\delta(\mathbf{r})$ describes a local increase in the paramagnetic–ferromagnetic transition temperature near the point defect. The magnetic stiffness parameter a is comparable in order of magnitude to the interatomic distance.

The minimum-energy equilibrium state of the system is found by solving the Euler–Lagrange equations associated with functional (1):

$$\left.\begin{pmatrix} \hat{\Delta}_{zz}-\tau & \hat{L}_{z\rho} & \hat{L}_{z\phi} \\ \hat{L}_{\rho z} & \hat{\Delta}_{\rho\rho}-\tau & \hat{L}_{\rho\phi} \\ \hat{L}_{\phi z} & \hat{L}_{\phi\rho} & \hat{\Delta}_{\phi\phi}-\tau \end{pmatrix}\right|_{\mathbf{r}} \times \begin{pmatrix} M^{*z}(\mathbf{r}') \\ M^{\rho}(\mathbf{r}') \\ M^{\phi}(\mathbf{r}') \end{pmatrix} = \begin{pmatrix} f^z(\mathbf{r}) \\ f^{\rho}(\mathbf{r}) \\ f^{\phi}(\mathbf{r}) \end{pmatrix}, \qquad (2)$$

where the operators $\hat{\Delta}_{zz} = \Delta$, $\hat{\Delta}_{\rho\rho} = \Delta - 1/\rho^2$, and $\hat{\Delta}_{\phi\phi} = \Delta - 1/\rho^2$ are expressed in terms of the Laplacian Δ written in the cylindrical coordinates $\mathbf{r} = (z, \rho\cos\phi, \rho\sin\phi)$;

$$\begin{aligned} \hat{L}_{z\rho} &= -\hat{L}_{\rho z} = \frac{\lambda}{\rho}\frac{\partial}{\partial\phi}, \\ \hat{L}_{\rho\phi} &= -\hat{L}_{\phi\rho} = \lambda\frac{\partial}{\partial z} - \frac{2}{\rho^2}\frac{\partial}{\partial\phi}, \\ \hat{L}_{\phi z} &= -\hat{L}_{z\phi} - \frac{\lambda}{\rho^2} = \lambda\frac{\partial}{\partial\rho}; \end{aligned} \qquad (3)$$

and

$$\begin{aligned} f^z(\mathbf{r}) &= -C\frac{\delta(\rho)\delta(z)}{2\pi\rho} + bM^{*z}\mathbf{M}^2, \\ f^{\rho}(\mathbf{r}) &= bM^{\rho}\mathbf{M}^2, \quad f^{\phi}(\mathbf{r}) = bM^{\phi}\mathbf{M}^2. \end{aligned} \qquad (4)$$

Here, $C = \gamma(M^z_{(z\,=\,0,\,\rho\,=\,0)} + H/2\tau)$ with $M^{*z} = M^z - H/2\tau$ (the difference between the total magnetic moment parallel to the z axis and its homogeneous spatial part). The magnetic moment of the defect is parallel to the z axis.

Since Eqs. (2) are difficult to solve analytically, we make use of the following procedure. First, we find the eigenvalues and eigenfunctions of (2) with a zero right-hand side,

$$\left.\begin{pmatrix} \hat{\Delta}_{zz}-\tau & \hat{L}_{z\rho} & \hat{L}_{z\phi} \\ \hat{L}_{\rho z} & \hat{\Delta}_{\rho\rho}-\tau & \hat{L}_{\rho\phi} \\ \hat{L}_{\phi z} & \hat{L}_{\phi\rho} & \hat{\Delta}_{\phi\phi}-\tau \end{pmatrix}\right|_{\mathbf{r}} \times \begin{pmatrix} M^{*z}(\mathbf{r}')_{\alpha,\,(\omega,\,\sigma,\,\nu)} \\ M^{\rho}(\mathbf{r}')_{\alpha,\,(\omega,\,\sigma,\,\nu)} \\ M^{\phi}(\mathbf{r}')_{\alpha,\,(\omega,\,\sigma,\,\nu)} \end{pmatrix} = 0. \qquad (5)$$

The result is

$\tau_1 = -(\omega^2 + \sigma^2)$,

$$\begin{cases} M^{*z}_{1,(\omega,\sigma,\nu)}(z,\rho,\phi) = \dfrac{\omega}{\sqrt{\omega^2+\sigma^2}} J_\nu(\sigma\rho) e^{i\omega z} e^{i\nu\phi}, \\ M^{\rho}_{1,(\omega,\sigma,\nu)}(z,\rho,\phi) = \dfrac{i\sigma}{2\sqrt{\omega^2+\sigma^2}} (J_{\nu+1}(\sigma\rho) - J_{\nu-1}(\sigma\rho)) e^{i\omega z} e^{i\nu\phi}, \\ M^{\phi}_{1,(\omega,\sigma,\nu)}(z,\rho,\phi) = \dfrac{\sigma}{2\sqrt{\omega^2+\sigma^2}} (J_{\nu+1}(\sigma\rho) + J_{\nu-1}(\sigma\rho)) e^{i\omega z} e^{i\nu\phi}. \end{cases}$$

$\tau_2 = -(\omega^2 + \sigma^2 + \lambda\sqrt{\omega^2+\sigma^2})$,

$$\begin{cases} M^{*z}_{2,(\omega,\sigma,\nu)}(z,\rho,\phi) = \dfrac{1}{\sqrt{2}} \dfrac{\sigma}{\sqrt{\omega^2+\sigma^2}} J_\nu(\sigma\rho) e^{i\omega z} e^{i\nu\phi}, \\ M^{\rho}_{2,(\omega,\sigma,\nu)}(z,\rho,\phi) = \dfrac{i}{2\sqrt{2}} \dfrac{\sigma^2}{\sqrt{\omega^2+\sigma^2}} \left(\dfrac{J_{\nu+1}(\sigma\rho)}{\sqrt{\omega^2+\sigma^2}+\omega} + \dfrac{J_{\nu-1}(\sigma\rho)}{\sqrt{\omega^2+\sigma^2}-\omega} \right) e^{i\omega z} e^{i\nu\phi}, \\ M^{\phi}_{2,(\omega,\sigma,\nu)}(z,\rho,\phi) = \dfrac{1}{2\sqrt{2}} \dfrac{\sigma^2}{\sqrt{\omega^2+\sigma^2}} \left(\dfrac{J_{\nu+1}(\sigma\rho)}{\sqrt{\omega^2+\sigma^2}+\omega} - \dfrac{J_{\nu-1}(\sigma\rho)}{\sqrt{\omega^2+\sigma^2}-\omega} \right) e^{i\omega z} e^{i\nu\phi}. \end{cases} \tag{6}$$

$\tau_3 = -(\omega^2 + \sigma^2 - \lambda\sqrt{\omega^2+\sigma^2})$,

$$\begin{cases} M^{*z}_{3,(\omega,\sigma,\nu)}(z,\rho,\phi) = \dfrac{1}{\sqrt{2}} \dfrac{\sigma}{\sqrt{\omega^2+\sigma^2}} J_\nu(\sigma\rho) e^{i\omega z} e^{i\nu\phi}, \\ M^{\rho}_{3,(\omega,\sigma,\nu)}(z,\rho,\phi) = -\dfrac{i}{2\sqrt{2}} \dfrac{\sigma^2}{\sqrt{\omega^2+\sigma^2}} \left(\dfrac{J_{\nu+1}(\sigma\rho)}{\sqrt{\omega^2+\sigma^2}-\omega} + \dfrac{J_{\nu-1}(\sigma\rho)}{\sqrt{\omega^2+\sigma^2}+\omega} \right) e^{i\omega z} e^{i\nu\phi}, \\ M^{\phi}_{3,(\omega,\sigma,\nu)}(z,\rho,\phi) = -\dfrac{1}{2\sqrt{2}} \dfrac{\sigma^2}{\sqrt{\omega^2+\sigma^2}} \left(\dfrac{J_{\nu+1}(\sigma\rho)}{\sqrt{\omega^2+\sigma^2}-\omega} - \dfrac{J_{\nu-1}(\sigma\rho)}{\sqrt{\omega^2+\sigma^2}+\omega} \right) e^{i\omega z} e^{i\nu\phi}. \end{cases}$$

It can be shown that $M^{*z,\rho,\phi}_{\alpha}$ ($\alpha = 1, 2, 3$) make up a set of orthonormal functions:

$$\sum_{\nu} \int \sigma d\sigma \int d\omega \sum_{\alpha=1,2,3} M^{i}_{\alpha,(\omega,\sigma,\nu)}(\mathbf{r}_1) \times (M^{j}_{\alpha,(\omega,\sigma,\nu)}(\mathbf{r}_2))^{\text{c.c.}} = \delta(\mathbf{r}_1 - \mathbf{r}_2)\delta_{ij}.$$

Here, c.c. denotes a complex conjugate. Next, we introduce Green functions of (5),

$$G^{ij}(\mathbf{r}_1, \mathbf{r}_2) = \sum_{\nu} \int \sigma d\sigma \times \int d\omega \sum_{\alpha=1,2,3} \frac{M^{i}_{\alpha,(\omega,\sigma,\nu)}(\mathbf{r}_1)(M^{j}_{\alpha,(\omega,\sigma,\nu)}(\mathbf{r}_2))^{\text{c.c.}}}{\tau_\alpha - \tau}, \tag{7}$$

which satisfy the system of equations

$$\left.\begin{pmatrix} \hat{\Delta}_{zz}-\tau & \hat{L}_{z\rho} & \hat{L}_{z\phi} \\ \hat{L}_{\rho z} & \hat{\Delta}_{\rho\rho}-\tau & \hat{L}_{\rho\phi} \\ \hat{L}_{\phi z} & \hat{L}_{\phi\rho} & \hat{\Delta}_{\phi\phi}-\tau \end{pmatrix}\right|_{\mathbf{r}} \tag{8}$$
$$\times\begin{pmatrix} G^{zz}(\mathbf{r}_1,\mathbf{r}_2) & G^{z\rho}(\mathbf{r}_1,\mathbf{r}_2) & G^{z\phi}(\mathbf{r}_1,\mathbf{r}_2) \\ G^{\rho z}(\mathbf{r}_1,\mathbf{r}_2) & G^{\rho\rho}(\mathbf{r}_1,\mathbf{r}_2) & G^{\rho\phi}(\mathbf{r}_1,\mathbf{r}_2) \\ G^{\phi z}(\mathbf{r}_1,\mathbf{r}_2) & G^{\phi\rho}(\mathbf{r}_1,\mathbf{r}_2) & G^{\phi\phi}(\mathbf{r}_1,\mathbf{r}_2) \end{pmatrix} = \hat{I}\delta(\mathbf{r}_1-\mathbf{r}_2),$$

where $\hat{I}$ is the identity matrix. Thus, the formal solution to Eqs. (2) has the form

$$M^i(\mathbf{r}_1) = \sum_j \int d\mathbf{r}_2 G^{ij}(\mathbf{r}_1,\mathbf{r}_2) f^j(\mathbf{r}_2). \tag{9}$$

3. NUMERICAL RESULTS AND CONCLUSIONS

To compute the spatial distribution of magnetization, we solved (9) iteratively for several values of the external magnetic field.

Solutions to Eqs. (9) for the components of **M** are difficult to find in explicit form. However, if we drop the nonlinear terms in (4), then

$$\begin{aligned} f^{0z}(z,\rho,\phi) &= -C\frac{\delta(\rho)\delta(z)}{2\pi\rho}, \\ f^{0\rho}(z,\rho,\phi) &= 0, \\ f^{0\phi}(z,\rho,\phi) &= 0, \end{aligned} \tag{10}$$

and expressions for the magnetization components can readily be found by substituting (9) into (10) and using Green functions:

$$\begin{aligned} M^{0*z}(z,\rho) &= -C\int\rho' d\rho'\int dz'\int d\phi' G^{zz}(\mathbf{r},\mathbf{r}')\frac{\delta(\rho')\delta(z')}{2\pi\rho'}, \\ M^{0\rho}(z,\rho) &= -C\int\rho' d\rho'\int dz'\int d\phi' G^{\rho z}(\mathbf{r},\mathbf{r}')\frac{\delta(\rho')\delta(z')}{2\pi\rho'}, \\ M^{0\phi}(z,\rho) &= -C\int\rho' d\rho'\int dz'\int d\phi' G^{\phi z}(\mathbf{r},\mathbf{r}')\frac{\delta(\rho')\delta(z')}{2\pi\rho'}. \end{aligned} \tag{11}$$

Since the system is homogeneous with respect to ϕ, the eigenfunctions given by (6) reduce to

$$\tau_1 = -(\omega^2+\sigma^2),$$

$$\begin{cases} M^{*z}_{1,(\omega,\sigma)}(z,\rho) = \dfrac{\omega}{\sqrt{\omega^2+\rho^2}}J_0(\sigma\rho)e^{i\omega z}, \\ M^{\rho}_{1,(\omega,\sigma)}(z,\rho) = \dfrac{i\sigma}{\sqrt{\omega^2+\sigma^2}}J_1(\sigma\rho)e^{i\omega z}, \\ M^{\phi}_{1,(\omega,\sigma)}(z,\rho) = 0, \end{cases}$$

$$\tau_2 = -(\omega^2+\sigma^2+\lambda\sqrt{\omega^2+\sigma^2}),$$

$$\begin{cases} M^{*z}_{2,(\omega,\sigma)}(z,\rho) = \dfrac{1}{\sqrt{2}}\dfrac{\sigma}{\sqrt{\omega^2+\sigma^2}}J_0(\sigma\rho)e^{i\omega z}, \\ M^{\rho}_{2,(\omega,\sigma)}(z,\rho) = -\dfrac{i\omega}{\sqrt{2}\sqrt{\omega^2+\sigma^2}}J_1(\sigma\rho)e^{i\omega z}, \\ M^{\phi}_{2,(\omega,\sigma)}(z,\rho) = \dfrac{1}{\sqrt{2}}J_1(\sigma\rho)e^{i\omega z}, \end{cases} \tag{12}$$

$$\tau_3 = -(\omega^2+\sigma^2-\lambda\sqrt{\omega^2+\sigma^2}),$$

$$\begin{cases} M^{*z}_{3,(\omega,\sigma)}(z,\rho) = \dfrac{1}{\sqrt{2}}\dfrac{\sigma}{\sqrt{\omega^2+\sigma^2}}J_0(\sigma\rho)e^{i\omega z}, \\ M^{\rho}_{3,(\omega,\sigma)}(z,\rho) = -\dfrac{i\omega}{\sqrt{2}\sqrt{\omega^2+\sigma^2}}J_1(\sigma\rho)e^{i\omega z}, \\ M^{\phi}_{3,(\omega,\sigma)}(z,\rho) = -\dfrac{1}{\sqrt{2}}J_1(\sigma\rho)e^{i\omega z}. \end{cases}$$

Substituting the eigenfunctions from (12) into (7), we obtain

$$G^{zz}(\mathbf{r}_1,\mathbf{r}_2) = -\int\sigma d\sigma d\omega$$
$$\times\frac{((\omega^2+\sigma^2+\tau)^2-\lambda^2\omega^2)J_0(\sigma\rho_1)J_0(\sigma\rho_2)e^{i\omega(z_1-z_2)}}{(\omega^2+\sigma^2+\tau)((\omega^2+\sigma^2+\tau)^2-\lambda^2(\omega^2+\sigma^2))},$$

$$G^{\rho\rho}(\mathbf{r}_1,\mathbf{r}_2) = \int\sigma d\sigma d\omega$$
$$\times\frac{((\omega^2+\sigma^2+\tau)^2-\lambda^2\sigma^2)J_1(\sigma\rho_1)J_1(\sigma\rho_2)e^{i\omega(z_1-z_2)}}{(\omega^2+\sigma^2+\tau)((\omega^2+\sigma^2+\tau)^2-\lambda^2(\omega^2+\sigma^2))},$$

$$G^{\phi\phi}(\mathbf{r}_1,\mathbf{r}_2) = -\int\sigma d\sigma d\omega$$
$$\times\frac{(\omega^2+\sigma^2+\tau)J_1(\sigma\rho_1)J_1(\sigma\rho_2)e^{i\omega(z_1-z_2)}}{(\omega^2+\sigma^2+\tau)^2-\lambda^2(\omega^2+\sigma^2)},$$

$$G^{z\rho}(\mathbf{r}_1, \mathbf{r}_2) = \int \sigma d\sigma d\omega$$

$$\times \frac{i\sigma\omega\lambda^2 J_0(\sigma\rho_1) J_1(\sigma\rho_2) e^{i\omega(z_1 - z_2)}}{(\omega^2 + \sigma^2 + \tau)((\omega^2 + \sigma^2 + \tau)^2 - \lambda^2(\omega^2 + \sigma^2))}, \quad (13)$$

$$G^{\rho z}(\mathbf{r}_1, \mathbf{r}_2) = \int \sigma d\sigma d\omega$$

$$\times \frac{i\sigma\omega\lambda^2 J_1(\sigma\rho_1) J_0(\sigma\rho_2) e^{i\omega(z_1 - z_2)}}{(\omega^2 + \sigma^2 + \tau)((\omega^2 + \sigma^2 + \tau)^2 - \lambda^2(\omega^2 + \sigma^2))},$$

$$G^{z\phi}(\mathbf{r}_1, \mathbf{r}_2) = \int \sigma d\sigma d\omega \frac{\sigma\lambda J_0(\sigma\rho_1) J_1(\sigma\rho_2) e^{i\omega(z_1 - z_2)}}{(\omega^2 + \sigma^2 + \tau)^2 - \lambda^2(\omega^2 + \sigma^2)},$$

$$G^{\phi z}(\mathbf{r}_1, \mathbf{r}_2) = \int \sigma d\sigma d\omega \frac{\sigma\lambda J_1(\sigma\rho_1) J_0(\sigma\rho_2) e^{i\omega(z_1 - z_2)}}{(\omega^2 + \sigma^2 + \tau)^2 - \lambda^2(\omega^2 + \sigma^2)},$$

$$G^{\rho\phi(\phi\rho)}(\mathbf{r}_1, \mathbf{r}_2)$$

$$= -\int \sigma d\sigma d\omega \frac{i\omega\lambda J_1(\sigma\rho_1) J_1(\sigma\rho_2) e^{i\omega(z_1 - z_2)}}{(\omega^2 + \sigma^2 + \tau)^2 - \lambda^2(\omega^2 + \sigma^2)}.$$

Thus, combining (10) with (13) at the first iterative step, we obtain

$$M^{0*z}(z, \rho) = C \int_0^{+\infty} \sigma d\sigma \int_{-\infty}^{+\infty} d\omega$$

$$\times \frac{(\omega^2 + \sigma^2 + \tau)^2 - \omega^2\lambda^2}{(\omega^2 + \sigma^2 + \tau)((\omega^2 + \sigma^2 + \tau)^2 - \lambda^2(\omega^2 + \sigma^2))}$$

$$\times J_0(\sigma\rho) e^{i\omega z},$$

$$M^{0\rho}(z, \rho) = C \int_0^{+\infty} \sigma d\sigma \int_{-\infty}^{+\infty} d\omega$$

$$\times \frac{-i\omega\sigma\lambda^2}{(\omega^2 + \sigma^2 + \tau)((\omega^2 + \sigma^2 + \tau)^2 - \lambda^2(\omega^2 + \sigma^2))} \quad (14)$$

$$\times J_1(\sigma\rho) e^{i\omega z},$$

$$M^{0\phi}(z, \rho) = C \int_0^{+\infty} \sigma d\sigma \int_{-\infty}^{+\infty} d\omega$$

$$\times \frac{\sigma\lambda}{(\omega^2 + \sigma^2 + \tau)^2 - \lambda^2(\omega^2 + \sigma^2)} J_1(\sigma\rho) e^{i\omega z}.$$

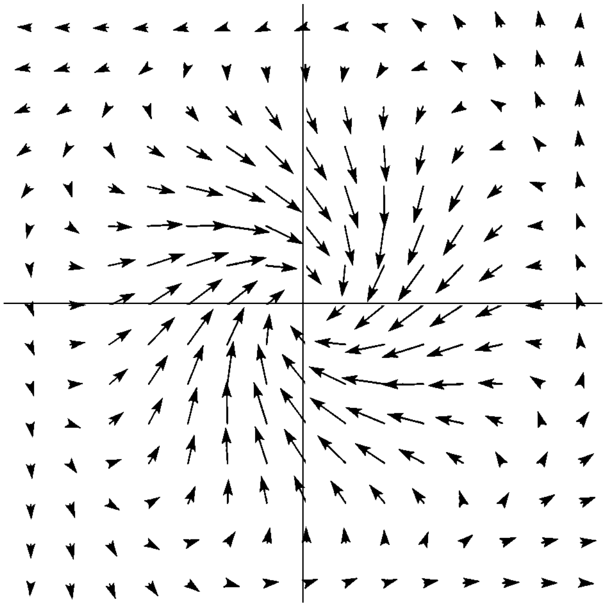

Fig. 1. Magnetization distribution in a plane perpendicular to the helicoid axis ($z = z_1 - z_2 = 2\pi$) in the absence of external magnetic field.

At the next iterative step, the magnetization components are calculated numerically by solving (2) with nonlinear terms (4). The results have the form

$$M^z \sim H/2\tau + I_{1z}H + I_{2z}bH^3,$$

$$M^\rho \sim I_{1\rho}H + I_{2\rho}bH^3,$$

$$M^\phi \sim I_{1\phi}H + I_{2\phi}bH^3,$$

where I_{zi}, $I_{\rho i}$, and $I_{\phi i}$ are numerical coefficients obtained by integrating expressions depending on G^{0ij} and M^{0i} with respect to ω and σ. To illustrate the results obtained, we used a Cartesian coordinate system to calculate the components M^x and M^y of the magnetization projected onto the plane $z = z_1 - z_2 = 2\pi$ perpendicular to the helicoid axis.

Figure 1 shows the two-dimensional magnetization pattern obtained in the plane perpendicular to the z axis for zero external field. This distribution agrees with that obtained in [6] in the absence of external magnetic field and nonlinear term $b\mathbf{M}^4/2$ in the Helmholtz free-energy functional.

Figure 2 illustrates the evolution of magnetic structure. The degree of helicity increases with the strength of the external magnetic field parallel to the z axis from Fig. 2a to Fig. 2d as the vortex formation due to the exchange interaction involves magnetic moments located at progressively larger distances from the defect.

The properties of the nonuniform states examined here are characteristic of a broad class of systems.

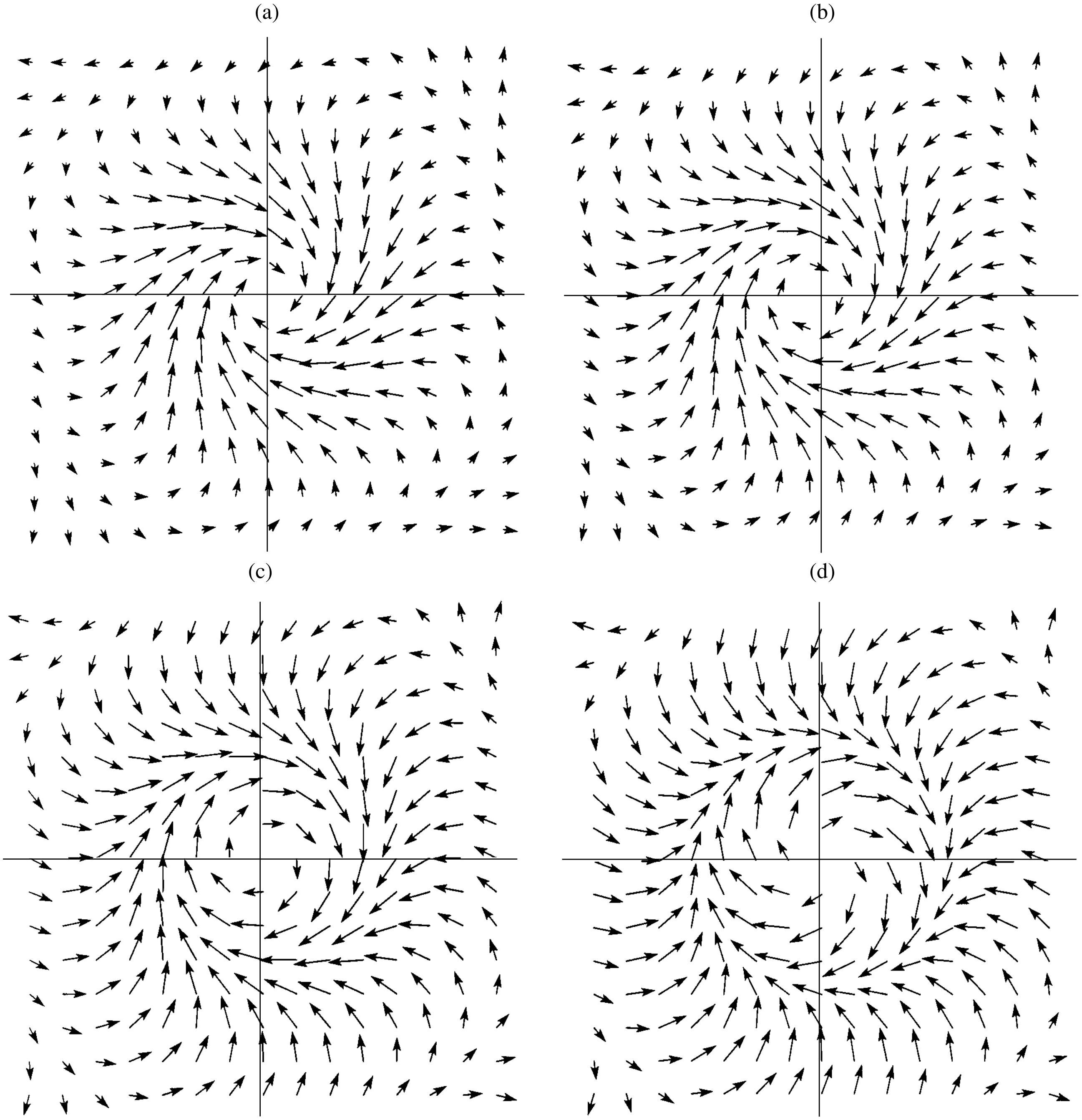

Fig. 2. Magnetization distribution in a plane perpendicular to the helicoid axis ($z = z_1 - z_2 = 2\pi$) at magnetic-field strengths (a) 3, (b) 4, (c) 5, and (d) 6 (in arbitrary units).

Therefore, both the proposed method for calculating the response of a system to an external magnetic field and the results obtained can be used in other areas of solid-state physics.

ACKNOWLEDGMENTS

This work was supported by the Russian Foundation for Basic Research, project no. 04-02-16688a.

REFERENCES

1. M. I. Kaganov and A. N. Omel’yanchuk, Zh. Éksp. Teor. Fiz. **61**, 1679 (1971) [Sov. Phys. JETP **34**, 895 (1972)].
2. I. N. Khlustikov and A. I. Buzdin, Adv. Phys. **36**, 271 (1987).
3. L. D. Landau and E. M. Lifshitz, *Course of Theoretical Physics*, Vol. 8: *Electrodynamics of Continuous Media*, 2nd ed. (Nauka, Moscow, 1982; Pergamon, Oxford, 1984).

4. M. L. Plumer and M. B. Walker, J. Phys. C **14**, 4689 (1981).
5. J. Beille, J. Voicon, and M. Roth, Solid State Commun. **47**, 399 (1983).
6. A. Buzdin and Y. Meurdesoif, Pis'ma Zh. Éksp. Teor. Fiz. **65**, 776 (1997) [JETP Lett. **65**, 814 (1997)].
7. A. Bogdanov, Pis'ma Zh. Éksp. Teor. Fiz. **68**, 296 (1998) [JETP Lett. **68**, 317 (1998)].
8. A. Zheludev, G. Shirane, Y. Sasago, *et al.*, Phys. Rev. B **54**, 15163 (1996).
9. A. Zheludev, S. Maslov, G. Shirane, *et al.*, Phys. Rev. B **59**, 11432 (1999).
10. M. D. Lumsden, B. C. Sales, D. Mandrus, *et al.*, Phys. Rev. Lett. **86**, 159 (2001).
11. A. N. Bogdanov, U. K. Rössler, M. Wolf, and K.-H. Müller, Phys. Rev. B **66**, 214410 (2002).
12. A. Zheludev, T. Sato, T. Masuda, *et al.*, Phys. Rev. B **68**, 024428 (2003).
13. I. E. Dzyaloshinskiĭ, Zh. Éksp. Teor. Fiz. **46**, 1420 (1964) [Sov. Phys. JETP **19**, 960 (1964)].
14. Yu. A. Izyumov, Usp. Fiz. Nauk **144**, 439 (1984) [Sov. Phys. Usp. **27**, 845 (1984)].
15. P. de Gennes, *The Physics of Liquid Crystals* (Clarendon Press, Oxford, 1974; Mir, Moscow, 1977).
16. A. A. Abrikosov, Zh. Éksp. Teor. Fiz. **32**, 1442 (1957) [Sov. Phys. JETP **5**, 1174 (1957)].
17. A. Bogdanov and A. Hubert, J. Magn. Magn. Mater. **138**, 255 (1994).

Translated by A. Betev

Journal of Experimental and Theoretical Physics, Vol. 99, No. 6, 2004, pp. 1214–1222.
Translated from Zhurnal Éksperimental’noĭ i Teoreticheskoĭ Fiziki, Vol. 126, No. 6, 2004, pp. 1391–1401.
Original Russian Text Copyright © 2004 by Tsymbalenko.

SOLIDS
Structure

Decay of the Anomalous State of a ^{4}He Crystal

V. L. Tsymbalenko
Russian Research Center Kurchatov Institute, Moscow, 123182 Russia
e-mail: vlt@isssph.kiae.ru

Received July 21, 2004

Abstract—The relaxation of the anomalous state, i.e., the return of the growth kinetics to the regime typical of crystals in the normal state, is studied experimentally in the temperature range 0.48–0.68 K. It is found that the relaxation process with the growth rate decreasing by two orders of magnitude mainly occurs 1–20 ms after the termination of the fast growth stage. Slow relaxation to the normal values of the kinetic growth coefficient is observed subsequently during a time interval equal approximately to 100 ms. *© 2004 MAIK “Nauka/Interperiodica”.*

1. INTRODUCTION

The growth kinetics for helium crystals with small deviations from equilibrium has been studied in detail both above the temperature of faceting transitions in the atomically rough state and below this temperature (in the atomically smooth state). The main features of the kinetics can be described using the model of layer growth of the crystal [1] taking into account the quantum effects described by Andreev and Parshin [2]. The phenomenon of anomalous growth, which does not fit this pattern, is manifested in a sharp increase in the facet growth rate by several orders of magnitude at strong supersaturation [3]. The conditions for the emergence of this state have been determined [4–6], the kinetics of its emergence has been studied [7], the growth rates after a transition to the anomalous state have been measured [7, 8], and the effect of impurities on these processes has been investigated [9]. These experiments have led to the rejection of possible explanations for anomalous growth based on the mechanisms studied on classical crystals (see [1]). However, the pattern of evolution of the anomalous state remained incomplete until the reverse process (return of the crystal to the normal state) was studied experimentally. We apply the term normal state to a state with a slow growth kinetics controlled by known mechanisms (spiral growth, Frank–Read sources, and two-dimensional nucleation [1]). In this case, the mobility of facets is determined by external supersaturation and is independent of the past history.

After transition to the anomalous state, the crystal rapidly grows and the pressure in the container drops to a value close to the phase-equilibrium pressure and is obviously smaller than the supersaturation pressure required for the emergence of the anomalous state. It is known from previous experiments that a second after this instant, the crystal behaves as a normal crystal [10]. Later, a smaller value equal to 100 ms was estimated for the return time [5]. These data characterized in general the return to the normal state. The details of the relaxation process were unknown. In particular, it remained unclear how the reverse process of relaxation occurs: abruptly, as during the formation of the anomalous state, or continuously with a monotonic decrease in the kinetic growth coefficient by several orders of magnitude.

A sharp increase in the growth rate for the (0001) facet free of growth dislocations was observed in the temperature range 0.002–0.25 K both in our experiments from the pressure jump and in [11], where optical methods were used. Pressure recording shows that after the pressure drop (fast growth phase), the pressure begins to increase, indicating an extremely low growth rate. Thus, the relaxation to the normal state is detected in this case also. However, the low time resolution of the capacitive sensor and optical recording (~1 s) does not permit the clarification of the details of the relaxation process.

Here, we study the relaxation of a helium crystal to the normal state.

2. EXPERIMENTAL TECHNIQUE

It was known from previous experiments that the crystals do not differ in appearance from normal crystals prior to the transition to their fast growth and after its termination [7, 12]. For the time being, the only indication of the anomaly is the high growth rate for facets, which exceeds the normal growth rate by several orders of magnitude. Thus, the process of return to the normal state (relaxation) can be traced so far only by studying the facet growth kinetics at weak supersaturation that does not induce a transition to the anomalous phase. In our experiments the crystal growth was ensured by a continuous supply of liquid helium to the container via a capillary connecting the experimental volume with the external high-pressure system. Since the mass of helium in the container and in the pressure system is constant, we can write the equations connecting the pressures in both parts of the system:

$$M_1 + M_2 = M = \text{const},$$

$$M_1 = \rho' V_c + \rho(p_1)(V_1 - V_c), \quad M_2 = p_2 V_2(t)\frac{m_4}{RT}, \quad (1)$$

$$\frac{dM_1}{dt} = -\frac{dM_2}{dt} = \frac{p_2 - p_1}{Z},$$

where subscripts 1 and 2 correspond to the container and to the outer part, respectively. Primed parameters pertain to solid helium, unprimed parameters correspond to liquid helium, V_c is the volume of the helium crystal, V_1 is the internal volume of the container, and Z is the impedance of the capillary. The volume V_2 of the outer part was changed by compression and extension of the bellow. Below a temperature of 0.8 K at which the experiments were performed, the effect of thermal expansion of helium and the heat of crystallization is negligibly weak [5]; for this reason, the corresponding corrections were not taken into account in formulas (1). Passing to more convenient variables, we obtain the system of equations

$$\frac{dp_1}{dt} + Dp_0\frac{df}{dt} = \frac{p_2 - p_1}{\tau_1},$$

$$\frac{dp_2}{dt} = -\frac{p_2 - p_1}{\tau_1} + \left(1 + \frac{\tau_1}{\tau_2}\right)\frac{dp_1}{dt}\bigg|_{t<0}, \quad (2)$$

$$\tau_1 = Z\rho V_1 k_L, \quad \tau_2 = Z\frac{m_4 V_2}{RT},$$

$$f = \frac{V_c}{V_1 \dfrac{\rho}{\Delta\rho} k_L D p_0},$$

where Dp_0 is the supersaturation beginning from which the crystal starts growing and k_L is the compressibility of liquid helium. It should be noted that the ratio of time constants τ_1 and τ_2 is independent of the impedance of the inlet capillary and is determined by the ratio of the helium masses in the container and in the outer part containing the gas. When the bellow is compressed at a constant rate, the external pressure exceeds the pressure in the container by

$$p_2 = p_1 + \tau_1\frac{dp_1}{dt}, \quad \frac{dp_1}{dt} \approx \text{const}. \quad (3)$$

After the transition of the crystal to the anomalous state, it grows upon supersaturation drop over a time approximately equal to 1 ms $\ll \tau_{1,2}$; consequently, the initial conditions for system of equations (2) are given by

$$p_1 = p_1(0),$$

$$p_2 = Dp_0 + \tau_1\frac{dp_1}{dt}\bigg|_{t=0}, \quad (4)$$

$$f = 1.$$

Here and below, the pressure is measured from the phase-equilibrium pressure. Substituting the experimentally measured dependence $p_1(t)$ into system (2) with initial conditions (4) and considering that the values of time constants considerably exceed the time of the experiment ($\tau_1 = 37$ s, $\tau_2 = 30$ s, $\tau_{1,2} \gg t_{\exp} \sim 0.2$ s), we obtain the following time dependence for the crystal volume:

$$V_c(t) = V_1\frac{\rho}{\Delta\rho}k_L\left(Dp_0 - p_1(t) + p_2(0)\frac{t}{\tau_1}\right). \quad (5)$$

Note that since this expression contains the difference between the current and initial pressures, the result given by formula (5) is insensitive to the value of pressure determined for the phase-equilibrium point.

Pressure measurements in the container and, accordingly, the determination of the crystal volume were performed with a step of 64 μs. However, it is possible to pass from the volume to the size and to determine the facet growth rate only in the following cases: (i) a single crystal is formed, (ii) the growth anisotropy is known, and (iii) the kinetics of closely packed facets is slower than the kinetics of surfaces with other crystallographic orientations. Then the crystal shape determined by the mobility of the basal and lateral facets is a hexagonal prism and the change in the volume is determined by the growth of the facets. A similar technique was used earlier for measuring rates at the fast growth stage [7]. It is clear from the above arguments that pressure measurements should be supplemented with direct photography of the crystal in the course of relaxation. The photographs of the crystal obtained with a time interval of 20 ms (separation between half-frames) provide reference points for reconstructing of the entire process of crystal growth; this allows us to use relation (5) for time intervals between frames for determining the growth rates of the facets.

Since the facet growth rate during relaxation changes by several orders of magnitude, we will disregard the anisotropy in the growth of equivalent facets and use the linear relation

$$V = K\frac{\Delta\rho}{\rho\rho'}p_1 \quad (6)$$

for connecting the growth rate with supersaturation; this relation approximately holds for facets in the atomically smooth state also (the applicability of this relation was discussed in [7]). The error in determining the coefficient of growth resistance $1/K$ is the sum of the errors in measuring the velocity and supersaturation. The supersaturation is measured from the phase-equilibrium pressure over the plane surface. In our experiments, this point was determined after termination of measurement during subsequent melting of the crystal. The typical radius of curvature of the crystal surface was approximately 1 mm, which leads to a correction of about 0.02 mbar. Together with the root mean square error ~0.07 mbar in pressure measurements, this leads to an overall indeterminacy of ~ 0.1 mbar. This contribution is significant in the region where supersaturation is on the same order of magnitude or smaller. To obtain an independent estimate of pressure in such cases, we measured the curvature of atomically rough surfaces from the photographs of the crystals. The error in the optical method increases with supersaturation and amounts approximately to 50% at 0.25 mbar. The combination of different techniques has made it possible to reduce the error of measurements up to 0.03–0.05 mbar in the entire pressure range.

The experimental technique was described in detail in a number of publications [5, 7]; we will outline here only the main points. Crystals were grown from helium purified by the thermomechanical technique in an optical container [13] mounted in an optical ^{3}He refrigerator [14]. Nucleation was initiated by a high-voltage pulse applied to a tungsten needle. The pressure drop was detected by a capacitive sensor with a band of 25 kHz. The crystal was photographed by a CCD camera; the frames were synchronized with the voltage pulse, pressure recording, and the pulsed source of light with a pulse duration of 15 μs.

3. EXPERIMENTAL RESULTS AND DISCUSSION

The maximal supersaturation attainable in the chamber is limited by spontaneous nucleation at the wall. In optical experiments, this value was 8–10 mbar. It turned out that the quality and shape of the crystal substantially depend on the growth regime in the anomalous state. For this reason, we determined at the first stage the growth conditions for crystals satisfying the criteria described in the previous section and suitable for measuring relaxation.

3.1. Growth Kinetics and Crystal Shape during the Fast Growth Phase at High Supersaturation

The crystal growth rate after the transition to the anomalous state was studied earlier with the help of optical methods for a supersaturation which does not exceed ~6 mbar [5, 7]. The photographs of the crystal showed that the crystal shape during the first ~200 μs is close to a hexagonal prism. Small ripples were observed on the facets in the photographs, but the crystal as a whole has clear faceting at this stage, reflecting the hexagonal symmetry and indicating a slight anisotropy on the order of 1.5–3 in the kinetic growth coefficient. This conclusion is also confirmed in the present observations.

The crystals beginning to grow at a supersaturation exceeding 6 mbar demonstrate strong deviations from the hexagonal shape (see Fig. 1). It can be seen that the crystal initially resembles a hexagonal prism. However, 120–200 μs after the transition, the shape of the crystal is close to a sphere with noticeable “mounds.” Such a shape is encountered the most frequently, although quite exotic forms of crystals are also observed sometimes (see Fig. 5c below). Figure 2 shows the region in which surface turbulence is observed. It can be seen that the conditional boundary separating the stability and instability regions (hatched band) lies approximately at 6 mbar. It should be noted that this graph reflects only the cases when instability developed during the growth over the first 200 μs. Most crystals grown above the instability boundary have liquid inclusions in the bulk (see Fig. 5c below) as well as extended defects emerging at the surface; these defects cause considerable distortion of the crystal surface, which is especially pronounced in the equilibrium state attained after the growth stage. This renders these crystals invalid for relaxation measurements. Thus, the region in which the return to the normal state can be studied using the given method is limited by a supersaturation of approximately 6 mbar from above and by the boundary between the anomalous and normal phases from below.

3.2. Possible Reasons for Crystal Shape Distortion

These observations lead to a new insight at the results of measurement of crystal growth rates at high supersaturation (Fig. 3). The method of determining the crystal growth rate from the ratio of pressure amplitudes is strongly substantiated by the assumption that the crystal has a convex shape close to a sphere [7]. This is observed for crystals acquiring a nearly spherical shape (see Fig. 1). However, for the crystal shown in Fig. 5c, this assumption is violated and the above-described computational method leads to elevated values of the rate and kinetic growth coefficient. Consequently, until the crystal shape above the instability region is determined, the results of calculating the fast growth rate based on the given method should be treated as the upper boundary of the real values. Taking into account these remarks, we will consider the values of the average growth rate at the first half-wave of pressure oscillations (in the first ~200 μs) for crystals with an initial supersaturation of approximately 10 mbar (Fig. 4). Attenuation of subsequent pressure oscillations is associated with the growth/melting of atomically rough regions. The damping decrement makes it

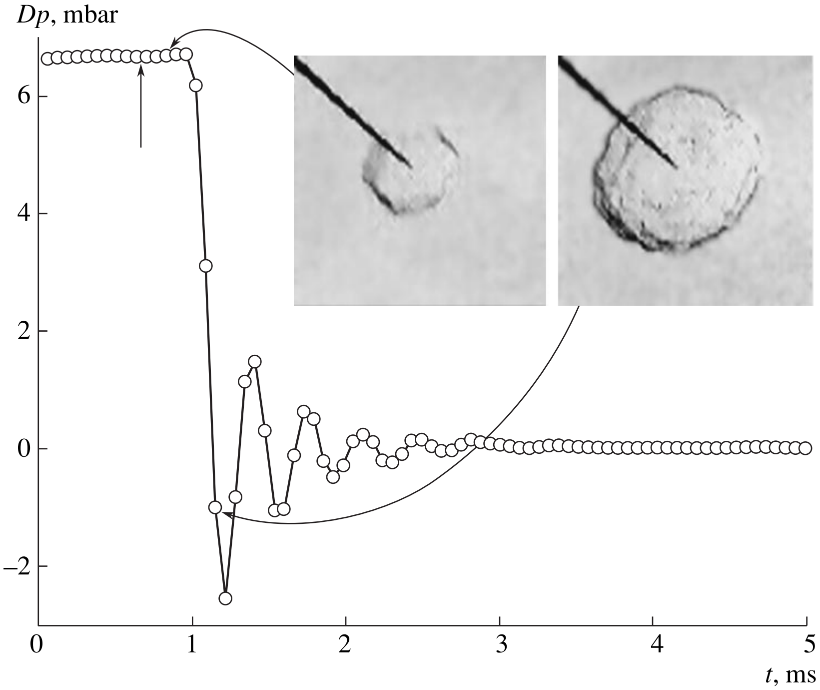

Fig. 1. Crystal growth at $T = 0.48$ K. The vertical arrow marks the instant corresponding to the application of a high-voltage pulse. At the initial stage, the crystal has a visible kinetic faceting with a slight anisotropy of growth. Instability leads to a nearly spherical shape of the crystal after about 200 μs.

possible to obtain an order-of-magnitude estimate of the kinetic growth coefficients for these surfaces for a supersaturation below 1 mbar (see Fig. 4). These values give the interval of values from which the return to the normal state begins.

According to experimental results, the crystal has well-defined facets prior to the transition to the anomalous state and grows due to mechanisms associated with defects [5, 7]. At this stage, the pattern of crystal growth suggests that the basal and lateral facets are in an atomically smooth state. Saturation as such does not violate the faceting transition. After a transition to the anomalous state, kinetic faceting of the crystal is observed in experiments [8], which only indicates an anisotropy in the crystal growth. This anisotropy can emerge during the growth of both atomically smooth and atomically rough facets. Indeed, the emergence of flat regions on the surface of a growing crystal was experimentally observed above the faceting transition also, when the boundary pertains to the atomically rough state [5, 15]. Consequently, it remains unclear whether the crystal surface returns to the atomically rough state or remains atomically smooth upon a transition to the anomalous phase.

Andreev [16] studied the stability of an atomically smooth surface in a tangential flow of a liquid and proved that the change in the energy of a stage leads to cylindrical faceting of the crystal. In our case, the liquid flows on the boundary mainly along the normal, which differs from the purely tangential flow considered in [16]. The experiments with a liquid jet directed to the basal facet of the crystals revealed that the facet remains undistorted at flow velocities up to 50 cm/s, which corresponds to growth rates of about 5 m/s [17].

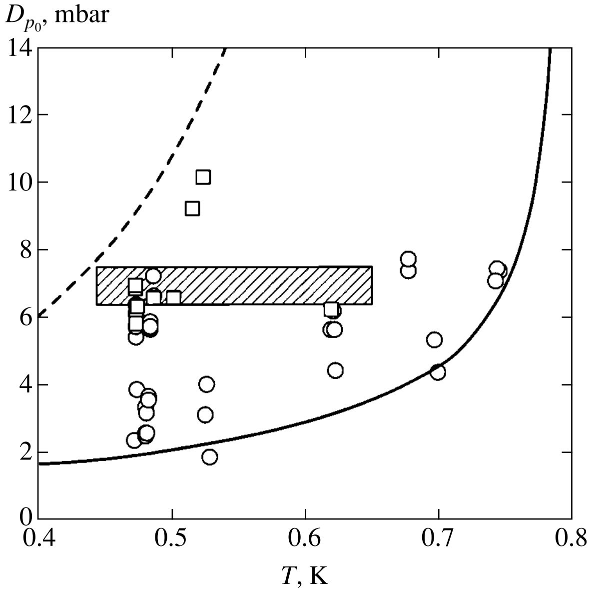

Fig. 2. Phase diagram of the anomalous state. The solid curve separates the regions of normal (below the curve) and anomalous growth. The circles indicate the growth series in which the instability of the crystal shape did not develop, while the squares correspond to crystals with a noticeable deviation from the hexagonal shape; the boundary between them is shown by the hatched region. The dashed curve shows the variation of limiting supersaturation for the tangential instability [18, 19].

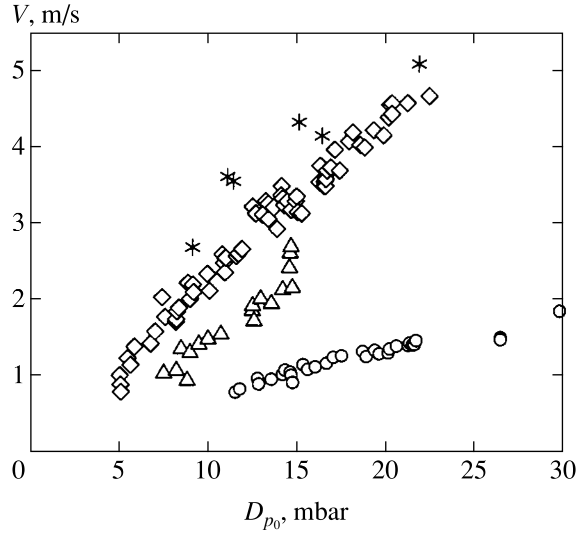

Fig. 3. Dependence of the crystal growth rate on supersaturation immediately after transition to the anomalous state: T = 0.653 (○), 0.533 (△), 0.421 (◇), and 0.206 K (∗).

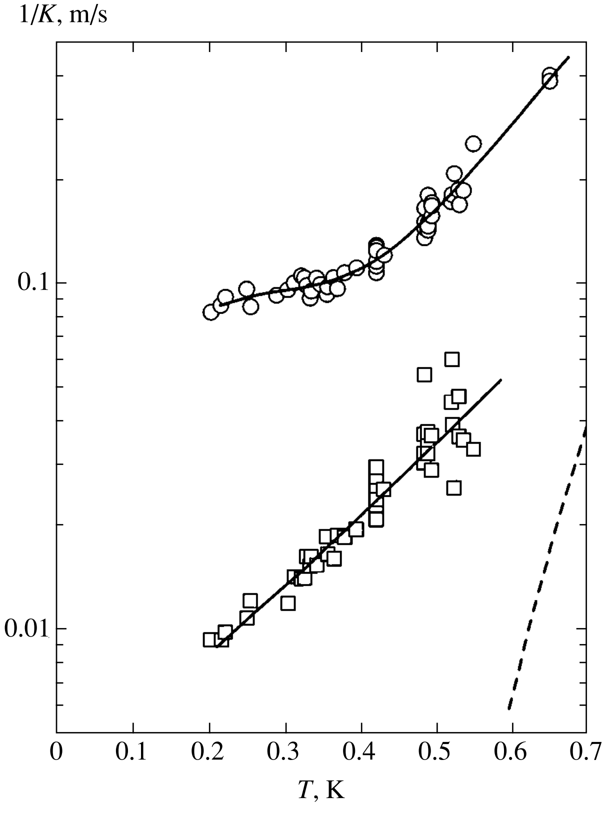

Fig. 4. Temperature dependence of the kinetic growth coefficient determined from pressure oscillations. The circles demonstrate the kinetics of the facets during the first ~200 μs after the formation of the fast phase, the squares show the kinetics of atomically rough surfaces at the final stage of oscillations. The dashed curve corresponds to the kinetic coefficient of the growth of atomically rough surfaces measured for small deviations from the equilibrium state by the crystallization wave technique.

Although the situation in experiments with a jet differs from the situation of crystal growth on a needle, the facet stability up to such high velocities speaks in favor of the conclusion about the stability of the crystal shape in the atomically smooth state in the case of a fast growth.

If, however, the transition to the anomalous phase leads to a transition of the facets to the atomically rough state, the singularity of the surface rigidity on closely packed facets disappears, and hydrodynamic instabilities associated either with crystallization waves of with the Kagan–Nozieres–Uwaha instability become possible [18, 19]. In the former case, ripples on the crystal surface could be due to generation and propagation of crystallization waves since the kinetic growth coefficients of the facets are quite large. The dispersion relation for the waves disregarding the gravitational contribution as well as the tangential liquid flow (see below) has the form [2]

$$\omega^2 + i\frac{1}{K}\frac{\rho\rho'}{\Delta\rho^2}\omega k - \frac{\alpha\rho}{\Delta\rho^2}k^3 = 0, \qquad (7)$$

where ω and k are the frequency and the wavevector of a crystallization wave and α is the surface rigidity. To estimate the surface rigidity, we disregard the dependence of the surface energy on the orientation and assume that the surface energy is about 0.2 erg/cm^2. For a running crystallization wave, the condition

$$k \ge \frac{1}{4K^2}\frac{\rho}{\alpha}\left(\frac{\rho'}{\Delta\rho}\right)^2 \qquad (8)$$

must be observed; for $1/K \sim 10$ cm/s (see Fig. 4), this condition makes it possible to estimate the minimal wavevector as $k \sim 10^4$ cm^{-1} and the damping time for wave damping proportional to $\exp(-t/\tau)$ as

$$\tau \le 4K^3\frac{\alpha}{\rho'}\left(\frac{\Delta\rho^2}{\rho\rho'}\right)^2 \sim 10^{-6}\ \text{s}. \qquad (9)$$

These estimates show that the length of crystallization wave propagating over a facet is on the order of 10^{-4} cm and is too short to form the observed distortions on the facet surface. In addition, these waves must attenuate over a time two orders of magnitude shorter than the characteristic growth time. Thus, the excitation of crystallization waves is not responsible for the observed deformation of the crystal shape.

The stream of liquid flowing over the surface change the dispersion relation for crystallization waves and, according to Nozieres and Uwaha [18] and Kagan [19], may lead to surface instability. These authors observed an instability similar to the Kelvin–Helmholtz tangential discontinuity instability and found that a liquid flow along the normal does not lead to instability.[1] In the

---

[1] The conclusion drown in [17] concerning the surface instability during crystal growth is erroneous. The authors are grateful to A.Ya. Parshin for pointing out this circumstance.

case of free crystal growth at the center of the container, its kinetic faceting in the form of a hexagonal prism generates a tangential flow of the liquid with velocity v_t in the region of the edges, which might be a source of instability. In the presence of a tangential liquid flow, the dispersion relation for crystallization waves has the form

$$\omega^2 + \left(i\frac{1}{K}\frac{\rho\rho'}{\Delta\rho^2}\omega k + 2v_t\frac{\rho}{\Delta\rho}\right) + k^2\left(v_t\frac{\rho}{\Delta\rho}\right)^2 - \frac{\alpha\rho}{\Delta\rho^2}k^3 = 0. \tag{10}$$

The positive imaginary part of frequency leads to an exponential increase in the perturbation amplitude. Since the observed instability develops over a time of approximately 100 μs, the values of the tangential velocity must be quite large. Assuming that the peak value of $\mathrm{Im}(\omega) = 10^4\ \mathrm{s}^{-1}$ and using the kinetic growth coefficient from Fig. 4, we can numerically calculate the required values of v_t. These values lie in the interval 25–40 cm/s. Assuming that tangential velocities are proportional to the velocity v_n of the normal flow of the liquid and this relation (geometrical factor) is approximately constant in the temperature interval studied here, we can calculate the temperature variation of supersaturation required for the development of tangential instability (see Fig. 2). The geometrical factor $v_t/v_n \sim 0.2$ is chosen in such a way that the stability boundary passes through point $Dp = 6$ mbar at $T = 0.4$ K. It can be seen that an increase in temperature leads to a decrease in the kinetic growth coefficient; consequently, a higher velocity of the liquid flow (and, hence, a higher pressure) is required. Such a steep dependence disagrees with the experimental data and the observed instability is hardly a consequence of the Kagan–Nozieres–Uwaha tangential instability [18, 19] developing due to nonuniformity of the helium flow.

The crystal surface distortions are probably associated with the emergence and development of turbulence in the liquid flow near the crystal since the flow velocities are high (see Fig. 3). Our results are insufficient to draw an unambiguous conclusion concerning this process.

3.3. *Relaxation to the Normal State in front of the Instability Boundary*

In this region, the crystals correspond to the above-formulated criteria, contain insignificant defects, and have the shape of a hexagonal prism. The reconstruction of the crystal dimensions from the projection introduces an error of about 0.01 mm in the measurement of linear sizes. The time interval between the shots was varied from 20 to 100 ms, which sets the lower limit on a facet growth rate of ~0.01 cm/s. The growth rate is limited from above by the helium inflow and does not exceed 0.1 cm/s in our experiments. For supersaturations $Dp \geq 0.1$ mbar, the corresponding kinetic growth coefficients lie in the region $1/K \geq 5$ m/s. The results for the growth coefficients for the fastest lateral facets will be given below. The values of K for the basal facets can be obtained from these data by multiplying them with

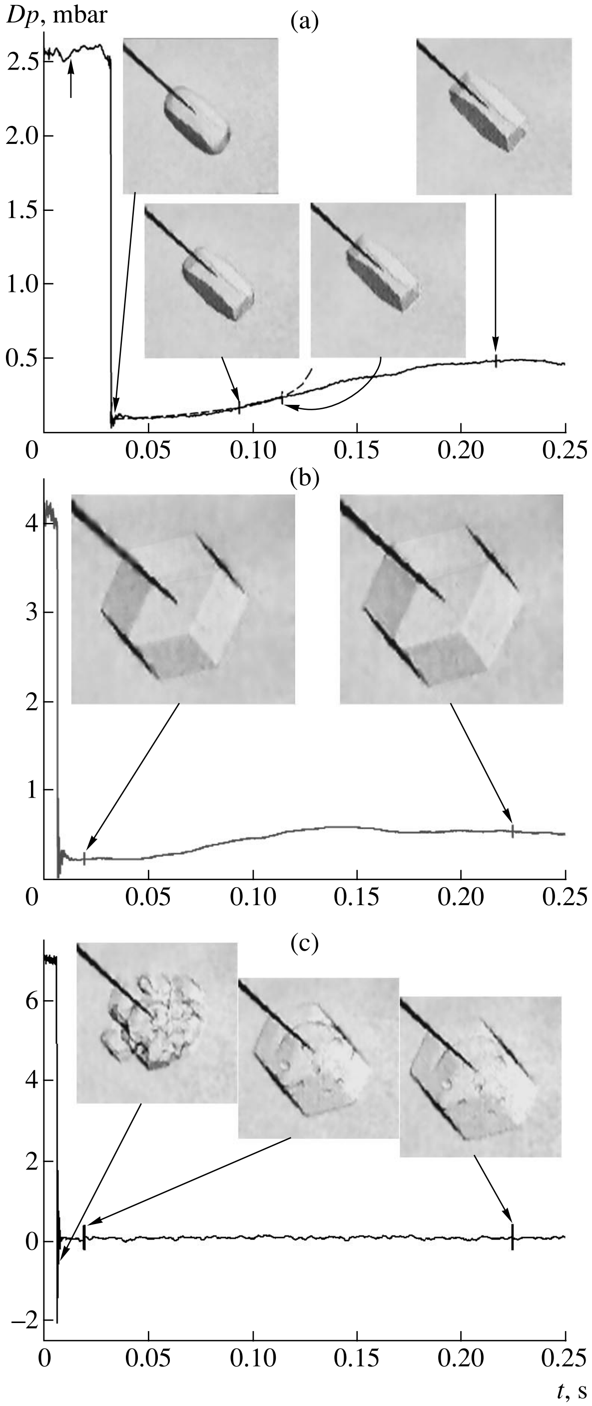

Fig. 5. Examples of crystal growth at the stage of relaxation to the normal state at 0.48 K. (a) Relaxation of the crystal with the initial supersaturation near the boundary of the anomalous region. (b) Relaxation of the crystal for a residual pressure of approximately up to 0.25 mbar. (c) The shape and relaxation of a crystal formed at a high supersaturation.

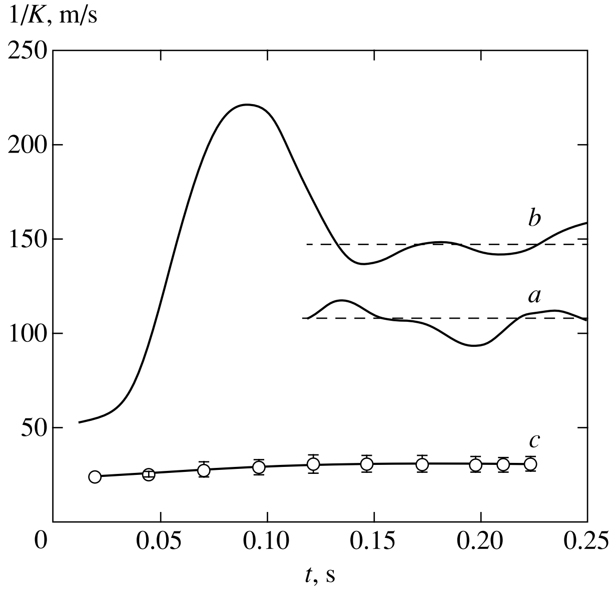

Fig. 6. Variation of the kinetic growth coefficient at the final stage of relaxation. The notation of the curves corresponds to the series in Fig. 5. The time is measured from the instant of pressure jump.

the anisotropy coefficient, which lies in the interval 0.3–0.6 at T ~ 0.5 K and in the range 0.05–0.15 at T ~ 0.7 K.

Crystal Relaxation at T = 0.48 K

Let us consider the relaxation of the crystals formed near the boundary of the anomalous phase (Fig. 5a). The kinetic coefficient of fast growth, which is determined from the amplitude ratio, is $1/K = 0.14$ m/s. After completion of the fast growth phase, the pressure in the container stabilizes at a value exceeding the equilibrium pressure by the Laplacian pressure for a plane surface. According to the rounded shape of the crystals in Fig. 5a, this difference amounts to about 0.07 mbar. The liquid inflow via the capillary leads to crystal growth primarily in the region of rounded edges, where the kinetic growth coefficient is higher than the growth coefficient for the facets. As long as atomically rough regions grow, the pressure variation reflects the increase in the curvature of these regions (dashed curve in Fig. 5a). Then the observed growth of the facets begins, and the kinetics of their growth can be determined using the technique proposed above (Fig. 6). It can be seen that, beginning at t ~ 100 ms, the kinetic growth coefficient remains unchanged within the measurement error. For time periods $t < 100$ ms, the lower boundary of coefficient $1/K \leq 10$ m/s. Thus, the mobility of the facets decreases at least by two orders of magnitude approximately 20 ms after the termination of the fast growth stage.

Crystal growth due to atomically rough regions increases the delay beginning from which out technique is applicable. From this standpoint, series of measurements in which the pressure in the container differs from the equilibrium pressure by a large value ($Dp \geq$ 0.2 mbar) after the termination of the fast growth stage are preferable. In this case, the curvature of the edges is small and the growth resource due to atomically rough regions is exhausted much more rapidly. Figure 5b shows an example of such a series of measurements. During the fast growth, the kinetic coefficient is 1/K = 0.14 m/s. It can be seen from the photographs that, beginning with t ~ 20 ms after the pressure jump, the crystal increases in size due to facet growth. The corresponding time dependence of the kinetic growth coefficient is shown in Fig. 6. During the period from 20 to 100 ms, a small (approximately by a factor of three) relaxation of coefficient K can be observed, which approaches the value $1/K = 150 \pm 24$ m/s. Thus, kinetics relaxation mainly occurs over a time shorter than 20 ms. It remains unclear whether the inverse transition occurs jumpwise or continuously.

It was noted above that analysis of relaxation for high supersaturations is limited by the instability of the crystal shape during the fast growth stage and, as a consequence, the defectiveness and strong distortion of the crystal facets. However, we managed to detect the growth of a crystal which, in spite of the above-mentioned circumstances, had a shape suitable for such measurements (see Fig. 5c). During fast growth, the kinetic coefficient $1/K$ is 0.097 m/s; i.e., this coefficient is approximately twice as large as that for the crystals shown in Figs. 5a and 5b. Liquid inclusions in the crystal do not change their positions. The pressure in the container at the relaxation stage changes insignificantly and is equal to 0.1 ± 0.06 mbar. The error in the measurement of the phase-equilibrium pressure may change the scale of K values by no more than a factor of two in either direction. Figure 6 shows the values of the kinetic growth coefficients calculated for Dp = 0.1 mbar as well as relative errors associated with noise. It can be seen that the kinetic growth coefficient slowly decreases, remaining approximately an order of magnitude larger than the equilibrium value, but two orders of magnitude smaller than the value measured during fast growth.

Relaxation at T = 0.69 K

At this temperature, the range of supersaturations at which the crystals suitable for measurements are formed is not large (see Fig. 2). However, an important advantage of experiments in this region is that the time interval between the instant of crystal formation and its transition to the anomalous state is quite large (Fig. 7). This makes it possible to measure the growth kinetics prior to the transition together with relaxation measurements. Figure 7 shows two series of growth with delays of 16 ms (a) and 3.6 ms (b). It should be noted that the crystal volume in series (a) with a high growth anisotropy of 0.053 prior to the jump amounted approxi-

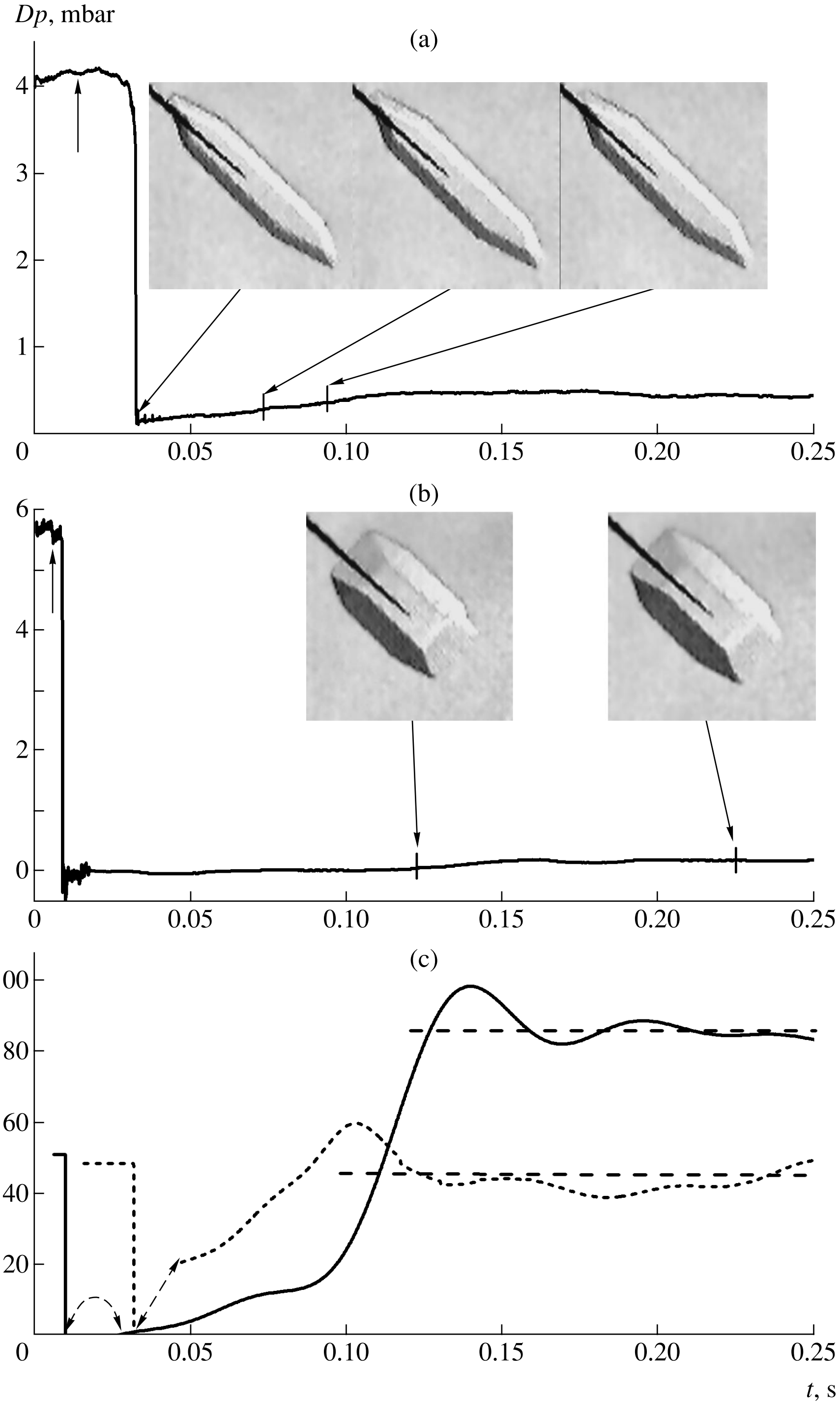

Fig. 7. Relaxation of crystals at 0.69 K for two different values of the initial supersaturation. The kinetic coefficients of crystal growth before and after the anomalous growth differ by no more than a factor of two. Two-sided arrows indicate the intervals outside the sensitivity limits of the given technique.

mately to 50% of the final volume; i.e., at the fast growth stage, the crystal size has increased by just 25%. For series (b), we managed to determine the fast kinetic growth coefficient $1/K_{\text{fast}} = 0.22$ m/s. The lower curve shows the variation of the kinetic growth coefficient. It can be seen that the value of K before the transition differs only slightly from the value after the relaxation. The difference by a factor of two is immaterial since, according to the observation of the shape of kinetic faceting in the normal growth regime determined by defects [5, 10], the growth rates differ by a factor of several units even for equivalent facets. The values of K

at $T = 0.68$ K are higher than at 0.48 K, which is in agreement with the available experimental data [10, 12].

As at a temperature of 0.48 K, fast relaxation occurs during approximately 20 ms after the transition and the kinetic coefficient $1/K$ assumes values equal to 10–20 m/s. Subsequently, the kinetics returns to the normal regime over a time approximately equal to 100 ms. Comparison of relaxation curves in Figs. 7a and 7b shows a tendency that can also be observed in Fig. 6: the time of slow relaxation to the normal state increases with the initial supersaturation.

4. DISCUSSION

The experiments show that the main (fast) relaxation occurs over a time approximately from 1 to 20 ms after the transition to the anomalous state. This time interval could not be resolved by our technique; it is known only that the kinetic growth coefficient $1/K$ was in the interval 0.05–0.25 m/s at the initial point of the transition and dropped to 10–20 m/s at the final point. It remains unclear whether the main return was jumplike or continuous. Furthermore, relaxation to normal values close to the growth coefficient prior to the transition occurs with a characteristic time of approximately 100 ms. A tendency towards an increase in the slow relaxation time (see Figs. 6 and 7) with increasing initial supersaturation is observed. However, this conclusion cannot be regarded as final since a considerable retardation of relaxation was observed in crystals formed at high supersaturations (see Figs. 5c and 6). In these cases, surface growth instability leading to the emergence of defects in the crystal, the formation of inclusions and, probably to saturation of the crystal with vacancies was observed. Observations of the last stage of the process complete the pattern of the effect.

Processes occurring during a long time and leading to a sharp increase in the growth rate as well as the fast growth mechanism itself still remain unclear. The only phenomenon having common features with the given effect (the phase diagram, the statistical nature of the transition, and the effect of impurities) is the effect described in [11]. A combination of these effect has further reduced the list of possible sources of the fast growth. Since acceleration took place in the latter case at a perfect facet, sources of the growth must be formed by the process itself. Two-dimensional nucleation is ineffective for such small deviations from equilibrium. A qualitatively new source of the growth was proposed in [20], where it was proved that collisions of the stages can lead to their transfer to the next crystallographic plane, thus ensuring the growth of the perfect facet. An increase in temperature and the introduction of impurities decelerates the stages, which requires a high supersaturation for realizing such a scenario. This picture is in qualitative agreement with the experiment and it is perhaps this mechanism that ensures a fast kinetics of the facets. However, the reason why this mechanisms is not triggered for a long time and the crystal grows in the conventional slow mode is not clear as yet. The explanation of the fast growth based on a model proposed in [21] does not agree qualitatively with the experimental results.

ACKNOWLEDGMENTS

The author is grateful to A.Ya. Parshin for a detailed and critical appraisal of this research. Thanks are also due to Yu.M. Kagan for his interest in this work and for fruitful discussion in the course of the experiments.

This study was financed by the Russian Foundation for Basic Research (project no. 02-02-16772).

REFERENCES

1. A. A. Chernov, in *Modern Crystallography,* Vol. 3: *Crystal Growth*, Ed. by B. K. Vaĭnshtein, A. A. Chernov, and L. A. Shuvalov (Nauka, Moscow, 1980; Springer, Berlin, 1984).
2. A. F. Andreev and A. Ya. Parshin, Zh. Éksp. Teor. Fiz. **75**, 1511 (1978) [Sov. Phys. JETP **48**, 763 (1978)].
3. V. L. Tsymbalenko, Phys. Lett. A **211**, 177 (1996).
4. V. L. Tsymbalenko, Phys. Lett. A **257**, 209 (1999).
5. V. L. Tsymbalenko, J. Low Temp. Phys. **121**, 53 (2000).
6. V. L. Tsymbalenko, Pis'ma Zh. Éksp. Teor. Fiz. **77**, 288 (2003) [JETP Lett. **77**, 243 (2003)].
7. V. L. Tsymbalenko, Zh. Éksp. Teor. Fiz. **119**, 1182 (2001) [JETP **92**, 1024 (2001)].
8. V. L. Tsymbalenko, Phys. Lett. A **274**, 223 (2000).
9. V. L. Tsymbalenko, Pis'ma Zh. Éksp. Teor. Fiz. **78**, 965 (2003) [JETP Lett. **78**, 493 (2003)].
10. V. L. Tsymbalenko, Fiz. Nizk. Temp. **21**, 162 (1995) [Low Temp. Phys. **21**, 120 (1995)].
11. P. J. Hakonen, J. P. Ruutu, G. Tvalashvili, *et al.*, J. Low Temp. Phys. **112**, 117 (1998).
12. S. Balibar, F. Gallet, P. Nozieres, *et al.*, J. Phys. (Paris) **46**, 1987 (1985).
13. V. L. Tsymbalenko, Cryogenics **36**, 65 (1996).
14. V. L. Tsymbalenko, Prib. Tekh. Éksp., No. 4, 161 (1997) [Instrum. Exp. Tech. **40**, 585 (1997)].
15. J. Bodensohn, P. Leiderer, and K. Nicolai, Z. Phys. B **64**, 55 (1986).
16. A. F. Andreev, Zh. Éksp. Teor. Fiz. **106**, 1219 (1994) [JETP **79**, 660 (1994)].
17. L. A. Maksimov and V. L. Tsymbalenko, Zh. Éksp. Teor. Fiz. **122**, 530 (2002) [JETP **95**, 455 (2002)].
18. P. Nozieres and M. Uwaha, J. Phys. (Paris) **47**, 263 (1986).
19. M. Yu. Kagan, Zh. Éksp. Teor. Fiz. **90**, 498 (1986) [Sov. Phys. JETP **63**, 288 (1986)].
20. A. Ya. Parshin and V. L. Tsymbalenko, Pis'ma Zh. Éksp. Teor. Fiz. **77**, 372 (2003) [JETP Lett. **77**, 321 (2003)].
21. N. Gov, J. Low Temp. Phys. **129**, 25 (2002).

Translated by N. Wadhwa

Journal of Experimental and Theoretical Physics, Vol. 99, No. 6, 2004, pp. 1223–1232.
Translated from Zhurnal Éksperimental'noĭ i Teoreticheskoĭ Fiziki, Vol. 126, No. 6, 2004, pp. 1402–1412.
Original Russian Text Copyright © 2004 by Borisenko, Constantinian, Kislinskiĭ, Ovsyannikov.

SOLIDS
Electronic Properties

Andreev States and Shot Noise in Bicrystal Junctions of Cuprate Superconductors

I. V. Borisenko, K. Y. Constantinian*, Yu. V. Kislinskiĭ, and G. A. Ovsyannikov

Institute of Radio Engineering and Electronics, Russian Academy of Sciences,
Moscow, 125009 Russia
**e-mail: karen@hitech.cplire.ru*

Received February 6, 2004

Abstract—Experimentally observed features of the electrical and noise characteristics of bicrystal junctions of cuprate superconductors, such as linearity of the critical current density versus square root of the junction transparency and increase in the spectral density of shot noise for small bias voltages (below the superconducting gap), indicate that the superconducting current in cuprate bicrystal junctions is determined by the passage of quasi-particles through a potential barrier at the superconductor boundaries. This process involves bound states appearing as a result of multiple Andreev reflections in superconductors with dominant wavefunction components of the $d_{x^2-y^2}$ symmetry type. At the same time, interpretation of the experimental current–phase and current–magnetic field curves requires that the character of faceting at the bicrystal junctions would be also taken into account. *© 2004 MAIK “Nauka/Interperiodica”.*

1. INTRODUCTION

Shortly after the discovery of the Josephson effect, according to which Cooper pairs penetrate through a thin insulator layer (potential barrier) between two superconductors, it was pointed out [1] that the superconducting current I_S is proportional to the probability of electron tunneling, or the barrier transparency D, averaged over directions of the carrier momentum: $I_S \propto D$. Note that this behavior differs from that expected for a two-particle process, in which case the current would be proportional to D^2. Thus, the superconducting current I_S is on the same order of magnitude as the normal (single-particle) current ($I_N \propto D$). In this context, it was suggested [1] that the transport of Cooper pairs is a complex process proceeding via an “intermediate” electron–hole state in which the pair are dissociated so that the barrier transparency for such a pair is the same as that for single charge carriers. It was theoretically established, first for the superconductor–normal metal–superconductor (SNS) junctions [2] and somewhat later (in the 1990s) for the superconductor–insulator–superconductor (SIS) junctions [3], that these intermediate states are related to multiple Andreev reflections in superconductors.

In the case of tunneling junctions with a small transparency of the boundary, the midgap states (called the Andreev bound states) have energies close to the superconducting gap width Δ. In SNS junctions (with $D \approx 1$ [2]), as well as in the tunneling junctions involving cuprate superconductors with dominating wavefunction components of the $d_{x^2-y^2}$ symmetry type (D-type superconductors), Andreev levels occur near the Fermi surface (low-energy levels) [4–6]. Since the superconducting current is determined by the derivative of the level energy with respect to the phase difference φ of the wavefunctions of superconductors [7], the behavior of superconducting currents in DID and SNS junctions differ from that in SIS junctions. In particular, SNS junctions are characterized by the critical current $I_c(T)$ linearly increasing in a broad temperature range, whereas the temperature dependence of the critical current in SIS junctions rapidly reaches saturation [8]. In addition, the behavior of $I_c(T)$ in DID junctions depends on the orientation of D-type superconductors [5, 9, 10].

The influence of Andreev states on the phase and temperature dependences of the critical current in bicrystal junctions of cuprate superconductors has been experimentally studied in [11–14]. Alff *et al.* [12] also observed peculiarities in the current–voltage characteristics of such junctions that were caused by the presence of low-energy Andreev levels. Previously, we have pointed out certain features in the properties of bicrystal junctions, related to the low-energy Andreev levels in bicrystal junctions of cuprate superconductors. These peculiarities were manifested both in the electrical characteristics of junctions [13, 14], and in the appearance of excess shot noise at small voltages in such contacts [15–18]. However, despite a large number of publications on the physical properties of contacts involving metal oxide superconductors with high critical temperatures (see, e.g., review [19] and references therein), no systematic experimental investigations into the features of shot noise in such systems have been performed so far. The $1/f$ type noise in a bicrystal junction was studied by Kawasaki *et al.* [20], but

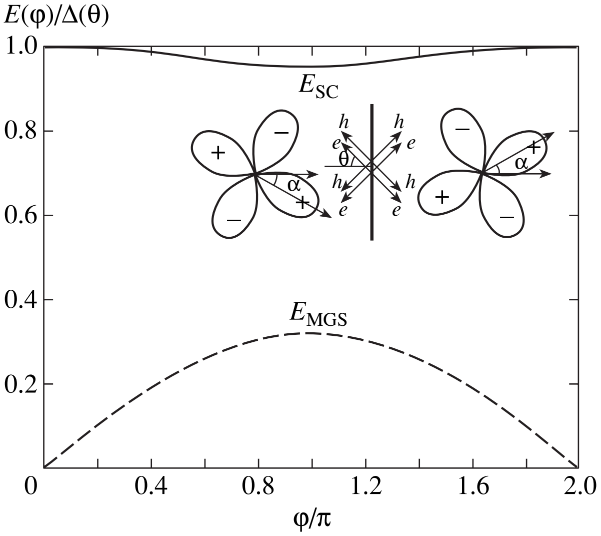

Fig. 1. The phase dependence of the energy of Andreev levels in a tunneling junction between S-type superconductors (solid curve) and the low-energy Andreev levels in a $D_\alpha ID_{-\alpha}$ junction (dashed curve) with a transparency of $D = 0.1$. The inset shows a schematic diagram of the bicrystal junction between two D-type superconductors with symmetric misorientation of the crystallographic axes relative to the direction of incidence of electrons and holes.

their data cannot be used to evaluate the effective transferred charge Q, which requires measurements of the shot noise to be performed at much higher frequencies. It should be noted that measurements of the spectral density of shot noise and the dependence of Q on the applied voltage provides additional information about the mechanism of charge transfer in the junction.

This paper presents the results of experimental investigations of the electrical and noise characteristics of bicrystal junctions of cuprate superconductors and considers the influence of low-energy Andreev bound states on the current transport in such junctions.

2. ANDREEV STATES IN SYMMETRIC SUPERCONDUCTING BICRYSTAL JUNCTIONS

It was theoretically established [2, 3] that, in the course of multiple Andreev reflections at the boundaries of usual (S-type) superconductors, one electron is reflected as a hole and the Cooper pair passes to a superconductor. The Andreev bound states are localized within a boundary layer at the interface, which has a thickness on the order of the coherence length. The energy of Andreev levels in the junctions between S-type superconductors can be expressed as

$$E_{SC} = \pm\Delta\sqrt{1 - D\sin^2(\varphi/2)}, \qquad (1)$$

where Δ is the superconducting energy gap width.

For junctions with a low transparency of the barrier ($D \ll 1$), the levels occur near the superconducting gap (Fig. 1). Most properties of the SIS junctions can be described both using the tunneling Hamiltonian model and in terms of the Andreev bound states.

The superconducting order parameter in a D-type superconductor changes sign when the momentum of a quasi-particle rotates by 90° (see the inset to Fig. 1). As a result, the phases of Andreev reflections in the junctions between D-type superconductors may have opposite signs for the incident and mirror-reflected quasi-particles. The sequence of mirror and Andreev reflections in the (110) plane leads to the formation of bound states with the energy E_{MGS} at the Fermi level [4]. On the current–voltage characteristics of junctions between a normal metal and a D-type superconductor (NID contacts), a peak in the density of states is manifested by anomalous conductivity observed at low applied voltage [21, 22].

The dependence of the energy of Andreev levels on the phase difference in a junction is determined by the angles of misorientation ($\alpha_{L(R)}$) of the crystallographic axes of D-type superconductors and by the angle of incidence (θ) of the quasi-particle. For mirror-symmetric ($\alpha_L = -\alpha_R = \alpha$) junctions ($D_\alpha ID_{-\alpha}$), the energy E_{MGS} of Andreev states for the angle $\alpha = 45°$ and the energy gap $\Delta_{R(L)} = \Delta_0\cos(2\theta + 2\alpha_{L(R)})$ (where $\Delta_0 = \Delta(\alpha = 0)$ depend on the phase as [5, 6]

$$E_{MGS} = \pm\Delta_{R(L)}\sin(\varphi/2)\sqrt{D(\theta)}. \qquad (2)$$

In contrast to the case described by Eq. (1), Andreev levels with the energies $E_{MGS}(\varphi)$ occur near the Fermi level even for $D \ll 1$, and their amplitudes do not exceed $\Delta_0\sqrt{D(\pi/4)}$.

Figure 2 shows the maximum energy of the Andreev bound states at $\varphi = \pi$ as a function of the incidence angle θ for various misorientation angles α in a symmetric junction with the typical transparency $D = 10^{-2}$. In the symmetric junction with $\alpha = 45°$, the low-energy Andreev states (E_{MGS}) are observed for all incident quasi-particles. As the misorientation angle decreases ($\alpha < 45°$), the angles θ for which the E_{MGS} levels are observed range within a 2α-wide interval relative to the directions $\theta = \pm\pi/4$. In other directions, the states with energies (E_{SC}) close to the energy gap appear. For $\alpha = 0$, the situation is close to that in the SIS junction, where the energies of Andreev states are described by formula (1).

Since the superconducting current is determined by the energies of Andreev states,

$$I_S \propto dE/d\varphi,$$

both contributions (1) and (2) should be taken into account for $0 < \alpha < 45°$ by adding the corresponding current components [6, 7, 11]. It should be noted that the current is proportional to the first power of the transparency D for the states described by formula (1), and to the square root of D for the states described by formula (2). The cone (angular range) of tunneling, which determines the fraction of quasi-particles producing the main contribution to the current, can be either wide ($D(\theta) = D_0\cos\theta$, $D_0 = D(\theta = 0)$, for δ-shaped barriers), or rather narrow ($D \propto \exp(-2\theta)$ for thick barriers) [23]. In bicrystal junctions, the case of a thin barrier is more likely to take place, since the barrier thickness for superconducting current must not exceed the coherence length ξ_0.

3. METHODS OF PREPARATION AND CHARACTERIZATION OF SUPERCONDUCTING JUNCTIONS

3.1. Sample Preparation

The Josephson junctions were formed on $(1\bar{1}02)$-oriented Al_2O_3 bicrystal substrates with a misorientation angle of ±12° between the $\langle 11\bar{2}0 \rangle$ crystallographic axes. The epitaxial films of $YBa_2Cu_3O_x$ (YBCO) cuprate with a thickness of 100–200 nm were grown at a substrate temperature of 750–770°C by means of cathode sputtering in an oxygen atmosphere at a pressure of 4 mbar. The cuprate films were deposited onto a CeO_2 buffer layer that was necessary to prevent the diffusion of aluminum from the substrate to the YBCO film at a high growth temperature. The 30-nm-thick epitaxial CeO_2 buffer layer was obtained by RF magnetron sputtering of a Ce target at 600–700°C in an $Ar–O_2$ gas mixture at a total pressure of 0.01 mbar. The epilayers were grown for the following epitaxial relations: $(001)YBCO/(001)CeO_2/(1\bar{1}02)Al_2O_3$ and $\langle 110\rangle YBCO/\langle 001\rangle CeO_2/\langle 11\bar{2}0\rangle Al_2O_3$. Then, 5-μm-long and 10-μm-wide bridges were formed in the YBCO film by means of ion-plasma etching and liquid-phase etching (0.5% Br_2 solution in ethanol) via a photoresist mask. In each sample, the bridges crossed the boundary at various angles γ (within 0–54°) relative to the normal to the interface. The deposition of CeO_2 film by sputtering a metallic Ce target, as well as the combined (ion-plasma and liquid-phase) etching of YBCO film, is an important original feature of the proposed technology [13, 14].

3.2. Methods of Measurements

The Josephson junctions obtained had the critical current density within $j_c = 10^4$–10^5 A/cm^2 and the characteristic voltage $V_0 = I_cR_N = 1$–2 mV (R_N is the junction resistance in the normal state) at $T = 4.2$ K. The current–voltage characteristics of these junctions were measures in a range of temperatures ($4.2\text{ K} < T < 77$ K), magnetic fields ($H \le 100$ Oe), and under the action of a monochromatic microwave radiation with the frequency $f_e = 30$–100 GHz. In order to reduce the influence of external electromagnetic fields, all measurements were performed in a shielded room, with signal filtration in all leads connected to the samples. The critical temperatures of the superconducting films, as determined from the results of resistance measurements at an ac current below 1 μA, fell within $T_c = 87$–89 K.

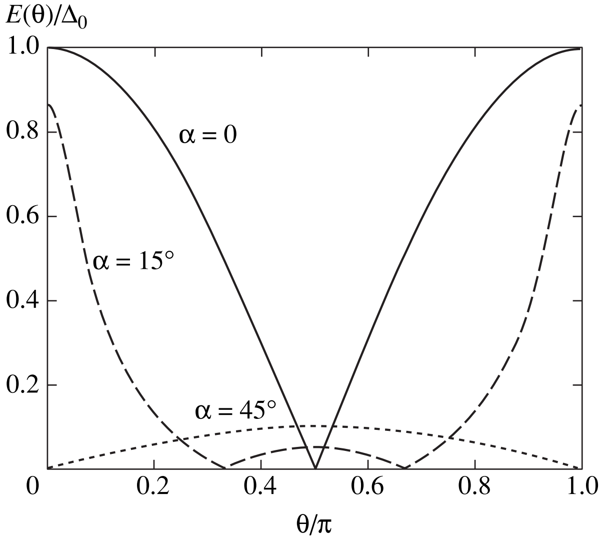

Fig. 2. Plots of the maximum energy of the Andreev bound states at $\varphi = \pi$ versus the quasi-particle incidence angle θ for various misorientation angles α in a symmetric bicrystal junction of D-type superconductors with a transparency of $D = 10^{-2}$.

The barrier layer transparency D (averaged over the momentum directions) was defined by the relation

$$D = \frac{2\pi^2\hbar^3}{e^2 p_F^2}\frac{1}{R_N S} = \frac{2\rho l}{3R_N S}, \tag{3}$$

where p_F is the Fermi momentum in YBCO, ρ is the resistivity of YBCO, l is the mean free path of electrons in the ab plane, and S is the contact area. For $\rho l = 4 \times 10^{-9}\ \Omega$ cm^2 and the typical values of $R_N S = (1–3) \times 10^{-7}\ \Omega$ cm^2, we obtain $D = (1–3) \times 10^{-2}$ [20, 22].

Figure 3 shows a schematic diagram of our experimental setup for the noise measurements. The measurements were performed in the decimeter wavelength range, where $1/f$ type noise is absent. The setup employed low-noise high-electron mobility transistors operating in the frequency range $f_a = 1$–2 GHz, with an intrinsic noise temperature of $T_{N1} = 8 \pm 2$ K and a gain of $G_1 = 20$ dB at $T = 4.2$ K. The balance input circuit ensured stable operation in a broad range of loads (10–100 Ω) and reduced the temperature of a background radiation reaching the sample via a coaxial cable. The noise temperature of the measuring circuitry contained contributions from the second amplification stage

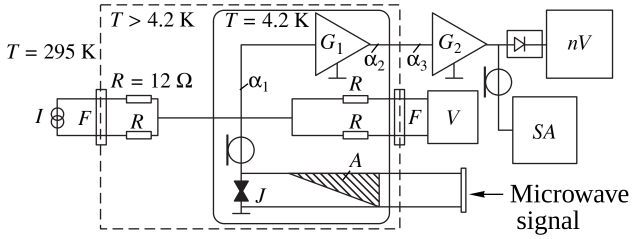

Fig. 3. Schematic diagram of the experimental setup for the noise measurements: (J) sample; (I) dc current source; (V) low-frequency voltage amplifier; (F) low-frequency filters; (SA) HP8563A spectrum analyzer; (G_1, G_2) first- and second-stage amplifiers; (nV) analog nanovoltmeter; diode symbol denotes a quadratic detector. Microwave signal is transmitted via a waveguide with cooled 20-dB attenuator A eliminating background irradiation of the sample.

(which occurred at room temperature and had an intrinsic noise temperature of $T_{N2} = 130$ K and a gain of $G_2 = 40$ dB) and the coaxial cable (with a damping coefficient of $\alpha_1 \leq 0.2$ dB) connecting the sample to the low-noise amplifier. This amplifier was connected to the second-stage amplifier occurring at $T = 300$ K via a rigid coaxial cable in a stainless-steel braid. This cable could be considered as consisting of two parts: the first, with an effective temperature of $T_{T1} \approx 30$ K and a damping factor of $\alpha_2 \leq 1.5$ dB, and the second, with $\alpha_3 \leq 0.5$ dB at $T_{T2} = 295$ K (see Fig. 3). As a result, the total noise temperature of the measuring system was

$$T_0 \approx T_{N1}$$
$$+ \frac{1}{G}\left[T_{T1}(1 - \alpha_2^{-1}) + T_{T2}(1 - \alpha_3^{-1}) + \frac{T_{N2}}{\alpha_1 + \alpha_2}\right] = 12\ \text{K},$$

which was on the same order of magnitude as the background radiation temperature ($T_b \approx 10$ K). Under conditions of good impedance matching between the sample junction and the low-noise amplifier, the accuracy of noise temperature determination was ±5 K. In order to minimize the influence of the background radiation reaching the sample via the rectangular waveguide, we used a cooled microwave absorber ensuring a 20-dB attenuation. The noise temperature of the measuring system was calibrated by varying the temperature of a 50-Ω-impedance matched load connected instead of the sample.

Parameters of bicrystal junctions measured at liquid helium temperature ($T = 4.2$ K)

Parameter	Sample			
	BC-9	BC-15	BC-16	BC-21
Misorientation angle α	33°	12°	12°	12°
I_c, μA	70	18	55	32
R_N, Ω	16	90	40	60
R_NS, Ω μm^2	10	45	20	30
Q_{max}/e	10	–	16	15
V_Q, μV	300 ($H = 0$)	–	30 ($H = 65$ Oe)	10 ($H = 45$ Oe)
ΔV, mV (for $Q \sim e$)	$V > 4$	25–70	20–60	5–20

The response signal voltage (proportional to the noise power P_N) was measured at the output of a quadratic detector. Simultaneously, the amplitude–frequency characteristic was measured at the amplifier output. The absence of resonance features on this characteristic in the course of noise measurements was evidence of a good impedance matching between the sample junction and the measuring circuit. By varying the inductance of the cable connecting the sample to the amplifier, it was possible to ensure nonresonance impedance matching in a broad range of normal resistances of the sample junctions ($R_N = 15$–$90\ \Omega$). However, exact quantitative determination of the spectral density of current fluctuations $S_I(V) \propto P_N/R_d$ (R_d is the differential resistance of the junction) and the corresponding effective transferred charge $Q(V) = S_I(V)/2I$ was possible only for the junctions with normal resistances within a narrower interval, $R_N = 20$–$60\ \Omega$. Data on the maximum effective transferred charge Q_{max}, the range of voltages ΔV where this charge was constant and equal to the electron charge, and the electric parameters of several junctions are presented in the table.

4. RESULTS AND DISCUSSION

4.1. Electrical Properties of Superconducting Bicrystal Junctions

Figure 4 shows the typical current–voltage characteristic of a bicrystal junction, which is well described by a resistive model with two channels of charge transfer, including the current of quasi-particles (V/R_N) and the superconducting current ($I_S(\varphi) = I_c\sin\varphi$). A small level of the excess current (deviation from the Ohm law) at voltages above 10 mV is evidence of the absence of direct (nontunneling) conductivity. However, the temperature dependence of the critical current (left inset to Fig. 4) is close to linear (to within the experimental accuracy), in contrast to a theoretical curve obtained for the tunneling junctions between S-type superconductors [8] that exhibits saturation for $kT < \Delta$. The junctions with direct conductivity, in which the low-energy Andreev states determine the superconducting current transport, usually exhibit an almost linear behavior of $I_c(T)$ in a broad temperature interval.

According to Fig. 2, the states of both types described by Eqs. (1) and (2) can be observed in the tunneling DID junctions depending on the incidence angle of quasi-particles, and the superconducting current consists of two parts [6, 11]:

$$I_S(f) = I_{\mathrm{SC}}(\varphi) + I_{\mathrm{MGS}}(\varphi).$$

The contribution due to Andreev states near the gap, which is described by Eq. (1), rapidly increases with the temperature (in proportion to $\Delta^2(T)$ according to the Ambegaokar–Baratoff law [8]) and exhibits saturation at low temperatures:

$$I_{\mathrm{SC}} \propto D_0\Delta_0\cos(2\alpha)\sin\varphi.$$

The contribution due to states near the Fermi level increases in proportion to $1/T$ with decreasing temperature and (for $kT \ll \Delta\sqrt{D}$) saturates at

$$I_{\mathrm{MGS}} \propto -\Delta_0\sin(2\alpha)D_0\cos\frac{\varphi}{2}\operatorname{sgn}\left(\sin\frac{\varphi}{2}\right)$$

(with the minus sign). Therefore, there must exist a certain temperature T^* at which the $I_c(T)$ curve exhibits a dip and the $I_S(\varphi)$ curve deviates from the sinusoidal law. For a barrier with the transparency $D = 10^{-2}$ and an YBCO superconducting gap of $\Delta_0 = 20$ meV, the estimation yields $T^* = 12$ K. The typical experimental curve of $I_c(T)$ presented in the left inset to Fig. 4 exhibits no such dip, which is probably related to faceting developed at the interface during epitaxial growth [19, 22]. Il'ichev *et al.* [11] studied bicrystal junctions of small thickness (comparable with the facet size) and observed a dip in $I_c(T)$ for a temperature at which the current versus phase curve deviates from the sinusoidal law. A nonmonotonic $I_c(T)$ curve was also observed for junctions of rather large thickness (on the order of several microns), but only for asymmetric bicrystal junctions [24].

At high temperatures ($T_c - T \ll T_c$), where the influence of thermal fluctuations is large, the temperature dependence of I_c is close to $(T_c - T)^{1/2}$ [6, 25]. This temperature interval features the most pronounced suppression of the D-type component of the order parameter near the bicrystal junction [26].

According to Eqs. (1) and (2), the superconducting current at $T \ll T_c$ depends on the transparency D in the DID junctions ($I_c \propto \sqrt{D}$) not in the same manner as in the SIS junctions ($I_c \propto D$). This difference is related to the fact that low-energy Andreev levels in the DID junctions occur at the Fermi level ($E \sim \Delta\sqrt{D}$, see formula (2)), whereas these levels in S-type superconductors occur near the gap ($E \sim \Delta$, see formula (1)). The behavior observed in our experiments seems more like it obeys the root law: $I_c \propto 1/\sqrt{R_{\mathrm{N}}S} \propto \sqrt{D}$ (see the right inset to Fig. 4). Despite a rather large scatter of experimental points (characteristic of the junctions involving cuprate superconductors [19]), the best fit (minimum deviation) of $I_c(D)$ was observed for the $I_c \propto \sqrt{D}$ curve. We believe that the observed dependence of the energy of Andreev levels on the junction transparency is quite stable to the action of various factors, including the boundary faceting, which leads to the appearance of both symmetric ($\mathrm{D}_\alpha\mathrm{ID}_{-\alpha}$) and asymmetric ($\mathrm{D}_\alpha\mathrm{ID}_0$ junctions). However, the $\mathrm{D}_\alpha\mathrm{ID}_{-\alpha}$ junctions according to formula (2) at low temperatures have $I_S \propto \Delta_0 D_0$, whereas the $\mathrm{D}_\alpha\mathrm{ID}_0$ junctions are characterized by $I_S \propto \Delta_0 D_0^2$ [5]. Therefore, the superconducting current for $D_0 < 1$ is determined by the regions with symmetric misorientation of the crystallographic axes.[1] It is not excluded that, in the case of suppression of the order parameter, the D-type component may influence the behavior of $I_c(D)$ [26]. It should be noted that a dependence of the $I_c \propto \sqrt{D}$ type was theoretically predicted for SIS contacts with a thick potential barrier [28]. For such SIS junctions, the difference of the spectrum of the Andreev bound states from the spectrum according to Eq. (1) leads to a different dependence of I_c on the barrier transparency. However, realization of the mechanism described in [28] requires low transparency of the boundary ($D \leq 10^{-8}$) and weak influence of the depairing factors on the density of states.

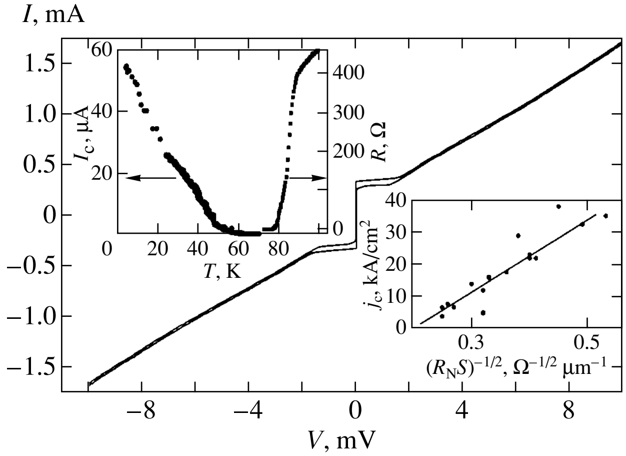

Fig. 4. The typical current–voltage characteristic of a bicrystal junction measured at $T = 4.2$ K. The left inset shows the temperature dependence of the critical current I_c and the resistance R; the right inset shows a plot of the critical current density versus characteristic normal resistance ($R_{\mathrm{N}}S$) of the junction.

---

[1] Inhomogeneity (roughness) of the bicrystal junction on a smaller scale (on the order of the Fermi wavelength of quasi-particles ($\lambda_F \approx 0.01$ μm) breaks the coherence of Andreev reflections for small incidence angles of quasi-particles ($4\pi\eta(\lambda)\cos\theta > \pi$, where η is the characteristic size of the junction inhomogeneity in the direction of current flow [27].)

4.2. The Dependence of the Critical Current on the Magnetic Field

Figure 5 presents the experimental dependence of the critical current on the magnetic field, $I_c(H)$, for one of the bicrystal junctions studied. As can be seen, the curve is significantly different from the Fraunhofer diffraction pattern typical of junctions with a small characteristic inhomogeneity size, $w < \lambda_J$ (in this case, w is the width of bridges crossing the bicrystal junction), where λ_J is the Josephson penetration depth [8]. The observed $I_c(H)$ curve can be related to inhomogeneity (roughness) of the junction related to faceting at the interface: previously, such patterns were observed for the misorientation angles greater than 10° (but smaller than 45°) [29]. It was demonstrated [30] that the experimental behavior presented in Fig. 5 could be well described in terms of a system of parallel Josephson junctions with a certain distribution of critical currents. Some bicrystal junctions exhibited $I_c(H)$ curves in which the ratio of the critical current to local maximum was below two and the subsequent $I_c(H)$ peaks weakly decreased with increasing magnetic field. It was shown [30] that the junctions of this kind have to be considered with regard to the presence of facets possessing the properties of π-contacts [6, 25].

4.3. The Phase Dependence of the Critical Current

The phase dependence of the superconducting current, $I_S(\varphi)$, in a Josephson junction is determined by the character of conductivity between two superconductors in contact with each other. At relatively high temperatures ($T_c - T \ll T_c$), the $I_S(\varphi)$ curve shape is very close to sinusoidal for the junctions of any type: $I_S(\varphi) = I_c \sin\varphi$. This dependence is retained in all low-transparency SIS junctions ($D \ll 1$) at low temperatures ($T \ll T_c$) [1, 5, 8], while in thick SNS junctions ($L > \hbar v_F/kT$) this law holds for $T < T_c$. In order to reveal deviations of the $I_S(\varphi)$ curve shape from sinusoidal, we have measured the current–voltage characteristics of bicrystal junctions exposed to a monochromatic microwave radiation $A\sin(2\pi f_e t)$ in the millimeter range (f_e = 40–100 GHz) [14]. The experiments were performed for the junctions featuring both symmetric (the bridge was perpendicular to the interface) and asymmetric current flow (the bridge was oriented at γ = 0–72° relative to the interface). Previously, the appearance of the subharmonic Shapiro steps in the junctions with nonsinusoidal $I_S(\varphi)$ curve was used to study the phase dependence of the critical current of thin tin bridges [31] and hybrid Pb/Au/YBCO superconducting heterojunctions [32].

Figure 6 presents the dependences of the first ($I_1(A)$) and subharmonic ($I_{1/2}(A)$) Shapiro steps on the radiation amplitude for the bicrystal junctions with $\gamma = 0$ and 54°. The inset to Fig. 6 shows theoretical curves calculated using a resistive model for $f_e > 2eI_cR_N/h$. The calculations were performed for the sinusoidal relation

$$I_S(\varphi) = I_c \sin\varphi$$

and for a system with small deviation from the sinu-

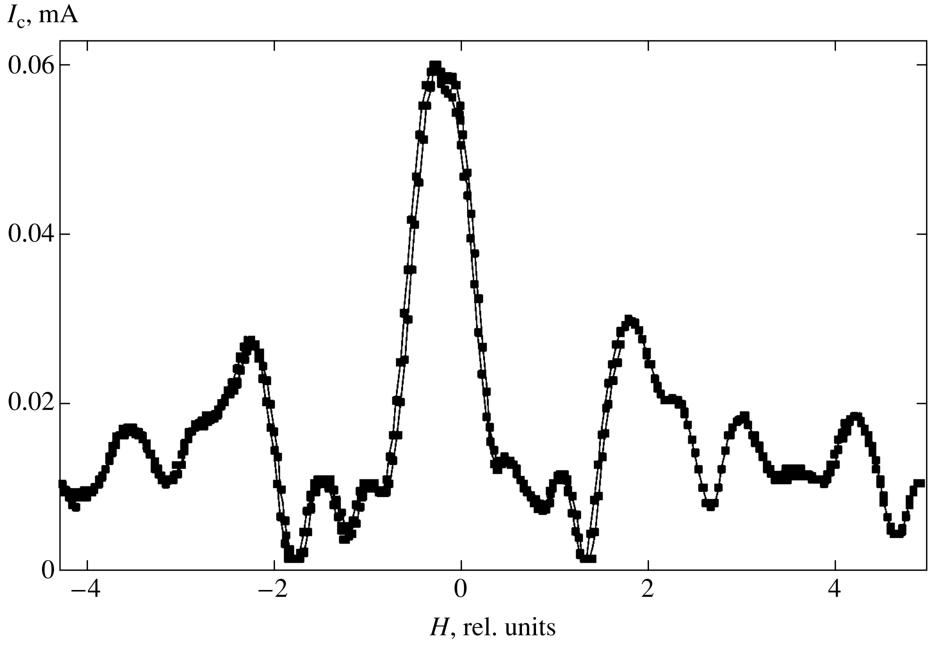

Fig. 5. Experimental curve of the critical current versus magnetic field applied to a bicrystal junction.

soidal law:

$$I_S(\varphi) = (1-\delta)I_c\sin\varphi + \delta I_c\sin(2\varphi), \quad \delta = 0.2.$$

As can be seen, the difference between the two theoretical and experimental $I_1(A)$ curves is relatively small. However, even a small deviation of the phase dependence from sinusoidal leads to the appearance of noticeable subharmonic Shapiro steps. The results of experimental measurements of the amplitude of subharmonic steps as a function of the bridge orientation angle γ showed the absence of $\sin(2\varphi)$ components in the angular interval $\gamma = 0$–36° (to within 5%). For the angles $\gamma > 40°$, the contribution of $\sin(2\varphi)$ exhibits monotonic growth.[2]

The deviation of the phase dependence from sinusoidal for the bicrystal junctions with asymmetric bias current is probably related to the current component along the bicrystal interface, which changes the spectrum of low-energy Andreev states. The maximum energy of Andreev states, $\Delta_0\sqrt{D_0} \approx 2$ meV, is comparable to the value ($\varepsilon = ev_F j_S \lambda^2 \approx 5$ meV) of the longitudinal component of the superconducting current for $j_S = 10^3$ A/cm^2, $v_F = 5 \times 10^4$ cm/s, and $\lambda = 0.1$ μm (here, λ is the London penetration depth).

4.4. Shot Noise in Bicrystal Junctions

Indirect evidence for the existence of excess nonthermal noise in the junctions involving cuprate superconductors has been obtained from data on the broadening of the line of intrinsic Josephson generation [33, 34] and on the noise characteristics of SQUIDs and electromagnetic radiation detectors [35]. However, the $1/f$ type fluctuations do not always explain the growth of noise (in particular, for processes in the microwave frequency range). From this standpoint, it was of interest to study the appearance of shot noise—a factor determining both broadening of the generation line and deterioration of the device characteristics.

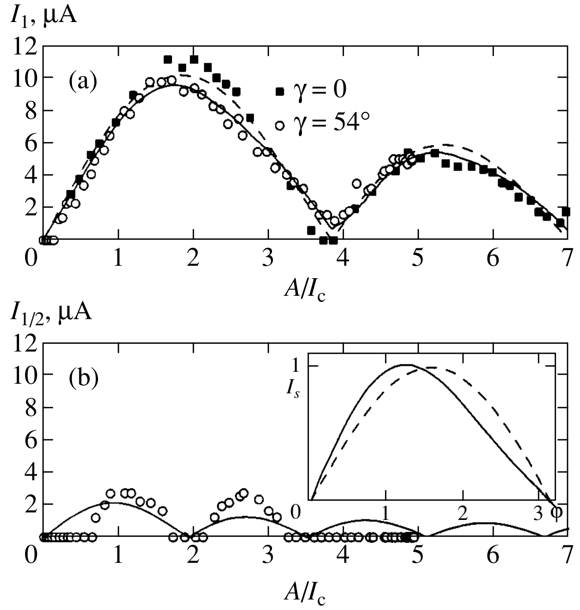

Fig. 6. Plots of (a) the first and (b) the subharmonic Shapiro steps versus microwave radiation amplitude (f_e = 100 GHz, T = 4.2 K). Curves show the dependences calculated using the resistive model for $I_S(\varphi) = I_c\sin\varphi$ (dashed) and $I_S(\varphi) = (1-\delta)I_c\sin\varphi + \delta I_c\sin2\varphi$ ($\delta = 0.2$) (solid); symbols present the experimental data for two orientations of bridges. The inset shows the corresponding $I_S(\varphi)$ curves.

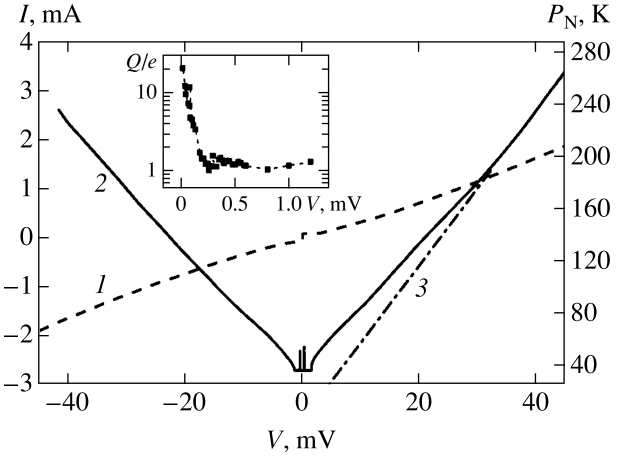

Fig. 7. Symmetric bicrystal junction: (*1*) current–voltage characteristic at T = 4.2 K; (*2*) noise power $P_N(V)$ expressed in kelvins; (*3*) theoretical shot noise temperature $T_{SH}(V) = (e/2k)I(V)R_d$. The inset shows the normalized effective charge $Q(V) = S_I(V)/2I$.

The noise characteristics of junctions were studied both in the autonomous regime ($H = 0$, $A = 0$) and in a weak magnetic field ($H < 100$ Oe) sufficient to suppress the critical current in the junction. Figure 7 shows the current–voltage characteristic and the noise power as a function of the bias voltage, $P_N(V)$), in the autonomous regime.[3] In the region of large voltages ($V > 30$ mV), the experimental $P_N(V)$ curve coincides with the classical dependence of the shot noise temperature,

$$T_{SH}(V) = (e/2k)I(V)R_d,$$

where R_d is the differential resistance of the junction.

---

[2] For a high-frequency external action ($f_e > 2eI_cR_N/h$), the ratio of the maximum amplitude of the subharmonic step to the critical current within the framework of the resistive model is equal to the ratio of the second and first harmonics in the phase dependence of the critical current.

[3] The noise power is expressed in the temperature units due to the special features of calibration of the experimental setup described in Section 3.2.)

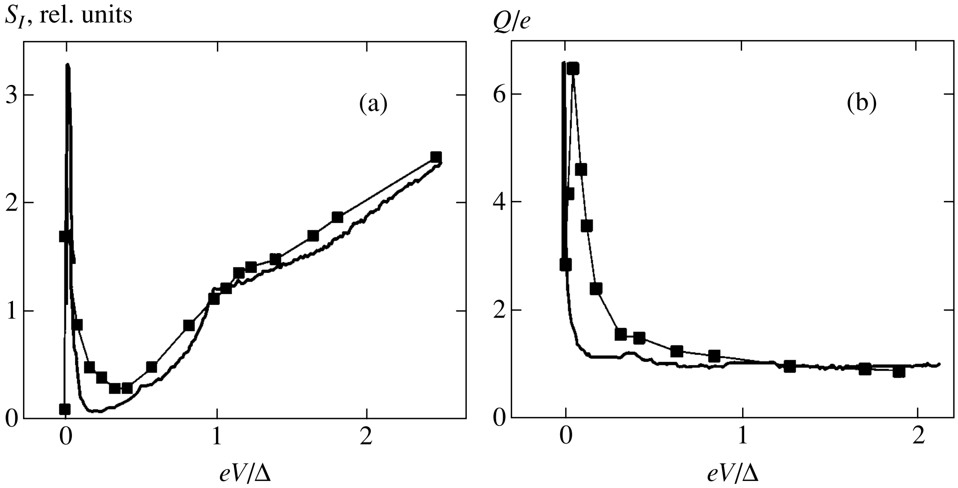

Fig. 8. (a) Spectral density of the noise current $S_I(V)$ at $T = 4.2$ K for a bicrystal junction with $R_N = 18\ \Omega$ (squares represent experimental data; the thick solid curve shows the results of theoretical calculation for a DID junction with $D = 0.01$ and $e\Delta_0 = 5$ mV [18]); (b) normalized effective charge $Q(V) = S_I(V)/2I$ (squares present experimental data; thick solid curve shows the results of theoretical calculation).

Calculations of $Q(V)$ were performed for the spectral density of noise $S_I = 2eI$ at $eV > kT, hf$ (this condition was satisfied in the experiment for $V > 0.7$ mV at $T = 4.2$ K and the amplifier operating at $f_a = 1$–2 GHz). Previously, an analogous dependence (similar to the curve in Fig. 7) of the spectral density of noise in a superconducting junction was observed for SIS contacts [36–39] in the region of voltages above Δ/e.

As can be seen from Fig. 7, the junction noise temperature T_N exceeds the shot noise temperature $T_{SH}(V)$ in a broad range of lower voltages ($0 < V < 30$ mV). In the region of small voltages ($V < 2$ mV) the $T_N(V)$ curve exhibits peaks caused by the appearance of the intrinsic Josephson radiation at the amplifier input. At small voltages, a sharp increase in the value of $R_d(V)$ (this dependence is not depicted in Fig. 7) affects impedance matching between the sample and amplifier. For this reason, below we will consider only the spectral density of shot noise $S_I(V) \propto 4kT_N/R_d$ and the effective charge $Q(V) = S_I(V)/2I$, since these quantities are independent of R_d. Taking into account variation of the $R_d(V)$ value, we observe an almost linear increase in $S_I(V)$ at $V > 4$ mV and a distinct peak at $V < 2$ mV. The inset to Fig. 7 shows the effective charge variation in the same junction, which reveals the growth in $Q(V)$ that is characteristic of the superconductor structures featuring multiple Andreev reflections [15–18]. The ratio Q_{max}/e exceeded ten (see table).

Figure 8 shows $S_I(V)$ and $Q(V)$ curves measured in the presence of an external constant magnetic field decreasing I_c and R_d of the junction. At a large bias voltage ($V > 10$ mV), the $S_I(V)$ curves observed in the magnetic field (Fig. 8a) and at $H = 0$ (Fig. 7) coincide, which allows us to use the noise density calibration performed for $S_I(V)$ in the autonomous regime.[4] As can be seen, the R_d variations at small bias voltages do not influence the shape of the curve of transferred charge versus voltage (Fig. 8b). The bias voltage in Fig. 8 is normalized to $V = \Delta_0/e = 5$ mV and the experimental values of S_I and Q are expressed in relative units. Solid curves show the results of theoretical calculations for a mirror-symmetric junction $D_{45}ID_{-45}$ with $D = 0.1$ at a fixed value of the inelastic scattering parameter (0.003Δ). As can be seen, the experimental data fit to the theory well taking into account multiple Andreev reflections in the junctions involving D-type superconductors [18]. However, the values of the transparency and gap evaluated for the D-type superconductor using this comparison to the theory differ from the values determined using electrical measurements. It should be also noted that we did not observe subharmonic gap features on the current–voltage characteristic predicted in [18], which is probably related to the low transparency of the junction.

At the same time, the values of V_Q for which $Q(V) = Q_{max}$ in the magnetic field proved to be much lower than in the autonomous regime. The measurements for the autonomous transitions could be performed only for the junctions with low values of the normal resistance ($R_N < 20\ \Omega$), which were poorly impedance-matched to the measuring amplifier. As a result, the error in these measurements exhibited a severalfold increase. For such

---

[4] The range of voltages for which the shot noise obeys the classical relation $Q = e$ changed from one sample to another. The upper boundary of this range is probably related to the potential barrier height (see table).

junctions, comparison of theory and experiment [18] was performed using normalized dependences.

The fact that the intensity of noise caused by multiple Andreev reflections exceeds the level of thermal fluctuations explains the experimentally observed broadening of the Josephson generation line in the junctions of cuprate superconductors [33–35]. This result should be taken into account in applications based on the Josephson effect. Note also that, in the region of high bias voltages, the Nyquist noise in the junction is much lower than the shot noise.

5. CONCLUSIONS

The results of our experimental study of the critical current as a function of the temperature, transparency, and phase difference between superconducting electrodes, as well as the measured current–voltage characteristics showed that the most probable mechanism of superconducting current transport in bicrystal junctions of cuprate superconductors is electron tunneling through the barrier with participation of the bound states formed at the superconductor-insulator interface as a result of multiple Andreev reflections. However, the shapes of the experimental current–phase and current–magnetic field curves cannot be described within the framework of a homogeneous junction model, without taking into account the roughness caused by faceting at the interface in the course of epitaxial layer growth. At present, there is no consistent theory adequately describing the experimental situation. In the region of relatively large bias voltages ($V > 5$ mV), the junction noise level exceeds the level of thermal fluctuations, in agreement with the voltage dependence of the shot noise in the junction (analogous to that observed for the junctions of S-type superconductors). In the region of small voltages, a noise peak is observed that is characteristic of superconducting junctions featuring multiple Andreev reflections.

ACKNOWLEDGMENTS

The authors are grateful to F.V. Komissinski, V.K. Kornev, and P.B. Mozhaev for their help in conducting experiments and to Yu.S. Barash, A.V. Zaitsev, A. Kadigrobov, J. Mygind, N. Pedersen, and V. Shumeĭko for fruitful discussions of results.

This study was supported in part by the Federal Program “Current Problems in Physics of Condensed State” (“Superconductivity” Subprogram), the Presidential Program of Support for Leading Scientific Schools in Russia (project no. NSh-1344.2004.2), the Russian Foundation for Basic Research (project no. 04-02-16818a), the INTAS Foundation (grant no. 2001-0809), and the International Scientific-Technological Center (grant no. 2369).

REFERENCES

1. I. O. Kulik and I. K. Yanson, in *Josephson Effect in Superconducting Tunnel Structures* (Nauka, Moscow, 1970) [in Russian].
2. I. O. Kulik, Zh. Éksp. Teor. Fiz. **57**, 1745 (1969) [Sov. Phys. JETP **30**, 944 (1970)].
3. A. Furusaki and M. Tsukada, Phys. Rev. B **43**, 10164 (1991).
4. C.-R. Hu, Phys. Rev. Lett. **72**, 1526 (1994).
5. R. A. Riedel and P. F. Bagwell, Phys. Rev. B **57**, 6084 (1998).
6. Yu. S. Barash, Phys. Rev. B **61**, 678 (2000).
7. C. W. Benaker, Phys. Rev. Lett. **67**, 3836 (1991).
8. K. K. Likharev, Rev. Mod. Phys. **51**, 101 (1979).
9. Y. Tanaka and S. Kashiwaya, Phys. Rev. B **53**, 11957 (1996).
10. Yu. S. Barash, H. Burkhardt, and D. Rainer, Phys. Rev. Lett. **77**, 4070 (1996).
11. E. Il’ichev, M. Grajcar, R. Hlubina, *et al.*, Phys. Rev. Lett. **86**, 5369 (2001).
12. L. Alff, A. Beck, R. Gross, *et al.*, Phys. Rev. B **58**, 11197 (1998).
13. G. A. Ovsyannikov, A. D. Mashtakov, I. V. Borisenko, and K. Y. Constantinian, J. Low Temp. Phys. **117**, 605 (1999).
14. A. D. Mashtakov, K. Y. Constantinian, G. A. Ovsyannikov, and E. A. Stepantsov, Pis’ma Zh. Tekh. Fiz. **25** (7), 1 (1999) [Tech. Phys. Lett. **25**, 249 (1999)].
15. E. V. Bezuglyi, E. N. Bratus’, V. S. Shumeiko, and G. Wendin, Phys. Rev. Lett. **83**, 2050 (1999).
16. Y. Naveh and D. V. Averin, Phys. Rev. Lett. **82**, 4090 (1999).
17. K. Y. Constantinian, G. A. Ovsyannikov, I. V. Borisenko, *et al.*, IEEE Trans. Appl. Supercond. **13**, 610 (2003).
18. J. C. Cuevas and M. Fogelström, Phys. Rev. B **64**, 104502 (2001); Phys. Rev. Lett. **89**, 227003 (2002).
19. H. Hilgenkamp and J. Mannhart, Rev. Mod. Phys. **74**, 485 (2002).
20. M. Kawasaki, P. Chaudhari, and A. Gupta, Phys. Rev. Lett. **68**, 1065 (1992).
21. M. Covington, M. Aprili, E. Paraoanu, *et al.*, Phys. Rev. Lett. **79**, 277 (1997).
22. F. V. Komissinski, G. A. Ovsyannikov, Yu. V. Kislinskiĭ, *et al.*, Zh. Éksp. Teor. Fiz. **122**, 1247 (2002) [JETP **95**, 1074 (2002)].
23. T. Lofwander, V. S. Shumeiko, and G. Wendin, Supercond. Sci. Technol. **14**, R53 (2001).
24. Z. G. Ivanov, E. A. Stepantsov, A. Y. Tzalenchuk, *et al.*, IEEE Trans. Appl. Supercond. **3**, 2925 (1993).
25. H. Hilgenkamp, J. Mannhart, and B. Mayer, Phys. Rev. B **53**, 14586 (1996).
26. L. J. Buchholtz, M. Palumbo, D. Rainer, and J. A. Sauls, J. Low Temp. Phys. **101**, 10789 (1995).
27. M. B. Walker and P. Pairor, Physica C (Amsterdam) **341–348**, 1523 (2000).

28. G. Wendin and V. S. Shumeiko, Phys. Rev. B **53**, R6006 (1996).
29. F. V. Komissinski, G. A. Ovsyannikov, and Z. G. Ivanov, Fiz. Tverd. Tela (St. Petersburg) **43**, 769 (2001) [Phys. Solid State **43**, 801 (2001)].
30. V. K. Kornev, I. I. Soloviev, N. V. Klenov, *et al.*, IEEE Trans. Appl. Supercond. **13**, 825 (2003).
31. V. N. Gubankov, V. P. Koshelets, and G. A. Ovsyannikov, Zh. Éksp. Teor. Fiz. **71**, 348 (1976) [Sov. Phys. JETP **44**, 181 (1976)].
32. R. Kleiner, A. S. Katz, A. G. Sun, *et al.*, Phys. Rev. Lett. **76**, 2161 (1996).
33. L. É. Amatuni, R. M. Martirosyan, and K. Y. Constantinian, Pis'ma Zh. Tekh. Fiz. **20** (3), 86 (1994) [Tech. Phys. Lett. **20**, 128 (1994)].
34. Y. Y. Divin, U. Poppe, K. Urban, *et al.*, IEEE Trans. Appl. Supercond. **9**, 3346 (1999).
35. O. Harnack, M. Darula, S. Beuven, and H. Kohlstedt, Appl. Phys. Lett. **76**, 1764 (2000).
36. P. L. Richards and T.-M. Shen, Appl. Phys. Lett. **36**, 480 (1980).
37. Y. Blanter and M. Buttiker, Phys. Rep. **336**, 1 (2000).
38. P. Dieltman, H. G. Bukkems, T. M. Klapwijk, *et al.*, Phys. Rev. Lett. **79**, 3486 (1997).
39. K. Y. Constantinian, G. A. Ovsyannikov, I. V. Borisenko, *et al.*, Supercond. Sci. Technol. **14**, 1035 (2001).

Translated by P. Pozdeev

Journal of Experimental and Theoretical Physics, Vol. 99, No. 6, 2004, pp. 1233–1243.
Translated from Zhurnal Éksperimental'noĭ i Teoreticheskoĭ Fiziki, Vol. 126, No. 6, 2004, pp. 1413–1424.

SOLIDS
Electronic Properties

Spin Relaxation of Quadrupole Nuclei in Paramagnetic and Magnetically Ordered Insulators

N. P. Fokina[a] **and M. O. Elizbarashvili**[b]
[a]*Tbilisi State University, Tbilisi, 380028 Georgia*
[b]*Institute of Cybernetics, Academy of Sciences of Georgia, Tbilisi, 380086 Georgia*
e-mail: n_fokina@caucasus.net

Received February 24, 2004

Abstract—The longitudinal and transverse spin relaxation through a (generally anisotropic) electron–nucleus interaction in paramagnetic and magnetically ordered insulators is theoretically studied for nuclei with a resolved quadrupole structure. Expressions are derived for the relaxation rates of both the transverse nuclear magnetization components when individual transitions are excited in the quadrupole structure and the total longitudinal nuclear magnetization component. These expressions are reduced to a form that contains the Fourier transforms of the time correlation functions only for the electron spins. Given the specific form of these correlation functions corresponding to different phase states of the electron spins and different origins of their fluctuations, the temperature dependences of the nuclear relaxation rates are ascertained in various cases, including those for dipole and isotropic hyperfine interactions. Calculations are performed for arbitrary electron and half-integer nuclear spins by taking into account the possible quadrupole splitting of the NMR spectrum without any restriction on the smallness of the ratio $\hbar\omega_s/k_BT$ (ω_s is the resonance frequency of the electron spins). The derived expressions are compared with available experimental data on the longitudinal and transverse nuclear relaxation in colossal-magnetoresistance lanthanum manganites in the part of their phase diagram where the corresponding samples are either paramagnetic or magnetically ordered insulators and near the points of transition to an ordered state. Interpretations alternative to the existing ones are offered. © *2004 MAIK "Nauka/Interperiodica".*

1. INTRODUCTION

In a paramagnetic or magnetically ordered insulator, the nuclear relaxation is generally attributable to the fluctuating local magnetic fields generated on the nuclei by the electron spins. The corresponding relaxation rates are well known for nuclei with an equidistant NMR spectrum (nuclei with the spin $I = 1/2$ or $I > 1/2$ [1]). On the other hand, generalizing these results to the case of nuclear spins with a nonequidistant NMR spectrum, which ensures, for example, a resolved quadrupole NMR structure, is of current interest. These nuclei are exemplified by ^{139}La and ^{55}Mn in $La_{1-x}A_xMnO_3$ lanthanum manganites (where A is an alkali-earth metal; doping gives rise to holes in the e_g state of the Mn^{3+} ions of the initial $LaMnO_3$ material). Heightened interest in these materials is aroused by their unusual magnetic and electric transport properties (see reviews [2–4]). Studying the temperature dependences of the longitudinal (T_1) and transverse (T_2) relaxation times for ^{139}La and ^{55}Mn nuclei is highly informative for investigating lanthanum manganites. This is because NMR experiments provide local probing at a lattice site of the sample where the intensity and correlation times of the fluctuating local magnetic fields and the electric field gradients causing nuclear relaxation [5–12] determine the times T_1 and T_2. Which local fields, magnetic or electric, play the dominant role depends on the composition and temperature of the sample. Since these local fields for the specific samples studied were found in several papers [5–7] to be produced by the interactions of nuclear spins with those of electrons, the times T_1 and T_2 in these samples bear an imprint of the degree of order in the electron spin system and the origin of the electron spin fluctuations. When the experimental nuclear relaxation data [5–7] are interpreted theoretically, the difference between the behaviors of the electron spin system in a magnetically ordered sample and a paramagnet is generally disregarded quantitatively. On the other hand, lanthanum manganites manifest the most interesting and promising properties precisely near the transition to the ferromagnetic state.

Therefore, the goal of this study is to draw attention to the possibility of different interpretations of the temperature dependences of the times T_1 and T_2 for different degrees of order in a system of localized electron spins and different origins of their fluctuations. To this end, we first reduce the problem of calculating the rates of nuclear relaxation through an arbitrary anisotropic electron–nucleus interaction to a form that contains the correlation functions of only the electron spin system. Subsequently, as an illustration of the results obtained, we consider the regions of the phase diagram for lanthanum manganites (with a hole concentration of $0 \leq x < 0.15$; see [8–14]) where the sample is either a paramagnetic or magnetically ordered insulator; hence, the presence of delocalized spins is disregarded in the formulation of the problem. We perform our calculations for arbitrary electron and half-integer nuclear spins, taking into account the possible quadrupole splitting of the NMR spectrum.

2. CALCULATING THE NUCLEAR RELAXATION RATES

Let us consider the electron–nucleus system of a dielectric sample composed of localized electron and nuclear spins. This can be both a paramagnet and a ferro- or antiferromagnet in which the magnetic moments of the sublattices are directed along the corresponding easy axes. To simplify the problem, we assume that these axes are directed along or opposite to the crystallographic z axis of the crystal (a collinear structure) that coincides with the principal axis of the electric field gradient and the direction of the external constant magnetic field $\mathbf{H}_0$.[1] The quantization axes of the electron and nuclear spins are assumed to coincide. In addition to the Zeeman energies of the electron (S) and nuclear (I) spins (the first two terms), the main Hamiltonian of this system,

$$\mathcal{H}_0 = \hbar\omega_s S^z - \hbar\omega_I I^z - 2J\sum_{j,k}\mathbf{S}_j\cdot\mathbf{S}_k + \frac{\hbar}{2}(\omega_Q + \delta\omega_Q)\left[(I^z)^2 - \frac{1}{3}I(I+1)\right], \tag{1}$$

includes the electron-spin exchange energy (J is the exchange integral of the closest neighboring electron spins) and the effective quadrupole Hamiltonian of the nuclei. Here, $\omega_s = (-g\mu_B/\hbar)H$, where H is the sum of the external field H_0, the demagnetizing field of the sample surface, and the effective fields of the magnetic anisotropy. The nuclear frequency ω_I includes the static shifts due to the interaction with the electron spins (see below). The last term in Eq. (1) is the axisymmetric quadrupole Hamiltonian of the nuclei, where

$$\hbar\omega_Q = \frac{3e^2qQ}{2I(2I-1)},$$

Q is the quadrupole moment of the nucleus, and $eq = V_{zz}$ is the tensor component of the electric field gradient. Equation (1) also takes into account the fact [16] that, even for a cubic crystal with $\omega_Q = 0$, the virtual processes of emission and absorption of a spin wave by the nucleus of a magnetic ion attributable to hyperfine interaction at low temperatures ($T \ll T_C, T_N$, where T_C and T_N are the Curie and Néel temperatures, respectively) are described by an axisymmetric quadrupole Hamiltonian with

$$\delta\omega_Q = -\frac{SA^2}{N_s\hbar^2}\sum_k \omega_k^{-1},$$

where A is the isotropic hyperfine coupling constant, ω_k is the frequency of the spin wave with wavevector $\mathbf{k}$, and N_s is the number of magnetic spins. Below, we consider the case where $\omega_Q + \delta\omega_Q \ll \omega_I$.

Here, we investigate an experimental situation where the role of the quadrupole Hamiltonian (irrespective of its causes) reduces only to the transformation of equidistant nuclear levels into nonequidistant ones. In this case, either the frequency difference between the neighboring NMR transitions is assumed to be larger than the NMR line width, which ensures a resolved quadrupole structure (e.g., the multicomponent quadrupole structure in high-quality lanthanum manganite monocrystals at helium temperatures [8] or the characteristic powder spectrum in a strong magnetic field [7]) or the quadrupole structure is unresolved and one NMR line is observed [5, 6]. In particular, we exclude from our analysis the case of low hole concentrations and temperatures at which the nuclear relaxation in the state of a ferromagnetic insulator is attributable to the fluctuations of the electric field gradients on the nuclei. In the latter case, as was shown in [11–13], the broad spectrum of the corresponding correlation times leads to such fast inhomogeneous transverse nuclear relaxation with a characteristic time T_2^* that the signal from the nuclear spin echo becomes unobservable.

In writing the electron–nucleus interaction $\mathcal{H}'$ that causes the relaxation of the nuclear spins when their direct coupling with the lattice and the direct or indirect interaction between themselves are disregarded, we take into account the fact that the fluctuating part of the local field generated by the electron spins on the nuclei causes the relaxation. Therefore, the terms responsible for the static local field on the nuclei should be subtracted from the total Hamiltonian of the electron–nucleus interaction (as was noted above, together with the external field $\mathbf{H}_0$, they form the nuclear resonance frequency ω_I):

$$\mathcal{H}' = \hbar\sum_j\sum_{m,m'=-1}^{1} D_{ij}^{-mm'}\tilde{I}_i^m\delta\tilde{S}_j^{m'}, \tag{2}$$

where $D_{ij}^{-mm'}$ are the coupling constant between the ith nuclear spin and the jth electron spin; $\delta\tilde{S}_j^m = \tilde{S}_j^m - \langle\tilde{S}_j^m\rangle$, $m, m' = -1, 0, +1$; and the following notation [1] is used:

$$\tilde{S}_j^{\pm} = \mp\frac{1}{\sqrt{2}}(S_j^x \pm iS_j^y), \quad \tilde{I}_i^{\pm} = \pm\frac{1}{\sqrt{2}}(I_i^x \pm iI_i^y).$$

---

[1] Note that generalizing the problem to other orientations of the field $\mathbf{H}_0$ reduces to renormalizing ω_Q (see [15]).

Note that the interaction of the nuclear spin only with the proper electron shell ($i = j$) or the closest paramagnetic centers is implied in (2) (e.g., in [6], the sum over the eight closest Mn ions is taken for the indirect local field on the ^{139}La nucleus), because the contribution from each of the centers to the relaxation of nucleus i rapidly decreases with distance r_{ij}. Some of the multiparticle (electron–electron and nucleus–nucleus) interaction effects are mentioned below.

We calculate the transverse nuclear relaxation rate by the Kubo–Tomita method [17] (see also [1]). In contrast to the calculations in [1], we impose no restrictions on the smallness of the ratio $\hbar\omega_s/k_BT$ in the paramagnetic region and take into account the fact that the quadrupole structure of the NMR spectrum may be resolved (for $I > 1/2$). To determine the longitudinal nuclear relaxation rate, we use the Kubo–Tomita and Moriya [18] formulas (see also [16]); i.e., we use the approximation of short correlation times for the electron correlation functions where these times do not exceed the reciprocal of the fluctuation amplitude in frequency units.

For an experimental situation where the resonance frequency of the electron spins is much higher than the nuclear frequency, we obtain the following relations for the width of the $M \longrightarrow M+1$ transition in the quadrupole NMR structure and for the relaxation rate of the longitudinal component of the total nuclear magnetization:

$$\begin{aligned}T_{2M}^{-1} = {} & \tau_{s\|}(\omega_{s\|})\sum_j (D_{ij}^{00})^2 + \left(C_M + \frac{1}{2}C_{M+1} + \frac{1}{2}C_{M-1}\right) \\ & \times \tau_{s\|}(\omega_{s\|} - \omega_I)\sum_j(-D_{ij}^{+10}D_{ij}^{-10}) + \tau_{s\perp}(\omega_{s\perp}) \\ & \times \sum_j(-D_{ij}^{0+1}D_{ij}^{0-1}) + \frac{1}{2}\Big[C_M\tau_{s\perp}(\omega_{s\perp}) + \frac{1}{2}C_{M+1}\tau_{s\perp}^{+-}(\omega_{s\perp}) \\ & + \frac{1}{2}C_{M-1}\tau_{s\perp}^{-+}(\omega_{s\perp})\Big]\sum_j D_{ij}^{+1+1}D_{ij}^{-1-1} \\ & + \frac{1}{2}\Big[C_M\tau_{s\perp}(\omega_{s\perp}) + \frac{1}{2}C_{M+1}\tau_{s\perp}^{-+}(\omega_{s\perp}) \\ & + \frac{1}{2}C_{M-1}\tau_{s\perp}^{+-}(\omega_{s\perp})\Big]\sum_j D_{ij}^{+1-1}D_{ij}^{-1+1},\end{aligned} \tag{3}$$

$$\begin{aligned}T_1^{-1} = {} & \tau_{s\|}(\omega_{s\|} - \omega_I)\sum_j(-2D_{ij}^{+10}D_{ij}^{-10}) \\ & + \tau_{s\perp}(\omega_{s\perp})\sum_j(D_{ij}^{+1+1}D_{ij}^{-1-1} + D_{ij}^{+1-1}D_{ij}^{-1+1}),\end{aligned} \tag{4}$$

where

$$\tau_{s\|}(\omega_{s\|}) = \mathrm{Re}\int_0^\infty \langle\delta S_j^z(t)\delta S_j^z\rangle dt,$$

$$\tau_{s\|}(\omega_{s\|} - \omega_I) = \mathrm{Re}\int_0^\infty \langle\delta S_j^z(t)\delta S_j^z\rangle \exp(-i\omega_I t)dt,$$

$$\tau_{s\perp}(\omega_{s\perp}) = \mathrm{Re}\int_0^\infty \langle\{\delta S_j^+(t)\delta S_j^-\}\rangle \exp(-i\omega_I t)dt,$$

$$\tau_{s\perp}^{\overset{+-}{-+}}(\omega_{s\perp}) = \mathrm{Re}\int_0^\infty \langle\delta S_j^\pm(t)\delta S_j^\mp\rangle \exp(-i\omega_I t)dt,$$

the angular brackets denote an equilibrium averaging with the Hamiltonian $\mathcal{H}_0$, and the braces denote the symmetrized product $\{AB\} = (AB + BA)/2$. The quantities $C_M = I(I+1) - M(M+1)$ characterize the intensity of the component of the quadrupole NMR structure related to the change in the z component of the nuclear spin $M \longrightarrow M+1$. The meaning of the designations $\omega_{s\|}$ and $\omega_{s\perp}$ is explained below in each specific case. Formulas (3) and (4) are valid for any paramagnetic and magnetically ordered insulators if the pair interaction between the electron and nuclear spins is effective in the nuclear relaxation.

As we see from Eqs. (3) and (4), at fixed electron–nucleus coupling constants, the nuclear relaxation is determined by the electron correlation functions, their physical nature and the specific form of the time dependence, which determine the corresponding correlation times. Since this all depends on the degree of order in the electron spin system, the latter clearly shows up in the nuclear relaxation.

The time dependence of the electron spin operators is determined by the Hamiltonian H_0 with the addition of any interactions that can cause these operators to decay in paramagnetic and magnetically ordered insulators. Since we study here the situation where $\omega_Q + \delta\omega_Q \ll \omega_I$, it was assumed in formulas (3) and (4) that

$$\tau_s[\omega - (2M+1)(\omega_Q + \delta\omega_Q)] \approx \tau_s(\omega).$$

The result of this assumption is that the total longitudinal magnetization of a nuclear spin system with split quadrupole structure approaches equilibrium along a single exponential with the characteristic rate T_1^{-1} denoted in [6, 7] by $2W$ and τ^{-1}, respectively. The spin relaxation of one selected pair of levels in the quadrupole-split spectrum (the corresponding transition is determined by the choice of the frequency of exciting and reading pulses) experimentally observed in [19–22] is multiexponential. The corresponding theoretical analysis was performed in [18–21] in terms of level populations, i.e., in a reduced description of the spin dynamics where the nondiagonal elements of the spin density matrix were assumed to have decayed by the time of observation. Experimentally, such a situation in a spin system with a strong inhomogeneous broadening of the magnetic resonance with a width $\delta^* \gg T_{2M}^{-1}$ is ensured by the condition $t \gg T_2^* = (\delta^*)^{-1}$, where t is the interval between the radio-frequency pulses. In this time, the precession dephasing of the individual isochromates destroys the transverse magnetization components, which is equivalent to the nondiagonal elements of the density matrix becoming equal to zero. In this case, the observed multiexponential longitudinal relaxation is described by the formulas from [19–22] with $2W$ (or τ^{-1}) given by Eq. (4) and its versions presented below. If, however, an experiment records the total longitudinal magnetization component, then its relaxation for $\omega_Q + \delta\omega_Q \ll \omega_I$ is one-exponential.

If there is no quadrupole structure (i.e., the NMR signal is of the same form as that at $I = 1/2$), then we should set $C_{M=-1/2} = 1$, $C_{M+1} = 0$, and $C_{M-1} = 0$ in Eqs. (3) and (4). Then, as should be in this case [24],

$$T_1^{-1} = 2(T_2^{-1})_{\text{nonsec}},$$

where $(T_2^{-1})_{\text{nonsec}}$ is the nonsecular width.

When the isotropic indirect hyperfine interaction dominates in the local field on the nucleus, we have

$$D_{ij}^{00} = D_{ij}^{+1+1} = D_{ij}^{-1-1} \equiv A_{ij}/\hbar,$$

the remaining $D_{ij}^{mm'} = 0$. Such a situation is also possible for some of the nuclei of nonmagnetic ions where the isotropic hyperfine interaction is ensured by the overlapping of the electron shells [16].

The overlapping of the inner t_{2g}-orbitals of manganese ions with the s-wave functions on the ^{139}La nucleus in $\text{La}_{1-x}\text{Ca}_x\text{MnO}_3$ may serve as an example (see [6] and, for more detail, [9]). In this case, the hyperfine field on ^{139}La is insensitive to the e_g-state population in manganese ions.

If the dipole–dipole interaction between the electron and nuclear spins acts as the anisotropic interaction (which is most characteristic of the nuclear relaxation of nonmagnetic ions), then

$$\begin{gathered} D_{ij}^{00} = a_{ij}(1 - 3\cos^2\theta_{ij}), \\ -D_{ij}^{+10}D_{ij}^{-10} = -D_{ij}^{0+1}D_{ij}^{0-1} = \frac{9}{2}a_{ij}^2\sin^2\theta_{ij}\cos^2\theta_{ij}, \\ D_{ij}^{+1+1}D_{ij}^{-1-1} + D_{ij}^{+1-1}D_{ij}^{-1+1} \\ = \frac{a_{ij}^2}{4}(1 - 3\cos^2\theta_{ij})^2 + \frac{9}{4}a_{ij}^2\sin^4\theta_{ij}. \end{gathered} \tag{5}$$

Here, $a_{ij} = \gamma_I\gamma_s r_{ij}^{-3}$; γ_I and γ_s are the gyromagnetic ratios for the nucleus and the electron, respectively; and θ_{ij} is the angle that the vector $\mathbf{r}_{ij}$ indicating the position of the ith nucleus with respect to the jth electron spin makes with the z axis. The anisotropic contribution to the local field on the nucleus can also come from the "proper" electron shell. For example, the field on the ^{55}Mn nucleus in Mn^{3+} ions has a strong anisotropic contribution from the spin–dipole field of the e_g-electron orbital $d(x^2 - y^2)$ of the ion [5], while the hyperfine field on the ^{55}Mn nucleus in Mn^{4+} ions has no such contribution.

In paramagnets, $\omega_{s\parallel} = 0$, $\omega_{s\perp} = \omega_s$, and the following should be substituted in (3) and (4) [1]:

$$\frac{\langle \delta S_j^z(t)\delta S_j^z\rangle}{\langle(\delta S_j^z)^2\rangle} = f_{s\parallel}(t),$$

$$\frac{\langle \delta S_j^{\pm}(t)\delta S_j^{\mp}\rangle}{\langle \delta S_j^{\pm}\delta S_j^{\mp}\rangle} = \exp(\pm i\omega_s t)f_{s\perp}(t),$$

where at arbitrary temperatures

$$\langle \delta S_j^+\delta S_j^-\rangle = -\frac{2\langle S_j^z\rangle}{\exp(\hbar\omega_s/k_\text{B}T) - 1},$$

$$\langle \delta S_j^-\delta S_j^+\rangle = -\frac{2\langle S_j^z\rangle\exp(\hbar\omega_s/k_\text{B}T)}{\exp(\hbar\omega_s/k_\text{B}T) - 1},$$

$$\langle\{\delta S_j^+\delta S_j^-\}\rangle = -\langle S_j^z\rangle\coth\left(\frac{\hbar\omega_s}{2k_\text{B}T}\right),$$

$$\langle S_j^z\rangle = -SB_s\left(\frac{S\hbar\omega_s}{k_\text{B}T}\right),$$

B_s is the Brillouin function. The quantities $\langle(\delta S_j^z)^2\rangle$ should be calculated numerically for the specific electron spin.

In the high-temperature (HT) approximation, i.e., at a low ratio $\hbar\omega_s/k_\text{B}T$, when

$$\begin{gathered} \langle\{\delta S_j^+\delta S_j^-\}\rangle \approx \langle\delta S_j^+\delta S_j^-\rangle \approx \langle\delta S_j^-\delta S_j^+\rangle \\ \approx 2\langle(\delta S_j^z)^2\rangle \approx \frac{2}{3}S(S+1), \end{gathered}$$

Eqs. (3) and (4) simplify to

$$\begin{gathered} (T_{2M}^{-1})^{HT} = W_{\text{sec}}^{HT} + (2C_M - 1)W_{\text{nonsec}}^{HT}, \\ (T_1^{-1})^{HT} = 2W_{\text{nonsec}}^{HT}. \end{gathered} \tag{6}$$

Here, we use the identity

$$C_M + \frac{1}{2}C_{M+1} + \frac{1}{2}C_{M-1} = 2C_M - 1$$

and the notation

$$W_{\text{sec}}^{HT} = \frac{S(S+1)}{3}\left\{\tau'_{s\parallel}(0)\sum_j (D_{ij}^{00})^2 \right.$$

$$\left. + \tau'_{s\perp}(\omega_s)\sum_j(-2D_{ij}^{0+1}D_{ij}^{0-1})\right\},$$

$$W_{\text{nonsec}}^{HT} = \frac{S(S+1)}{3}\left\{\tau'_{s\parallel}(\omega_I)\sum_j(-D_{ij}^{+10}D_{ij}^{-10})\right.$$

$$\left. + \tau'_{s\perp}(\omega_s)\sum_j(D_{ij}^{+1+1}D_{ij}^{-1-1} + D_{ij}^{+1-1}D_{ij}^{-1+1})\right\}, \tag{7}$$

$$\tau'_{s\parallel}(0) = \frac{3\tau_{s\parallel}(0)}{2S(S+1)}, \quad \tau'_{s\parallel}(\omega_I) = \frac{3\tau_{s\parallel}(\omega_I)}{S(S+1)},$$

$$\tau'_{s\perp}(\omega_s) = \frac{3\tau_{s\perp}^{+-}(\omega_s)}{2S(S+1)} = \frac{3\tau_{s\perp}^{-+}(\omega_s)}{2S(S+1)}.$$

If the concentration of magnetic ions is low, then the sample is a diluted paramagnet. $LaGa_{1-x}Mn_xO_3$ crystals with $0 \le x \le 0.2$, where most of the magnetic Mn^{3+} ions are substituted with nonmagnetic Ga^{3+} ions, may serve as examples of a magnetically diluted lanthanum manganite. The NMR and the nuclear spin relaxation of ^{69}Ga and ^{71}Ga in such samples were investigated in [22].

The correlation functions $f_{s\parallel}(t)$ and $f_{s\perp}(t)$ for the electron spin fluctuations in a diluted paramagnet may be assumed to be simple exponentials [1]. Then, $\tau'_{s\parallel}(0) = \tau_{s\parallel}$, where $\tau_{s\parallel}$ is the time constant of the function $f_{s\parallel}(t)$,

$$\tau'_{s\parallel}(\omega_I) = \frac{\tau_{s\parallel}}{\omega_I^2\tau_{s\parallel}^2 + 1}, \quad \tau'_{s\perp}(\omega_s) = \frac{\tau_{s\perp}}{\omega_s^2\tau_{s\perp}^2 + 1},$$

where $\tau_{s\perp}$ is the time constant of the function $f_{s\perp}(t)$. Expression (7) for T_1^{-1} at $I = 1/2$ with such electron correlation functions is identical to the corresponding expression in [1] for an arbitrary anisotropic electron–nucleus interaction. If the relaxation rates are dominated by the dipole–dipole interaction and if the terms with $\tau_{s\perp}(\omega_s)$ are negligible due to the relation $\omega_s \gg \omega_I$, then expressions (6) and (7) for a magnetically diluted sample with a random distribution of paramagnetic centers (PC) reduce to

$$(T_{2M}^{-1})_{PC}^{HT} \approx \frac{S(S+1)}{3}$$

$$\times[0.8\tau'_{s\parallel}(0) + 0.6(2C_M - 1)\tau'_{s\parallel}(\omega_I)]\sum_j a_{ij}^2, \tag{8}$$

$$(T_1^{-1})_{PC}^{HT} \approx \frac{S(S+1)}{3}1.2\tau'_{s\parallel}(\omega_I)\sum_j a_{ij}^2. \tag{9}$$

If, however, the isotropic hyperfine interaction is effective in the nuclear relaxation, then expressions (6) and (7) take the form

$$(T_{2M}^{-1})_{PC}^{HT} \approx \frac{S(S+1)}{3\hbar^2}$$

$$\times\sum_j A_{ij}^2[\tau'_{s\parallel}(0) + (2C_M - 1)\tau'_{s\perp}(\omega_s)], \tag{10}$$

$$(T_1^{-1})_{PC}^{HT} \approx \frac{2S(S+1)}{3\hbar^2}\tau'_{s\perp}(\omega_s)\sum_j A_{ij}^2. \tag{11}$$

In the limit of long correlation times, $\omega_s^2\tau_{s\perp}^2 \gg 1$ (nevertheless, for the method of short correlation times to be applicable, $\tau_{s\parallel} = \tau_{s\perp} = \tau_s$ must not exceed $\hbar(S(S+1)\sum_j A_{ij}^2/3)^{-1/2}$ that we use in our estimation), we obtain from (10) and (11)

$$(T_{2M}^{-1})_{PC}^{HT} \approx \frac{1}{\hbar}\left(S(S+1)\sum_j\frac{A_{ij}^2}{3}\right)^{1/2},$$

$$(T_1^{-1})_{PC}^{HT} \approx \frac{2}{\omega_s^2\hbar^3}\left(S(S+1)\sum_j\frac{A_{ij}^2}{3}\right)^{3/2} \ll (T_{2M}^{-1})_{PC}^{HT}. \tag{12}$$

Under strong-narrowing conditions where $\omega_s^2\tau_{s\perp}^2 \ll 1$, the line width (10) of an individual transition is proportional to C_M, the square of the matrix element of the dipole transition $M \longrightarrow M + 1$:

$$(T_{2M}^{-1})_{PC}^{HT} \approx \frac{C_M}{\hbar^2}\frac{2S(S+1)}{3}\tau_s\sum_j A_{ij}^2.$$

This result seems quite natural for an arbitrary isotropic relaxation mechanism in systems with a quadrupole structure attributable to a quadrupole Hamiltonian of any origin (see, e.g., [23]); it is important that the Fourier transform of the correlation function for the z component of the fluctuating spin at a zero frequency is approximately equal to the spectral density of the correlation functions for the transverse components at its resonance frequency. The longitudinal relaxation rate for the total magnetization is approximately equal to

$$(T_1^{-1})_{PC}^{HT} \approx \frac{2S(S+1)}{3\hbar^2}\tau_s \sum_j A_{ij}^2;$$

i.e., the following relation holds:

$$(T_{2M}^{-1})_{PC}^{HT} \approx C_M (T_1^{-1})_{PC}^{HT}. \qquad (13)$$

In [6], the longitudinal relaxation rate for ^{139}La nuclei ($I = 7/2$) was measured by using a stimulated echo and the recovery of the NMR signal detected by the spin echo method after saturation. The observed multiexponential time dependence of the nuclear magnetization z component that corresponds to the population difference at the detected central transition is dominated by the relaxation rate

$$T_{1\text{eff}}^{-1} = 28 \times 2W_{\text{nonsec}}^{HT}.$$

According to (6), the transverse relaxation rate measured by the decay of the spin echo that was also excited at the central frequency is

$$T_{2(-1/2)}^{-1} = W_{\text{sec}}^{HT} + 31W_{\text{nonsec}}^{HT}.$$

In our opinion, Fig. 8 from [6] shows the quantities

$$2W_1 = T_{\text{eff}}^{-1}/28 = 2W_{\text{nonsec}}^{HT} = T_1^{-1}, \qquad (14)$$

$$2W_2 = \frac{T_{2(-1/2)}^{-1}}{16} = \frac{W_{\text{sec}}^{HT}}{16} + \frac{31}{16}W_{\text{nonsec}}^{HT}, \qquad (15)$$

which differ from $2W_1$ and $2W_2$ in expressions (3) from that paper. Expressions (14) and (15) proposed above seem to be correct.

For strong NMR line narrowing ($T \geq 300$ K), the equality $W_{\text{sec}}^{HT} = W_{\text{nonsec}}^{HT}$ holds; a corollary of this equality is $2W_1 = 2W_2$, as observed experimentally. For slow fluctuations, i.e., at low temperatures, but in the paramagnetic region ($T_{\text{C}} < T \leq 250$ K) where $W_{\text{sec}}^{HT} \gg W_{\text{nonsec}}^{HT}$, it follows from the theory that $2W_1 \ll 2W_2$, in agreement with the experimental data. In the intermediate temperature range, the general formulas (14) and (15) should be used to determine T_1^{-1} from data on the spin-echo decay at the central transition.

On the other hand, it seems that the ordering in the electron spin system should be taken into account at $T < T_{\text{C}}$. The fact that W_{nonsec}^{HT} and T_1^{-1}, attributable to the involvement of free spin waves in the case where the external constant magnetic field is negligible compared to the exchange field, become equal to zero may then be the result of a prohibition from the energy conservation law (see below).

The fluctuations of the electron spin components in a conventional paramagnet are attributable to its spin–lattice and (or) spin–spin (dipole–dipole and exchange) interaction [1]:

$$\tau_{s\parallel}^{-1} \approx T_{1s}^{-1} + \Delta\omega_s, \quad \tau_{s\perp}^{-1} \approx \Delta\omega_s, \qquad (16)$$

where T_{1s} is the electron spin–lattice relaxation time and $\Delta\omega_s \sim (\gamma_s^2\hbar)^2 c_s$ is the homogeneous EPR line width (c_s is the electron spin concentration). Here, we took into account the fact that, since the projection operator of an individual electron spin onto the z axis does not commute even with the secular part of the dipole–dipole interaction between the electron spins, the processes that lead to a (homogeneous) EPR line broadening also cause relaxation of the z component of the electron spin [1]. The experimental temperature dependences are successfully fitted theoretically by using the activation laws of the variations in $\tau_{s\parallel}$ and $\tau_{s\perp}$ with temperature [6, 24].

A comparison of Eqs. (8), (9) and (10), (11) shows that the assumption about the effectiveness of a particular electron–nucleus interaction in the nuclear relaxation in the theoretical formulas significantly affects the quantitative interpretation of the experimental data. For example, the dependence of T_1 for the ^{139}La nuclei in $\text{La}_{1-x}\text{Ca}_x\text{MnO}_3$ ($x = 1/3$) on the square of the constant magnetic field shown in Fig. 11 from [7] was interpreted by assuming the dipole–dipole interaction to be effective (formula (9)). The values of 10^{-8} s and 130 G were obtained for the correlation time of the electron spins and the amplitude of the fluctuating local field on the ^{139}La nuclei, respectively. It is pointed out in [7] that the measured correlation time proved to be much larger than its expected value. However, if this plot were interpreted in terms of an isotropic hyperfine interaction (see formula (11)), then the correlation time would be much shorter, $\tau_{s\perp} \approx 10^{-12}$ s, while the amplitude of the local field would be much larger that suggested in [7]. For this interpretation, both these quantities prove to be within the expected ranges [6] (the spin–spin and spin–lattice interactions were assumed in [6, 7] to be the source of fluctuations in the localized electron spins). The assumption made in [6] about an isotropic pattern of the fluctuating local field on the ^{139}La nuclei seems to be more realistic. Therefore, Eqs (3), (4), and (10) with an isotropic hyperfine interaction should be used for the width of the detectable (in ceramic samples) relatively narrow central transition $-1/2 \longrightarrow 1/2$ in the quadrupole structure of the NMR signal (it is observed against the pedestal of merged satellite lines [6, 7]) and for the longitudinal relaxation rate T_1^{-1} measured in both studies.

The assumption that the electron spin dynamics slows down in $\text{La}_{1-x}\text{Ca}_x\text{MnO}_3$ ($x = 1/3$) due to the transition to the spin glass state [25] seems not to be confirmed by the EPR data [26]. It should be noted, however, that adding nonmagnetic trivalent ions (instead of bivalent ones) to lanthanum manganites can give rise to slow electron spin dynamics, as confirmed by a series of NMR and EPR experiments in $LaGa_{1-x}Mn_xO_3$ (x = 0–0.2) [21]. According to [22], the nuclear relaxation scenario for ^{69}Ga and ^{71}Ga in $LaGa_{1-x}Mn_xO_3$ is the following.

The Jahn–Teller static cooperative pulling of the MnO_6 octahedrons related to the orbital ordering, i.e., the strictly alternating orbitals $d(3x^2 - r^2)$ and $d(3y^2 - r^2)$ of the Mn^{3+} ions, takes place in the distorted rhombohedral phase of $LaMnO_3$ at room temperature. A dilution and a rise in temperature cause a breakdown of the Jahn–Teller cooperative deformations and a slow reorientation of the orbitals. As was theoretically substantiated in [27], thermally activated reorientations of the Jahn–Teller configurations take place in Mn^{3+} clusters or near defects. These reorientations are the source of fluctuations that ensure a relatively slow relaxation of the Mn^{3+} spins. According to [16], long electron relaxation times serve as the source of large $\tau_{s\|}$ and $\tau_{s\perp}$. The latter, in turn, ensure the nuclear relaxation of ^{69}Ga and ^{71}Ga by a mechanism based on the effectiveness of the dipole–dipole electron–nucleus interaction [22].

In crystals with a high concentration of magnetic ions, the main type of interactions between them is the exchange interaction; at $T < T_{C,N}$, the sample is in an ordered state, ferromagnetic (FM) or antiferromagnetic (AFM). The existence of a region corresponding to a ferromagnetic insulator on the phase diagram for lanthanum manganites with a low hole concentration was proven theoretically [28] and experimentally [29, 30]. According to [8, 10], only the phase of a ferromagnetic insulator with a spontaneous field of ~3.5 T [12] is detected in ceramic $La_{1-x}Ca_xMnO_3$ samples for $T \ll T_C$ and $0 < x \le 0.15$ by the NMR method, while in pure $LaMnO_3$ at $T \ll T_N$, there is a spontaneous field of ~0.03 T attributable to lattice distortion [8]. The electron spin components in ordered crystals fluctuate due to the exchange interactions between themselves. This pattern at a high concentration of magnetic ions is preserved even in the paramagnetic region of a magnetic, i.e., at $T \gg T_{C,N}$ (in this case, $\omega_{s\|} = 0$ and $\omega_{s\perp} \approx 0$). As follows from the results of [18] (see also [16]), the electron correlation functions are then Gaussian:

$$\langle \delta S_i^z(t)\delta S_i^z\rangle \approx \frac{1}{2}\langle \delta S_i^+(t)\delta S_i^-\rangle$$
$$\approx \frac{1}{2}\langle \delta S_i^-(t)\delta S_i^+\rangle \approx \frac{S(S+1)}{3}\exp\left(-\frac{\omega_E^2 t^2}{2}\right).$$

It should be noted, however, that when this expression was derived, the external constant magnetic field was assumed to be weak compared to the spontaneous field of the magnetic; i.e., it was assumed that the exchange frequency defined by the equality

$$\omega_E^2 = \frac{2S(S+1)}{3}Z\left(\frac{J}{\hbar}\right)^2 \qquad (17)$$

(Z is the number of closest neighbors of the electron spin) was higher than the electron Zeeman frequency. In this case, $\tau_{s\|} = \tau_{s\perp} = \sqrt{\pi/2}/\omega_E$; hence, we obtain for the paramagnetic (PM) region of a magnetic

$$(T_{2M}^{-1})_{PM}^{HT} = \sqrt{\frac{\pi}{2}}\frac{S(S+1)}{3\omega_E}\sum_j[(D_{ij}^{00})^2 - 2D_{ij}^{0+1}D_{ij}^{0-1}$$
$$+ (2C_M - 1)(-D_{ij}^{+10}D_{ij}^{-10} + D_{ij}^{+1+1}D_{ij}^{-1-1} + D_{ij}^{+1-1}D_{ij}^{-1+1})], \qquad (18)$$

$$(T_1^{-1})_{PM}^{HT} = \sqrt{2\pi}\frac{S(S+1)}{3\omega_E}$$
$$\times\sum_j[(-D_{ij}^{+10}D_{ij}^{-10} + D_{ij}^{+1+1}D_{ij}^{-1-1} + D_{ij}^{+1-1}D_{ij}^{-1+1})]. \qquad (19)$$

If we write expressions (18) and (19) for nuclei with $I = 1/2$ whose relaxation is dominated by the fluctuations of the isotropic local field, then the longitudinal and transverse relaxation rates in the paramagnetic region will be equal:

$$(T_1^{-1})_{PM}^{HT} = (T_2^{-1})_{PM}^{HT} = \frac{\sqrt{2\pi}}{\omega_E}\frac{S(S+1)}{3\hbar^2}\sum_j A_{ij}^2. \qquad (20)$$

This result matches expression (5.35) in [16].

Let us now take into account the fact that the exchange mechanism of the electron spin fluctuations in an ordered insulator (sample va.16 with a high Curie temperature investigated in [6] may serve as an example) at low temperatures is effected through the inelastic scatterings of spin waves by the nuclear magnetic moments [16]. Experiments on the inelastic scattering of neutrons in $La_{1-x}Ca_xMnO_3$ in a zero external field [30, 31] suggest the presence of spin waves (which are also interpreted as the coherent waves of magnetic polarons) with a quadratic dispersion law (both gapless and with a gap).

The electron spin deviation produced at a certain lattice site of a magnetically ordered crystal propagates in the crystal as an oscillatory wave of electron magnetic moments—a spin wave or a magnon. For free spin waves (i.e., those that do not interact with one another and with the lattice), the fluctuations of the spin components at site j can be roughly written as [16]

$$\delta S_j^z = \pm(\langle a_j^\dagger a_j\rangle - a_j^\dagger a_j),$$
$$\delta S_j^\pm = \sqrt{2S}a_j, \quad \delta S_j^\mp = \sqrt{2S}a_j^\dagger, \qquad (21)$$

where $a_j^\dagger$ and a_j are the creation and annihilation operators for the spin deviation at the lattice site j. In these formulas, we should take the upper sign for FM and the upper and lower signs for one and the other sublattices, respectively, for AFM. Let us pass from $a_j^\dagger$ and a_j to their spatial Fourier components and take into account the time dependence of the collective variables,

$$a_k^\dagger(t) = a_k^\dagger \exp(i\omega_k t), \quad a_k(t) = a_k \exp(-i\omega_k t),$$

where ω_k is the frequency of a magnon with a wave vector **k**. If we now disregard the influence of the constant magnetic field and make the only assumption that the NMR frequency (attributable to the local field) is low compared to the frequency of the homogeneous FM or AFM resonance, $\omega_{FMR,\,AFMR} = \omega_{k=0}$, then we can easily verify that only the Raman processes involving magnons [16, 32] contribute to the nuclear relaxation. An elementary act of these processes is the emission of one magnon by a nucleus and the absorption of another; the nuclear relaxation results from their energy difference. As we see from (21), these processes are described by the correlation function of the electron spin z components, which contains exponentials of the form $\exp[i(\omega_k - \omega_{k'})_t]$ $(\omega_{s\parallel} = \omega_k - \omega_{k'})$. However, it is well known that impurities (e.g., rare-earth ions) and the interaction between the magnons can cause the spin wave to be damped out. The nuclear relaxation through the emission or absorption of one magnon by a nucleus $(\omega_{s\perp} = \omega_k)$ then becomes possible. In calculating the corresponding relaxation rates, we take into account the fact that, in general, the scattering of spin waves can ensure the fluctuations of an arbitrary anisotropic field from the electron spins on the nucleus. For a ferromagnet,

$$\langle \delta S_j^z(t)\delta S_{j'}^z\rangle = \frac{1}{N_s^2}$$
$$\times \sum_{k,\,k'} \exp[i(\omega_k - \omega_{k'})t - (\Gamma_k + \Gamma_{k'})t]\bar{n}_k(\bar{n}_{k'} + 1),$$
$$\langle \delta S_j^+(t)\delta S_{j'}^-\rangle = \frac{2S}{N_s}\sum_k \exp(-i\omega_k t - \Gamma_k t)\bar{n}_k,$$
$$\langle \delta S_j^-(t)\delta S_{j'}^+\rangle = \frac{2S}{N_s}\sum_k \exp(i\omega_k t - \Gamma_k t)(\bar{n}_k + 1),$$

where N_s is the total number of localized electron spins, Γ_k is the damping of spin waves with a wave vector **k**, and the mean (at a given temperature) spin wave numbers are given by the Bose–Einstein distribution function

$$\bar{n}_k = [\exp(\hbar\omega_k/k_BT - 1)]^{-1}.$$

Given the damping of spin waves at $T \ll T_C$ (the low-temperature (LT) approximation), the following expressions can be derived for the transverse and longitudinal nuclear relaxation rates in FM from (3) and (4):

$$(T_{2M}^{-1})_{FM}^{LT} = \left[\sum_j (D_{ij}^{00})^2 + \sum_j (-D_{ij}^{+10}D_{ij}^{-10})(2C_M - 1)\right]$$
$$\times \frac{1}{N_s^2}\sum_{k,\,k'}\bar{n}_k(\bar{n}_{k'} + 1)\frac{\Gamma_k + \Gamma_{k'}}{(\omega_k - \omega_{k'})^2 + (\Gamma_k + \Gamma_{k'})^2}$$
$$+ p\frac{S}{N_s}\sum_k \Bigg\{(2\bar{n}_k + 1)\sum_j (-D_{ij}^{0+1}D_{ij}^{0-1})$$
$$+ \frac{1}{2}[C_M(2\bar{n}_k + 1) + C_{M+1}\bar{n}_k + C_{M-1}(\bar{n}_k + 1)] \tag{22}$$
$$\times \sum_j D_{ij}^{+1+1}D_{ij}^{-1-1}$$
$$+ \frac{1}{2}[C_M(2\bar{n}_k + 1) + C_{M+1}(\bar{n}_k + 1) + C_{M-1}\bar{n}_k]$$
$$\times \sum_j D_{ij}^{+1-1}D_{ij}^{-1+1}\Bigg\}\frac{\Gamma_k}{\omega_k^2 + \Gamma_k^2},$$

$$(T_1^{-1})_{FM}^{LT} = \sum_j (-D_{ij}^{+10}D_{ij}^{-10})\frac{2}{N_s^2}$$
$$\times \sum_{k,\,k'}\bar{n}_k(\bar{n}_{k'} + 1)\frac{\Gamma_k + \Gamma_{k'}}{(\omega_k - \omega_{k'})^2 + (\Gamma_k + \Gamma_{k'})^2} \tag{23}$$
$$+ \frac{S}{N_s}\sum_j (D_{ij}^{+1+1}D_{ij}^{-1-1} + D_{ij}^{+1-1}D_{ij}^{-1+1})$$
$$\times \sum_k \frac{(2\bar{n}_k + 1)\Gamma_k}{\omega_k^2 + \Gamma_k^2}.$$

When the damping of spin waves in the sample is negligible, we should let all Γ_k in formulas (22) and (23) tend to zero. Then,

$$(T_{2M}^{-1})_{FM}^{LT} = \pi\sum_j [(D_{ij}^{00})^2 - D_{ij}^{+10}D_{ij}^{-10}(2C_M - 1)] \tag{24}$$
$$\times \frac{1}{N_s^2}\sum_{k,\,k'}\bar{n}_k(\bar{n}_{k'} + 1)\delta(\omega_k - \omega_{k'}),$$

$$(T_1^{-1})_{FM}^{LT} = 2\pi\sum_j (-D_{ij}^{+10}D_{ij}^{-10})\frac{1}{N_s^2} \tag{25}$$
$$\times \sum_{k,\,k'}\bar{n}_k(\bar{n}_{k'} + 1)\delta(\omega_k - \omega_{k'}).$$

According to [16], when the isotropic fluctuating local field on the nucleus dominates, expression (25) becomes equal to zero. The well-known expression (5.41) from [16] is obtained for the transverse relaxation rate at $I = 1/2$. The physical cause of the longitudinal relaxation rate T_1^{-1} becoming equal to zero in this case differs significantly from the cause of the large decrease in T_1^{-1} for slow fluctuations (see formulas (12)). Expression (25) pertains to the case (pointed out in [17]) where a perturbation (the Hamiltonian of an isotropic electron–nucleus interaction) cannot produce the absorption or emission of a nuclear-frequency quantum. Naturally, both the longitudinal relaxation rate and the nonsecular contribution to the NMR line width then simultaneously become equal to zero.

However, for the nuclei of nonmagnetic ions, the dipole fields of the surrounding magnetic ions can contribute significantly to the local field. Expressions (22) and (23) with the substitution of (5) yield the relaxation rates in the case where the scattering of spin waves produces the fluctuations of the dipole field on the nuclei.

To find out how expressions (24) and (25) depend on temperature, the following should be substituted in them [16]:

$$\begin{aligned}&\frac{\pi}{N_s^2}\sum_{k,\,k'}\bar{n}_k(\bar{n}_{k'+1})\delta(\omega_k-\omega_{k'})\\ &= \frac{1}{16\pi^3\omega_E}\left(\frac{k_{\mathrm{B}}T}{\hbar\omega_E}\right)^2\ln\left\{\left[1-\exp\left(-\frac{\hbar\omega_{FMR}}{k_{\mathrm{B}}T}\right)\right]^{-1}\right\}.\end{aligned} \tag{26}$$

This expression is valid for a quadratic dispersion law of spin waves: $\omega_k = \omega_{FMR} + \omega_E(ak)^2$, where a is the lattice parameter.

For completeness, we provide similar results for a cubic AFM at $T \ll T_{\mathrm{C,\,N}}$ obtained in [16] for an isotropic local field on the nucleus:

$$\begin{aligned}(T_2^{-1})_{AFM}^{LT} &\approx \frac{C}{6\pi\hbar^2\omega_E^{AFM}}\\ &\times\sum_j A_{ij}^2\left(\frac{k_{\mathrm{B}}T}{\hbar\omega_E^{AFM}}\right)^3\left[1-I_1\left(\frac{\hbar\omega_{AFMR}}{k_{\mathrm{B}}T}\right)\right],\end{aligned} \tag{27}$$

where C is a constant on the order of unity determined by the number of spins in an elementary cell and by the geometry of the latter;

$$I_1(x) = \frac{6}{\pi^2}\int_0^x\frac{ydy}{e^y-1}, \quad \omega_E^{AFM} = \frac{4S}{\sqrt{3}}\frac{J_{1,\,2}(0)}{\hbar},$$

where $J_{1,\,2}(0)$ is the Fourier component with $k = 0$ for the exchange integral between the AFM sublattices.

Expression (27) from [16] is valid in the long-wavelength approximation for spin waves when their spectrum in AFM is

$$\omega_k^2 \approx \omega_{AFMR}^2 + (\omega_E^{AFM})^2(ak)^2.$$

Since $\omega_E^{AFM} \ll \omega_E$, it follows from (24), (25), and (27) that the longitudinal and transverse nuclear relaxation rates in AFMs will be much larger than those in FMs, which is observed experimentally [5]. A more detailed and comprehensive theory of the nuclear spin relaxation in AFMs is presented in [33].

At intermediate (IT) temperatures ($T \le T_{\mathrm{C,\,N}}$), the temperature dependence of the relaxation rates in cubic crystals in a zero external field is [16, 32]

$$\begin{aligned}(T_2^{-1})_{FM}^{IT} &= (T_1^{-1})_{FM}^{IT} = C'(T_1^{-1})_{PM}^{HT}\left(\frac{T_{\mathrm{C}}}{T-T_{\mathrm{C}}}\right)^{3/2},\\ (T_2^{-1})_{AFM}^{IT} &= (T_1^{-1})_{AFM}^{IT} = C'(T_1^{-1})_{PM}^{HT}\left(\frac{T_{\mathrm{N}}}{T-T_{\mathrm{N}}}\right)^{1/2},\end{aligned} \tag{28}$$

where $C' \sim 0.1$.

Here, it should be noted that formulas (28) are valid in a very narrow temperature range [16, 32]:

$$\left(\frac{\omega_I}{\omega_E}\right)^{1/2} \ll \frac{T-T_{\mathrm{C,\,N}}}{T_{\mathrm{C,\,N}}} \ll 1$$

for FMs and

$$\frac{\omega_I}{\omega_E^{AFM}} \ll \frac{T-T_{\mathrm{C,\,N}}}{T_{\mathrm{C,\,N}}} \ll 1$$

for AFMs. In addition, applying a sufficiently strong constant magnetic field suppresses (particularly strongly in FMs) the divergence of T_1^{-1} [32] predicted by expressions (28). Therefore, this effect was not observed in the experimental works on the nuclear relaxation in lanthanum manganites under consideration [5–13].

In conclusion, we will describe the role of the multiparticle nucleus–nucleus interactions that are indirect in a magnetically ordered crystal and are effected through the electron spins due to the hyperfine interaction. The indirect interaction between the nuclear spins of a magnetically ordered crystal through the emission of a magnon by one nucleus and its absorption by another (Suhl–Nakamura (SN) interaction) at high concentrations of magnetic nuclei can contribute to the line width of the nuclear quadrupole structure (see [16]). This contribution is estimated as the square root of the second moment of the lines. As was shown in [34, p. 443], this moment for a resolved quadrupole structure changes from line to line and, for the $M \longrightarrow M + 1$ transition, is

$$(M_{2M})^{SN} = \frac{2}{N_I(2I+1)} \times \sum_{i,j} U_{ij}^2 \left[C_M^2 + \frac{1}{2} C_{M+1}^2 + \frac{1}{2} C_{M-1}^2 \right]. \tag{29}$$

Here, N_I is the number of magnetic nuclei, and U_{ij} is the temperature-independent Suhl–Nakamura coupling constant. In contrast to the Suhl–Nakamura interaction, the indirect interaction between the nuclear spins through the electron spins in crystals with a cubic symmetry becomes isotropic (scalar) with increasing temperature, when the spontaneous magnetization is absent or small, and its constant depends on temperature as T^{-2} [32]. As a result of the scalar form, this interaction will not contribute to the second moment of the NMR signal from identical nuclei. On the other hand, for identical nuclei with a symmetry lower than the cubic one and for different nuclei with any symmetry, this indirect interaction will make a contribution to the line width that will decrease with increasing temperature as T^{-2}. In the immediate vicinity of the point of transition to an ordered state, the Moriya theory [32] yields a contribution to the line width for both FM and AFM that diverges as $(T/|T - T_{\mathrm{C, N}}|)^{1/4}$.

3. CONCLUSIONS

We calculated the transverse relaxation rates T_{2M}^{-1} for the nuclear magnetization at the frequencies of individual transitions of the quadrupole NMR structure and the relaxation rate T_1^{-1} for the total longitudinal magnetization component by using methods that assume short correlation times for the fluctuating local fields generated on the nuclei by the electron spins. The corresponding formulas were derived for an arbitrary anisotropic electron–nucleus relaxation mechanism and arbitrary electron and nuclear spins; they are valid for any ratio $\hbar\omega_s/k_{\mathrm{B}}T$. The cases of dipole–dipole and isotropic hyperfine relaxation mechanisms were concretized. We discussed the fact noted in [7] that, when the results of experiments on the relaxation of ^{139}La nuclei in $\mathrm{La}_{1-x}\mathrm{Ca}_x\mathrm{MnO}_3$ are interpreted under the assumption made in [7] about the effectiveness of the dipole–dipole electron–nucleus interaction, the correlation times prove to be unusually long, while the fluctuating local fields prove to be weak. We showed that these results interpreted by assuming the isotropic hyperfine interaction to be effective [5, 6] yield correlation times and local field amplitudes within the ranges expected from the EPR data. It should be noted that the nuclear relaxation model based on the effectiveness of the electron–nucleus dipole–dipole interaction can yield good results for magnetically diluted manganites [22].

In a diluted paramagnet, the correlation functions of the longitudinal (transverse) electron spin components are simple exponentials with correlation times equal to, respectively, the spin–lattice and spin–spin electron relaxation times (a LaMnO_3 material strongly diluted with nonmagnetic Ga^{3+} ions [22]). In samples with a high concentration of magnetic ions (e.g., in $\mathrm{La}_{1-x}\mathrm{Ca}_x\mathrm{MnO}_3$), the fluctuations of the electron spins both below and above the magnetic ordering temperature are attributable to their exchange interaction. In the latter case, the formulas for T_{2M}^{-1} and T_1^{-1} were obtained by taking into account the well-known Gaussian time dependence of the electron correlation functions with the correlation times that are the reciprocals of the exchange frequency. In magnetically concentrated samples below the ordering temperature, the nuclear relaxation could be attributable to the exchange fluctuations of the spatially correlated electron spins, which is faithfully described in terms of spin waves. Without allowance for the damping of spin waves, only the Raman magnon absorption–emission processes, which contribute only to the transverse nuclear relaxation, are effective in the nuclear relaxation. Therefore, we might expect a sharp slowdown of the longitudinal nuclear relaxation at $T < T_{\mathrm{C}}$, which is attributable in our case to the energy prohibition on the single-magnon interaction with nuclei rather than to the slowdown of the electron spin fluctuations. This mechanism can qualitatively explain the relation $2W_1 \ll 2W_2$ observed in [6] at $T < T_{\mathrm{C}}$.

ACKNOWLEDGMENTS

We are grateful to V.A. Atsarkin for valuable remarks and for the opportunity to familiarize ourselves with the content of paper [22] before its publication.

REFERENCES

1. I. V. Aleksandrov, *Theory of Magnetic Relaxation. Relaxation in Liquids and Solid Nonmetallic Paramagnets* (Nauka, Moscow, 1975), Chap. III [in Russian].
2. J. M. D. Coey, M. Viret, and S. von Molnar, Adv. Phys. **48**, 167 (1999).
3. E. L. Nagaev, Phys. Rep. **346**, 387 (2001).
4. E. Dagotto, J. Hotta, and A. Moreo, Phys. Rep. **344**, 1 (2001).
5. G. Allodi, R. De Renzi, G. Guidi, *et al.*, Phys. Rev. B **56**, 6036 (1997).
6. G. Allodi, R. De Renzi, and G. Guidi, Phys. Rev. B **57**, 1024 (1998).
7. K. E. Sakaie, C. P. Slichter, P. Lin, *et al.*, Phys. Rev. B **59**, 9382 (1999).
8. K. Kumagai, A. Iwai, Y. Tomioka, *et al.*, Phys. Rev. B **59**, 97 (1999).
9. G. Papavassiliou, M. Fardis, M. Belesi, *et al.*, Phys. Rev. B **59**, 6390 (1999).

10. G. Papavassiliou, M. Fardis, M. Belesi, *et al.*, Phys. Rev. Lett. **84**, 761 (2000).
11. G. Papavassiliou, M. Belesi, and D. Dimitropoulos, Phys. Rev. Lett. **87**, 177204 (2001).
12. G. Allodi, M. Gestelli Guidi, R. De Renzi, *et al.*, Phys. Rev. Lett. **87**, 127206 (2001).
13. M. M. Savosta, V. I. Kamenev, V. A. Borodin, *et al.*, Phys. Rev. B **67**, 094403 (2003).
14. A. Urushibara, Y. Morimoto, T. Arima, *et al.*, Phys. Rev. B **51**, 14103 (1995).
15. A. Abragam, *The Principles of Nuclear Magnetism* (Clarendon Press, Oxford, 1961; Inostrannaya Literatura, Moscow, 1963).
16. E. A. Turov and M. P. Petrov, *Nuclear Magnetic Resonance in Ferro- and Antiferromagnets* (Nauka, Moscow, 1969; Wiley, New York, 1972), Chap. V.
17. R. Kubo and K. Tomita, J. Phys. Soc. Jpn. **9**, 888 (1954).
18. T. Moriya, Prog. Theor. Phys. **16**, 23, 641 (1956).
19. T. Rega, J. Phys.: Condens. Matter **3**, 1871 (1991).
20. W. W. Simmons, W. J. O'Sullivan, and W. A. Robinson, Phys. Rev. **127**, 1168 (1962).
21. A. Narath, Phys. Rev. **162**, 320 (1967).
22. N. Noginova, E. Arthur, T. Weaver, *et al.*, Phys. Rev. B **69**, 024406 (2004).
23. T. Plefka, Phys. Status Solidi B **55**, 129 (1973).
24. C. P. Slichter, *Principles of Magnetic Resonance*, 3rd ed. (Springer, Berlin, 1990; Mir, Moscow, 1967), Chap. V.
25. R. H. Heffner, L. P. Le, M. F. Hundley, *et al.*, Phys. Rev. Lett. **77**, 715 (1996).
26. S. E. Lofland, P. Kim, P. Dahiroc, *et al.*, Phys. Rev. Lett. **79**, 476 (1997).
27. J. B. Goodenough, A. Wold, R. J. Arnott, and N. Meniuk, Phys. Rev. **124**, 373 (1961).
28. S. Yunoki, A. Moreo, and E. Dagotto, Phys. Rev. Lett. **81**, 5612 (1998).
29. Y. Endoh, K. Hirota, S. Ishihara, *et al.*, Phys. Rev. Lett. **82**, 4328 (1999).
30. M. Hennion, F. Moussa, J. Rodriguez-Carvajal, *et al.*, Phys. Rev. B **56**, R497 (1997).
31. J. W. Lynn, R. W. Erwin, J. A. Borchers, *et al.*, Phys. Rev. Lett. **76**, 4046 (1996).
32. T. Moriya, Prog. Theor. Phys. **28**, 371 (1962).
33. S. Chakravarty, M. P. Gefland, P. Kopietz, *et al.*, Phys. Rev. B **43**, 2796 (1991).
34. M. A. H. McClausen and I. S. Mackenzie, Adv. Phys. **28**, 307 (1979).

Translated by V. Astakhov

Journal of Experimental and Theoretical Physics, Vol. 99, No. 6, 2004, pp. 1244–1252.
Translated from Zhurnal Éksperimental'noĭ i Teoreticheskoĭ Fiziki, Vol. 126, No. 6, 2004, pp. 1425–1434.
Original Russian Text Copyright © 2004 by Okotrub, Bulusheva, Gusel'nikov.

SOLIDS
Electronic Properties

Effect of Purification on the Electron Structure and Field Emission Characteristics of a Carbonaceous Material Containing Single-Wall Carbon Nanotubes

A. V. Okotrub*, L. G. Bulusheva, and A. V. Gusel'nikov
Nikolaev Institute of Inorganic Chemistry, Siberian Division, Russian Academy of Sciences,
Novosibirsk, 630090 Russia
**e-mail: spectrum@che.nsk.su*

Received April 21, 2004

Abstract—A carbonaceous material containing single-wall carbon nanotubes (SWNTs) has been synthesized by arc-discharge evaporation of graphite with a catalytic additive of nickel and cobalt powders. The synthesized SWNTs were purified from an amorphous carbon component (soot) and the catalyst particles by boiling in nitric acid. A comparison of the X-ray fluorescence spectra measured before and after this treatment showed that acid etching significantly decreased the content of soot in the material. The material enriched with SWNTs is characterized by a reduced threshold for the appearance of the field emission current, which is explained by a decrease in the screening effect of soot. The current–voltage characteristics of SWNTs exhibit a hysteresis, which is suggested to be due to the adsorption of molecules and radicals on the surface and at the ends of carbon nanotubes. *© 2004 MAIK "Nauka/Interperiodica".*

1. INTRODUCTION

Single-wall carbon nanotubes (SWNTs) are of considerable interest both from the standpoint of basic science, being the ideal object for direct observation of the effects characteristic of low-dimensional structures, and in view of the possible practical applications [1]. One of the most impressive features of SWNTs is the cold emission of electrons at low electric field strengths [2–4], which provides for a real possibility of creating a new generation of small-size electronic devices capable of operating in a broad range of frequencies at high working currents. The dependence of the tunneling current on the composition of the environment makes it possible to develop effective gas sensors based on SWNTs [5].

The field emission properties of SWNTs are determined by the ratio of the tube length to diameter and by the structure of the tube surface. Using high-temperature electric arc, it is possible to obtain carbon nanotubes containing a small number of defects, which is an important factor favoring stability of the emission current. The average nanotube diameter is determined by the catalyst composition [6, 7] and varies within 1.0–1.4 nm. Powdered Ni–Co mixtures with various ratios of components (sometimes, with additives of rare earth metals) are among the most effective catalysts for SWNT synthesis.

In addition to nanotubes combined in bundles, the as-synthesized material contains amorphous carbon and residual catalyst particles. For effective utilization of SWNTs in various devices, it is necessary to remove these by-products. This can be achieved by a special chemical treatment of the carbonaceous material, in particular, by etching in concentrated mineral acids. However, the chemical treatment also modifies the structure of carbon nanotubes by opening their ends, grafting various functional groups, and creating vacancies [8–11]. Evidently, these changes in the chemical structure of SWNTs must influence their electron structure and, hence, the field emission characteristics of the SWNT-containing material.

This study was aimed at determining changes in the electron structure and field emission properties of an SWNT-containing carbonaceous material synthesized by arc-discharge evaporation of graphite and then subjected to a chemical treatment. The electron structure of the material was studied by ultrasoft X-ray fluorescence (XRF) spectroscopy, which provides information about the local partial density of occupied electron states. The XRF spectra were interpreted based on the results of quantum-chemical calculations of model structures using the local density functional approximation. The dynamic characteristics of the field emission from SWNTs were studied by varying the frequency of the applied sawtooth voltage.

2. SYNTHESIS OF SWNT-CONTAINING MATERIAL

The SWNT-containing carbonaceous material was obtained via arc-discharge evaporation of graphite

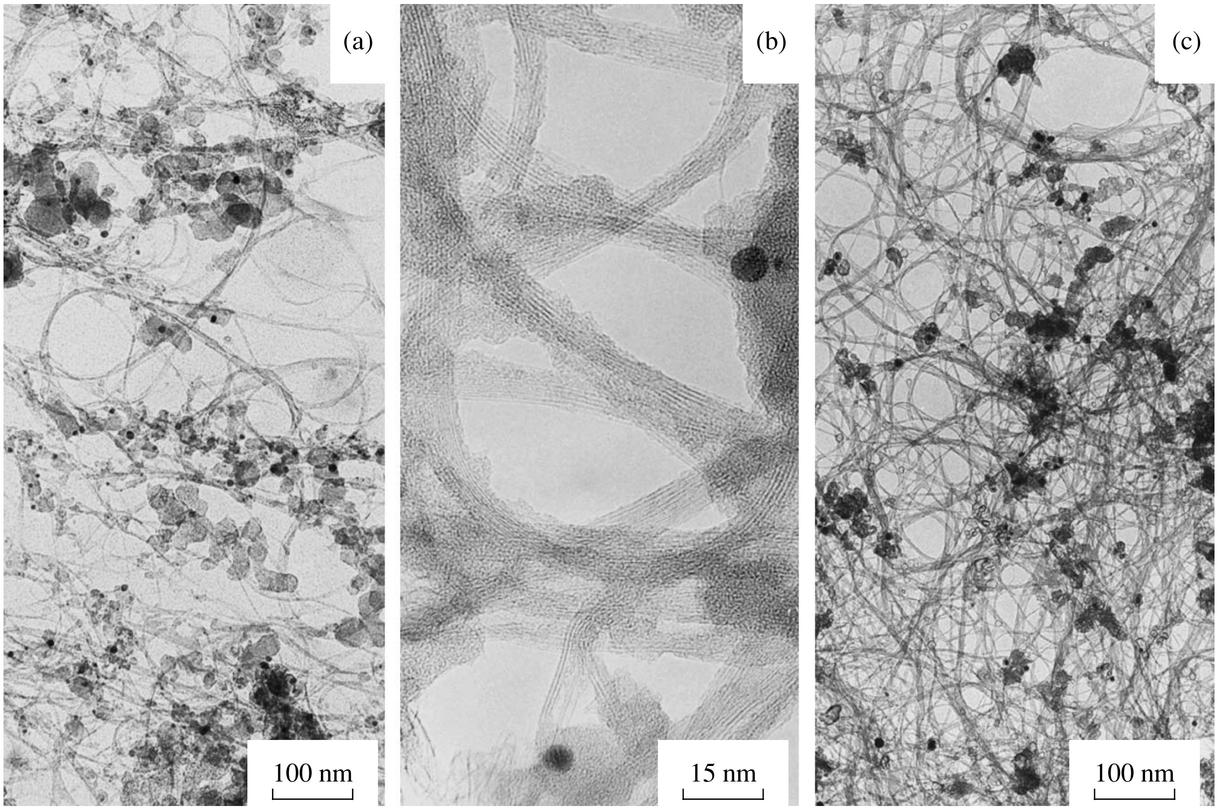

Fig. 1. TEM micrographs of a carbonaceous material synthesized by arc-discharge evaporation of graphite with Ni–Co catalyst additives: (a, b) before treatment with nitric acid; (c) after the chemical treatment. Magnified image (b) shows the bundles of SWNTs.

using a setup described in detail elsewhere [12, 13]. The synthesis was carried out in a stainless-steel reactor with a diameter of 0.5 m and a working volume of about 150 with water-cooled walls. The buffer gas was helium at a pressure of 1.2×10^5 Pa. The arc discharge was power supplied from a current generator ensuring a discharge current of about 1000 A at an applied voltage of 35–40 V. The electrodes were arranged in a vertical geometry. The movable upper electrode (cathode) was a graphite rod with a diameter of 60 mm. The lower consumable electrode (anode) was a 200-mm-long graphite rod with a 14×14 mm^2 cross section and a 10-mm-diameter axial cavity filled with a catalyst powder.

In the first stage of synthesis, the anode cavity was filled with a mixture of powdered graphite, nickel, and cobalt at a total metal content of 5% (relative to the electrode weight). Upon the graphite anode evaporation in the arc discharge, soot was deposited on the water-cooled reactor walls. The deposit contained metal nanoparticles and a small proportion of SWNTs (about 1% according to electron microscopy data). This soot was used to fill the cavity of the evaporated electrode in the second stage of synthesis. In this stage, the synthesized carbonaceous material was deposited onto a nickel screen situated at a distance of 100 mm from the arc and heated to a temperature of 1200°C. A deposit formed on this screen had a denser structure than the soot formed on the water-cooled reactor walls in the first stage.

3. ELECTRON-MICROSCOPIC EXAMINATION OF CARBONACEOUS MATERIAL

The structure of a material deposited on the nickel screen was studied by transmission electron microscopy (TEM). The measurements were performed using a JEM-100CX electron microscope (JEOL, Japan) with a spatial resolution of 5 Å. The samples were prepared by ultrasonic dispersion of soot in cavitation-boiling suspension deposited onto a colloid substrate. The TEM micrographs showed that the synthesized material contained carbon nanotubes, metal particles, and soot (Fig. 1a). Carbon nanotubes synthesized in the presence of a Ni–Co catalyst have a diameter of 1.2–1.4 nm and form bundles including up to several tens of nanotubes (Fig. 1b). The weight fraction of nanotubes in the material obtained by two-stage synthesis was about 50%.

The particles of metal and amorphous carbon were removed by boiling the carbonaceous material for 2 h in concentrated nitric acid. As can be seen from Fig. 1c,

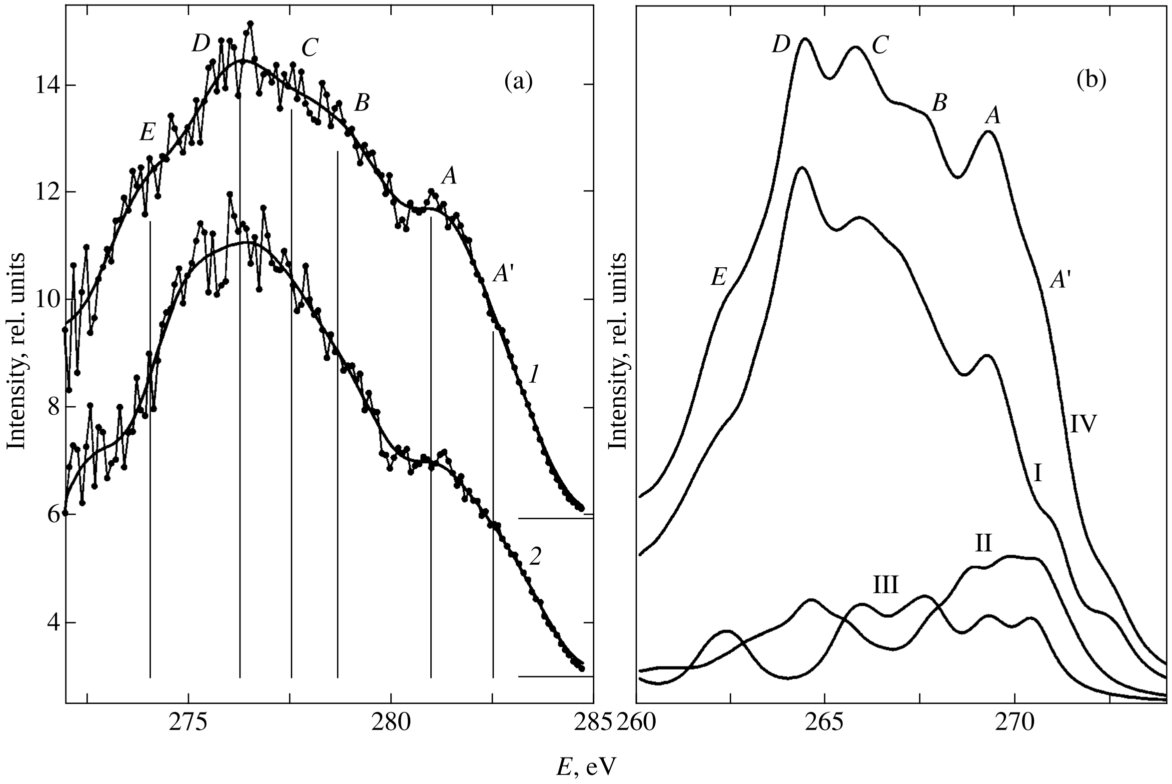

Fig. 2. The CK_α spectra: (a) experimental spectra of an SWNT-containing material (*1*) before and (*2*) after purification; (b) theoretical spectra constructed using the results of quantum-chemical calculations for model structures of (I) a carbon nanotube, (II) a stripe of carbon hexagons, and (III) a carbon chain (Fig. 3); spectrum IV shows a sum of curves I, II, and III with a component ratio of 7 : 1.5 : 1.5.

the material upon this treatment is enriched with carbon nanotubes. The purified material is characterized by a significantly lower content of metal particles and soot. In addition, there appear hollow spherical graphite particles. Some of the metal particles retained after synthesis are covered by graphite layers. In the case when the number of such layers is small and they contain defects, the acid dissolves metal to leave hollow graphite shells. Since thick and continuous graphite shells prevent acid penetration, the etched material still contains a certain fraction of graphite-encapsulated metal particles. The weight fraction of SWNTs relative to the total carbon content in the purified material is about 90%.

4. X-RAY FLUORESCENCE SPECTRA AND ELECTRON STRUCTURE OF CARBONACEOUS MATERIAL

XRF spectra of the SWNT-containing material before and after boiling in nitric acid were measured with a laboratory-made spectrometer. The samples were applied onto a copper substrate and cooled down to liquid nitrogen temperature in the course of measurements. The X-ray fluorescence was excited using bremsstrahlung radiation from a copper anode operating at $U = 6$ kV, $I = 0.5$ A. The output radiation was analyzed by an ammonium biphthalate (NH_4AP) single crystal. Because of the phenomenon of anomalous reflection, the NH_4AP crystal exhibits nonuniform reflectance near the *K*-edge of carbon absorption [14]. For this reason, the XRF spectra were corrected by means of a special mathematical algorithm [15]. The analyzer crystal employed in our setup allowed the CK_α spectra to be obtained with an energy resolution of 0.5 eV and the maximum statistics in a short-wavelength range (279–285 eV). The XRF spectra were normalized to maximum intensity; the accuracy of determining spectral line positions on the energy scale was about 0.3 eV.

Figure 2a compares the CK_α spectra of the initial (as-synthesized) and acid-treated carbonaceous SWNT-containing material. The XRF spectra exhibit the main maximum *D* at an energy of 276.2 eV and a less intense peak *A* at 281.0 eV. Such peaks with close energies of the emitted radiation are characteristic of the CK_α spectra of graphite [16], arc-discharge synthesized multiwall carbon nanotubes [17], and SWNTs obtained by laser ablation [18]. The XRF fluorescence spectrum arises when valence electrons occupy the vacancies created by exciting radiation on the core levels of atoms (1*s* for carbon). Owing to the dipole selection rules, the CK_α spectrum contains information about the density of occupied 2*p* states of a carbon

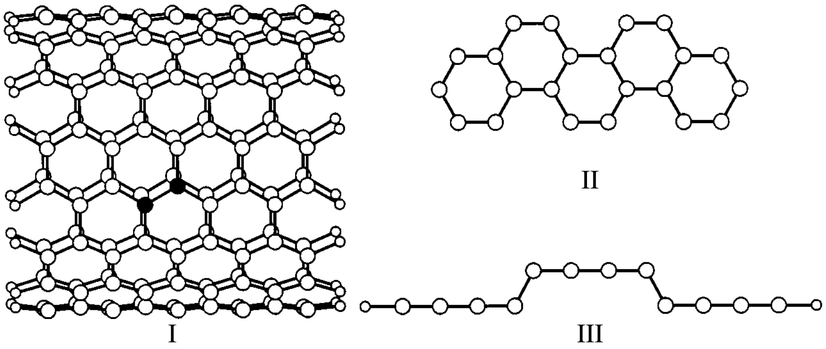

Fig. 3. Calculated fragments of an (8, 8)-armchair-type SWNT (model I), a stripe of graphite carbon hexagons (model II), and a carbon chain (model III). Large open circles denote carbon atoms; small open circles are hydrogen atoms attached to terminal carbon atoms in the nanotube and chain structures. Black circles indicate two structurally nonequivalent carbon atoms in the nanotube for which the theoretical CK_α spectrum was constructed.

atom, which can be compared to the results of quantum-chemical calculations for atoms in the given compound [19]. Based on such a comparison, peaks *A* and *D* in the CK_α spectra of our samples were assigned to π and σ electron systems, respectively. The electrons of both π and σ systems are also responsible for the intensities of peaks *C* and *B*.

The CK_α spectrum of a material enriched with carbon nanotubes is characterized by a decrease in the relative intensities of high-energy features (Fig. 2a, curve *2*). This spectrum is much like the CK_α spectrum of SWNTs synthesized by laser evaporation of a graphite target with additives of a Ni–Co catalyst [18], which is evidence that carbon atoms occur in the like electron states in the nanotubes of both types. The main difference of purified material from the initial one is a decrease in the content of soot. Therefore, it is suggested that the peaks of maximum intensity in the CK_α spectrum of the initial sample are most probably related to features of the electron state of amorphous carbon.

The structure of soot formed in the course of arc-discharge evaporation of graphite is undetermined. The results of measurements using various spectral and structure-sensitive techniques show that most probable components in this soot are small graphite fragments [20] and linear carbon chains [21]. In order to reveal the differences in electron structure of the carbon atoms constituting the surface of nanotubes and those entering into the fragments contained in soot, we have analyzed three model structures (Fig. 3). Model I is a fragment of the (8, 8)-armchair-type nanotube configuration. Two types of bonds can be distinguished in this structure: (i) perpendicular to the tube axis and (ii) making an angle with this axis (a bond of this type links atoms indicated by black circles in Fig. 3). The results of optimization of the nanotube fragment geometry performed within the framework of the semiempirical MNDO method [22], showed that the lengths of the bonds of two types are 1.42 and 1.45 Å at a tube diameter of 10.9 Å. The shorter bond is perpendicular to the tube axis, in agreement with the results of calculations for the armchair-type nanotube of a greater diameter performed using the local electron density functional approximation [23]. The structure of model II comprises five carbon hexagons sharing edges, and model III represents a fragment of the α-carbyne chain with alternating single and triple bonds [24]. The structures of these models were calculated within the framework of the local density functional approximation using the B3LYP method [25], implemented in the quantum-chemical program package Jaguar [26]. The calculation was performed using a 3-21G basis set of atomic orbitals; the dangling bonds at the boundaries of nanotube and carbyne fragments were saturated with hydrogen atoms.

The results of quantum-chemical calculations of the model structures were used to simulate the corresponding theoretical CK_α spectra. The X-ray transition energy was assumed to be equal to the difference between one-electron energies of the valence (*i*) and core (*j*) levels:

$$E_{ij} = \varepsilon_i - \varepsilon_j. \qquad (1)$$

The X-ray transition intensity was calculated assuming that localization of the C 1*s* orbitals allows these transitions to occur within the same carbon atom A. Then, the line intensity was calculated using the formula

$$I_{ij} = \sum_{\mathrm{A}, n, m} \left|C_{jm}^{\mathrm{A}} C_{in}^{\mathrm{A}}\right|^2, \qquad (2)$$

where A denotes carbon atoms of the model, and C_{jm} and C_{in} are the weight coefficients with which the 1*s* and 2*p* atomic orbitals enter into the *j*th and *i*th molecular orbitals, respectively. Theoretical spectra of the carbon nanotubes according to model I were calculated for two structurally nonequivalent carbon atoms indi-

Absolute (E) and relative (ΔE) energies of peaks in the experimental CK_α spectra of SWNT-containing materials and in the theoretical spectra of model carbon structures

Peak	$E^{\rm exp}$, eV	$E^{\rm theor}$, eV	$\Delta E^{\rm exp}$, eV	$\Delta E^{\rm theor}$, eV
A'	282.6	270.9	–1.6	–1.6
A	281.0	269.3	0	0
B	279.0	267.6	2.0	1.7
C	277.6	265.9	3.4	3.4
D	276.2	264.4	4.8	4.9
E	274.0	262.3	7.0	7.0

cated in Fig. 3. By considering only these central atoms, we reduced the influence of the fragment boundaries so as to model the electron state of carbon atoms in a long nanotube. In simulating the spectra of structures according to models II and III, we took into account all carbon atoms. Theoretical spectra were constructed as the superpositions of 0.6 eV-wide Lorentzian lines and normalized to maxima.

The theoretical CK_α spectra of the carbon-based structures according to models I–III and their sum (curve IV) are presented in Fig. 2b. The spectrum of the carbon nanotube (curve I) exhibits the main maximum *D*, a shoulder *C* on the short-wavelength side, and a less intense component *A*. The same features are resolved in the spectrum of purified SWNTs (Fig. 2a, curve *2*). The calculated energies of X-ray transitions are about 12 eV lower than the corresponding experimental values. This difference is related to the fact that calculations of the system in the ground state were performed with neglect of relaxation processes accompanying the X-ray emission. The calculated distances between the main spectral features agree well with the experimental values (see table). The calculation somewhat overstated the relative intensity of the short-wavelength peak *A* in comparison to that in the measured XRF spectra of nanotubes, which can be explained by the limitations of model I and the calculation method employed. The length of the calculated fragment may be insufficient to completely exclude the effect of fragment boundaries on the electron state of central carbon atoms. Indeed, investigation of the dependence of the density of C 2*p* electrons on the length of fragments in a (6, 0)-zigzag-type nanotube showed that the optimum tube length corresponds to five hexagons [27]. Moreover, the calculated tube has a smaller diameter than the SWNTs studied. High curvature of the graphite cylinder leads to a significant alternation of bonds in the (8, 8)-armchair-type nanotube configuration and, as a result, to localization of the π electron density. An increase in the length and diameter of the nanotube fragment (selected taking into account limitations of the software used in the calculations) might be expected to result in a decrease in the relative intensity of peak *A* in the theoretical spectrum of the carbon nanotube according to model I.

The CK_α spectra of the fragments representing a stripe of carbon hexagons and a carbon chain (Fig. 2b, curves II and III, respectively) significantly differ both from each other and from the spectrum of the carbon nanotube. The spectrum of fragment II displays two pronounced features with their maxima at about 265 and 270 eV. As a result, account of the electron state of condensed carbon hexagons leads to an increase in the relative intensity of peaks *D* and *A*, as well as of the most short-wavelength feature *A*' in the total spectrum IV. The shape of profile III is indicative of a significant delocalization of the electron density in this model. Thus, the presence of carbon chains in the sample must provide for an increase in the intensity of peaks *C*, *B*, *A* and a long-wavelength shoulder *E* in the total spectrum. All the above tendencies are observed in the CK_α spectrum of the initial material in comparison to that of the purified sample. It should be noted that adding only one of the spectra of models II or III to the spectrum of nanotube I does no provide satisfactory reproduction of the experimental profile.

Thus, the results of modeling show that the particles of soot must contain both graphite fragments and carbon chains. In order to obtain the relative intensities observed in the spectrum of the initial carbonaceous material, we constructed the total profile IV with a 70% contribution of the nanotubes and the remainder distributed approximately equally between the contributions of models II and III. As was noted above, the content of nanotubes in the product of two-stage synthesis according to electron microscopy data is about 50%. An additional contribution may be provided by the graphite coatings on metal particles. This is confirmed by similarity of the CK_α spectra of multilayer polyhedral carbon particles and graphite [28]. An increase in the relative intensities of features *A* and *B* in the total profile IV in comparison to the theoretical spectrum of carbon nanotube I is due to a high density of states in structures II and III in the energy interval 267–272 eV (Fig. 2b). An analysis of the results of quantum-chemical calculations showed that the electron density profile in this interval is formed by overlapped atomic orbitals oriented perpendicularly to the C–C bonds. In contrast to the case of a graphite cylinder, the carbon chain and stripe fragments include carbon atoms in the hybridized sp^1 state, which accounts for the increased density of weakly bound electron states responsible for peak *A* in the total profile IV.

5. FIELD ELECTRON EMISSION

The electron emission properties of SWNT-containing samples were studied in a diode regime. The measurements were performed at room temperature in a vacuum of 5×10^{-4} Pa. The powdered material was

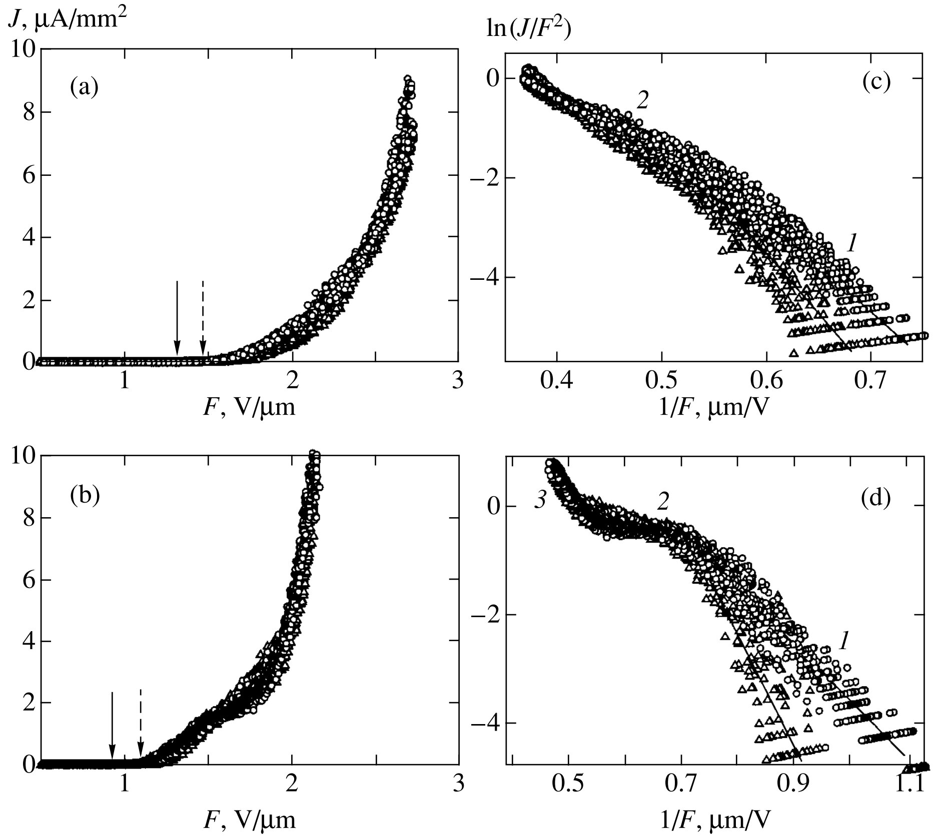

Fig. 4. Current–voltage characteristics plotted (a, b) as the electron emission current density *J* versus the electric field strength *F* and (c, d) in the Fowler–Nordheim coordinates for an SWNT-containing material (a, c) before and (b, d) after purification. Circles (triangles) present the data obtained in the course of increase (decrease) of the sawtooth voltage. (a, b) Solid and dashed arrows indicate the fields at which the emission current appears and disappears, respectively. (c, d) Regions *1* correspond to low-current field electron emission via an adlayer; region *2* reflects the most significant adsorption–desorption processes on the SWNT surface; region *3* corresponds to high-current electron emission from heated nanotubes.

pressed into a 0.5-mm-deep 1-mm-diameter cavity on the surface of a stainless steel cathode. The cavity was filled with the powder by means of a scraper and leveled flush with the cathode surface. The sample prepared in this way is characterized by a random orientation of nanotubes relative to each other and to the cathode surface. This may lead to differences in the threshold voltage for the onset of field emission. The results of measurements performed on four samples prepared from the same batch of carbonaceous material showed the same character of current–voltage curves, with the scatter of threshold voltages not exceeding 5% of the mean value. The distance from the cathode to a flat molybdenum anode was $d = 500 \pm 5$ μm. The value of the tunneling current as a function of the electric field strength was measured on applying a sawtooth voltage with an amplitude of up to $U = 1500$ V and a frequency of 0.025 Hz. The discrete character of measurements at small currents is related to a limited sensitivity of the analog-to-digital converter operating in a broad range of currents. The response had the form of a periodic signal whose constant amplitude value was evidence of stable electron emission characteristics. The data were obtained by averaging over the results of 40 measurements for each sample.

Figures 4a and 4b show the current–voltage (*J*–*F*) characteristics of the carbonaceous SWNT-containing material in the initial state and after the treatment with nitric acid, respectively. As can be seen, the two materials differ in slope of the *J*–*F* curves and in values of the hysteresis loop width and the threshold electric field strength. Owing to a relatively large area of the sample (about 1 mm^2), hundreds of individual carbon nanotubes contribute to the emission current, and the measured values represent averaged characteristics of the whole sample.

The field emission of electrons from flat metal cathodes is described by the Fowler–Nordheim equation [29]

$$J(F) = \frac{e^3F^2}{4(2\pi)^2\eta\varphi}\exp\left(-\frac{4\sqrt{2m_e}\varphi^{1.5}}{3\eta eF}\right), \tag{3}$$

where *J* is the emission current density, *F* is the electric field strength, φ is the work function of a given cathode material, e and m_e are the electron charge and mass, respectively, and η is the field enhancement factor. The J–F curve of the initial material is typical of SWNTs [30]. The emission current appears when the field strength reaches 1.45 V/μm, which is two to three orders of magnitude lower than the values expected for carbon-based materials according to Eq. (3). The difference is explained by the special morphology of carbon nanotubes. In the ideal case, the applied electric field strength exhibits local enhancement at the end of a separate tube as compared to the macroscopic value $F \sim U/d$. The field enhancement factor η in the hemisphere-on-rod approximation is given by the ratio of the rod length to hemisphere radius [31]. For a sloped nanotube, the η value is lower, as determined by the projection of the tube length onto the normal to the sample surface. The local field enhancement factor further decreases as a result of the field screening by the neighboring particles. The parameter η plays a determining role in decreasing the threshold for the emission onset in materials containing carbon nanotubes.

A comparison of Figs. 4a and 4b shows that the acid treatment led to an increase in the emission current and decreased the threshold field strength down to 1.1 V/μm (Fig. 4b). This is related primarily to a decrease in the screening action of soot particles and an increase in the content of SWNTs in the material (see Fig. 1). Indeed, calculation of the densities of occupied states for the models I–III considered above confirmed that carbon nanotubes are characterized by a lower ionization potential (see Fig. 2). Higher ionization potentials of the stripes of condensed carbon hexagons and especially of the carbon chain structures lead to an increase in the tunneling threshold for the particles of soot. The field emission from such structures begins at higher field strengths than the emission from carbon nanotubes.

In Figs. 4c and 4d, the results of measurements for the samples with SWNTs are plotted as $\ln(J/F^2)$ versus $1/F$ (Fowler–Nordheim coordinates). Using this representation, it is possible to determine the work function φ for a given cathode material by measuring the slope of the linear dependence. The current–voltage characteristics of the initial and purified material plotted in the Fowler–Nordheim coordinates can be divided into two and three linear portions, respectively. Breaks in the characteristics may reflect either changes in the work function or saturation of the emission current related to limited density of the conduction electrons, especially in the case of nonmetallic tubes [32]. The minimum slope in region *2* of the Fowler–Nordheim plot for the purified sample could just be indicative of the emission current saturation, but the subsequent increase in the slope observed in region *3* of this curve rejects this possibility. The most probable reasons for the work function of carbon nanotubes to change in the course of measurements of the current–voltage characteristics are adsorption processes. Molecules adsorbed on the surface and ends of nanotubes may form either chemical bonds (chemisorption) or the polarization and van der Waals contacts (physical adsorption). It was shown that the adsorption of polar molecules leads to a decrease in the emission threshold [33] and increases the field emission properties of nanotubes [34]. The influence of physically adsorbed molecules on the emission properties of multiwall nanotubes was confirmed by direct mass spectrometry measurements, which showed an increase in the partial densities of H_2, H_2O, CO, and CO_2 at high field strengths (about 24 V/μm) [35].

The results of measurements of the electron emission current using sawtooth voltage with a period on the order of several seconds revealed a hysteresis in the current–voltage characteristics. The magnitude and sign of this hysteresis depend on the structure of nanotubes, the electron state of emitting surfaces, and the chemical nature of residual gases. In our experiments, the threshold electric field strength on the ascending branch of the current–voltage characteristic was 0.2 V/μm higher than that on the descending branch for the samples of both initial and purified materials (Fig. 4). This is evidence of an additional barrier for the field emission of electrons from unheated nanotubes. We believe that the barrier can be related to the presence of functional groups chemically bound to the terminal atoms of carbon nanotubes. An analysis of the electron structure of SWNT clusters with and without hydrogen-saturated terminal atoms calculated using the local density functional approximation showed that the ionization potential is about 0.5 eV higher for a carbon nanotube with hydrogen atoms [36], which may explain the observed increase in the tunneling barrier. After the onset of electron emission (at a field strength of about 1 V/μm), the ends of nanotubes begin to clean: chemically bound molecules are removed first, while the physically adsorbed molecules influence the field emission in the fields up to 2.0–2.5 V/μm. It should be noted that the desorption of a chemisorbed particle is a single event taking place upon the appearance of tunneling current, whereas the physical adsorption–desorption process has a dynamical character and continuously influences the field electron emission. At a field strength above 2.5 V/μm and a high emission current, the temperature of nanotubes increases up to 1300–2000 K [37–39]. Under these conditions, the hysteresis decreases because of a considerable contribution due to thermoelectron emission that is independent of the adsorption properties of the emitter material.

6. CONCLUSIONS

We have synthesized an SWNT-containing carbonaceous material by arc-discharge evaporation of graphite and studied the electron structure and properties of this material by methods of ultrasoft XRF, electron microscopy, and field electron emission measurements. The CK_α spectrum of a sample treated with nitric acid reveals a significant decrease in the density of high-energy states as compared to that for the initial material. According to TEM data, the chemical treatment leads to partial removal of the amorphous carbon fraction and metal catalyst particles, thus increasing the SWNT fraction in the material. The CK_α spectra were successfully interpreted based on the results of quantum-chemical calculations for the model carbon structures performed using the local density functional approximation. It is established that the amorphous fraction must include a considerable amount of carbon in the hybridized sp^1 state forming chain structures and boundaries of graphite fragments. Such carbon atoms account for the high density of electron states forming the high-energy maximum in the CK_α spectrum of the initial material.

Carbon nanotubes possess the minimum ionization potential among the calculated model structures, which explains the increase in the field electron emission properties of the material after chemical purification. The amorphous carbon covering the surface and ends of nanotubes probably produces a screening action, thus influencing the appearance of tunneling current. The current–voltage characteristics of both the initial and purified samples exhibit deviations from the Fowler–Nordheim relation, which are probably related to the influence of adsorbed molecules and functional groups on the work function of SWNT-containing materials. The results of measurements in a dynamical regime revealed a hysteresis in the current–voltage characteristics of samples. More significant changes observed in the characteristics of purified samples may reflect the attachment of functional groups (chemisorption) to defects and ends of the chemically treated carbon nanotubes. An increase in the field strength leads to detachment of the adsorbed functional groups, which results in the corresponding increase in the emission current. A small hysteresis observed in the current–voltage characteristics at high values of the applied bias voltage probably reflects the physical adsorption. This dynamical phenomenon can be used for the development of gas sensors.

ACKNOWLEDGMENTS

The authors are grateful to A.L. Chuvilin for conducting electron-microscopic measurements.

This study was supported by the Russian foundation for Basic Research (project nos. 03-03-32286 and 03-03-32336).

REFERENCES

1. M. S. Dresselhaus, G. Dresselhaus, and P. C. Eklund, *Science of Fullerenes and Carbon Nanotubes* (Academic, New York, 1996).
2. A. G. Rinzler, J. H. Hafner, P. Nikolaev, *et al.*, Science **269**, 1550 (1995).
3. G. Zhou, W. Duan, and B. Gu, Appl. Phys. Lett. **79**, 836 (2001).
4. D. Lovall, M. Buss, E. Graugnard, *et al.*, Phys. Rev. B **61**, 5683 (2000).
5. A. Modi, N. Koratkar, E. Lass, *et al.*, Nature **424**, 171 (2003).
6. H. Kataura, Y. Kumazawa, Y. Manwa, *et al.*, Carbon **38**, 1691 (2000).
7. H. Kanzow, Ch. Lenski, and A. Ding, Phys. Rev. B **63**, 125402 (2001).
8. D. W. Mawhinney, V. Naumenko, A. Kuznetsova, *et al.*, Chem. Phys. Lett. **324**, 213 (2000).
9. Ch.-M. Yang, K. Kaneko, M. Yudasaka, and S. Iijima, Physica B (Amsterdam) **323**, 140 (2002).
10. Ch. Kim, K. Seo, and B. Kim, Phys. Rev. B **68**, 115403 (2003).
11. L. G. Bulusheva, A. V. Okotrub, A. V. Gusel'nikov, *et al.*, in *Molecular Nanostructures*, Ed. by H. Kuzmany, J. Fink, M. Mehring, and S. Roth (AIP, Melville, N.Y., 2003); AIP Conf. Proc. **685**, 108 (2003).
12. A. V. Okotrub, Yu. V. Shevtsov, L. I. Nasonova, *et al.*, Prib. Tekh. Éksp., No. 1, 193 (1995).
13. A. V. Okotrub, Yu. V. Shevtsov, L. I. Nasonova, *et al.*, Neorg. Mater. **32**, 974 (1996).
14. A. V. Okotrub, G. S. Belikova, T. N. Turskaya, and L. N. Mazalov, in *Applications of Synchrotron Radiation Techniques to Materials Science IV,* Ed. by S. M. Mini, S. R. Stock, D. L. Perry, and L. J. Terminello; Mater. Res. Soc. Symp. Proc. **524**, 161 (1997).
15. A. V. Okotrub and L. G. Bulusheva, Fullerene Sci. Technol. **6**, 405 (1998).
16. Chr. Beyreuther, R. Hierl, and G. Wiech, Ber. Bunsen-Gess. Phys. Chem. **79**, 1081 (1895).
17. A. V. Okotrub, L. G. Bulusheva, A. I. Romanenko, *et al.*, Appl. Phys. A **71**, 481 (2001).
18. S. Eisebitt, A. Karl, W. Eberhardt, *et al.*, Appl. Phys. A **67**, 89 (1998).
19. É. Z. Kurmaev, in *X-ray and Electron Spectroscopy of Solids*, Ed. by V. N. Antonov (Naukova Dumka, Kiev, 1993), p. 1 [in Russian].
20. L. J. Dunne, A. K. Sarkar, H. W. Kroto, *et al.*, J. Phys.: Condens. Matter **8**, 2127 (1996).
21. R. J. Lagow, J. J. Kampa, H.-Ch. Wei, *et al.*, Science **267**, 362 (1995).
22. M. J. S. Dewar and W. Thiel, J. Am. Chem. Soc. **99**, 4899 (1977).
23. Y.-K. Kwon, S. Saito, and D. Tomanek, Phys. Rev. B **58**, R13314 (1998).
24. R. B. Heimann, J. Kleiman, and N. M. Salansky, Nature **306**, 164 (1983).
25. A. D. Becke, J. Chem. Phys. **98**, 5648 (1993).
26. *Jaguar 3. 5* (Schrödinger, Portland, OR, 1998).
27. L. G. Bulusheva, A. V. Okotrub, D. A. Romanov, and D. Tomanek, Phys. Low-Dimens. Semicond. Struct., No. 3–4, 107 (1998).

28. A. V. Okotrub, L. G. Bulusheva, V. L. Kuznetsov, *et al.*, J. Phys. Chem. A **105**, 9781 (2001).
29. R. H. Fowler and L. W. Nordheim, Proc. R. Soc. London **119**, 173 (1928).
30. W. Zhu, C. Bower, O. Zhou, *et al.*, Appl. Phys. Lett. **75**, 873 (1999).
31. F. H. Read and N. J. Bowring, Nucl. Instrum. Methods Phys. Res. A **519**, 305 (2004).
32. P. G. Collins and A. Zettl, Phys. Rev. B **55**, 9391 (1997).
33. M. Grujicic, G. Cao, and B. Gersten, Appl. Surf. Sci. **206**, 167 (2003).
34. K. A. Dean and B. R. Chalamala, Appl. Phys. Lett. **76**, 375 (2000).
35. W. I. Milne, K. B. K. Teo, S. B. Lansley, *et al.*, in *Molecular Nanostructures*, Ed. by H. Kuzmany, J. Fink, M. Mehring, and S. Roth (AIP, Melville, N.Y., 2003); AIP Conf. Proc. **685**, 605 (2003).
36. G. Zhou, W. Duan, B. Gu, and Y. Kawazoe, J. Chem. Phys. **116**, 2284 (2002).
37. S. T. Purcell, P. Vicent, C. Journet, and V. T. Binh, Phys. Rev. Lett. **88**, 105502 (2002).
38. J.-M. Bonard, Ch. Klinke, K. A. Dean, and B. F. Coll, Phys. Rev. B **67**, 115406 (2003).
39. J. P. Sun, Z. H. Zhang, S. M. Hou, *et al.*, Appl. Phys. A **75**, 479 (2002).

Translated by P. Pozdeev

Journal of Experimental and Theoretical Physics, Vol. 99, No. 6, 2004, pp. 1253–1263.
Translated from Zhurnal Éksperimental'noĭ i Teoreticheskoĭ Fiziki, Vol. 126, No. 6, 2004, pp. 1435–1445.
Original Russian Text Copyright © 2004 by Kirichenko, Peschanskii, Stepanenko.

SOLIDS
Electronic Properties

Collective Modes in Quasi-Two-Dimensional Conductors under Strong Spatial Dispersion

O. V. Kirichenko, V. G. Peschanskii, and D. I. Stepanenko
Verkin Institute for Low Temperature Physics and Engineering, National Academy of Sciences of Ukraine,
Kharkov, 61103 Ukraine
e-mail: vpeschansky@ilt.kharkov.ua

Received June 8, 2004

Abstract—Propagation of electromagnetic and spin waves in layered conductors with a quasi-two-dimensional dispersion law of charge carriers is investigated theoretically in the presence of an external magnetic field with induction $\mathbf{B}_0$. In layered conductors, the drift velocity $\mathbf{v}_D$ of electrons along $\mathbf{B}_0$ is an oscillatory function of the angle between the magnetic field direction and the normal to the layers. For certain orientations of the magnetic field with respect to the layers of the conductor, $\mathbf{v}_D$ is close to zero. In these directions, there is no collision-free absorption, and weakly damped waves may propagate even under strong spatial dispersion. In the short-wavelength limit, there may exist collective modes with frequencies in the neighborhood of resonances for arbitrary orientation of the wavevector $\mathbf{k}$ relative to $\mathbf{B}_0$. Similar types of excitations in quasi-isotropic metals are possible only when $\mathbf{k}$ is perpendicular to the direction of the external magnetic field. *© 2004 MAIK “Nauka/Interperiodica”.*

1. INTRODUCTION

Layered structures with strongly anisotropic metallic-type electric conductivity have been intensively studied recently. These structures include a large family of organic conductors based on tetrathiofulvene, dichalcogenides of transition metals, graphite, and other materials. In the absence of an external magnetic field, the electric conductivity $\sigma_\parallel$ along the layers in these materials is several orders of magnitude greater than the conductivity $\sigma_\perp$ across the layers. The sharp anisotropy of the kinetic coefficients of layered conductors is attributed to the quasi-two-dimensional character of the energy spectra of electrons. The maximal velocity of electrons with Fermi energy ε_F along the normal $\mathbf{n}$ to the layers, $v_z = \mathbf{v}\cdot\mathbf{n}$, is much less than the characteristic velocity of electrons in the plane of layers, v_F, while their energy weakly depends on the momentum projection $p_z = \mathbf{p}\cdot\mathbf{n}$ and can be represented as a rapidly divergent series

$$\varepsilon(\mathbf{p}) = \varepsilon_0(p_x, p_y) + \sum_{n=1}^{\infty} \varepsilon_n(p_x, p_y, \eta)\cos\frac{np_z}{p_0}. \qquad (1)$$

The functions $\varepsilon_n(p_x, p_y, \eta)$ rapidly decrease as their number increases, and the greatest of these functions is $\varepsilon_1(p_x, p_y, \eta) \sim \eta\varepsilon_F$. Here, $\eta = (\sigma_\perp/\sigma_\parallel)^{1/2}$ is the quasi-two-dimensionality parameter of a conductor, $p_0 = \hbar/a$, and $\hbar$ is the Planck constant. Formula (1) corresponds to the strong-coupling approximation when the overlapping of the electron shells of atoms belonging to different layers is small, while the distance a between them is much greater than the interatomic distance within a layer. The Fermi surface (FS) $\varepsilon(\mathbf{p}) = \varepsilon_F$ for charge carriers with the dispersion law (1) is an open surface with small corrugation along axis p_z; it may be multisheeted and consist of topologically different elements, for example, of cylinders and planes. In what follows, we will assume that the FS of a layered conductor represents a weakly corrugated cylinder all of whose sections by the plane $p_B = (\mathbf{p}\cdot\mathbf{B}_0)/B_0 = p_z\cos\vartheta + p_x\sin\vartheta =$ const are closed for $\pi/2 - \vartheta > \eta$, where $\mathbf{B}_0 = (B_0\sin\vartheta, 0, B_0\cos\vartheta)$ is the induction of the external magnetic field. Numerous experimental investigations of magnetic oscillations have shown that a considerable part of tetrathiofulvene-based organic conductors have such an FS [1–3].

At low temperatures, various types of weakly damped Bose-type collective modes (electromagnetic, acoustic, and spin waves) may exist in normal metals placed in a magnetic field. There is a large number works devoted to the study of electromagnetic and spin waves in quasi-isotropic metals; a survey of the results of these studies is given, for example, in the monographs [4, 5]. In the present paper, we consider collective modes in layered conductors with quasi-two-dimensional energy spectrum of electrons. Wave processes in layered conductors are characterized by a number of features associated with the topology of the FS. For certain orientations of the magnetic field with respect to the layers of a conductor, the projection of electron velocity onto the direction of $\mathbf{B}_0$, averaged over the period of motion along a cyclotron orbit, is negligibly small. There is no collision-free absorption for these directions of $\mathbf{B}_0$, and weakly damped waves may propagate even under strong spatial dispersion.

2. SYSTEM OF EQUATIONS OF THE PROBLEM

The kinetic properties of a system of fermions in an electromagnetic field are described by the equation for the density matrix and the Maxwell system of equations. Consider the quasiclassical case $\hbar\omega_B \lesssim T \ll \eta\varepsilon_F$, when the quantization of the energy levels of charge carriers in a magnetic field does not have any significant effect on the magnitude of magnetization $\mathbf{M}$ and the quantum oscillatory component of the magnetization does not exceed its paramagnetic part. Here, ω_B is the cyclotron frequency of conduction electrons and T is temperature. Under these conditions, the density matrix in the quasiclassical approximation represents an operator in the space of spin variables and a quasiclassical function depending on the coordinates and momenta. An equation for the one-particle density matrix is given by

$$\begin{gathered}\frac{\partial\hat{\rho}}{\partial t} - \frac{i}{\hbar}[\hat{\varepsilon}, \hat{\rho}]_S + \frac{1}{2}\{\hat{\varepsilon}, \hat{\rho}\} + \frac{1}{2}\{\hat{\rho}, \hat{\varepsilon}\} + e\mathbf{E}\cdot\frac{\partial\hat{\rho}}{\partial\mathbf{p}} \\ + \frac{1}{2}\frac{e}{c}\left(\left[\frac{\partial\hat{\varepsilon}}{\partial\mathbf{p}}\times\mathbf{B}\right]\cdot\frac{\partial\hat{\rho}}{\partial\mathbf{p}} + \frac{\partial\hat{\rho}}{\partial\mathbf{p}}\cdot\left[\frac{\partial\hat{\varepsilon}}{\partial\mathbf{p}}\times\mathbf{B}\right]\right) = \hat{I}_{\mathrm{coll}},\end{gathered} \tag{2}$$

where $[\hat{\varepsilon}, \hat{\rho}]_S$ is the commutator of matrices in the space of spin variables, $\{\hat{\varepsilon}, \hat{\rho}\}$ is the classical Poisson bracket, $\hat{I}_{\mathrm{coll}}$ is the collision operator, e is the electron charge, c is the velocity of light, $\mathbf{E}$ is electric field, and $\mathbf{B} = \mathbf{B}_0 + \mathbf{B}^{\sim}(\mathbf{r}, t)$, where $\mathbf{B}^{\sim}(\mathbf{r}, t)$ is a high-frequency field. The operator

$$\hat{\varepsilon} = \varepsilon(\mathbf{p})\delta_{\alpha\beta} - \mu_0\boldsymbol{\sigma}\cdot\mathbf{B} + \delta\hat{\varepsilon}(\mathbf{p}, \mathbf{r}, t) \tag{3}$$

is a sum of the energy of a quasiparticle in the one-electron approximation in a magnetic field and the energy of a quasiparticle due to electron–electron interaction; within the Landau–Silin Fermi-liquid theory [6, 7], the latter energy can be represented as

$$\begin{gathered}\delta\hat{\varepsilon}(\mathbf{p}, \mathbf{r}, t) \\ = \mathrm{Tr}_{\sigma'}\int\frac{d^3p'}{(2\pi\hbar)^3}\mathbb{L}(\mathbf{p}, \boldsymbol{\sigma}, \mathbf{p}', \boldsymbol{\sigma}')\delta\hat{\rho}(\mathbf{p}', \mathbf{r}, \boldsymbol{\sigma}', t).\end{gathered} \tag{4}$$

Here,

$$\mathbb{L}(\mathbf{p}, \hat{\boldsymbol{\sigma}}, \mathbf{p}', \hat{\boldsymbol{\sigma}}') = L(\mathbf{p}, \mathbf{p}') + S(\mathbf{p}, \mathbf{p}')\hat{\boldsymbol{\sigma}}\hat{\boldsymbol{\sigma}}' \tag{5}$$

is the Landau correlation function, $\delta_{\alpha\beta}$ is the Kronecker delta, μ_0 is the magnetic moment of a conduction electron, $\boldsymbol{\sigma}$ is the Pauli matrix, and $\delta\hat{\rho}$ is the nonequilibrium component of the density matrix. The term on the right-hand side of (5) that depends on spin operators corresponds to the exchange interaction of electrons.

The ac electric $\mathbf{E}$ and magnetic $\mathbf{B}^{\sim}(\mathbf{r}, \mathbf{t})$ fields are determined from the Maxwell equations

$$\begin{gathered}\mathrm{curl}\mathbf{B}^{\sim} = \frac{1}{c}\frac{\partial\mathbf{E}}{\partial t} + \frac{4\pi}{c}\mathbf{j}, \\ \mathrm{curl}\mathbf{E} = -\frac{1}{c}\frac{\partial\mathbf{B}^{\sim}}{\partial t}, \quad \mathrm{div}\mathbf{B}^{\sim} = 0,\end{gathered} \tag{6}$$

supplemented with the material equation for the density of current induced in the medium:

$$\begin{gathered}\mathbf{j}(\mathbf{r}, t) = e\mathrm{Tr}_{\sigma}\int\frac{d^3p}{(2\pi\hbar)^3}\hat{\rho}(\mathbf{p}, \mathbf{r}, \boldsymbol{\sigma}, t)\frac{\partial\hat{\varepsilon}}{\partial\mathbf{p}} \\ + c\mu_0\mathrm{curl}\mathrm{Tr}_{\sigma}\int\frac{d^3p}{(2\pi\hbar)^3}\boldsymbol{\sigma}\hat{\rho}(\mathbf{p}, \mathbf{r}, \boldsymbol{\sigma}, t).\end{gathered} \tag{7}$$

For angles ϑ between $\mathbf{B}_0$ and $\mathbf{n}$ that are not too close to $\pi/2$, namely, for $\pi/2 - \vartheta \gg \eta$, closed electron orbits in the momentum space for different values of the momentum projection onto the magnetic field direction are nearly indistinguishable, while the area $S(\varepsilon, p_B)$ of the cross section of the FS by the plane p_B = const and the components v_x and v_y of the velocity $\mathbf{v} = \partial\varepsilon(\mathbf{p})/\partial\mathbf{p}$ of conduction electrons in the plane of layers depend weakly on p_B. This means that the energy of quasiparticles in the one-electron approximation, the Landau correlation function, and the cyclotron frequency can be expanded into an asymptotic series in the quasi-two-dimensionality parameter η, and the leading term of the asymptotics is independent of p_B. In the zeroth-order approximation in η, the functions $L(\mathbf{p}, \mathbf{p}')$ and $S(\mathbf{p}, \mathbf{p}')$ can be represented as the Fourier series

$$\begin{gathered}L(\mathbf{p}, \mathbf{p}') = \sum_{n=-\infty}^{\infty} L_n(\varepsilon_F)e^{in(\varphi-\varphi')}, \\ S(\mathbf{p}, \mathbf{p}') = \sum_{n=-\infty}^{\infty} S_n(\varepsilon_F)e^{in(\varphi-\varphi')}.\end{gathered} \tag{8}$$

The integrals of motion of charge carriers in a magnetic field, ε and p_B, as well as the phase of the electron velocity $\varphi = \omega_B t_1$, where t_1 is the time of motion along a trajectory $\varepsilon = \varepsilon_F$, p_B = const, are chosen as the variables in the $\mathbf{p}$-space. Due to the symmetry $\mathbb{L}(\mathbf{p}, \hat{\boldsymbol{\sigma}}, \mathbf{p}', \hat{\boldsymbol{\sigma}}') = \mathbb{L}(\mathbf{p}', \hat{\boldsymbol{\sigma}}', \mathbf{p}, \hat{\boldsymbol{\sigma}})$ with respect to the permutation of arguments, the coefficients in (4) are related by the formulas $L_{-n} = L_n$ and $S_{-n} = S_n$. Consideration of the subsequent terms of the expansion of the correlation function in powers of η results in negligibly small corrections to the spectrum of collective modes.

Instead of the matrix equation (2), it is convenient to consider a system of four equations for the distribution function

$$f(\mathbf{r}, \mathbf{p}, t) = \underset{\sigma}{\mathrm{Tr}}\hat{\rho}$$

and the spin density

$$\mathbf{g}(\mathbf{r}, \mathbf{p}, t) = \operatorname*{Tr}_{\sigma}(\boldsymbol{\sigma}\hat{\rho}).$$

One of these equations is obtained by applying the operation of taking the trace with respect to the spin variables to the matrix equation for $\hat{\rho}$, while the other three are obtained by applying the operation Sp to the original equation (2) multiplied by $\boldsymbol{\sigma}$. The function $\mathbf{g}(\mathbf{r}, \mathbf{p}, t)$, together with the second term on the right-hand side of (7), describes paramagnetic spin waves, which were predicted by Silin [8] and experimentally observed by Dunifer and Schultz [9] in alkaline metals.

For small deviations of the electron system from equilibrium, one can represent the functions f and $\mathbf{g}$ as the respective sums of equilibrium parts and small non-equilibrium components,

$$f(\mathbf{r}, \mathbf{p}, t) = f_0(\varepsilon) - \psi(\mathbf{r}, \mathbf{p}, t)\frac{\partial f_0}{\partial \varepsilon},$$

$$\mathbf{g}(\mathbf{r}, \mathbf{p}, t) = \mathbf{g}_0 - \frac{\partial f_0}{\partial \varepsilon}\boldsymbol{\xi}(\mathbf{r}, \mathbf{p}, t).$$

Here, $f_0(\varepsilon)$ is the Fermi function, and $\mathbf{g}_0(\varepsilon) = -\mu\mathbf{B}_0(\partial f_0/\partial\varepsilon)$. The integral of $\mu_0\mathbf{g}_0(\varepsilon)$ over a unit cell in the $\mathbf{p}$-space represents the magnetization $\mathbf{M}_0 = \chi_0\mathbf{B}_0$ in a uniform constant magnetic field of induction $\mathbf{B}_0$, $\chi_0 = \mu_0\mu\nu(\varepsilon_F)$ is the static paramagnetic susceptibility, and $\nu(\varepsilon_F)$ is the density of states at the Fermi level. The non-equilibrium component of the distribution function satisfies the linearized Boltzmann equation

$$\begin{gathered}\frac{\partial\psi}{\partial t} + \left(\mathbf{v}\cdot\frac{\partial}{\partial \mathbf{r}} + \frac{e}{c}[\mathbf{v}\times\mathbf{B}_0]\cdot\frac{\partial}{\partial \mathbf{p}}\right)(\psi + \langle L\psi\rangle) \\ + e\mathbf{v}\cdot\mathbf{E} = \hat{I}^{(1)}_{\text{coll}},\end{gathered} \tag{9}$$

while the kinetic equation for the perturbed spin density in the case when $\boldsymbol{\xi}$ is perpendicular to $\mathbf{B}_0$ is given, according to [8], by

$$\begin{gathered}\frac{\partial\boldsymbol{\xi}}{\partial t} + \left(\mathbf{v}\cdot\frac{\partial}{\partial \mathbf{r}} + \frac{e}{c}[\mathbf{v}\times\mathbf{B}_0]\cdot\frac{\partial}{\partial \mathbf{p}}\right)(\boldsymbol{\xi} + \langle S\boldsymbol{\xi}\rangle) \\ - \frac{2\mu}{\hbar}[B_0\times(\boldsymbol{\xi} + \langle S\boldsymbol{\xi}\rangle)] \\ - \mu_0\mathbf{v}\frac{\partial\mathbf{B}^{\sim}}{\partial\mathbf{r}} + \frac{2\mu\mu_0}{\hbar}[\mathbf{B}_0\times\mathbf{B}^{\sim}] = \hat{I}^{(2)}_{\text{coll}},\end{gathered} \tag{10}$$

where angular brackets denote averaging over the Fermi surface:

$$\langle L\psi\rangle \equiv \int\frac{2d^3p'}{(2\pi\hbar)^3}\left(-\frac{\partial f_0(\varepsilon')}{\partial\varepsilon'}\right)L(\mathbf{p}, \mathbf{p}')\psi(\mathbf{r}, \mathbf{p}', t).$$

The collision integrals $\hat{I}^{(1)}_{\text{coll}}$ and $\hat{I}^{(2)}_{\text{coll}}$ determine the characteristic relaxation times of momentum, τ_1, and spin density, τ_2 ($\tau_2 \gg \tau_1$). Henceforth, we will consider processes that correspond to the range of frequencies

$$\omega \gg \tau^{-1} = \tau_1^{-1} + \tau_2^{-1},$$

where the asymptotics of the spectrum of collective modes is independent of the specific form of the collision integral and $\mathbf{k}$ is the wavevector.

System of equations (6)–(10) describes natural oscillations of electromagnetic field and spin density in layered conductors with arbitrary energy spectrum and correlation function.

3. CYCLOTRON WAVES

The so-called cyclotron waves represent a type of excitations that is characteristic of both a solid-state and a gas plasma. These waves, with frequencies in the neighborhood of the cyclotron resonance $\omega \approx n\omega_B$, $n = 0, 1, 2, \ldots$, propagate predominantly in the direction perpendicular to the external magnetic field under conditions of nonlocal coupling between the current density and the electric field. In this section, we restrict our consideration to the one-electron approximation and do not take into account a Fermi-liquid interaction between charge carriers.

Assuming that the space–time dependence of all variable quantities is given by $\exp(i\mathbf{k}\cdot\mathbf{r} - i\omega t)$, we can easily derive from the Maxwell equations (6) the dispersion equation

$$\det\left[k^2\delta_{ij} - k_ik_j - \frac{\omega^2}{c^2}\varepsilon_{ij}(\omega, \mathbf{k})\right] = 0, \tag{11}$$

which determines the spectrum $\omega(\mathbf{k})$ of natural oscillations of electromagnetic field. Here,

$$\varepsilon_{ij}(\omega, \mathbf{k}) = \delta_{ij} + \frac{4\pi i}{\omega}\sigma_{ij}(\omega, \mathbf{k})$$

is the tensor of permittivity, δ_{ij} is the Kronecker delta,

$$\begin{gathered}\sigma_{ij}(\omega, \mathbf{k}) = \frac{2e^2}{(2\pi\hbar)^3} \\ \times\int dp_B\frac{m^*\omega_B^{-1}}{1 - \exp\frac{2\pi i}{\omega_B}(\omega - \langle\mathbf{k}\cdot\mathbf{v}\rangle_\varphi)}\int_0^{2\pi}d\varphi\, v_i(\varphi) \\ \times\int_0^{2\pi}d\varphi_1\, v_j(\varphi - \varphi_1)\exp\left(i\frac{\tilde{\omega}}{\omega_B}\varphi_1 - iR(\varphi, \varphi_1)\right)\end{gathered} \tag{12}$$

is the conductivity tensor,

$$R(\varphi, \varphi_1) \equiv \frac{1}{\omega_B}\int_{\varphi - \varphi_1}^{\varphi}d\varphi'\,\mathbf{k}\cdot\mathbf{v}(\varphi'),$$

m^* is the cyclotron effective mass of charge carriers, and

$$\langle \mathbf{k}\cdot\mathbf{v}\rangle_\varphi = \frac{1}{2\pi}\int_0^{2\pi} d\varphi' \mathbf{k}\cdot\mathbf{v}(\varphi'), \quad \tilde{\omega} = \omega + i0.$$

If the wavevector $\mathbf{k} = (k\sin\phi, 0, k\cos\phi)$ lies in the plane xz, then, expanding the determinant, we obtain

$$A\left(\frac{kc}{\omega}\right)^4 + B\left(\frac{kc}{\omega}\right)^2 + C = 0, \tag{13}$$

where

$$A = \varepsilon_{xx}\sin^2\phi + 2\varepsilon_{xz}\sin\phi\cos\phi + \varepsilon_{zz}\cos^2\phi,$$

$$B = -\varepsilon_{xx}\varepsilon_{zz} - (\varepsilon_{yy}\varepsilon_{zz} + \varepsilon_{yz}^2)\cos^2\phi$$
$$-(\varepsilon_{xx}\varepsilon_{yy} + \varepsilon_{xy}^2)\sin^2\phi + \varepsilon_{xz}^2 + 2(\varepsilon_{xy}\varepsilon_{yz} - \varepsilon_{xz}\varepsilon_{yy})$$
$$\times \sin\phi\cos\phi,$$

$$C = \det[\varepsilon_{ij}] = \varepsilon_{zz}(\varepsilon_{xx}\varepsilon_{yy} + \varepsilon_{xy}^2)$$
$$+ \varepsilon_{xx}\varepsilon_{xy}^2 + 2\varepsilon_{xy}\varepsilon_{xz}\varepsilon_{yz} - \varepsilon_{yy}\varepsilon_{xz}^2,$$

and ϕ is the angle between the vectors $\mathbf{n}$ and $\mathbf{k}$.

In the case of strong spatial dispersion, $kr_0 \gg 1$, $\eta kr_0 \sim 1$, where $r_0 = v_F/\omega_B$ is the Larmor radius of conduction electrons, the integrals with respect to φ and φ_1 in (12) are calculated by the stationary phase method [10]; moreover, if $\omega \sim \omega_B$, the stationary points are determined from the equations $v_x(\varphi) = 0$ and $v_x(\varphi - \varphi_1) = 0$. One can easily see that the maximal of the components σ_{ij} of the conductivity tensor is σ_{yy}, which is proportional to $(kr_0)^{-1}$; the expansion of the components σ_{xj} ($j = x, y, z$), in powers of $(kr_0)^{-1}$ starts from higher order terms; and the components $\sigma_{z\alpha}$ ($\alpha = x, y$), are proportional to η, while $\sigma_{zz} \propto \eta^2$. In the main approximation in the small parameters $(kr_0)^{-1}$ and η, we obtain the following dispersion equation from (13):

$$\frac{k^2c^2}{\omega^2} = \frac{4\pi i}{\omega}\sigma_{yy}, \tag{14}$$

$$\sigma_{yy}(\omega, \mathbf{k}) = \frac{e^2 m^* \omega_B^{-1}}{2\pi^2\hbar^3}\int dp_B \frac{1}{1 - \exp\left(2\pi i\dfrac{\tilde{\omega} - \langle\mathbf{k}\cdot\mathbf{v}\rangle_\varphi}{\omega_B}\right)}$$
$$\times \sum_\alpha \kappa(\boldsymbol{\varphi}^{\boldsymbol{\alpha}})\{|\det(R''_{\varphi\varphi_1}(\varphi^{(\alpha)}, \varphi_1^{(\alpha)}))|\}^{-1/2}$$
$$\times \exp\left[i\frac{\tilde{\omega}}{\omega_B}\varphi_1^{(\alpha)} - iR(\varphi^{(\alpha)}, \varphi_1^{(\alpha)}) + i\frac{\pi}{4}s\right] \tag{15}$$
$$\times v_y(\varphi^{(\alpha)})v_y(\varphi^{(\alpha)} - \varphi_1^{(\alpha)}).$$

The summation is over all stationary points $\boldsymbol{\varphi}^{(\alpha)} = (\varphi^{(\alpha)}, \varphi_1^{(\alpha)})$; $\kappa(\boldsymbol{\varphi}^{(\alpha)}) = 1$ if a stationary point belongs to the domain of integration $0 < \varphi^{(\alpha)} < 2\pi$, $0 < \varphi_1^{(\alpha)} < 2\pi$, and $\kappa(\boldsymbol{\varphi}^{(\alpha)}) = 1/2$ if it lies on the boundary of the domain; and $s = \operatorname{sgn} R''_{\varphi\varphi_1}(\varphi^{(\alpha)}, \varphi_1^{(\alpha)}) = \nu_+(R''_{\varphi\varphi_1}) - \nu_-(R''_{\varphi\varphi_1})$, where $\nu_+(R''_{\varphi\varphi_1})$ and $\nu_-(R''_{\varphi\varphi_1})$ are the numbers of positive and negative eigenvalues of the matrix $R''_{\varphi\varphi_1} \equiv \partial^2 R(\varphi^{(\alpha)}, \varphi_1^{(\alpha)})/\partial\varphi\partial\varphi_1$, respectively. The dependence of the cyclotron frequency on p_B should be taken into account only in the expression $k_x v_x/\omega_B$ in the exponent provided that $\eta k v_F \sim \omega_B$; therefore, we took $m^*\omega_B^{-1}$ outside the integral.

Outside the domain of values of ω, $\mathbf{k}$ corresponding to the condition

$$|\omega - n\omega_B| > \max|\langle\mathbf{k}\cdot\mathbf{v}\rangle_\varphi|, \tag{16}$$

the integrand in (15) has a pole; after integrating with respect to p_B, the dispersion equation acquires an imaginary part that is responsible for a strong absorption of a wave. In layered conductors, the drift velocity $\mathbf{v}_B = \langle\mathbf{v}\rangle_\varphi$ of electrons along a magnetic field oscillates as the angle ϑ between the magnetic field and the normal to the layers is varied. For certain directions of $\mathbf{B}_0$ relative to the conductor layers, $\mathbf{v}_B$ is close to zero, and there is no Landau damping. In this case, the wave attenuation is determined by collision processes, and collective modes may exist even under the condition that $\eta k v_F \gtrsim \omega_B$. In the range of values of ω and $\mathbf{k}$ such that $\mathbf{k}\cdot\mathbf{v}_m \gg \omega_B$ and $\omega \ll \mathbf{k}\cdot\mathbf{v}_m$, where $\mathbf{v}_m$ is the maximal velocity in the direction $\mathbf{k}$, there exist solutions to the dispersion equation (14) in the region of the resonance

$$\omega = n\omega_B + \Delta\omega, \tag{17}$$

where $n\omega_B$ is the frequency corresponding to the cyclotron resonance, $n = 1, 2, 3, \ldots$, and $|\Delta\omega|$ ranges in the interval $0 < |\Delta\omega| < \omega_B$.

Let us take into account only the zeroth- and first-order terms in formula (1) for the dispersion law of charge carriers. Neglecting the anisotropy in the plane of layers and assuming that $\varepsilon_1(p_x, p_z)$ is a constant equal to $\eta v_F p_0$ ($v_F = \sqrt{2\varepsilon_F/m}$, m = const is the effective mass in the plane of layers), we express the energy of a quasiparticle as

$$\varepsilon(\mathbf{p}) = \frac{p_x^2 + p_y^2}{2m} - \eta v_F p_0 \cos\frac{p_z}{p_0}. \tag{18}$$

The velocity components of a conduction electron that correspond to the dispersion law (18) satisfy the equations

$$\frac{dv_x}{dt_1} = \frac{eB_0}{mc}\cos\vartheta\, v_y,$$

$$\frac{dv_y}{dt_1} = \frac{eB_0}{mc}(-v_y\cos\vartheta + v_z\sin\vartheta), \qquad (19)$$

$$v_z = \eta v_{\mathrm{F}}\sin\left(\frac{p_{\mathrm{B}}}{p_0\cos\vartheta} - \frac{mv_x}{p_0}\tan\vartheta\right).$$

Asymptotic (up to terms of order η) solutions to system (19) are easily obtained by standard methods of nonlinear mechanics [11]:

$$v_x(t_1) = v_x^{(0)}(t_1) + v_x^{(1)}(t_1),$$

$$v_x^{(0)}(t_1) = v_\perp\cos\omega_{\mathrm{B}}(\beta)t_1,$$

$$v_x^{(1)}(t_1) = \eta v_{\mathrm{F}}\tan\vartheta J_0(\alpha)\sin\beta - \eta v_{\mathrm{F}}\tan\vartheta \qquad (20)$$

$$\times\sum_{n=2}^{\infty}\frac{J_n(\alpha)\sin(\beta - n\pi/2)}{n^2-1}\cos n\omega_{\mathrm{B}}(\beta)t_1,$$

$$v_z(t_1) = \eta v_F\sin(\beta - \alpha\cos\omega_{\mathrm{B}}(\beta)t_1).$$

Here,

$$\omega_{\mathrm{B}}(\beta) = \omega_{\mathrm{B}}^{(0)}\left(1 + \frac{1}{2}\eta\tan\vartheta J_1(\alpha)\cos\beta\right)$$

is the cyclotron frequency of quasiparticles with energy (18) in the field $\mathbf{B}_0 = (B_0\sin\vartheta, 0, B_0\cos\vartheta)$, $\omega_{\mathrm{B}}^{(0)} = (|e|B_0/mc)\cos\vartheta$, $\alpha = (mv_{\mathrm{F}}/p_0)\tan\vartheta$, $\beta = p_{\mathrm{B}}/p_0\cos\vartheta$, $J_n(\alpha)$ is the Bessel function, the initial phase is chosen so that $v_y(0) = 0$, and

$$v_\perp = v_{\mathrm{F}}\left(1 - \frac{v_x^{(1)}(0)}{v_{\mathrm{F}}} + \frac{\eta p_0}{mv_{\mathrm{F}}}\cos(\beta - \alpha)\right)$$

is the amplitude of the first harmonic of $v_x(t)$ that is determined from the condition

$$mv_x^2(0)/2 + \eta v_{\mathrm{F}}p_0\cos(p_z(0)/p_0) = \varepsilon_{\mathrm{F}}.$$

For electrons with the dispersion law (18), the component σ_{yy} of the conductivity tensor is expressed as

$$\sigma_{yy}(\omega, k) = i\frac{e^2\nu(\varepsilon_{\mathrm{F}})v_{\mathrm{F}}^2}{\omega_{\mathrm{B}}k_xr_0}\left\langle\cot\frac{\pi}{\omega_{\mathrm{B}}}(\tilde{\omega} - \langle\mathbf{k}\cdot\mathbf{v}\rangle_\varphi) - \frac{\sin\left(R\left(\frac{\pi}{2}, \pi\right) - \frac{\pi}{\omega_{\mathrm{B}}}\langle\mathbf{k}\cdot\mathbf{v}\rangle_\varphi\right)}{\sin\frac{\pi}{\omega_{\mathrm{B}}}(\tilde{\omega} - \langle\mathbf{k}\cdot\mathbf{v}\rangle_\varphi)}\right\rangle_\beta. \qquad (21)$$

Here, $\nu(\varepsilon_{\mathrm{F}}) = p_0m/\pi\hbar^3$ is the density of states of quasiparticles with energy (18), and

$$\langle\ldots\rangle_\beta = \frac{1}{2\pi}\int_0^{2\pi}d\beta\ldots.$$

Averaging the velocity components of electrons over a period of their motion along a cyclotron orbit, we obtain

$$\langle\mathbf{k}\cdot\mathbf{v}\rangle_\varphi = \eta v_{\mathrm{F}}J_0(\alpha)(k_x\tan\vartheta + k_z)\sin\beta. \qquad (22)$$

For the directions of $\mathbf{B}_0$ in which α is equal to one of the zeros $\alpha_i = (mv_{\mathrm{F}}/p_0)\tan\vartheta_i$ of the Bessel function $J_0(\alpha)$, the average $\langle\mathbf{k}\cdot\mathbf{v}\rangle_\varphi \propto \eta^2$, and the dispersion equation is rewritten as

$$1 + 2\frac{(kr_0)^{-3}}{\sin\phi}\left(\frac{\omega_{\mathrm{p}}v_{\mathrm{F}}}{\omega_{\mathrm{B}}^{(0)}c}\right)^2\frac{\omega}{\omega_{\mathrm{B}}^{(0)}}$$

$$\times\frac{\left(\cos\frac{\pi\tilde{\omega}}{\omega_{\mathrm{B}}^{(0)}} - \langle\sin R(\vartheta_i)\rangle_\beta\right)}{\sin\frac{\pi\tilde{\omega}}{\omega_{\mathrm{B}}^{(0)}}} = 0, \qquad (23)$$

where

$$R(\vartheta_i) = \int_{-\pi/2}^{\pi/2}\frac{\mathbf{k}\cdot\mathbf{v}(\varphi)}{\omega_{\mathrm{B}}(\beta_i)}d\varphi = 2\frac{k_xv_\perp}{\omega_{\mathrm{B}}(\beta_i)}$$

$$-\pi\eta\frac{k_zv_{\mathrm{F}}}{\omega_{\mathrm{B}}^{(0)}}\mathrm{H}_0(\alpha_i)\cos\beta_i \qquad (24)$$

$$+\eta\frac{k_xv_{\mathrm{F}}}{2\omega_{\mathrm{B}}^{(0)}}\tan\vartheta_i\cos\beta_i\sum_{n=1}^{\infty}\frac{J_{2n+1}(\alpha_i)}{n(n+1)(2n+1)},$$

where

$$\mathrm{H}_0(\alpha) = \frac{2}{\pi}\int_0^{\pi/2}d\varphi\sin(\alpha\cos\varphi)$$

is the Struwe function, $\beta_i = p_{\mathrm{B}}/p_0\cos\vartheta_i$, $\omega_{\mathrm{p}} = \sqrt{4\pi n_0e^2/m}$ is the plasma frequency, and $n_0 = p_0m^2v_{\mathrm{F}}^2/2\pi\hbar^3$ is the density of charge carriers.

When

$$\frac{1}{(kr_0)^3}\left(\frac{\omega_{\mathrm{p}}v_{\mathrm{F}}}{\omega_{\mathrm{B}}^{(0)}c}\right)^2 \gg 1,$$

which can easily be realized in conductors with the density of charge carriers on the order of one carrier per atom, the solution to Eq. (23) can be represented as (17) with

$$\Delta\omega = \omega_{\mathrm{B}}^{(0)}\left(\frac{1}{2} - \frac{(-1)^n}{\pi}\arcsin\langle\sin R(\vartheta)\rangle_\beta\right). \tag{25}$$

In the inverse limit case

$$\frac{1}{(kr_0)^3}\left(\frac{\omega_{\mathrm{p}} v_{\mathrm{F}}}{\omega_{\mathrm{B}}^{(0)} c}\right)^2 \ll 1,$$

the spectrum of cyclotron waves is determined by

$$\begin{aligned}\omega = n\omega_{\mathrm{B}}^{(0)}\Bigg(1 - 2\frac{(kr_0)^{-3}}{\pi\sin\phi}\left(\frac{\omega_{\mathrm{p}} v_{\mathrm{F}}}{\omega_{\mathrm{B}}^{(0)} c}\right)^2 \\ \times (1 - (-1)^n\langle\sin R(\vartheta)\rangle_\beta)\Bigg).\end{aligned} \tag{26}$$

In layered conductors, for certain directions of the external magnetic field with respect to the layers, electromagnetic waves with frequencies in the neighborhood of the cyclotron resonance may propagate for arbitrary orientations of the vectors **k** and $\mathbf{B}_0$. Formulas (25) and (26) show that, under strong spatial dispersion, the frequencies of cyclotron waves are oscillatory functions of the projection k_x of the wavevector onto the plane of layers.

4. FERMI-LIQUID MODES

Consider propagation of electromagnetic waves in the electron Fermi liquid along the normal to the layers. In the linear approximation (9) with respect to a weak perturbation of the electron system by the electric field of the wave,

$$\mathbf{E}(\mathbf{r}, t) \propto \exp(-i\omega t + i\mathbf{k}\cdot\mathbf{r}),$$

the kinetic equation is transformed into the integral equation

$$\psi + \langle L\psi\rangle = \hat{R}\{e\mathbf{v}\cdot\mathbf{E} - i\omega\langle L(\mathbf{p}, \mathbf{p}')\psi(\mathbf{p}')\rangle\}, \tag{27}$$

where

$$\begin{aligned}\hat{R}\{g\} &= \frac{1}{\omega_{\mathrm{B}}}\int_{-\infty}^{\varphi} d\varphi' g(\varphi') \\ &\times \exp\left[-i\frac{\tilde{\omega}}{\omega_{\mathrm{B}}}(\varphi' - \varphi) + i\frac{1}{\omega_{\mathrm{B}}}\mathbf{k}\cdot(\mathbf{r}(\varphi') - \mathbf{r}(\varphi))\right], \\ \mathbf{r}(\varphi') - \mathbf{r}(\varphi) &= -\int_{\varphi'}^{\varphi} d\varphi''\mathbf{v}(\varphi'').\end{aligned} \tag{28}$$

Let us invoke the model representation of the Landau correlation function in the form

$$L(\mathbf{p}, \mathbf{p}') = \Lambda\mathbf{v}\cdot\mathbf{v}', \tag{29}$$

which quite satisfactorily describes the Fermi-liquid phenomena in the propagation of electromagnetic waves with $\mathbf{k} = (0, 0, k)$.

Using this expression, we can rewrite a renormalized correction to the distribution function $\Psi = \psi + \langle L\psi\rangle$ as

$$\Psi = \psi + e\Lambda v_k\chi_k, \tag{30}$$

where $\chi_k = \langle v_k\psi\rangle/e$.

Equating Eqs. (30) and (27), we obtain

$$\psi = \sum_k\{e\hat{R}(v_k)E_k - ie\omega\Lambda\hat{R}(v_k)\chi_k - e\Lambda v_k\chi_k\}. \tag{31}$$

Multiplying formula (31) by v_j and averaging the result over the Fermi surface, we obtain a system of linear algebraic equations in χ_j:

$$\begin{aligned}\chi_j + \Lambda\sum_k\langle v_j v_k\rangle\chi_k + i\omega\Lambda\sum_k\langle v_j\hat{R}(v_k)\rangle\chi_k \\ = \sum_k\langle v_j\hat{R}(v_k)\rangle E_k.\end{aligned} \tag{32}$$

Substituting a solution to this system into the expression for the current density $\mathbf{j} = \langle e\mathbf{v}\Phi\rangle$, which, with regard to (29), is rewritten as

$$j_i = e^2\sum_k\langle v_i\hat{R}(v_k)\rangle(E_k - i\omega\Lambda\chi_k), \tag{33}$$

we obtain the relation between **j** and **E**.

Thus, Eqs. (31), combined with the Maxwell equations for the Fourier components

$$E_x = \zeta j_x, \quad E_y = \zeta j_y, \quad j_z = 0, \tag{34}$$

yield a system of six linear algebraic equations in the functions E_j and χ_j:

$$\begin{aligned}e^2\chi_j + e^2\Lambda\sum_k\langle v_i v_k\rangle\chi_k + i\omega\Lambda\sum_k\sigma_{ik}\chi_k - \sigma_{ik}E_k &= 0, \\ \sum\sigma_{zk}(E_k - i\omega\Lambda\chi_k) &= 0, \\ E_x - \zeta\sum_k\sigma_{xk}(E_k - i\omega\Lambda\chi_k) &= 0, \\ E_y - \zeta\sum_k\sigma_{yk}(E_k - i\omega\Lambda\chi_k) &= 0.\end{aligned} \tag{35}$$

Here,

$$\zeta = \frac{4\pi i\omega}{k^2c^2 - \omega^2},$$

and the quantities $\sigma_{ik} = e^2\langle v_i\hat{R}(v_k)\rangle$ coincide with the components of the conductivity tensor in a gas approximation. A condition for the existence of a nontrivial solution to this system of equations (the vanishing of its determinant) represents a dispersion equation for waves. After straightforward calculations, we can represent it as

$$\begin{aligned}&\left[1 - \zeta(\tilde{\sigma}_{xx} + \Lambda_x\tilde{\sigma}_{xy}B_{xy}) + \frac{i\omega}{e^2}\Lambda_x\tilde{\sigma}_{xx}\right]\\ &\times\left[1 - \zeta(\tilde{\sigma}_{yy} + \Lambda_y\tilde{\sigma}_{yx}B_{xy}) + \frac{i\omega}{e^2}\Lambda_y\tilde{\sigma}_{yy}\right]\\ &-\left[\zeta\tilde{\sigma}_{yx} - \frac{i\omega}{e^2}\Lambda_x\tilde{\sigma}_{yx} - \Lambda_xB_{xy}\right]\\ &\times\left[\zeta\tilde{\sigma}_{xy} - \frac{i\omega}{e^2}\Lambda_y\tilde{\sigma}_{xy} - \Lambda_yB_{xy}\right] = 0.\end{aligned} \tag{36}$$

Here,

$$B_{\alpha\beta} = \langle v_\alpha v_\beta\rangle - \Lambda\frac{\langle v_\alpha v_z\rangle\langle v_z v_\beta\rangle}{1 + \Lambda\langle v_z^2\rangle},$$

$$\tilde{\sigma}_{\alpha\beta} = \sigma_{\alpha\beta} - (\sigma_{\alpha z}\sigma_{z\beta})/\sigma_{zz}, \quad \Lambda_\alpha = \frac{\Lambda}{1 + \Lambda B_{\alpha\alpha}},$$

$$\alpha, \beta = x, y.$$

A peculiar behavior of a layered conductor is associated with the fact that the in-plane velocities of charge carriers are much greater than their projection onto the normal to the layers (axis z). The in-plane anisotropy does not produce any appreciable effect on the phenomena associated with the specific feature of the quasi-two-dimensional energy spectrum of such a conductor, and we do not take it into account. In this case, $B_{xy} = 0$, $\Lambda_x = \Lambda_y$, and one can easily verify that Eq. (36) holds if

$$\begin{aligned}&k^2c^2 - \omega^2 - 4\pi\omega\left\{\frac{\omega}{e^2}\Lambda_x\right.\\ &\left.- i\frac{\tilde{\sigma}_{xx} + \tilde{\sigma}_{yy} \pm \sqrt{(\tilde{\sigma}_{xx} - \tilde{\sigma}_{yy})^2 + 4\tilde{\sigma}_{xy}\tilde{\sigma}_{yx}}}{2(\tilde{\sigma}_{xx}\tilde{\sigma}_{yy} - \tilde{\sigma}_{xy}\tilde{\sigma}_{yx})}\right\}^{-1} = 0.\end{aligned} \tag{37}$$

One can easily verify that the quantities $\tilde{\sigma}_{\alpha\beta}$ ($\alpha, \beta = x, y$) are mainly determined by the components $\sigma_{\alpha\beta}$ because the components σ_{ik} that contain index z are small due to the smallness of the quasi-two-dimensionality parameter η.

Assume, for simplicity, that the dispersion law of charge carriers is given by (18). Calculating σ_{ik} by the equation of motion (20) of a charged particle in a magnetic field, we can easily verify that, for $\vartheta \ll 1$, Eq. (37) is rewritten as

$$\begin{aligned}&k^2c^2 - \omega^2\\ &- \frac{\omega\omega_p^2}{\omega\lambda - \sqrt{(\tilde{\omega} \mp \omega_B^{(0)})^2 - (k\eta v_F J_0(\alpha))^2}} = 0.\end{aligned} \tag{38}$$

Here, $\lambda = \Lambda_x v_F^2\langle 1\rangle/2$ is a dimensionless quantity that characterizes the Fermi-liquid interaction between electrons.

If the condition

$$(\omega \mp \omega_B^{(0)})^2 - (\lambda\omega)^2 < (\eta k v_F J_0(\alpha))^2 < (\omega \mp \omega_B^{(0)})^2 \tag{39}$$

holds, then, in the collision-free limit ($\tau_1 \longrightarrow \infty$), there exist real solutions to the dispersion equation (38). They describe collective modes that are associated with correlation phenomena and are absent in a gas approximation. These excitations exist even for $k > k_{\min} = \omega_p/c\sqrt{\lambda}$. Application of a magnetic field removes the degeneracy of the spectrum of electromagnetic oscillations, thus resulting in two waves with the frequencies

$$\omega^\pm = \frac{((\eta k v_F J_0(\alpha))^2 - [(\eta k v_F J_0(\alpha))^2 - \omega_B^{(0)^2}](\lambda - \omega_p^2/k^2c^2))^{1/2} \pm \omega_B^{(0)}}{1 - (\lambda - \omega_p^2/k^2c^2)}. \tag{40}$$

The threshold frequencies of these waves $\omega_{\min}^\pm = (\omega_p\eta v_F/c\sqrt{\lambda}) \pm \omega_B^{(0)}$ may be much lower than ω_p; this provides more favorable conditions for observing Fermi-liquid modes in layered conductors compared with ordinary metals.

An increase in the angle between the magnetic field and the normal to the layers enhances the influence of the dependence of the electron velocity projection onto the wavevector on its phase on the trajectories. If the condition $\eta k v_F/\omega_B^{(0)} \gg 1$ holds, then one can apply the method of stationary phase to calculate $\sigma_{\alpha\beta}$. When $\tan\vartheta < \pi p_0/2p_F$, there may be either two or none of such points on the electron orbit. However, for a sufficiently large deviation of the magnetic field from the normal to the layers, there may be a sufficiently large number of points of stationary phase on the orbits that

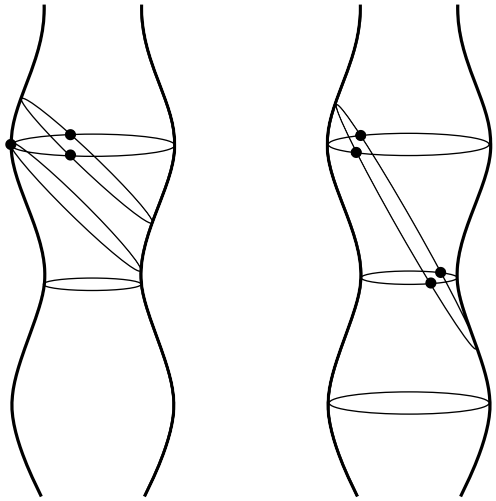

(a) (b)

Points of stationary phase at which $\mathbf{k}\cdot\mathbf{v}=\omega$ on the electron orbits (a) for $\tan\vartheta < \pi p_0/2p_F$ and (b) for $\tan\vartheta > \pi p_0/2p_F$. Thin lines connect the points at which $kv_z=\omega$.

intersect several unit cells of the momentum space (see figure).

After integrating with respect to φ and φ', the expression for $\sigma_{\alpha\beta}$ in a strong magnetic field ($\omega_B\tau_1 \gg 1$) is rewritten as

$$\sigma_{\alpha\beta} = \frac{\omega_p^2}{4\pi^2 k v_F^2}$$

$$\times \sum_e \int_0^{2\pi} d\beta \left\{1 - \exp\frac{2\pi i}{\omega_B}(\omega - \langle k v_z\rangle_\varphi)\right\}^{-1}$$

$$\times \left\{\left[\frac{v_\alpha(\varphi_e)v_\beta(\varphi_e)}{2|v'_z(\varphi_e|} + \frac{v_\alpha(\pi-\varphi_e)v_\beta(\pi-\varphi_e)}{2|v'_z(\pi-\varphi_e)|}\right]\right.$$

$$\times\left(1 + \exp\frac{2\pi i}{\omega_B}(\omega - \langle k v_z\rangle_\varphi)\right) \qquad (41)$$

$$+ \frac{1}{(|v'_z(\varphi_e)v'_z(\pi-\varphi_e)|)^{1/2}}\Big[v_\alpha(\varphi_e)v_\beta(\pi-\varphi_e)$$

$$\times \exp\left(-i\frac{\tilde{\omega}}{\omega_B}\Delta\varphi + ik\Delta z + i\frac{\pi}{2} + \frac{2\pi i}{\omega_B}(\omega - \langle k v_z\rangle_\varphi)\right)$$

$$\left.+ v_\alpha(\pi-\varphi_e)v_\beta(\varphi_e)\exp\left(i\frac{\tilde{\omega}}{\omega_B}\Delta\varphi - ik\Delta z - i\frac{\pi}{2}\right)\Big]\right\},$$

where φ_e are the points on the electron trajectory at which $v_z(\varphi_e) = 0$, $v'_z(\varphi_e) > 0$, $\Delta\varphi_e = \pi - 2\varphi_e$, and $\Delta z_e = z(\pi-\varphi_e) - z(\varphi_e)$.

In formula (41), $\Delta\varphi$ and Δz are essentially different on different electron orbits. At certain inclination angles $\vartheta = \vartheta_i$ of the magnetic field, an electron nearly ceases to drift along the wavevector, and, in a linear approximation in the quasi-two-dimensionality parameter, the projection averaged over the period, of the velocity of a charged particle onto the normal to the layers,

$$\langle v_z\rangle_\varphi = \eta v_F J_0(\alpha)\sin\beta,$$

vanishes.

The integration of the last two terms of alternating sign with respect to β significantly reduces the contribution of these terms to the electric conductivity even for $\eta k v_F/\omega_B \approx 1$. As a result, for $\vartheta = \vartheta_i$, in the range of frequencies close to the frequency of rotation of charge carriers along closed trajectories in a magnetic field or to the multiples of this frequency,

$$\omega = n\omega_B^{(0)} + \Delta\omega,$$

one can neglect the nondiagonal components of the tensor $\sigma_{\alpha\beta}$, while, for the components $\sigma_{\alpha\alpha}$, one can apply the following asymptotic expression:

$$\sigma_{\alpha\alpha} = \frac{i\omega_p^2}{4\pi^2 k v_F^2}\sum_e \int_0^{2\pi} d\beta \frac{v_\alpha^2(\varphi_e)}{|v'_z(\varphi_e)|}\cot\frac{\pi\tilde{\omega}}{\omega_B}. \qquad (42)$$

In this case, the dispersion equation reduces to

$$k^2c^2 - \omega^2 - \frac{\omega\omega_p^2}{\omega\lambda - i\omega_p^2/4\pi\sigma_{\alpha\alpha}} = 0, \quad \alpha = x, y. \qquad (43)$$

When $|\Delta\omega| > \eta\omega$, dispersion equation (38) may have a real solution that describes a cyclotron wave, and the relation between $\Delta\omega$ and k in the collision-free limit is given by

$$\Delta\omega = \frac{n\omega_B^{(0)^2}}{C_\alpha \eta k v_F}\left(\lambda - \frac{\omega_p^2}{k^2c^2 - n^2\omega_B^{(0)^2}}\right), \qquad (44)$$

where

$$C_\alpha = \frac{\pi^2 v_F}{\eta}\left(\sum_e \int_0^{2\pi} \frac{d\beta\, v_\alpha^2(\varphi_e, \beta)}{|v'_z(\varphi_e, \beta)|}\right)^{-1}.$$

Formula (44) shows that, in the absence of Fermi-liquid electron correlations, an undamped cyclotron wave may only exist when $\Delta\omega < 0$. The consideration of Fermi-liquid effects increases the transparency windows of a layered conductor, and a cyclotron wave may propagate even for $\Delta\omega > 0$, i.e., above the cyclotron resonance frequency.

5. SPIN WAVES

Paramagnetic spin waves represent space–time perturbations of spin density. Oscillations of this type are attributed to the exchange interactions between electrons and cannot be excited in a gas of noninteracting particles. In the main approximation in the small parameter η, the Landau correlation function is given by (8) and kinetic equation (10) for the spin density can be substantially simplified. Let us expand the functions $\mathbf{\Phi} = \boldsymbol{\xi} + \langle S\boldsymbol{\xi}\rangle$ into Fourier series in the variable φ:

$$\mathbf{\Phi}(\mathbf{p}) = \sum_{n=-\infty}^{\infty} \mathbf{\Phi}_n(\varepsilon_F, p_B)e^{in\varphi},$$

$$\boldsymbol{\xi}(\mathbf{p}) = \sum_{n=-\infty}^{\infty} \boldsymbol{\xi}_n(\varepsilon_F, p_B)e^{in\varphi};$$

applying formula (8), we obtain

$$\boldsymbol{\xi}(\mathbf{p}) = \mathbf{\Phi}(\mathbf{p}) - \sum_{n=-\infty}^{\infty} \lambda_n \overline{\mathbf{\Phi}}_n e^{in\varphi}, \tag{45}$$

where

$$\lambda_n = \frac{S^{\sim}_n}{1 + S^{\sim}_n},$$

$$\overline{\mathbf{\Phi}}_n = \frac{1}{(2\pi)^2}\int_0^{2\pi} d\varphi e^{-in\varphi}\int_{-\pi}^{\pi} d\beta \mathbf{\Phi}(\varepsilon_F, \beta, \varphi) \equiv \langle e^{-in\varphi}\mathbf{\Phi}\rangle_{\beta,\varphi},$$

$$S^{\sim}_n = \nu(\varepsilon_F)S_n.$$

Substituting (45) into Eq. (10), we find that the components of the renormalized spin density $\Phi_\pm = \Phi_{x_1} \pm i\Phi y \propto \exp(i\mathbf{k}\cdot\mathbf{r} - i\omega t)$ of conduction electrons with the quasi-two-dimensional dispersion law (1) satisfy the equation

$$\frac{\partial\Phi_\pm}{\partial\varphi} - \frac{i}{\omega_B}(\omega - \mathbf{k}\cdot\mathbf{v} \mp \Omega)\Phi_\pm$$
$$= i\frac{\mu_0}{\omega_B}(\mathbf{k}\cdot\mathbf{v} \pm \Omega)B^{\sim}_{\pm} \tag{46}$$
$$- \frac{i\omega}{\omega_B}\sum_{n=-\infty}^{\infty}\lambda_n\overline{\Phi}{}_n^{(\pm)}e^{in\varphi} + \frac{1}{\omega_B}I_{\text{coll}}^{(2)}(\Phi_\pm).$$

Here, $\Phi_{x_1} = \Phi_x\cos\vartheta - \Phi_z\sin\vartheta$, the axis x_1 is perpendicular to the axis y and the vector $\mathbf{B}_0$, $\Omega = -2\mu B_0/\hbar = \omega_s/(1 + S^{\sim}_0)$, and $\omega_s = -2\mu_0 B_0/\hbar$ is the spin paramagnetic resonance frequency. The ac magnetic field $B^{\sim}_{\pm} = B_{x_1} \pm iB_y$ induced by spin oscillations is determined from the equation

$$\mathbf{B}^{\sim}(\omega, \mathbf{k}) = 4\pi\left(\mathbf{M}^{\sim}(\omega, \mathbf{k}) - \frac{\mathbf{k}}{k^2}(\mathbf{k}\cdot\mathbf{M}^{\sim}(\omega, \mathbf{k}))\right), \tag{47}$$

where $\mathbf{M}^{\sim}(\omega, \mathbf{k}) = \mu_0\langle\boldsymbol{\xi}(\mathbf{p}, \omega, \mathbf{k})\rangle$ is the high-frequency magnetization.

After straightforward transformations, Eq. (46) for the renormalized spin density is reduced to

$$\Phi^{(\pm)} = \int_{-\infty}^{\varphi} d\varphi' \exp\left(\frac{i}{\omega_B}\int_{\varphi'}^{\varphi} d\varphi''(\tilde{\omega} \mp \Omega - \mathbf{k}\cdot\mathbf{v}(\varphi''))\right)$$
$$\times\left(i\frac{\mu_0}{\omega_B}(\mathbf{k}\cdot\mathbf{v}(\varphi') \pm \Omega)B^{\sim}_{\pm} - i\frac{\omega}{\omega_B}\sum_{p=-\infty}^{\infty}\lambda_p\overline{\Phi}{}_p^{(\pm)}e^{ip\varphi'}\right). \tag{48}$$

Multiplying Eq. (48) by $e^{-in\varphi}$ and integrating the result with respect to the variables β and φ, for the Fourier coefficients $\overline{\Phi}{}_n^{(\pm)}$ of the function

$$\langle\Phi^{(\pm)}\rangle_\beta = \frac{1}{2\pi}\int_0^{2\pi} d\beta\Phi^{(\pm)}(\varepsilon_F, \beta, \varphi),$$

we obtain the following system of linear equations:

$$\sum_{p=-\infty}^{\infty}\left(\delta_{np} - \lambda_p\frac{\omega}{\omega_B}\langle f_{np}(\beta)\rangle_\beta\right)\overline{\Phi}{}_p^{(\pm)}$$
$$= -\mu_0 B^{\sim}_{\pm}\left\langle\frac{1}{2\pi i}\left\{1 - \exp\left(2\pi i\frac{\tilde{\omega} - (\langle\mathbf{k}\cdot\mathbf{v}\rangle_\varphi \mp \Omega)}{\omega_B}\right)\right\}^{-1}\right.$$
$$\times\int_0^{2\pi}\int_0^{2\pi} d\varphi d\varphi_1(\mathbf{k}\cdot\mathbf{v}(\varphi - \varphi_1) \mp \Omega) \tag{49}$$
$$\left.\times\exp\left(i(p - n)\varphi - ip\varphi_1 + i\frac{\tilde{\omega} \mp \Omega}{\omega_B}\varphi_1 - iR(\varphi, \varphi_1)\right)\right\rangle_\beta,$$

$$f_{np}(\beta) = \frac{1}{2\pi i}\left\{1 - \exp\left(2\pi i\frac{\tilde{\omega} - (\langle\mathbf{k}\cdot\mathbf{v}\rangle_\varphi \mp \Omega)}{\omega_B}\right)\right\}^{-1}$$
$$\times\int_0^{2\pi}\int_0^{2\pi} d\varphi d\varphi_1 \tag{50}$$
$$\times\exp\left(i(p - n)\varphi - ip\varphi_1 + i\frac{\tilde{\omega} \mp \Omega}{\omega_B}\varphi_1 - iR(\varphi, \varphi_1)\right).$$

The Fourier coefficients of the smooth function $\nu(\varepsilon_F)S(\mathbf{p}, \mathbf{p}')$ rapidly decrease as their number increases; therefore, one may restrict oneself to a finite number of terms of the series. System of equations (49), combined with Eq. (47), which links the high-frequency magnetic field to the magnetization, describes natural oscillations of spin density in layered conductors with arbitrary energy spectrum and correlation function. It is obvious that, to determine the spectrum of spin waves, it suffices to use the homogeneous system of equations corresponding to (49). Let us neglect the small nonhomogeneous parameter in (49), which is proportional to $\mu_0 \tilde{B}_{\pm}$ and takes into account the effect of the self-consistent field $\tilde{B}_{\pm}$. The dispersion equation of "free" oscillations of spin density is given by [12]

$$D(\omega^{(0)}, \mathbf{k}) \equiv \det\left[\delta_{n\mathrm{p}} - \lambda_{\mathrm{p}}\frac{\omega^{(0)}}{\omega_{\mathrm{B}}}\langle f_{n\mathrm{p}}(\beta)\rangle_{\beta}\right] = 0. \quad (51)$$

The frequency ω of natural oscillations of magnetization coincides, up to the terms proportional to $\chi_0 \sim \mu_0^2\nu(\varepsilon_{\mathrm{F}})$, with the frequency $\omega^{(0)}$ of free oscillations of spin density. At this frequency, the magnetic susceptibility has a sharp maximum and the determinant $D(\omega, \mathbf{k})$ is equal to χ_0 in order of magnitude.

The condition that there is no collision-free attenuation of spin waves reduces to the inequality

$$|\omega - n\omega_{\mathrm{B}} \mp \Omega| > \max|\langle \mathbf{k}\cdot\mathbf{v}\rangle_{\varphi}|. \quad (52)$$

Under strong spatial dispersion, $\mathbf{k}\cdot\mathbf{v}_m \gg \omega_{\mathrm{B}}$, $\omega \mp \Omega \ll \mathbf{k}\cdot\mathbf{v}_m$, for the directions of $\mathbf{B}_0$ relative to the conductor layers such that $\mathbf{v}_{\mathrm{B}}$ is close to zero, there exist solutions to the dispersion equation (51) in the neighborhood of the resonance

$$\begin{gathered} \omega = n_1\omega_{\mathrm{B}} \pm \Omega + \Delta\omega, \\ \Delta\omega \ll \omega_{\mathrm{B}}, \quad n_1 = 0, 1, 2, \ldots. \end{gathered} \quad (53)$$

The correction to the resonance frequency can be represented as

$$\Delta\omega = \frac{n_1\omega_{\mathrm{B}} \pm \Omega}{\pi k_x r_0}\gamma_i, \quad (54)$$

where γ_i are the roots of the equation

$$\det\left|\delta_{n\mathrm{p}} - \lambda_{\mathrm{p}}\gamma_i^{-1}\langle I_{n\mathrm{p}}(\beta)\rangle_{\beta}\right| = 0, \quad (55)$$

where

$$I_{n\mathrm{p}}(\beta) = \sum_{\alpha}\kappa(\boldsymbol{\varphi}^{\alpha})\frac{\exp\left[-iR(\varphi^{(\alpha)}, \varphi_1^{(\alpha)}) - i(n-p)\varphi^{(\alpha)} + ip\varphi_1^{(\alpha)} + i\frac{\pi}{4}\mathrm{s}\right]}{\left|\det(R''_{\varphi\varphi_1}(\varphi^{(\alpha)}, \varphi_1^{(\alpha)}))\right|^{1/2}}. \quad (56)$$

The summation is over all stationary points determined from the equations $v_x(\varphi) = 0$ and $v_x(\varphi - \varphi_1) = 0$. By ω_{B} in (51), (53), and (54), we mean the zeroth-order term in the expansion of the cyclotron frequency in powers of η.

In a model where the energy of conduction electrons is defined by (18) and the velocity components are defined by (20), asymptotic expressions for the coefficients $f_{n\mathrm{p}}(\beta)$ are given by

$$\begin{aligned} f_{n\mathrm{p}}(\beta) = \frac{1}{k_x r_0}\Bigg(&\cot\frac{\pi(\tilde{\omega} \mp \Omega)}{\omega_{\mathrm{B}}}\cos\frac{\pi}{2}(n-p) \\ &+ \frac{\sin\left(R(\vartheta_i) + \frac{\pi}{2}(n+p)\right)}{\sin\frac{\pi(\tilde{\omega} \mp \Omega)}{\omega_{\mathrm{B}}}}\Bigg) \end{aligned} \quad (57)$$

and Eq. (55) reduces to

$$\begin{aligned} \det\Bigg|\delta_{n\mathrm{p}} - \lambda_{\mathrm{p}}\gamma_i^{-1}\Bigg(&\cos\frac{\pi}{2}(n-p) \\ &+ (-1)^{n_1}\left\langle \sin\left(R(\vartheta_i) + \frac{\pi}{2}(n+p)\right)\right\rangle_{\beta}\Bigg)\Bigg| = 0. \end{aligned} \quad (58)$$

When the correlation function is defined by the zeroth and first Fourier harmonics,

$$S(\mathbf{p}, \mathbf{p}') = S_0 + 2S_1\cos(\varphi - \varphi'),$$

Eq. (58) is reduced to a quadratic equation whose roots are given by

$$\begin{aligned} \gamma_{1,2} = \frac{1}{2}\Big(&\lambda_0 + 2\lambda_1 + (-1)^{n_1}(\lambda_0 - 2\lambda_1)g \\ &\pm\{(\lambda_0 + 2\lambda_1 + (-1)^{n_1}(\lambda_0 - 2\lambda_1)g)^2 \\ &+ 8\lambda_0\lambda_1(-1 + g^2 + h^2)\}^{1/2}\Big), \end{aligned} \quad (59)$$

where $g = \langle \sin R(\vartheta_i) \rangle_\beta$ and $h = \langle \sin R(\vartheta_i) \rangle_\beta$.

In the short-wavelength limit, for certain directions of the external magnetic field, there exist spin waves with frequencies (53) close to the resonance frequencies $\omega_r = n\omega_B \pm \Omega$. An analogous type of excitations in quasi-isotropic metals occurs only when the wavevector $\mathbf{k}$ is perpendicular to $\mathbf{B}_0$.

REFERENCES

1. J. Wosnitza, Springer Tracts Mod. Phys. **134**, 1 (1996).
2. M. V. Kartsovnik and V. N. Laukhin, J. Phys. I **6**, 1753 (1996).
3. J. Singelton, Rep. Prog. Phys. **63**, 1111 (2000).
4. P. M. Platzman and P. A. Wolf, *Waves and Interactions in Solid State Plasma* (Academic, New York, 1973; Mir, Moscow, 1975).
5. A. I. Akhiezer, V. G. Bar’yakhtar, and S. V. Peletminskii, *Spin Waves* (Nauka, Moscow, 1967; North-Holland, Amsterdam, 1968).
6. L. D. Landau, Zh. Éksp. Teor. Fiz. **30**, 1058 (1956) [Sov. Phys. JETP **3**, 920 (1956)].
7. V. P. Silin, Zh. Éksp. Teor. Fiz. **33**, 495 (1957) [Sov. Phys. JETP **6**, 387 (1958)].
8. V. P. Silin, Zh. Éksp. Teor. Fiz. **35**, 1243 (1958) [Sov. Phys. JETP **8**, 870 (1959)].
9. S. Schultz and G. Dunifer, Phys. Rev. Lett. **18**, 283 (1967).
10. M. V. Fedoryuk, *Asymptotic. Integrals and Series* (Nauka, Moscow, 1987) [in Russian].
11. N. N. Bogolyubov and Yu. A. Mitropol’skii, *Asymptotic Methods in the Theory of Nonlinear Oscillations* (Nauka, Moscow, 1974; Gordon and Breach, New York, 1962).
12. V. G. Peschanskiĭ and D. I. Stepanenko, Pis’ma Zh. Éksp. Teor. Fiz. **78**, 772 (2003) [JETP Lett. **78**, 322 (2003)].

Translated by I. Nikitin

Journal of Experimental and Theoretical Physics, Vol. 99, No. 6, 2004, pp. 1264–1278.
Translated from Zhurnal Éksperimental'noĭ i Teoreticheskoĭ Fiziki, Vol. 126, No. 6, 2004, pp. 1446–1464.
Original Russian Text Copyright © 2004 by Kuleeva, Kuchinskii, Sadovskii.

SOLIDS
Electronic Properties

Superconductivity in the Pseudogap State in the Hot Spot Model: The Influence of Impurities and the Phase Diagram

N. A. Kuleeva*, E. Z. Kuchinskii, and M. V. Sadovskii*****
Institute of Electrophysics, Russian Academy of Sciences, Ural Branch, Yekaterinburg, 620016 Russia
**e-mail: strigina@iep.uran.ru*
***e-mail: kuchinsk@iep.uran.ru*
****e-mail: sadovski@iep.uran.ru*

Received June 10, 2004

Abstract—We analyze the peculiarities of the superconducting state (*s*- and *d*-wave paring) in the model of the pseudogap state induced by Heisenberg antiferromagnetic short-range order spin fluctuations. The model is based on the pattern of strong scattering near hot spots at the Fermi surface. The analysis is based on the microscopic derivation of the Ginzburg–Landau expansion with the inclusion of all Feynman diagrams of perturbation theory for the interaction of an electron with short-range order fluctuations and in the ladder approximation for the scattering by normal (nonmagnetic) impurities. We determine the dependence of the critical superconducting transition temperature and other superconductor characteristics on the pseudogap parameters and the degree of impurity scattering. We show that the characteristic shape of the phase diagram for high-temperature superconductors can be explained in terms of the model under consideration. © *2004 MAIK "Nauka/Interperiodica".*

1. INTRODUCTION

One of the most important problems in the physics of high-temperature superconductors (HTSCs) based on copper oxides is the theoretical description of the characteristic shape of their phase diagram [1]. Elucidating the nature of the pseudogap state that is observed over wide ranges of temperatures and carrier concentrations [2] and that undoubtedly plays the central role in shaping the properties of the normal and superconducting states of these systems arouses particular interest. Despite ongoing discussions, the pseudogap formation scenario based on the pattern of strong scattering of current carriers by antiferromagnetic[1] (AFM, SDW) short-range order spin fluctuations seems to be preferred [2, 3]. In the momentum space, this scattering takes place with the transfer of the wavevectors of order $\mathbf{Q} = (\pi/a, \pi/a)$ (a is the two-dimensional lattice constant) and leads to precursors of the rearrangement of the electron spectrum that arises when a long-range AFM order is established (the period doubles). This results in a non-Fermi liquid behavior (dielectrization) of the spectral characteristics near the so-called hot spots at the Fermi surface that emerge at the points of intersection of this surface with the boundaries of the "future" antiferromagnetic Brillouin zone [2].

A simplified model of the pseudogap behavior [4, 5] in which the scattering by real (dynamical) spin fluctuations was replaced (which is valid at fairly high temperatures) with a static Gaussian random field of pseudogap fluctuations with a characteristic wavevector from the vicinity of $\mathbf{Q}$ whose width is determined by the inverse correlation length of the short-range order $\kappa = \xi^{-1}$ has been intensively studied in terms of this approach. An overview of the works, as applied to the properties of the normal state and for simple models of the influence of pseudogap fluctuations on superconductivity, can be found in [2].

In our recent paper [6], based on the microscopic derivation of the Ginzburg–Landau expansion,[2] we have studied the influence of pseudogap fluctuations in the hot spot model on the basic characteristics of the superconducting state (*s*- and *d*-type pairing) that forms against the background of these fluctuations. We considered a slightly simplified version of the model where the Heisenberg spin fluctuations were replaced with Ising or spin-independent charge CDW fluctuations. These pseudogap fluctuations of a "dielectric" nature were shown to generally suppress conductivity, causing a decrease in superconducting transition temperature, a reduction in the jump in specific heat, and several other anomalies of the superconductor characteristics. We found two possible types of interaction between the superconducting order parameter and pseudogap fluctuations that lead to distinctly different scales of their influence on superconductivity.

The goal of this work is to generalize the approach proposed in [6] to the "realistic" case of Heisenberg

---

[1] The role of similar charge (CDW) fluctuations cannot be ruled out either.

[2] A similar analysis was performed in [7] on the basis of Gorkov's equations.

1063-7761/04/9906-1264$26.00 © 2004 MAIK "Nauka/Interperiodica"

spin fluctuations and to calculate the influence of (nonmagnetic) impurities (disorder) on superconductivity in the pseudogap state. We show that the typical phase diagram for a HTSC can be semiquantitatively modeled in terms of the model under consideration.

2. THE HOT SPOT MODEL AND THE RECURRENCE PROCEDURE FOR CALCULATING THE GREEN FUNCTIONS AND THE VERTEX PARTS

The basic ideas of the hot spot model under consideration and the method for calculating the single-electron Green function were presented in detail in [4, 5]; the methods for determining the vertex parts of interest were described previously [6, 8]. Therefore, in this section, we provide only the basic equations and introduce the necessary notation by briefly describing the changes required to allow for the spin structure of the interaction in the Heisenberg model of antiferromagnetic fluctuations.

An effective interaction between electrons and spin fluctuations is introduced in the model of an "almost antiferromagnetic" Fermi liquid [4]. This interaction is described by the dynamical susceptibility characterized by the correlation length ξ of the spin fluctuations and their characteristic frequency ω_{sf} to be determined experimentally, which can depend significantly on the carrier concentration (and, for ξ, on the temperature). This dynamical susceptibility together with the effective interaction have (in momentum representation) a maximum in the vicinity of $\mathbf{Q} = (\pi/a, \pi/a)$, which gives rise to two types of quasi-particles: hot quasi-particles whose momenta lie near the points of the Fermi surface coupled by the scattering vector of order $\mathbf{Q}$ and cold quasi-particles whose momenta lie near the regions of the Fermi surface surrounding the diagonals of the Brillouin zone [2, 4, 5].

At high temperatures, $2\pi T \gg \omega_{sf}$, the spin dynamics may be disregarded [4]. The interaction with spin (pseudogap) fluctuations then reduces to the scattering of electrons by the corresponding static Gaussian random field. In this model, we can suggest a simplified form of the effective interaction (the correlator of the random fluctuation field) [4, 5] that allows full summation of the Feynman series of perturbation theory, which gives rise to the following recurrence procedure for determining the single-electron Green function:

$$G_k(\varepsilon_n, \mathbf{p}) = \frac{1}{i\varepsilon_n - \xi_k(\mathbf{p}) + ikv_k\kappa - \Sigma_k(\varepsilon_n, \mathbf{p})}, \quad (1)$$

$$\Sigma_k(\varepsilon_n, \mathbf{p}) = W^2 s(k+1) G_{k+1}(\varepsilon_n, \mathbf{p}). \quad (2)$$

This is shown in the form of a symbolic Dyson equation in Fig. 1a, where the following function is introduced:

$$G_{0k}(\varepsilon_n, \mathbf{p}) = \frac{1}{i\varepsilon_n - \xi_k(\mathbf{p}) + ikv_k\kappa}. \quad (3)$$

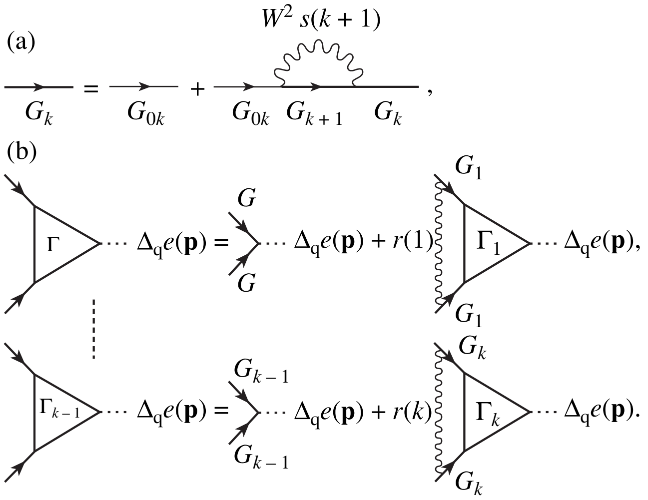

Fig. 1. Recurrence equations for (a) the Green function and (b) the triangular vertex.

Here, $\kappa = \xi^{-1}$ is the inverse correlation length of the pseudogap fluctuations; $\varepsilon_n = 2\pi T(n + 1/2)$ (to be specific, we assume that $\varepsilon_n > 0$);

$$\xi_k(\mathbf{p}) = \begin{cases} \xi_{\mathbf{p}+\mathbf{Q}} & \text{for odd } k, \\ \xi_{\mathbf{p}} & \text{for even } k; \end{cases} \quad (4)$$

$$v_k = \begin{cases} |v_x(\mathbf{p}+\mathbf{Q})| + |v_y(\mathbf{p}+\mathbf{Q})| & \text{for odd } k, \\ |v_x(\mathbf{p})| + |v_y(\mathbf{p})| & \text{for even } k; \end{cases} \quad (5)$$

$\mathbf{v}(\mathbf{p}) = \partial\xi_{\mathbf{p}}/\partial\mathbf{p}$ is the velocity of a free quasi-particle with the spectrum $\xi_{\mathbf{p}}$ that is taken in standard form [4]:

$$\xi_{\mathbf{p}} = -2t(\cos p_x a + \cos p_y a) - 4t' \cos p_x a \cos p_y a - \mu; \quad (6)$$

t and t' are the transfer integrals between the closest neighbors and between the second closest neighbors on the square lattice, respectively; a is the lattice constant; and μ is the chemical potential.

The parameter W has the dimensions of energy. It defines the effective pseudogap width and can be written in the model of Heisenberg spin fluctuations as [4]

$$W^2 = g^2 \frac{\langle \mathbf{S}_i^2 \rangle}{3} = g^2 \langle (n_{i\uparrow} - n_{i\downarrow})^2 \rangle, \quad (7)$$

where g is the coupling constant between electrons and spin fluctuations, $\langle \mathbf{S}_i^2 \rangle$ is the mean square of the spin at the lattice site, and $n_{i\uparrow}$ and $n_{i\downarrow}$ are the particle number operators at the site with the corresponding spin projections. Clearly, like the correlation length ξ, the parameter W in the semiphenomenological approach [4, 5] is

The choice of the sign in the recurrence procedure for the vertex part

Pairs	CDW fluctuations	SDW (Ising) fluctuations	SDW (Heisenberg) fluctuations
s	+	–	+
d	–	+	–

also a function of the carrier concentration (and temperature) to be determined experimentally.

The factor $s(k)$ is determined by the Feynman diagram combinatorics and is

$$s(k) = k \tag{8}$$

in the simplest case of commensurable short-range order charge (CDW) fluctuations, while for the most interesting case of Heisenberg spin (SDW) fluctuations [4],[3]

$$s(k) = \begin{cases} \dfrac{k+2}{3} & \text{for odd } k, \\ \dfrac{k}{3} & \text{for even } k. \end{cases} \tag{9}$$

The validity conditions for the approximation under consideration were discussed in detail in [4, 5].

A remarkable feature of the model under consideration is the possibility of full summation of the entire series of Feynman diagrams[4] for the vertex functions that describe the response of the system to an arbitrary external perturbation. This was considered in detail in [8]. Here, we immediately give the recurrence equations for the "triangular" vertices in the Cooper channel that arise in the corresponding analysis. These equations are similar to those derived in [6] and describe the response to an arbitrary fluctuation of the superconducting order (gap) parameter,

$$\Delta(\mathbf{p}, \mathbf{q}) = \Delta_{\mathbf{q}} e(\mathbf{p}), \tag{10}$$

where the symmetry factor that determines the type (symmetry) of pairing is taken in the form

$$e(\mathbf{p}) = \begin{cases} 1, & s\text{-wave paring}, \\ \cos(p_x a) - \cos(p_y a), & d_{x^2-y^2}\text{-type pairing}, \end{cases} \tag{11}$$

and it is implied that the pairing is singlet in spin. It is convenient to write the vertex of interest as

$$\Gamma(\varepsilon_n, -\varepsilon_n, \mathbf{p}, -\mathbf{p}+\mathbf{q}) \equiv \Gamma_{\mathbf{p}}(\varepsilon_n, -\varepsilon_n, \mathbf{q}) e(\mathbf{p}). \tag{12}$$

$\Gamma_{\mathbf{p}}(\varepsilon_n, -\varepsilon_n, \mathbf{q})$ is then defined by the recurrence procedure

$$\begin{aligned} &\Gamma_{\mathbf{p}k-1}(\varepsilon_n, -\varepsilon_n, \mathbf{q}) \\ &= 1 \pm W^2 r(k) G_k(\varepsilon_n, \mathbf{p}+\mathbf{q}) G_k(-\varepsilon_n, \mathbf{p}) \\ &\times \left[1 + \frac{2ik\kappa v_k}{G_k^{-1}(\varepsilon_n, \mathbf{p}+\mathbf{q}) - G_k^{-1}(-\varepsilon_n, \mathbf{p}) - 2ik\kappa v_k}\right] \\ &\times \Gamma_{\mathbf{p}k}(\varepsilon_n, -\varepsilon_n, \mathbf{q}), \end{aligned} \tag{13}$$

which is shown as graphs in Fig. 1b. The "physical" vertex corresponds to $\Gamma_{\mathbf{p}k=0}(\varepsilon_n, -\varepsilon_n, \mathbf{q})$. The additional combinatorial factor is $r(k) = s(k)$ for the simples case of charge (or Ising spin) pseudogap fluctuations considered in [6]. For the most interesting case of Heisenberg spin (SDW) fluctuations considered below, this factor is [4] (see also the Appendix)

$$r(k) = \begin{cases} k & \text{for even } k, \\ \dfrac{k+2}{9} & \text{for odd } k. \end{cases} \tag{14}$$

The choice of the sign of W^2 on the right-hand side of Eq. (13) depends on the symmetry of the superconducting order parameter and the type of pseudogap fluctuations [6] (for details, see the Appendix). The corresponding cases are listed in the table. In particular, we see from this table that in the most interesting case of *d*-type pairing and Heisenberg pseudogap fluctuations, we should take the minus, so the recurrence procedure for the vertex part becomes an alternating one. At the same time, for the case of *s*-wave paring and fluctuations of the same type, we should take the plus, and the recurrence procedure becomes a constant-sign one. It was shown in [6] (using other examples from the table) that this difference in the types of recurrence procedure leads to two qualitatively different behaviors of all basic superconductor characteristics.

3. THE INFLUENCE OF IMPURITIES

The influence of the scattering by normal (nonmagnetic) impurities can be easily taken into account in the self-consistent Born approximation by writing the Dyson equation shown graphically in Fig. 2a for the single-electron Green function. Compared to Fig. 1a, the standard contribution from the impurity scattering to the intrinsic-energy part [9] was added to this figure.

---

[3] The Feynman diagram combinatorics for the model of Heisenberg fluctuations is analyzed in detail in the Appendix.

[4] Including all of the diagrams with crossing interaction lines.

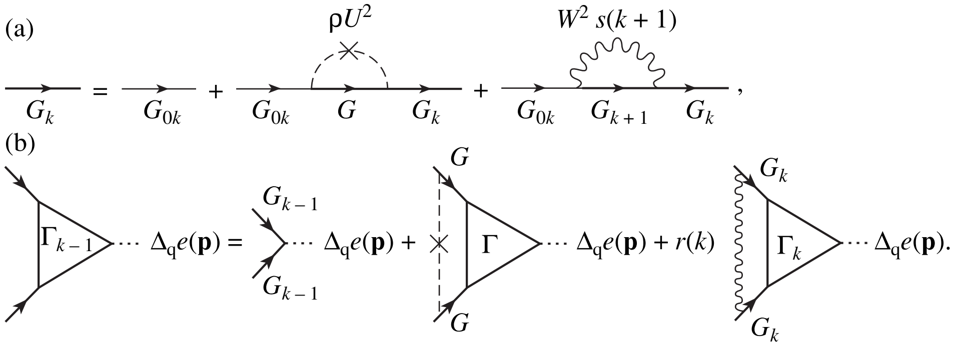

Fig. 2. Recurrence equations for (a) the Green function and (b) the triangular vertex including the impurity scattering

As a result, the recurrence equation for the Green function can be written as

$$G_k(\varepsilon_n, \mathbf{p}) = \left[G_{0k}^{-1}(\varepsilon_n, \mathbf{p}) - \rho U^2 \sum_{\mathbf{p}} G(\varepsilon_n, \mathbf{p}) - W^2 s(k+1) G_{k+1}(\varepsilon_n, \mathbf{p})\right]^{-1}, \tag{15}$$

where ρ is the impurity concentration with a point potential U and the "impurity" intrinsic-energy part includes the full Green function $G(\varepsilon_n, \mathbf{q}) = G_{k=0}(\varepsilon_n, \mathbf{p})$, which must generally be determined in a self-consistent way by using the written procedure. The contribution from the real part of the Green function to this intrinsic-energy part typically reduces [9] to an insignificant renormalization of the chemical potential, so Eq. (15) takes the form

$$G_k(\varepsilon_n, \mathbf{p}) = \left[i\left(\varepsilon_n - \rho U^2 \sum_{\mathbf{p}} \mathrm{Im}\, G(\varepsilon_n, \mathbf{p}) + k v_k \kappa\right) - \xi_k(\mathbf{p}) - W^2 s(k+1) G_{k+1}(\varepsilon_n, \mathbf{p})\right]^{-1}. \tag{16}$$

Therefore, compared to the impurity-free case, the following substitution (renormalization) actually takes place:

$$\varepsilon_n \longrightarrow \varepsilon_n - \rho U^2 \sum_{\mathbf{p}} \mathrm{Im}\, G(\varepsilon_n, \mathbf{p}) \equiv \varepsilon_n \eta_\epsilon, \tag{17}$$

$$\eta_\epsilon = 1 - \frac{\rho U^2}{\varepsilon_n} \sum_{\mathbf{p}} \mathrm{Im}\, G(\varepsilon_n, \mathbf{p}). \tag{18}$$

If no full self-consistent calculation is performed for the intrinsic-energy part of the impurity scattering, then we have in the simplest approximation

$$\varepsilon_n \longrightarrow \varepsilon_n - \rho U^2 \sum_{\mathbf{p}} \mathrm{Im}\, G_{00}(\varepsilon_n, \mathbf{p}) \equiv \varepsilon_n \eta_\epsilon = \varepsilon_n + \gamma_0 \,\mathrm{sgn}\, \varepsilon_n, \tag{19}$$

$$\eta_\epsilon = 1 + \frac{\gamma_0}{|\varepsilon_n|}, \tag{20}$$

where $\gamma_0 = \pi \rho U^2 N_0(0)$ is the standard Born impurity scattering frequency [9] ($N_0(0)$ is the density of state of the free electrons at the Fermi level).

For the triangular vertices of interest, the recurrence equation that includes the impurity scattering is shown as a graph in Fig. 2b. For the vertex that describes the interaction with the fluctuation of the superconducting order parameter (10) with d-wave symmetry (11), this equation simplifies significantly, because the contribution of the second diagram in the right-hand part of Fig. 2b is virtually equal to zero in view of the condition $\sum_{\mathbf{p}} e(\mathbf{p}) = 0$ (cf. the discussion of a similar situation in [10]). The recurrence equation for the vertex then has the form (13), where the expressions derived from (15) and (16), i.e., the "dressed" (by the impurity scattering) Green functions defined by Fig. 2a, should be used as $G_k(\pm\varepsilon_n, \mathbf{p})$. For the vertex that describes the interaction with the fluctuation of the order parameter with s-wave symmetry, we have the equation

$$\begin{aligned} &\Gamma_{\mathbf{p}k-1}(\varepsilon_n, -\varepsilon_n, \mathbf{q}) \\ &= 1 + \rho U^2 \sum_{\mathbf{p}} G(\varepsilon_n, \mathbf{p}+\mathbf{q}) G(-\varepsilon_n, \mathbf{p}) \Gamma_{\mathbf{p}}(\varepsilon, -\varepsilon_n, \mathbf{q}) \\ &\pm W^2 r(k) G_k(\varepsilon_n, \mathbf{p}+\mathbf{q}) G_k(-\varepsilon_n, \mathbf{p}) \\ &\times \left\{1 + \frac{2ik\kappa v_k}{G_k^{-1}(\varepsilon_n, \mathbf{p}+\mathbf{q}) - G_k^{-1}(-\varepsilon_n, \mathbf{p}) - 2ik\kappa v_k}\right\} \\ &\times \Gamma_{\mathbf{p}k}(\varepsilon_n, -\varepsilon_n, \mathbf{q}), \end{aligned} \tag{21}$$

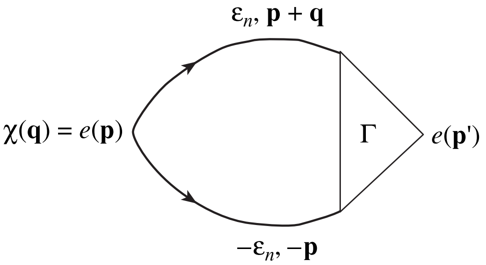

Fig. 3. Diagram for the generalized susceptibility $\chi(\mathbf{q})$ in the Cooper channel.

where expressions (15) and (16) should again be used as $G_k(\pm\varepsilon_n\mathbf{p})$ and the sign of W^2 is determined by the above rules. The difference between this vertex and the vertex of the interaction with *d*-wave symmetry fluctuations lies in the appearance of the second term on the right-hand side of Eq. (21), i.e., in the substitution

$$1 \longrightarrow \eta_\Gamma = 1 + \rho U^2 \sum_{\mathbf{p}} G(\varepsilon_n, \mathbf{p}+\mathbf{q}) \times G(-\varepsilon_n, \mathbf{p})\Gamma_{\mathbf{p}}(\varepsilon, -\varepsilon_n, \mathbf{q}). \tag{22}$$

Therefore, the self-consistent calculation procedure now looks as follows. Starting from the zero approximation $G = G_{00}$ and $\Gamma_{\mathbf{p}} = 1$, we then have in Eqs. (16) and (21)

$$\eta_\varepsilon = \eta_\Gamma = 1 - \frac{\rho U^2}{\varepsilon_n \sum_{\mathbf{p}} \mathrm{Im} G_{00}(\varepsilon_n, \mathbf{p})}.$$

We run the corresponding recurrence procedures (starting from a certain value of *k*) and determine the new values of $G = G_{k=0}$ and $\Gamma_{\mathbf{p}} = \Gamma_{k=0}$. We again calculate η_ε and η_Γ using (18) and (22), use these values in (16) and (21), and so on until convergence is achieved.

When considering the vertex of the *d*-wave symmetry, we should set $\eta_\Gamma = 1$ at all steps of our calculations. In this case, there is actually no particular need to perform full self-consistent impurity scattering calculation, because it leads to relatively small corrections to the results of non-self-consistent calculation using the simplest substitution (19) [7].

4. CALCULATING THE SUPERCONDUCTING TRANSITION TEMPERATURE AND THE GINZBURG–LANDAU COEFFICIENTS

The critical superconducting transition temperature is defined by the normal-phase Cooper instability equation

$$1 - V\chi(0; T) = 0, \tag{23}$$

where the generalized Cooper susceptibility is indicated by the graph in Fig. 3 and is

$$\chi(\mathbf{q}; T) = -T\sum_{\varepsilon_n}\sum_{\mathbf{p}} G(\varepsilon_n, \mathbf{p}+\mathbf{q}) \times G(-\varepsilon_n, -\mathbf{p})e^2(\mathbf{p})\Gamma_{\mathbf{p}}(\varepsilon_n, -\varepsilon_n, \mathbf{q}). \tag{24}$$

The pairing interaction constant *V*, which is nonzero in a layer $2\omega_c$ in width around the Fermi level, determines the seed transition temperature T_{c0} in the absence of pseudogap fluctuations by means of the standard BCS equation:[5]

$$1 = \frac{2VT}{\pi^2}\sum_{n=0}^{\bar{m}}\int_0^{\pi/a} dp_x \int_0^{\pi/a} dp_y \frac{e^2(\mathbf{p})}{\xi_{\mathbf{p}}^2 + \varepsilon_n^2}, \tag{25}$$

where $\bar{m} = [\omega_c/2\pi T_{c0}]$ is the dimensionless cutoff parameter of the Matsubara frequency sum. As in [6], all of our calculations were performed for the typical spectrum (6) of quasi-particles in HTSCs for various relations between *t*, *t*', and μ. By arbitrarily choosing $\omega_c = 0.4t$ and $T_{c0} = 0.01t$, we can easily find a value of the pairing parameter *V* in (25) that yields this value of T_{c0} for different types of pairing. In particular, we obtain $V/ta^2 = 1$ and $V/ta^2 = 0.55$ for *s*-type and $d_{x^2-y^2}$-type pairing, respectively.

The fact that the Cooper susceptibility at $q = 0$ is required to calculate T_c significantly simplifies the calculations [6]. In general, for example, knowledge of $\chi(q; T)$ at arbitrary (small) *q* is required to calculate the Ginzburg–Landau expansion coefficients.

The Ginzburg–Landau expansion for the difference between the free energy densities of the superconducting and normal states can be written in standard form:

$$F_s - F_n = A|\Delta_{\mathbf{q}}|^2 + q^2C|\Delta_{\mathbf{q}}|^2 + \frac{B}{2}|\Delta_{\mathbf{q}}|^4; \tag{26}$$

it is defined by the loop expansion for the free energy in the fluctuation field of the order parameter (10).

It is convenient to normalize the Ginzburg–Landau coefficients *A*, *B*, and *C* to their values in the absence of pseudogap fluctuations by writing them as [6]

$$A = A_0K_A, \quad C = C_0K_C, \quad B = B_0K_B, \tag{27}$$

---

[5] We do not discuss the microscopic nature of this interaction; it can be associated with the exchange by the same antiferromagnetic spin fluctuations, phonons, or a combination of the electron–phonon and spin–fluctuation interactions.

where

$$A_0 = N_0(0)\frac{T-T_c}{T_c}\langle e^2(\mathbf{p})\rangle,$$

$$C_0 = N_0(0)\frac{7\zeta(3)}{32\pi^2T_c^2}\langle|\mathbf{v}(\mathbf{p})|^2e^2(\mathbf{p})\rangle, \qquad (28)$$

$$B_0 = N_0(0)\frac{7\zeta(3)}{8\pi^2T_c^2}\langle e^4(\mathbf{p})\rangle;$$

the angular brackets denote an ordinary averaging over the Fermi surface:

$$\langle\ldots\rangle = \frac{1}{N_0(0)}\sum_p\delta(\xi_{\mathbf{p}})\ldots;$$

and $N_0(0)$ is the state density at the Fermi surface for free electrons.

We then obtain the following general expressions [6]:

$$K_A = \frac{\chi(0;\,T)-\chi(0;\,T_c)}{A_0}, \qquad (29)$$

$$K_C = \lim_{q\to0}\frac{\chi(\mathbf{q};\,T_c)-\chi(0;\,T_c)}{q^2C_0}, \qquad (30)$$

$$K_b = \frac{T_c}{B_0}\sum_{\varepsilon_n}\sum_{\mathbf{p}}e^4(\mathbf{p})G^2(\varepsilon_n,\mathbf{p}) \times G^2(-\varepsilon_n,-\mathbf{p})\Gamma^4_{\mathbf{p}}(\varepsilon_n,-\varepsilon_n,0), \qquad (31)$$

which were used for our direct numerical calculations.

In the presence of impurities, all of the Green functions and the vertices appearing in these expressions should be calculated using Eqs. (16) and (21) written above.

Knowledge of the Ginzburg–Landau expansion coefficients allows all of the basic superconductor characteristics near the transition temperature T_c to be determined. The coherence length is defined as

$$\frac{\xi^2(T)}{\xi^2_{BCS}(T)} = \frac{K_C}{K_A}, \qquad (32)$$

where $\xi_{BCS}(T)$ is the value of this length in the absence of a pseudogap. For the magnetic-field penetration depth, we have

$$\frac{\lambda(T)}{\lambda_{BCS}(T)} = \sqrt{\frac{K_B}{K_AK_C}}, \qquad (33)$$

where this quantity was also normalized to its value of $\lambda_{BCS}(T)$ in the absence of pseudogap fluctuations.

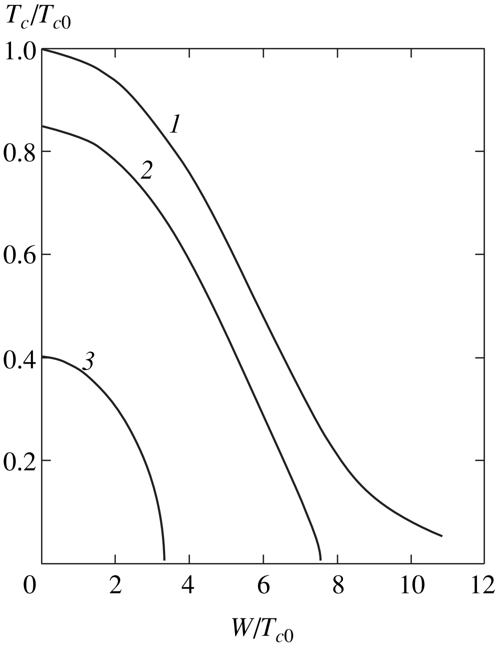

Fig. 4. T_c versus effective pseudogap width W for d-type pairing for three impurity scattering frequencies: γ_0/T_{c0} = 0 (*1*), 0.18 (*2*), and 0.64 (*3*). The inverse correlation length is $\kappa a = 0.2$.

The normalized slope of the upper critical field near T_c,

$$\left|\frac{dH_{c2}}{dT}\right|_{T_c}\bigg/\left|\frac{dH_{c2}}{dT}\right|_{T_{c0}} = \frac{T_c}{T_{c0}}\frac{K_A}{K_C}, \qquad (34)$$

and the relative jump in specific heat at the transition point,

$$\Delta C = \frac{(C_s-C_n)_{T_c}}{(C_s-C_n)_{T_{c0}}} = \frac{T_c}{T_{c0}}\frac{K_A^2}{K_B}, \qquad (35)$$

are determined in a similar way.

5. RESULTS OF CALCULATIONS

The results of calculations for the charge (CDW) and spin (SDW) Ising fluctuations of the short-range order were presented in [6]. Here, we focus on the analysis of the most important and interesting case of Heisenberg spin (SDW) fluctuations and on the discussion of the role of impurity scattering (disorder). Since the case of d-type pairing is of particular importance in the physics of HTSCs based on copper oxides, we pay slightly more attention to this case.

We performed all of the calculations in this section for the typical parameters of the initial electron spectrum $t'/t = -0.4$ and $\mu/t = -1.3$ and took $\kappa a = 0.2$ for the inverse correlation length. To save space, we do not present the results of our calculations for the dimen-

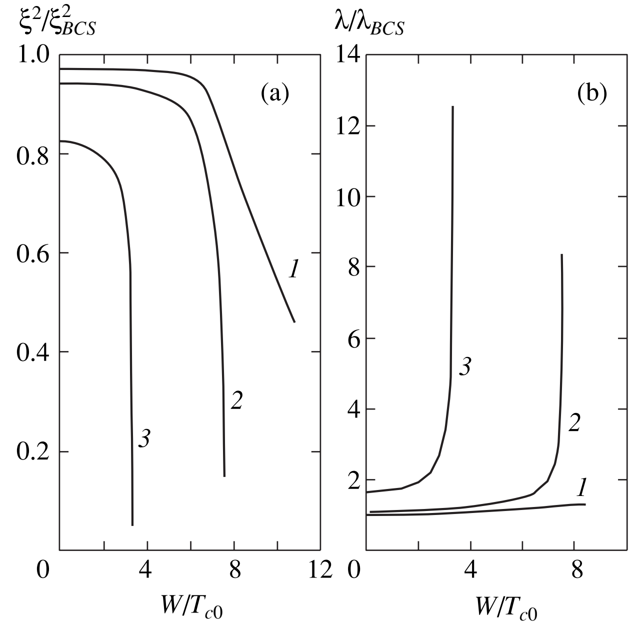

Fig. 5. Square of the coherence length (a) and magnetic-field penetration depth (b) versus effective pseudogap width W for d-type pairing for three impurity scattering frequencies: $\gamma_0/T_{c0} = 0$ (*1*), 0.18 (*2*), and 0.64 (*3*)

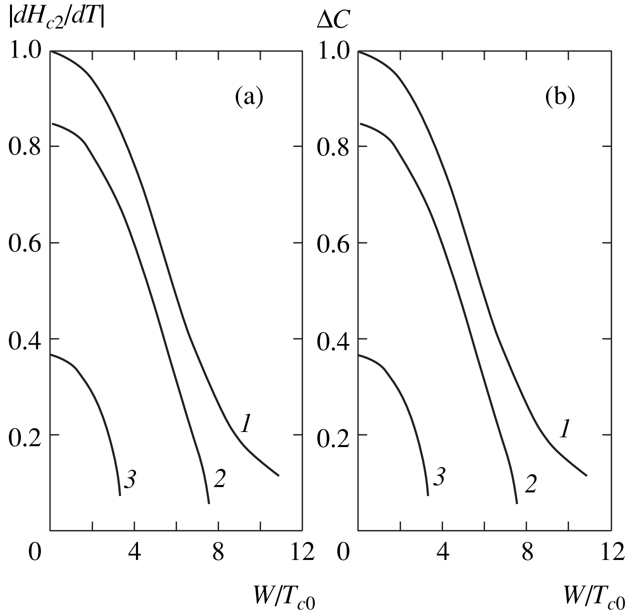

Fig. 6. Slope of the upper critical field and jump in specific heat at the transition point versus effective pseudogap width for d-type pairing for three impurity scattering frequencies: $\gamma_0/T_{c0} = 0$ (*1*), 0.18 (*2*), and 0.64 (*3*).

sionless Ginzburg–Landau expansion coefficients K_A, K_B, and K_C, but immediately show the typical dependences for the basic physical parameters.

When considering the dependences on the pseudogap width and the impurity scattering frequency γ_0, we give all of the characteristics normalized to their values, respectively, at $T = T_{c0}$ and $T = T_{c0}(W)$, i.e., at the seed transition temperature at a given W, but in the absence of impurity scattering ($\gamma_0 = 0$).

5.1. The d-Type Paring

In Fig. 4, the superconducting transition temperature T_c is plotted against the effective pseudogap width W for several impurity scattering frequencies. We see that pseudogap fluctuations lead to noticeable suppression of superconductivity; in the presence of finite disorder, a critical value of W at which T_c becomes zero arises. This suppression of T_c is naturally related to the partial dielectrization of the electron spectrum near hot spots [4, 5].

Similar dependences are shown in Fig. 5 for the coherence length and the magnetic-field penetration depth and in Fig. 6 for the slope of the temperature dependence of the upper critical field and the jump in specific heat at the transition point. The latter superconductor characteristics are rapidly suppressed by pseudogap fluctuations.

The dependence on the correlation length of the short-range order fluctuations is slower: in all cases, the increase in ξ (the decrease in parameter κ) enhances the pseudogap fluctuation effect.

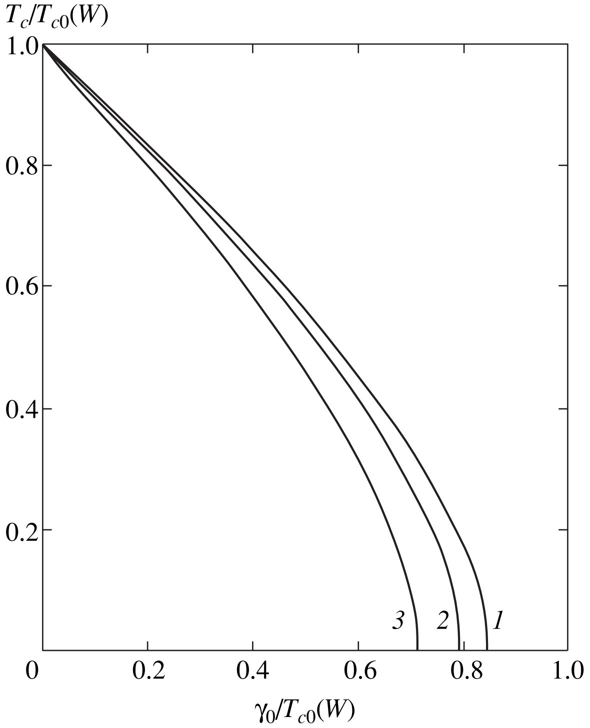

Fig. 7. T_c versus impurity scattering (disorder) frequency for d-type pairing for three effective pseudogap widths: $W/T_{c0} = 0$ (*1*), 2.8 (*2*), and 5.5 (*3*).

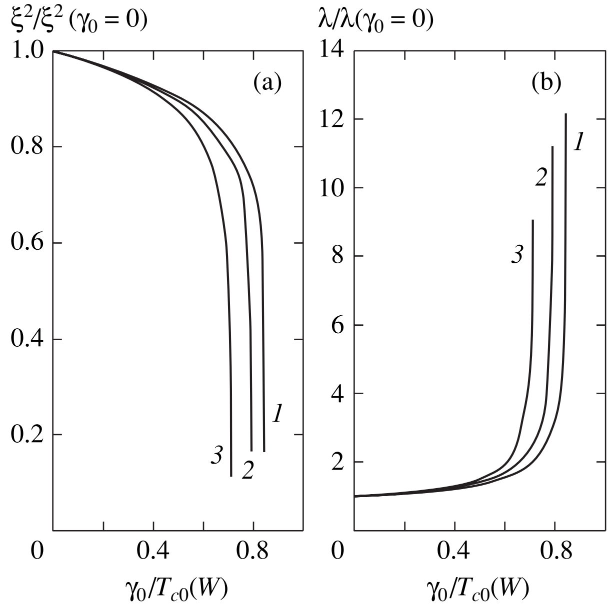

Fig. 8. Square of the coherence length (a) and magnetic-field penetration depth (b) versus impurity scattering frequency γ_0 for *d*-type pairing for three effective pseudogap widths: W/T_{c0} = 0 (*1*), 2.8 (*2*), and 5.5 (*3*).

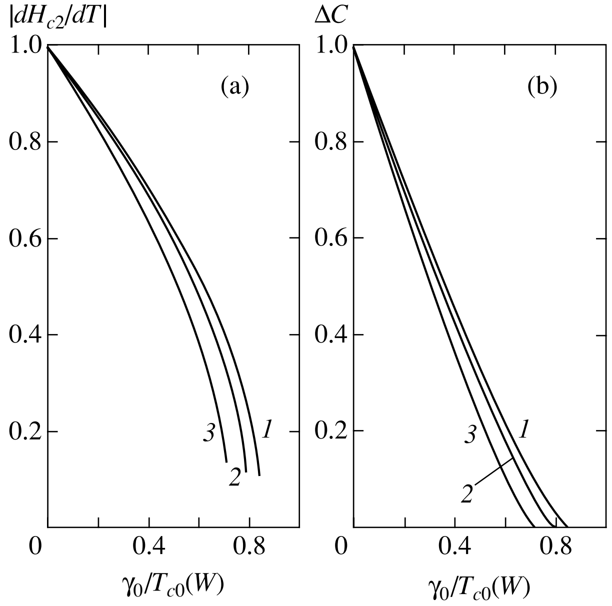

Fig. 9. Slope of the upper critical field and jump in specific heat at the transition point versus impurity scattering frequency γ_0 for *d*-type pairing for three effective pseudogap widths: W/T_{c0} = 0 (*1*), 2.8 (*2*), and 5.5 (*3*).

In Fig. 7, the superconducting transition temperature is plotted against the impurity scattering frequency γ_0 for several effective pseudogap widths. We see that, in the presence of pseudogap fluctuations, the suppression of T_c with growing disorder is appreciably faster that in their absence (W = 0) when the dependence $T_c(\gamma_0)$ for *d*-type paring is described by the standard Abrikosov–Gorkov curve [10, 11]. Similar dependences are shown in Fig. 8 for the coherence length and the penetration depth and in Fig. 9 for the slope of the $H_{c2}(T)$ curve and the jump in specific heat. We again see that impurity scattering (disorder) causes the last two parameters to rapidly decrease; i.e., it enhances the pseudogap fluctuation effect.

The derived dependences on the pseudogap parameters are qualitatively similar to those obtained in [6] for the case of charge (CDW) pseudogap fluctuations where, as in the case considered here, an alternating recurrence procedure arises for the vertex part. At the same time, certain quantitative differences associated with different diagram combinatorics also arise. The dependences on the impurity scattering (disorder) frequency have not been studied previously in this model.[6]

The dependences found are in qualitative agreement with most of the data from the experiments aimed at studying the superconductivity in the domain of existence of the pseudogap (the underdoped region in the cuprate phase diagram). Below, we show that the results obtained can be used to directly model the typical phase diagram for HTSC cuprates.

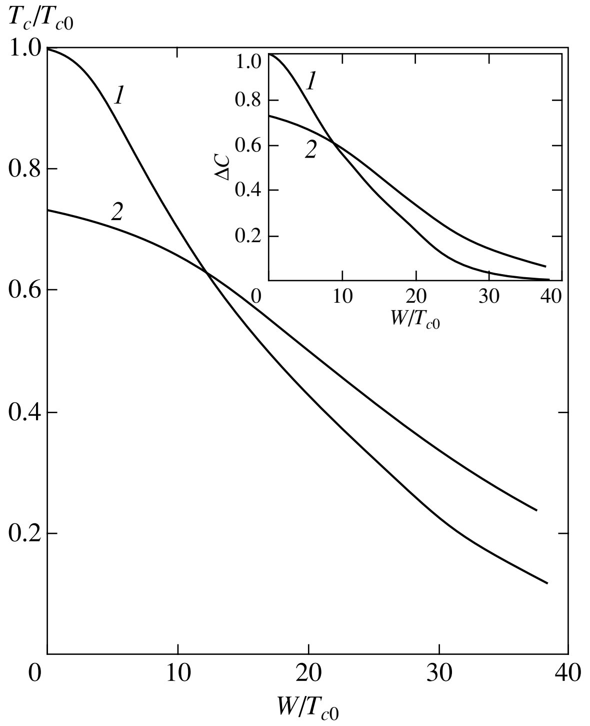

Fig. 10. T_c versus effective pseudogap width W for *s*-type pairing for two impurity scattering frequencies: γ_0/T_{c0} = 0 (*1*) and 20 (*2*). The inverse correlation length is κa = 0.2. The insert shows the characteristic behavior of the jump in specific heat for similar parameters.

---

[6] The corresponding dependences of T_c were considered in [7] for the constant-sign recurrence procedure that arises in the case of Ising SDW fluctuations where the suppression of superconductivity is much slower.

5.2. The s-Type Pairing

The *s*-type pairing is mainly of interest in revealing the characteristic differences from the *d*-type pairing. There are virtually no experimental data on the *s*-type conductivity in systems with a pseudogap, although it may well be that the corresponding systems will be discovered in the future.

Our calculations indicate that pseudogap fluctuations suppress appreciably the superconducting transition temperature in this case as well (Fig. 10), although the scale length of these fluctuations required for significant suppression of superconductivity is much larger than that for the *d*-type pairing. This result has already been obtained in [6]. Note, however, that in the case of Heisenberg SDW fluctuations under consideration, there is no characteristic "shelf" on the $T_c(W)$ curve that is present in the case of scattering by CDW pseudogap fluctuations [6]. The jump in specific heat at the superconducting transition point is also significantly suppressed on the same scale of *W*, as shown in the insert to Fig. 10. The corresponding dependences for the coherence length and the penetration depth are similar to those obtained previously in [6] and are not given here. Figure 11 shows the calculated dependence of T_c on the impurity scattering (disorder) frequency. Apart from the relatively weak suppression of T_c by disorder related [7] to the state density smearing at the Fermi level, a weak effect of increase in T_c with γ_0 that is probably related to the smearing of the pseudogap in the state density by impurity scattering can also be observed.

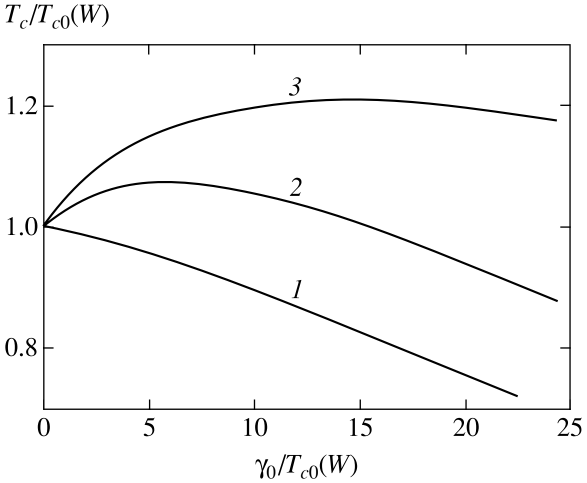

Fig. 11. Superconducting transition temperature T_c versus impurity scattering (disorder) frequency γ_0 for *s*-type pairing for three pseudogap widths: W/T_{c0} = 0 (*1*), 8 (*2*), and 15 (*3*).

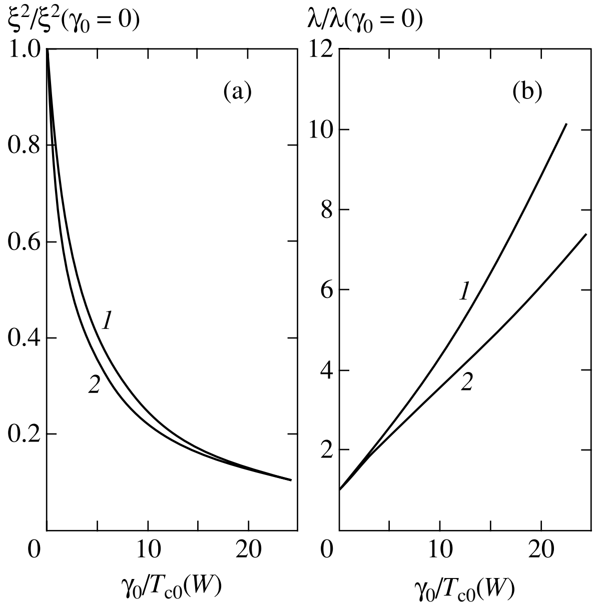

Fig. 12. Square of the coherence length (a) and magnetic-field penetration depth (b) versus impurity scattering (disorder) frequency γ_0 for *s*-type pairing for two effective pseudogap widths: W/T_{c0} = 0 (*1*) and 15 (*2*).

Figure 12 shows how impurity scattering (disorder) affects the coherence length and the magnetic-field penetration depth in the case of *s*-type pairing.

Finally, Fig. 13 shows how impurity scattering (disorder) affects the slope of the upper critical field and the jump in specific heat. The jump in specific heat is significantly suppressed by disorder, and the behavior of the slope of $H_{c2}(T)$ qualitatively differs from that in the case of *d*-type pairing: the growth of disorder causes this parameter to increase appreciably, as in the standard theory of "dirty" superconductors [20], while pseudogap fluctuations increase the slope of $H_{c2}(T)$. In the absence of pseudogap fluctuations, similar differences in the behavior of the slope of the $H_{c2}(T)$ curve for disorder have been pointed out [10].

6. MODELING THE PHASE DIAGRAM

The described model of the influence of pseudogap fluctuations on superconductivity allows the typical phase diagram for HTSC cuprates to be modeled.[7] Modeling of this kind, based on an extremely simplified version of our model, was originally attempted in [13]. The main idea is to identify the parameter *W* with the experimentally observed effective pseudogap width (the temperature of the crossover to the pseudogap region of the phase diagram), $E_g \approx T^*$, determined from many experiments [1–3]. This parameter is known to decrease almost linearly with increasing dopant (current carriers) concentration from values of ~10^3 K, becoming zero at a certain critical concentration $x_c \approx$

---

[7] We ignore the existence of a narrow region of antiferromagnetic ordering in the state of a Mott insulator that exists in the range of low dopant concentrations by restricting our analysis to the wide domain of existence of a "bad" metal.

0.19–0.22 that slightly exceeds the “optimal value” $x_{\text{opt}} \approx 0.15$–0.17 [1, 14]. Accordingly, we may take[8] a similar concentration dependence of our pseudogap width parameter $W(x)$. In this sense, the dependence $W(x)$ may be considered to be determined directly from experiments. The only parameter to be determined is then the concentration dependence of the seed superconducting transition temperature $T_{c0}(x)$ that would exist in the absence of pseudogap fluctuations. Its knowledge will allow the concentration behavior of the actual transition temperature $T_c(x)$ to be determined by solving the equations of our model. Unfortunately, as was pointed out in [6], the dependence $T_{c0}(x)$ is generally unknown and cannot be determined from experiments, remaining a fitting parameter of the theory.

Assuming, as was done in [13], that $T_{c0}(x)$ can be described by a linear function of x that becomes zero at $x = 0.3$ and choosing $T_{c0}(x = 0)$ to obtain the desired $T_c(x = x_{\text{opt}})$, we can calculate the form of the “observed” dependence $T_c(x)$. As an example, the results of such calculations for d-type pairing and the scattering by charge (CDW) pseudogap fluctuations [6] using a typical dependence $W(x)$ are shown in Fig. 14. We see that, even under such arbitrary assumptions, the hot spot model yields a dependence $T_c(x)$ close to the experimentally observed one. Similar calculations for the Ising model of the interaction with spin fluctuations (a constant-sign procedure for the vertex part [6]) indicate that reasonable values of $T_c(x)$ can be obtained only at nonrealistic values of $W(x)$ that are about an order of magnitude larger than the observed values.

In the BCS model for the seed temperature T_{c0} under consideration, the assumption of a noticeable concentration dependence of this parameter seems rather unrealistic.[9] Therefore, we assume that T_{c0} does not depend on the carrier concentration x at all, but take into account the fact that doping inevitably gives rise to impurity scattering (internal disorder), which can be described by the corresponding linear function $\gamma(x)$. Let us assume that this growth of disorder leads to total suppression of the d-type pairing at $x = 0.3$ in accordance with the standard Abrikosov–Gorkov dependence [11]. The phase diagram for a $La_{2-x}Sr_xCuO_4$ system calculated in our model for Heisenberg pseudogap fluctuations by taking into account the described role of impurity scattering is shown in Fig. 15. The parameters of the problem for this system used in our calculations are given in Fig. 15. The “experimental” values of $T_c(x)$ indicated in this figure (as well as in Fig. 14) by

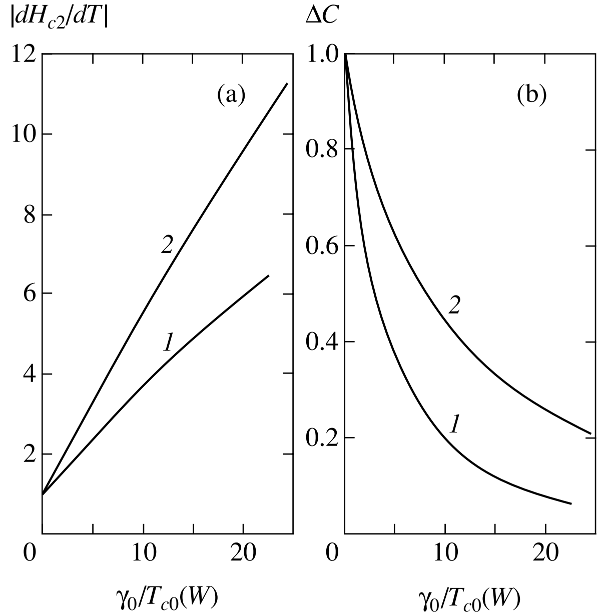

Fig. 13. Slope of the upper critical field and jump in specific heat at the transition point versus impurity scattering (disorder) frequency γ_0 for s-type pairing for two effective pseudogap widths: $W/T_{c0} = 0$ (*1*) and 15 (*2*).

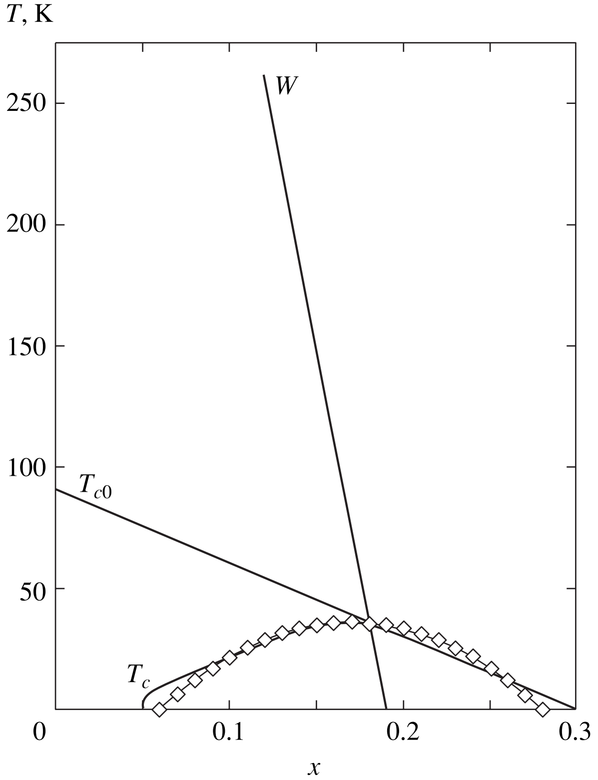

Fig. 14. Model phase diagram for the scattering by charge (CDW) pseudogap fluctuations (d-type pairing) and the seed superconducting transition temperature T_{c0} that is a linear function of the carrier concentration. The diamonds represent the “experimental” data; $W(x = 0) = 708$ K; $T_{c0}(x = 0) = 90$ K; $\kappa a = 0.2$; $T_c(x = 0.17) = 36$ K.

---

[8] Naturally, this identification can be made to the unknown proportionality factor of the order of unity.

[9] In this approach, the dependence $T_{c0}(x)$ may be attributable only to the corresponding relatively weak dependence of the state density at the Fermi level.

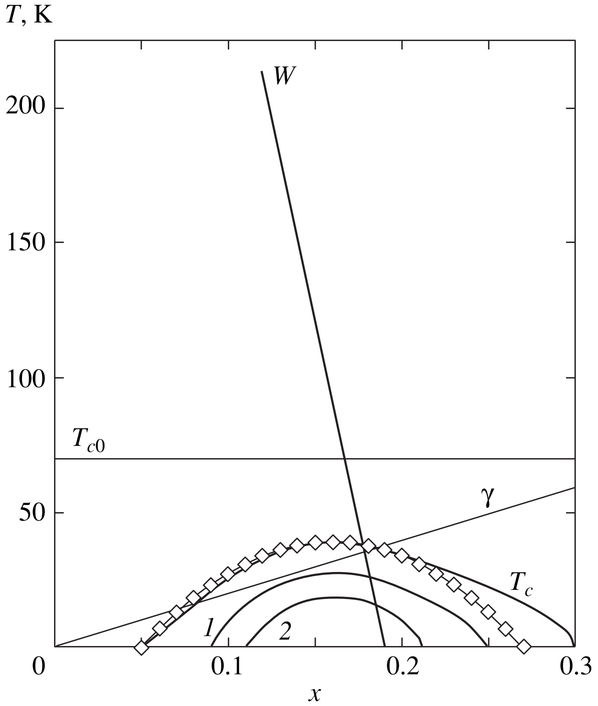

Fig. 15. Model phase diagram for the scattering by Heisenberg (SDW) pseudogap fluctuations (d-type pairing) and the seed superconducting transition temperature T_{c0} that does not depend on the carrier concentration with the inclusion of internal disorder $\gamma(x)$ that is linear in dopant concentration. The diamonds represent the "experimental" data; $\gamma_0 = 0.15T_{c0}$ (curve *1*), $\gamma_0 = 0.25T_{c0}$ (curve *2*); $W_m(x = 0) = 580$ K; $T_{c0} = 70$ K; $t'/t = -0.25$; $\mu/t = -0.8$; $\kappa a = 0.2$; $T_{\max}(x = 0.16) = 39$ K.

diamonds were obtained by using the empirical formula [14, 15]

$$\frac{T_c(x)}{T_c(x = x_{\rm opt})} = 1 - 82.6(x - x_{\rm opt})^2. \qquad (36)$$

This formula satisfactorily describes the concentration behavior of T_c for a number of HTSC cuprates. We see that our model gives an almost ideal description of the "experimental" data at reasonable values of $W(x)$ in the entire underdoped region. The description becomes poorer at the end of the overdoped region. It should be borne in mind, however, that formula (36) does not yield satisfactory results either; in addition, our superconductivity suppression model in the overdoped region is clearly very crude, and no special parameter fitting that would improve the agreement with the data in this region has been performed.

It is interesting to consider the behavior of the superconducting transition temperature T_c for additional disordering of the system for various compositions (carrier concentrations). There are many experimental works in which such disordering was achieved by doping [16, 17] or by fast neutron [18] and electron [19, 20] irradiation. The role of the additional disorder was discussed in the context of the existence of a pseudogap state only in [17].

In our model, this disordering can be simulated by introducing the additional impurity scattering parameter γ_0 that is added to the internal disorder parameter $\gamma(x)$. The calculated superconducting transition temperature for two values of this parameter is also shown in Fig. 15. We see that, in close agreement with the experiment [17], doping (disorder) causes the domain of existence of superconductivity to narrow rapidly. Also in close agreement with the conclusion drawn above from Fig. 7 and with the experimental data [17, 18], the suppression of superconductivity by disorder in the underdoped region (the pseudogap region) is much faster than that for the optimal composition. It might be expected that "normal" disorder, which clearly causes the pseudogap in the state density to slightly decrease, could lead to a certain "delay" of the decrease in T_c, but this effect is absent for d-type pairing.

However, the problem is that, in all cases, the decrease in T_c is faster than that implied by the standard Abrikosov–Gorkov curve for d-type pairing [11]. At the same time, attempts to properly process most of the experimental data on disordering in HTSC cuprates [16, 19, 20] lead to the conclusion that this decrease is actually much slower than that predicted by the Abrikosov–Gorkov dependence. This as yet unsolved problem is among the main problems in the theory of high-temperature superconductors [12]. One way to solve this problem may be associated with a consistent description of the role of disorder in superconductors located in the transition region from "loose" pairs of the BCS theory to "compact" pairs that emerge in the limit of strong coupling [21]. Another interesting possibility of explaining this delay of the decrease in T_c is related to the anisotropy of elastic impurity scattering considered in detail in [10, 22]. This effect can be included relatively easily in our calculations. It seems particularly interesting in connection with the established strong anisotropy of elastic scattering (with d-type symmetry) observed in ARPES experiments on a $Bi_2Sr_2CaCuO_{8+\delta}$ system [23, 24]. The corresponding scattering frequency varies over the range 20–60 meV [24], which is almost an order of magnitude higher than the maximum value of $\gamma(x)$ used in our calculations and points once again to the unusual stability of the d-type pairing in cuprates against static disorder. It should be noted that our model for the intrinsic-energy part of the electron actually describes a similar anisotropy of elastic scattering that corresponds to its increase near hot spots. However, no delay of the decrease in T_c was observed in our calculations.

The results show that, despite the obvious crudeness of our assumptions, the hot spot model gives a reasonable (occasionally even semiquantitative) description of the domain of existence of superconductivity on the phase diagram for HTSC cuprates.[10] The significant uncertainty in the formation scenario for the concentration dependence of the seed superconducting transition temperature remains a major shortcoming in the approach.

7. CONCLUSIONS

Our analysis shows that the pseudogap state model based on the concept of hot spots can provide a fairly consistent description of the basic properties of the superconducting phase for HTSC cuprates and their phase diagram with a relatively small number of fitting parameters most of which can be determined from independent experiments.

It should be emphasized that our analysis was performed entirely under the standard assumption [12] about the self-averaging of the superconducting order (gap) parameter in the field of random impurities and pseudogap fluctuations. This assumption is generally justified for superconductors whose coherence length (the Cooper pair size) is much larger than other microscopic lengths in the system, such as the mean free path or the correlation length ξ of the pseudogap fluctuations. In the class of pseudogap state models under consideration, this is not necessarily the case, and significant non-self-averaging effects [25, 26] that lead to the qualitative picture of an inhomogeneous superconducting state with superconducting-phase drops existing at temperatures $T > T_c$ can arise. In principle, there are direct experimental data that confirm this picture of inhomogeneous superconductivity in HTSC cuprates [27–29]. Of course, we are far from asserting that these real experiments confirm the picture that has been theoretically developed by using simplified models in [25, 26]. Nevertheless, these results emphasize the importance of a consistent analysis of the non-self-averaging effects in relatively realistic pseudogap state models, such as the hot spot model considered above.[11]

ACKNOWLEDGMENTS

This work was supported in part by the Russian Foundation for Basic Research (project no. 02-02-16031), the Basic Research Programs of the Presidium of the Russian Academy of Sciences “Quantum Macrophysics” and the Department of Physical Sciences of the Russian Academy of Sciences “Strongly Correlated Electrons in Semiconductors, Metals, Superconductors, and Magnetic Materials,” and the Project of the Ministry of Education and Science of Russia “Studies of Collective and Quantum Effects in Condensed Media.”

APPENDIX

DIAGRAM COMBINATORICS IN THE MODEL OF HEISENBERG PSEUDOGAP FLUCTUATIONS

To analyze the diagram combinatorics, let us consider the limit of an infinite correlation length of spin fluctuations. In this case, the spin density by which an electron is scattered can be expressed as

$$\mathbf{S}_{\mathbf{q}} = \mathbf{S}\delta(\mathbf{q}-\mathbf{Q}), \tag{A.1}$$

and averaging over Gaussian spin fluctuations reduces to ordinary integration [4]:

$$\langle\ldots\rangle = \frac{g^3}{(2\pi)^{3/2}W^3}\int d\mathbf{S}\exp\left(-\frac{g^2\mathbf{S}^2}{2W^2}\right)\ldots. \tag{A.2}$$

Consequently, in this limit, we can first solve the problem of an electron in the coherent field of the spin density (A.1) and then perform averaging (A.2) over its fluctuations. For the subsequent analysis, it is convenient to introduce the fluctuating field $\boldsymbol{\delta} = (g/\sqrt{3})\mathbf{S}$, the potential by which an electron is scattered. Averaging (A.2) over the spin fluctuations then reduces to averaging over the fluctuations of this field:

$$\begin{aligned}\langle\ldots\rangle = {} & \sqrt{\frac{3}{2\pi W^2}}\int_{-\infty}^{\infty} d\delta_l \exp\left(-\frac{3\delta_l^2}{2W^2}\right)\frac{3}{2\pi W^2} \\ & \times\int_0^{2\pi} d\varphi\int_0^{\infty} d|\boldsymbol{\delta}_t||\boldsymbol{\delta}_t|\exp\left(-\frac{3|\boldsymbol{\delta}_t|^2}{2W^2}\right)\ldots.\end{aligned} \tag{A.3}$$

Thus, there are two fluctuating fields by which free carriers are scattered: the real longitudinal field $\delta_l = (g/\sqrt{3})S_z$ and the complex transverse field $\boldsymbol{\delta}_t$ with amplitude $|\boldsymbol{\delta}_t|$ and phase φ that is associated with the two transverse components of the vector $\mathbf{S}$.

This averaging gives rise to a diagram technique with two types of effective interactions [4]: one is represented by the dashed line,

$$V_{\mathrm{eff}1} = \frac{g^2}{3}\langle S_{z\mathbf{q}}S_{z-\mathbf{q}}\rangle = \pm\frac{W^2}{3}\delta(\mathbf{q}-\mathbf{Q}), \tag{A.4}$$

where the minus refers to the case of a change in spin projection under this line (e.g., when the dashed line encloses an odd number of spin flip operators S_+ and S_-); the other is represented by the wavy line,

$$V_{\mathrm{eff}2} = \frac{g^2}{3}\langle S_{+\mathbf{q}}S_{--\mathbf{q}}\rangle = 2\frac{W^2}{3}\delta(\mathbf{q}-\mathbf{Q}). \tag{A.5}$$

The means $\langle S_+S_+\rangle$ and $\langle S_-S_-\rangle$ are equal to zero due to the phase averaging in (A.3).

---

[10] Above, we always implied hole-doped systems for which the dependence $T^*(x)$ is well established [1, 14]. The pseudogap state data for electron-doped systems are rather fragmentary.

[11] In principle, several experiments that are usually interpreted in favor of the superconducting nature of the pseudogap in HTSCs can also be understood in terms of the pattern of existence of superconducting drops.

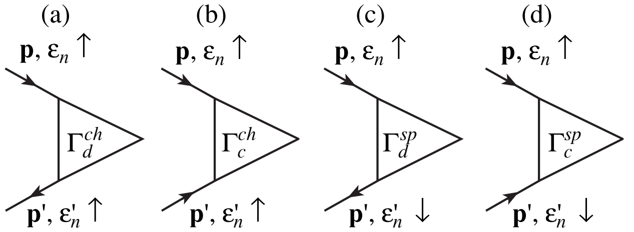

Fig. 16. Two-particles vertices with different diagram combinatorics.

Let us now solve the problem of an electron in the coherent field of the spin density (A.1). In this case, the matrix single-particle Green function has four independent components[12] that can be determined from the system of equations

$$\begin{aligned} G_{1\uparrow;\,1\uparrow} &= G_1 + G_1\delta_l G_{2\uparrow;\,1\uparrow} + G_1\delta_t G_{2\downarrow;\,1\uparrow}, \\ G_{2\uparrow;\,1\uparrow} &= G_2\delta_l G_{1\uparrow;\,1\uparrow} + G_2\delta_t G_{1\downarrow;\,1\uparrow}, \\ G_{2\downarrow;\,1\uparrow} &= -G_2\delta_l G_{1\downarrow;\,1\uparrow} + G_2\delta_t^* G_{1\uparrow;\,1\uparrow}, \\ G_{1\downarrow;\,1\uparrow} &= -G_1\delta_l G_{2\downarrow;\,1\uparrow} + G_1\delta_t^* G_{2\uparrow;\,1\uparrow}, \end{aligned} \qquad (A.6)$$

where we use the short designations (ε_n, $\mathbf{p}$) $\longrightarrow$ 1, (ε_n, $\mathbf{p} + \mathbf{Q}$) $\longrightarrow$ 2 and

$$G_1 = \frac{1}{i\varepsilon_n - \xi_{\mathbf{p}}}, \quad G_2 = \frac{1}{i\varepsilon_n - \xi_{\mathbf{p}+\mathbf{Q}}}.$$

It thus follows that

$$\begin{aligned} G_{1\uparrow;\,1\uparrow} &= \frac{G_2^{-1}}{G_1^{-1}G_2^{-1} - |\boldsymbol{\delta}|^2}, \\ G_{2\uparrow;\,1\uparrow} &= \frac{\delta_l}{G_1^{-1}G_2^{-1} - |\boldsymbol{\delta}|^2}, \\ G_{1\downarrow;\,1\uparrow} &= 0, \quad G_{2\downarrow;\,1\uparrow} = \frac{\delta_t^*}{G_1^{-1}G_2^{-1} - |\boldsymbol{\delta}|^2}, \end{aligned} \qquad (A.7)$$

where $|\boldsymbol{\delta}| = \sqrt{\delta_l^2 + |\boldsymbol{\delta}_t|^2}$ is the amplitude of the field $\boldsymbol{\delta}$.

In this case, the fluctuation-averaged single-particle Green function is

$$G = \langle G_{1\uparrow;\,1\uparrow}\rangle = \sqrt{\frac{2}{\pi}}\left(\frac{3}{W^2}\right)^{3/2} \times \int_0^\infty d|\boldsymbol{\delta}||\boldsymbol{\delta}|^2 \exp\left(-\frac{3|\boldsymbol{\delta}|^2}{2W^2}\right)\frac{G_2^{-1}}{G_1^{-1}G_2^{-1} - |\boldsymbol{\delta}|^2}. \qquad (A.8)$$

This integral representation can be easily written [4] as the continued fraction (1), (2) with κ = 0 and the combinatorial coefficients $s(k)$ defined by Eq. (9).

The combinatorial coefficients $r(k)$ for the two-particle vertices are slightly more difficult to determine. Four types of vertices (see Fig. 16) may be considered. For all four types of vertices, the recurrence procedure has the form (13), but the signs in the procedure and the combinatorial coefficients $r(k)$ can be different. Let us consider all vertices in the coherent field δ.

(1) The charge vertex (the spin projection is conserved at the vertex) in the diffusion channel (particle–hole), Fig. 16a:

$$\Gamma_d^{ch} = \sum_{i,\sigma} G_{1\uparrow;\,i\sigma}G_{i'\sigma;\,1'\uparrow} = \frac{(G_2G_{2'})^{-1} + |\boldsymbol{\delta}|^2}{d_\delta}, \qquad (A.9)$$

where i and σ take on values of 1, 2 and ↑, ↓, and the designations (ε_n', $\mathbf{p}'$) $\longrightarrow$ 1'), (ε_n', $\mathbf{p}' + \mathbf{Q}$) $\longrightarrow$ 2'), and $d_\delta = [(G_1G_2)^{-1} - |\boldsymbol{\delta}|^2][(G_{1'}G_{2'})^{-1} - |\boldsymbol{\delta}|^2]$ are used.

(2) The charge vertex in the Cooper channel (particle–particle),[13] Fig. 16b:

$$\Gamma_c^{ch} = \sum_{i,\sigma} G_{1\uparrow;\,i\sigma}G_{1'\uparrow;\,i'\sigma} = \frac{(G_2G_{2'})^{-1} + \delta_l^2}{d_\delta}. \qquad (A.10)$$

(3) The spin vertex (the spin projection changes sign at the vertex) in the diffusion channel (particle–hole), Fig. 16c:

$$\Gamma_d^{sp} = \sum_{i,\sigma} G_{1\uparrow;\,i\sigma}G_{i'-\sigma;\,1'\downarrow} = \frac{(G_2G_{2'})^{-1} - \delta_l^2}{d_\delta}. \qquad (A.11)$$

(4) The spin vertex in the Cooper channel (particle–particle), Fig. 16d:

$$\begin{aligned} \Gamma_c^{sp} &= \sum_{i,\sigma} G_{1\uparrow;\,i\sigma}G_{1'\downarrow;\,i'-\sigma} \\ &= \frac{(G_2G_{2'})^{-1} + (|\boldsymbol{\delta}_t|^2 - \delta_l^2)}{d_\delta}. \end{aligned} \qquad (A.12)$$

The physical vertices can be obtained from these vertices with the coherent field δ by averaging (A.3) over the fluctuations of the corresponding field.

Thus, we see that the vertex Γ_d^{ch} is defined by Eq. (A.9), while all of the other vertices have the form[14]

$$\Gamma = \frac{(G_2G_{2'})^{-1} \pm |\boldsymbol{\delta}|^2/3}{d_\delta}, \qquad (A.13)$$

---

[12] The components that differ from these by the change of sign of all spin projections can be obtained by the substitution $\delta_l \longrightarrow -\delta_l$ and $\delta_t \longleftrightarrow \delta_t^*$.

[13] It emerges when the triplet pairing is described.

[14] This form is equivalent to (A.10)–(A.12) when averaged.

where the plus corresponds to the vertices Γ_c^{ch} and Γ_c^{sp}, and the minus corresponds to the vertex Γ_d^{sp}.

Obviously, $r(k) = s(k)$ for the vertex Γ_d^{ch}. Indeed, the expansion for the physical vertex $\langle \Gamma_d^{ch} \rangle$ can be obtained by inserting the corresponding free vertex in all the electron lines of an arbitrary diagram for the single-particle Green function. Inserting this vertex changes neither the direction of the electron line nor the spin projection; accordingly, the diagram combinatorics does not change either.

In the limit of an infinite correlation length, any skeleton diagram for the vertex differs from the ladder diagram of the same order with the interaction $(W^2/3)\delta(\mathbf{q} - \mathbf{Q})$ only by the sign and the factor 2^p, where p is the number of wavy lines. Thus, the sum of all skeleton diagrams of a given order may be replaced with the corresponding ladder diagram with the interaction $(W^2/3)\delta(\mathbf{q} - \mathbf{Q})$ multiplied by the combinatorial factor, which we call the number of skeleton diagrams of a given order.

The first term in Eqs. (A.9)–(A.12) is the same for all vertices and generates the numbers of skeleton diagrams of even (in W^2) order when averaged (since this term corresponds to the terms with $i = 1$ in these equations). Thus, the numbers of skeleton diagrams of even order are the same for all four vertices. The second term in these equations generates the numbers of diagrams of odd order (it corresponds to the terms with $i = 2$). Consequently, the numbers of skeleton diagrams of odd order for all three vertices defined by (A.13) are ±1/3 of the corresponding numbers of for the vertex Γ_d^{ch}. The minus corresponding to the vertex Γ_d^{sp} can be offset by changing the sign in the recurrence procedure for this vertex. Consequently, the sign of the second term in (A.13) determines the sign in the recurrence procedure (13) for these vertices, and the combinatorial coefficients $r(k)$ are the same for these three vertices.

The number of skeleton diagrams of order L is[15]

$$3^L \prod_{1 \le k \le L} r(k). \tag{A.14}$$

Thus, we obtain

$$\prod_{1 \le k \le 2n} r(k) = \prod_{1 \le k \le 2n} s(k) \tag{A.15}$$

for even $L = 2n + 1$ and

$$\prod_{1 \le k \le 2n+1} r(k) = \frac{1}{3} \prod_{1 \le k \le 2n+1} s(k) \tag{A.16}$$

for odd $L = 2n + 1$; whence, given (9), follows (14).

In this paper, we were mainly interested in the vertex Γ_c^{sp}. The above analysis shows that a constant-sign procedure emerges for this vertex for the case of s-type paring where the symmetry factor $e(\mathbf{p})$, which must appear in the vertex, is equal to unity. In contrast, in the case of d-type paring where the superconducting gap when switching over to $\mathbf{Q}$ changes sign (i.e., $e(\mathbf{p}) = -e(\mathbf{p} + \mathbf{Q})$), the sign of the recurrence procedure must be reversed [6], and the procedure becomes an alternating one. For the Ising spin fluctuations considered in [6], the situation with the sign of the recurrence procedure for the vertex is reverse. This somewhat surprising result can be easily understood from Eq. (A.12) for the vertex Γ_c^{sp}. The two transverse components (i.e., the field δ_t) vanish in the Ising model, causing the sign of the second term in (A.12) and, hence, in the recurrence procedure to change.

REFERENCES

1. J. L. Tallon and J. W. Loram, Physica C (Amsterdam) **349**, 53 (2000).
2. M. V. Sadovskiĭ, Usp. Fiz. Nauk **171**, 539 (2001) [Phys. Usp. **44**, 515 (2001)].
3. D. Pines, cond-mat/0404151.
4. J. Schmalian, D. Pines, and B. Stojkovic, Phys. Rev. B **60**, 667 (1999).
5. É. Z. Kuchinskiĭ and M. V. Sadovskiĭ, Zh. Éksp. Teor. Fiz. **115**, 1765 (1999) [JETP **88**, 968 (1999)].
6. É. Z. Kuchinskiĭ, M. V. Sadovskiĭ, and N. A. Strigina, Zh. Éksp. Teor. Fiz. **125**, 854 (2004) [JETP **98**, 748 (2004)].
7. N. A. Kuleeva and É. Z. Kuchinskiĭ, Fiz. Tverd. Tela (St. Petersburg) **46**, 1557 (2004) [Phys. Solid State **46**, 1604 (2004)].
8. M. V. Sadovskiĭ and N. A. Strigina, Zh. Éksp. Teor. Fiz. **122**, 610 (2002) [JETP **95**, 526 (2002)].
9. A. A. Abrikosov, L. P. Gor'kov, and I. E. Dzyaloshinskiĭ, *Methods of Quantum Field Theory in Statistical Physics* (Fizmatgiz, Moscow, 1962; Prentice Hall, Englewood Cliffs, N.J., 1963).
10. A. I. Posazhennikova and M. V. Sadovskiĭ, Pis'ma Zh. Éksp. Teor. Fiz. **63**, 347 (1996) [JETP Lett. **63**, 358 (1996)]; Zh. Éksp. Teor. Fiz. **112**, 2124 (1997) [JETP **85**, 1162 (1997)].
11. R. J. Radtke, K. Levin, H.-B. Schüttler, and M. R. Norman, Phys. Rev. B **48**, 653 (1993).
12. M. V. Sadovskii, *Superconductivity and Localization* (World Sci., Singapore, 2000).
13. A. Posazhennikova and P. Coleman, Phys. Rev. B **67**, 165109 (2003).

---

[15] The factor 3^L emerges, because the recurrence procedure (13) and the combinatorial coefficients $r(k)$ correspond to the expansion in a power series of W^2, while the number of skeleton diagrams was determined for the expansion in a power series of $W^2/3$.

14. S. H. Naqib, J. R. Cooper, J. L. Tallon, *et al.*, cond-mat/0312443.
15. M. R. Presland, J. L. Tallon, R. G. Buckley, *et al.*, Physica C (Amsterdam) **176**, 95 (1991).
16. Y. Fukuzumi, K. Mizuhashi, K. Takenaka, and S. Uchida, Phys. Rev. Lett. **76**, 684 (1996).
17. J. L. Tallon, C. Bernhard, G. V. M. Williams, and J. W. Loram, Phys. Rev. Lett. **79**, 5294 (1997).
18. A. E. Kar'kin, S. A. Davydov, B. N. Goshchitskiĭ, *et al.*, Fiz. Met. Metalloved. **76**, 103 (1993).
19. S. K. Tolpygo, J.-Y. Lin, M. Gurvitch, *et al.*, Phys. Rev. B **53**, 12454 (1996); **53**, 12462 (1996).
20. F. Rullier-Albenque, H. Alloul, and R. Tourbot, Phys. Rev. Lett. **91**, 047001 (2003).
21. A. I. Posazhennikova and M. V. Sadovskiĭ, Pis'ma Zh. Éksp. Teor. Fiz. **65**, 258 (1997) [JETP Lett. **65**, 270 (1997)].
22. G. Haran and A. D. S. Nagy, Phys. Rev. B **54**, 15463 (1996).
23. T. Valla, A. V. Fedorov, P. D. Johnson, *et al.*, Phys. Rev. Lett. **85**, 828 (2000).
24. A. Kaminski, H. M. Fretwell, M. R. Norman, *et al.*, cond-mat/0404385.
25. É. Z. Kuchinskiĭ and M. V. Sadovskiĭ, Zh. Éksp. Teor. Fiz. **117**, 613 (2000) [JETP **90**, 535 (2000)].
26. É. Z. Kuchinskiĭ and M. V. Sadovskiĭ, Zh. Éksp. Teor. Fiz. **121**, 758 (2002) [JETP **94**, 654 (2002)].
27. S. H. Pan, J. P. O'Neil, R. L. Badzey, *et al.*, Nature **413**, 282 (2001).
28. K. McElroy, D.-H. Lee, J. E. Hoffman, *et al.*, cond-mat/0404005.
29. A. Fang, C. Howald, N. Kanenko, *et al.*, cond-mat/0404452.

Translated by V. Astakhov

Journal of Experimental and Theoretical Physics, Vol. 99, No. 6, 2004, pp. 1279–1290.
Translated from Zhurnal Éksperimental'noĭ i Teoreticheskoĭ Fiziki, Vol. 126, No. 6, 2004, pp. 1465–1478.
Original Russian Text Copyright © 2004 by Glazov, Ivchenko.

SOLIDS
Electronic Properties

Effect of Electron–Electron Interaction on Spin Relaxation of Charge Carriers in Semiconductors

M. M. Glazov and E. L. Ivchenko
Ioffe Physicotechnical Institute, Russian Academy of Sciences, St. Petersburg, 194021 Russia
e-mail: glazov@coherent.ioffe.ru

Received March 30, 2004

Abstract—An analysis of spin dynamics is presented for semiconductor systems without inversion symmetry that exhibit spin splitting. It is shown that electron–electron interaction reduces the rate of the Dyakonov–Perel (precession) mechanism of spin relaxation both via spin mixing in the momentum space and via the Hartree–Fock exchange interaction in spin-polarized electron gas. The change in the Hartree–Fock contribution with increasing nonequilibrium spin polarization is analyzed. Theoretical predictions are compared with experimental results on spin dynamics in GaAs/AlGaAs-based quantum-well structures. The effect of electron–electron collisions is examined not only for two-dimensional electron gas in a quantum well, but also for electron gas in a bulk semiconductor and a quantum wire. © *2004 MAIK "Nauka/Interperiodica".*

1. INTRODUCTION

Spin dynamics in semiconductors and semiconductor heterostructures is the subject of intensive ongoing research in view of possible applications in spintronics [1–5]. There exist four principal mechanisms of free-electron spin relaxation in semiconductors (see [6–8] and references therein). In the Elliott–Yafet mechanism, spin flip due to electron–electron scattering is explained by admixture of valence-band states to the conduction-band wave functions. In the Dyakonov–Perel (DP) mechanism, spin polarization decays during intervals between successive collisions, rather than in collisions (as in the Elliott–Yafet mechanism), owing to wavevector-dependent spin splitting of the conduction band [9]. In *p*-type structures, electrons are spin-depolarized as they are scattered by holes (the Bir–Aronov–Pikus mechanism). In samples with paramagnetic impurities, spin flip is partly due to the exchange interaction between free electrons and electrons bound to paramagnetic impurities.

For two-dimensional *n*-type quantum-well structures, the DP mechanism, also known as the precession mechanism (due to spin splitting in systems without inversion symmetry), is the most likely scenario of spin depolarization in wide ranges of carrier temperature and concentration [10–21]. Spin splitting is equivalent to spin precession in magnetic field, with a Larmor frequency $\mathbf{\Omega}_{\mathbf{k}}$ depending on the magnitude and direction of the electron wavevector **k**. The spin relaxation rate can be estimated as

$$\tau_s^{-1} \propto \langle \mathbf{\Omega}_{\mathbf{k}}^2 \tau \rangle,$$

where the angle brackets denote averaging over the electron energy distribution and τ is a microscopic relaxation time. We were the first to note [22] that the inverse relaxation time τ^{-1} is the sum of contributions due not only to various momentum-scattering mechanisms (which control the carrier mobility), but also to electron–electron collisions (which do not change the mean electron quasimomentum). Indeed, it does not matter whether a change in **k** (and the corresponding change in the axis of Larmor precession) is due to the scattering by a static defect or a phonon, or due to cyclotron motion of free carriers in magnetic field [11, 23], or it is caused by a collision with another electron. In particular, this implies that there exists a natural upper limit of spin relaxation rate in high-quality structures: $\tau_s^{-1} \le \langle \mathbf{\Omega}_{\mathbf{k}}^2 \rangle \tau_{ee}^{(s)}$, where the time scale $\tau_{ee}^{(s)}$ characterizing the electron–electron collision frequency can be found by solving an equation for the component $\delta \mathbf{s}_{\mathbf{k}}$ of the spin density matrix that is an odd function of **k**. The important role played by electron–electron scattering was demonstrated experimentally in [24], where spin dynamics were studied for optically oriented electrons in *n*-type GaAs/AlGaAs-based quantum wells.

In [22, 25], $\tau_{ee}^{(s)}$ was calculated for a nondegenerate two-dimensional electron system by solving a master equation for the spin density matrix. In [26], the theory was extended to the case of a bulk crystal, when electron–electron collisions can be described in the quasi-elastic approximation [27]. Extensions of kinetic theory from nondegenerate to arbitrary electron statistics were outlined in [28]. The contribution of electron–electron collisions to spin dynamics was allowed for in the theoretical study presented in [29], where the Hartree–Fock corrections to the one-electron energy in a spin-polarized electron gas introduced in [16, 17] were also taken into account. The numerical results pre-

1063-7761/04/9906-1279$26.00 © 2004 MAIK "Nauka/Interperiodica"

sented in [29] were obtained for only one value of two-dimensional quantum-well electron concentration in nonzero magnetic field at temperatures above 120 K. They cannot be used to evaluate the relative contributions of electron–electron and electron–phonon scattering and distinguish between the effects due to Hartree–Fock corrections to electron energy and electron–electron collisions.

In this paper, we present a kinetic theory of spin relaxation of conduction electrons that takes into account the contribution of electron–electron interaction for arbitrary degrees of degeneracy and spin polarization of the electron system. We calculate the spin relaxation time for a two-dimensional electron gas at temperatures ranging from low values to 120 K in the case when electron–phonon interaction weakly affects spin relaxation. The results obtained are compared with experiment [24] (see preliminary comparison in [30]). We find conditions under which the Hartree–Fock corrections are negligible as compared to the effect of electron–electron collisions on spin dynamics. The effect of these collisions on the Dyakonov–Perel mechanism is analyzed for systems with dimensions varying from $d = 3$ to $d = 1$.

The paper is organized as follows. In Section 2, we derive a master equation for spin-polarized electrons that takes into account electron–electron interaction. In Section 3, a general expression is obtained for the tensor of inverse spin-relaxation times. In Section 4, we calculate the spin relaxation time for a quantum well. In Section 5, the spin relaxation time is calculated for a bulk semiconductor and a quantum wire.

2. MASTER EQUATION FOR THE SPIN DENSITY MATRIX

In the kinetic theory of the electron gas, the joint distribution of the wavevector **k** and spin is described by a 2-by-2 density matrix that can be represented in terms of basis matrices as

$$\rho_{\mathbf{k}} = f_{\mathbf{k}} + \mathbf{s}_{\mathbf{k}} \cdot \boldsymbol{\sigma}. \qquad (1)$$

Here, $\boldsymbol{\sigma}$ is the vector whose components are the Pauli matrices, $f_{\mathbf{k}} = \mathrm{Tr}[\rho_{\mathbf{k}}/2]$ is the spin-averaged electron distribution function, and $\mathbf{s}_{\mathbf{k}} = \mathrm{Tr}[\rho_{\mathbf{k}}(\boldsymbol{\sigma}/2)]$ is the spin per **k**-state electron (the 2-by-2 identity matrix is omitted in this representation). The master equation for the density matrix $\rho_{\mathbf{k}}$ can be written as

$$\frac{d\rho_{\mathbf{k}}}{dt} + \frac{i}{\hbar}[\mathcal{H}_{\mathrm{SO}}(\mathbf{k}) + V_{\mathrm{C}}(\mathbf{k}), \rho_{\mathbf{k}}] + \hat{Q}_{\mathbf{k}}\{\rho\} = 0. \qquad (2)$$

Here, $\mathcal{H}_{\mathrm{SO}}(\mathbf{k})$ is the contribution of spin-dependent terms to the effective one-electron Hamiltonian, and $V_{\mathrm{C}}(\mathbf{k})$ is the Hartree–Fock contribution to the effective one-electron Hamiltonian due to the exchange interaction between the spin-polarized electron gas and an electron in the **k**-state [16, 17, 29, 31]:

$$V_{\mathrm{C}}(\mathbf{k}) = 2\sum_{\mathbf{k}'} V_{\mathbf{k}'-\mathbf{k}}(\mathbf{s}_{\mathbf{k}'} \cdot \boldsymbol{\sigma}). \qquad (3)$$

The last term on the left-hand side is the collision integral. The electron–electron scattering processes that do not conserve the total spin are ignored in this study.

To derive an expression for the contribution of electron–electron interaction to the collision integral $\hat{Q}_{\mathbf{k}}\{\rho\}$, we apply the standard Keldysh diagram technique and use the fact that the matrix element associated with the electron–electron scattering process **k**, $s_{\mathbf{k}}$ + **k**', $s_{\mathbf{k}'} \longrightarrow$ **p**, $s_{\mathbf{p}}$ + **p**', $s_{\mathbf{p}'}$ can be represented as

$$\begin{aligned} &M(\mathbf{p}, s_{\mathbf{p}}; \mathbf{p}', s_{\mathbf{p}'}|\mathbf{k}, s_{\mathbf{k}}; \mathbf{k}', s_{\mathbf{k}'}) \\ &= V_{\mathbf{k}-\mathbf{p}}\delta_{s_{\mathbf{p}}, s_{\mathbf{k}}}\delta_{s_{\mathbf{p}'}, s_{\mathbf{k}'}} - V_{\mathbf{k}-\mathbf{p}'}\delta_{s_{\mathbf{p}}, s_{\mathbf{k}'}}\delta_{s_{\mathbf{p}'}, s_{\mathbf{k}'}}, \end{aligned} \qquad (4)$$

where $s_{\mathbf{k}}$, $s_{\mathbf{k}'}$, … denote projections of spin ±1/2 on the z axis and $V_{\mathbf{q}}$ is a Fourier component of the Coulomb potential $V(\mathbf{r})$ in a d-dimensional space. We can use (4) to write the matrix element for arbitrary spin orientations in the initial and final states. Expression (4) can be rewritten in a convenient invariant matrix form by assigning index 1 to the spin states $s_{\mathbf{k}}$ and $s_{\mathbf{p}}$ of electrons with wavevectors **k** and **p**, respectively, and index 2 to the spin states $s_{\mathbf{k}'}$ and $s_{\mathbf{p}'}$. Furthermore, Eq. (4) can be written in the following operator form in terms of the 2-by-2 identity matrices $I^{(1)}$ and $I^{(2)}$ and the Pauli matrices $\sigma_\alpha^{(1)}$ and $\sigma_\alpha^{(2)}$ ($\alpha = x, y, z$):

$$\hat{M} = AI^{(1)}I^{(2)} + B\boldsymbol{\sigma}^{(1)} \cdot \boldsymbol{\sigma}^{(2)}, \qquad (5)$$

where

$$A = V_{\mathbf{k}-\mathbf{p}} - \frac{1}{2}V_{\mathbf{k}-\mathbf{p}'}, \quad B = -\frac{1}{2}V_{\mathbf{k}-\mathbf{p}'}. \qquad (6)$$

This expression for $\hat{M}$, as well as the starting expression (4), has a simple form because the scattering processes that do not conserve the total spin are ignored in this study. We write out the following useful expression for the squared operator $\hat{M}$:

$$\hat{M}^2 = (A^2 + 3B^2)I^{(1)}I^{(2)} + 2B(A - B)\boldsymbol{\sigma}^{(1)} \cdot \boldsymbol{\sigma}^{(2)}.$$

The matrix $\hat{M}$ is then used to rewrite the collision integral in (2) in compact form as

$$\begin{aligned} \hat{Q}_{\mathbf{k}}\{\rho\} = \frac{\pi}{2\hbar}\sum_{\mathbf{k}', \mathbf{p}, \mathbf{p}'} &\delta_{\mathbf{k}+\mathbf{k}', \mathbf{p}+\mathbf{p}'}\delta(E_k + E_{k'} - E_p - E_{p'}) \\ &\times \mathrm{Tr}_2 G(\mathbf{p}, \mathbf{p}'; \mathbf{k}, \mathbf{k}'), \end{aligned} \qquad (7)$$

where a matrix depending on the spin indices 1 and 2 is introduced,

$$\begin{aligned} G(\mathbf{p}, \mathbf{p}'; \mathbf{k}, \mathbf{k}') = {} & \hat{M}(I^{(1)} - \rho_{\mathbf{p}}^{(1)})(I^{(2)} - \rho_{\mathbf{p}'}^{(2)})\hat{M}\rho_{\mathbf{k}}^{(1)}\rho_{\mathbf{k}'}^{(2)} \\ & + \rho_{\mathbf{k}}^{(1)}\rho_{\mathbf{k}'}^{(2)}\hat{M}(I^{(1)} - \rho_{\mathbf{p}}^{(1)})(I^{(2)} - \rho_{\mathbf{p}'}^{(2)})\hat{M} \\ & - \hat{M}\rho_{\mathbf{p}}^{(1)}\rho_{\mathbf{p}'}^{(2)}\hat{M}(I^{(1)} - \rho_{\mathbf{k}}^{(1)})(I^{(2)} - \rho_{\mathbf{k}'}^{(2)}) \\ & - (I^{(1)} - \rho_{\mathbf{k}}^{(1)})(I^{(2)} - \rho_{\mathbf{k}'}^{(2)})\hat{M}\rho_{\mathbf{p}}^{(1)}\rho_{\mathbf{p}'}^{(2)}\hat{M}, \end{aligned} \tag{8}$$

and Tr_2 denotes the sum of diagonal matrix elements with index 2. The equation for the density matrix is equivalent to the following system of scalar and (pseudo)vector equations for $f_{\mathbf{k}}$ and $\mathbf{s}_{\mathbf{k}}$, respectively:

$$\frac{df_{\mathbf{k}}}{dt} + Q_{\mathbf{k}}\{f, \mathbf{s}\} = 0, \tag{9}$$

$$\frac{d\mathbf{s}_{\mathbf{k}}}{dt} + \mathbf{s}_{\mathbf{k}} \times (\mathbf{\Omega}_{\mathbf{k}} + \mathbf{\Omega}_{\mathrm{C},\mathbf{k}}) + \mathbf{Q}_{\mathbf{k}}\{\mathbf{s}, f\} = 0. \tag{10}$$

Here, the angular frequencies are defined by the relations

$$\mathcal{H}_{\mathrm{SO}}(\mathbf{k}) \equiv \frac{\hbar}{2}\mathbf{\Omega}_{\mathbf{k}} \cdot \boldsymbol{\sigma}, \quad \mathbf{\Omega}_{\mathrm{C},\mathbf{k}} = \frac{2}{\hbar}\sum_{\mathbf{k}'} V_{\mathbf{k}'-\mathbf{k}}\mathbf{s}_{\mathbf{k}'}, \tag{11}$$

the scalar and vector collision integrals, by the relations

$$\begin{aligned} Q_{\mathbf{k}}\{f, \mathbf{s}\} = {} & \frac{\pi}{4\hbar}\sum_{\mathbf{k}', \mathbf{p}, \mathbf{p}'} \delta_{\mathbf{k}+\mathbf{k}', \mathbf{p}+\mathbf{p}'}\delta(E_k + E_{k'} - E_p - E_{p'}) \\ & \times \mathrm{Tr}_1\mathrm{Tr}_2[G(\mathbf{p}, \mathbf{p}'; \mathbf{k}, \mathbf{k}')], \end{aligned}$$

$$\begin{aligned} \mathbf{Q}_{\mathbf{k}}\{\mathbf{s}, f\} = {} & \frac{\pi}{4\hbar}\sum_{\mathbf{k}', \mathbf{p}, \mathbf{p}'} \delta_{\mathbf{k}+\mathbf{k}', \mathbf{p}+\mathbf{p}'}\delta(E_k + E_{k'} - E_p - E_{p'}) \\ & \times \mathrm{Tr}_1\mathrm{Tr}_2[\boldsymbol{\sigma}^{(1)}G(\mathbf{p}, \mathbf{p}'; \mathbf{k}, \mathbf{k}')]. \end{aligned}$$

Performing the operations Tr_1 and Tr_2, we obtain

$$\begin{aligned} Q_{\mathbf{k}}\{f, \mathbf{s}\} = {} & \frac{2\pi}{\hbar} \\ & \times \sum_{\mathbf{k}', \mathbf{p}, \mathbf{p}'} \delta_{\mathbf{k}+\mathbf{k}', \mathbf{p}+\mathbf{p}'}\delta(E_k + E_{k'} - E_p - E_{p'}) \\ & \times \{(2V_{\mathbf{k}-\mathbf{p}}^2 - V_{\mathbf{k}-\mathbf{p}}V_{\mathbf{k}-\mathbf{p}'}) \\ & \times [f_{\mathbf{k}}f_{\mathbf{k}'}(1 - f_{\mathbf{p}} - f_{\mathbf{p}'}) - f_{\mathbf{p}}f_{\mathbf{p}'}(1 - f_{\mathbf{k}} - f_{\mathbf{k}'})] \\ & + 2(V_{\mathbf{k}-\mathbf{p}}^2 - V_{\mathbf{k}-\mathbf{p}}V_{\mathbf{k}-\mathbf{p}'}) \\ & \times [(f_{\mathbf{p}} - f_{\mathbf{k}})(\mathbf{s}_{\mathbf{k}'} \cdot \mathbf{s}_{\mathbf{p}'}) + (f_{\mathbf{p}'} - f_{\mathbf{k}'})(\mathbf{s}_{\mathbf{k}} \cdot \mathbf{s}_{\mathbf{p}})] \\ & - V_{\mathbf{k}-\mathbf{p}}V_{\mathbf{k}-\mathbf{p}'}[(f_{\mathbf{k}} + f_{\mathbf{k}'})(\mathbf{s}_{\mathbf{p}} \cdot \mathbf{s}_{\mathbf{p}'}) \\ & - (f_{\mathbf{p}} + f_{\mathbf{p}'})(\mathbf{s}_{\mathbf{k}} \cdot \mathbf{s}_{\mathbf{k}'})]\}, \end{aligned} \tag{12}$$

$$\begin{aligned} \mathbf{Q}_{\mathbf{k}}\{\mathbf{s}, f\} = {} & \frac{2\pi}{\hbar} \\ & \times \sum_{\mathbf{k}', \mathbf{p}, \mathbf{p}'} \delta_{\mathbf{k}+\mathbf{k}', \mathbf{p}+\mathbf{p}'}\delta(E_k + E_{k'} - E_p - E_{p'}) \\ & \times \{(2V_{\mathbf{k}-\mathbf{p}}^2 - V_{\mathbf{k}-\mathbf{p}}V_{\mathbf{k}-\mathbf{p}'}) \\ & \times [\mathbf{s}_{\mathbf{k}}F(\mathbf{k}'; \mathbf{p}, \mathbf{p}') - \mathbf{s}_{\mathbf{p}}F(\mathbf{p}'; \mathbf{k}, \mathbf{k}')] \\ & - V_{\mathbf{k}-\mathbf{p}}V_{\mathbf{k}-\mathbf{p}'}[\mathbf{s}_{\mathbf{k}'}F(\mathbf{k}; \mathbf{p}, \mathbf{p}') - \mathbf{s}_{\mathbf{p}}F(\mathbf{p}'; \mathbf{k}, \mathbf{k}') \\ & - (\mathbf{s}_{\mathbf{k}'} - \mathbf{s}_{\mathbf{k}})(\mathbf{s}_{\mathbf{p}} \cdot \mathbf{s}_{\mathbf{p}'})] \\ & + 2(V_{\mathbf{k}-\mathbf{p}}^2 - V_{\mathbf{k}-\mathbf{p}}V_{\mathbf{k}-\mathbf{p}'})(\mathbf{s}_{\mathbf{p}} - \mathbf{s}_{\mathbf{k}})(\mathbf{s}_{\mathbf{k}'} \cdot \mathbf{s}_{\mathbf{p}'})\}, \end{aligned} \tag{13}$$

where

$$F(\mathbf{k}_1; \mathbf{k}_2, \mathbf{k}_3) = f_{\mathbf{k}_1}(1 - f_{\mathbf{k}_2} - f_{\mathbf{k}_3}) + f_{\mathbf{k}_2}f_{\mathbf{k}_3}. \tag{14}$$

When the terms of third order in f and $\mathbf{s}$ can be neglected for a nondegenerate electron system, the vector collision integral reduces to [22]

$$\begin{aligned} \mathbf{Q}_{\mathbf{k}}\{\mathbf{s}, f\} = {} & \frac{2\pi}{\hbar} \\ & \times \sum_{\mathbf{k}', \mathbf{p}, \mathbf{p}'} \delta_{\mathbf{k}+\mathbf{k}', \mathbf{p}+\mathbf{p}'}\delta(E_k + E_{k'} - E_p - E_{p'}) \\ & \times [2(V_{\mathbf{k}-\mathbf{p}}^2 - V_{\mathbf{k}-\mathbf{p}}V_{\mathbf{k}-\mathbf{p}'})(\mathbf{s}_{\mathbf{k}}f_{\mathbf{k}'} - \mathbf{s}_{\mathbf{p}}f_{\mathbf{p}'}) \\ & + V_{\mathbf{k}-\mathbf{p}}V_{\mathbf{k}-\mathbf{p}'}(\mathbf{s}_{\mathbf{k}}f_{\mathbf{k}'} - \mathbf{s}_{\mathbf{k}'}f_{\mathbf{k}})]. \end{aligned} \tag{15}$$

The case when all spins are oriented along a certain axis and the case of weak spin polarization ($|\mathbf{s}_{\mathbf{k}}| \ll f_{\mathbf{k}}$) were discussed in [26]. The contributions to (12) and (13) proportional to $V_{\mathbf{k}-\mathbf{p}}^2$ and $V_{\mathbf{k}-\mathbf{p}}V_{\mathbf{k}-\mathbf{p}'}$ represent direct Coulomb interaction and exchange interaction between electrons, respectively. A kinetic equation for spin-polarized electron gas taking into account electron–electron interaction was discussed in a series of papers [16, 17, 29, 31]. The Hartree–Fock term in (9) is consistent with analogous terms in the equations for spin density-matrix components discussed in [16, 17]. Note that the electron–electron collision integral considered in [29, 31] did not include exchange interaction. Moreover, the expressions for $Q_{\mathbf{k},x}\{\mathbf{s}, f\}$ and $Q_{\mathbf{k},y}\{\mathbf{s}, f\}$ that follow from (13) substantially differ from the corresponding collision integral $(\partial\rho_{\mathbf{k}}/\partial t)_{\mathrm{scatt}}$ for $\rho_{\mathbf{k}} = s_{\mathbf{k}x} - is_{\mathbf{k}y}$ used in [29, 31]. In the case of a nondegenerate electron system, the term $V_{\mathbf{k}-\mathbf{p}}^2$ in (15) is multiplied by $\mathbf{s}_{\mathbf{k}}f_{\mathbf{k}'} - \mathbf{s}_{\mathbf{p}}f_{\mathbf{p}'}$, whereas the corresponding multiplicand in [29, 31] is proportional to

$$s_{\mathbf{k},\alpha}(2f_{\mathbf{p}} + f_{\mathbf{k}'} + f_{\mathbf{p}'}) - s_{\mathbf{p},\alpha}(2f_{\mathbf{k}} + f_{\mathbf{k}'} + f_{\mathbf{p}'}),$$

where $\alpha = x, y$. Note also the wavevectors $\mathbf{k}$, $\mathbf{k}'$, $\mathbf{p}$, and $\mathbf{p}'$ are used here instead of $\mathbf{k}$, $\mathbf{k}' - \mathbf{q}$, $\mathbf{k} - \mathbf{q}$, and $\mathbf{k}'$ in [29, 31], respectively. Both analysis of (15) and general considerations show that the collision integral corresponding to the latter combination of wavevectors is incorrect, because it does not vanish for the spin-polarized electron gas characterized by the Maxwell–Boltzmann equilibrium distribution of kinetic energy in each spin branch.

The Larmor frequencies due to spin–orbit interaction can be expressed for specific semiconductors as follows. The valence-band spin-orbit splitting in a bulk semiconductor with zinc-blende-type lattice scales with the electron wavevector cubed. The corresponding Larmor frequency is

$$\mathbf{\Omega}_{\mathbf{k}} = \frac{\alpha\hbar^2}{\sqrt{2m^3E_g}}\boldsymbol{\kappa}, \tag{16}$$

where $\alpha \approx 0.07$ is the Dresselhaus constant, E_g is the band gap, m is the effective electron mass, $\kappa_z = k_z(k_x^2 - k_y^2)$, and the remaining components of $\boldsymbol{\kappa}$ are obtained by cyclic permutation of indices (the x, y, and z axes are aligned with the [100], [010], and [001] directions, respectively) [32].

For a [001]-grown quantum well that has symmetric interfaces and is symmetric under the point group D_{2d}, spin splitting is due to bulk inversion asymmetry. It is represented by the Dresselhaus term [10]

$$\mathcal{H}_{\mathrm{SO}}(\mathbf{k}) = \beta_1(\sigma_y k_y - \sigma_x k_x), \tag{17}$$

obtained by averaging the three-dimensional Hamiltonian $\mathcal{H}_{\mathrm{SO}}(\mathbf{k})$, with $\mathbf{\Omega}_{\mathbf{k}}$ given by (16), over the size-quantized states of an electron moving along the growth axis; here, $\beta_1 \propto \alpha\langle k_z^2\rangle$.

For an asymmetric quantum well that is symmetric under the point group C_{2v}, spin splitting involves an additional contribution (represented by the Rashba term) due to the inversion asymmetry of the heterostructure-confining potential (see [8] and references therein):

$$\mathcal{H}_{\mathrm{SO}}(\mathbf{k}) = \beta_2(\sigma_x k_y - \sigma_y k_x), \tag{18}$$

where β_2 is a constant factor.

In the principal axes of the C_{2v} group, $x' \parallel [1\bar{1}0]$, $y' \parallel [110]$, and $z \parallel [001]$, the Larmor frequency corresponding to these contributions to spin splitting has the components

$$\Omega_{\mathbf{k},x'} = \beta_- k_{y'}/\hbar, \quad \Omega_{\mathbf{k},y'} = -\beta_+ k_{x'}/\hbar, \quad \Omega_{\mathbf{k},z} = 0, \tag{19}$$

where $\beta_\pm = 2(\beta_2 \pm \beta_1)$.

For a quantum wire, the Larmor frequency can be expressed as follows [33–35]:

$$\mathbf{\Omega}_{k_z} = \boldsymbol{\lambda} k_z, \tag{20}$$

where the constant vector $\boldsymbol{\lambda}$ determines the splitting and the direction of the spin precession axis.

Thus, the angle dependence of the Larmor-frequency components $\Omega_{\mathbf{k},\alpha}$ is described by the third-order spherical harmonics $Y_{3,m}(\mathbf{k}/k)$ for zinc-blende-based bulk crystals, by the first-order harmonics $\cos\varphi_{\mathbf{k}}$ and $\sin\varphi_{\mathbf{k}}$ and terms linear in the two-dimensional wavevector $\mathbf{k}$ for quantum-well structures ($\varphi_{\mathbf{k}}$ is the azimuthal angle of $\mathbf{k}$), and by the function $\mathrm{sgn}\{k_z\}$ for quantum wires.

3. SPIN RELAXATION TIME

We consider the DP mechanism of spin relaxation in the case when the spin splitting $\hbar\Omega_{\mathbf{k}}$ is small as compared to $\hbar/\tau$, where τ is the electron wavevector relaxation time; i.e., $\Omega_{\mathbf{k}}\tau \ll 1$ can be used as the small parameter in perturbation theory. When spin splitting is neglected, it is assumed that the electron energy distribution is uniform and the spins of all electrons are parallel to a unit vector $\mathbf{o}_s$. Therefore, the zeroth-approximation spin density matrix $\rho_{\mathbf{k}}^0$ is diagonal in the basis of spin states with spin projection on the $\mathbf{o}_s$ direction, and its diagonal elements are the Fermi–Dirac functions

$$f_{k,\pm} = \left[\exp\left(\frac{E_{\mathbf{k}} - \mu_\pm}{k_B T}\right) + 1\right]^{-1},$$

where μ_+ and μ_- are chemical potentials, $E_{\mathbf{k}} = \hbar^2k^2/2m$ is the kinetic energy of an electron, k_B is Boltzmann's constant, and T is temperature. In the basis of states with spin projection on the z axis, a quasi-equilibrium density matrix can be represented as follows [9]:

$$\rho_{\mathbf{k}}^0 = f_k^0 + \mathbf{s}_k^0 \cdot \boldsymbol{\sigma},$$

where the mean occupation f_k^0 and mean spin $\mathbf{s}_k^0$ for $\mathbf{k}$-state electrons are expressed in terms of $f_{k,\pm}$ as

$$f_k^0 = \frac{1}{2}(f_{k,+} + f_{k,-}), \quad \mathbf{s}_k^0 = \frac{1}{2}(f_{k,+} - f_{k,-})\mathbf{o}_s.$$

Introducing the quasi-equilibrium components of $\mathbf{s}_{\mathbf{k}}$ and $\mathbf{\Omega}_{\mathrm{C},\mathbf{k}}$, we write

$$\mathbf{s}_{\mathbf{k}} = \mathbf{s}_{\mathbf{k}}^0 + \delta\mathbf{s}_{\mathbf{k}}, \quad \mathbf{\Omega}_{\mathrm{C},\mathbf{k}} = \mathbf{\Omega}_{\mathrm{C},\mathbf{k}}^0 + \delta\mathbf{\Omega}_{\mathrm{C},\mathbf{k}},$$

where

$$\boldsymbol{\Omega}^0_{\mathrm{C},\mathbf{k}} = \frac{2}{\hbar}\sum_{\mathbf{k}'} V_{\mathbf{k}'-\mathbf{k}}\mathbf{s}^0_{\mathbf{k}'},$$
$$\delta\boldsymbol{\Omega}_{\mathrm{C},\mathbf{k}} = \frac{2}{\hbar}\sum_{\mathbf{k}'} V_{\mathbf{k}'-\mathbf{k}}\delta\mathbf{s}_{\mathbf{k}'}. \tag{21}$$

The first-order perturbative correction does not modify the distribution function $f_{\mathbf{k}}$, while $\delta\mathbf{s}_{\mathbf{k}}$ is proportional to the spin splitting. Note that the order of the angular harmonic associated with $\mathbf{s}_{\mathbf{k}}$ is preserved by the collision operator $\mathbf{Q}_{\mathbf{k}}\{\mathbf{s}, f^0\}$ and operator (3); i.e., the angle-dependent components $\delta s_{\mathbf{k},\alpha}$ and $\delta\Omega_{\mathrm{C},\mathbf{k},\alpha}$ involve the same harmonics as does $\boldsymbol{\Omega}_{\mathbf{k}}$. Note also that $\boldsymbol{\Omega}^0_{\mathrm{C},\mathbf{k}} \parallel \mathbf{o}_s$ and $\sum_{\mathbf{k}}\delta\boldsymbol{\Omega}_{\mathrm{C},\mathbf{k}} = 0$.

Taking the sum of (10) over $\mathbf{k}$, we obtain a balance equation for the total spin $\mathbf{S}_0 = \sum_{\mathbf{k}}\mathbf{s}^0_{\mathbf{k}}$:

$$\frac{d\mathbf{S}_0}{dt} + \sum_{\mathbf{k}}\delta\mathbf{s}_{\mathbf{k}}\times\boldsymbol{\Omega}_{\mathbf{k}} = 0. \tag{22}$$

Retaining the terms in (10) depending on the orientation of $\mathbf{k}$, we derive the following equation for the nonequilibrium correction:

$$\mathbf{L}_{\mathbf{k}}\{\delta\mathbf{s}\} = -\mathbf{S}_0\times\boldsymbol{\Omega}_{\mathbf{k}},$$
$$\mathbf{L}_{\mathbf{k}}\{\delta\mathbf{s}\} = \mathbf{Q}_{\mathbf{k}}\{\mathbf{s}, f^0\} + (G_k - H_k)\delta\mathbf{s}_{\mathbf{k}}\times\mathbf{s}^0_{\mathbf{k}} + \frac{\delta\mathbf{s}_{\mathbf{k}}}{\tau_p}, \tag{23}$$

where

$$G_k = \frac{1}{\hbar}\sum_{\mathbf{k}'} V_{\mathbf{k}'-\mathbf{k}}\frac{f_{k',+} - f_{k',-}}{|\mathbf{S}_0|}$$

and the function H_k is defined by the relation

$$\frac{2}{\hbar}\sum_{\mathbf{k}'} V_{\mathbf{k}'-\mathbf{k}}\delta\mathbf{s}_{\mathbf{k}'} = H_k\delta\mathbf{s}_{\mathbf{k}}.$$

In addition to the electron–electron collision operator $\mathbf{Q}_{\mathbf{k}}$, we introduce a term in $\mathbf{L}_{\mathbf{k}}$ that represents the momentum scattering characterized by a constant time τ_p. The momentum scattering time is used as an additional parameter in the theory developed below.

The contribution of the time derivative $d\delta\mathbf{s}_{\mathbf{k}}/dt$ to (23) is neglected here, because it is a quantity of higher order in $\Omega_{\mathbf{k}}\tau$. Since the collision integral must vanish for $\rho^0_{\mathbf{k}}$, the expression for

$$\mathbf{Q}_{\mathbf{k}}\{\mathbf{s}, f^0\} = \mathbf{Q}_{\mathbf{k}}\{\mathbf{s}^0 + \delta\mathbf{s}, f^0\}$$

can be substantially simplified by introducing an operator $\mathbf{Q}_{\mathbf{k}}\{\delta\mathbf{s}, \mathbf{s}^0, f^0\}$ linear in $\delta\mathbf{s}_{\mathbf{k}}$. An analysis of the symmetry of $\mathbf{L}_{\mathbf{k}}$ shows that $\delta\mathbf{s}_{\mathbf{k}} \perp \mathbf{S}_0$. Therefore, we can replace $\mathbf{s}_{\mathbf{k}}$, $\mathbf{s}_{\mathbf{k}'}$, and $\mathbf{s}_{\mathbf{p}}$ with $\delta\mathbf{s}_{\mathbf{k}}$, $\delta\mathbf{s}_{\mathbf{k}'}$, and $\delta\mathbf{s}_{\mathbf{p}}$, respectively, in the summands in (13) that are linear in the spin density matrix. Moreover, we can perform the following change in the cubic terms:

$$(\mathbf{s}_{\mathbf{k}'} - \mathbf{s}_{\mathbf{k}})(\mathbf{s}_{\mathbf{p}}\cdot\mathbf{s}_{\mathbf{p}'}) \longrightarrow (\delta\mathbf{s}_{\mathbf{k}'} - \delta\mathbf{s}_{\mathbf{k}})(\mathbf{s}^0_{\mathbf{p}}\cdot\mathbf{s}^0_{\mathbf{p}'}).$$

Then, the solution to Eq. (23) can be represented as

$$\delta s_{\mathbf{k},\alpha} = F_{1k}(\mathbf{S}_0)\mathbf{S}_0\times\boldsymbol{\Omega}_{\mathbf{k}} + F_{2k}(\mathbf{S}_0)[\mathbf{S}_0\times(\mathbf{S}_0\times\boldsymbol{\Omega}_{\mathbf{k}})], \tag{24}$$

where $F_{1k}(\mathbf{S}_0)$ and $F_{2k}(\mathbf{S}_0)$ are even functions of $\mathbf{S}_0$ depending on $k = |\mathbf{k}|$. Figure 1a illustrates the equilibrium distribution for a nondegenerate electron system, the nonequilibrium spin distribution in the absence of splitting, and the correction $\delta\mathbf{s}_{\mathbf{k}}$ due to precession with $\boldsymbol{\Omega}_{\mathbf{k}} \perp z$ in the case of $\mathbf{S}_0 \parallel z$ and spin splitting linear in the wavevector. If spin splitting is controlled by the Rashba term (18), then $\delta\mathbf{s}_{\mathbf{k}}$ is parallel to $\mathbf{k}$ (see Fig. 1b). When the dominant role is played by Dresselhaus term (17), the angle dependence of $\delta\mathbf{s}_{\mathbf{k}}$ has a more complicated form (see Fig. 1c).

Substituting the nonequilibrium correction given by (24) into (22), we find that the decay of the total spin is governed by the equation

$$\frac{d\mathbf{S}_0}{dt} + \sum_{\mathbf{k}}\{F_{1k}(\mathbf{S}_0)[\mathbf{S}_0|\boldsymbol{\Omega}_{\mathbf{k}}|^2 - \boldsymbol{\Omega}_{\mathbf{k}}(\mathbf{S}_0\cdot\boldsymbol{\Omega}_{\mathbf{k}})] + F_{2k}(\mathbf{S}_0)(\mathbf{S}_0\cdot\boldsymbol{\Omega}_{\mathbf{k}})(\mathbf{S}_0\times\boldsymbol{\Omega}_{\mathbf{k}})\} = 0.$$

If there exists a coordinate system in which the angle-averaged product $\langle\Omega_{\mathbf{k},\alpha}\Omega_{\mathbf{k},\beta}\rangle$ is proportional to $\delta_{\alpha,\beta}$, then we can rewrite the balance equation for spin as

$$\frac{dS_{0,\alpha}}{dt} + \frac{S_{0,\alpha}}{\tau_{\alpha\alpha}} + \sum_{\mathbf{k}} F_{2k}\varepsilon_{\alpha\beta\gamma}\langle\Omega^2_{\mathbf{k},\beta}\rangle S_{0,\beta}S_{0,\gamma} = 0,$$

where $\varepsilon_{\alpha\beta\gamma}$ is the Levi-Civita permutation symbol and

$$\frac{1}{\tau_{\alpha\alpha}} = \sum_{\mathbf{k}} F_{1k}(\mathbf{S}_0)(|\boldsymbol{\Omega}_{\mathbf{k}}|^2 - \Omega^2_{\mathbf{k},\alpha}). \tag{25}$$

When $\mathbf{S}_0$ is parallel to a coordinate axis α, the contribution proportional to F_{2k} vanishes, and spin relaxation can be described in terms of $\tau_{\alpha\alpha}$ only.

4. SPIN RELAXATION OF CONDUCTION ELECTRONS IN A QUANTUM WELL

Consider conduction electrons occupying the ground size-quantized subband ($e1$) in a [001]-grown zinc-blende-based quantum-well structure. In view of the quasi-two-dimensional form of the wavefunction envelope $\varphi_{e1}(z)$ and the effect of screening, the Fourier transform of the Coulomb potential has the following form (see [25]):

$$V_{\mathbf{q}} = \frac{2\pi e^2}{\kappa(q+q_s)}H(q), \qquad (26)$$

where $\mathbf{q}$ is a two-dimensional vector with components q_x and q_y,

$$q_s = 2me^2\{\kappa\hbar^2[1+\exp(-\mu/k_BT)]\}^{-1}$$

is the inverse screening length [36], μ is the chemical potential, and the sample area in the interface plane is unity. The form factor

$$H(q) = \iint \exp(-q|z-z'|)\varphi_{e1}^2(z)\varphi_{e1}^2(z')dzdz'$$

describes the spread of the electron wavefunction in a quantum well and strongly depends on the quantum-well width a. In the strictly two-dimensional limit, when $a \longrightarrow 0$ and the well is infinitely deep, $H(q)$ tends to unity. In a well of finite width, $H(q) < 1$; when $qa \ll 1$ (distances between electrons are relatively large), $H(q) \longrightarrow 1$; when $qa \gg 1$ (for relatively small distances between electrons), the form factor is inversely proportional to q and $V_{\mathbf{q}} \propto q^{-2}$ (if screening is neglected), as in the case of a three-dimensional electron gas.

The contribution of the Hartree–Fock field to the DP spin relaxation mechanism is controlled by the parameter $\Omega_C\tau$, where Ω_C is the mean value of the frequency $\Omega_{C,\mathbf{k}}$ defined in (11), and τ is the relaxation time of the electron wavevector in any collision. The spin-precession frequency controlled by the Hartree–Fock exchange interaction can be estimated as

$$\Omega_C \sim \frac{e^2}{\hbar\kappa\bar{k}}PN,$$

where $\hbar\bar{k}$ is the mean electron quasimomentum, N is the two-dimensional electron concentration, and $P = 2S_0/N$ is the degree of spin polarization. The time τ can be estimated by using the relation $\tau^{-1} = \tau_p^{-1} + \tau_{ee}^{-1}$, where the time τ_{ee} characterizes the frequency of electron–electron collisions. For the Boltzmann gas,

$$\tau_{ee}^{-1} = \frac{c_1e^4N}{\hbar\kappa^2k_BT}. \qquad (27)$$

In the case of a highly degenerate electron system, when the thermal energy k_BT is much smaller than the

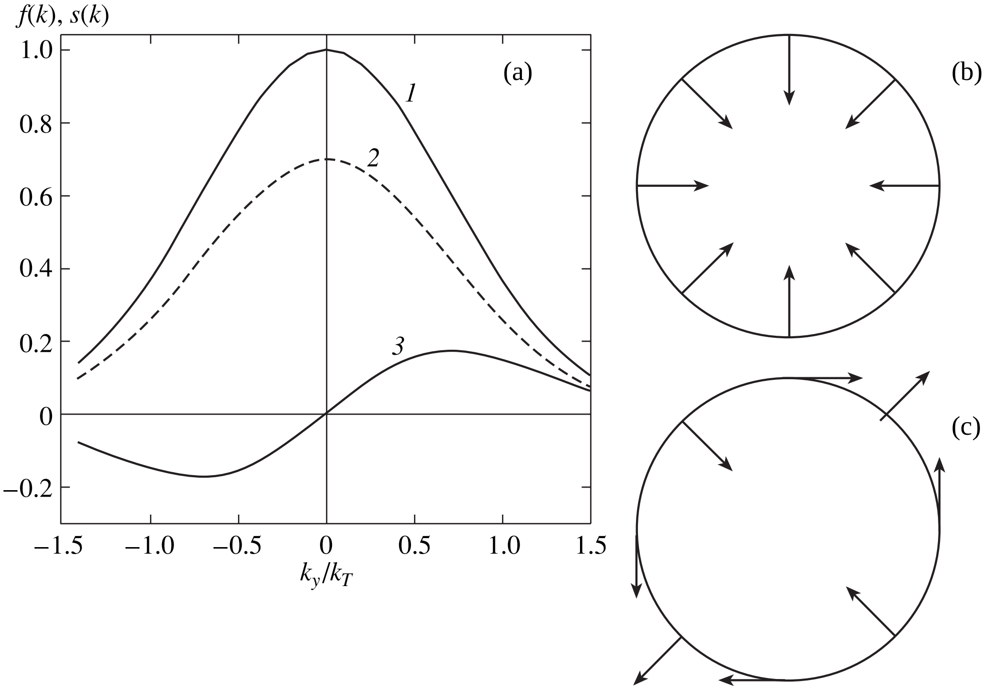

Fig. 1. (a) Electron distributions in the $\mathbf{k}$ space: (*1*) Maxwell–Boltzmann distribution, (*2*) quasi-equilibrium distribution of electrons with spin parallel to the z axis, and (*3*) nonequilibrium correction $\delta s_{\mathbf{k},x}$ due to spin splitting; (b) spin orientation controlled by the Rashba field in the (x, y) plane of a quantum well; (c) spin orientation controlled by the Dresselhaus field in the (x, y) plane of a quantum well.

Fermi energy E_F, we can use the estimate

$$\tau_{ee}^{-1} = c_2(T)\frac{E_F}{\hbar}\left(\frac{k_BT}{E_F}\right)^2, \tag{28}$$

where $c_1 \sim \pi^2/2$ [37, 38] and $c_2(T)$ is a slowly varying function of temperature, which behaves as $(\pi/4)\ln(E_F/k_BT)$ for a Fermi-level electron [39–42].

In what follows, we separately analyze the case of low degree of spin polarization, when $\Omega_C\tau \ll 1$ and the Hartree–Fock field can be neglected, and the case of relatively high P, when the frequency Ω_C is at least comparable to the inverse time τ^{-1}.

4.1. Weakly Polarized Electron Gas

In the case of a two-dimensional electron gas, the quasi-elastic approximation cannot be applied to collision integral (13) [37, 38, 43, 44]. Indeed, the energy transferred in an electron–electron collision is on the order of k_BT; i.e., the relative change in energy is comparable to those in $\mathbf{s}_k^0$ and $\delta\mathbf{s}_\mathbf{k}$. For this reason, Eq. (23) for the nonequilibrium correction was solved numerically.

When $\Omega_C\tau \ll 1$, we neglect the contributions of Hartree–Fock exchange interaction (3) and cubic in $\mathbf{s}_\mathbf{k}$ terms to the collision integral by taking the limits of $\Omega_{C,\mathbf{k}} \longrightarrow 0$ and $\mathbf{Q}_\mathbf{k}\{\delta\mathbf{s}, \mathbf{s}^0, f^0\} \longrightarrow \mathbf{Q}_\mathbf{k}\{\delta\mathbf{s}, \mathbf{s}^0 = 0, f^0\}$. In this case, the tensor of inverse spin-relaxation times given by (25) is independent of the total spin, and its nonzero components in the C_{2v} principal axes are

$$\frac{1}{\tau_{x'x'}} = \left(\frac{\beta_+k_0}{\hbar}\right)^2\tau, \quad \frac{1}{\tau_{y'y'}} = \left(\frac{\beta_-k_0}{\hbar}\right)^2\tau, \quad \frac{1}{\tau_{zz}} = \frac{1}{\tau_{x'x'}} + \frac{1}{\tau_{y'y'}}. \tag{29}$$

Here, the collision time τ that controls DP spin relaxation is defined as

$$\tau = \frac{1}{2}\sum_\mathbf{k}\frac{k^2}{k_0^2}F_{1k}(0), \tag{30}$$

with $F_{1k}(\mathbf{S})$ defined in (24) and a reference wavevector k_0 introduced to simplify the analysis of the dimensions of individual multiplicands in expressions for spin relaxation times. In the cases of nondegenerate and degenerate electron systems, reasonable estimates for k_0 are given by the "thermal" wavevector $k_T = \sqrt{2mk_BT}/\hbar$ and the Fermi wavevector $k_F^0 = \sqrt{2\pi N}$ ($T = 0$), respectively.

For nondegenerate electron gas, τ was calculated in [22, 25, 26] without allowance for momentum scattering. In this case, $k_0 = k_T$ and

$$\tau^{-1} = \tau_{ee}^{(s)-1} = \frac{c_1'e^4N}{\hbar\kappa^2k_BT}, \tag{31}$$

where the constant factor c_1' is approximately 35.7 (for strictly two-dimensional gas), i.e., several times greater than c_1 in (27). For degenerate (low-temperature) electrons, the function $\tau_{ee}^{(s)}(T)$ calculated in this study can be accurately approximated as follows:

$$\tau_{ee}^{(s)-1} = c_2'\frac{E_F}{\hbar}\left(\frac{k_BT}{E_F}\right)^2,$$

where $c_2' \approx 3.4$. This expression does not contain the factor $c_2(T)$, because its presence in (28) is due to the assumption that the electron energy relative to the Fermi level is small as compared to k_BT. Thus, we have $\tau_{ee}^{(s)} \propto T^{-2}$ at low temperatures and linear growth with temperature at high temperatures (when the chemical potential is negative); i.e., $\tau_{ee}^{(s)}(T)$ is a nonmonotonic function. The minimum value of $\tau_{ee}^{(s)}$ corresponds to the point of transition between the degenerate and nondegenerate statistics at $T \sim E_F/k_B$.

Now, we focus on the case when spin splitting in a quantum well is controlled by only one of the terms that are linear in $\mathbf{k}$ (either β_1 or β_2 is zero). If $\beta_2 = 0$, then the Larmor frequency is independent of $\varphi_\mathbf{k}$ ($\Omega_\mathbf{k} = |\beta_1|k$). Therefore, we can represent $\tau_{\alpha\alpha}$ as

$$\frac{1}{\tau_{zz}} = \frac{2}{\tau_{xx}} = \frac{2}{\tau_{yy}} = \Omega_0^2\tau, \tag{32}$$

where $\hbar\Omega_0 = \beta_1k_F^0$ is the spin splitting for Fermi-level electrons at $T = 0$.

Figure 2 compares our theoretical results with the experiment reported in [24] (see also the preliminary comparison in [30]). Here, the time τ in (32) is used as the ordinate to simplify presentation. Squares and circles represent the values of τ and τ_p measured in an n-type GaAs/AlGaAs-based quantum-well structure characterized by a high carrier mobility [24, 30], with a concentration of 1.86×10^{11} cm^{-2}, a well width of 100 Å, a barrier height of 250 MeV, an effective mass of $m = 0.067m_0$ (m_0 is the free-electron mass), and $\kappa = 13$. All values of τ, except for that at $T = 1.8$ K, were determined by measuring τ_{zz} and using (32). At $T = 1.8$ K, the condition $\Omega_0\tau \ll 1$ corresponding to the collision-dominated regime was violated in the sample ($\Omega_0\tau \sim 2$) and

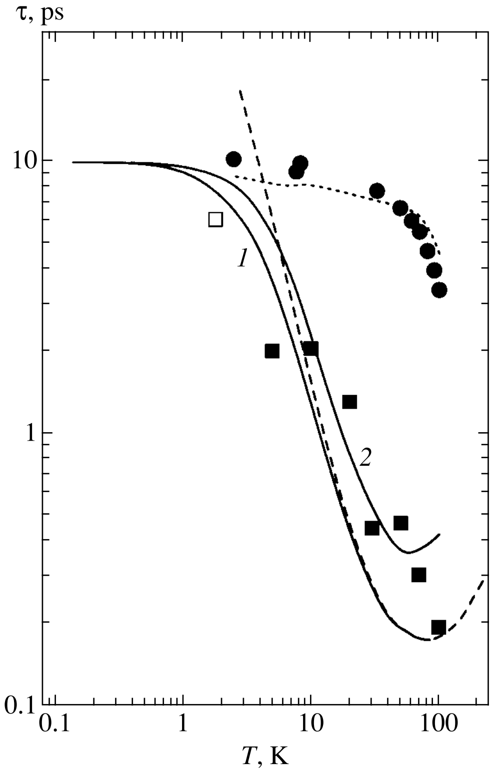

Fig. 2. Temperature dependence of microscopic collision time τ that controls spin relaxation according to (32) and transport time τ_p that controls carrier mobility for an *n*-GaAs/AlGaAs quantum-well structure. Experimental values of τ and τ_p are represented by circles and squares, respectively [24, 30]. Dashed and dotted curves represent the time τ calculated, respectively, by neglecting momentum scattering and electron–electron collisions. Solid curves are obtained by taking into account both electron–electron collisions and momentum scattering with τ_p = 10 ps for strictly two-dimensional (curve *1*) and quasi-two-dimensional (curve *2*) electrons.

an oscillatory spin-polarization decay was observed (see [45]):

$$S_{0,z}(t) \propto e^{-t/2\tau}\cos\Omega_0 t.$$

The corresponding result (τ = 6 ps at T = 1.8 K) is the open square in Fig. 2.

Calculated results are represented in Fig. 2 by four curves. The dotted curve was calculated by neglecting electron–electron collisions ($\tau_{ee}^{(s)-1} = 0$) and retaining both linear and cubic in wavevector contributions to spin splitting [6, 8]. It disagrees with the drop in τ observed experimentally at $T > 5$ K. The remaining three curves were calculated for three models with $\beta_1 \neq 0$ and $\beta_2 = 0$. The dashed curve corresponds to two-dimensional electron–electron collisions in the absence of momentum scattering ($\tau_{ee}^{(s)-1} \neq 0$, $\tau_p^{-1} = 0$). Curves *1* and *2* were calculated for two-dimensional and quasi-two-dimensional electron wavefunctions (in a quantum well with $H(q) < 1$), respectively, by taking into account both electron–electron collisions and momentum scattering with τ_p = 10 ps. The parameter values used in the calculations correspond to the experimental conditions. The figure demonstrates that our results are in good agreement at temperatures up to 80 K. This means that the reduction of the DP spin relaxation rate in the experiment reported in [24] was dominated by electron–electron collisions at $T > 5$ K.

4.2. Highly Polarized Electron Gas

When the degree of spin polarization is high, kinetic equation (23) for $\delta\mathbf{s}_\mathbf{k}$ contains two contributions proportional to the total spin: the Hartree–Fock term $(G_k - H_k)\mathbf{S}_0$ and the terms quadratic in $\mathbf{s}^0_\mathbf{k}$ in the linearized collision integral $\mathbf{Q}_\mathbf{k}\{\delta\mathbf{s}, \mathbf{s}^0, f^0\}$. Estimates show that these terms can be neglected for P below 20% considered here; i.e., the collision integral $\mathbf{Q}_\mathbf{k}\{\delta\mathbf{s}, \mathbf{s}^0 = 0, f^0\}$ can be used in this case as well. For this reason, we examine how the field induced by the Hartree–Fock interaction modifies the results presented in the preceding subsection when $\mathbf{S}_0 \neq 0$. It follows from (21) that the average Hartree–Fock field is parallel to $\mathbf{S}_0$. It gives rise to precession of $\delta\mathbf{s}_\mathbf{k}$ about the vector $\mathbf{S}_0$; i.e., it reduces the rate of spin relaxation (by analogy with Larmor precession in external magnetic field [23]). To be specific, we henceforth assume that the spin polarization is parallel to the growth axis of the quantum well ($\mathbf{o}_s \parallel z$) in the case of $\beta_1 \neq 0$ and $\beta_2 = 0$ (i.e., linear in wavevector splitting of the subband $e1$ due to the Dresselhaus term).

First, we calculate the effect of the Hartree–Fock field on spin relaxation in the case of $T \longrightarrow 0$, when electron–electron collisions are ruled out by the Pauli exclusion principle and spin relaxation is due to elastic carrier scattering by defects of quantum-well interfaces, which is characterized by a momentum relaxation time τ_p satisfying the condition $\Omega_0\tau_p \ll 1$. The result can be obtained in analytical form by assuming that the difference between μ_+ and μ_- is small for electrons with $s_z = \pm 1/2$. The corresponding $\mathbf{s}^0_\mathbf{k}$ and $\delta\mathbf{s}_\mathbf{k}$ can be approximated by delta functions of the magnitude of $\mathbf{k}$:

$$\mathbf{s}^0_\mathbf{k} = P\bar{\mu}\delta(E_\mathbf{k} - \bar{\mu})\mathbf{o}_s,$$

$$\delta\mathbf{s}_\mathbf{k} = (\mathbf{A}_c\cos\varphi_\mathbf{k} + \mathbf{A}_s\sin\varphi_\mathbf{k})\delta(E_\mathbf{k} - \bar{\mu}),$$

where $P = (\mu_+ - \mu_-)/2\bar{\mu}$, $\bar{\mu} = (\mu_+ + \mu_-)/2$, and the constant vectors $\mathbf{A}_c$ and $\mathbf{A}_s$ lie in the (x, y) plane. The Hartree–Fock contribution to (23) can be rewritten as

$$(G_k - H_k)\delta\mathbf{s}_\mathbf{k} \times \mathbf{S}_0 = \delta\mathbf{s}_\mathbf{k} \times \mathbf{\Omega}_\mathrm{C},$$

where the frequency of spin precession in the exchange field generated by the spin-polarized electron gas is expressed as

$$\mathbf{\Omega}_{\mathrm{C}} = \frac{2\pi\hbar NP}{m}\Lambda\mathbf{o}_{\mathbf{s}}, \qquad (33)$$

$$\Lambda = \frac{m}{(2\pi\hbar)^2}\int_0^{2\pi} V\left(2k_{\mathrm{F}}^0\sin\frac{\varphi}{2}\right)$$

$$\times(1-\cos\varphi)d\varphi = r_{\mathrm{s}}^2\mathcal{F}(r_{\mathrm{s}}) - \frac{r_{\mathrm{s}}^2}{2} + \frac{\sqrt{2}r_{\mathrm{s}}}{\pi};$$

with $V(q) \equiv V_{\mathbf{q}}$, the constant $r_{\mathrm{s}} = \sqrt{2}\,me^2/\kappa\hbar^2k_{\mathrm{F}}^0$ characterizes the Coulomb-to-kinetic energy ratio, and (see [46, 47])

$$\mathcal{F}(x) = \frac{x}{\pi}\begin{cases}\operatorname{arccosh}(\sqrt{2}/x)/\sqrt{2-x^2}, & x \le \sqrt{2},\\ \arccos(\sqrt{2}/x)/\sqrt{x^2-2}, & x > \sqrt{2}.\end{cases}$$

The relaxation time for the spin parallel to the growth axis is obtained by using general expression (25):

$$\frac{1}{\tau_{zz}} = \frac{\Omega_0^2\tau_p}{1+(\Omega_C\tau_p)^2}. \qquad (34)$$

It follows that $(\Omega_{\mathrm{C}}\tau_p)^2 \approx 0.4$ for $P = 1\%$ and $N = 1.86 \times 10^{11}$ cm^{-2}.

Figure 3 shows the spin relaxation rates calculated numerically versus P for the same parameters of the electron gas as those used in calculating curve *1* in Fig. 2 ($N = 1.86 \times 10^{11}$ cm^{-2} and $\tau_p = 10$ ps). The reduction of spin relaxation rate due to increase in degree of spin polarization is qualitatively consistent with the results of a numerical analysis of spin dynamics in an external magnetic field [29].

Figure 3 demonstrates that, if the starting degree of spin polarization is held constant, the effect of the Hartree–Fock field decreases as the electron–electron collision frequency increases with temperature according to (28). We conclude that the experimental conditions in [24] correspond to the regime of weak spin polarization considered in Section 4.1.

5. EFFECT OF ELECTRON–ELECTRON COLLISIONS IN SYSTEMS OF DIFFERENT DIMENSIONS

It is interesting to compare the effects of electron–electron collisions on the reduction of the spin relaxation rate in semiconductor-based systems of different dimensions: a bulk semiconductor, a quantum well, and a quantum wire. In this section, we compare the DP spin relaxation times calculated for a bulk semiconductor and a quantum wire by allowing only for electron–electron collisions with those due to the elastic scattering by ionized impurities whose concentration is equal to the electron concentration. The calculations are simplified by assuming that spin polarization is weak, which makes it possible to ignore the spin-dependent Hartree–Fock corrections to the electron energy.

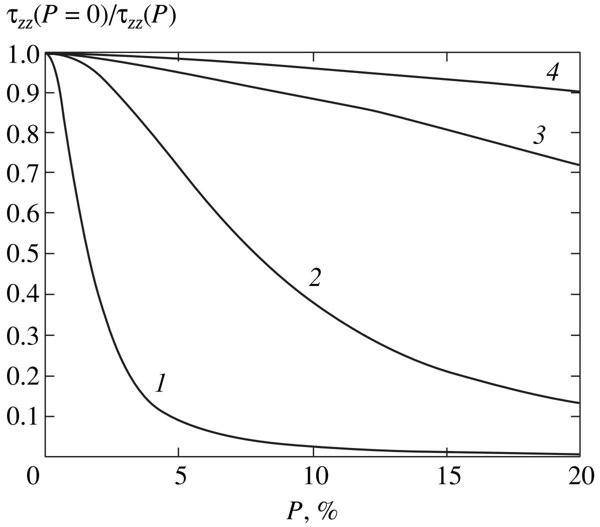

Fig. 3. Reduction of the rate of spin relaxation in strongly polarized electron gas at $T = 0$ (*1*), 10 (*2*), 20 (*3*), and 40 K (*4*).

5.1. Spin Relaxation in a Bulk Semiconductor

When the three-dimensional nondegenerate electron gas satisfies the condition

$$\frac{e^2}{\kappa r_{\mathrm{D}}}\frac{1}{k_{\mathrm{B}}T} \ll 1,$$

where $r_{\mathrm{D}} = (\kappa k_{\mathrm{B}}T/4\pi e^2N)^{1/2}$ is the Debye screening radius, electron–electron collisions can be treated as quasi-elastic [27, 28, 48]. This means that the wavevector $\mathbf{q} = \mathbf{p} - \mathbf{k}$ exchanged in the collision transforming a ($\mathbf{k}$, $\mathbf{k}'$) state into a ($\mathbf{p}$, $\mathbf{p}'$) state is small as compared to the “thermal” wavevector. In this case, electrons diffuse in the momentum space, and the collision integral can be represented as the divergence of the electron flux density in this space [27]. Moreover, we can use the following differential operator (see [28]):

$$\left(\frac{\partial}{\partial t}\delta s_{\mathbf{k},l}\right)_{\mathrm{sc}} \equiv Q_{\mathbf{k}}\{\delta s_l, f\} = \sum_i \frac{\partial}{\partial k_i}W_{i,l}(\mathbf{k}), \qquad (35)$$

with the spin flux density in the $\mathbf{k}$ space defined as

$$W_{i,l}(\mathbf{k}) = -A_i(\mathbf{k})s_{\mathbf{k},l} - D_{ij}(\mathbf{k})\frac{\partial}{\partial k_j}s_{\mathbf{k},l} \qquad (36)$$

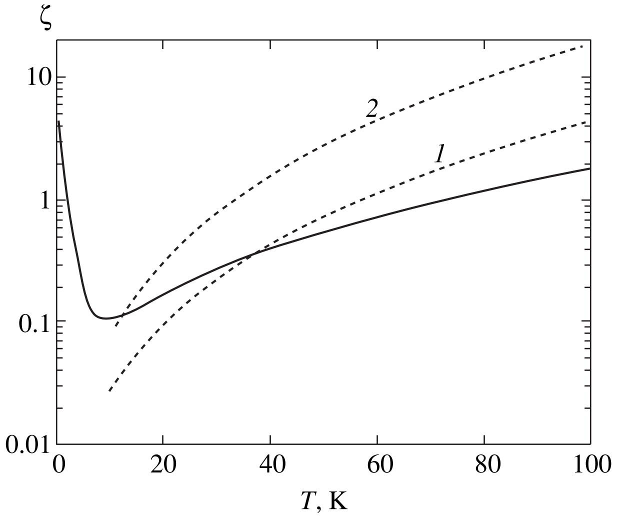

Fig. 4. Dimensionless parameter ζ in (40) versus temperature for spin relaxation in a quantum wire controlled by electron–electron collisions only (solid curve) and scattering by ionized impurities localized at the center of the wire (curve *1*) and uniformly distributed over the wire cross section (curve *2*).

and $A_i(\mathbf{k})$ and $D_{ij}(\mathbf{k})$ expressed as

$$A_i(\mathbf{k}) = \frac{\hbar^2 k^2}{2mk_{\rm B}T}\frac{k_i}{\tau_\parallel(E_{\mathbf{k}})},$$

$$D_{ij}(\mathbf{k}) = \frac{1}{2}\left[\delta_{ij}\frac{k^2}{2\tau_\perp(E_{\mathbf{k}})} + k_i k_j\left(\frac{1}{\tau_\parallel(E_{\mathbf{k}})} - \frac{1}{2\tau_\perp(E_{\mathbf{k}})}\right)\right].$$

The inverse electron–electron collision times [48]

$$\tau_\parallel^{-1}(E) = \tau_{ee}^{-1}(E)\frac{\mu(x)}{x},$$

$$\tau_\perp^{-1}(E) = \tau_{ee}^{-1}(E)[2\mu'(x) + \mu(x)(2 - x^{-1})]$$

characterize the spread in the momentum space along the vector $\mathbf{k}$ and in the perpendicular plane, respectively; the scattering time is

$$\tau_{ee}(E) = E^{3/2}\kappa^2 m^{1/2}/\sqrt{2}\pi N e^4 \Lambda,$$

where Λ is the Coulomb logarithm; $x = E/k_{\rm B}T$; and $\mu(x) = \mathrm{erf}(\sqrt{x}) - 2\sqrt{x/\pi}\, e^{-x}$.

Numerically solving Eq. (23) with collision operator (35), we obtain the following final expression for the principal values of the tensor of inverse spin relaxation times:

$$\frac{1}{\tau_{xx}} = \frac{1}{\tau_{yy}} = \frac{1}{\tau_{zz}} = \alpha^2\frac{(k_{\rm B}T)^3}{\hbar^2 E_{\rm g}}\tau, \qquad (37)$$

where α is defined by (16) and

$$\tau \equiv \tau_{ee}^{(s)} \approx 1.22\frac{\kappa^2\sqrt{m}}{Ne^4\Lambda}(k_{\rm B}T)^{3/2}. \qquad (38)$$

5.2. Spin Relaxation of Conduction Electrons in a Quantum Wire

For electron–electron collisions in a one-dimensional system schematized as $k + k' \longrightarrow p + p'$, the energy and momentum conservation laws imply that either $p = k$ and $p' = k'$ or $p = k'$ and $p' = k$ [49]. Therefore, collisions do not change the state of a pair of electrons having equal spins. Otherwise, collisions can result in spin exchange, as in the process

$$(k, 1/2) + (k', -1/2) \longrightarrow (k', 1/2) + (k, -1/2).$$

Thus, electron–electron collisions in a quantum wire can reduce the DP spin relaxation rate in a quantum wire, as in two- and three-dimensional systems.

In a cylindrical quantum wire characterized by weak spin polarization and arbitrary degree of degeneracy of the electron system, the electron–electron collision integral for $\mathbf{s}_{\mathbf{k}}$ reduces to

$$Q\{\mathbf{s}, f\} = \frac{1}{\tau_0}\int_{-\infty}^{\infty} dp\frac{v^2(k-p)}{|k-p|} \times [\mathbf{s}_k F(k'; p, p') - \mathbf{s}_p F(p'; k, k')]. \qquad (39)$$

Here, $\tau_0^{-1} = (me^4/\pi\hbar^3\kappa)$, the function $F(k'; p, p')$ is defined by (14), and the Fourier transform of the dimensionless quasi-one-dimensional potential of electron–electron interaction [50],

$$v(q) = \frac{72}{(qR_0)^2}\left[\frac{1}{10} - \frac{2}{3(qR_0)^2} + \frac{32}{3(qR_0)^4} - \frac{64}{(qR_0)^4}\mathrm{I}_3(qR_0)\mathrm{K}_3(qR_0)\right],$$

is expressed in terms of the quantum-wire radius R_0 and the Bessel and Macdonald functions $\mathrm{I}_3(x)$ and $\mathrm{K}_3(x)$. Effects of Luttinger-liquid behavior on spin dynamics in one-dimensional systems were considered in [34, 51]. Analogous effects on DP spin relaxation are left outside the scope of the present analysis.

The spin component parallel to the vector $\boldsymbol{\lambda}$ in linear relation (20) is preserved, whereas the decay of the spin component in the perpendicular plane is characterized by the rate constant

$$\frac{1}{\tau_\perp} = \left(\frac{\lambda}{\hbar R_0}\right)^2\zeta\tau_0. \qquad (40)$$

The solid curve and dotted curves in Fig. 4 represent the dimensionless factors $\zeta(T)$ calculated, respectively, for electron–electron collisions in a quantum wire with $N = 3.2 \times 10^5$ cm^{-1} and $R_0 = 100$ Å and for the scattering of electrons by ionized impurities whose concentration is equal to the electron concentration. These results demonstrate that the effect of electron–electron collisions is stronger in a wide temperature range.

According to (37) and expression (3.40) in [32], the ratio of the respective spin relaxation times due to electron–electron collisions and the elastic scattering by ionized impurities whose concentration is equal to the electron concentration, τ_s^{ee}/τ_s^i, is about 2.5 for an undeformed bulk semiconductor; i.e., the effect of electron–electron collisions is stronger. For a two-dimensional electron gas, the ratio is 3.6 [26, 28]. Curve *2* in Fig. 4 demonstrates that the effect of electron–electron collisions is stronger than that due to the elastic scattering by ionized impurities uniformly distributed over the wire cross section by an order of magnitude at $T = 100$ K. Thus, the effect of electron–electron collisions on the DP spin relaxation rate increases with decreasing dimension.

6. CONCLUSIONS

A theoretical analysis of the effect of electron–electron interactions on the Dyakonov–Perel spin relaxation is presented. It is shown that this mechanism of spin relaxation is controlled by electron–electron collisions to an extent comparable to the effect of other electron scattering processes. In the case of strong spin polarization, the Hartree–Fock field additionally reduces the rate of spin relaxation. The results obtained here agree with experimental studies of spin dynamics in *n*-type quantum-well structures characterized by high carrier mobility.

ACKNOWLEDGMENTS

We thank L.E. Golub for helpful discussions. This work was supported in part by the Russian Foundation for Basic Research and Russian Academy of Sciences. One of us (M.M.G.) appreciates the support provided by the Dynasty Foundation affiliated with the International Center for Fundamental Physics in Moscow.

REFERENCES

1. S. Das Sarma, J. Fabian, Zuedong Hu, *et al.*, Solid State Commun. **119**, 207 (2001).
2. M. Oestreich, M. Bender, J. Hübner, *et al.*, Semicond. Sci. Technol. **17**, 285 (2002).
3. *Semiconductor Spintronics and Quantum Computation*, Ed. by D. D. Awschalom, D. Loss, and N. Samarth (Springer, Berlin, 2002).
4. V. F. Motsnyi, V. I. Safarov, P. van Dorpe, *et al.*, J. Supercond.: Incorp. Novel Magn. **16**, 671 (2003).
5. M. I. Dyakonov, cond-mat/0401369.
6. E. L. Ivchenko and G. E. Pikus, *Superlattices and Other Heterostructures: Symmetry and Optical Phenomena* (Springer, Berlin, 1995), Springer Ser. Solid-State Sci., Vol. 110.
7. Pil Hun Song and K. W. Kim, Phys. Rev. B **66**, 035207 (2002).
8. N. S. Averkiev, L. E. Golub, and M. Willander, J. Phys.: Condens. Matter **14**, 271 (2002).
9. M. I. D'yakonov and V. I. Perel', Fiz. Tverd. Tela (Leningrad) **13**, 3581 (1971) [Sov. Phys. Solid State **13**, 3023 (1971)].
10. M. I. D'yakonov and V. Yu. Kachorovskiĭ, Fiz. Tekh. Poluprovodn. (Leningrad) **20**, 178 (1986) [Sov. Phys. Semicond. **20**, 110 (1986)].
11. E. L. Ivchenko, P. S. Kop'ev, V. P. Kochereshko, *et al.*, Pis'ma Zh. Éksp. Teor. Fiz. **47**, 407 (1988) [JETP Lett. **47**, 486 (1988)].
12. R. S. Britton, T. Grevatt, A. Malinowski, *et al.*, Appl. Phys. Lett. **73**, 2140 (1998).
13. Y. Ohno, R. Terauchi, T. Adachi, *et al.*, Phys. Rev. Lett. **83**, 4196 (1999).
14. A. Tackeuchi, T. Kuroda, S. Muto, *et al.*, Jpn. J. Appl. Phys. **38**, 4680 (1999).
15. K. C. Hall, S. W. Leonard, H. M. van Driel, *et al.*, Appl. Phys. Lett. **75**, 4156 (1999).
16. M. W. Wu and H. Metiu, Phys. Rev. B **61**, 2945 (2000).
17. M. W. Wu and C. Z. Ning, Phys. Status Solidi B **222**, 523 (2000).
18. W. H. Lau, J. T. Olesberg, and M. E. Flatté, Phys. Rev. B **64**, 161301 (2001).
19. M. W. Wu, J. Phys. Soc. Jpn. **70**, 2195 (2001).
20. M. W. Wu and M. Kuwata-Gonokami, Solid State Commun. **121**, 509 (2002).
21. J. Kainz, U. Rössler, and R. Winkler, Phys. Rev. B **68**, 075322 (2003).
22. M. M. Glazov and E. L. Ivchenko, Pis'ma Zh. Éksp. Teor. Fiz. **75**, 476 (2002) [JETP Lett. **75**, 403 (2002)].
23. E. L. Ivchenko, Fiz. Tverd. Tela (Leningrad) **15**, 1566 (1973) [Sov. Phys. Solid State **15**, 893 (1973)].
24. M. A. Brand, A. Malinowski, O. Z. Karimov, *et al.*, Phys. Rev. Lett. **89**, 236601 (2002).
25. M. M. Glazov, Fiz. Tverd. Tela (St. Petersburg) **45**, 1108 (2003) [Phys. Solid State **45**, 1162 (2003)].
26. M. M. Glazov and E. L. Ivchenko, J. Supercond.: Incorp. Novel Magn. **16**, 735 (2003).
27. L. D. Landau, Zh. Éksp. Teor. Fiz. **7**, 203 (1937).
28. M. M. Glazov and E. L. Ivchenko, in *Optical Properties of 2D Systems with Interacting Electrons*, Ed. by W. J. Ossau and R. Suris (Kluwer Academic, Dordrecht, 2003), p. 181.
29. M. Q. Weng and M. W. Wu, Phys. Rev. B **68**, 75312 (2003); Phys. Status Solidi B **239**, 121 (2003).
30. M. M. Glazov, E. L. Ivchenko, M. A. Brand, *et al.*, in *Proceedings of 11th International Symposium on Nanostructures: Physics and Technology* (St. Petersburg, 2003), p. 273; cond-mat/0305260.

31. M. Q. Weng and M. W. Wu, J. Phys.: Condens. Matter **15**, 5563 (2003).
32. G. E. Pikus and A. N. Titkov, in *Optical Orientation*, Ed. by F. Meier and B. P. Zakharchenya (North-Holland, Amsterdam, 1984; Nauka, Leningrad, 1989).
33. T. Nishimura, Xue-Lun Wang, M. Ogura, *et al.*, Jpn. J. Appl. Phys. **38**, L941 (1999).
34. M. Governale and U. Zülicke, Phys. Rev. B **66**, 073311 (2002).
35. E. A. de Andrada e Silva and G. C. La Rocca, Phys. Rev. B **67**, 165318 (2003).
36. F. Stern, Phys. Rev. Lett. **18**, 546 (1967).
37. S. É. Esipov and I. B. Levinson, Pis'ma Zh. Éksp. Teor. Fiz. **42**, 193 (1985) [JETP Lett. **42**, 239 (1985)].
38. S. É. Esipov and I. B. Levinson, Zh. Éksp. Teor. Fiz. **90**, 330 (1986) [Sov. Phys. JETP **63**, 191 (1986)].
39. C. Hodges, H. Smith, and J. W. Wilkins, Phys. Rev. B **4**, 302 (1971).
40. G. F. Giuliani and J. J. Quinn, Phys. Rev. B **26**, 4421 (1982).
41. T. Jungwirth and A. H. MacDonald, Phys. Rev. B **53**, 7403 (1996).
42. Lian Zheng and S. Das Sarma, Phys. Rev. B **53**, 9964 (1996).
43. R. N. Gurzhi, A. N. Kalinenko, and A. I. Kopeliovich, Phys. Rev. B **52**, 4744 (1995).
44. Ben Yu Kuang Hu and K. Flensberg, Phys. Rev. B **53**, 10072 (1996).
45. V. N. Gridnev, Pis'ma Zh. Éksp. Teor. Fiz. **74**, 417 (2001) [JETP Lett. **74**, 380 (2001)].
46. J. F. Janak, Phys. Rev. **178**, 1416 (1969).
47. Guang-Hong Chen and M. E. Raikh, Phys. Rev. B **60**, 4826 (1999).
48. V. F. Gantmakher and I. B. Levinson, *Scattering of Carriers in Metals and Semiconductors* (Nauka, Moscow, 1984) [in Russian].
49. F. Prengel and E. Schöll, Phys. Rev. B **59**, 5806 (1999).
50. A. Gold and A. Ghazali, Phys. Rev. B **41**, 7626 (1990).
51. A. V. Moroz, K. V. Samokin, and C. H. W. Barnes, Phys. Rev. Lett. **84**, 4164 (2000).

Translated by A. Betev

Journal of Experimental and Theoretical Physics, Vol. 99, No. 6, 2004, pp. 1291–1306.
Translated from Zhurnal Éksperimental'noĭ i Teoreticheskoĭ Fiziki, Vol. 126, No. 6, 2004, pp. 1479–1495.
Original Russian Text Copyright © 2004 by Ivanov, Kulagin.

SOLIDS
Electronic Properties

Instanton Paths for the Problem of Coherent Quantum Tunneling in Small Ferromagnetic Particles

B. A. Ivanov[a] **and N. E. Kulagin**[b]

[a]*Institute of Magnetism, National Academy of Sciences of Ukraine, Kiev, 03142 Ukraine*
[b]*Lukin Institute of Physical Problems, Zelenograd, Moscow, 124460 Russia*
e-mail: bivanov@i.com.ua

Received May 19, 2004

Abstract—It is shown that the problem of instantons in ferromagnetic materials in a large-spin model is reduced to an exactly integrable dynamical system with a finite number of variables. For a rather wide class of models, there exists a continuum of instanton paths that form a one-parameter family of paths with essentially different shapes but with the same value of the Euclidean action. On the basis of the formalism developed, exact instanton solutions are constructed that describe macroscopic quantum tunneling for a small ferromagnetic particle with uniaxial or biaxial quadratic anisotropy in the presence of a magnetic field applied perpendicularly to the easy axis. These solutions are valid for any relations between the anisotropy parameters and for any magnitude of the magnetic field and its direction in the base plane. Based on the solutions obtained, the principles of macroscopic quantum tunneling in high-spin-molecule-type magnetic particles are described. Tunneling regimes of two types are obtained: (1) regimes that are characterized by destructive interference of instanton trajectories and oscillatory dependence of the transition probability on the magnitude of the magnetic field and (2) regimes in which all instantons have the same purely real value of the Euclidean action and there is no destructive interference. *© 2004 MAIK "Nauka/Interperiodica".*

1. INTRODUCTION AND FORMULATION OF THE MODEL

In the last decade, the problems of macroscopic quantum tunneling in macroscopic (or, more precisely, mesoscopic) magnetic systems have been intensively studied both experimentally and theoretically (see surveys [1, 2]). In the physics of magnetism, these systems include small magnetic particles, magnetic clusters, and high-spin molecules. Special attention has been focused on the phenomenon of coherent macroscopic quantum tunneling between energy equivalent but physically different states in systems with discrete degeneracy of the ground state. In such systems, a typical effect of coherent quantum tunneling consists in the mixing of two equivalent classical states that correspond to two identical minima of the anisotropy energy (see [1, 2]). The mixing results in the tunnel splitting of these states, which are degenerate in the classical case. Interest in this phenomenon is due to the two following reasons. First, mesoscopic objects that exhibit quantum-mechanical properties are of interest as potential elements of quantum computers (see [3, 4]). Second, these problems involve fine and beautiful effects of interference between instanton trajectories. In ferromagnetic particles, these effects lead to the suppression of tunneling for systems with half-integer total spin in the absence of a magnetic field [5, 6], as well as to the oscillatory dependence of the tunnel splitting of levels on external parameters, first of all, on the magnetic field. In the case of $H \neq 0$, tunneling was theoretically studied (by an instanton method) by Garg, who discovered an interesting interference phenomenon: oscillations of the splitting of levels as a function of a magnetic field applied along the hard axis [7]. The effects of coherent macroscopic quantum tunneling can be observed experimentally by the resonance absorption of electromagnetic waves by tunnel-split levels. The controllability of the tunneling phenomena (the switching on and off of tunneling) is an important factor for the application of magnetic elements in quantum computers [3, 4].

The first studies in the theory of quantum tunneling [8–10] were performed for small ferromagnetic particles under the assumption that all spins in a particle are parallel to each other (a large-spin model). For these systems, the effects of destructive interference of instanton trajectories and suppression of tunneling due to interference were predicted in [5, 6]. Then, it was long believed that antiferromagnets are more convenient objects for the experimental observation of tunneling because they are characterized by higher tunneling probability and less stringent temperature constraints compared with ferromagnets [11–14]. It is worth noting that the effects of coherent quantum tunneling were first observed, by resonance methods, in antiferromagnetic particles of ferritin of biological origin [15].

In recent years, there has been increased interest in tunneling in ferromagnets and, hence, in large-spin models. This interest has been stimulated by experimental investigations of tunneling phenomena in oriented single-crystals of high-spin molecules (see the survey by Wernsdorfer [16]). In fact, the synthesis and investigation of high-spin molecules have started a new period in the study of macroscopic quantum phenomena. The main advantage of these objects, which include both ferromagnets (in fact, high-spin molecules or molecular magnets) and antiferromagnets (spin rings), is their well-defined magnetic structure [17]. The total magnetic moment of high-spin molecules amounts to 26 Bohr magnetons [18]. The states of the most thoroughly studied high-spin molecules, which are denoted for brevity by Fe_8 and Mn_{12}, are well described under the assumption that all spins of a molecule are coupled by a strong exchange interaction and form a total spin of $S = 10$. There also exist high-spin molecules with half-integer spin, which include Mn_4 complexes with the spin 9/2 [19]. In these systems, tunneling phenomena were observed both between excited levels, which have greater splitting [20, 21], and in the ground state [22–26]. Actually, a system of such molecules represents an ensemble of identical particles (in contrast, for example, to the particles of ferritin, in which the number of magnetic ions in a particle may range from 20 to 30, i.e., about one percent of the total number of ions, which is on the order of 3500). Moreover, it is possible to produce high-quality single crystals of high-spin molecules with exactly oriented anisotropy axes. This made it possible to pose the question concerning the observation of tunnel-splitting oscillations, predicted by Garg [7], as a function of an external magnetic field applied along the hard axis of a magnetic particle. Such oscillations were observed by Wernsdorfer and Sessoli in Fe_8 [24] and by Wernsdorfer and coauthors in Mn_{12} [25]; experiments were also carried out on systems with half-integer spin [26]. The measurements of the relaxation time at low temperatures showed that this quantity periodically depends on a magnetic field when the field is directed along the hard axis of such high-spin molecules.

The observation of these beautiful phenomena stimulated new theoretical investigations of the problem of tunneling for ensembles of oriented ferromagnetic particles [27, 28]. The states of high-spin molecules are well described under the assumption that all spins in a molecule are coupled by a strong exchange interaction, so that the total spin of a molecule is S. Thus, we arrive at a model of large spin S in the presence of single-ion magnetic anisotropy in a magnetic field $\mathbf{H}$. In all the works devoted to this problem that we are aware of, the dynamics of high-spin molecules is described by a Hamiltonian

$$\hat{H} = \frac{1}{2}(K_1 S_x^2 + K_2 S_y^2) + g\mu_B \mathbf{H}\cdot\mathbf{S} + \tilde{K}[S_{(+)}^4 + S_{(-)}^4]. \qquad (1)$$

Here, K_1 and K_2 are constants of rhombic anisotropy, the term with $\tilde{K}$ corresponds to tetragonal anisotropy that exists in the case of Mn_{12}, S_x and S_y are components of the spin operator, $S_\pm = S_x \pm iS_y$, g is the gyromagnetic ratio, and μ_B is the modulus of the Bohr magneton. The constants K_1, K_2, and $\tilde{K}$ are positive; i.e., the z axis is the easy axis for the spin. The magnitude of $\tilde{K}$ is small: $\tilde{K} \ll K_1, K_2$; its contribution is significant only for an undeformed Mn_{12} molecule, which has no natural rhombic anisotropy. For Fe_8 molecules, as well as for deformed Mn_{12} complexes, the main contribution to anisotropy is made by the first two terms in (1), i.e., by rhombic anisotropy. In what follows, we restrict our consideration to the case of $\tilde{K} = 0$.

The simplest way to analyze the tunneling between different classically degenerate ground states $\mathbf{m}^{(+)}$ and $\mathbf{m}^{(-)}$ of a system and to determine the tunnel splitting of energies of these states is to apply the instanton formalism (see, for example, [29, 30]). For the classical magnetization $\mathbf{m}$, we have to pass to imaginary time in the classical Landau–Lifshits equations by the formula $t = i\tau$ and find instanton solutions $\mathbf{m} = \mathbf{m}(\tau)$ to these equations such that the magnetization tends to two different ground states, $\mathbf{m}(\tau) \longrightarrow \mathbf{m}^{(\pm)}$, as $\tau \longrightarrow \pm\infty$. This approach can be applied more carefully within the formalism of coherent spin states [30]. Within this approach, a magnetization vector $\mathbf{m}$ of constant magnitude represents a dynamical variable. Taking into account that the magnetization is antiparallel to the spin, we write $\mathbf{m} = -\mathbf{S}/S$. It is convenient to parameterize the vector $\mathbf{m}$ in terms of angular variables θ and φ: $m_x + im_y = \sin\theta\exp(i\varphi)$ and $m_z = \cos\theta$. Instantons correspond to the extrema of the Euclidean action $A_E[\mathbf{m}]$ and represent solutions to the Euler–Lagrange equations for the Euclidean version of the Lagrangian of a ferromagnet. Only equivalent trajectories that have the minimal value of the real part of the Euclidean action $A_E[\mathbf{m}]$ contribute to splitting. This contribution is proportional to the tunneling exponential $\exp\{-\mathrm{Re}A_E[\mathbf{m}]/\hbar\}$. The Euclidean action can be represented in terms of the magnetization vector $\mathbf{m}$ as follows:

$$A_E[\mathbf{m}] = \int d\tau\left[-i\hbar S\frac{\mathbf{n}[\mathbf{m}\times d\mathbf{m}/d\tau]}{1+\mathbf{m}\cdot\mathbf{n}} + W(\mathbf{m})\right], \qquad (2)$$

where $W(\mathbf{m})$ is the energy of a ferromagnet that includes the ferromagnetic anisotropy energy and the

Zeeman energy of a spin in an external magnetic field. The first term in the case of real time determines the dynamics of magnetization; variation of it gives the well-known Landau–Lifshits equations. The dynamical part of the Lagrangian (2) has a singularity at $\mathbf{m}\cdot\mathbf{n} = -1$. The origin of this singularity and possible ways to remove it become clear when we pass to the variable $\mathbf{M} = M\mathbf{m}$, which is not subject to the condition $\mathbf{M}^2 = \text{const}$. In terms of $\mathbf{M}$, the expression for the Lagrangian can be written as

$$\begin{aligned} L &= -i\mathbf{A}\partial\mathbf{M}/\partial\tau + W(\mathbf{m}), \\ \mathbf{A} &= \hbar S[\mathbf{n}\times\mathbf{M}]/M[M+\mathbf{n}\cdot\mathbf{M}], \end{aligned} \tag{3}$$

where the vector $\mathbf{A}$ has a singularity on the line $(\mathbf{n}, \mathbf{M}) = -M$. The dynamical part of Lagrangian (1), represented in terms of $\mathbf{M}$ and $\partial\mathbf{M}/\partial t$, formally coincides with the Lagrangian of a charged particle with coordinate $\mathbf{M}$ in a magnetic field with the vector potential $\mathbf{A}$. It can easily be shown that the vector $\mathbf{B} = \operatorname{curl}\mathbf{A} = \hbar S\mathbf{M}/\mathbf{M}^3$ has no singularities when $M \neq 0$. Thus, expression (2) for $\mathbf{A}$ describes the vector potential of a magnetic monopole situated at the origin. The vector potential $\mathbf{A}$ for a monopole certainly has a singularity on the line (the Dirac string) that starts at the location point of the monopole and goes to infinity [30]. The admissible transformations (2) or (3) are reduced to gauge transformations, in particular, to changing the orientation of the Dirac string. The singularities of the Lagrangian are closely related to the so-called Berry phase (see [5, 6, 30]), i.e., to the total time derivative in the Lagrangians (2) or (3), which does not manifest itself in the equations of motion but is responsible for the interference of instanton trajectories. The nontrivial contribution of the Berry phase to the tunneling probability is determined by the integral $\oint\mathbf{A}d\mathbf{M}$ along a closed contour and can be transformed into a two-dimensional integral of $\mathbf{B} = \operatorname{curl}\mathbf{A}$ over a surface bounded by this contour, whereby the result should not depend on calibration [5, 6, 30].

Usually, the Lagrangian of a ferromagnet is expressed in angular variables. When $\mathbf{n}\parallel\mathbf{e}_z$, the Euclidean action acquires the well-known form

$$A_E(\theta, \varphi) = \int d\tau[-i\hbar S(1-\cos\theta)\delta\varphi/d\tau + W(\theta, \varphi)].$$

The dynamical part of the Lagrangian in this form also contains singularities associated with the nondifferentiability of the azimuth φ at the points $\theta = 0, \pi$. However, we will use more general expression (2) because the calculation of the Euclidean action can often be significantly simplified by an appropriate choice of the direction of the Dirac string (see Section 4).

It has often been pointed out that instantons are formally similar to domain-wall-type solitons. Sometimes, this similarity is quite striking; for instance, in Lorentz-invariant models, the analysis of solutions for instantons is analogous to that for domain walls. However, we will show that, for a ferromagnet, there is a fundamental difference between the analyses of instantons and domain walls. In contrast to the problem of a moving domain wall, which is integrable only in a few particular cases, the construction of an instanton solution in a ferromagnet is reduced to an exactly integrable dynamical problem.

The Euclidean version of the equations for magnetization dynamics has an obvious integral of motion $W(\theta, \varphi) = \text{const}$; within the instanton formalism, the value of this constant should be chosen so that $W(\theta^{(\pm)}, \varphi^{(\pm)}) = 0$ for the equilibrium states $\theta = \theta^{(\pm)}$, $\varphi = \varphi^{(\pm)}$ between which the tunneling is considered. Hence, $W(\theta, \varphi) = 0$ on the instanton solution; therefore, for a ferromagnet, the quantity $A_E[\theta, \varphi]$ is determined only by the first term in the Lagrangians (2) or (3), i.e., by its dynamical part. This, in particular, implies that the instanton solution cannot be real because the realization of the quasiclassical dynamics requires that the Euclidean action must have a considerable real part of A_E (2).

2. A MODEL OF A PURELY UNIAXIAL FERROMAGNET AND SOME GENERAL CONSIDERATIONS

We begin the analysis with the case of a purely uniaxial magnet by setting

$$K_1 = K_2 = K$$

in (1). In this case, equations for the angular variables are expressed as

$$\begin{aligned} \sin\theta d\varphi/d\tau &= \omega_0\cos\theta(\sin\theta - h\cos\varphi), \\ d(\cos\theta)/d\tau &= +h\sin\theta\sin\varphi, \end{aligned} \tag{4}$$

where $h = H/H_a = g\mu_B H/KS$ is a characteristic dimensionless field, $H_a = KS/g\mu_B$ has the meaning of the anisotropy field, and $\hbar\omega_0 = KS$. If we assume that $\cos\theta$ and φ may take complex values, the system of equations (4) represents a dynamical system with two degrees of freedom. It is convenient to introduce dimensionless imaginary time by changing $\tau \longrightarrow \tau\omega_0$. Next, instead of the first equation, we can use the first integral $W(\theta, \varphi) = \text{const}$ of this system. The equation $W(\theta, \varphi) = 0$ yields $\sin\theta = h\exp(i\sigma\varphi)$, where $\sigma = \pm 1$. Using this formula, we can eliminate φ from the equation for $d(\cos\theta)/d\tau$ and obtain a first-order equation for the quantity $P = \cos\theta$ in the following form:

$$2\dot{P} = \sigma(1-h^2-P^2). \tag{5}$$

Here and below, a dot denotes a derivative with respect to dimensionless τ. It is clear that the presence of a discrete parameter $\sigma = \pm 1$ in this problem corresponds to

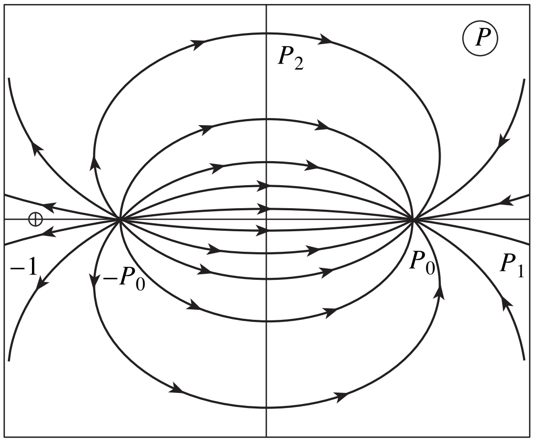

Fig. 1. Phase trajectories of the system of equations (6) with $\sigma = +1$ on the plane of complex variable $P = P_1 + iP_2$. The circle denotes a pole (at the point $P = -1$) of the integrand of (8), which determines the value of the Euclidean action.

the invertibility of the original equations with respect to the imaginary time τ. Obviously, the replacement of σ by $-\sigma$ corresponds to the replacement of τ by $-\tau$, i.e., of an instanton by an anti-instanton; henceforth, we can set $\sigma = 1$.

Taking into account that P in an instanton may be complex, we write $P = P_1 + iP_2$. Separating the real and imaginary parts, we arrive at a system of two real equations:

$$2\dot{P}_1 = 1 - h^2 - P_1^2 + P_2^2, \quad \dot{P}_2 = -P_1 P_2. \tag{6}$$

These equations have two singular points on the phase plane (P_1, P_2), $P_1 = \pm\sqrt{1-h^2}$ and $P_2 = 0$. A simple analysis shows that both these points are degenerate nodes. For $\sigma = +1$ (see above), one has an unstable node at $P_1 = -\sqrt{1-h^2}$ and a stable node at $P_1 = \sqrt{1-h^2}$ (see Fig. 1). Hence, all phase trajectories that emanate from the point $P_1 = -\sqrt{1-h^2}$, $P_2 = 0$ reach the point $P_1 = \sqrt{1-h^2}$, $P_2 = 0$, and Eqs. (5) or (6) describe a continuous one-parameter family of instantons in which $\mathbf{m} \longrightarrow h\mathbf{e}_y - \mathbf{e}_z\sqrt{1-h^2}$ as $\tau \longrightarrow -\infty$ and $\mathbf{m} \longrightarrow h\mathbf{e}_y + \mathbf{e}_z\sqrt{1-h^2}$ as $\tau \longrightarrow +\infty$. Similarly, when $\sigma < 0$, one obtains an analogous family of anti-instantons. The general instanton solution of Eqs. (6) can explicitly be expressed as

$$\begin{aligned} P_1 &= \sqrt{1-h^2}\frac{\sinh\omega\tau}{\cosh\omega\tau + \cos\psi}, \\ P_2 &= \sqrt{1-h^2}\frac{\sin\psi}{\cosh\omega\tau + \cos\psi}, \end{aligned} \tag{7}$$

where $\omega = \sqrt{1-h^2}\,\omega_0$ and the arbitrary real parameter ψ takes values $0 \le \psi \le 2\pi$.

The presence of a continuous family of separatrix trajectories is a usual property of integrable Hamiltonian systems with two degrees of freedom [31]. One should expect that this situation is also realized in our case, i.e., that system (4) with two degrees of freedom is integrable. Below, we will show that all instanton problems in ferromagnets are exactly integrable. Now, we discuss the properties of the family of solutions (7).

For a particular case $\psi = 0$, we have $P_2 = 0$; i.e., $\cos\theta$ is real, while φ is purely imaginary. Such solutions were discussed by Garg in [7]; but he considered only discontinuous solutions, i.e., those that have jumps near equilibrium positions. Among solutions (7), there is a discontinuous solution, which corresponds to $\psi = \pi$.

At first sight, instantons of type (7) with different values of ψ are essentially inequivalent. For example, when $\psi = \pi$, a solution has a singularity. However, it turns out that all such solutions have the same value of the Euclidean action. One can easily verify this fact by applying formula (2) and expressing $\dot{\varphi}$ in terms of θ by the formula $h\exp(i\varphi) = \sin\theta$ obtained above. The latter formula implies that $i\sin\theta d\varphi = \cos\theta d\theta$, and the Euclidean action is represented as the contour integral

$$A_{\mathrm{E}} = \int\limits_{-\sqrt{1-h^2}}^{\sqrt{1-h^2}} \frac{PdP}{1+P} \tag{8}$$

in the complex plane P, i.e., on the plane (P_1, P_2) depicted in Fig. 1 above. Since all the contours that determine the integration path for different $\psi \ne \pi$ do not intersect the real axis and the only pole at the point $P = -1$ does not fall within the domain bounded by the trajectory with $\psi = 0$ and a trajectory with a certain $\psi \ne 0$, π, the value of A_{E} is the same for all these contours,

$$\frac{A_{\mathrm{E}}}{\hbar S} = -2\sqrt{1-h^2} + \ln\frac{1+\sqrt{1-h^2}}{1-\sqrt{1-h^2}}.$$

Analyzing the improper integral, one can easily verify that the special case $\psi = \pi$ leads to the same expression for A_{E}. Hence, there exist an infinite number of instanton paths in this problem that possess different structures but have the same value of the Euclidean action.

To explain this, at first sight strange, result, one should notice that all solutions (7) can actually be rewritten using a complex shift of the argument of a single real solution. Indeed, taking a real solution derived from (7) for $\psi = 0$ and writing $P = \sqrt{1-h^2}\tanh(\omega\tau/2 + i\psi)$, we arrive at (7). A question arises as to whether the possibility of such a proliferation of instanton solutions is a specific property of model (5) or continuous families of instantons that are characteristic of integrable dynamical systems also exist in other models of a ferromagnet.

To answer this question, we express the equation of motion for $P = \cos\theta$ and $Q = \varphi$, without specifying the form of the ferromagnet energy $W(\theta, \varphi)$, as complex Hamilton equations

$$i\dot{P} = -\frac{\partial W}{\partial Q}, \quad i\dot{Q} = \frac{\partial W}{\partial P}. \qquad (9)$$

Let us write $W = H_1 + iH_2$, where H_1 and H_2 are real-valued functions and—assuming that P and Q are complex, $P = P' + iP''$ and $Q = Q' + iQ''$—separate the real and imaginary parts of Eqs. (9). As a result, we obtain a system of four real equations whose right-hand sides contain the derivatives of H_1 and H_2 with respect to the variables P', P'', Q', and Q''. However, if we require that the function W be an analytic function of complex variables P and Q, i.e., that the function W should independently satisfy the Cauchy–Riemann conditions with respect to these variables, then the right-hand sides can be rewritten in terms of the derivatives of H_1 or H_2 alone. As a result, this system of equations becomes a Hamiltonian system. In particular, choosing the pairs of canonical variables as

$$p_1 = P', \quad q_1 = Q'', \quad p_2 = P'', \quad q_2 = Q', \qquad (10)$$

we can rewrite the system as $\dot{p}_i = -\partial H_1/\partial q_i$, $\dot{q}_i = \partial H_1/\partial p_i$, i.e., as a Hamiltonian system with two degrees of freedom, with the Hamilton function $H_1 = H_1(p_1, q_1, p_2, q_2)$ and an additional integral of motion H_2. Again, using solely the Cauchy–Riemann condition for W, one can show that the Poisson bracket for H_1 and H_2, calculated in terms of the canonical variables p_i and q_i, vanishes. Thus, we can conclude that any model of a ferromagnet with energy W that is analytic with respect to $\cos\theta$ and φ in the above sense is reduced to an exactly integrable dynamical system and in fact admits the construction of an infinite system of instanton trajectories.

A concrete procedure for solving this problem can be substantially facilitated when one takes into account the fact that the canonical pairs of variables (10) consist of one real and one imaginary part of the complex variables P and Q. Therefore, one can seek a partial solution in which only one pair of variables, $p_1 = p_1^{(0)}(\tau)$, $q_1 = q_1^{(0)}(\tau)$, is changed, while the other pair is identically zero, $p_2 = 0$, $q_2 = 0$. As we have seen above, this condition corresponds to a solution of the form (7) with $\psi = 0$; in this case, the value of φ is purely imaginary (or $\varphi = 0$). Further, using a complex shift of the argument,

$$P(\tau) = p_1^{(0)}(\tau + i\psi), \quad Q(\tau) = iq_1^{(0)}(\tau + i\psi),$$

we can obtain a general solution with $p_{1,2}, q_{1,2} \neq 0$. Partial solutions in which some of the variables are real and others are either purely imaginary or zero are known to occur in many models of magnets (see, for example, [32]). Below, we will demonstrate the efficiency of this technique as applied to many physically interesting models of a ferromagnet.

One may have the impression that the condition for the analyticity of energy W with respect to both complex variables $P = \cos\theta$ and $Q = \varphi$ is rather stringent. For instance, energy of the form (5) does not satisfy this requirement because it contains $\sin\theta = \sqrt{1-P^2}$ and branching points with respect to the variable P. However, this problem can be resolved by an appropriate choice of the polar axis in a coordinate system. Indeed, the energy of a ferromagnet includes the energy of magnetic anisotropy W_a and the Zeeman energy $W_H = g\mu_B \mathbf{H} \cdot \mathbf{S}$ in an external magnetic field $\mathbf{H}$. Choosing the polar axis along $\mathbf{H}$, we obtain $W_H = -g\mu_B HS\cos\theta = g|\mu_B|HSP$. The anisotropy energy represents a polynomial in even powers of the spin components and, for magnets with symmetry no lower than that of rhombic crystals, contains only the squares of the spin components (except for rhombohedral magnets, whose energy contains an invariant of the form $\sin^3\theta\cos\theta\cos 3\varphi$). Thus, for all magnets with symmetry no lower than that of rhombic crystals, except for rhombohedral magnets, the condition for the analyticity of energy W is fulfilled when the magnetic field is directed along the symmetry axes. We think that this constraint on the choice of a model is not very stringent. Moreover, it seems that the existence of a finite number of branching-point-type singularities does not impede the manifestation of integrability properties, in particular, the existence of degenerate families of instantons and the possibility of constructing them. Below, in Section 4, we verify this fact by a concrete example, where we construct such families of instantons in the case when the direction of a magnetic field is different from a symmetry axis of a crystal. However, since the analysis of this case is rather cumbersome, it is expedient to begin with the simpler case of a rhombic ferromagnet in a magnetic field parallel to a certain symmetry axis; this will be done in the following section.

3. ANALYSIS OF A FERROMAGNETIC MODEL WITH A MAGNETIC FIELD DIRECTED ALONG RHOMBIC ANISOTROPY AXES

Consider instanton solutions for a magnet with rhombic anisotropy assuming that $\tilde{K} = 0$ in (1). We begin with the simple case when the field is directed along one of the symmetry axes and $W(\cos\theta, \varphi)$ is an analytic function of its arguments in the entire domain of their definition. In what follows, it is convenient to assume that the magnetic field is always directed along the same axis, say, along the y axis. Let us introduce a dimensionless parameter $\lambda = K_1/K_2$; the case $\lambda < 1$ corresponds to the situation when the y axis is the hard axis of a ferromagnet and the x axis is an intermediate axis; when $\lambda > 1$, the classification of axes is reversed. Thus, by varying the parameter λ, we can obtain all interesting cases: when $\lambda < 1$, the magnetic field is directed along the hard anisotropy axis, whereas, when $\lambda > 1$, the magnetic field is parallel to an intermediate axis. While constructing instantons and calculating the Euclidean action, it suffices to consider only those values of magnetization for which $W = 0$; therefore, we will omit the coefficient $K_2/2$ in the expression for energy and the parameter $\omega_0 = K_2S/\hbar$ in a solution. Choose a reference point of energy so that $W = 0$ in the ground state. Then, the energy of a ferromagnet in the dimensionless form is expressed as

$$W(\mathbf{m}) = \frac{\lambda}{2}m_x^2 + \frac{1}{2}(m_y - h)^2, \tag{11}$$

where $h = g\mu_B H/K_2S$.

In this model of a ferromagnet, the system of equations for instantons has the form

$$\begin{gathered}\frac{dm_x}{d\tau} = i(m_y - h)m_z, \quad \frac{dm_y}{d\tau} = -i\lambda m_x m_z,\\ \frac{dm_z}{d\tau} = i[(\lambda - 1)m_y + h]m_x,\end{gathered} \tag{12}$$

and instanton solutions are situated on the level surfaces of the integrals

$$\lambda m_x^2 + (m_y - h)^2 = 0 \quad \text{and} \quad m_x^2 + m_y^2 + m_z^2 = 1.$$

Hence, $m_y - h = i\sigma\sqrt{\lambda}\, m_x$, where $\sigma = \pm 1$; i.e., the relation between m_x and m_y in an instanton solution is linear. The system of equations (12) has an exact class of solutions

$$m_x = ix, \quad m_y = y, \quad m_z = z, \tag{13}$$

where x, y, and z are real variables. Then, we obtain the following system of real equations for x, y, and z:

$$\begin{gathered}\frac{dx}{d\tau} = (y - h)z,\\ \frac{dy}{d\tau} = \lambda xz, \quad \frac{dz}{d\tau} = -[(\lambda - 1)y + h]x.\end{gathered} \tag{14}$$

Note that we may not restrict the analysis to real solutions of (14); we can consider the substitutions (13) simply as a change of variables assuming that x, y, and z are complex variables. Actually, one should do so when constructing a general instanton solution that belongs to a one-parameter family. However, as we pointed out in the preceding section, for the simplest case of a uniaxial ferromagnet, it is much more convenient to first construct a certain simple symmetric solution with real x, y, and z and then continue it by an imaginary shift along the independent variable τ. A similar procedure of shifting along τ applies to the case of a rhombic ferromagnet.

The instanton solutions of interest are situated on the level surfaces of the first integrals

$$\lambda x^2 - (y - h)^2 = 0 \quad \text{and} \quad -x^2 + y^2 + z^2 = 1, \tag{15}$$

whereby one obtains a linear relation between the variables x and y, $y - h = \sigma\sqrt{\lambda}\, x$, where $\sigma = \pm 1$, and a simple relation between the variables x and z,

$$(\lambda - 1)\left(x + \frac{\sigma h\sqrt{\lambda}}{\lambda - 1}\right)^2 + z^2 = 1 + \frac{h^2}{\lambda - 1}. \tag{16}$$

This analysis of a real class of solutions clearly shows that the variation of the parameters of the problem gives rise to bifurcations. Equation (16) describes various second-order curves on the plane (x, y): when $\lambda > 1$, one has an ellipse, whereas when $\lambda < 1$, one has a system of hyperbolas that belong to different sectors of the plane (x, y) for small and large fields, $h^2 < 1 - \lambda = h_c^2$ and $1 - \lambda < h^2 < 1$, respectively. In the limit cases when $\lambda = 1$ (a uniaxial ferromagnet) or $h^2 = h_c^2$, Eq. (16) describes a parabola or two intersecting straight lines, respectively. Naturally, all these curves pass through the points that correspond to equilibrium positions, $z = \pm\sqrt{1 - h^2}$, $x = 0$; however, they exhibit essentially different behavior (see below). Taking into account the fact that the ground state is not degenerate for $h^2 > 1$ and tunneling is impossible, we obtain three different domains for instantons. We will show below that instanton solutions possess essentially different properties in these three domains. In particular, the value of h_c coincides with the critical value of the field (which was introduced earlier by Garg [7] and then by the authors of [27, 28]) above which the effects of destructive interference vanish. However, the authors of the cited works obtained this value of h_c from other considerations; namely, they assumed that there are no continuous instanton solutions for $h > h_c$ and that one should introduce either discontinuous instantons [27] or instantons that partially proceed in ordinary real time [28]. It is quite possible that such exotic instanton paths will be useful for certain other tunneling problems. However, we will show that, within the ferromagnetic model (1), taking into account the existence of an infinite family of instantons obtained by a complex shift of the type described above, there exist continuous standard instanton solutions with purely real τ for all domains indicated above. In fact, only the solutions with certain specific values of the complex shift parameter ψ are discontinuous. This fact is most easily illustrated by an example of the case $1 - h^2 < \lambda < 1$, when the magnetic field is small, $h^2 < h_c^2 = 1 - \lambda$, and $\lambda < 1$, i.e., the magnetic field is applied along the hard axis of a magnet.

A Weak Field Parallel to the Hard Axis

It is this case that was considered in detail by Garg [7] and for which oscillations of the transition probability as a function of a field were predicted and experimentally observed [16–26]. The instanton paths used in [7] do not satisfy the assumption that m_y and m_z are real and m_x is purely imaginary. However, we begin with seeking precisely such solutions in order to obtain general solutions by a complex shift of the argument. In particular, we obtain instantons similar to those of [7] in this way. Let us rewrite (16) in the canonical form:

$$-\frac{(x - x_0)^2}{a^2} + \frac{z^2}{b^2} = 1, \tag{17}$$

where

$$x_0 = \frac{\sigma h\sqrt{\lambda}}{1-\lambda}, \quad a^2 = \frac{1}{1-\lambda}\left(1 - \frac{h^2}{1-\lambda}\right),$$
$$b^2 = \frac{1-\lambda-h^2}{1-\lambda}. \tag{18}$$

The branches of the hyperbola described by this equation are the integral curves of the system of equations (14). For real x, y, and z, these curves do not connect points corresponding to different equilibrium positions, i.e., the point $x = 0$, $z = \sqrt{1-h^2}$ with the point $x = 0$, $z = -\sqrt{1-h^2}$, in a finite domain of the plane (x, z). However, there does exist an instanton solution that connects these points. To construct this solution, we introduce a parametrization $x = x_0 + a\sinh\phi$, $z = b\cosh\phi$ and, using the first equation of system (14), obtain the following equation for ϕ:

$$a\frac{d\phi}{d\tau} = \sigma\sqrt{\lambda}(x_0 + a\sinh\phi)b.$$

A solution to this equation can easily be expressed in explicit form:

$$\tanh\frac{\phi}{2} = \sinh\gamma + \cosh\gamma\tanh\left[\frac{1}{2}(\xi + i\psi)\right],$$
$$\xi = \sigma\lambda^{1/2}(1-h^2)^{1/2}(\tau - \tau_0), \tag{19}$$
$$\sinh\gamma = \frac{\sigma(1-\lambda)^{1/2}(1-h^2)^{1/2}}{h\lambda^{1/2}}.$$

In this formula, ψ is an arbitrary complex number; this clearly indicates the possibility of both a complex and a real shift of the argument. Explicit expressions for the spin components in an instanton are rather lengthy; however, after trivial calculations, they can be simplified by shifting the argument by the real quantity γ introduced above. Henceforth, we use the notation $\bar{\xi} = \omega\tau + \gamma + i\psi$ with the characteristic frequency $\omega = \omega_0\lambda^{1/2}(1-h^2)^{1/2} = (S/\hbar)\sqrt{K_1K_2(1-h^2)}$. This yields

$$m_z = \sigma\sqrt{1-h^2}\frac{\cosh\bar{\xi}}{1/\sinh\gamma - \sinh\bar{\xi}},$$
$$m_x = i\frac{1-h^2}{(1-\lambda-h^2)^{1/2}}\frac{1}{1/\sinh\gamma - \sinh\bar{\xi}}, \tag{20}$$
$$m_y = \left[\frac{\sigma\lambda^{1/2}}{(1-\lambda-h^2)^{1/2}} - h\sinh\bar{\xi}\right]\frac{1}{1/\sinh\gamma - \sinh\bar{\xi}}.$$

(From this point on, we omit the bar over ξ, thus admitting arbitrary shifts of the argument, both real and complex.) Then, we immediately obtain, in particular, that a solution has the above-mentioned singularity only for certain specific values of ψ, namely, for $\psi = 0$ and π. For all other values of ψ, a solution has no singularity; more precisely, the singularity moves to the complex plane and does not manifest itself for real values of the imaginary time τ. It is interesting to note that, when the polar axis is chosen along a magnetic field (y axis), the azimuth φ of magnetization, which is purely imaginary in solutions of the form (13),

$$\tan\varphi = \frac{m_x}{m_z} = i\sigma\frac{(1-h^2)^{1/2}}{(1-\lambda-h^2)^{1/2}}\frac{1}{\cosh\xi},$$

becomes real for $\psi = \pi/2$, when $\cosh(\xi + i\pi/2) \longrightarrow i\sinh\xi$. When $\psi = \pi/2$, the angle φ ranges from zero to π through $\pi/2$ as τ varies from ∞ to $-\infty$; in this case, the angle θ, as well as all components of the magnetization, are complex. The structure of the solution for $\psi = \pi/2$ resembles that of the instanton path that was used by Garg in [7]. For all other values of ψ, both θ and φ are complex; moreover, the real part of the angle ψ does not reach $\pi/2$.

Thus, we have arrived at a very complicated structure of instanton paths, with complex values of all spin components or angular variables θ and φ for magnetization. Among the solutions obtained, there are singular ones as well. However, the situation with a physically interesting quantity, the Euclidean action A_E, turns out to be very simple and clear just as in the preceding section. Here as before, the Euclidean action can conveniently be calculated in terms of contour integrals. However, it is more convenient to use the complex variable ξ and choose the direction of a singular ray (the Dirac string) along the negative direction of the axis m_y. The point is that the case involving the integration over a complex plane P for a rhombic ferromagnet is not so clear and simple as the purely uniaxial case considered above because, when $\lambda \neq 1$, branching points arise in the plane P. As a result, the Euclidean action is represented as the integral

$$A_{\mathrm{E}} = \sigma\hbar S\frac{(1-h^2)^{3/2}}{(1+h)(1-\lambda-h^2)^{1/2}}\int\limits_{-\infty}^{\infty} d\xi \frac{\sinh(\xi+i\psi)}{[\sinh(\xi+i\psi)-(\sigma/h\cdot\sinh\gamma)][\sinh(\xi+i\psi)-\sigma/\sinh\gamma]}, \tag{21}$$

where we have restored a complex shift along ξ. This integral can be considered as an integral along a certain contour L in the complex plane $z = \xi$,

$$A_{\mathrm{E}} = \hbar S\int\limits_L dz F(z),$$

$$F(z) = \sigma\frac{(1-h^2)^{3/2}}{(1+h)(1-\lambda-h^2)^{1/2}} \tag{22}$$

$$\times\frac{\sinh z}{[\sinh z-(\sigma/h\cdot\sinh\gamma)][\sinh z-\sigma/\sinh\gamma]},$$

where the contour L represents a straight line in the complex plane that is parallel to the real axis ($\mathrm{Im}z = \psi$) and passes at a distance of ψ from it. Hence, it is clear that one can easily find a difference between the Euclidean actions A_{E} for different values of ψ via a simple integral along a closed contour (see Fig. 2).

Let us fix two values ψ_1 and ψ_2, $\psi_1 < \psi_2$. Consider a contour (rectangle) $ABCD$, where $A = -R + i\psi_1$, $B = R + i\psi_1$, $C = R + i\psi_2$, $D = -R + i\psi_2$, and R is a real number. It is obvious that

$$\int\limits_{BC} F(z)dz \longrightarrow 0 \quad\text{and}\quad \int\limits_{DA} F(z)dz \longrightarrow 0,$$

as $R \longrightarrow \infty$, so that

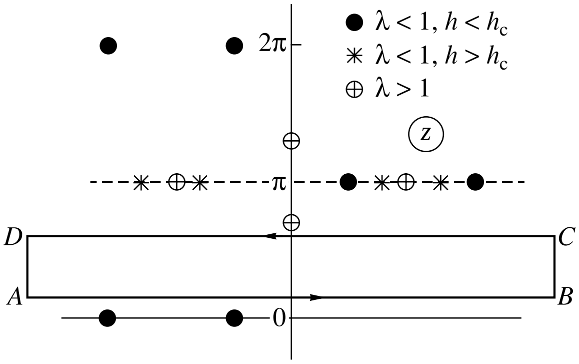

Fig. 2. Complex plane z, integration contour $ABCD$, and the arrangement of poles of the function $F(z)$. Closed circles correspond to the case of a weak field considered in this section; other symbols correspond to other domains of the problem parameters λ and h that are considered below.

$$\lim_{R\to\infty}\int\limits_{AB} F(z)dz - \lim_{R\to\infty}\int\limits_{DC} F(z)dz = \oint\limits_{ABCD} F(z)dz$$

and this limit is determined by the integral along a closed contour that encloses the rectangle $ABCD$. Hence, the difference

$$A_{\mathrm{E}}(\psi_1) - A_{\mathrm{E}}(\psi_2) = \hbar S\oint\limits_{ABCD} F(z)dz$$

between the Euclidean actions for different ψ is expressed in terms of the sum of residues of the function $F(z)$ that fall within this rectangle (the strip $\psi_1 < \psi_2$). Thus, the Euclidean action is independent of ψ in certain intervals of ψ, and the function $A_{\mathrm{E}}(\psi)$ changes stepwise as the contour $ABCD$ crosses a pole as ψ varies. Since the function $F(z)$ is periodic in ψ with period 2π, the function $A_{\mathrm{E}}(\psi)$ is also periodic; therefore, it suffices to consider a variation in $A_{\mathrm{E}}(\psi)$ in a strip of width 2π. It is obvious that this strip contains four poles of the function $F(z)$ and the sum of all these four residues equals zero. Note also that the integral (22) does not change under the substitutions $\psi \longrightarrow \psi + \pi$ and $\sigma \longrightarrow -\sigma$, so that one can restrict the consideration to a certain one sign of σ, say, $\sigma = 1$. This is also valid for other relations between the values of the parameters h and λ of the problem (see below), but the properties of the residues will be different, which results in a variation in the dependence of A_{E} on ψ.

In the case considered here, of a weak field applied along the hard axis, $h^2 < h_c^2 = 1 - \lambda$, $\lambda < 1$, two poles of the function $F(z)$, z_1 and z_2, lie on the real axis at the points $z_1 = \zeta_1$ and $z_2 = \zeta_2$, where ζ_1 and ζ_2 are real solutions of the equations $\sinh\zeta_1 = 1/\sinh\gamma$ and $\sinh\zeta_2 = 1/(h\sinh\gamma)$, while the other two poles lie at the points $z_3 = -\zeta_1 + i\pi$ and $z_4 = -\zeta_2 + i\pi$. The sums of residues at the pairs of points z_1, z_3 and z_2, z_4 are equal to zero, whereas the sums of residues at the pairs of points z_1, z_2 and z_3, z_4 with different values of ζ are real; for example, $\mathrm{Res}[F(z_1)] + \mathrm{Res}[F(z_2)] = 1 - h/\sqrt{1-\lambda}$. Hence, when the parameter ψ passes through the values 0, π, 2π, etc., the Euclidean action $A_{\mathrm{E}}(\psi)$ acquires a purely imaginary term $\pm 2\pi i\hbar S[1 - h/\sqrt{1-\lambda}]$. For a certain concrete value of ψ, one can easily calculate the quantity A_{E} (it is convenient to take $\psi = \pi/2$). Then, taking into account the above-described properties of A_E, we arrive at the expression

$$A_E = \hbar S\left[\ln\frac{\sqrt{1-h^2}+\lambda}{\sqrt{1-h^2}-\lambda} - \frac{h}{\sqrt{1-\lambda}} \times \ln\frac{\sqrt{(1-h^2)(1-\lambda)}+h\sqrt{\lambda}}{\sqrt{(1-h^2)(1-\lambda)}-h\sqrt{\lambda}}\right] + \frac{i\pi\hbar S}{\sqrt{1-\lambda}}\frac{\sin\psi}{|\sin\psi|}(\sqrt{1-\lambda}-h), \quad h^2 < h_c^2 = 1-\lambda. \tag{23}$$

Thus, we have found that, for the case of a weak field directed along the hard axis, the real part of the Euclidean action is independent of ψ, and all instanton trajectories, either regular or singular, real or complex, make identical contributions to the tunneling exponential factor $\exp(-\mathrm{Re}[A_E]/\hbar)$. In this case, the imaginary part of A_E depends only on $\sin\psi/|\sin\psi|$. This means that all trajectories for which the parameter ψ lies in different strips of the same width π behave identically and that interference occurs between instanton trajectories for which the values of ψ lie in these neighboring strips.

Below, we will analyze instanton solutions in two other cases that arise when the external magnetic field is directed along symmetry axes. In the case of a strong field, $1 - \lambda < h^2 < 1$, directed along the hard axis for $\lambda < 1$, as well as when the field is directed along an intermediate axis, i.e., $\lambda > 1$, the integral curves of the system of equations (14) connect points corresponding to different but equivalent equilibrium positions for real x, y, and z. This means that there exist nonsingular instantons with real x, y, and z in these two cases. However, taking into account the complex nature of instantons, one cannot observe any fundamental difference in the structure of general instanton solutions.

Instantons in the Case of a Strong Field Directed along the Hard Axis

Instanton solutions for a strong field $h^2 > 1 - \lambda > 0$ are analyzed in virtually the same way as in the preceding subsection. Just as for a weak field, the integral curves of the system (14) are second-order curves with the parameters defined by formulas of type (18). When $1 - \lambda < h^2 < 1$, one has a hyperbola of the form $(x - x_0)^2/a^2 - z^2/b^2 = 1$, where the expression for x_0 is the same as in the case of a weak field (see (18)) and expressions for a^2 and b^2 differ in sign from those given in (18). To construct an instanton solution that connects equilibrium points, we introduce a parametrization $x = x_0 + a\cosh\phi$, $z = b\sinh\phi$. Then, using the first equation of system (14), we obtain the following equation for ϕ:

$$a\frac{d\phi}{d\tau} = \sigma\sqrt{\lambda}(x_0 + a\cosh\phi)b.$$

Its convenient to seek a solution to this equation in the form

$$\tanh\frac{\phi}{2} = \frac{h\sqrt{\lambda}+\sigma(h^2+\lambda-1)^{1/2}}{((1-h^2)(1-\lambda))^{1/2}}\tanh\left[\frac{1}{2}(\xi + i\psi)\right],$$

where the variable ξ is similar to that used in the case of a weak field (see (19)). Next, we can write explicit expressions for the spin components in the instanton:

$$m_z = \sigma(1-h^2)^{1/2}\frac{(h^2+\lambda-1)^{1/2}\sinh z}{\sigma h\lambda^{1/2}-(h^2+\lambda-1)^{1/2}\cosh z},$$

$$m_x = \frac{i\sigma(1-h^2)}{h\lambda^{1/2}-\sigma(h^2+\lambda-1)^{1/2}\cosh z}, \tag{24}$$

$$m_y = \frac{\lambda^{1/2}-h\sigma(h^2+\lambda-1)^{1/2}\cosh z}{h\lambda^{1/2}-\sigma(h^2+\lambda-1)^{1/2}\cosh z},$$

where $z = \xi + i\psi$. The Euclidean action can easily be represented as an integral of the same type as (21) or (22),

$$A_E = \hbar S\int_L dzF(z),$$

with the only difference that now the function $F(z)$ is defined by

$$F(z) = \frac{(1-h)(1-h^2)^{1/2}(\lambda+h^2-1)^{1/2}\cosh z}{[(\lambda+h^2-1)^{1/2}\cosh z-\sigma\lambda^{1/2}h][(\lambda+h^2-1)^{1/2}\cosh z-\sigma\lambda^{1/2}]}. \tag{25}$$

Instantons for a Field Directed along an Intermediate Axis

Now, consider the final case when the field is directed along an intermediate axis, i.e., when $\lambda > 0$. In this case, the integral curve is the ellipse $(x - x_0)^2/a^2 + z^2/b^2 = 1$ with the same x_0 and with a^2 and b^2 given by $a^2 = (\lambda + h^2 - 1)/(\lambda - 1)^2$ and $b^2 = (\lambda + h^2 - 1)/(\lambda - 1)$. We choose a parametrization of a solution in the form

$x = x_0 + a\cos\phi$, $z = b\sin\phi$, where ϕ is described by the equation

$$a\frac{d\phi}{d\tau} = -\sigma\sqrt{\lambda}(x_0 + a\cos\phi)b.$$

Like the formulas for the spin components, the solution to this equation can easily be expressed in explicit form. However, we will not write out these cumbersome expressions since they can be obtained from formulas (24). To this end, it suffices to note that the constant λ of rhombic anisotropy enters formulas (24) for the spin components, as well as the expression for the Euclidean action in terms of the integral (25), only as $\sqrt{h^2 - 1 + \lambda}$ and $\sqrt{\lambda}$, and the combination $(1 - \lambda)$, whose sign distinguishes these two cases, does not appear under the square-root sign. In this situation, one should expect that the corresponding formulas for the two domains of parameter values will be equivalent. Hence, the expressions for the spin components and for the function $F(z)$ in the case $\lambda > 1$ coincide with (24) and (25), respectively, provided that σ is replaced by $-\sigma$ in the latter formulas. Since such a substitution is equivalent to a complex shift of the argument by $i\pi$, i.e., to the substitution $\psi \longrightarrow \psi + \pi$, both cases can be considered using the same expression for the function $F(z)$, which we choose as

$$F(z) = \frac{(1-h^2)^{3/2}}{(1+h)(1-\lambda-h^2)^{1/2}}$$

$$\times\frac{\cosh z}{[\cosh z + \cosh\beta][\cosh z + h\cosh\beta]}, \qquad (26)$$

where

$$\cosh\beta = \frac{\lambda^{1/2}}{(h^2+\lambda-1)^{1/2}}.$$

Formula (26) is valid both in the case of a strong field directed along the hard axis and in the case of an arbitrary magnitude of a magnetic field directed along an intermediate axis. However, we will see that the behavior of the Euclidean action as a function of ψ in these two cases is essentially different and is also different from the case of a weak field directed along the hard axis, which was considered at the beginning of this section.

Calculation of the Euclidean Action for $h^2 > 1 - \lambda$

The inequality $h^2 > 1 - \lambda$ involves both cases discussed above: a strong field directed along the hard axis and an arbitrary field directed along an intermediate axis. To calculate the Euclidean action, we apply the same method as that used above in the case of a weak field. For a function of the form (26), there are no singular points on the real axis for $\psi = 0$, and the value of the integral is real; it can readily be calculated in an explicit form (see formula (27) below). Next, the values of $A_E(\psi)$ for $\psi \neq 0$ are expressed in terms of the contour integral along the rectangle *ABCD*, and the difference between the values $A_E(\psi)$ and $A_E(0)$ is determined by the sum of residues of the poles that fall within the corresponding strip.

Note that, in both cases of interest, $h^2 > 1 - \lambda$ and $\cosh\beta > 1$; i.e., β is real. Therefore, two of the four poles contained in the strip $0 \le \psi < 2\pi$ lie at the points $z_{1,2} = i\pi \pm \beta$. The sum of residues at these points is equal to zero, and the value of $A_E(\psi)$ is not changed when the contour crosses the line $z = i\pi$. Next, for a strong field applied along the hard axis, $h_c^2 < h^2 < 1$ for $\lambda < 1$, we have $h\cosh\beta > 1$, and the second pair of poles also lies on the same line $z_{3,4} = i\pi \pm \beta'$, where β' is real. For this pair of poles, the sum of residues is also zero. Hence, in the case of a strong field applied along the hard axis, A_E is independent of ψ, $A_E(\psi) = A_E(0)$. Since $A_E(0)$ is real, the imaginary part of the Euclidean action is equal to zero, and there is no interference. The vanishing of interference as the field increases is in agreement with the experiment of [24, 25] (see also the survey [16]) and with the results of calculations performed with the use of discontinuous instanton solutions or test functions [27, 28]. Note that, in our calculations for the case of a strong field, solutions with discontinuities for real τ only exist for $\psi = \pi$; but these solutions are not distinguished among other trajectories of the infinite one-parameter family. Thus, in the case of a strong magnetic field applied along the hard axis, the real part of A_E is independent of ψ,

$$A_E = \hbar S\left[\ln\frac{\lambda + \sqrt{1-h^2}}{\lambda - \sqrt{1-h^2}} - \frac{h}{\sqrt{1-\lambda}}\right.$$

$$\left.\times\ln\frac{h\sqrt{\lambda} + \sqrt{(1-h^2)(1-\lambda)}}{h\sqrt{\lambda} - \sqrt{(1-h^2)(1-\lambda)}}\right], \qquad (27)$$

$$0 < 1 - \lambda = h_c^2 < h^2,$$

and all instanton trajectories with parameter ψ in the strip $0 \le \psi < 2\pi$ make equal contributions to A_E.

In the case of a field directed parallel to an intermediate axis, the two poles of the function $F(z)$, z_1 and z_2, again lie on the axis $\mathrm{Im}(z) = \pi$ at the points $z_{1,2} = i\pi \pm \beta$. However, in the case of $\lambda > 1$, we have $h\cosh\beta < 1$, and the two other poles move away from the line $\mathrm{Im}(z) = \pi$; they are situated at the points $z_3 = i(\pi - b)$ and

$z_4 = i(\pi + b)$, where b is a real solution to the equation $\cos b = h\cosh\beta < 1$. The values of the residues at these points are purely imaginary; they have equal absolute values but opposite signs: $\mathrm{Res}[F(z_3)] = -ih/\sqrt{\lambda - 1}$ and $\mathrm{Res}[F(z_4)] = +ih/\sqrt{\lambda - 1}$. Thus, just as in the case of a weak field, the Euclidean action $A_\mathrm{E}(\psi)$ depends on ψ. It changes stepwise when the contour *ABCD* passes through a pole under the variation of ψ. However, when $\lambda > 1$, the jump $\Delta A_\mathrm{E}(\psi)$ of the function is real and occurs at $\psi = \pi - b$ and $\psi = \pi + b$, i.e., at values of ψ that depend on the parameters of the problem. Thus, in the strip $0 \le \psi \le \pi - b$, the Euclidean action is independent of ψ and attains its minimal value $A_\mathrm{E}^{(\min)}$,

$$A_\mathrm{E}^{(\min)} = \hbar S\left[\ln\frac{\lambda + \sqrt{1-h^2}}{\lambda - \sqrt{1-h^2}} - \frac{4h}{\sqrt{\lambda - 1}} \times \arctan\frac{\sqrt{(1-h^2)(1-\lambda)}}{h\sqrt{\lambda} + \sqrt{h^2 + \lambda - 1}}\right], \tag{28}$$

at $\psi = \pi - b$, it increases stepwise to the value

$$A_\mathrm{E}^{(\max)} = A_\mathrm{E}^{(\min)} + 2\pi\hbar Sh/\sqrt{1-\lambda},$$

and remains equal to this value in the entire strip $\pi - b \le \psi \le \pi + b$; at $\psi = \pi + b$, the Euclidean action returns stepwise to the value $A_\mathrm{E}^{(\min)}$ and remains equal to this value as ψ increases further up to 2π, i.e., in the strip $\pi + \beta \le \psi \le 2\pi$. In the spirit of the instanton approach, we have to take into account only paths with the minimal value of the Euclidean action. Hence, such behavior of $A_\mathrm{E}(\psi)$ under the variation of a field results in a continuous variation in the relative weight of instanton paths that guarantees the minimal value of the exponential factor $\exp(-\mathrm{Re}[A_\mathrm{E}]/\hbar)$ and make a contribution to the tunneling. The relative width $(\pi - \beta)/\pi$ of this interval tends to 1/2 as $h \longrightarrow 0$ and attains its maximal value of unity when $h \longrightarrow 1$. The emergence of an additional coefficient, associated with this factor, in the expression for the probability of tunneling transition is a remarkable result of the structure of instanton paths. This structure, namely, the presence of one-parameter families of instanton trajectories instead of a finite number of instantons in the standard theory, is indicated by the present authors for the first time. We will discuss this question in greater detail in the final section of the paper.

4. INSTANTON SOLUTIONS UNDER AN ARBITRARY ORIENTATION OF A FIELD IN THE BASE PLANE

In [24, 25], the tunnel splitting of levels was measured both under the variation of the magnitude of the external magnetic field and under the rotation of the field in the base plane of a magnet. Therefore, the analysis of the case with an arbitrary orientation of the field in the plane (x, y) perpendicular to the easy axis of a magnet is important for the interpretation of experimental data. However, this case has not been studied by theoreticians. To our knowledge, [33] is the only work in which the analysis of instantons was carried out on the basis of an approximate reduction of the Lagrangian to the problem on the dynamics of a particle with a certain effective mass; however, this technique is certainly inapplicable to the most interesting case of $\lambda \sim 1$. Below, we will show that the method developed in this paper allows the construction of exact instanton solutions in this complicated case too.

In the case of an arbitrary orientation of a field, the condition that energy is equal to its minimal value yields the relation $\lambda(m_x - h_x/\lambda)^2 + (m_y - h_y)^2 = 0$. Therefore, there is a linear relation between m_x and m_y on the instanton solution as well; in complex terms (13), we have

$$y = \sigma x\sqrt{\lambda} + h_y - ih_x\sigma/\sqrt{\lambda};$$

however, all magnetization components are now complex. But this fact does not prevent us from choosing a parametrization in terms of ϕ of the same type as before, writing an equation for ϕ, and solving it. As a result, we obtain rather cumbersome formulas for the function $\phi = \phi(\tau)$ in the solution and a few less cumbersome expressions for the magnetization components,

$$\begin{aligned} m_x &= \frac{(h_x/\lambda)(H_1^2 + \lambda - 1)^{1/2}\cosh z - i\sigma(1 - h_y H_1)}{\sigma H_2\lambda^{1/2} + (H_1^2 + \lambda - 1)^{1/2}\cosh z}, \\ m_y &= \frac{h_y(H_1^2 + \lambda - 1)^{1/2}\cosh z + \sigma\lambda^{1/2}(1 - i\sigma h_x H_1/\lambda^{3/2})}{\sigma H_2\lambda^{1/2} + (H_1^2 + \lambda - 1)^{1/2}\cosh z}, \\ m_z &= \sigma(1 - H_0^2)^{1/2}\frac{(H_1^2 + \lambda - 1)^{1/2}\sinh z}{\sigma H_2\lambda^{1/2} + (H_1^2 + \lambda - 1)^{1/2}\cosh z}. \end{aligned} \tag{29}$$

Here,

$$H_1 = h_y - ih_x\sigma/\lambda^{1/2}, \quad H_2 = h_y - ih_x\sigma/\lambda^{3/2},$$

$$H_0 = (h_y^2 + h_x^2/\lambda^2)^{1/2},$$

and $z = \xi + i\psi$ as before; the last equation allows us to take into account a complex shift of the variable τ in the solution.

The value $H_0 = 1$ corresponds to the main bifurcation in the problem. The effects of degeneracy of the classical ground state, tunneling, and instantons manifest themselves only for $H_0 < 1$. The symmetry of this solution is lower than that in the case of a symmetric orientation of a field considered above; therefore, the expression for the Euclidean action with a standard choice of the Dirac string **n** along the hard axis turns out to be rather cumbersome. However, choosing **n** to be antiparallel to the magnetic field normalized by a local value of the anisotropy filed, i.e., in the form $\mathbf{n} = (\mathbf{e}_x h_x/\lambda + \mathbf{e}_y h_y)/H_0$, one can significantly simplify this expression and represent the Euclidean action as

$$A_\mathrm{E} = \hbar S\int_L dz F(z),$$

$$F(z) = \frac{H_1(1-H_0^2)^{3/2}}{H_0(1+H_0)(\lambda-1+H_1^2)^{1/2}} \times \frac{\cosh z}{[\cosh z + R][\cosh z + H_0 R]}, \tag{30}$$

where

$$R = \frac{\sigma\lambda^{1/2}}{H_0(\lambda-1+H_1^2)^{1/2}}H_2.$$

As before, this integral is taken along the contour L, i.e., along a straight line z on the complex plane, that is parallel to the real axis. This fact allows us to take into account a complex shift along the argument ξ in the instanton solution. Next, we can calculate A_E for a certain value of ψ (it is convenient to take $\psi = 0$) and determine the difference between the values of A_E for different ψ. The function $A_\mathrm{E} = A_\mathrm{E}(\psi)$ is determined by the position of the poles of the integrand (30), which are situated at the points

$$z_1 = 2i\pi k + i\pi \pm \zeta_1, \quad z_2 = 2i\pi k + i\pi \pm \zeta_2,$$

where ζ_1 and ζ_2 are the roots of the equations $\cosh\zeta_1 = R$ and $\cosh\zeta_2 = H_0 R$, respectively, where k is integer. The analysis is significantly simplified if we take into account the fact that, for our choice of the Dirac string, the residues of the function $F(z)$ at appropriate poles are given by simple expressions. The residues at points of the type z_1 do not depend on the parameters of the problem and are equal to ±1, while the residues at points of the type z_2 are equal to $\mp H_1/\sqrt{1-\lambda}$. Here, the pairs of poles corresponding to the signs ± at ζ_1 or ζ_2 are characterized by opposite signs of the residues.

To investigate the effect of the field rotation in the plane (x, y), we represent its components as

$$h_y = h\cos\chi, \quad h_x = h\sin\chi.$$

For definiteness, assume that $\lambda < 1$ and that the angle $\chi = 0$ corresponds to the field orientation along the hard axis of a particle. Since $\zeta_{1,2}$ are complex, the positions of poles could not be found analytically; the corresponding numerical data are given in Fig. 3. As expected, the poles exhibit essentially different behavior in a weak ($h < h_\mathrm{c} = \sqrt{1-\lambda}$) and a strong ($h_\mathrm{c} < h < 1$) field under the rotation of the field.

We begin with the most interesting case of a weak field (see Fig. 3a). In this case, for $\chi = 0$, the poles lie on the lines $\mathrm{Im}z = \pi/2$ and $\mathrm{Im}z = 3\pi/2$ symmetrically with respect to the point $z = i\pi$. (Note that the picture here differs from that presented in Fig. 2 in the preceding section because of the different choice of the reference point for ψ.) As χ increases, the poles move toward each other, so that, as $\chi \longrightarrow \pi/2$, the points of type z_1 with the residues $\mathrm{Res}[F(z_1)] = \pm 1$ lie on the axis $\mathrm{Im}z = \pi$, while the points of type z_2 with the residues equal to $\pm H_1/h_\mathrm{c}$ lie on the imaginary axis $\mathrm{Res} = 0$. Expressing the positions of poles in the strip $0 \le \mathrm{Im}z < 2\pi$ as

$$z_1 = i\pi \pm [A_1(\chi) + iB_1(\chi)],$$
$$z_2 = i\pi \pm [A_2(\chi) + iB_2(\chi)],$$

where $A_{1,2}$ and $B_{1,2}$ are positive real numbers, we can easily verify that $B_1(\chi) < B_2(\chi)$ for any $0 \le \chi < \pi/2$. Therefore, the function $A_\mathrm{E}(\psi)$ and a classification of contributions of paths with different ψ turn out to be as follows.

When the reference point for ψ is chosen as at the beginning of this section, the minimal value of the real part of A_E, equal to $A_\mathrm{E}^{(\min)}$, is attained at $\psi = 0, 2\pi$. This value remains minimal for ψ in the two strips $0 < \psi < \pi - B_2$ and $\pi + B_2 < \psi < 2\pi$. The boundaries of these strips are determined by the condition that the integration path passes through poles of the type z_2. Since the residue at the point z_2 equals $\pm H_1/(1-\lambda)^{1/2}$, the value of A_E increases stepwise by $2\pi i\hbar S H_1/(1-\lambda)^{1/2}$ when the integration path passes through these poles. Note that, in this case, the real part of A_E increases stepwise by $2\pi h_x\hbar S/h_c$, and, for appreciable values of h_x, the contribution of this strip should be neglected. This value of A_E is preserved in the two strips $\pi - B_2 < \psi < \pi - B_1$ and $\pi + B_1 < \psi < \pi + B_2$. When the trajectory enters into the central part of the domain $(0, 2\pi)$, i.e., into the strip $\pi - B_1 < \psi < \pi + B_1$, the value of A_E again varies stepwise, but now by a purely imaginary value of $2\pi i\hbar S$.

Thus, the contribution of instanton paths to the tunneling amplitude is determined by the following principles. The paths with the minimal value of $\mathrm{Re}A_E$ contribute with a relative weight of $1 - B_2/\pi$. The remaining paths, whose relative weight is $B_2/\pi \le 1/2$, make a contribution with the exponentially small coefficient $\exp(-\Delta A_E/\hbar)$, $\Delta A_E = 2\pi h_x S\hbar/h_c$, as well as with various phase coefficients. In the spirit of the instanton approach, we should take into account only the paths with the minimal value of A_E, except, maybe, the case $\Delta A_E/\hbar \le 1$. In our case, this inequality is satisfied only for extremely small angles of deviation from the hard axis, $h_x \le h_c/2\pi S$. For $h \ge 0.5h_c$, this fact corresponds to $\chi \le 1/\pi S$, which amounts to several degrees for $S \approx 10$. For smaller fields, the critical value of the angle increases. This fact corresponds to the experimentally observed tunneling pattern in which the tunnel splitting exhibits nonmonotonic behavior only for small χ; moreover, even for small but nonzero angles, the oscillations are smoothed out as the field increases.

In the most interesting case of small $h_x \ll h_y$, one can carry out a quite comprehensive analysis of the problem. In this case, the values of B_1 and B_2 are close to $\pi/2$,

$$\begin{aligned} B_1 &= \frac{\pi}{2} - h_x\frac{1-\lambda}{\lambda h_y(1-\lambda-h_y^2)}(1-h_y^2)^{1/2}, \\ B_2 &= \frac{\pi}{2} - h_x\frac{(1-\lambda)^{1/2}}{\lambda(1-\lambda-h_y^2)}(1-h_y^2)^{1/2}. \end{aligned} \tag{31}$$

The difference $B_1 - B_2$ is small, and, in the first approximation in h_x, the contribution of strips of the type $\pi \pm B_2 < \psi < \pi \pm B_1$, whose width is proportional to h_x, i.e., containing an additional power of a small parameter, can be neglected. Then, the tunnel splitting Δ of levels versus the angle χ (recall that Δ is proportional to the sum of tunneling exponential factors over all paths),

$$\Delta \propto \left|\sum_\psi \exp\left(-\frac{A_E}{\hbar}\right)\right|,$$

is described by the approximate expression

$$\left|\sum_\psi e^{-A_E/\hbar}\right| \approx \frac{1}{2}\exp\left(-\frac{A_E^{(\min)}}{\hbar}\right)$$

$$\times\left|1 + \exp\left[-\frac{2\pi h_x S}{\sqrt{1-\lambda}} + 2\pi i S\left(1 - \frac{h_y}{\sqrt{1-\lambda}}\right)\right]\right|.$$

For $h_x = h\sin\chi = 0$, this expression gives the earlier obtained result

$$\Delta \approx \exp\left(-\frac{A_E^{(\min)}}{\hbar}\right)\left|\cos\left[\pi S\left(1 - \frac{h_y}{\sqrt{1-\lambda}}\right)\right]\right|.$$

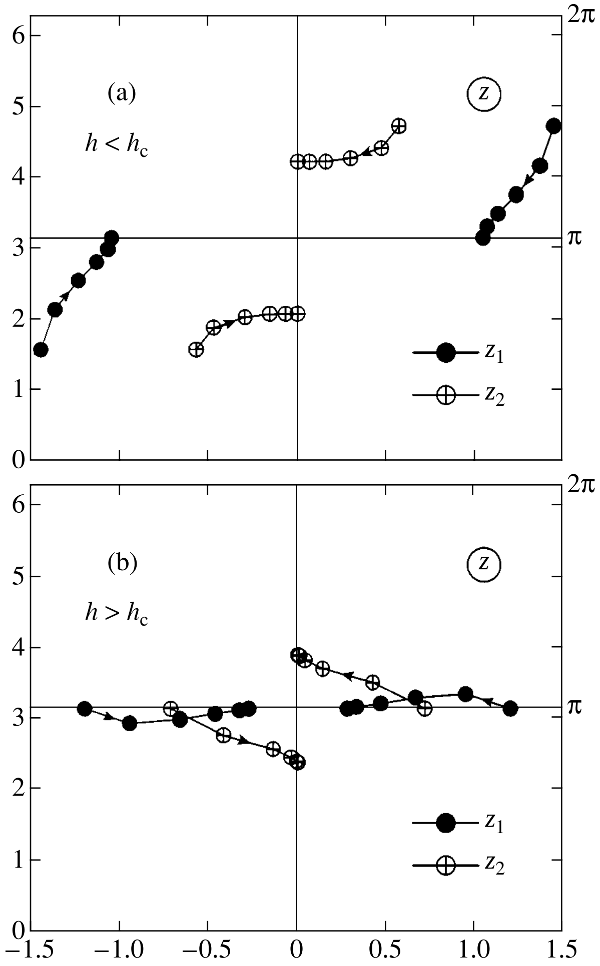

Fig. 3. The dynamics of the poles of the function $F(z)$ under the rotation of a magnetic field in the basal plane for various values of its magnitude $|\mathbf{h}| = h$. The dots indicate successive positions of poles as the angle χ between the field direction and the axis y increases from $\chi = 0$ to $\chi = \pi/2$; to improve clarity, the indicated positions of points correspond to the values of χ that differ by $\pi/10$. The arrows show the direction of motion as χ increases starting from $\chi = 0$. For specific numerical calculations, the following values of the parameters are chosen: $\lambda = 0.73$, which approximately corresponds to Fe_8, (a) $h/h_c = 0.6$, and (b) $h/h_c = 1.35$.

For small but nonzero $h_x \neq 0$, incomplete destructive interference occurs when the tunnel splitting is proportional to

$$\left|\sum_{\psi} e^{-A_{\mathrm{E}}/\hbar}\right| \approx \exp\left(-\frac{A_{\mathrm{E}}^{(\min)}}{\hbar}\right)$$
$$\times\left(\frac{1}{4}\left(1-\exp\left(-\frac{2\pi h_x S}{h_{\mathrm{c}}}\right)\right)^2+\exp\left(-\frac{2\pi h_x S}{h_{\mathrm{c}}}\right)\right. \qquad (32)$$
$$\left.\times\cos^2\left[\pi S\left(1-\frac{h_y}{h_{\mathrm{c}}}\right)\right]\right)^{1/2}.$$

When $h_x \neq 0$, this expression does not vanish for any value of h_y.

In the case of a strong field, $h > h_{\mathrm{c}}$, the arrangement of poles is different (see Fig. 3b). When $\mathbf{h} \parallel \mathbf{e}_y$, i.e., $\chi = 0$, all poles lie on the line $\mathrm{Im}z = \pi$ In this case, they do not contribute to the function $A_{\mathrm{E}}(\psi)$ (see the previous section). When the direction of the field deviates from the hard axis, the poles move away from this line and two strips with different values of A_{E} are formed near the line $\mathrm{Re}s = \pi$. Again, as ψ deviates from the value $\psi = 0$, a pole of type z_2 is the first one traversed by ψ, and the real part of the Euclidean action increases stepwise. However, when $h > h_{\mathrm{c}}$, there is an essential difference from the case of a weak field: for small h_x, when it is expedient to consider the contribution of paths with large values of $\mathrm{Re}A_{\mathrm{E}}$, the width of an appropriate strip is small and proportional to h_x. Accordingly, the relative weight of a trajectory with a different value of the phase factor, which could contribute to interference, is small. When h_x are not small, the contribution of such paths is suppressed by the exponential factor $\exp(-\Delta A_{\mathrm{E}}/\hbar)$. Therefore, when $h > h_{\mathrm{c}}$, there are no effects of partial interference for any orientation of the field, which agrees with the experiment of [16].

5. DISCUSSION OF THE RESULTS AND CONCLUDING REMARKS

We have considered two problems, a general and a specific one. Specifically, we have given a full description of quantum tunneling between levels corresponding to the ground state of a Fe_8-type high-spin molecule (which are degenerate in the classical case) with rhombic anisotropy in a magnetic field directed arbitrarily in the plane perpendicular to the easy axis of the molecule. As far as we are concerned, we are the first to construct exact instanton solutions for this model for arbitrary values and orientations of the magnetic field. To our knowledge, the results obtained describe all basic features of the experimental behavior of tunnel splitting Δ of levels as a function of the magnitude and orientation of a magnetic field. In the case of a magnetic field parallel to the hard axis, our analysis yields either (1) the interference pattern, predicted by Garg [7], with a nonmonotonic variation of the splitting Δ of levels and the vanishing of Δ at certain values of weak field $H < H_{\mathrm{c}} = S\sqrt{K_2(K_2-K_1)}/g\mu_{\mathrm{B}}$, or (2) the absence of interference and a monotonic increase of $\Delta(H)$ in the entire domain of admissible values of the field $H_{\mathrm{c}} < H < KS/g\mu_{\mathrm{B}}$. To our knowledge, the results of our calculations made it possible to describe, for the first time, partial interference on the basis of exact instanton solutions, i.e., to describe the nonmonotonic behavior of $\Delta(H)$ without vanishing of Δ for a small deviation of the field from the hard axis by an angle of $\chi < \chi_{\mathrm{c}} \approx 1/\pi S$ and a monotonic behavior of $\Delta(H)$ for all other orientations of the field.

Such a full description of this specific problem has become possible owing to analysis of the general problem concerning the structure of instanton paths in ferromagnets. We could reduce the problem of searching for instanton paths for a wide class of ferromagnetic models to an exactly integrable problem of Hamiltonian dynamics. We have established that, for nearly all physically meaningful ferromagnetic models, instanton paths form a system of continuous one-parameter families. Each instanton belonging to a certain family is characterized by its own function $\mathbf{m}(\tau)$, but the value of the Euclidean action A_{E} is the same for all instantons in this family. We have established that all instanton paths are characterized by a single real parameter ψ that varies in the interval $0 \leq \psi < 2\pi$, while the Euclidean action is a periodic, with period 2π, stepwise function of ψ. This picture is fundamentally different from that usually described in the literature, which involves a finite number of instanton paths.

Depending on the situation, our scheme may give different results: those that can, in principle, be reduced to a standard scenario where certain families of instantons with the same A_{E} can be represented by a single path, and those that cannot by described by such a simplified scheme. Examples of such a “reducible” problem are given by the model of a purely uniaxial ferromagnet, considered in Section 2, in which all instanton paths with $0 \leq \psi < 2\pi$ have the same value of A_{E}, or by a more complicated model with rhombic anisotropy and a field exactly parallel to the hard axis. In the latter case, two families of instantons with equal real parts of A_{E} but different imaginary parts of A_{E} correspond to two strips with the same width $\Delta\psi = \pi$. In this case, each family of paths can be represented by a single equivalent instanton. However, a full description of the experimental results requires the use of “irreducible” problems. A clear example of such problems is obtained from the analysis of the effect of deviation of a magnetic field from the hard axis. In this case, both for $H < H_{\mathrm{c}}$ and $H > H_{\mathrm{c}}$, there exist instanton solutions with slightly different values of $\mathrm{Re}A_{\mathrm{E}}$, such that $A_{\mathrm{E}}^{(2)} - A_{\mathrm{E}}^{(1)} = \Delta A_{\mathrm{E}} \ll A_{\mathrm{E}}^{(1,2)}$, and significantly different imaginary parts of A_E. If the problem consisted only in the existence of two different instantons, it would be difficult to account for the different behavior of the system in these two cases. The result, namely, the fact that the splitting of levels is significantly different for $H < H_c$ and $H > H_c$, is associated precisely with the concept of continuous families of instantons that exist in the intervals $\Delta\psi$. In the specific case $H < H_c$, the characteristic intervals $\Delta\psi_{1,2}$ for instantons with $A_E^{(1)}$ and $A_E^{(2)}$ are on the same order of magnitude, which results in partial interference of type (32), whereas, for $H > H_c$, the width of one of the intervals is small, and no interference occurs.

Here, it is relevant to note that the picture of instanton families that depend on a continuous parameter admits a realization of more general tunneling scenarios that do not occur in the simple model (1) with $\tilde{K} = 0$ considered here, i.e., in a model in which the anisotropy energy is quadratic in the spin components. Suppose that, in a certain model of a ferromagnet, there are two instanton families that have different imaginary parts but the same real parts of A_E and are realized in different intervals $\Delta\psi$. Then, one can obtain a different form of partial interference, without exponential suppression. Another interesting scenario could occur if, for a certain value of the external parameter, the interval width for instantons with the minimal value of A_E would tend to zero. Then, in the neighborhood of this value of the parameter, the tunneling would be determined by paths with nonminimal A_E. This, as well as many other possibilities, cannot be excluded a priori. However, the analysis of more complicated ferromagnetic models, including model (1) with $\tilde{K} \neq 0$, falls outside the scope of this paper. There are no fundamental difficulties here: the function $W(\cos\theta, \varphi)$ in model (1) with $\tilde{K} \neq 0$ is analytic; however, the analysis of this model requires the solution of complicated algebraic equations, which can only be done numerically.

As was pointed out above, the presence of instanton families is associated with the admissibility of complex values for magnetization **m** (or for angular variables θ and φ) in an instanton and can be described by a complex shift of the reference point of imaginary time in the instanton solution, $\mathbf{m}(\tau) \longrightarrow \mathbf{m}(\tau + i\psi)$. These properties are closely related to the analyticity of the classical energy of a ferromagnet with respect to the variables $\cos\theta$ and φ. Many authors pointed out that it is necessary to take into account complex values of magnetization. In the clearest form, this property of instantons was formulated in the works [34], which are devoted to the analysis of the mathematical nature of integrals along instanton paths in ferromagnets. However, the authors of these works used a parametrization of magnetization in terms of a complex stereographic projection, $w = (m_x + im_y)/(1 + m_z)$. Under such a parametrization, the energy of a ferromagnet contains nonanalytic multipliers of the type $|w|^2$ for which the Cauchy–Riemann conditions are violated on the entire complex plane w rather than at certain specific singular points. Therefore, the integrability of the problem in these variables, as well as the possibility of using a complex shift of the argument for obtaining solutions with the same value of A_E, is not obvious a priori.

ACKNOWLEDGMENTS

This work is dedicated to the blessed memory of V.M. Eleonskiĭ. We thank E.G. Galkina for assistance in work. We are grateful to V.G. Bar'yakhtar, A.B. Borisov, V.E. Kireev, V.V. Kiselev, A.S. Kovalev, A.K. Kolezhuk, L.M. Lerman, and A.F. Popkov for useful discussions.

This work was supported by the Russian Foundation for Basic Research, project no. 03-01-00100.

REFERENCES

1. *Quantum Tunneling of Magnetization*, Ed. by L. Gunter and B. Barbara (Kluwer Academic, Dordrecht, 1995), NATO ASI Ser., Ser. E, Vol. 301.
2. E. M. Chudnovsky and J. Tejada, *Macroscopic Quantum Tunneling of the Magnetic Moment* (Cambridge Univ. Press, Cambridge, 1998).
3. L. N. Leuenberger and D. Loss, Nature **410**, 789 (2001).
4. W. Wernsdorfer, N. Aliaga-Alcalde, D. N. Hendrickson, and G. Christou, Nature **416**, 406 (2002).
5. D. Loss, D. P. DiVincenzo, and G. Grinstein, Phys. Rev. Lett. **69**, 3232 (1992).
6. J. von Delft and C. L. Henley, Phys. Rev. Lett. **69**, 3236 (1992).
7. A. Garg, Europhys. Lett. **22**, 205 (1993).
8. M. Enz and R. Schilling, J. Phys. C **19**, L711 (1986).
9. J. L. van Hemmen and A. Sütö, Physica B (Amsterdam) **141**, 37 (1986).
10. E. M. Chudnovsky and L. Gunther, Phys. Rev. Lett. **60**, 661 (1988).
11. B. Barbara and E. M. Chudnovsky, Phys. Lett. A **145**, 205 (1990).
12. I. V. Krive and O. B. Zaslavskii, J. Phys.: Condens. Matter **2**, 9457 (1990).
13. V. Y. Golyshev and A. F. Popkov, Europhys. Lett. **29**, 327 (1995).
14. E. M. Chudnovsky, J. Magn. Magn. Mater. **140–144**, 1821 (1995).
15. D. D. Awschalom, J. F. Smyth, G. Grinstein, *et al.*, Phys. Rev. Lett. **68**, 3092 (1992).
16. W. Wernsdorfer, Adv. Chem. Phys. **118**, 99 (2001).
17. S. M. J. Aubin, N. R. Dilley, M. B. Wemple, *et al.*, J. Am. Chem. Soc. **120**, 839 (1998).
18. G. Christou, D. Gatteschi, D. N. Hendrickson, and R. Sessoli, MRS Bull. **25**, 66 (2000).
19. R. S. Edvards, S. Hill, S. Bhaduri, *et al.*, Polyhedron **22**, 1911 (2003).

20. J. R. Friedman, M. P. Sarachik, J. Tejada, and R. Ziolo, Phys. Rev. Lett. **76**, 3830 (1996).
21. L. Thomas, F. Lionti, R. Ballou, *et al.*, Nature **383**, 145 (1996).
22. C. Sangregorio, T. Ohm, C. Paulsen, *et al.*, Phys. Rev. Lett. **78**, 4645 (1997).
23. S. M. J. Aubin, N. R. Dilley, M. W. Wemple, *et al.*, J. Am. Chem. Soc. **120**, 839 (1998).
24. W. Wernsdorfer and R. Sessoli, Science **284**, 133 (1999).
25. W. Wernsdorfer, M. Soler, G. Christou, and D. N. Hendrickson, J. Appl. Phys. **91**, 7164 (2002).
26. W. Wernsdorfer, S. Bhaduri, C. Boskovic, *et al.*, Phys. Rev. B **65**, 180403(R) (2002).
27. E. Kececioglu and A. Garg, Phys. Rev. Lett. **88**, 237205 (2002); Phys. Rev. B **67**, 054406 (2003).
28. E. M. Chudnovsky and X. Martines Hidalgo, Europhys. Lett. **50**, 395 (2000).
29. A. I. Wainshtein, V. I. Zakharov, V. A. Novikov, and M. A. Shifman, Usp. Fiz. Nauk **136**, 553 (1982) [Sov. Phys. Usp. **25**, 195 (1982)].
30. E. Fradkin, *Field Theories of Condensed Matter Systems* (Addison-Wesley, Redwood City, CA, 1991), Frontiers in Physics, Vol. 82.
31. V. M. Eleonskiĭ and N. E. Kulagin, Zh. Éksp. Teor. Fiz. **84**, 616 (1983) [Sov. Phys. JETP **57**, 356 (1983)]; **93**, 1436 (1987) [Sov. Phys. JETP **66**, 819 (1987)]; V. M. Eleonskiĭ, N. N. Kirova, and N. E. Kulagin, Zh. Éksp. Teor. Fiz. **77**, 409 (1979) [Sov. Phys. JETP **50**, 209 (1979)].
32. B. A. Ivanov and V. E. Kireev, Zh. Éksp. Teor. Fiz. **121**, 320 (2002) [JETP **94**, 270 (2002)].
33. R. Lu, J. L. Zhu, Y. Zhou, and B. L. Gu, Phys. Rev. B **62**, 11661 (2000).
34. E. A. Kochetov, J. Phys. A: Math. Gen. **31**, 4473 (1998); M. Stone, K.-S. Park, and A. Garg, J. Math. Phys. **41**, 8025 (2000); A. Garg, E. A. Kochetov, K.-S. Park, and M. Stone, J. Math. Phys. **44**, 48 (2003).

Translated by I. Nikitin